Mixed Matrix Membranes of Polybenzimidazoles as Proton and Anion Exchange Membranes

A Thesis Submitted for the degree of

DOCTOR OF PHILOSOPHY

By

Anupam Das

School of Chemistry
University of Hyderabad
Hyderabad-500 046
INDIA
March 2023

Dedicated to Thesis Supervisor,

All my teachers,

my parents and family members

UNIVERSITY OF HYDERABAD
Central University (P.O.), Hyderabad-500046, INDIA

DECLARATION

I hereby declare that the matter embodied in the thesis entitled ***“Mixed Matrix Membranes of Polybenzimidazoles as Proton and Anion Exchange Membranes”*** is the combined results of investigation carried out by me in the School of Chemistry, University of Hyderabad, Hyderabad-500,046, India, under the supervision of Prof. Tushar Jana. The thesis has not been submitted elsewhere for the award of any degree or diploma or membership etc.

In keeping with the general practice of reporting scientific investigations, due acknowledgements have been made wherever the work described is based on the findings of other investigations. Any omission or error that might have persist here is regretted.

Anupam Das.

March 2023

Anupam Das
16CHPH37

UNIVERSITY OF HYDERABAD
Central University (P.O.), Hyderabad-500046, INDIA

Professor Tushar Jana
School of Chemistry

Web: http://chemistry.uohyd.ac.in/~tj

Tel: 91-40-23134808 (Office)
91-9440127016 (Mobile)
Fax: 91-40-23012460
E-mail: tusharjana@uohyd.ac.in
tjscuoh@gmail.com

CERTIFICATE

This is to certify that the thesis entitled "***Mixed Matrix Membranes of Polybenzimidazoles as Proton and Anion Exchange Membranes***" submitted by **Anupam Das** bearing registration number **16CHPH37** in partial fulfilment of the requirements for award of Doctor of Philosophy in the School of Chemistry is a bonafide work carried out by him under my supervision and guidance. This thesis is free from plagiarism and has not been submitted previously in part or in full to this or any other University or Institution for award of any degree or diploma. Further the student has three publications before submission of the thesis for adjudication and has produced evidences for the same in the form of reprints.

Parts of this thesis have been published in the following publications:

1. Mukhopadhyay, S.;† , **Das, A.;**† , Jana, T.; Das, S. K. *ACS Appl. Energy Mater.* **2020**, *3*, 7964–7977. **[†] Co-First Authors. (Chapter 3)**
2. **Das, A.;** Mukherjee. N.; Jana, T. *ACS Appl. Nano. Mater.* **2023**, **[Article in Press]**. ***(Chapter 5)***
3. **Das, A.;** Sana, B.; Bhattacharyya, R.; Ghosh, P. C.; Jana, T. *ACS Appl. Polym. Mater.* **2022**, *4*, 1523−1534. **(Chapter 6)**

He has also made presentation in the following Conferences:

- **ORAL presentation** in the ChemFest-2021, (University of Hyderabad).
- **ORAL presentation** in the 13th International Conference on Advance Polymeric Materials (APM-2022).
- **Presented POSTER** in 16th International conference on Polymer Science & Technology (SPSI-MACRO-November 2022)

Further the student has passed the following courses towards fulfilment of course work:

Course	*Title*	*Credits*	*Pass/fail*
CY-801	**Research Proposal**	**3**	**Pass**
CY-802	**Chemistry Pedagogy**	**3**	**Pass**
CY-805	**Instrumental method A**	**3**	**Pass**
CY-806	**Instrumental method B**	**3**	**Pass**

Ashwini Nangia

Dean
School of Chemistry, UoH

Dean
SCHOOL OF CHEMISTRY
University of Hyderabad
Hyderabad-500 046

Jana 27/03/2023

Prof. Tushar Jana
(Thesis Supervisor)

Prof. TUSHAR JANA
School of Chemistry
University of Hyderabad
HYDERABAD-500 046. INDIA.

[Preface]

The current thesis entitled ***"Mixed Matrix Membranes of Polybenzimidazoles as Proton and Anion Exchange Membranes"*** has been divided into eight chapters. **Chapter 1** is the introductory chapter which discusses the working principle of the PEMFC, AAEMFC, alkaline water electrolysis, various fabrication techniques of PBI based blends and nanocomposite membranes and a brief discussion about the surface initiated RAFT polymerization techniques. **Chapter 2** explains the detailed characterization methods of the various types of samples and fabricated membranes (both AEMs and PEMs) included in the thesis. In the **Chapter 3,** post synthetically modified (PSM) UiO-66-NH_2 MOFs (PSM1 & PSM2) were incorporated into the OPBI matrix in order to fabricate efficient Polymer-MOF nanocomposite MMMs, their super proton conductivity and various other membrane based properties improvements were discussed thoroughly. In the **Chapter 4,** phosphoric acid impregnated melamine based Schiff base network type covalent organic framework (COF) materials have been incorporated in the PBI matrix in order to develop super proton conducting Polymer-COF nanocomposite PEMs. In the **Chapter 5,** SI-RAFT initiated polymer-*g*-GO materials have been incorporated into the OPBI matrix in order to fabricated OPBI@GOP nanocomposite membranes with remarkably high proton conductivity and mechanical durability for their utilization in the PEMFC. **Chapter 6** demonstrates the synthesis and characterizations of ionically crosslinked (ICL) non porous and porous blended AAEMs for their potential application in the alkaline water electrolysis treatment. In the **Chapter 7,** SI-RAFT initiated polymer-*g*-GOPILs have been incorporated into the alkylated PyPBI-BuI-OBA matrix in order to develop mechanically robust nanocomposite mixed matrix anion exchange membranes with high OH^- conductivity for their potential utilization in the AAEMFC. **Chapter 8** summaries all the important findings of the current thesis work with a concluding remarks and demonstrates the future scopes of various scientific findings associated with this thesis.

Anupam Das.

March 2023 **Anupam Das**

[Acknowledgement]

The journey of my Ph.D. for the last five and a half years is combined with a bunch of struggles, failures, new learnings, constructive criticism through which I could able to make myself a calm composed and mature person with time, which helps me to find the path of success and achievements during the process. It cannot be expressed in words that how much difference I could feel in my character and my thinking process after pursuing Ph.D. It has been a great learning experience for life beside academics, which will help me to become an honest and responsible human being in future. Therefore, it is a genuine pleasure for me to express my deep sense of thanks to one and all who were directly or indirectly involved in this successful journey. In this note of thanks, I will try to briefly elaborate my journey of life through remembering all of your valuable contribution in the way of my journey.

Firstly, I would like to express my sincere gratitude towards my research supervisor, Prof. Tushar Jana, for his constant guidance and support throughout my journey of Ph.D. I have learned various aspects of polymer chemistry and always motivated by him to pursue challenging research problems. Not only academics, but I have learned the lessons of life from him to be a good human being. His ideology has make a significant impact on my thinking process towards research, science, people, society, daily life and other facts of the world. I truly feel fortunate to have him as my guide who always give me freedom to look towards various aspects of research according to my knowledge, interests and skills. He has perfectly analysed my strong points and week points and have given me the licence to utilize my skills in the laboratory in whatever best possible way I can deliver it. As a result of that, I started loving my work and I could able to put my best effort in each and every problems of research as well as daily life to resolve it in a positive way with critical and effective thinking. This process helps me to drive towards the way of success and have kept me always positive during my Ph.D. Whatever I could able to achieve that is purely due to the belief and trust Sir showed on me. I have always been an admirer of how nicely sir organize and represent things in an attractive way towards the audience. I have learned various aspects of representation and organization skills from him over the years, which will always help me in my career growth. Also, I would like to thank him for his constant financial support (when I joined at 2017 initially as a project assistant, and also after the 5th year fellowship tenure got over). Thank you Sir for everything. I also want to thank to Madam Mrs. Sutapa Sinha for her warm welcoming attitude whenever we go to Sir's home or any lab parties. I would like to convey my best wishes to Buchan and Babli for their great successful career ahead. I know both of you will be successful in your career, will be good and responsible human being and make us proud.

I would like to express my warm regards to my doctoral committee member and our research collaborator Prof. Samar K. Das for his constant guidance, motivation and appreciation. Whenever I met him, his words and wisdom has impressed me. Such a humble and down to earth personality I have rarely seen in my entire life. I have felt always motivated by seeing his enthusiasm towards science and research. I have been fortunate enough to contribute in some of the collaborative research findings with Sir, and every time I felt enthusiastic and positive while working with him. Thank you Sir for valuing and appreciating all my efforts. Your words and appreciative remarks always motivate me to work harder with more care. I also enjoyed a lot while discussing with you about various scientific problems/facts and their probable solutions/reasons. The education and the value of life which I have learned from you will be always remain in my heart. You will be always an inspiration. I thank all the SKD lab members for treating me like their own lab mate, I have enjoyed every moment of get together with all of you. I would like to convey my gratitude and thanks to my doctoral committee member Dr. Murali Banavoth for his valuable suggestions. I would like to thank the present and former Dean(s), School of Chemistry, for providing all the facilities for pursuing my research. I have learned the ideology of simplicity and simple living high thinking from Prof. Samudranil Pal, *a kind hearted human being have always helped me, my lab members and Sir when we need him. I sincerely acknowledge Dr. Krishna Kumar from MMMUT, Gorakhpur and Prof. Suresh K. Jewrajka (CSIR-SCMCRI, Bhavnagar, Gujrat) with whom I have contributed in few collaborative projects. It has been always good and learning experience while discussing with them regarding the work. I would like to thank our collaborator Prof. Prakash C. Ghosh, IIT-Bombay for helping us with the alkaline water electrolysis treatment of our AEM samples, and our collaborator Dr. Manju Sharma, SoC-UoH for helping us in DFT studies for one of our collaborative project. I would like to convey my warm regards to Prof. Roy Shenhar, whom I met in the SPSI-Macro Conference at Pune 2018, In one day of city tour we have made several memories. Roy you are such a humble and down to earth person, I will continue to remember the day of 21st December, 2018 through my entire life. Also, the Centre for Nanotechnology, UoH is greatly acknowledged for providing the TEM facilities and School of Physics, UoH for PXRD facilities. I am thankful to Dr. Uday (for PXRD), Mr. Pankaj (for TEM), Dr. Durgaprasad (for TEM, AFM, Raman), Mr. Sunil (for FESEM), Mr. Durgesh and Mahindar for helping me with the NMR studies. I thank all the non-teaching staff in School of Chemistry for their support and help. specially Mr. Venkatesh for managing several labs related official work. Also, would like to give special gratitude to Mr. Abraham for official works, Mrs. Geetha and Mrs. Rani for helping me regarding several bills payments towards the vendors. I would like to deeply thank the Deputy Registrar of UoH Dr. Bipin P. Varghese Sir for helping me during my Ph.D. admission time and allow me to take admission without migration certificate. The effort Mr. Azhgar Khan and Mr. Md. Jaffar Sir had put regarding my fellowship and all the lab project related bills are highly acknowledged. Financial assistance from DST, India is greatly acknowledged, it is a huge financial support for being a INSPIRE scholar since my B.Sc. days. Being a student from the middle class family it was really difficult to pursue my study without financial support from DST. My special thanks to INSPIRE for providing me the fellowship during my Ph.D.*

Now, I would like to convey my deep sense of thanks to all my co-workers and co-authors without whom this journey was incomplete. First, I would like to specially thank Dr. Subhabrata Mukhopadhyay, who has been a great co-worker, an elder brother beside a friend and guide. He has been always my idol, I respect and love him a lot and I will continue to do so. I would like to convey my warm regards to Dr. Balakondareddy Sana, it has been a great experience to work with you in a significant no. of research problems. Next, I would like to convey my heartfelt thanks towards my colleague and best friend in lab Dr. Nilanjan Mukherjee, without you my journey of research would have been incomplete. You have given me all possible assistance whenever I required your help the most for each and everything. I am happy that we could able to solve a significant no. of scientific problems together in the lab. Also, my personal life become easy for having a friend like you. Thank you Nilu for everything. Then comes Dr. Moumita Dhara, an elder sister, a well-wisher always. You have been there always in my support beside me like my own elder sister, whenever I required you the most in my difficult time. Your guidance, suggestions simplicity and humble attitude have always helps me towards improvement in my academic career and personal life. Also, you and Nitai Da used to warmly welcome us and cook several delicious foods for us when we visit your home. I want to congratulate both of you for your Son, I wish Munu all the success and happiness in life. I want to covey my sincere acknowledgement towards our lab alumni Dr. Mousumi Hazarika, who have been very humble towards me during her visit to our lab, while working with you I have learned several laboratory experiments. I express my warm wishes to your husband Dr. Naba kamal Nath, your son and family a prosperous life ahead. I want to convey my heartfelt gratitude and warm wishes to my very good friends Dr. Olivia Basu and Dr. Kolli Hema Kumari. Working with both of you in different collaborative projects have been *great experience for me. I could able to learn and understand several things regarding MOF and POM chemistry from both of you. Thanks to both of you for being there always beside me in my difficult time. Furthermore, I thank all of my lab mates and other co-workers for their valuable contribution in my professional career and personal life for making several good memories with me during work.*

I would like to thank all my other lab seniors Dr. Arindam Sannigrahi, Dr. Dhamodaran Arunbabu, Dr. Sandip Ghosh, Dr. Shudhangshu Maity, Dr. Shuvra Singha, Dr. Kuruma Malkappa, Dr. K.S.N Raju, Dr. Billa Narasimha Rao, Dr. Bikash Sikdar, Dr. K. Rambabu, Dr. Harilal, Dr. Niranjan Yeole, Mr. Murali Sankar, Dr. K. Ramesh, Dr. Konda Reddy Kundru, Dr. Mutyala Naidu, Dr. Mithun Chakraborty, Dr. Amarnath Jasti and Dr. Sateesh malkapuri for their help and useful discussions. I specially mention the bonding and discussions I have had with Harilal anna during his last days of lab. I felt extremely happy for your postdoctoral position in DTU, I wish you will do exceptional research work there. I thank my lab mates Srinivas, Suchismita di, Nilanjan, Prasanntha, Arunava, Somdatta, Akhil, Ritu, Sourav and Vikali for being always humble and helpful towards me. I thank all my lab mates for keeping a friendly atmosphere in the lab. I would like to thank Ms. Anjana Ram and Ms. Poushali Naskar, who have completed their M.Sc. projects with me. I would also like to thank Mr. Pravin Parasakthi Aravindhan and Mr. Anirudh Devrajan who has kept constant relation with me over the years. I would like to thank all my campus mates of Ph.D. and M.Sc. juniors - Satyam, Shyam, Vinay, Suraj, Sasikanth, Ajay, Daradi, Sneha, Arghyadeep, Debu, Somratan, Avijit, Ujjwal, Subham, Sagar, Soudipta, Sujan, Sovon, Atanu, Prajit, Dighanchal, Joydeb, Sampita, Avijit, Dipanjan, Supratik, Mafidul, Sohel, Sampurna and all of our Bengali juniors for having some enjoyable memories especially during the festivals like Saraswati puja and Parichiti.

I cherish my special bonding with my seniors Dr. Subhabrata Mukhopadhyay Da and Dr. Sneha Paul Di, they have given me uncountable memories, valuable guidance and have been always great friends in the campus. I cherish those memories of rehearsal nights before Saraswati puja, campus tea break, campus picnic, high rock and mushroom rock tour with Subha Da, Sneha Di and Nilanjan. Also, I am thankful to god for having my seniors like Dr. Sugata Goswami, Dr. Rudraditya Sarkar, Dr. Sudipta Seth, Dr. Apurba De, Dr. Nitai Giri, Dr. Bappaditya Sankhari, Dr. Koushik Ghosh, Dr. Suman Ghosh, Dr. Kollol Mukherjee, Dr. Arijit Mukherjee, Dr. Arijit Sarkar, Dr. Kuntal Bhattacharyya, Dr. Debika Debnath, Dr. Chandni Singh, Dr. Tasnim Ahmed, Dr. Sameeta Sahoo, Dr. Mou Mondal, Dr. Sabari Ghosh, Dr. Ankit Kumar Srivastava, Dr. Anirban Debnath. There are uncountable memories I have shared with all of you. In addition, I would like to specially mention about all of my good friends in campus, without all of you my Ph.D. life would have been incomplete. Firstly, I would like to talk about Dr. Shubham Debnath, a flamboyant personality with a kind and generous heart become one of my close friend since I joined my Ph.D. I could not count how many good memories we will have on campus. I have never ever seen any big biriyani lover than you in my life. Also, the memories I shared with my friends Dr. Soutrick Das, Dr. Suman Mandal, Dr. SK Alim, Alamgir, Sumanta, Soumen in the NRS-Hostel will be forever remembered. I will miss those Saturday night hostel picnics with all of you, which have given me uncountable good memories over the years. Now I would like to mention about two of my dear friend in campus Dr. Somnath Das and Dr. Saradamoni Mondal, the bonding and the friendship associated with both of you is something special. In the tough time of lockdown because of both of you I could able to manage my lifestyle properly without feeling depressed in the campus. Special thanks to both of you for that. During lockdown period beside our work life, the quality time spending, playing games, having food together, those lockdown days I will never forget in my life. Saradamoni and Olivia thanks to both of you for cooking several delicious foods for us that time, when no outside food was allowed. Somnath has been a great friend with whom I have a special *bonding. I have been inspired by your academic dedication which have helped me to grow in my career as well. You are such a humble and great human being I have ever met. I wish Saradamoni and Somnath a prosperous future ahead with all the achievements and success. I would like to give my special thanks to Mr. Dipankar Das (dasbabu), Sanju Da, Mithun Da. and Mr. Moinuddin in the UGC-NRC canteen for serving us quality food in reasonable price during the lockdown and post lockdown period. Their effort is truly acknowledged. I would like to express warm wishes & gratitude towards my sister Mrs. Maitrayee Sinha. Thank you for cooking all such delicious items for me. Both Nilanjan and you have become family members far away from home and never make me feel outside home. I also convey respect towards Uncle and Aunty for giving me so much love. I convey my well wishes to Atrayee.*

Now I would like to extrapolate a bit about my Master of Science (M.Sc.) days in the University of Calcutta (Rajabazar Science College). In this regards, I would like to convey my deep sense of gratitude towards Prof. Dilip K. Maiti, Prof. Susanta Sekhar Adhikari, Prof. Asutosh Ghosh, Prof. Achintya Kumar Sarkar, Prof. Goutam Chattopadhyay, Prof. Debasis Das, Prof. Asish Ranjan Das, Prof. Nikhil Guchhait, Prof. Chanda Mukhopadhyay, Dr. Sanchita Goswami and Dr. Ramananda Maity who have always motivated us to choose research as career path. Thank you all my professors for guiding us towards the positive direction. It will be incomplete if I don't mention some of my great friends from my M.Sc. days. I felt blessed to share my M.Sc. classroom with Soumya, Koustav, Tathagata, Supriyo, Somali, Ankita, Treena, Bilkis, Rituparna, Jayisha, Rima, Sukanya, Debarati, Sayantani, Poulami, Dibyojyoti, Sumit, Suman, Chandan, Alamgir, Subhasis, Anik, Ranadip, Mijan, Apurba, Palash, Aritra, Pushpendu, Vaswar and many others. I would like to mention about Mr. Arnab Datta dada specially, dada you were my friend and guide during the M.Sc. days. I could remember we used to roam old Calcutta (Vidyasagar's house, Rammohan Roy's house, Coffee house, Presidency College, College street, paramount, Babughat, Bagbazar ghat, Eden Gardens, City tour in Tram etc.) to feel the soul and culture of the city. I was blessed to have you those days with whom I can discuss on various topics and take suggestions. I will also be grateful to Dr. Md. Yousuf, and Dr. Subhajit Guria with whom I have pursued my M.Sc. project in the laboratory of Prof. Susanta Sekhar Adhikari. I have learned a lot from that experience.

Now would like to reminiscence those evergreen memories of the Ramakrishna Mission Residential College, Narendrapur, where I have pursued my Bachelor of Science (B.Sc.) degree in Chemistry. First of all, I would like to take the blessings of Sri Sri Thakur Ramakrishna Paramahamsa Dev, Maa Sarada, Swami Vivekananda and all the other monks and Maharaja's associated with this great institution. I would like to convey my heartfelt respect towards my RKM professors Dr. Arogya Varam Saha, Dr. Hrishikesh Chatterjee, Dr. Pulak Ganguly, Dr. Santosh Kumar Maji, Dr. Ramaprasad Chakraborty, Dr. Prasanta Ghosh, Dr. Bikash Baran Ghosh, Dr, Bimal Kumar Sadhukhan, Dr. Rathindranath Ghosh, Dr. Dinabandhu Mondal, and our guest lecturers Dr. Azizul Haq and Dr. Amit Saha. Specially AVS Sir, PrG Sir and PG Sir, inspiring by their dedication towards science and research I decided to go for higher studies in Chemistry after pursuing my bachelor's degree from RKMRC. I would like to specially mention about a name Dr. Chandan Saha (Professor, School of tropical medicine), Sir the way you have shared the aesthetics and philosophy of Organic Chemistry with all of us that actually triggers me to take the challenging Organic Chemistry as my Specialization subject in M.Sc. later. I was blessed enough to share my B.Sc. classroom with Rajarshi, Saptarshi, Swarup, Aishik, Mijan, Sougata, Snehasis, Arpan Sasmal, Subhajit, Sohel, Subir, Supriya, Arunabha, Ranadip, Palash, Apurba, Anik, Pritam, Ratan, Sahabuddin, Sunny, Firdous, Jayanta, Umesh and Arpan Patra. I feel proud for all of you as many of you have already established in your career. My special thanks to my friend and well-wisher Mr. Rajarshi Panigrahi, who has always helped me to develop my knowledge in Chemistry. I would *like to give my special thanks to my roommates in B.Sc. days, Dr. Sourav Manna, Dr. Ramesh Ch. Sau and Mr. Souporno Mondal for being so much humble with me. Also, I have inspired by my seniors in RKM Dr. Pritam Das, Dr. Banshi Das, Dr. Sajal Sen, Dr. Pratik Roy, Dr. Mangaldeep Kundu, Dr. Monosij Mondal, Dr. Biswarup Jash, Dr. Korak Biswas, Dr. Rupayan Mukherjee, Dr. Jayjeet Mukherjee, Dr. Mihir Sasmal, Dr. Debdeep Chatterjee, Dr. Sabyasachi Chakraborty, Mr. Achintya Mondal, Mr. Satyaki Sen and many others. Pritam Da. You have been my idol over the years. You have inspired me in many ways. By seeing you I stated the dream of pursuing higher studies in abroad. Korak Da and Rupayan Da you have been great friends always. We used to have so much fun and enjoyment in the RKMRC nara-narayan seba, Foundation day, Thakur's birth anniversary, Swamizi's birth anniversary, kalpataru utsav, Ramakrishna Mela, Vidyarthi Brata and various other festivals. RKM has given me uncountable memories and friends which I will continue to cherish forever.*

Now I would like to remember those incredible memories of evergreen School life. From Class V-Class XII, I have studied in Karimpur Jagannath High School for my Secondary and higher Secondary examination. I convey my deep sense of regards to all the Sir's and madams of my school who gave me the social knowledge beside subjective knowledge. Subrata Sarkar Sir, Kajal Sir, Netabuddin Sir, Dinesh sir, Kanai Sir, Achintya Biswas Sir, Achintya K. Mondal Sir, Prabir K. Mondal Sir, Prabir Kundu Sir, Nilotpal Sir, Arijit Sir, Pranati Madam, Pragati Madam, Tapas Sir, Sujit Sir, Kalyan Sir, Parthasarathi sir, Sanchayan Sir, Sheela Madam, Parameswar Tudu Sir, Amrita Ghosh Sir, Dipankar Sir, Mahitosh sir, Suman Sir, I will never forget all of your contribution in my life from Class V- Class XII. I would like to thank all of my School friends for making my school life so special and memorable. Dr. Sourav Biswas was my first ever school friend since Class V. I have inspired by you Sourav in several occasions, and in several phases of my life specially in school days. I am very much proud of you that you have completed your Ph.D. from MUN, Canada. Best wishes for your new journey in RWTH-AACHEN. Also, I would like to give special thanks to my another dear friend Mrs. Sanghita Biswas. You are such an amazing person, friend and always a well-wisher, blessed to have you in my life. It's always lots of happiness, and trust associated with our bonding and friendship. I am proud of you as you involved yourself in social welfare being a responsible teacher. I will always stand beside both of you as a friend and well-wisher. Through Sourav I have met Mr. Santu Mondal (Santu Da), Santu da you have inspired all of us towards Science and Chemistry, you have always inspired us to set big dreams in life. The section will be incomplete without mentioning of my dear friend Dr. Sankarsan Biswas. I would like to congratulate you for completing your Ph.D. from City University of New York and for getting Job in Bausch & Lomb, USA. There are uncountable good memories we have shared together. Another one friend is Dr. Nilabrata Saha. Nilabrata, I am proud of you that you have become an Orthopaedic Surgeon in the Burdwan Medical College. Through Korak Da I met Dr. Soumalya Joarder Da (both Korak Da and Soumalya Da belongs to my hometown Karimpur which creates a special bonding). I could remember all three of us watched the 2014 Football World cup together in Soumalya Da's house. The golden goal of Mario Gotze in the 2014 Football World Cup final and the WC lifting moment of Philipp Lahm's Germany was one of the memorable and happy moment in my life beside Mahendra Singh Dhoni's finishing Six against Sri Lanka in the 2011 Cricket WC final, that day the nation chants together Vande-Mataram in the mighty Wankhede Stadium. Also, I would like to congratulate both of you for Argentina's famous World cup win in Qatar, 2022. I am extremely blessed to watch the great Leo Messi lifting the WC trophy as a world cup winning captain.

Now, I would like to thank all my relatives and family members. I would like to thank all my maternal uncles and aunts, My cousin brother Mr. Dipankar Raha, and my cousin Sisters Mrs. Dipanwita Raha (Dipa) and Ms. Aitihya Raha (Nipa). It cannot be expressed in words here *that how many good memories we have together as it will require an entire book to note it down. Also, I would like to give my love and thanks to my other cousin brothers and sister in laws - Bijoy Da & Sonali Boudi, Badal Da & Mala Boudi, Joy Da, Samir Da, Chandan Da, Nandan Da and all others. My childhood was evergreen being loved and adored by all of you. Now I would like to convey my warm regards towards my paternal uncles, aunts and my father's childhood friend Mr. Brajakishor Pal (Mahadev Pal). I would like to convey my thanks and love towards my cousin brothers, sisters and sister in laws. Nelu didi & Animesh Jamaibabu, Tutu didi & Partha Jamaibabu, Sonamoni didi & Nilratan Jamaibabu, Shukla didi & Lal jamaibabu, Raju dada & Swarupa Boudi, Bhola Dada & Supriya Boudi, Mana Dada & Papiya boudi, Nabin dada & Mili boudi, Biswanath dada & Papia boudi, Hari dada & Gouri boudi, all of you were so special to me in my childhood and during my bachelors and masters' degree. Thank you for giving me all your unconditional love and blessings. I would like to convey my love and best wishes to all my nephew and nieces. I had a great childhood bonding and friendship with Tutu di's son Ratul. Shukla Di's daughter Dipanjali has been a good friend and a well-wisher, I wish you and your husband all the best for your prosperous future. I would like to convey my heartfelt gratitude and respect towards Aloke Mama, Sikha Mami, Mintu Mama, Sampa Mami, Dida, my love and warm wishes to Liton Dada, Tuka boudi, Megha, Sankha, Rik and Rai and the entire Dumdum family. I cherish the Jagaddhatri Puja celebration together in the Janaki Apartment, Motijheel Dumdum every year. This address has been a nostalgia for me over the years.*

Finally, last but not the least I want to convey my heartfelt gratitude, respect, love and pranam to my Grandparents (thakurda & thakuma, dadu & dida), my Father Shri. Niranjan Kumar Das and my Mother Shreemati. Akhi Rani Das. Being a middle class family whatever sacrifices they have made for me to raise me that cannot be expressed in word. Their love towards me also cannot be expressible in words. Today I want to thank both of you maa and baba for everything. Thank you for giving me so much freedom in life. I like freedom so you have never ever restricted me for anything which I likes to pursue, or you have never imposed your own choices on me. You have given me every space so that I can grow up in my feet like the way I want in my life. Most probably that only makes me a practical minded, matured and emotional person with certain values and ideology towards life and its journey. I would like to convey my love to my elder brother Shri. Nirupam Das, my Sister in law Shreemati Tumpa Das and my Niece Nirnita Das (kuttus) for your unconditional love, care and support towards me. Dada I never said you thank you in life, but as you were there with us in our difficult time with financial and mental support being the elder son of a middle class family with so many responsibilities, so we could able to overcome those difficult times slowly towards the way of hope and development. Nirnita, I wish you all the best for your future. Be a good human being. Do whatever you like to do, and be there where you find peace and happiness in life. Also, I would like to give thanks to boudi's family members (her father, mother and brother) for their love and wises towards me. I wish Riju all the success in life.

Sorry I could not mention all the names; I convey my sincere gratitude to all the people who have been associated with this journey and make it a memorable one.

Anupam Das.

Anupam Das

March 2023

[Contents]

Introduction

Fuel cell

Fuel cell is an energy conversion device discovered by Sir William Grove who is known as the father of fuel cell as he was the first to put forward the concept of fuel cell. Christian Friedrich Schonbein first published research article in the philosophical magazine in January 1839. Another name associated with this concept of fuel cell is Francis Thomas Bacon. He experimented with alkaline electrolytes instead of acid based electrolytes and found that the potassium hydroxide electrolytes worked as good as acid based electrolytes.

Fuel cells are electrochemical energy conversion devices that convert chemical energy of hydrogen directly into the electrical energy via a chemical reaction.[1–3] Fuel cell (FC) composed of three main components: anode, cathode and electrolyte. The oxidant is reduced at the cathode and fuel is oxidized at anode. Ions move through the electrolyte and a current is produced at the external circuit that is used to power a device. In the operational FC a membrane consists of electrolyte sandwiched between cathode and the anode which is known as membrane electrode assembly (MEA).[4–6] The anode acts as an interface between the electrolyte and the fuel (e.g. H_2), which catalyses the oxidation reaction and generates free electron and H^+. The electrons conduct to the load via the external circuit. Whereas, the cathode provides an interface region between the electrolytes and the oxygen, which catalyzes reduction reaction of oxygen, and provides a path through which the flow of free electrons is conducted from the load to the electrode via the external circuit. The electrolyte layer acts as a physical barrier developed between the oxygen and the hydrogen, which prevents direct mixing of H_2 and O_2 but enable for the conduction of ionic charges between the electrodes (cathode and anode) and the complete cell electric circuit. The cell reactions and a fuel cell are schematically represented in the Figure 1.1.

In general, fuel cells are various types according to their operating temperature, electrolyte type, efficiency and applications. Fuel cells (FC) can be classified into five types based on the choice and types of the electrolytes. These are: 1) Polymer electrolyte fuel cell (PEFC), more specifically Proton exchange membrane fuel cell (PEMFC),[7] 2) Alkaline fuel cell (AFC) or Alkaline anion exchange membrane fuel cell (AAEMFC),[8] 3) Solid oxide fuel cell (SOFC),[9] 4) Molten carbonate fuel cell (MCFC)[10] and 5) Phosphoric acid fuel cell (PAFC).[11]

In this thesis, we have aimed to focus on fabrication of various of polybenzimidazoles based mixed matrix membranes (MMMs) for PEMFC and polybenzimidazole MMMs for the development of alkaline anion exchange membranes (AEMs). Therefore, in the following section, we will discuss in details the working environment and requirement for the PEMFC and AAEMFC fuel cells.

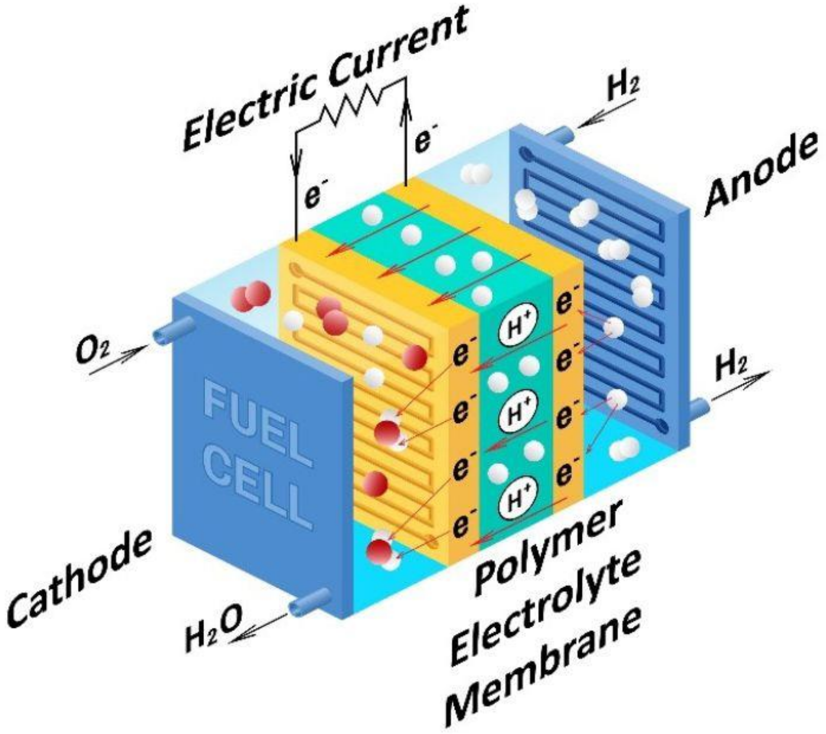

Cell reaction

At Anode: $2H_2 \rightarrow 4H^+ + 4e^-$

At Cathode: $O_2 + 4H^+ + 4e^- \rightarrow 2H_2O$

Overall cell: $2H_2 + O_2 \rightarrow 2H_2O$ **+ electrical energy + heat**

Figure 1.1. Schematic representation of a fuel cell. (Image adopted from google).

Proton exchange membrane fuel cell (PEMFC)

Proton exchange membrane or polymer electrolyte membrane fuel cells (PEMFCs) are considered to be promising candidates and more attractive fuel cell technology among various types of FCs due to their simplicity in use in automobile, portable power and stationary applications.[12–15] The PEMFC was first developed for utilization in the Gemini space vehicle. The important features of the PEMFCs are: pollution free operation, and all-solid construction and therefore less corrosion. The PEMFC is highly cost effective more efficient with respect to all other types of FCs. Depending upon the nature of polymer electrolytes, PEMFCs can operate ranges from lower to elevated temperature (30 to 180 °C) and generates high power density in comparison to other type of fuel cells.[15,16]

Desired properties of efficient PEM

Generally, a superior PEM working under operational fuel cell should consists (1) efficient proton conduction with zero electronic conductivity, (2) low permeation of oxygen and fuel, (3) good oxidative and hydrolytic stability, (4) excellent mechanical robustness in both dry and hydrated states, (5) cost effective synthesis, and (6) membrane durability for the membrane electrode assembly (MEA) fabrication and testing.[12] In the modern years, significant efforts have been made by the researchers worldwide to develop efficient PEM and alternatives to replace costly Nafion based membrane which operates up to 180 ºC without humidification.

Phosphoric acid (PA) doped polybenzimidazoles as PEM

In general, perfluorinated membrane Nafion has been widely utilized in literature to develop efficient PEM.[17] Nafion membranes displays thermal and chemical stability hence can be utilized safely as efficient membrane for PEMFC use[18] and that is the reason for the wide use of the perfluorinated based membrane as PEM in the last one-two decade. But the perfluorinated based polymers are consisting of significantly lower glass transition temperature (T_g) around 120 °C.[19] which causes deterioration of mechanical stability beyond 120 °C,[19] Perfluorinated membranes are highly costly and can conducts protons efficiently only up to 80 °C under 100% humidification. Temperature beyond 100 °C and less humidification, Nafion or any other perfluorinated types membranes are unable to conduct. There are additional drawbacks also like high methanol crossover which decays membranes performances.[20,21] In order to mitigate these problems associated with Nafion, extensive research have been performed by synthesizing non-perfluorinated based polymers structure.[15] Phosphoric acid (PA) doped PEM has emerged as a most efficient membrane towards this. The first ever synthesis of polybenzimidazole (PBI) structure was developed by Marvel and co-workers which was mechanically strong even at elevated temperature with good chemical stability.[22,23] PBI membranes were also used by the U.S. Air force due to its extraordinary properties like thermal, chemical and mechanical durability etc.[24] The PA doped PBI based membranes are currently being evolved and popular in literature as efficient PEM, as it conducts proton at elevated temperature (150 ºC – 200 ºC) without any humidification.[25–27] PBI is an amorphous aromatic heterocyclic polymer where the polymeric repeat unit consists of both the proton donor (-NH-) and proton acceptor (-N=) H-bonding sites through which PBI structure generates specific interactions with both the polar protic and aprotic solvents.[28] Most of the PBI based polymers are separated from reaction mixture as noodles or strong threads having good film forming proiperties.[29–31] Savinell et al[32] have first ever introduced acid doped PBI to improve the qualities of PEM. This work has been the path breaking development for the fabrication of cost effective PBI membrane with high performances. Several authors reported that PA loaded PBI membrane exhibits very high proton conductivity, low gas permeability/crossover, decent thermal and oxidative stability and lower water drag coefficient. PA doped PBI membrane produces low vapour pressure even at high temperature because of the development of 3D networking of phosphoric acid molecules.[33]

Synthesis of polybenzimidazoles

In the late 20th century, many research groups have started synthesized PBI for diverse applications. The PBI structure developed by Marvel et al[22,23] has exhibited high temperature and chemical resistance. Various synthetic methodology has been evolved in literature which consists of utilization of different tetramine monomers and dicarboxylic acids to synthesize various structural variation of PBI (Table 1.1). PBI can be synthesized by polycondensation reaction of tetraamines (TAB) and di-acids (Scheme 1.1). Literature reports consists various types of polycondensations: 1) melt condensation polymerization[34] 2) solution condensation polymerization[35] 3) catalytic condensation polymerization.[36]

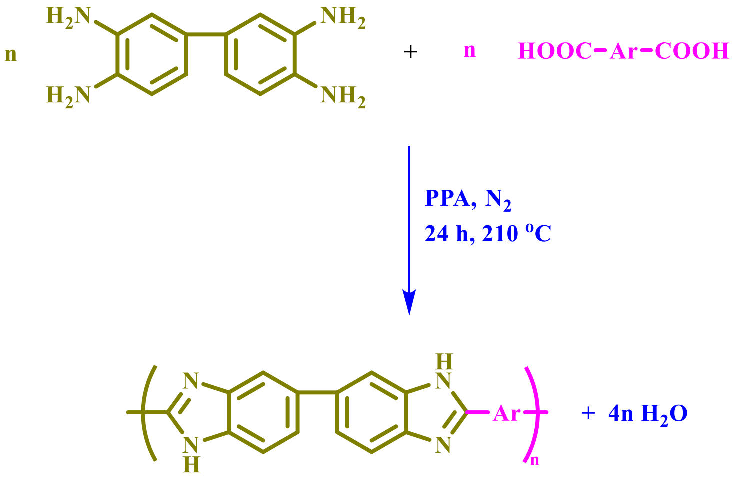

Scheme 1.1. Synthesis of polybenzimidazole (PBI) by polycondensation using polyphosphoric acid (PPA) medium.

For solution induced polycondensation, effects of several solvents have been investigated. Various high boiling solvents such as *N*, *N*-dimethylformamide (DMF), *N*, *N*-dimethyl acetamide (DMAc) have been utilized.[37,38] But the drawback associated with these solvents are the generation of polymers with very low molecular weight. This draw back was resolved by Iwakura et al.[39] in which all compounds [equimolar mixture of dicarboxylic acids and tetramine monomers were taken into polyphosphoric acid (PPA) medium] were taken in a three neck round bottom flask connected to N_2 flow for 24 h -26 h reaction at 180-210 °C. Here PPA acted as catalyst cum solvent. Various tetra ammine and di-acid monomers were synthesized and varied to developed alternative types of polybenzimidazoles (Table 1.1).

Table 1.1. Different types of aromatic tetraamines and dicarboxylic acid monomers for polybenzimidazole (PBI) synthesis.

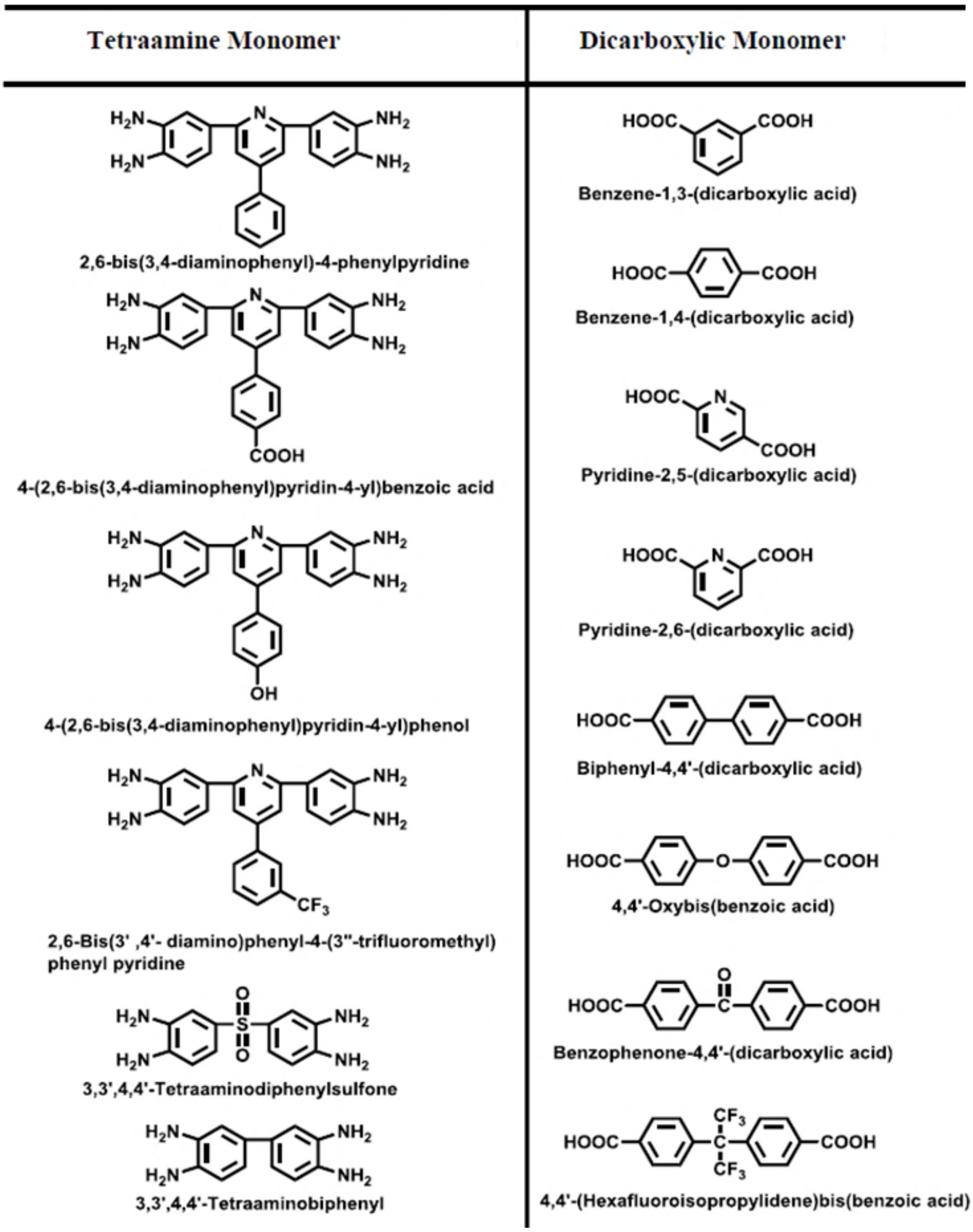

Tetraamine Monomer	Dicarboxylic Monomer
2,6-bis(3,4-diaminophenyl)-4-phenylpyridine	Benzene-1,3-(dicarboxylic acid)
4-(2,6-bis(3,4-diaminophenyl)pyridin-4-yl)benzoic acid	Benzene-1,4-(dicarboxylic acid)
4-(2,6-bis(3,4-diaminophenyl)pyridin-4-yl)phenol	Pyridine-2,5-(dicarboxylic acid)
2,6-Bis(3' ,4'- diamino)phenyl-4-(3"-trifluoromethyl) phenyl pyridine	Pyridine-2,6-(dicarboxylic acid)
3,3',4,4'-Tetraaminodiphenylsulfone	Biphenyl-4,4'-(dicarboxylic acid)
3,3',4,4'-Tetraaminobiphenyl	4,4'-Oxybis(benzoic acid)
	Benzophenone-4,4'-(dicarboxylic acid)
	4,4'-(Hexafluoroisopropylidene)bis(benzoic acid)

Since 1961, after the synthesis of PBI by Marvell et al, several research groups have been exploring and modifying the structure of PBI for employing them in a wide variety of areas and advanced fields. PBI possesses very unique properties as well as some restraints, so in order to improve their properties as per the requirements; researchers have synthesized different varieties of PBI. The varieties of PBI include poly[2,2′-(1,4-phenylene)-5,5′-benzimidazole] (known as *p*-PBI),[40] poly(4,4′-diphenylether-5,5′-bibenzimidazole) (OPBI),[41] poly(2,5- benzimidazole) (AB-PBI),[42] pyridine based PBI (Py-PBI),[43,44] sulfonated PBI,[45] crosslinked and hyperbranched PBI,[46,47] naphthalene based PBI,[48] fluorinated PBI,[49] N-substituted PBI (N-PBI),[50] meta-para random PBI copolymer,[51] PBI with sulfone or sulfonic acid groups in the backbone[52] and many others (Scheme 1.2).

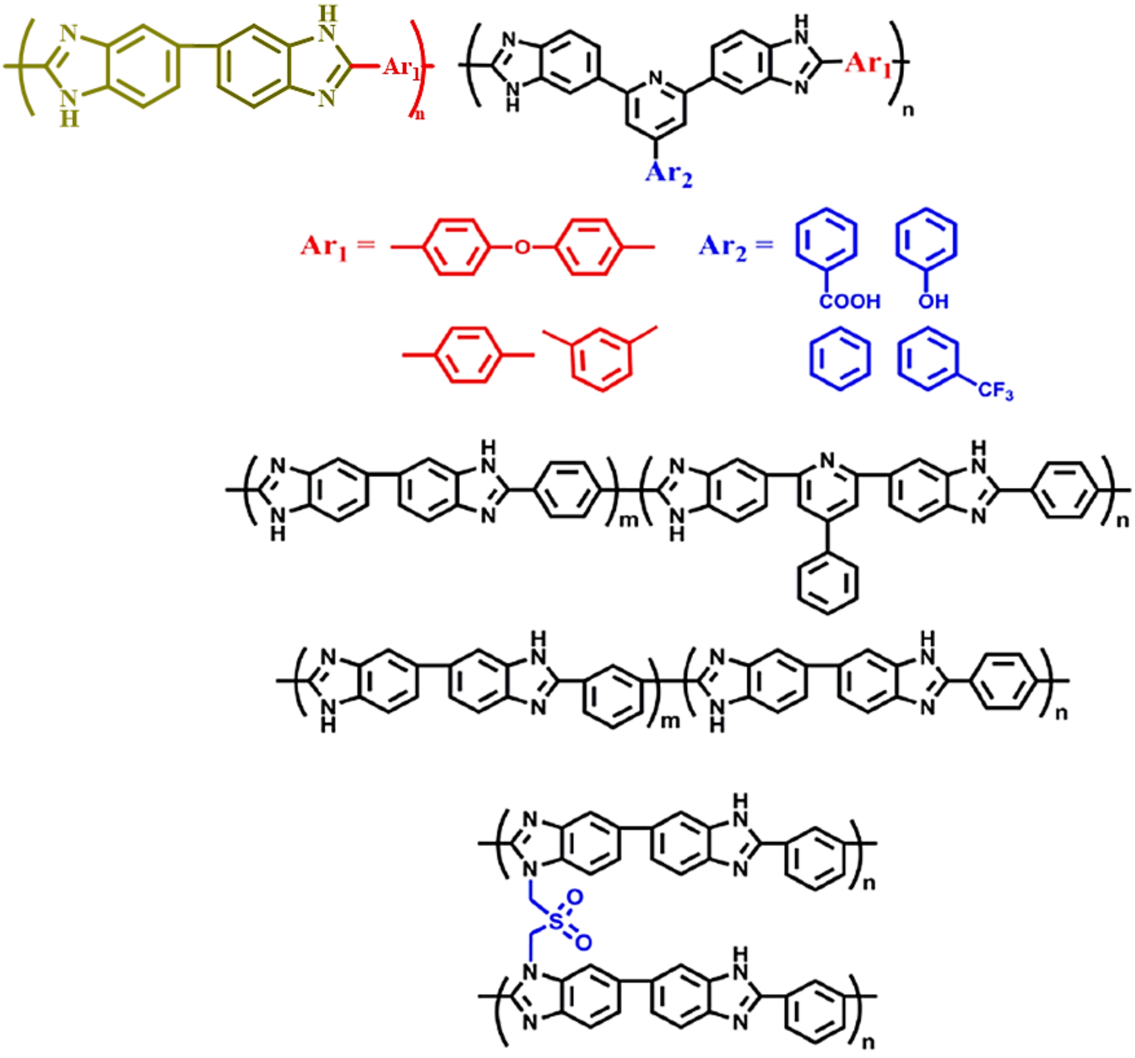

Scheme 1.2. Various types of PBI structure reported in the literature.

PBI possesses strong intermolecular and intra-molecular chain hydrogen bonding and also a highly rigid rod structure that results in poor solubility in common organic solvents. The incorporation of the hetero atoms[53] in the polymer main chain or by N-substitution post polymerization with sulfonic or the aliphatic groups have been found by the researchers to improve the solubility, acid uptake capability and thereby increasing the acid doping level for application in fuel cells. Flexibility was increased by modifying the main chain or side chain with the incorporation of flexor groups like para linkage monomer or aliphatic group or bulky group containing hetero atom. The presence of sulfonated acid groups in PBI increases its water and acid uptake capacity. Likewise, various other modification strategies have been developed to improve the quality of the membranes. Recently, our group also has implemented certain modifications with side and the main chain of PBI which increases solubility, flexibility and acid doping capability.

Various casting methods for PBI based membranes

By analysing the nature and the types of PBI based polymers, various types of membrane casting strategies have been evolved in the literature. Three main casting methods have been utilized extensively for preparation of efficient PEMs. Benicewiz et al have first ever reported the *sol-gel* method for development of PBI membranes.[54] In this process, after completion of the polycondensation polymerization reaction in presence of polyphosphoric acid (PPA) medium, the viscous solution was directly casted onto a glass petri dishes. Hence the resulted membranes will exhibit a sol-gel transformation or transition through surrounding moisture absorption. These membranes displayed high proton conducting behaviours in nature, in addition to their efficient thermal and mechanical durability. Another method was developed by Savinell et al[55] is the imbibing process using DMAC and LiCl solutions, where the LiCl acts as a stabilizer. After evaporation of the DMAC solvent, the PBI membrane was peeled out from the glass petri dishes followed by washing with water to remove trace amount of LiCl and DMAc as the DMAc solvent is poisonous to platinum catalyst which is used in MEA. In this process the PA holding level of PBI were 5 to 16 moles per repeating unit.[56] In addition, utilization of porogen also evolved in literature in order to fabricated porous PBI based PEMs. In this approach, after porogen treatment during membrane casting, the low molecular weight porogen were removed by dipping those membranes in suitable solvents (MeOH, hydrazine and water) (Figure 1.2).[57] The generation of pores all over the membranes interfaces resulted superior PA uptake in the membranes followed by improved proton conductivity.[57–59]

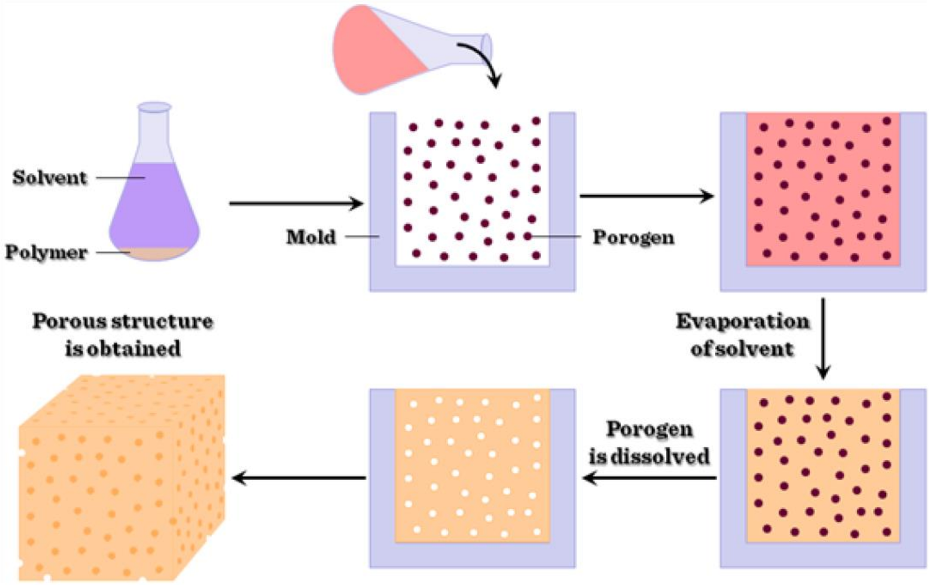

Figure 1.2. Method development for porous structure in the PBI membrane. (Taken from reference 57).

U.S. Pat. No. 5,525,436 described a strategy of doping the PBI film in presence of a strong acid (ex. phosphoric acid or sulfuric acid) to develop a single phase system.[60] In another *U.S. Pat. No. 5,945,233 Onorato et al.* mentioned that PBI based paste or gel can be formed by mixing PBI polymer with a suitable acid solution, which allows to generate a gel-like or paste-like consistency at room temperature.[61] Sannigrahi et al. have reported the thermoreversible gelation of PBI in phosphoric acid by studying the gel morphology, thermodynamics of the gelation, and gelation kinetics utilizing test tube tilting and UV-Vis spectroscopy techniques.[62] Also several synthetic strategies have been utilized in literature to develop super quality PEM by applying modification in the polymer backbone and in the polymeric side chains.[51,63,64] The major problem is to develop a membrane by maintaining the high PA doping level along with decent mechanical stability. Sometime, the acid content present in the membrane found to be too high to process the membrane due to its very poor mechanical stability.[30] Also, the PA doped membrane should have superior thermal stability to avoid the leaching out of the free PA molecules from the membrane above 160ºC, to achieve promising proton conductivity during fuel cell operation.[65] Hence, it is important to maintain a balance between the acid uptake level and the mechanical robustness of the membranes to obtain a PEM with improved quality.

Polymer nanocomposite mixed matrix membranes as PEM

Several nanofillers can play a vital role in order to improve the quality of the membranes by their incorporation into the membrane matrix during solution casting blending. The nanofillers are basically inorganic solid nanoparticles comprise of inorganic materials which differs from the polymer matrix in terms of structure and composition. The impregnation of suitable nanoparticles as nanofillers into the PBI matrix can develop mixed matrix PEM with improved PA doping level, proton conductivity and mechanical durability.[66,67] As the name suggests, polymer nanocomposite comprises of a mixture of two main components: the nanofiller and the polymer matrix in which the nanofiller is embedded. Emergence of nanocomposites opened a huge area of research as they provide a wide range of applications in industrial as well as daily life applications.[68–71] Up to now, a variety of nanofiller have emerged like carbon nanotube,[72] graphene,[71] chemically modified silica particles,[73–77] clay,[78–80] fullarene.[81] etc. Among all, carbon nanotube, graphene and chemically modified silica which provide high performance of the resulting nanocomposites is the major attraction. Incorporation of hydrophilic post synthetically modified metal organic framework as nanofillers into PBI matrix can develop superior quality PEM.[67,82,83] The addition of even a small amount of nanomaterials brings about a huge change in the polymer properties without disturbing the polymer backbone and processability of the polymer. The change is observed in the polymer properties particularly decreased gas permeability and flammability, increased mechanical strength and heat resistance, enhanced biodegradability of the biodegradable polymers, mechanical robustness, increase thermal and oxidative stability and acid loading capacity as well as the proton conductivity. The nanofillers have this much impact on the polymer properties as a result of its unique properties such as: (i) low percolation threshold, (ii) arising a low volume fraction due to particle-particle correlation (orientation and position), (iii) extensive interfacial area (communication between matrix and filler) per volume of particles, (iv) short distances between the particles and (v) comparable size scales among the rigid nanoparticles inclusion. Nanofillers can be mainly classified into three groups, on the basis of dimensions, that is, (i) one dimension (e.g., clay)[84] (ii) two dimension (e.g., carbon nanotube, graphene, MOFs, COFs)[85–87] and (iii) three dimension (e.g., silica, MOFs, COFs).[88,89] In the recent times, various modifications have been developed on PBI using different types of nano fillers.[90–93] The phosphoric acid doping level as well as the proton conductivity and the mechanical stability can be improved using MOF materials as potential nanofillers. Recently, a post synthetically modified MIL based flexible MOFs (53-S and 88B-

S) have been incorporated into the PBI matrix to generate MOF loaded MMMs (Figure 1.3).[94] Carbon nanotube and surface modified GO are also capable of increasing the several properties of the PBI.[93,95] Shao et.al. synthesized the multiwall carbon nanotubes (MWNTs) containing 0.1-1 wt% nanofillers in OPBI nanocomposites.[93] Mukherjee et al have developed SI-RAFT initiated block-co-polymers *grafted* on the surface of MWCNT in order to utilize those materials as potential nanofillers with OPBI (Figure 1.4).[96] In recent times, our group has synthesized the ammine modified silica particle[73] and the montmorillonite clay to influence the properties of the OPBI (Figure 1.5, Figure 1.6).[80,97] Sulfonated PS (SPS) and reduced GO based nanocomposite materials have been employed by Hazarika et al.[98] Maity et al.[77] have developed ionic liquid modified silica/OPBI MMMs with high proton conductivity and less PA leaching (Figure 1.5). Singha et al.[73] have synthesized long chain amine modified SiNP and utilized them to fabricate OPBI matrix supported MMMs for PEMFC applications. Recently, Kutcherlapati et al.[76] have reported the synthesis of poly (N-vinylimidazole) *grafted* SiNP as nanofillers with OPBI to fabricate efficient mixed matrix PEMs. Mukherjee et al have developed block co-polymer *grafted* on SiNP (pNVI-b-pNVT-*g*-SiNP, pNVT-b-pNVI-*g*-SiNP) for their potential utilization as nanofillers into OPBI matrix (Figure 1.7).[74] To solve the PA leaching problem of PEMs our research group have also developed organically modified cloisite clay impregnated OPBI as super proton conducting PEMs (Figure 1.6).[80,99]

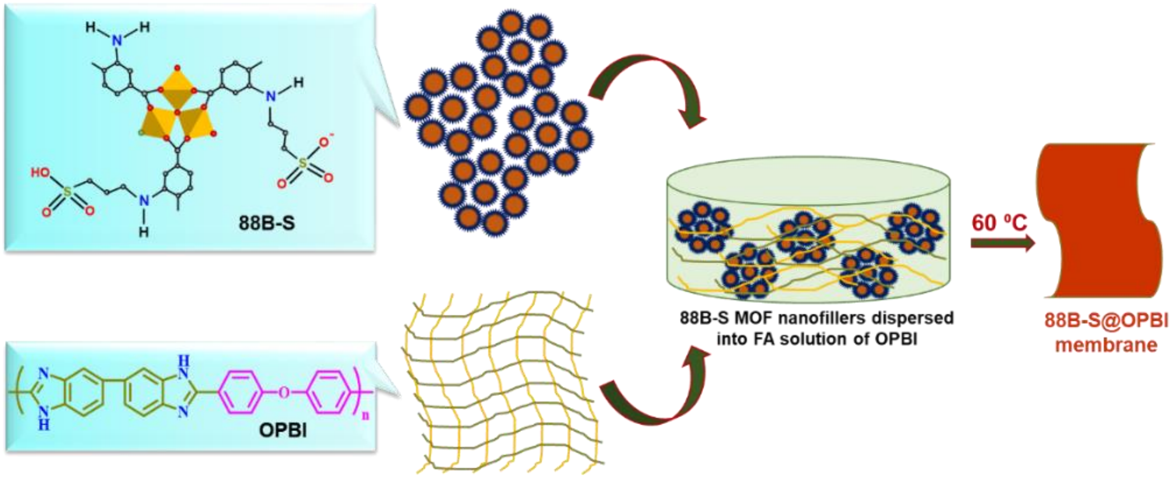

Figure 1.3. Schematic representation of the fabrication of **53-S@OPBI** and **88B-S@OPBI** MMMs.[94]

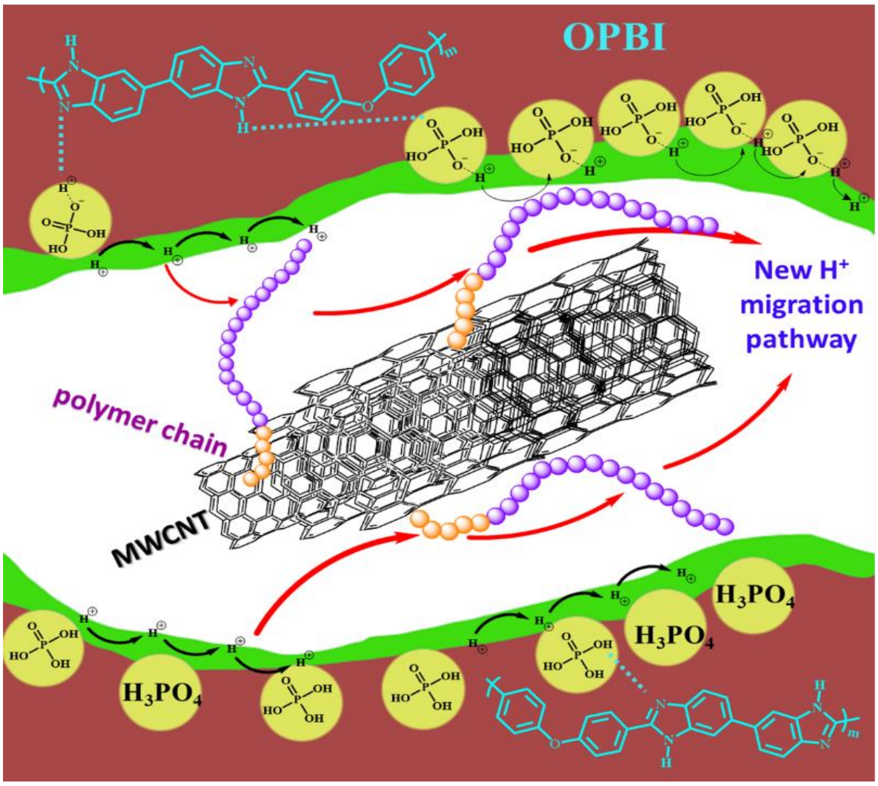

Figure 1.4. Schematic diagram of preparation of SI-RAFT initiated surface polymer *grafted* MWCNT loaded PGNT@OPBI nanocomposite membrane.[96]

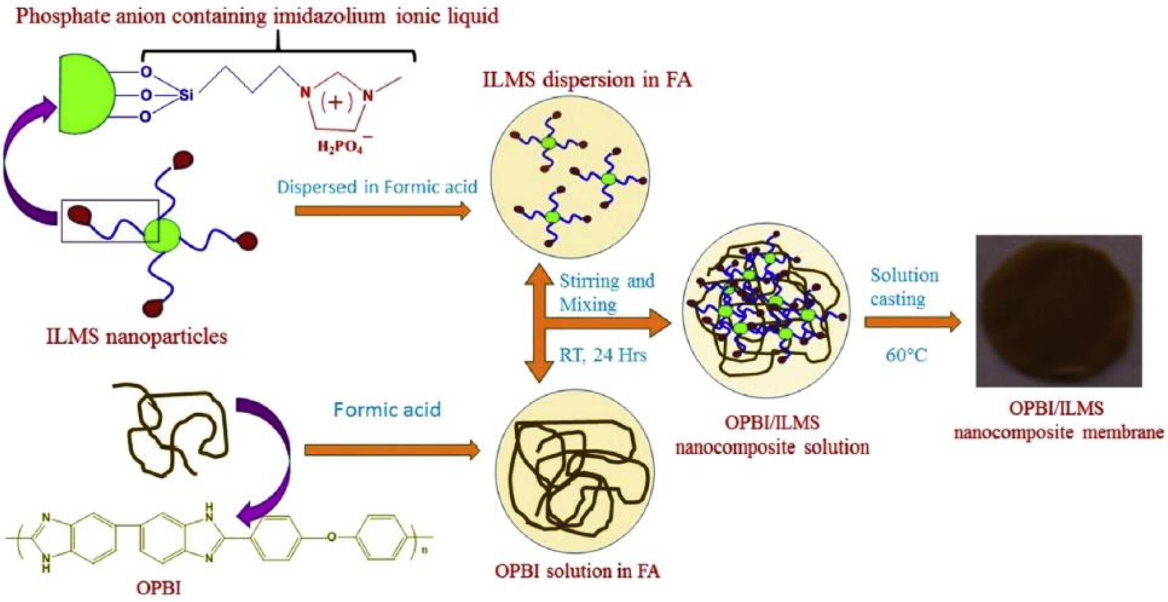

Figure 1.5. Schematic diagram of preparation of OPBI/ILMS nanocomposite membrane.[77]

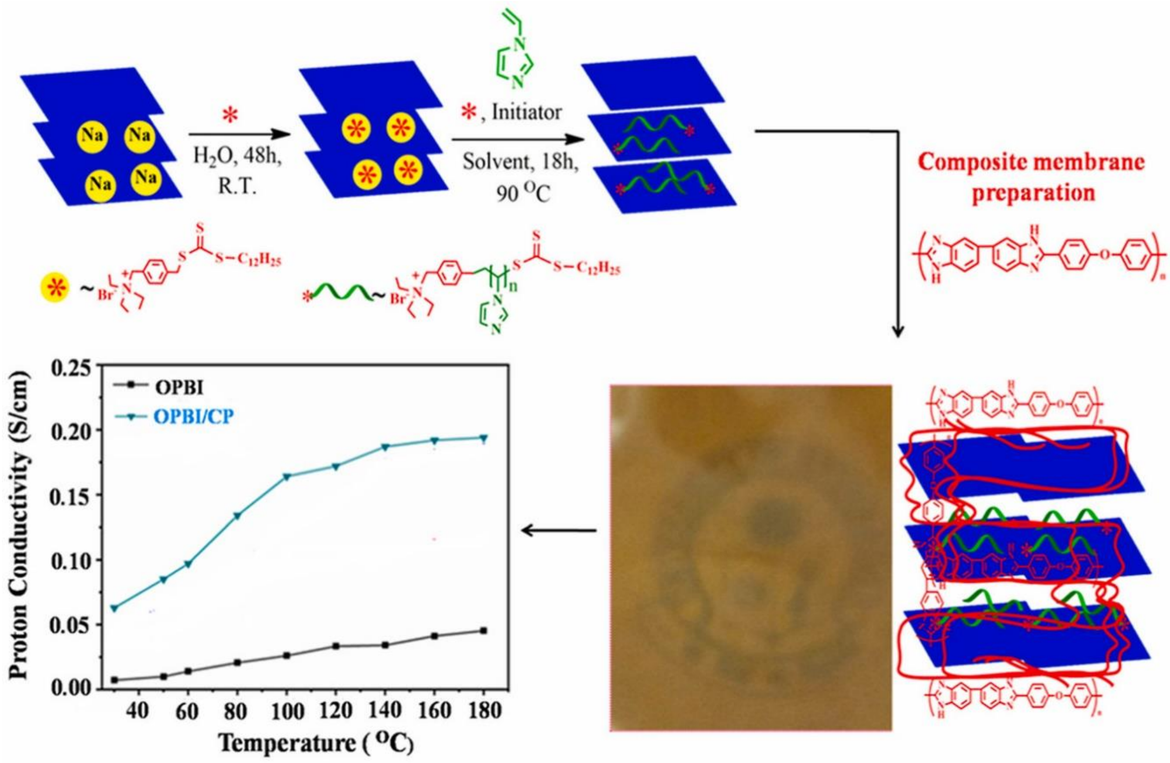

Figure 1.6. Schematic diagram of preparation of SI-RAFT modified surface polymer grafted cloisite nanoclay loaded OPBI nanocomposite membrane.[99]

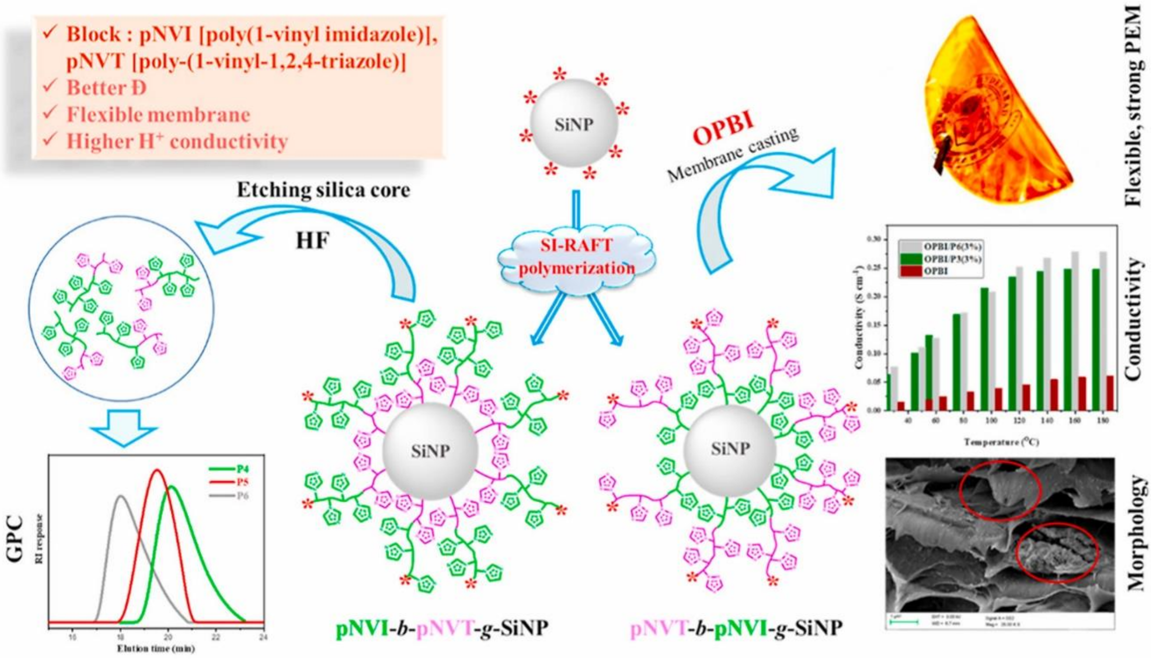

Figure 1.7. Schematic diagram of preparation of pNVI-*b*-pNVT-*g*-SiNP and pNVT-*b*-pNVI-*g*-SiNP loaded OPBI nanocomposite membrane.[74]

Alkaline fuel cell (AFC)

In 1950s, the AFC technology has been introduced by NASA Apollo space program which is still utilized for today's shuttle missions. Researchers around the globe started focusing on AFCs for various other applications. In the 1970s Kordesch,[100] built a car, which works under AFC when combined with a lead-acid battery. The AFC was the first ever introduced fuel cell technology to be developed towards practical application in the 20th century. In AFC, aqueous potassium hydroxide (KOH) used as an electrolyte in which hydroxide ions in an alkaline electrolyte solution passes from cathode to anode (Figure 1.8), which is entirely reverse directional when compared to PEMFCs. The operational condition of AFC is relatively low temperature varying from 20 °C to 80 °C which offers less thermal and chemical degradation.[101–104] The anode and cathode cell reactions and AFC diagram are presented in the Figure 1.8.

Cell reaction

At Anode: $2H_2 + 4OH^- \rightarrow 4H_2O + 4e^-$

At Cathode: $O_2 + 2H_2O + 4e^- \rightarrow 4OH^-$

Overall cell: $2H_2 + O_2 \rightarrow 2H_2O$ **+ electrical energy + heat**

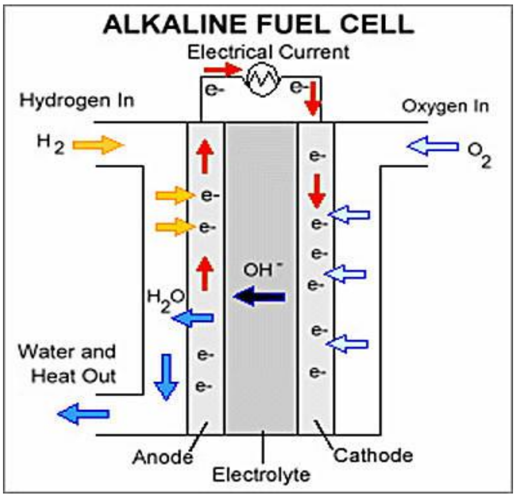

Figure 1.8. Schematic representation of the general fuel cell diagram. (Image adopted from google)

Drawbacks of AFC

In AFC, the liquid solution of electrolyte (aqueous KOH) has been the major cause of concerns. Generally, in AFC highly concentrated alkaline solution (6 M KOH) used as electrolyte which has more affinity towards CO_2 from the air and hence resulted in the generation of carbonates or bicarbonate ions under the carbonate process as shown below.[105,106]

$$CO_2 + 2OH^- \rightarrow CO_3^{2-} + H_2O$$

$$CO_2 + OH^- \rightarrow HCO_3^-$$

Hence, the number of hydroxide ions availability decreases and CO_3^{2-} or HCO_3^- ions are increases at the electrode. The mobility of CO_3^{2-} or HCO_3^- ions is slower than OH^- ions which results in the decrease in conductivity of OH- ion thus reducing the fuel cell performance. Furthermore, carbonate deposition can result in a precipitate that resulted blocking of micro pores of the electrodes which results further decrement in the AFC performance.[107,108] Management of corrosion problem under operational FC is also quite challenging as the KOH electrolyte is prone to degrade most of the materials. Therefore, all the necessary materials needed for the electrolyte fabrication needs to be highly stable which can introduce higher cost for the operation. The performance of AFC also depends upon the amount of added electrolytes, less amount of liquid electrolytes can dry the electrode, while the excess flow of liquid electrolyte may cause flooding of the electrode.

Anion exchange membrane fuel cell (AEMFC)

In order to address the above mentioned drawbacks, the researchers have started developing the anion exchange membrane fuel cell (AEMFC) by introducing anion conducting solid polymer electrolytes or membrane materials to replace the KOH solution as liquid electrolyte. In this design, the solid polymer electrolyte membrane (ion conducting membranes) acts as separator materials between the anode and cathode. In this design membrane is sandwiched between the two electrodes which include the gas diffusion layer along with the catalyst layer. The reaction scheme associated with the solid electrolyte fuel cell is quite similar to the liquid fuel cell. The oxygen reduction and hydrogen oxidation can take place at the cathode and the anode, respectively.[101,103]

In the working principle (Figure 1.9), the functioning of AAEMFC occurs using H_2 as fuel and O_2 as oxidant. In the AEMFC, during the electrochemical oxygen reduction, generation of hydroxide ions occurs at the cathode. The transportation of OH^- ions from cathode to anode through the anion conducting polymer electrolyte where in the OH^- ions remains combined with H_2 to form water molecules. The generation of electrons during the hydrogen oxidation passes through the external circuit to the cathode where the process of the electrochemical reduction of oxygen to form hydroxyl ions occurs through the electrons participations.

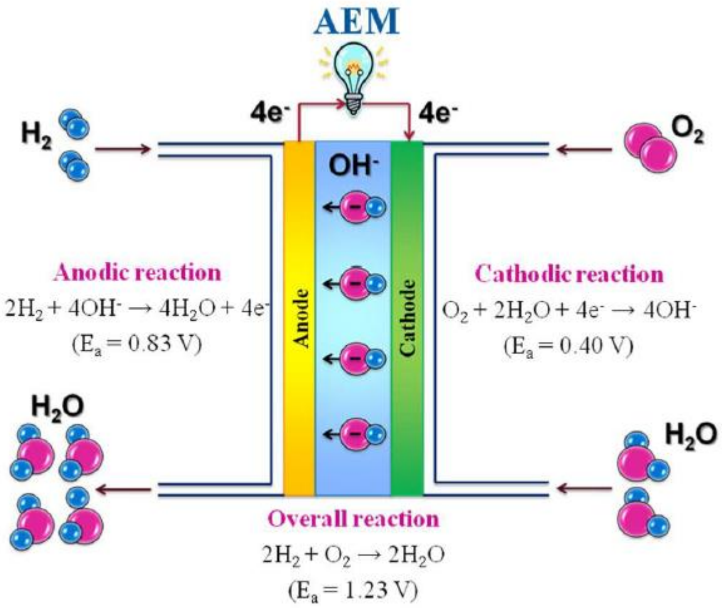

Figure 1.9. Schematic representation of the anion exchange membrane fuel cell (AEMFC) diagram. (Adapted from Hadis Zarrin thesis from University of Waterloo)

Advantages of AEMFC over PEMFC

- ✓ Use non precious metal catalyst ex, Co, Ni.[109]
- ✓ Cost effective and very easy to handle.
- ✓ The operational temperature is relatively low (60 °C – 80 °C).[109]
- ✓ Higher reaction kinetics at the electrodes than that of PEMFC.
- ✓ Higher cell voltage.
- ✓ Low gas crossover.

Disadvantages of AEMFC compare to PEMFC

- ✓ The OH^- ions conducted in the AEMFC is larger size compared to a proton H^+ conducting PEMFC resulting in lower mobility of the former one.[110]
- ✓ The hydroxide ionic conductivity highly depends on humidified condition, without humidification OH^- ions are unable to conduct, which limits their wide applications.[111]
- ✓ AEM shows low ionic conductivity and instability than PEM.

Desired properties of anion exchange membrane (AEM)

The efficiency of AAEMFC can be affected by several factors. AEM is considered as the core component of AAEMFC. An efficient AAEM should have these listed qualities:

- ✓ The AEM should tethered at least one cationic site or anion exchange site for hydroxide conduction. Various types of cationic sites are reported in the literature. They are 1) quaternary ammonium groups (QA),[112] & N-Spirocyclic QAs[113,114] 2) imidazolium or benzimidazolium based systems,[109,115,116] 3) pyridinium,[117] 4) guanidinium,[118] 5) phosphonium[119] 6) sulfonium[120] types and 7) metal-based systems.
- ✓ The membrane must retain their thermal and chemical stability under harsh alkaline conditions at elevated temperature.
- ✓ Polymer backbones and cationic sites should be mechanically stable in order to prepare mechanically durable membranes for operational AEMFC.
- ✓ AEM should produce high hydroxide ionic conductivity.
- ✓ The AEM electrolyte ion conductivity must be high under variant temperature along with altered humidity.
- ✓ The AEM should act as electronic insulators and also should acts as a barrier to prevent fuel cross over along the membrane.
- ✓ The fabrication strategy of the membranes should be cost effective.

Different cationic functional groups (anion exchange sites) and polymer backbones have been utilized and established in literature as efficient AAEMs.[101,102,107,108] The structure of these cationic sites are shown in **Scheme 1.3.**

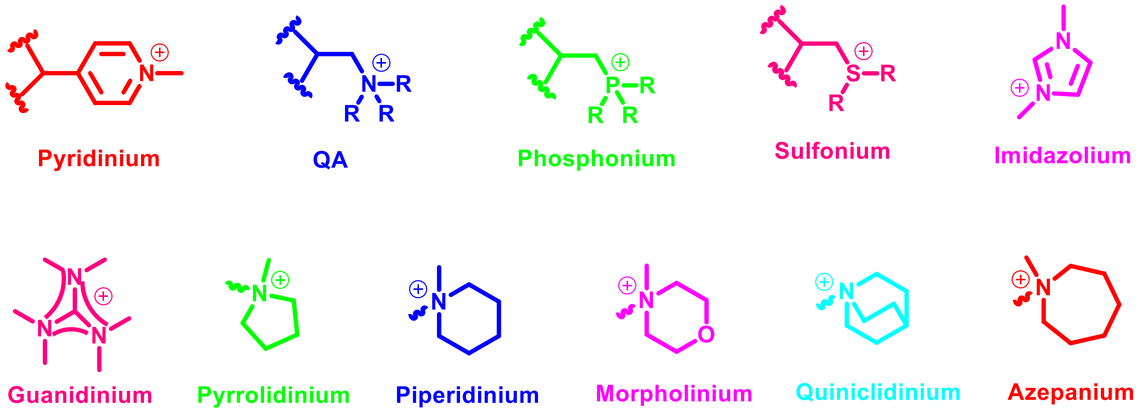

Scheme 1.3. Structures of cationic groups used as anion exchange sites in AAEM. (Ref 101, 102, 107, 108

AAEM based on quaternary ammonium (QA) cation

In order to develop QA based AAEM polymer backbones functionalization with QA groups is the widely utilized feasible strategy to introduce any tethered cationic functionalities.

Initially, it was considered that the QA groups containing AAEM are chemically more stable than the other cationic groups. Unfortunately, QA groups are degraded by hydroxide ion (OH-) nucleophilic attack and showed severe drawbacks The degradation in quaternary ammonium cation has been seen by nucleophilic substitution of hydroxide ion, Hofmann elimination and chloromethylation (Scheme 1.4).[121–123]

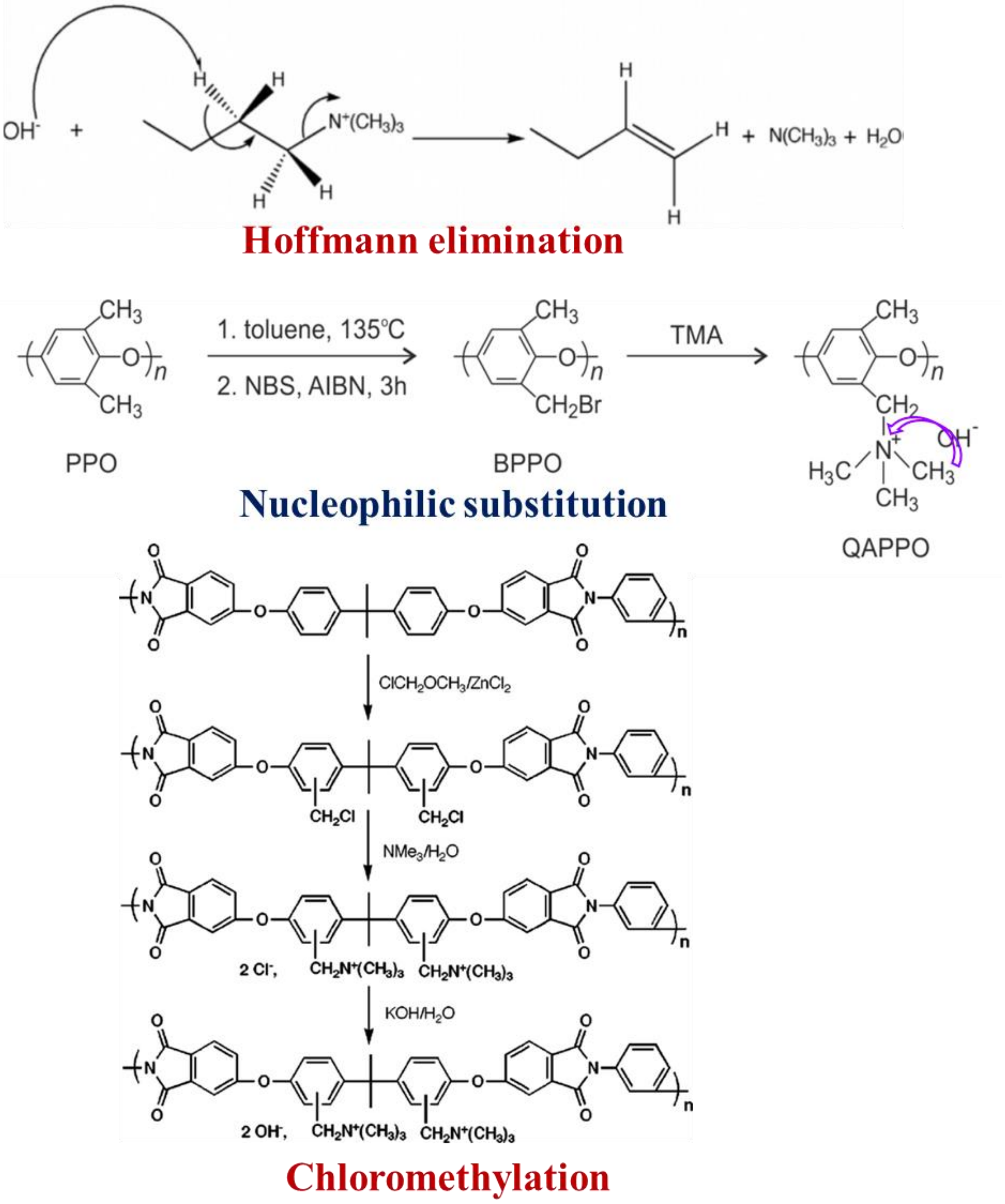

Scheme 1.4. Schematic representation of the various issues associated with QA based AAEM.[122,123]

A comparative study of tethered cycloaliphatic ring containing nitrogen atom on polyphenylene oxide was studied by Jannasch and co-workers, from which it has been found that the alkaline stability is affected by the factors like ring size as well their positions (**Scheme 1.5**). In addition, it was concluded that rings possessing low strain like piperidinium, pyrrolidine do not suffer degradation while large membered ring like azepanium degraded under alkaline conditions which was confirmed by ^{1}HNMR.[124]

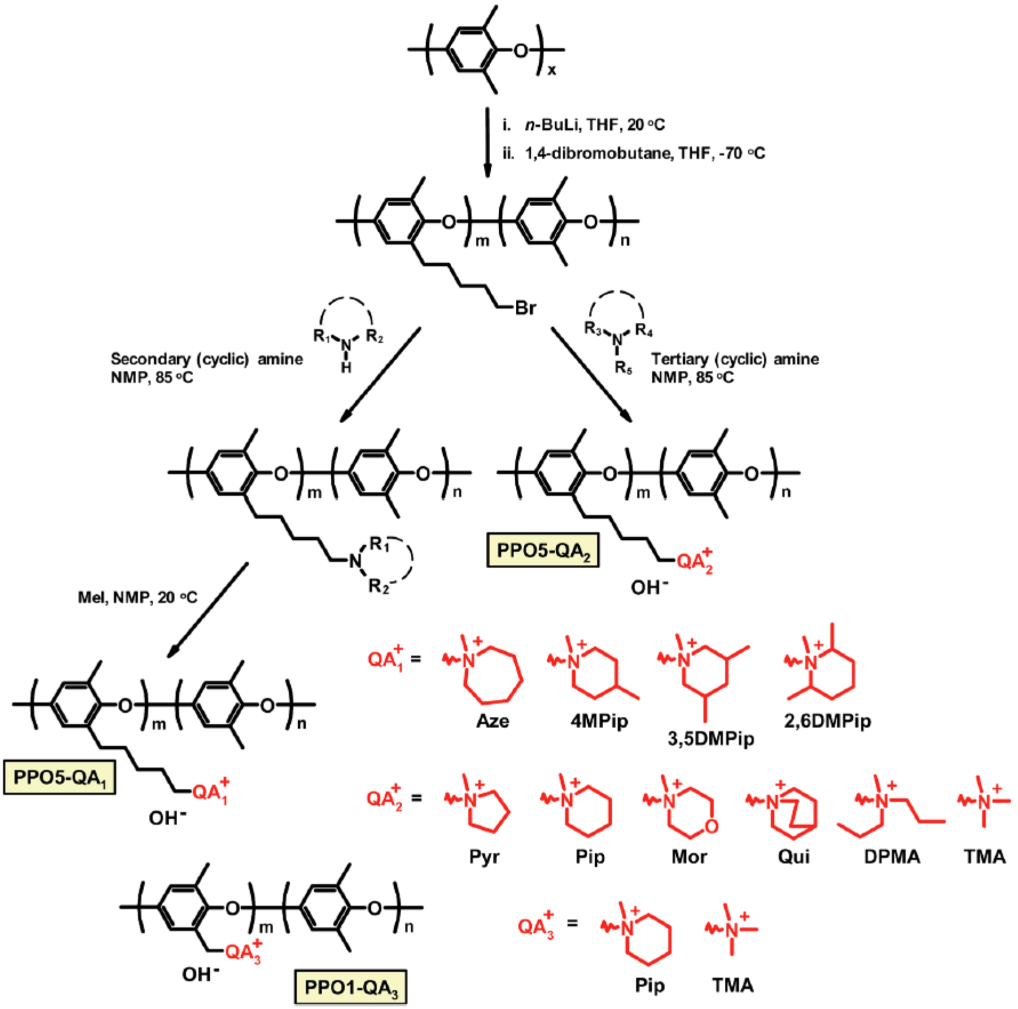

Scheme 1.5. Structures of various cycloaliphatic QA cationic groups of different ring sizes used as anion exchange sites in polyphenylene oxide based AAEM.[124]

Pyridinium and Imidazolium based AAEMs

Huang's and Xiuhua's groups have shown that the pyridinium based AAEMs may not be very suitable because these membranes show low ionic conductivity and are not stable in alkaline medium because of the irreversible formation of pyridone from pyridinium group in the presence of oxygen at high temperature (Scheme 1.6).[125,126] Later, Kallitisis and co-workers suggested that degradation in pyridinium moiety can be reduced by using 2,6-substituted pyridine based monomers.[117]

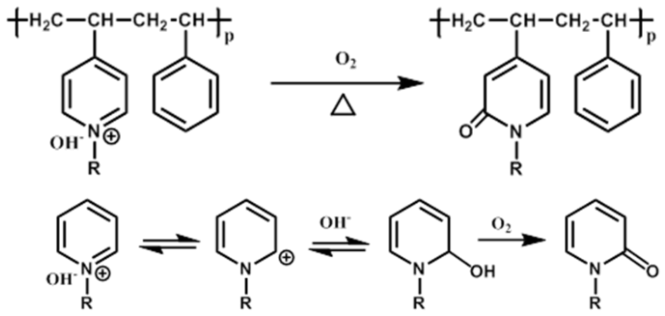

Scheme 1.6. Degradation of pyridinium site to pyridone.[125]

AAEM containing imidazolium groups also undergo degradation via nucleophilic attack of hydroxide ion on C2 position. To improve alkaline stability and better efficiency, Fang' and co-workers synthesized the imidazolium containing AAEMs which resulted good thermal and chemical stability in comparison to that of quaternary ammonium based AAEM.[127] AAEM containing PBI has been showed good ion conductivity but low ion exchange capacity was the obstacle in it. Later on, Henkensmeier and co-workers suggested that the alkaline stability can be improved further and studied the degradation mechanism.[128] Recently, our group have developed the AAEM by creating twin hydroxide conducting sites which includes imidazolium and pyridinium into the same polymer backbone which does not suffer the pyridone formation and proved to achieve moderate hydroxide conductivity and alkaline stability (Scheme 1.7).[116]

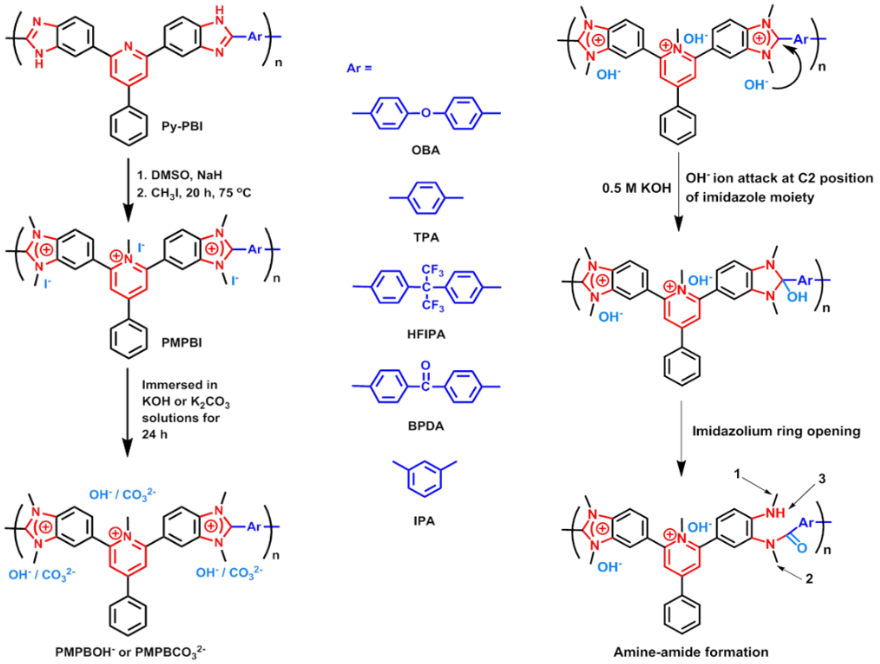

Scheme 1.7. Synthesis of PMPBI membrane and degradation of imidazolium site by nucleophilic attack of OH- ion at C2 position.[116]

Imidazolium cation degrades via different pathways like ring-opening reaction, heterocyclic deprotonations, substituents deprotonation, nucleophilic substitution. To prevent this degradation, scientists came up with the idea of substituting the C2-position of the imidazolium cationic sites with several moieties like methyl, ethyl, aryl etc. Among these aryl group having bulkier size will give utmost stability by hindering the proximity for attacking nucleophile.[129] Coates et al. have reported stable cationic moieties under harsh alkaline condition as a critical component AAEM for their application in alkaline fuel cells (AFCs); though, the commonly employed organic cations are prone to exhibit limited alkaline stability. In order to mitigate this problem, they have synthesized and checked the stability of the synthesized imidazolium cations in 1, 2, or 5 M KOH/CD_3OH at 80 °C (Scheme 1.8) in order to evaluate the effect of substituted alkylated moieties in the imidazolium backbone to enhance the alkaline stability of the imidazolium cationic functionalities.[130] The substituent identity at each position of the imidazolium ring has a dramatic effect on the overall cation stability. They have reported exceptionally stable imidazolium cations with superior alkaline stabilities (>99% cation remaining after 30 days in 5 M KOH/CD_3OH at 80 °C).[130] Another idea has been impregnated to block the imidazolium C2-position with bulky mesitylene group. The aliphatic methyl groups completely hinder the approach the nucleophile.[129]

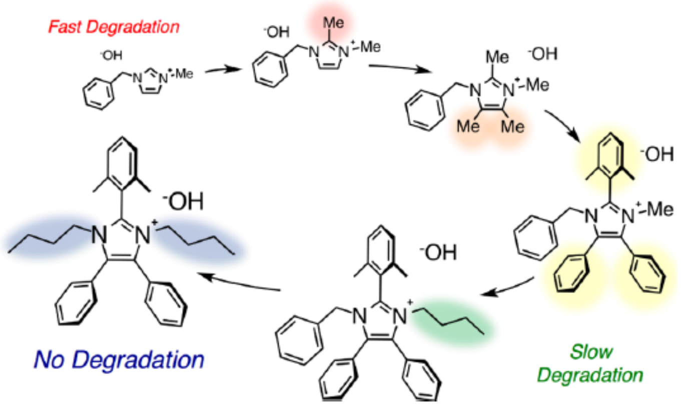

Scheme 1.8. Schematic strategy for prevention of imidazolium cation degradation.[130]

Our group recently reported, the effect of different alkyl group structure on the various properties improvement especially the hydroxide conductivity and alkaline stability of the AAEM with dual anion exchange sites consisting of imidazolium and pyridinium. Three different types of polymers namely PBI, PyPBI and t_{But}-PyPBI were converted to their iodide forms following base induced alkylation treatment of the imidazole ring by reacting with different kinds of alkyl iodides such as the methyl iodide (MeI), butyl iodide (BuI) and isobutyl iodide (IbuI). After that, all the iodide (I^-) forms polybenzimidazolium based membranes were converted into OH^- form membranes in order to develop OH^- ion conducting AAEMs by immersing them in 1 M KOH solution (Scheme 1.9).[115]

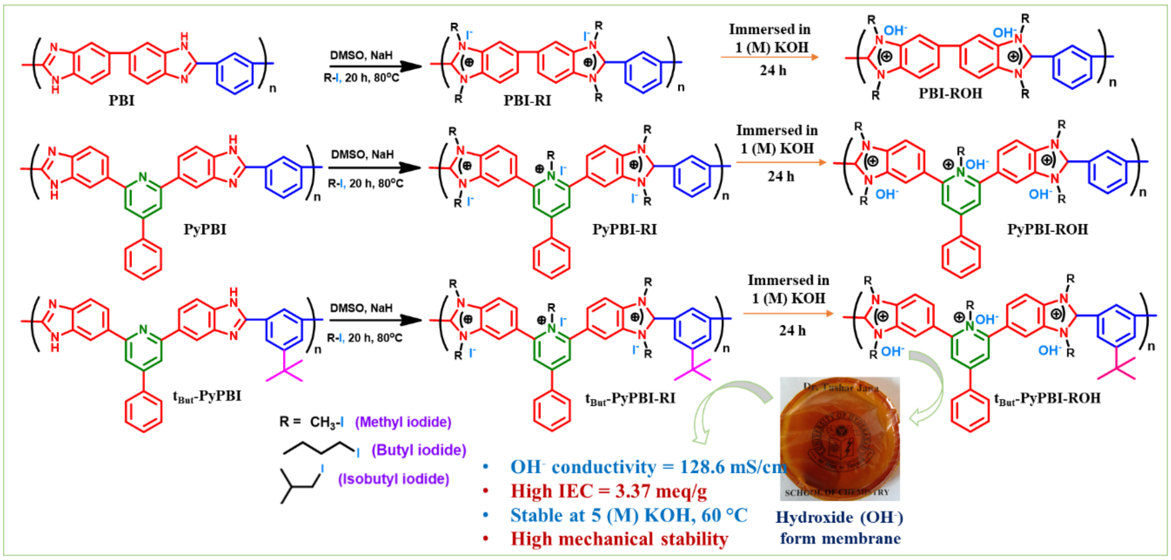

Scheme 1.9. Synthetic pathway of PyPBI-RI and PyPBI-ROH.[115]

The important observation noted from this study are:

- Among the alkylated polymer structures, PyPBI-BuI membrane showed the highest IEC 3.37 meq/g (at 1 M KOH) with maximum hydroxide conductivity of 128.6 mS/cm at 80 °C.
- Development of twin hydroxide conducting cationic sights by introducing pyridinium and imidazolium in a same AAEM backbone, and the electrophilic centres (2, 4 and 6 positions) surrounded the pyridinium groups prevents the natural pyridone formation due to the induced steric and electronic factors.
- All the PBI based polymer backbone structure when alkylated with butyl and isobutyl chain exhibited exceptional alkaline stability even in 5 M KOH aqueous solution at elevated temperature (60 °C), for prolong treatment period of 21 days without any noticeable degradation (<1%). The bulky nature of the alkylated side chains responsible for increasing steric factors, which prevents the OH^- attacks on both the imidazolium and pyridinium groups.
- DFT & molecular simulation studies also confirmed, structural and geometrical aspects along with electronically induced factors are the significantly responsible factors for such exceptional alkaline stability in case of butyl, isobutyl alkylated chains particularly in case of PyPBI and t_{But}-PyPBI.

AAEM for water electrolysis

AAEM can also be utilized in alkaline water electrolysis to produce green hydrogen. Alkaline water electrolysis (AEL) is a well-known proven for green hydrogen production, in this technique water splits into the formation of hydrogen and oxygen using electrical renewable energy.[103,104,131,132] The purpose associated with the membrane based AEL treatment is to separate the cathode loop (catholyte) from the anode loop (anolyte) in presence of electrolyte solution or a fluid, by avoiding any secondary unwanted reaction, so as to combine the electrode reaction with a separation step or to isolate separately the products formed on the electrode. The chemical reactions of AEM based electrolysis are represented in the cell reaction portrayed here. At the cathode side, the water molecules are get reduced by the electrons to generate H_2 and negatively charged OH^- ions. While, in the anode electrode, OH^- ions gets oxidized to form O_2 and water molecules while releasing electrons. Overall, a water molecule reacts to H_2 and O_2 in the ratio of 2:1 (Figure 1.10).[133]

Cell reaction

Cathode: $4H_2O + 4e^- \longrightarrow 2H_2 + 4OH^-$

Anode: $4OH^- \longrightarrow O_2 + 2H_2O + 4e^-$

Overall reaction: $2H_2O \longrightarrow 2H_2 + O_2$

The developed designs and models of the AEL stacks depends on the manufacturer; however, it contains some general similarities. Earlier models of alkaline water electrolyzers generally used a conventional assembled system with a defined distance between both electrodes. Later, this concept was replaced and developed by fabrication of the zero-gap assembly in the AEL stack, where the electrodes are directly pressed onto the separator to minimize ohmic loss associated with the electrolyte. Porous materials like Zirfon™ Perl UTP 500, dense AAEMs, cross-linked porous AAEMs can be used as the separator.[104,133]

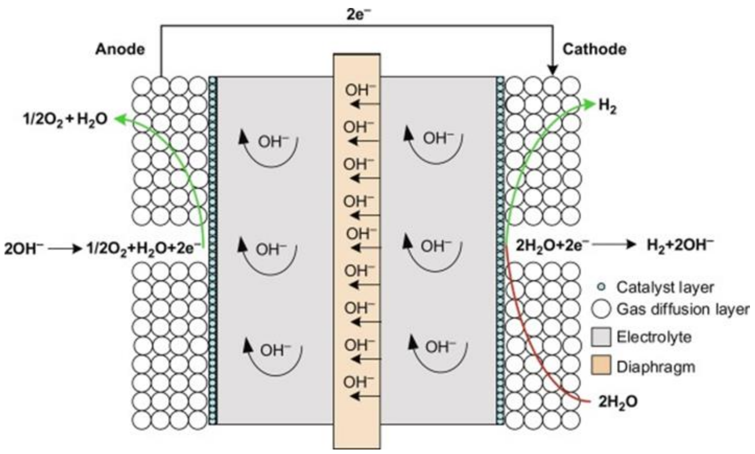

Figure 1.10. Membrane based Alkaline water electrolysis for H_2 generation (adapted from google).

RAFT Polymerization

In the modern world, 50% of the commercial polymerization are performed by free radical polymerization (FRP) method, and this process have been utilized extensively in the academics and industrial sectors.[134] But due to the high reactivity associated with the propagating radicals, bimolecular transitions, and other additional side reactions resulted higher molecular weight polymers, and hence the FRP technique kept restrained for various applications. Now, if we consider about Living anionic polymerization (LAP) technique, in this process the targeted molecular weight of the polymers is achievable with high degree accuracy with well controlled molar mass and distribution, but the high sensitivity towards formation of impurities results quick chain termination, which restricts this process utility than that of radical process polymerization.[135] In fact, due to the generation of overall low yield, difficult operational set up, long term reaction duration related issues associated with the ring opening polymerization (ROP) technique is also not much feasible polymerization technique.[136] Researchers have tirelessly worked in the process to develop efficient polymerization techniques over the years where these present issues can be mitigated. In this regard, controlled radical polymerization (CRP) technique is a versatile polymerization strategy. CRP technique allows the researchers to develop various architecture and functionalities induced polymers with well obtained molar mass and narrow polydispersity index (PDI). Nitroxide mediated polymerization (NMP), [21] Atom transfer radical polymerization (ATRP),[137,138] and reversible addition fragmentation chain transfer (RAFT) polymerization,[139,140] these are the three most widely utilized CRP techniques by researchers across the globe. Because of presence of vast number of advantages associated with the RAFT technique over the other methods, RAFT has emerged as a most useful strategy in modern era for the development of simple structures to variety of complex structures like star, graft, gradient, block, multiblock, comb copolymers, hyperbranched etc. (Figure.1.11).[141]

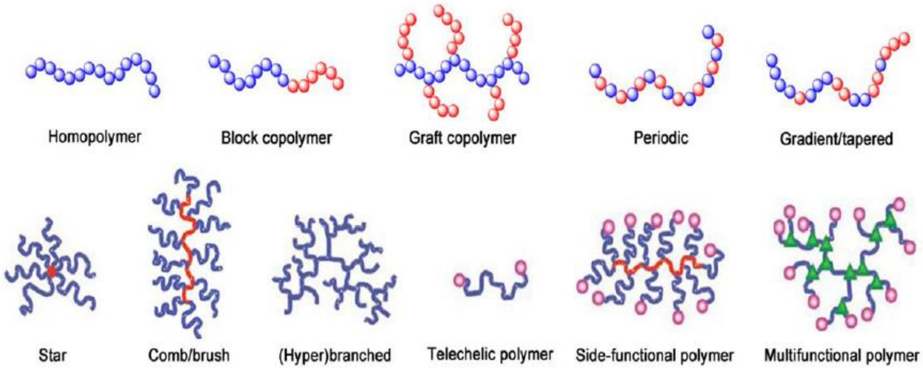

Figure 1.11. Different macromolecular structures developed from RAFT polymerization.[141]

Aim of the thesis.

The current thesis elaborates the detailed fabrication techniques and detailed characterization procedures of the PBI-MOF, PBI-COF, PBI-GO nanocomposite mixed matrix membranes (MMMs) for their utilization as efficient PEMs for the PEMFC. In addition, the thesis demonstrates the synthesis of ionically crosslinked blends and nanocomposite AAEMs for their efficient utilization in the AAEMFC, alkaline water electrolysis and various other electrochemical devices. **Chapter 1** is the introductory chapter, which demonstrates the working principle of the PEMFC, AAEMFC, alkaline water electrolysis, various fabrication techniques of PBI based blends and nanocomposite membranes and a brief discussion about the surface initiated RAFT polymerization techniques. **Chapter 2** explains the detailed characterization methods of the various types of samples and fabricated membranes (both AEMs and PEMs) included in the thesis. In the **Chapter 3,** post synthetically modified (PSM) UiO-66-NH_2 MOFs (PSM1 & PSM2) were incorporated into the OPBI matrix in order to fabricate efficient PBI-MOF nanocomposite MMMs, their super proton conductivity and various other membrane based properties improvements were discussed thoroughly. In the **Chapter 4,** phosphoric acid impregnated melamine based Schiff base network type covalent organic framework (COF) materials have been incorporated in the PBI matrix in order to develop super proton conducting PBI-COF nanocomposite PEMs. In the **Chapter 5,** SI-RAFT initiated polymer-g-GO materials have been incorporated into the OPBI matrix in order to fabricated OPBI@GOP nanocomposite membranes with remarkably high proton conductivity and mechanical durability for their utilization in the PEMFC. **Chapter 6** demonstrates the synthesis and characterizations of ionically crosslinked (ICL) non porous and porous blended AAEMs for their potential application in the alkaline water electrolysis treatment. In the **Chapter 7,** SI-RAFT initiated polymer-g-GOPILs have been incorporated into the alkylated PyPBI-BuI matrix in order to develop mechanically robust nanocomposite mixed matrix anion exchange membranes with high OH^- conductivity for their utilization in the AAEMFC. **Chapter 8** summaries all the important findings of the current thesis work with a concluding remarks and demonstrates the future scopes of various scientific findings associated with this thesis. The more detailed objectives of each working chapter is included in the introductory part of each individual chapters.

References:

(1) Yeager, E. *Science* **1961**, *134*, 1178.

(2) *Fuel Cell Handbook, 6th Edition, EG & G Technical Services, Inc. U. S. Department of Energy;* November, **2002**.

(3) Rikukawa, M.; Sanui, K. *Prog. Polym. Sci.* **2000,** *25*, 1463-1502.

(4) Peighambardoust, S. J.; Rowshanzamir, S.; Amjadi, M. *Int. J. Hydrogen Energy* **2010**, *35*, 9349–9384.

(5) Kraytsberg, A.; Ein-Eli, Y. *Energy and Fuels* **2014**, *28*, 7303–7330.

(6) Daud, W. R. W.; Rosli, R. E.; Majlan, E. H.; Hamid, S. A. A.; Mohamed, R.; Husaini, T. *Renew. Energy* **2017**, *113*, 620–638.

(7) Walkowiak-Kulikowska, J.; Wolska, J.; Koroniak, H. *Phys. Sci. Rev.* **2017**, *2*, 1–36.

(8) You, W.; Noonan, K. J. T.; Coates, G. W. *Prog. Polym. Sci.* **2020**, *100*, 101177.

(9) Stambouli, A. B.; Traversa, E. *Renewable & Sustainable Energy Reviews* **2002**, *6*, 433–455.

(10) Antolini, E. *Appl. Energy* **2011**, *88*, 4274–4293.

(11) Mistry, E. *Journal of Appl. Electrochemistry* **1992**, *22*, 995–1001.

(12) Hickner, M. A.; Ghassemi, H.; Kim, Y. S.; Einsla, B. R.; Mcgrath, J. E. *Chem. Rev.* **2004,** *104*, 4587–4612

(13) Kerres, J. A. *J. Membr. Sci.* **2001**, *185*, 3–27.

(14) Li, Q.; He, R.; Jensen, J. O.; Bjerrum, N. J. *Chem. Mater.* **2003,** *15*, 4896–4915

(15) Roziére, J.; Jones, D. J. *Annu. Rev. Mater. Res.* **2003**, *33*, 503–555.

(16) Maier, G. Haack, J. M.; Sulfonated Aromatic Polymers for Fuel Cell Membranes. Advances in polymer science book series (POLYMER,volume 216)

(17) Osborn, S. J.; Hassan, M. K.; Divoux, G. M.; Rhoades, D. W.; Mauritz, K. A.; Moore, R. B. *Macromolecules* **2007,** *40*, 3886–3890

(18) Kreuer, K. *Chem. Mater***.** **1996,** *8*, 610–641.

(19) Satterfield, M. B.; Majsztrik, P. W.; Ota, H.; Benziger, J. A. Y. B.; Bocarsly, A. B. *Journal of Polymer Science: Part B: Polymer Physics*, **2006,** *44*, 2327–2345.

(20) Thompson, E. L.; Capehart, T. W.; Fuller, T. J.; Jorne, J. *J. Electrochem. Soc.* **2006**, *153*, A2351

(21) Wu, L.; Zhang, Z.; Ran, J.; Zhou, D.; Li, C.; Xu, T. *Phys. Chem. Chem. Phys.* **2013**, *15*, 4870–4887.

(22) Vogel, H.; Marvel, S. Journal of polymer science. **1961**, *50*, 511–539.

(23) Vogel, H.; Marvel, C. S. *J. Polym. Sci. A* **1963**, *1*, 1531.

(24) Chen, B.; Luan, D.; Jiao, G.; Zhao, D.; Zhu, Y. *Front. Chem. China* **2009**, *4*, 207–209.

(25) Xiao, L.; Zhang, H.; Jana, T.; Scanlon, E.; Chen, R.; Choe, E. W.; Ramanathan, L. S.; Yu, S.; Benicewicz, B. C. *Fuel Cells* **2005**, *5*, 287–295.

(26) Xiao, L.; Zhang, H.; Scanlon, E.; Ramanathan, L. S.; Choe, E. W.; Rogers, D.; Apple, T.; Benicewicz, B. C. *Chem. Mater.* **2005**, *17*, 5328–5333.

(27) Savinell, R.; Yeager, E.; Tryk, D.; Landau, U.; Wainright, J.; Weng, D.; Lux, K.; Litt, M.; Rogers, C. *J. Electrochem. Soc.* **1994**, *141*, L46–L48.

(28) Sannigrahi, A.; Arunbabu, D.; Murali Sankar, R.; Jana, T. *Macromolecules* **2007**, *40*, 2844–2851.

(29) George, G. *Int J Plast Technol*. **2012,** *16*, 101–116.

(30) Li, Q.; Jensen, J. O.; Savinell, R. F.; Bjerrum, N. J. *Prog. Polym. Sci.* **2009**, *34*, 449–477.

(31) Qingfeng, L.; Hjuler, H. A.; Bjerrum, N. J. *J. Appl. Electrochem.* **2001**, *31*, 773–779.

(32) Wainright, J. S.; Wang, J. -T.; Weng, D.; Savinell, R. F.; Litt, M. *J. Electrochem. Soc.* **1995**, *142*, L121–L123.

(33) Berkelbach, T. C.; Lee, H.; Tuckerman, M. E. *Phys. Rev. Lett.* **2009,** *103*, 238302.

(34) Plummer. L.; Marvel, C. S. *J. Polym. Sci. A* **1964**, *2*, 2559.

(35) Geigerflex, R. *Macromolecules* **1986,** *19,* 481–484.

(36) Makowski, P.; Weber, J.; Thomas, A.; Goettmann, F. *Catal. Commun.* **2008**, *10*, 243–247.

(37) Mauritz, K. A.; Moore, R. B. *Chem. Rev.* **2004,** *104*, 4535–4586.

(38) Mehta, V.; Cooper, J. S. *Journal of Power Sources* **2003**, *114*, 32-53.

(39) Iwakura, Y.; Uno, K.; Imai, Y. *J. Polym. Sci. Part A Gen. Pap.* **1964**, *2*, 2605–2615.

(40) Rodrigo, M. A.; Linares, J. J.; Manjavacas, G. *J. Membr. Sci.* **2006**, *280*, 351–362.

(41) Ghosh, S.; Sannigrahi, A.; Maity, S.; Jana, T. *J. Phys. Chem. B* **2010**, *114*, 3122–3132.

(42) Asensio, J. N.; Borros, S.; Gomez-Romero, P. *J. Electrochem. Soc.* **2004**, *151*, A304.

(43) Maity, S.; Jana, T. *Macromolecules* **2013**, *46*, 6814–6823.

(44) Sana, B.; Jana, T. *Polymer.* **2018**, *137*, 312–323.

(45) Singha, S.; Jana, T.; Modestra, J. A.; Naresh Kumar, A.; Mohan, S. V. *J. Power Sources* **2016**, *317*, 143–152.

(46) Wang, K. Y.; Xiao, Y.; Chung, T. *Chemical Engineering Sci.* **2006**, *61*, 5807–5817.

(47) Xu, H.; Chen, K.; Guo, X.; Fang, J.; Yin, J. *Journal of Membr. Sci.* **2007**, *288*, 255–260.

(48) Carollo, A.; Quartarone, E.; Tomasi, C.; Mustarelli, P.; Belotti, F.; Magistris, A. *Journal of power Sources* **2006**, *160*, 175–180.

(49) Chuang, S.; Hsu, S. L. *Journal of Polym. Sci Part A: Polymer Chemistry* **2006**, *44*, 4508–4513.

(50) Maity, S.; Sannigrahi, A.; Ghosh, S.; Jana, T. *Eur. Polym. J.* **2013**, *49*, 2280–2292.

(51) Sannigrahi, A.; Arunbabu, D.; Sankar, R. M.; Jana, T. *J. Phys. Chem. B* **2007**, *111*, 12124–12132.

(52) Qing, S.; Huang, W.; Yan, D. *European Polymer Journal* **2005**, *41*, 1589–1595.

(53) Pu, H.; Liu, Q.; Liu, G. *J. Membr. Sci.* **2004**, *241*, 169–175.

(54) Xiao, L.; Zhang, H.; Scanlon, E.; Ramanathan, L. S.; Choe, E.; Rogers, D.; Apple, T.; Benicewicz, B. C.; York, N. *Chem. Mater.* **2005,** *17*, 5328–5333.

(55) Schechter, A.; Savinell, R. F. *Solid State Ionics* **2002**, *147*, 181–187.

(56) Qian, G.; Benicewicz, B. C. *J. Polymer Science: Part A: Polymer Chemistry*, **2009**, *47*, 4064–4073.

(57) Sampath, U. G.; Ching, Y. C.; Chuah, C. H.; Sabariah, J. J.; Lin, P. C. *Materials* **2016,** *9*, 991.

(58) Mecerreyes, D.; Grande, H.; Miguel, O.; Ochoteco, E.; Marcilla, R.; Cantero, I. *Chem. Mater.* **2004**, *16*, 604

(59) Chen, Z.; Holmberg, B.; Li, W.; Wang, X.; Deng, W.; Munoz, R.; Yan, Y. *Chem. Mater.* **2006,** 18, 5669–5675

(60) Sansone, M. J.; Heights, B.; French, S. M. *U.S. Pat. No. 5,525,436, issued Jun. 11, 1996.*

(61) Onorato et al. *U.S. Pat. No. 5,945,233, issued Aug. 31, 1999.*

(62) Sannigrahi, A.; Ghosh, S.; Jana, T. *Polymer* **2011**, *52*, 4319-4330.

(63) Maity, S.; Jana, T. *ACS Appl. Mater. Interfaces* **2014**, *6*, 6851–6864.

(64) Aili, D.; Yang, J.; Jankova, K.; Henkensmeier, D.; Li, Q. *J. Mater. Chem. A* **2020**, *8*, 12854–12886.

(65) Yu, S.; Xiao, L.; Benicewicz, B. C. *Fuel Cells* **2008**, *8*, 165–174.

(66) Bakangura, E.; Wu, L.; Ge, L.; Yang, Z.; Xu, T. *Prog. Polym. Sci.* **2016**, *57*, 103–152.

(67) Mukhopadhyay, S.; Das, A.; Jana, T.; Das, S. K. *ACS Appl. Energy Mater.* **2020**, *3*, 7964–7977.

(68) Wang, S.; Zhao, C.; Zhang, N.; Zhang, Y.; Zhang, G.; Liu, Z.; Na, H. *J. Mater. Chem. A*, **2013,** *1*, 621-629.

(69) Althues, H.; Henle, J.; Kaskel, S. *Chem. Soc. Rev.*, **2007,** *36*, 1454-1465.

(70) Kickelbick, G. *Prog. Polym. Sci.* **2003,** 28, 83-114.

(71) Verdejo, R.; Bernal, M. M.; Romasanta, L. J.; Lopez-manchado, M. A. *J. Mater. Chem.*, **2011,** *21*, 3301-3310.

(72) Ajayan, B. P. M.; Schadler, L. S.; Giannaris, C.; Rubio, A. *Adv. Mater.* **2000**, *10*, 750–753.

(73) Singha, S.; Jana, T. *ACS Appl. Mater. Interfaces* **2014**, *6*, 21286–21296.

(74) Mukherjee, N.; Das, A.; Dhara, M.; Jana, T. *Polymer* **2021**, *236*, 124315.

(75) Koyilapu, R.; Singha, S.; Kutcherlapati, S. N. R.; Jana, T. *Polymer* **2020**, *195*, 122458.

(76) Kutcherlapati, S. R.; Koyilapu, R.; Jana, T. *J. Polym. Sci. Part A Polym. Chem.* **2018**, *56*, 365–375.

(77) Maity, S.; Singha, S.; Jana, T. *Polymer*. **2015**, *66*, 76–85.

(78) Singha, S.; Jana, T. *Polymer*. **2016**, *98*, 20–31.

(79) Singha, S.; Jana, T. *Polymer*. **2016**, *98*, 20–31.

(80) Koyilapu, R.; Subhadarshini, S.; Singha, S.; Jana, T. *Polymer*. **2021**, *212*, 123175.

(81) Basu, O.; Mukhopadhyay, S.; De, A.; Das, A.; Das, S. K. *Mater. Chem. Front.* **2021**, *5*, 7654–7665.

(82) Escorihuela, J.; Sahuquillo, Ó.; García-Bernabé, A.; Giménez, E.; Compañ, V. *Nanomaterials* **2018**, *8*, 775.

(83) Escorihuela, J.; Narducci, R.; Compañ, V.; Costantino, F. *Adv. Mater. Interfaces* **2019**, *6*,

1801146.

(84) Singha, S.; Koyilapu, R.; Dana, K.; Jana, T. *Polymer*. **2019**, *167*, 13–20.

(85) Sun, H.; Tang, B.; Wu, P. *ACS Appl. Mater. Interfaces* **2017**, *9*, 26077–26087.

(86) Ding, S. Y.; Wang, W. *Chem. Soc. Rev*. **2013**, *42*, 548–568.

(87) Liang, X.; Zhang, F.; Feng, W.; Zou, X.; Zhao, C.; Na, H.; Liu, C.; Sun, F.; Zhu, G. *Chem. Sci*. **2013**, *4*, 983–992.

(88) Ghosh, S.; Maity, S.; Jana, T. *J. Mater. Chem*. **2011**, *21*, 14897–14906.

(89) Yoon, M.; Suh, K.; Natarajan, S.; Kim, K. *Angew. Chemie - Int. Ed*. **2013**, *52*, 2688–2700.

(90) He, R.; Li, Q.; Xiao, G.; Bjerrum, N. J. *J. membr. Sci*. **2003**, *226*, 169–184.

(91) Staiti, P.; Minutoli, M.; Hocevar, S. *J. Power Sources* **2000**, *90*, 231–235.

(92) Zaidi, S. M. J. *Electrochim. Acta*. **2005**, *50*, 4771–4777.

(93) Shao, H.; Shi, Z.; Fang, J.; Yin, J. *Polymer* **2009**, *50*, 5987–5995.

(94) Basu, O.; Das, A.; Jana, T.; Das, S. K. *ACS Appl. Energy Mater. DOI* : 10.1021/acsaem.2c02972

(95) Diaz-Abad, S.; Fernández-Mancebo, S.; Rodrigo, M. A.; Lobato, J. *Membranes*. **2022**, *12*, 116.

(96) Mukherjee, N.; Das, A.; Jana, T. *ACS Appl. Nano Mater*. **2022** (Article ASAP).

(97) Ghosh, S.; Sannigrahi, A.; Maity, S.; Jana, T. *J. Phys. Chem. C* **2011**, *115*, 11474–11483.

(98) Hazarika, M.; Jana, T. *Compos. Sci. Technol*. **2013**, *87*, 94–102.

(99) Singha, S.; Jana, T. *Polymer*. **2016**, *98*, 20–31.

(100) Kordesch, K. J. *Electrochem. Soc*. **1971**, *118*, 812.

(101) Merle, G.; Wessling, M.; Nijmeijer, K. *J. Membr. Sci*. **2011**, *377*, 1–35.

(102) Varcoe, J. R.; Slade, R. C. T. *Fuel Cells* **2005**, 2, 187–200.

(103) Hagesteijn, K. F. L.; Jiang, S.; Ladewig, B. P. *J. Mater. Sci*. **2018**, *53*, 11131–11150.

(104) Pushkareva, I. V.; Pushkarev, A. S.; Grigoriev, S. A.; Modisha, P.; Bessarabov, D. G. *Int. J. Hydrogen Energy* **2020**, *45*, 26070–26079.

(105) Cifrain, M.; Kordesch, K. V. *J. Power Sources* **2004**, *127*, 234–242.

(106) Gülzow, E.; Schulze, M. *J. Power Sources* **2004**, *127*, 243–251.

(107) Couture, G.; Alaaeddine, A.; Boschet, F.; Ameduri, B. *Prog. Polym. Sci*. **2011**, *36*, 1521–1557.

(108) Mclean, G. F.; Niet, T.; Djilali, N. *Int. J. Hydrogen Energy* **2002**, *27*, 507–526.

(109) Sana, B.; Das, A.; Jana, T. *ACS Appl. Energy Mater*. **2022**, *5*, 3626–3637.

(110) Hibbs, M. R.; Hickner, M. A.; Alam, T. M.; Mcintyre, S. K.; Fujimoto, C. H.; Cornelius, C. J.; Pennsyl, V. *Chem. Mater*. **2008,** *20*, 2566–2573.

(111) Varcoe, J. R. *Phys. Chem. Chem. Phys*., **2007,** *9*, 1479-1486.

(112) Dong, X.; Xue, B.; Qian, H.; Zheng, J.; Li, S.; Zhang, S. *J. Power Sources* **2017**, *342*, 605–615.

(113) Pham, T. H.; Jannasch, P. *ACS Macro Lett*. **2015,** *4*, 1370–1375.

(114) Das, A.; Sana, B.; Bhattacharyya, R.; Chandra Ghosh, P.; Jana, T. *ACS Appl. Polym. Mater.* **2022**, *4*, 1523–1534.

(115) Sana, B.; Das, A.; Sharma, M.; Jana, T. *ACS Appl. Energy Mater.* **2021**, *4*, 9792–9805.

(116) Sana, B.; Das, A.; Jana, T. *Polymer.* **2019**, *172*, 213–220.

(117) Vöge, A.; Deimede, V.; Kallitsis, J. K. *RSC Adv.* **2014**, *4*, 45040–45049.

(118) Xue, B.; Dong, X.; Li, Y.; Zheng, J.; Li, S.; Zhang, S. *J. Membr. Sci.* **2017**, *537*, 151–159.

(119) Noonan, K. J. T.; Hugar, K. M.; Kostalik, H. A.; Lobkovsky, E. B.; Abruña, H. D.; Coates, G. W. *J. Am. Chem. Soc.* **2012**, *134*, 18161–18164.

(120) Zhang, B.; Gu, S.; Wang, J.; Liu, Y.; Herring, A. M.; Yan, Y. *RSC Adv.* **2012**, *2*, 12683–12685.

(121) Bharath, V. J.; Jervis, R.; Millichamp, J.; Neville, T. P.; Mason, T.; Tjaden, B.; Shearing, P. R.; Brown, R. J. C.; Manos, G.; Brett, D. J. L. *Int. J. Hydrogen Energy* **2017**, *42*, 6243–6249.

(122) Yang, Z.; Peng, H.; Wang, W.; Liu, T. *J. Appl. Polym. Sci.* **2010**, *116*, 2658–2667.

(123) Pan, J.; Zhu, L.; Han, J.; Hickner, M. A. *Chem. Mater.* **2015**, *27*, 6689–6698.

(124) Dang, H. S.; Jannasch, P. A. *J. Mater. Chem. A* **2017**, *5*, 21965–21978.

(125) Huang, A.; Xia, C.; Xiao, C.; Zhuang, L. *J. Appl. Polym. Sci.* ***2006***, 100, 2248-2251.

(126) Li, X.; Yu, Y.; Liu, Q.; Meng, Y. *Int. J. Hydrogen Energy* **2013**, *38*, 11067–11073.

(127) Guo, M.; Fang, J.; Xu, H.; Li, W.; Lu, X.; Lan, C.; Li, K. *J. Membr. Sci.* **2010**, *362*, 97–104.

(128) Henkensmeier, D.; Cho, H. R.; Kim, H. J.; Nunes Kirchner, C.; Leppin, J.; Dyck, A.; Jang, J. H.; Cho, E.; Nam, S. W.; Lim, T. H. *Polym. Degrad. Stab.* **2012**, *97*, 264–272.

(129) Thomas, O. D.; Soo, K. J. W. Y.; Peckham, T. J.; Kulkarni, M. P.; Holdcroft, S. *J. Am. Chem. Soc.* **2012**, *134*, 10753–10756.

(130) Hugar, K. M.; Kostalik, H. A.; Coates, G. W. *J. Am. Chem. Soc.* **2015**, *137*, 8730–8737.

(131) Chu, X.; Shi, Y.; Liu, L.; Huang, Y.; Li, N. *J. Mater. Chem. A* **2019**, *7*, 7717–7727.

(132) Faraj, M.; Boccia, M.; Miller, H.; Martini, F.; Borsacchi, S.; Geppi, M.; Pucci, A. *Int. J. Hydrogen Energy* **2012**, *37*, 14992–15002.

(133) Cho, M. K.; Park, H. Y.; Lee, H. J.; Kim, H. J.; Lim, A.; Henkensmeier, D.; Yoo, S. J.; Kim, J. Y.; Lee, S. Y.; Park, H. S.; Jang, J. H. *J. Power Sources* **2018**, *382*, 22–29.

(134) Matyjaszewski, K.; Xia. J. *Chem. Rev.* **2001,** *101*, 2921-2990.

(135) Spencer, C. F.; Stammer, C. H. *J. Am. Chem. Soc.* **1956**, *78*, 2656–2657.

(136) Hu, Y.; Daoud, W. A.; Ka, K.; Cheuk, L.; Sze, C.; Lin, K. *Materials.* **2016**, *9*, 133.

(137) Wang; Shan, J.; Matyjaszewski, K *J. Am. Chem. Soc.* **1995,** *117*, 5614-5615.

(138) Sawamoto, M.; Higashimura, T. *Macromolecules* **1995,** *28*, 1721–1723.

(139) S. Perrier, *Macromolecules* **2017**, *50*, 7433–7447.

(140) John Chiefari, Y. K. (Bill) Chong, Frances Ercole, Julia Krstina, Justine Jeffery, Tam P. T. Le, Roshan T. A. Mayadunne, Gordon F. Meijs, Catherine L. Moad, Graeme Moad,* Ezio Rizzardo, and S. H. T. *Macromolecules* **1998**, *31*, 5559–5562.

(141) Moad, G.; Chong, Y. K.; Postma, A.; Rizzardo, E.; Thang, S. H. *Polymer.* **2005**, *46*, 8458–8468.

Materials & Methods

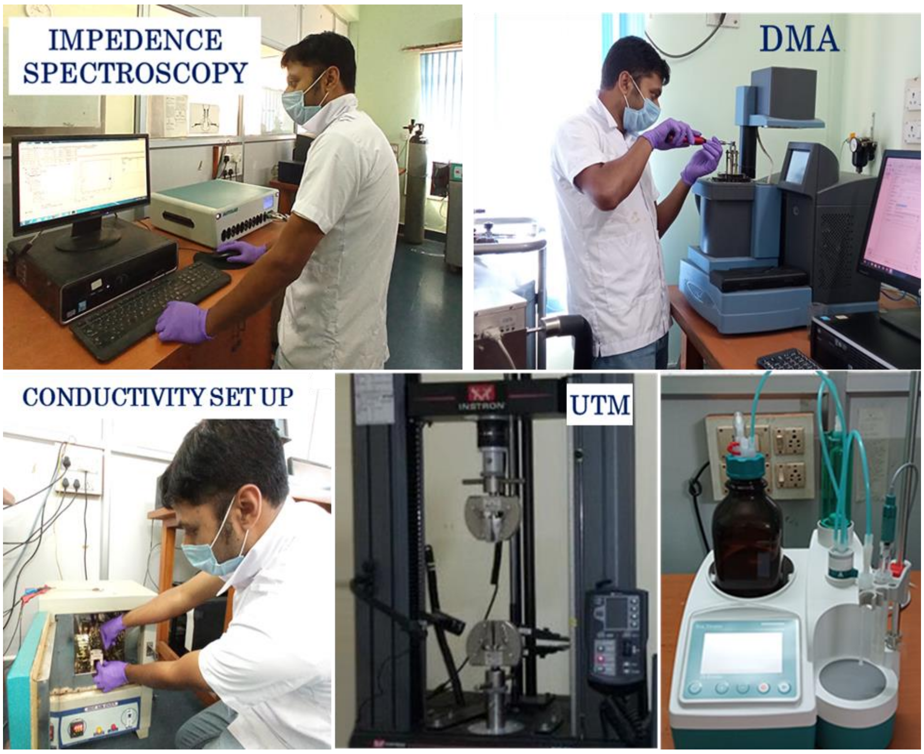

This chapter describes the detailed experimental procedures, all the characterization techniques and the details of the instruments used in working Chapters 3 to 7.

Source of materials

3,3',4,4'-tetraaminobiphenyl (TAB), 1,3-Benzenedicarboxilic acid (IPA), 4,4'-Oxybis(benzoic acid) (OBA) polyphosphoric acid (115%) (PPA), 2-Aminoteripthalic acid (99%), 1,3-Propane Sultone (98%), 1,3-Butane Sultone (98%), Melamine (>98%), terephthalaldeyde (>98%), Benzyl bromide (97%), 3-mercaptopropionic acid (3-MPA) (≥99%) and carbon disulfide (CS_2) (≥99%), 4-dimethylamino pyridine (DMAP), acrylamide (AAM) (99%), 2-acrylamido-2-methylpropane sulfonic acid (AMPS) (99%), 3-sulfopropyl acrylate potassium salt (SPAK) (≥99%), ethylene diamine (EDA), Durene (98%, Aldrich), *N*-bromosuccinimide (NBS, 99%, Acros), *N*-ethyldiisopropylamine (DIPEA, 99%, Sigma-Aldrich), 4,4'-trimethylenedipiperidine (97%, Aldrich), 1,3-dicyclohexyl carbodiimide (DCC), Vinyl benzyl chloride (VBC), 2-Methylimidazole (99%), [2-(Methacryloyloxy)ethyl]trimethylammonium chloride (99%), Butyl Iodide (BuI) (≥99%), 1-Vinylimidazole (≥99%), were purchased from Sigma Aldrich, India. 2,2′-Azobis(2-methylpropionitrile) (AIBN, 98%) from Sigma-Aldrich was freshly recrystallized from distilled methanol and kept under nitrogen till its use. NMR solvent dimethyl sulfoxide (DMSO-d_6), $CDCl_3$ and D_2O were procured from Sigma-Aldrich. Formic acid (99%), ortho phosphoric acid (85%), N-hydroxysuccinimide (NHS) (99.8%) and N, N'-dimethylformamide (HPLC grade), Graphite powder, potassium permanganate ($KMnO_4$), hydrogen peroxide (H_2O_2), were purchased from Merck, India. $ZrCl_4$ was purchased from Fischer Scientific. N-hexylamine, Sulphuric acid (98%), Hydrochloric acid (HCl), N, N- water for GPC (HPLC grade), Dimethylformamide (DMF), Anhydrous Dimethyl acetamide (DMAc), Dimethyl Sulfoxide (DMSO), Chloroform, Dichloromethane (DCM), Sodium bicarbonate ($NaHCO_3$), $FeSO_4$, Potassium hydroxide (KOH), Acetone, Tetrahydrofuran (THF), Ethanol, Methanol, were purchased from Finar Chemicals. [Fenton's reagent was prepared in the laboratory from Hydrogen peroxide (H_2O_2) and $FeSO_4$(3% H_2O_2 containing 2 ppm $FeSO_4$)]. 2, 6-bis(3′, 4′ diaminophenyl)-4-phenylpyridine (Py-TAB) monomer was synthesized using our previously reported procedure.[1] DDI water was used throughout the project.

Synthesis of poly [2,2′-(m-phenylene)-5,5′-benzimidazole] (m-PBI)

Following the modified literature reported procedure,[2] equimolar amounts of 3,3'-diaminobenzidine (TAB),1,3-Benzenedicarboxilic acid (IPA) along with the required amount of polyphosphoric acid (PPA) were placed in a three-necked RB. The reaction mixture was stirred at 60 rpm constant rotation with the help of a mechanical stirrer while a slow stream of nitrogen gas was purged into the reaction mixture to maintain the inert atmosphere. The polymerisation reaction was carried out at 190–210 °C for about 24 h-26 h. After that the reaction mixture was poured into distilled water to obtain the yellowish-brown colour product. The polymeric substance was then neutralized over sodium bicarbonate, washed thoroughly with distilled water and finally dried in a vacuum oven at 100 °C for 24 h to obtain dry m-PBI powder (see Figure 2.1 for schematic synthetic procedure and ^{1}H-NMR spectra of m-PBI). The inherent viscosity (I.V.) of the poly 2,2′-(m-phenylene)-5,5′-benzimidazole (m-PBI) polymer was measured at 30 °C in water bath with the help of Cannon (model F725) capillary dilution viscometer and the I.V. values are calculated from the flow time data. A solution of m-PBI in H_2SO_4 was used for the viscosity measurement. The concentration of the m-PBI solution in H_2SO_4 is 0.2 g/dL. The obtained I.V. value of the synthesised m-PBI is 1.02 dL/g.

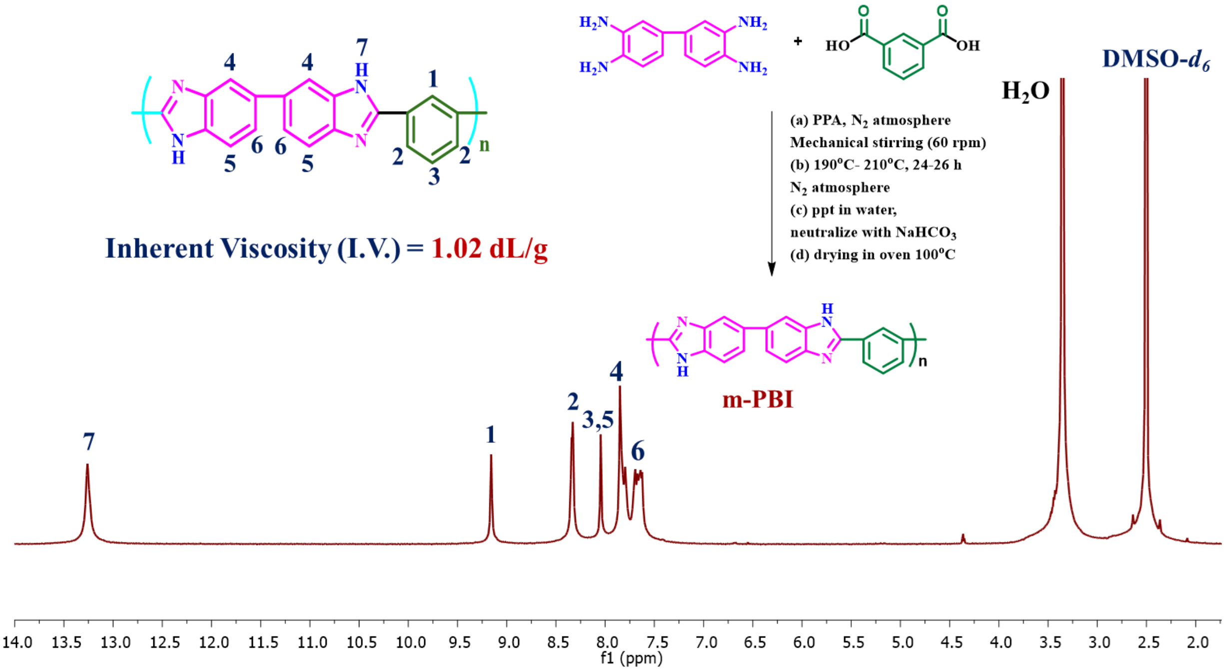

Figure 2.1. General synthetic procedure and ^{1}H-NMR spectra of m-PBI polymer in DMSO-d_6 solvent.

Synthesis of poly (4,4′-diphenylether-5,5′-bibenzimidazole) (OPBI)

According to literature reported procedure,[3] equimolar amounts of 3,3'-diaminobenzidine and 4,4'-oxybis(benzoic acid) (OBA) along with the required amount of polyphosphoric acid (PPA) were placed in a three-necked RB. The reaction mixture was subjected to mechanical stirring with an overhead stirrer while a slow stream of nitrogen gas was purged to maintain inert atmosphere. The polymerisation reaction was carried out at 190–220 °C for about 26 h. After that the reaction mixture was poured into distilled water where the polymer melt gets isolated as brown fibrous mass. This was then pulverized, neutralized with sodium bicarbonate, washed thoroughly with distilled water and finally dried in a vacuum oven at 100 °C for 24 h to obtain dry **OPBI** powder. The obtained I.V. value of the synthesised **OPBI** is 2.5 dL/g.

Synthesis of Pyridine Bridge Polybenzimidazole (PyOPBI)

Equal moles of 4,4′-oxybis(benzoic acid) (OBA), a dicarboxylic acid (DCA) and Py-TAB monomer were taken into a three-neck flask with polyphosphoric acid (PPA) for the synthesis of pyridine bridge PBI (PyPBI) polymer.[1] Monomers were taken along with polyphosphoric acid (PPA) in a 300 mL three-neck mercury sealed flask equipped with mechanical stirrer and nitrogen atmosphere. The reactions were carried in 100 mL PPA for 24 h at 210 °C. During reaction, the reaction time and temperature (which is often in the range of temperature 50-210 °C with appropriate ramp and soak times) were optimized. After the complete polymerization, the viscous polymer solutions were slowly poured into the deionized water and neutralized with sodium bicarbonate. The resulting polymer was filtered and washed with deionized water several times and dried in a vacuum oven for 24 h at 100 °C to remove the water completely. The reaction scheme for the synthesis is shown in **Scheme 2.1.** The ^{1}H-NMR spectra with peak assignments is shown in **Figure 2.2.**

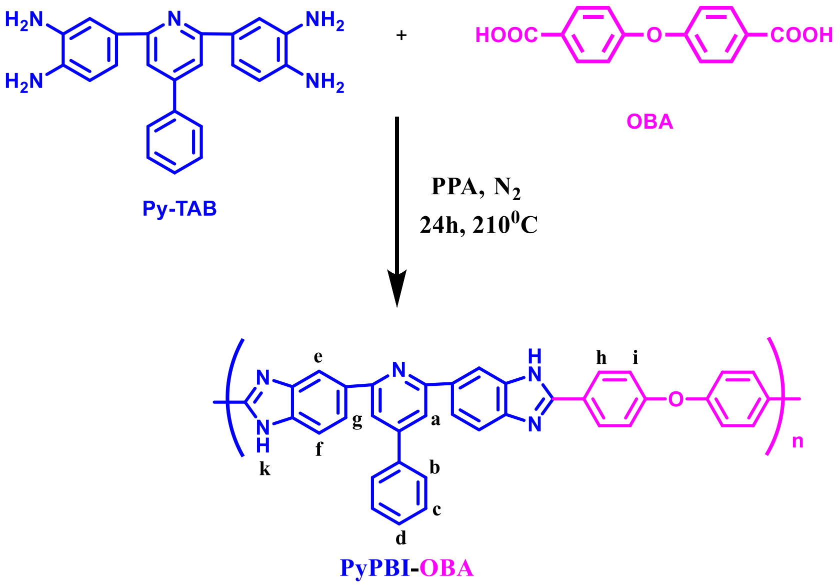

Scheme 2.1. Synthesis of PyPBI polymer.

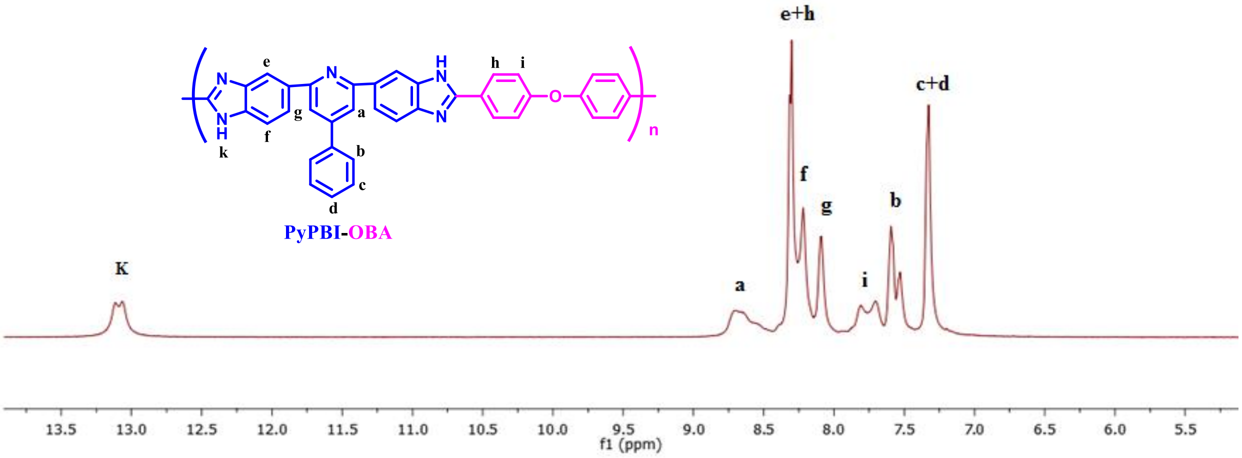

Figure 2.2. ^{1}H NMR spectra of PyPBI taken in a Bruker AV 500 MHz NMR using DMSO-d_6 solvent.

Preparation of PSM 1, PSM 2 MOFs, MCOF, P@MCOF, polymer-g-GOs (GOPs), spiro ionene polymer (SP), polymeric ionic liquid grafted GO (GOPIL) and other samples are discussed in the irrespective Chapters and its Appendix.

Details of experimental methods:

^{13}C CPMAS solid state NMR study

Solid-state ^{13}C CPMAS NMR spectra (in the Chapters 4) of the MCOF sample was obtained at ambient temperature with Bruker AV 500 MHz NMR spectrometer operating at 500 MHz at a spinning rate of 5 kHz and a contact time of 2 ms.

^{1}H NMR study

The proton NMR spectra of various starting materials, monomers, RAFT agents, and PBI, PyPBI based polymers (carried out for Chapters 5-7) were recorded by using Bruker AV 500 MHz NMR spectrometer at room temperature using $CDCl_3$ and DMSO-d_6 as NMR solvent.

Fourier transformed - infrared (FT-IR) spectra of the MOFs, COFs, polymer-*g*-GO samples, starting materials, monomers, RAFT agents, different types of polymers and various membranes (PEMs and AAEMs) (Chapter 3 – 7) were recorded on an iD7 ATR Thermo Fisher Scientific-Nicolet iS5 instrument. The powder samples were directly put on the sample holder without any modification. The membrane samples were also directly put on the sample holder to record the spectra.

Thermogravimetric analysis (TGA) of the MOFs, COFs, polymer-*g*-GO samples, starting materials, monomers, RAFT agents, different types of polymers and various membranes (PEMs and AAEMs) (Chapter 3 – 7) were carried out on TGA (TGA Q500, TA Instruments, USA) instrument operated in a temperature range from 35 °C to 700 °C with a scanning rate of 10°C / min under nitrogen gas flow. All the samples kept in isothermal condition at 80 °C for 30 minutes prior to analysis. (TGA) of undoped OPBI, m-PBI and its composite membranes and its PA doped membranes, and all the AAEM membranes were carried out on a TGA (TGA Q500, TA Instruments, USA) instrument operated in a temperature range from 35 °C to 700 °C with a scanning rate of 10°C / min under nitrogen gas flow.[3] All the membranes were kept isothermally at 100 °C for 30 minutes before measurement to evaporate the absorbed moisture from the membranes. After that, the samples were brought back to RT to start the experiment.

Field emission Scanning Electron Microscope (FE-SEM) imaging and EDX analysis of the MOFs, COFs, polymer-*g*-GO samples were carried out on a Carl Zeiss model Ultra 55 microscope. Samples were gold coated before imaging in FESEM. The surface and cross-sectional morphology of the pure OPBI, m-PBI, and all the composite membrane and different types of AAEMs were evaluated by using a field emission scanning electron microscope (FESEM) (Model: Zeiss Merlin Compact). The FESEM cross section morphology of the membrane samples were done by breaking the membranes in liquid nitrogen medium. Samples were gold coated before imaging in FESEM.[4]

Transmission electron microscopy (TEM) studies were conducted on JEOL (JEM Model No. F200) TEM machine at an accelerating voltage of 200 kV. The samples were prepared by placing a drop of ethanol dispersed MOFs, COFs, polymer-*g*-GO sample solution on carbon coated copper (200 mesh) grids. Transmission electron microscopy (TEM) studies of the polymer nanocomposite membranes and anion exchange membranes were conducted on JEOL (JEM Model No. F200) TEM machine at an accelerating voltage of 200 kV. The samples were prepared by placing a drop of formic acid, DMSO or DMAc dispersed 1% membrane solution on carbon coated copper (200 mesh) grids.

Atomic Force Microscope (AFM)

Surface AFM analysis, height profiles, 3D topology and surface roughness of the membranes were recorded (in the chapter 5 and 7) were carried out on NT-MDT-Solve-Probe & Oxford Asylum machine All calculations and image processing were carried out by using NOVA 1.0.26.1443 software provided by the manufacturer. The images were recorded in in tapping mode using a super sharp silicon cantilever (NSG 10-DLC) with a diamond-like carbon tip (NT-MDT, Moscow).

Powder X-ray diffraction (PXRD) patterns of the MOFs, COFs, polymer-*g*-GO samples, were recorded on D8 Advance Bruker diffractometer in the 2θ range (5º-60º). The diffraction patterns were analyzed using Bruker DIFFRAC plus EVA software. The powder x-ray diffraction patterns of OPBI, its dry composite membranes, PA loaded membranes, different types of AAEMs were collected in a Bruker D8 Advance powder diffraction apparatus. The samples were placed on a glass slide, and the diffractograms were recorded with Cu Kα radiation (λ = 1.5406 Å) operated at 40 kV and 30 mA current in the angular range (2θ) of 2-60° at a scanning rate of 1°/1.2 minutes.

N_2 gas sorption analysis of the powder samples (MOFs, COFs, polymer-g-GO) and ICL-AAEMs was carried out on the Quantachrome Autosorb IQ2 instrument (Chapter 3 – 6). All the samples were activated at 120 °C under vacuum for 18 hours, prior to N_2 sorption analysis. The temperature was maintained at 77 K during the experiment by a liquid nitrogen bath.

Inductively coupled plasma - optical emission spectrometry (ICP-OES) was performed in a ICP-OES Varian 720-ES instrument. All samples were activated at 140 °C for 12 hours prior to the experiments.

Zeta potential analysis of the surface functionalized GO samples and polymers (Chapter 5, 7) were measured utilizing Horiba Scientific nano partica nanoparticle analyser SZ-100. All the samples were dispersed in DDI water and sonicated for 5 min prior to experiment.

Dynamic vapour sorption (DVS) analysis of all the Polymer-*g*-GO samples (Chapter 5, 7) was performed on a TA Q5000 SA instrument at a temperature of 25 ºC and under N_2 atmosphere. All the samples were activated at 120 °C for 12 hours prior to the measurement.

The inherent viscosity (I.V.) values of the poly (4,4'-diphenyl-5,5'-bibenzimidazole) (OPBI) polymer, pyridine bridged polybenzimidazoles (PyPBIs) and [2,2′-(m-phenylene)-5,5′-benzimidazole] or m-PBI were measured at 30 °C in water bath with the help of Cannon (model F725) Ubbelohde capillary dilution viscometer and the I.V. values were calculated from the flow time data. A solution of polymers in H_2SO_4 was used for the viscosity measurement. The concentration of the polymer solution in H_2SO_4 was 0.2 g/dL.[1,2]

Thermo-mechanical properties of pristine polymers and various types of mixed matrix PEMs and AAEMs (Chapter 3 – 7) were studied by using a Dynamic Mechanical Analyser (DMA, model TA-Q-800). The membranes dimensions were 30 mm × 7 mm × 0.02 mm (L × W × T) and clamped on the films tension clamp of the pre-calibrated instrument. The samples were annealed at 400 °C for 15 minutes and then scanned from 100 °C to 400 °C with heating rate 4 °C/min. The storage modulus (E'), loss modulus (E″) and tan δ values were measured at a constant linear frequency 10 Hz with constant preload force of 0.01N.[5,6]

The tensile strength measurements (stress-strain profile) of all the water loaded AAEMs and PA doped mixed matrix PEMs of different wt% (Chapter 3 – 7) are performed in a universal testing machine (UTM, INSTRON-5965). Films of [50 mm × 10 mm × (thickness) mm] size were used for this experiment. For each sample, at least three times measurements were performed to check the reproducibility.

Phosphoric acid (PA) doping level, swelling ratio and water uptake and phosphoric acid doping level studies: Three similar size pieces of the OPBI, m-PBI and its nanocomposite membranes made from formic acid and DMAc (Chapter 3-5) were immersed in phosphoric acid (PA) for 5 days. The length, thickness and width of the dried membranes were measured before dipping in PA. After 5 days, the membranes were removed from PA container and quickly wiped to remove surface PA from the membranes and dried them in a vacuum oven at 100 °C for 24h followed by measuring again the length, thickness and width of the wet membranes. The phosphoric acid content was calculated as the number of PA moles per PBI repeat unit.[3,4,7]

$$\text{Doping level (PA moles/PBI repeat unit)} = \frac{W_{acid} - W_d}{W_d \text{ x } F_{PBI}} \text{ x } \frac{MW_{PBI}}{MW_{PA}} \qquad (1)$$

Where, MW_{PA} and MW_{PBI} are the molecular weights of PA and PBI, respectively. F_{PBI} is the weight fraction of PBI present in the blend composition. W_{acid} and W_d are the weight of the acid loaded and dry membrane, respectively.

The PA doping level of the membranes also measured through back titration method. The PA doped membranes were taken out from the PA bath, wiped with filter paper, and transferred into 50 ml of water. It was titrated against 0.1 N sodium hydroxide (NaOH) by using an Autotitrator (Model Metrohm702). The phosphoric acid content was calculated as the number of PA moles per PBI repeat unit.

Swelling ratio of the membranes were calculated from the following equation.

$$\%\text{Swelling Ratio} = \frac{L_w - L_d}{L_d} \times 100\% \qquad (2)$$

Where, L_w, and L_d are the length of the wet membranes and dry membranes, respectively.

Similarly, the swelling ratio and water uptake of **PBI** and its composite membranes were obtained by immersing the membranes in water for 5 days. The length, thickness and width of the dried membranes were measured before dipping in water. After 5 days, the membranes were removed from water bath and quickly wiped to remove surface water from the membranes and again the length, thickness and width of the wet membranes were measured. Water uptake was calculated from the following equation.

$$\%\text{Water Uptake} = \frac{W_w - W_d}{W_d} \times 100\% \qquad (3)$$

Where, W_w is wet membrane weight and W_d, is dry membrane weight. Similarly swelling ratio in water were calculated using equivalent equation like equation (2).

KOH uptake

Three similar size AAEMs (Chapter 6, 7) were dipped in 1 M KOH for 24 h. Then KOH treated membranes were removed from the KOH solution and wiped using a tissue paper to remove surface liquid. The weight of the KOH impregnated membrane (W_{KOH}) was measured and Eq. (4) was used to calculate the KOH uptake.[5]

$$\text{KOH uptake (\%)} = \frac{W_{w\text{-}KOH} - W_{d\text{-}KOH}}{W_{d\text{-}KOH}} \text{ x } 100\ \% \qquad (4)$$

Where, $W_{w\text{-}KOH}$ is weight of hydrated KOH loaded membrane & $W_{d\text{-}KOH}$ is weight of dried hydroxide form membrane.

Ion exchange capacity (IEC)

Ion exchange capacity (IEC) of the all the synthesized AAEMs (Chapter 6, 7) were determined by back titration method. The membranes were soaked in 35 mL of 0.01 M aqueous HCl solution for 48 h followed by back titration with 0.01 M aqueous KOH solution and using phenolphthalein as an indicator.[5] The IEC was calculated by the equation 5.

$$IEC\ (meq/g) = \frac{V_{x,KOH} \times C_{KOH} - V_{0,KOH} \times C_{KOH}}{W_{dry}} \qquad (5)$$

Where $V_{o,\ KOH}$ and $V_{x,\ KOH}$ are the volume of the KOH used in the titration without and with membrane, respectively. C_{KOH} is the molar concentration of the KOH which was titrated by the standard oxalic acid solution, and W_{dry} is the weight of the dried membrane.

Proton conductivity and OH^- conductivity measurement

Proton conductivity was carried out by four probe impedance analyser by using Auto lab Impedance analyser (PGSTAT302N) over a frequency range from 1 Hz to 100 KHz. The phosphoric acid doped OPBI@MOF, m-PBI@COF, OPBI@Polymer-*g*-GO composite membranes (Chapter 3-5) were cut in rectangular shape and then kept sandwiched between two Teflon plates with four platinum electrodes. Two outer electrodes (1.5 cm apart) supply current to the cell, while the two inner electrodes 0.5 cm apart on opposite sides of the membrane measure the potential drop. The whole conductivity cell set up was kept in an oven to measure the temperature dependence of proton conductivity. The conductivity cell was placed in an oven at 100 °C for 2h to avoid the conduction due to the presence of water molecules. The conductivity cell was cooled to room temperature in a vacuum oven and then before going to conductivity measurement, the cell was taken out to keep the sample dry. The conductivities of the membranes were measured from room temperature to 180 °C at intervals of 20 °C. At every temperature jump, the sample was kept for 30 minutes to attain isothermal equilibrium and then measurements were recorded.

Hydroxide (OH^-) form membranes (Chapter 6, 7) were cut into rectangular shape pieces and sandwiched between two Teflon plates with four platinum electrodes. The two outer electrodes (1.5 cm apart) supply the current to the cell, while the other two inner electrodes (0.5 cm apart) on the opposite sides of the membranes measure the potential drop. This whole conductivity cell set up was placed in deionized water to maintain 100% relative humidity. The ionic conductivities of the membranes were measured at an interval of 10 °C raised from room temperature to 90 °C. At each temperature of the measurement, the sample was kept for 30 minutes to attain isothermal equilibrium. The conductivities of the membranes were calculated using Eq. 6.

The conductivities of the membranes were calculated from the following equation:

$$\sigma = \frac{D}{RBL} \qquad (6)$$

where, D is the distance between the electrodes (here it is 0.5 cm), B is the thickness of the membrane, L is the width of the membrane and R is the bulk resistance obtained from the Nyquist plot.[4,5,7]

Isothermal proton conductivity/durability of proton conduction

The OPBI@MOF, m-PBI@COF, OPBI@Polymer-*g*-GO mixed matrix membranes (Chapter 3-5) were isothermally kept at 160 °C for 36 h. Under this condition, the conductivity the various nanocomposite PEMs and pristine membranes were measured for every 2 h up to 36 h. We exclude night time measurement (8 h gap) and kept the cell in equilibrium for overnight at isothermal condition (160 °C). Further measurement of proton conductivity was performed next morning up-to 36 h.

Oxidative stability

The oxidative stability of the OPBI@MOF, m-PBI@COF, OPBI@Polymer-*g*-GO membranes (used in Chapter 3-5) were investigated by immersing the membranes into Fenton's reagent (3% H_2O_2 aqueous solution containing 4 ppm ammonium iron (II) sulfate, or Mohr's Salt) at 70 °C. Three similar sized pieces of the membranes were taken for Fenton's test. The oxidative stability was measured for time variation up to 100 hours. The membranes were taken out at certain time intervals, dried in vacuum oven at 100 °C for 24 hours, and again weights were recorded. The oxidative stabilities of all the membranes were calculated as a weight remained after taking out the membranes from the Fenton's reagent.[8]

Alkaline stability

All the anion exchange membranes, and various other fabricated AAEMs (Chapter 7, 8) were immersed in 1 M, 2 M and 5 M aqueous KOH solution at room temperature and at RT, 60 °C and 80 °C for a longer period of time (500 h – 1000 h).[5,9] The alkaline stability of all the anion exchange membranes in basic condition was studied with the time by measuring the weight loss (%) through thermogravimetric analysis (TGA) before and after alkaline stability test and gravimetric analysis by taking the membrane weight before and after alkaline treatment, IEC & hydroxide ion conductivity measurement after 500 h alkaline treatment and comparing with the freshly alkali treated samples were also checked. Also FT-IR analysis before and after alkaline stability test were performed to check the alkaline stability.

Acid retention test (PA holding capacity measurement)

The acid leaching test was performed for OPBI and all the PA doped OPBI@MOF, m-PBI@COF, OPBI@Polymer-*g*-GO MMMs according to the previous reports.[4,7] The doped membranes were taken out from the phosphoric acid bath medium and excess phosphoric acid was removed by wiping with a tissue paper. The membranes were then placed under the vapour condition at 100 °C for a period of three hours and the weight of the membrane (W_t) after every one hour was recorded after removing the leached acid from the membrane. The weight loss ratio of acid in the membranes was calculated by using the following formula:

$$R = \frac{W_o - W_t}{W_a} \text{ x } 100\ \% \qquad (7)$$

Where W_o is weight of the PA doped membranes at the initial time of zero hour, W_t is the weight of the PA membrane after leaching at different times (t) and W_a is the original weight of PA present in the membranes calculated from the PA doping level of the membranes.

References

1. Maity, S.; Jana, T. *Macromolecules* **2013**, *46*, 6814–6823.
2. Hazarika, M.; Jana, T. *ACS Appl. Mater. Interfaces* **2012**, *4*, 5256–5265.
3. Mukherjee, N.; Das, A.; Dhara, M.; Jana, T. *Polymer* **2021**, *236*, 124315.
4. Mukhopadhyay, S.; Das, A.; Jana, T.; Das, S. K. *ACS Appl. Energy Mater.* **2020**, *3*, 7964–7977.
5. Das, A.; Sana, B.; Bhattacharyya, R.; Chandra Ghosh, P.; Jana, T. *ACS Appl. Polym. Mater.* **2022**, *4*, 1523–1534.
6. Koyilapu, R.; Subhadarshini, S.; Singha, S.; Jana, T. *Polymer* **2021**, *212*, 123175.
7. Kutcherlapati, S. R.; Koyilapu, R.; Jana, T. *J. Polym. Sci. Part A Polym. Chem.* **2018**, *56*, 365–375.
8. Harilal, A. Shukla, P. C. Ghosh, T. Jana. *ACS Appl. Energy Mater.* **2021,** *4*, 1644-1656.
9. Sana, B.; Das, A.; Sharma, M.; Jana, T. *ACS Appl. Energy Mater.* **2021**, *4*, 9792–9805.

Chapter 3

Fabricating a MOF Material with Polybenzimidazole into an Efficient Proton Exchange Membrane.

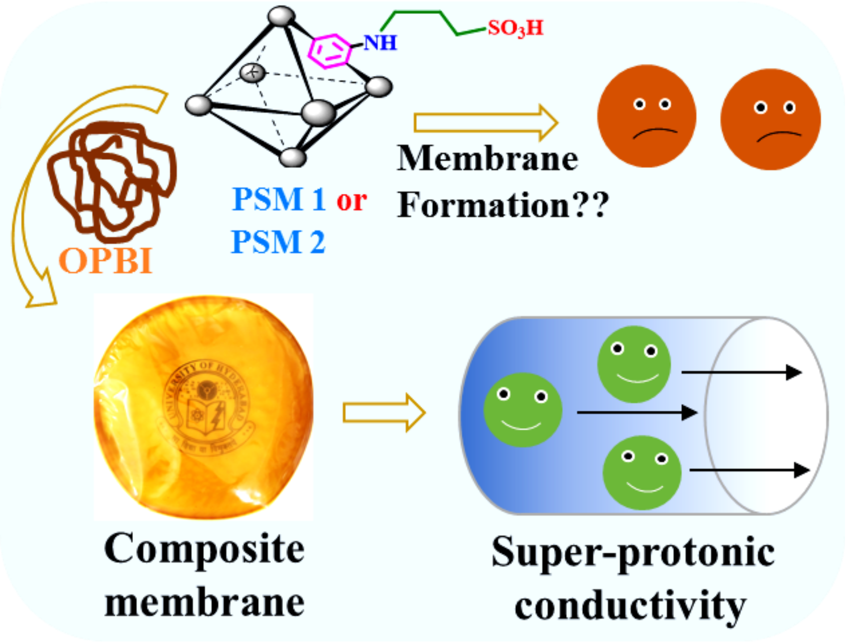

Subhabrata Mukhopadhyay†, **Anupam Das**†, Tushar Jana* and Samar K. Das*. Fabricating a MOF Material with Polybenzimidazole into an Efficient Proton Exchange Membrane. *ACS Appl. Energy Mater.* **2020**, *3*, 7964–7977. **[†] Co-First Authors.**

Abstract.

Metal organic frameworks (MOFs) have received considerable importance as proton conducting materials in recent times. However, most of the MOFs lack the ability to form film, which limits their application. In the present work, polybenzimidazole (PBI) composite membranes have been prepared by loading post synthetically modified (PSM) UiO-66-NH_2 MOFs, denoted as **PSM 1** and **PSM 2** into the arylether-type polybenzimidazole (**OPBI**) polymer. The pristine **OPBI**, and MOF nanofiller loaded membranes were doped with phosphoric acid (PA) to prepare proton exchange membranes (PEMs). Use of thermally stable, hydrophilic MOFs resulted into enhanced proton conductivity, higher PA retention capacity and increased stability against oxidative degradation for the composite membrane than the pristine OPBI polymer. Interestingly, the order of proton conductivity of the PA doped MOF containing polymer membranes were exactly opposite to that of the used MOFs as such. The proton conductivities of the composite membranes (0.29 Scm^{-1} for **PSM 1**-10% and 0.308 Scm^{-1} for **PSM 2**-10% membranes at 160˚C, anhydrous environment) were notably higher than the conductivities of the constituents and also higher than most of the MOF based polymer supported membranes. Extensive interfacial H-bonding plays the most crucial role behind the enhanced proton conductivities of the PA doped MOF containing polymer membranes reported here. This work clearly demonstrates the benefits of using rationally designed **PSM 1** and **PSM 2** MOFs as nanofiller to prepare OPBI supported membranes that perform excellent proton conduction in a wide temperature range spanning up to 160 °C. This provides a generalized approach towards achieving an efficient proton conducting membrane for the fuel cell.

Introduction

Heavy vehicles or automobiles are one of the major reasons behind high consumption of fossil fuels and environmental pollution. Replacement of such conventional engines by fuel cells can produce the best environment friendly solution to this existing problem. Fuel cell is an electrochemical energy conversion device which can convert chemical energy directly into electrical energy.[1–3] In fuel cell, hydrogen/ fuel gets oxidized in the anode while oxygen gets reduced in the cathode. Protons travel through the proton exchange membrane (PEM) from cathode to anode while electrical energy is obtained in the outer circuit. The efficiency of a fuel cell largely depends on the efficiency of proton conduction through the PEM.[2,4-6] Therefore, proton-conducting materials and proton transport phenomenon are very important for applied research in modern era.[7-10] In this context, polymers have been extensively studied in literature for PEMFC (proton exchange membrane fuel cell).[5] Perfluorosulfonated (Nafion) membranes have been evolved extensively as PEMs due to their promising conductivity, chemical and mechanical strength and long-term durability.[11,12] Recently, metal−organic framework (MOF) and other framework containing conducting compounds have been emerged as potential materials for scientific research which generates bridges between inorganic cluster-containing compounds and organic polymers in terms of availability of detailed crystal structure and their efficiency of proton conduction.[13-20] These MOFs are the coordination analogues of the conventional polymers and consist of organic molecules and metal ions.

Shimizu and co-workers developed two MOFs, namely, PCMOF2$^{1/2}$ (Pz) and PCMOF2$^{1/2}$ (Tz) (Pz = 1H-pyrazole and Tz = 1H-1,2,4-triazole) with promising proton conductivity under high relative humidity.[21] Lan and co-workers reported the synthesis of a sulfonic acid doped MIL-101 MOF (MIL-101- SO_3H) which displayed an excellent proton conductivity of 1.82 Scm^{-1} at 70 ºC and 90% RH (relative humidity) due to the presence of the sulfonic acid groups.[22] Elahi et al. reported polycarboxylate-templated coordination polymers (CPs) and achieved proton conductivity of 1.49×10^{-1} Scm^{-1} under 80 ºC and 98% RH.[23] Yang et al. reported a sulfonic acid rich flexible MOF and achieved super-protonic-conductivity of 1.27×10^{-1} Scm^{-1} (at 80 ºC under 100% RH).[24]

UiO-66, a subclass of MOFs, has also evolved as an efficient platform to design efficient MOF based proton conductors.[14,17,25-28] In an earlier report, we have synthesized two different kinds of post synthetically modified (PSM) MOFs named as **PSM 1** and **PSM 2**.[29] High stability and high proton conductivity were achieved with low '$-SO_3H$' content for these two MOFs. **PSM 1** is found to possess the undoped MOF based highest proton conductivity of (0.16 Scm^{-1} at 80 ºC) till date; while the proton conductivity of **PSM 2**, was almost 50 times lower than **PSM 1**. This profound variation of proton conduction was a direct consequence of the variation of length of side arm containing the -SO_3H group.

But MOFs have certain drawbacks, (a) most of the MOFs reported in literature produce relatively less proton conductivity compared to polymeric PEM, (b) their thermal stability is not always very promising and the most prominent drawback of MOFs is (c) the lack of ability to form a membrane. Generally, very thin PEM is used for proton conduction in a fuel cell.[11,30-32] Thus, the probability of using any material to perform proton conduction in fuel cell, largely depends on its processability into a membrane. Like most other MOFs, **PSM 1** and **PSM 2** also lack the ability to form a membrane. Thus, they are not suitable to design PEM as such. In recent years, several research groups have reported development of PEM from the composite membranes using Nafion as the polymer support and MOFs as the fillers.[33-37]

But, Nafion membranes have several limitations owing to their high cost and decrease in conductivity over 80 °C.[38-40] Sulfonated poly(ether ether ketone) (SPEEK) based blends and composites with MOFs are also reported to form proton conducting membranes.[41,42] Polybenzimidazole (PBI), a rigid polymer with high thermal stability, mechanical robustness and chemical stability, membrane has been found to show high proton conductivity in a fully anhydrous condition when loaded with phosphoric acid (PA); therefore it is considered to be a promising membrane material for PEMFC.[43-46] However, the PBI based membranes also suffer from less PA doping level, higher acid leaching at elevated temperature, and low oxidative stability. Due to excessive swelling, PA doped membranes also suffer from less mechanical strength. In this situation, nanofillers can play a vital role to improve these membrane properties. The nanofillers are basically solid nano-particles, which differ from the polymer matrix in terms of composition and structure. They generally comprise of inorganic materials. The incorporation of a suitable nanofiller component to PBI may give the composite membranes, the potential to overcome the excessive leaching of PA from the doped PBI membrane, and may also increase the mechanical strength and durability of the membranes.[47-49] Incorporation of MOFs as nanofillers into PBI matrix can produce high performing polymeric membranes superior for PEMFC.[50, 51]

Thus, in this work, our aim is to fabricate nanocomposite membranes utilizing solution blending method by mixing different amount of **PSM 1** and **PSM 2** as nanofillers with **OPBI** polymer. The structural properties of the **OPBI** matrix and the fillers suggest a high probability of H-bonded interfacial interactions between the fillers and **OPBI** matrix. Interaction between the 'N-H' groups of polymer and uncoordinated functional groups of PSM nanofillers are highly expected for such composite. We aim to achieve higher PA doping level followed by high proton conductivity and lower acid leaching in our composite membranes. Furthermore, the effect of membrane formation with **OPBI** matrix, in the order of the proton conductivity of the two PSM MOFs, may provide fundamental interesting information.

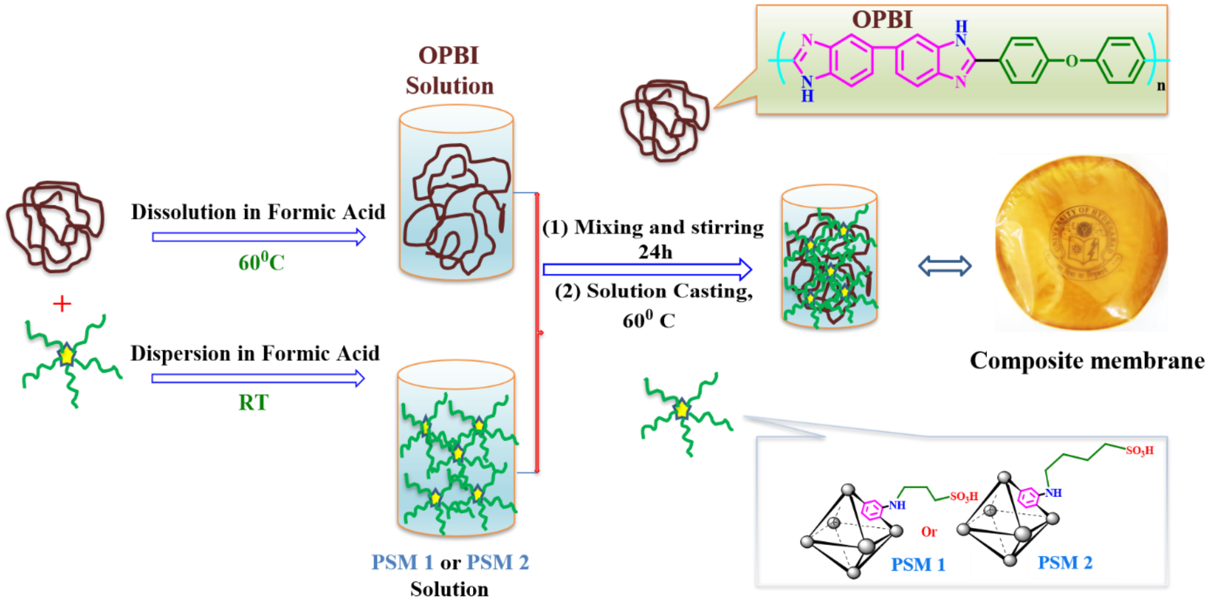

Scheme 3.1. Schematic representation of preparations of **PSM 1/PSM 2** nanocomposite membranes. Notably, the composite membrane shows the "University of Hyderabad logo" inscribed on it.

Four different concentrations of **PSM 1** composite membranes and two different concentrations of **PSM 2** composite membranes are synthesized. The proton conductivity, acid holding capacity, oxidative stability, high temperature stability *etc.* are measured for all of these composite membranes. In this work, we could achieve exceptional PA doping level, high proton conductivity, thermal and mechanical robustness along with exceptional chemical stability and acid retention properties for all the composite membranes. At higher filler concentration for both **PSM 1** and **PSM 2** composites, further improvements in membrane properties are observed. We achieved proton conductivity values of 0.290 Scm^{-1} and 0.308 Scm^{-1} for **PSM 1-10%** and **PSM 2-10%** composite membranes, respectively at 160 ^{o}C which are superior than most of the proton conductivity values, reported in literature till date.

Experimental Section

Synthesis of (4,4′-diphenylether-5,5′-bibenzimidazole) (**OPBI**) polymer was adapted from literature (detailed synthetic procedure given in **Chapter 2**).[52,53] The syntheses of UiO-66-NH$_2$, **PSM 1** and **PSM 2** have been adapted from our earlier report[29] and mentioned in details in the **Appendix 1**.

Fabrication of PSM-OPBI composite Membranes

Homogenous nanocomposite membranes were prepared by solution casting blending method by adding 3, 5, 7, and 10 wt % (with respect to polymer concentration) **PSM 1** and, 7 and 10 wt% of **PSM 2** dispersion in formic acid to 2 wt % **OPBI** solution in formic acid. The final **OPBI** concentration in solution was 1 wt %. Then the solution was stirred vigorously at room temperature for 24 h to form a homogeneous mixture after which it was poured on to a glass Petri dish and the solvent was evaporated at 60 °C slowly. The formed membranes were then peeled out and were dried in vacuum at 100 °C to remove the trace of solvent molecules. Composite membranes with 10% of unmodified parent MOF (UiO-66-NH_2) was also prepared following the same protocol. The synthesis protocols of **PSM-OPBI** nanocomposite membranes are shown in schematically in **Scheme 3.1.**

Phosphoric Acid (PA) Doping of Nanocomposite Membranes

The thoroughly vacuum-dried **OPBI** and the composite membranes were immersed in PA solution (85%) for 5 days to obtained PA doped films. After 5 days, the membranes were taken out from phosphoric acid (PA) bath, quickly wiped out the membrane-surface-adsorbed PA, and then stored in zip-lock air tight covers for further analysis.

Characterization Methods

All the prepared nanocomposite membranes were characterized by Fourier-transform infrared spectroscopy (FT-IR), structural analysis by powder X-ray diffraction (PXRD), Field emission scanning electron microscopy (FESEM) and transmission electron microscopy (TEM), thermogravimetric analysis (TGA), thermomechanical studies by dynamic mechanical analyser (DMA) and tensile stress-strain profile by universal testing machine (UTM). The experimental details are given in the **Chapter 2**. The detailed experimental procedure for PA loading, water uptake, swelling ratio studies, proton conductivity, acid leaching study are also included in the **Chapter 2.**

Results and discussion

X-ray study. The powder X-ray diffraction of **OPBI**, **PSM 1** and **PSM 2** composite membranes are presented in **Figure 3.1.** **PSM 1** and **PSM 2** were reported earlier and also confirmed here to have similar pattern as that of UiO-66 framework. On the other hand, the **OPBI** usually exhibits broad halo in the 2θ range of 20^0 to 30^0, which is attributed to amorphous nature of the polymer.[54-56] Similar kind of broad halo was not observed in case of **PSM 1** and **PSM 2** composite membranes, instead **PSM 1** and **PSM 2** composite membranes are observed to exhibit crystalline patterns, which are not identical with **PSM 1** and **PSM 2** MOF PXRD pattern. In the PXRD spectra of the **PSM 1** or **PSM 2** containing membranes, positional shifts of peaks could be observed when compared with the parent MOF (**Figure 1**). Moreover, extra peaks (marked with * in the **Figure 1**) could be observed indicating generation of new crystalline planes. This generation of new crystalline planes is a result of extensive H-bonding between **OPBI** and the nano fillers *i.e.*, **PSM 1** or **PSM 2**. The high peak intensity (counts) of the newly generated peaks (particularly between 2θ range 25° - 30°) provides strong argument in support of strong interfacial interaction between the **OPBI** and the **PSM 1** or **PSM 2**. Intensity of the * marked peaks were also found to be enhanced with enhancement of **PSM 1** and **PSM 2** loading in the composites. This is a result of the increase of the amount of the interfacial interactions between the MOF nanoparticles and **OPBI** matrix. As the amount of the non-coordinated '$-SO_3H$' groups and '$-NH_2$' groups of the MOF nanoparticles increase in the membrane (due to higher loading of MOF), the extent of H-bonding increases. Similar inference could also be drawn from the TEM analysis. A self–assembled network like structure was obtained for the PSM loaded composite membranes. The self–assembled network like structures (generated as a result of the interfacial interactions between **OPBI** and **PSM 1**/ **PSM 2**), obtained from TEM analysis, becomes prominent at higher loading of the nano-fillers. Self-assembly generates structural ordering which forms new crystalline planes in the composite matrix with respect to pristine amorphous polymer.[49,55,57]

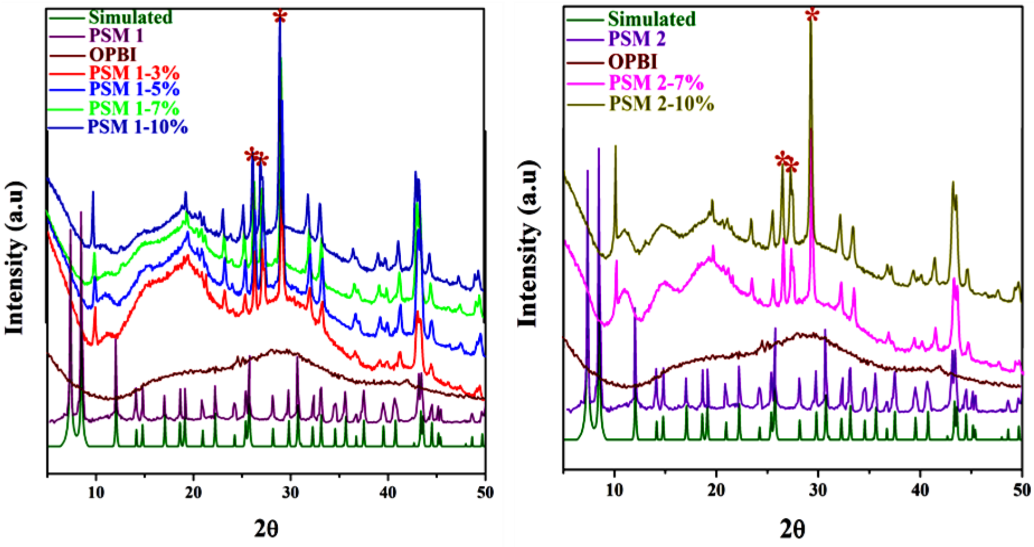

Figure 3.1. PXRD patterns of **OPBI**, **PSM 1**, **PSM 2** and nanocomposite membranes compared with the simulated PXRD pattern of UiO-66.[58]

Spectroscopy

The argument of extensive H-bonding in **PSM 1–OPBI** and **PSM 2–OPBI** composite is also further supported by FT-IR analysis of the membranes, as discussed below.

The intensity of the peak of the non-hydrogen bonded ‘N-H’ group of the **OPBI** in the FT-IR spectra of the nanofillers loaded **OPBI** membranes decrease with increasing loading of the **PSM 1**/ **PSM 2**. Especially for higher loaded membranes (7 and 10 % of **PSM 1**/ **PSM 2**), the ‘N-H’ peak disappears completely indicating the complete participation of the free N-H groups in **OPBI** molecule to form interfacial H-bonding. Also, due to the interaction between polymer ‘N-H’ with the dangling ‘$-SO_3H$’ groups of **PSM 1**/ **PSM 2**, few positional shifts of peaks in the FT-IR spectra are observed in case of both the **PSM 1** and **PSM 2** composite membranes [**Figure 3.2(a and b)** and **Figure A1.2(a and b)** of Appendix 1]. Spectral broadening obtained for **PSM 1-7%** and **PSM 1-10%** at 1216 cm^{-1} and for **PSM 2-7%** and **PSM 2-10%** at 1208 cm^{-1} due to presence of interfacial interactions between **OPBI** and the fillers. Thus, from FT-IR spectra, it can be inferred that, the nanofillers in **PSM 1** and **PSM 2** composite membranes perform extensive H-bonding interactions with **OPBI**. At higher loading of fillers, aliphatic C–H stretching peak becomes prominent at 2851 and 2921 cm^{-1} in the composites, which indicates the presence of aliphatic alkyl chains in the composites as a direct consequence of loading **PSM 1**/ **PSM 2**.

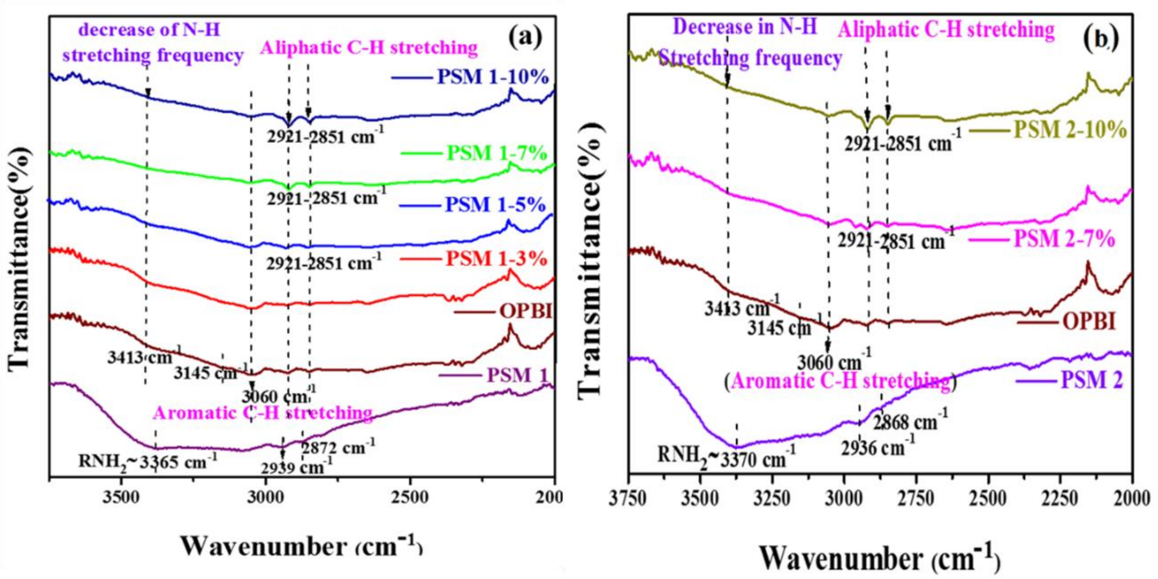

Figure 3.2. FT-IR spectra of (a) **OPBI** and **PSM 1** composite membranes (b) **OPBI** and **PSM 2** composite membranes at their indicated wt%.

Thus, the crystallinity, observed from the PXRD analysis of the undoped membrane along with the systematic analysis of the FT-IR spectral shifts of the composite membranes (both in position and intensity), indicate towards the H-bonding interactions and support the inference drawn from each other.

Morphology study

FESEM. The cross-section morphologies obtained by FESEM analysis of all six composite membranes appear to be different from the pristine **OPBI**. In both the cases of **PSM 1** and **PSM 2** composite membranes, thick fibre like network morphology is observed unlike pristine **OPBI** [**Figure 3.3(a-c)** & **Figure A1.3(a-d)** of Appendix 1]. The morphological variation is a result of interfacial interactions between **OPBI** and **PSM 1**/ **PSM 2** nanofiller (*vide supra*) and varies with variation of the amount of the nanofiller in the composite membranes. As the percentage of nanofiller is increased, the number of fibrils as well as the thickness of fibrils also increase, which makes the morphology of the composite membrane increasingly porous. This fibre like network and porous structure are more prominent all over the membrane matrix in case of **7%** and **10%** of **PSM 1 and PSM 2** composite membranes than the ones with lower loading of PSM.

TEM. From TEM images, the self-assembly of the **PSM 1** and **PSM 2** nano particles into **OPBI** matrix could be confirmed for both the nanofiller loaded **OPBI** composite membranes. In higher loading composite membranes, fillers have formed self-assembled network among themselves, as well as with the **OPBI** matrix. **PSM 2** nanofillers are observed to be scattered all over the **OPBI** matrix, which generates net-like clusters spreading throughout the composite membranes and further leads to structural anisotropy [**Figure 3.3(e and f)**]. Similar observation was recorded by us for a ILMS (ionic liquid modified silica) grafted composite membrane matrix.[57] Though the dispersion pattern of the fillers followed by net-like cluster formation is more prominent for **PSM 2-10%** composite over **PSM 1-10%**, where the **PSM 1** nanofillers undergo flower like self-aggregation in different portions of the **OPBI** matrix leading to self-assembled morphology [**Figure 3.3(d)**]. When the percentage of filler loading is high, two factors come into action, (a) Interfacial H-bonding interactions among the functional groups of **PSM 1** and **PSM 2**, which result into self-aggregation of fillers in the polymer matrix. (b) Also, the functional groups, present in the MOFs possess the affinity to undergo interfacial interactions with the polymeric 'N–H' through hydrogen bonding interactions. By maintaining the balance between these two factors, self-assembled network is formed in the composite network.[49] This anisotropic self-assembled structure of nanofillers causes generation of new crystalline planes, as observed in PXRD patterns of composite membranes between 2θ range 25º–30º (*vide supra*), which are absent in both **OPBI** and PSM MOFs.

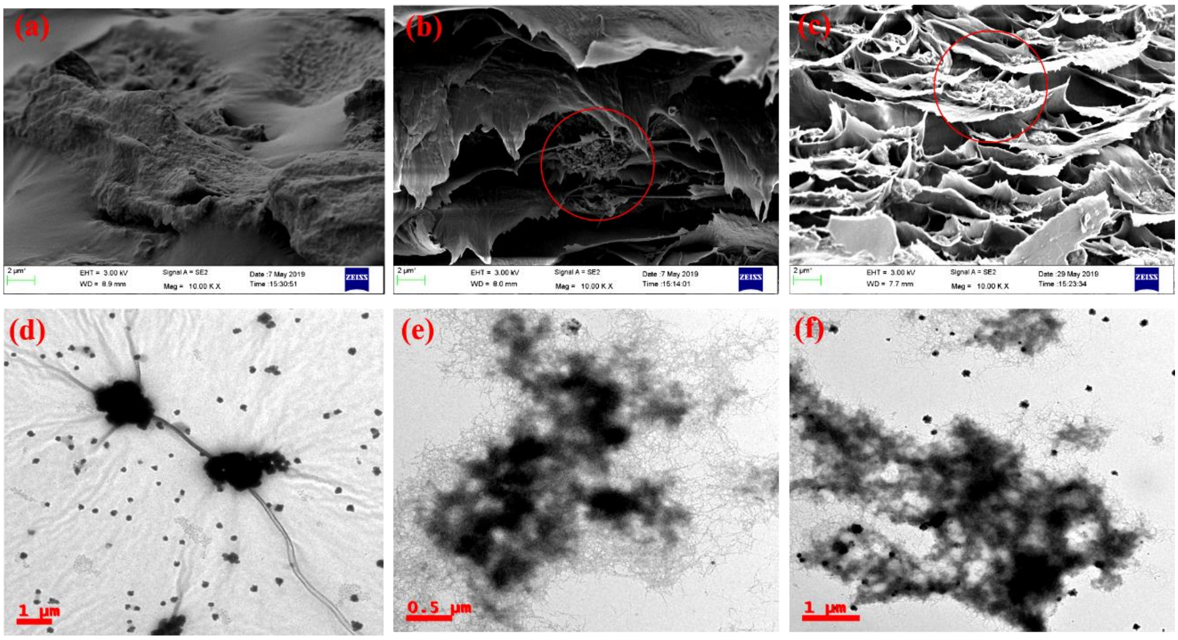

Figure 3.3 (a) FE-SEM cross-sectional image of pristine **OPBI**, **(b) PSM 1**-10% and **(c) PSM 2**-10% composite membranes. Nanofillers are scattered into the cross-section of composite membranes marked with red circle. **(d)** TEM images of **PSM 1**-10%, **(e and f)** TEM images of **PSM 2**-10% composite.

To prove this further, analysis of high resolution TEM image was carried out [**Figure A1.4 (a and b)** of Appendix 1]. The obtained d values are in the range between 0.31-0.34 nm (d value was calculated from reduced FFT generated by Digital Micrograph software) for both **PSM 1** and **PSM 2** composite membranes. These values are found to be in good agreement with the d values obtained from three different intense peaks between 2θ range 25º–30º, obtained from PXRD analysis. This proves the fact that interfacial interactions lead to structural anisotropy, causing generation of new crystalline planes in the composite matrix. This kind of strong interactions between **PSM 1** and **PSM 2** nano-fillers and polymer can provide mechanical reinforcement, higher stability and higher acid retention capacity.

Thermal Stability

TGA (**Figure 3.4**) of **OPBI**, **PSM 1** and **PSM 2** and their composite membranes (for details, see Appendix 1) show that, the weight loss starts after 200 ºC and with increase in loading of the nanofillers the weight loss percent also increases due to oxidation of alkyl chains and degradation of '–SO_3H' groups of **PSM 1** and **PSM 2** in case of both the **PSM 1** and **PSM 2** composite membranes. And for all the composite membranes as well as the pristine **OPBI**, degradation of polymeric backbone occurs after 550 °C. **PSM 1** composite membrane exhibits slightly higher thermal stability over **PSM 2** composite membranes. All the membranes exhibit thermal stability higher than the pristine **PSM 1** and **PSM 2** due to the high thermal stability of the **OPBI**, which is very useful for application in HT-PEMFC.

TGA of the **PA doped OPBI**, along with 7% and 10% composite membranes of **PSM 1** and **PSM 2** are represented in (**Figure A1.5** of Appendix 1). In between 100 -200 °C, the weight loss has been observed for the **PA doped** membranes due to evaporation of water molecules.[55,59,60] This is followed by a continuous weight loss up to 550 °C, either because of the degradation of corresponding composite or due to the self-condensation of phosphoric acid molecules. Beyond 550 °C, all the composites show sharp degradation of the polymer backbone. Two important observations can be obtained by comparing the TGA of the undoped and PA doped membranes (**Figure 3.4** and **Figure A1.5** in Appendix 1): (1) Unlike the undoped membranes, the thermal stability of PA loaded composite membranes are higher than the PA loaded pristine **OPBI** membrane. Similar observation was reported earlier by us for acidic surfactant like molecules (ASM) grafted composite membranes.[54] (2) Thermal stability is more or less similar for **PA** doped **PSM 1** and **PSM 2** composite membranes. This is because the composites form strong H-bonds with the PA molecules through the '–SO_3H' groups, primary and secondary amines of the PSM nanofillers and imidazole '–NH' group of the **OPBI** polymer.

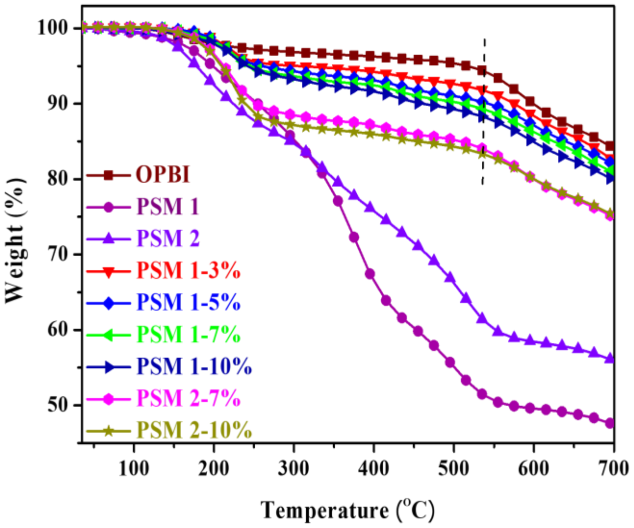

Figure 3.4. TGA plots of **OPBI**, **PSM 1**, **PSM 2** and nanocomposite membranes at their indicated wt%.

Mechanical study

The dispersion pattern of PSM MOFs possesses great influence over the thermo-mechanical properties of **OPBI**. **Figure 3.5** shows the temperature dependent storage modulus (E′) plots (obtained from the DMA study) of all the composite membranes along with the pristine **OPBI**. The storage moduli of the composite membranes at 100 ºC and 400 ºC are tabulated (**Table 3.1**). **Figure 3.5** and **Table 3.1** data unambiguously prove that the storage modulus of the nanocomposites is higher than the pristine **OPBI**. As shown in **Figure 3.5,** the storage modulus increases with increasing loading of the nanofiller in the membrane. Storage moduli of all the composite membranes are found to be higher than that of the pristine **OPBI**. The widely different morphology, associated with ionic crosslinking and fibrillar network of the composite membranes play a crucial role behind it. In other words, presence of nanoparticle clusters in the **OPBI** matrix creates a large amount of robust interfacial region, where the interfacial interactions (between **OPBI** chains and PSM MOF nanofillers) reduces the segmental mobility of the polymer chains and thereby make them more rigid and stiffer compared to the pristine **OPBI**.

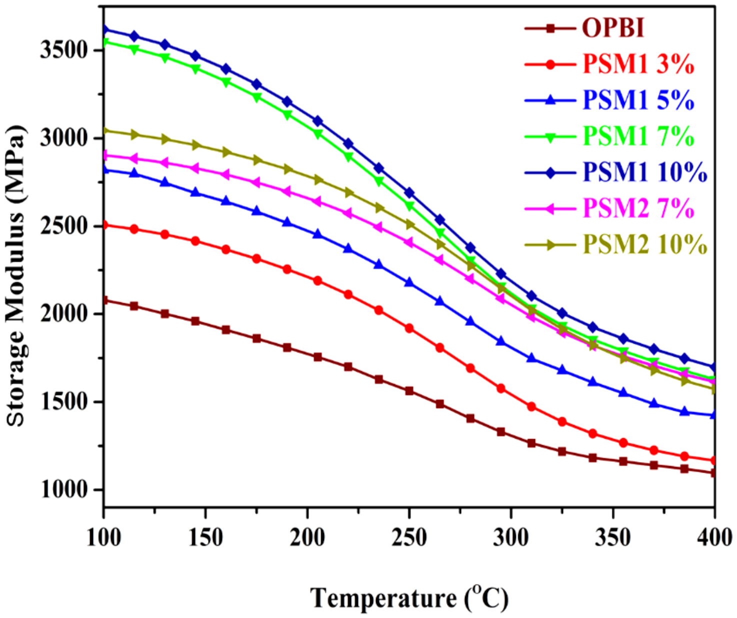

Figure 3.5. Storage modulus plots of **OPBI** nanocomposites, obtained from DMA analysis.

PSM 1-7% and **1-10%** composites are observed to have storage modulus higher than **PSM 2-7%** and **2-10%** composites. Since storage modulus has been analysed with respect to temperature, slightly higher thermal stability of undoped **PSM 1** composites over undoped **PSM 2** composites may have contributed to higher storage modulus of the former one.

Table 3.1. Temperature dependent storage modulus of PSM based **OPBI** nanocomposites obtained from DMA.

Sample	*E' (MPa) at 100 °C*	*% of increase*	*E' (MPa) at 400 °C*	*% of increase*
OPBI	2082		1105	
PSM 1-3%	2508	20.4	1168	5.70
PSM 1-5%	2821	35.4	1412	27.7
PSM 1-7%	3550	70.5	1649	49.2
PSM 1-10%	3624	74	1705	54.2
PSM 2-7%	2905	39.5	1614	46
PSM 2-10%	3045	46.25	1573	42.3

The loss modulus (E″) and tan δ plots against temperature (**Figure A1.6, a-b** in Appendix 1) exhibit only single relaxation peak for all the samples and the temperature corresponding to the peak is denoted as the glass transition temperature (T_g) of the **OPBI** and its composite membranes. The T_g values, obtained from loss modulus (E″) and tan δ plots of all the composite membranes, are summarized in **Table 3.2.** The T_g values, obtained for **OPBI** from loss modulus (E″) and tan δ are respectively 280 °C and 296 °C. In the case for **PSM 1** composites, T_g values are slightly less than those of **OPBI** and decreases with increase in the nanofiller loading from 3% to 10%. In a reverse trend, the T_g values, obtained in case for **PSM 2** composites, are slightly higher than those of pristine **OPBI** and increased with increase in the composite loading from 7% to 10% (**Table 3.2**). The reason behind the different trends of T_g of the **PSM 1** and **PSM 2** loaded composite membranes can be the difference in the nature of H-bonding interactions and complex structure formation between **PSM 1** and **OPBI** matrix when compared to **PSM 2** and **OPBI** matrix. From the TEM images, small differences in morphology can be observed between high loading **PSM 1** and **PSM 2** composite membranes. **PSM 2-10%** composite exhibits more prominent net like cluster morphology, attributed to prominent structural anisotropy over **PSM 1-10%** composite. This kind of morphology decreases the free volume fraction of the polymer and hence higher temperature is required to affect the segmental mobility of the polymer chains.[55] Thus, DMA studies of our nanocomposite membranes suggest the fact that post-synthetic installation of dangling side arm of different length, in the UiO-66 modified MOF nano-fillers, govern the dispersion pattern of PSM MOFs in the **OPBI** matrix which in turn dictates the structure and property of **OPBI** nanocomposites.

Table 3.2. Temperature dependent glass transition temperature (T_g) of PSM based **OPBI** composites obtained from Loss modulus and tan δ plot against temperature from the DMA study.

Sample	*Tg (° C) obtained from E"*	*T_g (° C) obtained from Tan δ*
OPBI	280	296
PSM 1-3%	278	289
PSM 1-5%	269	284
PSM 1-7%	262	280
PSM 1-10%	259	271
PSM 2-7%	282	297
PSM 2-10%	285	298

Oxidative stability

In order to analyse the effect of peroxide radical attack, membranes were immersed into Fenton's reagent (3% H_2O_2 containing 2 ppm $FeSO_4$) at 70 °C for a particular period of time. The oxidative stability as a function of time has been plotted and shown in **Figure 3.6.** All the nanocomposite membranes exhibit excellent chemical stability with respect to pristine **OPBI**. The stability increases with increase in concentration of **PSM 1** and **PSM 2** in the **OPBI** matrix providing evidence that the MOF nanofillers protect the polar groups of **OPBI** from HO• and HOO• radicals attack. The enhanced oxidative stability may be attributed to the formation of H-bonds between the PSM MOFs and the **OPBI** chains. At higher filler content, there are more ionic interactions and hence better shielding of polymer chains. This result into improvement of the durability of the composite membranes under an oxidative environment makes these nanocomposite membranes suitable for PEM applications. The slightly higher oxidative stability of **PSM 2** membranes over **PSM 1** membranes can be attributed to the net-like cluster morphology and better structural anisotropy of **PSM 2** composites at high concentration, over **PSM 1** composites. As, it was mentioned earlier that the slight difference in morphology is a direct consequence of the higher chain length of side arm of **PSM 2** than **PSM 1** and also the marginal higher loading of '$-SO_3H$' containing side arms. The presence of slightly more '$-SO_3H$' groups in **PSM 2** composite membrane over **PSM 1** composite membrane produce more ionic interaction causing more oxidative stability in **PSM 2** composites.

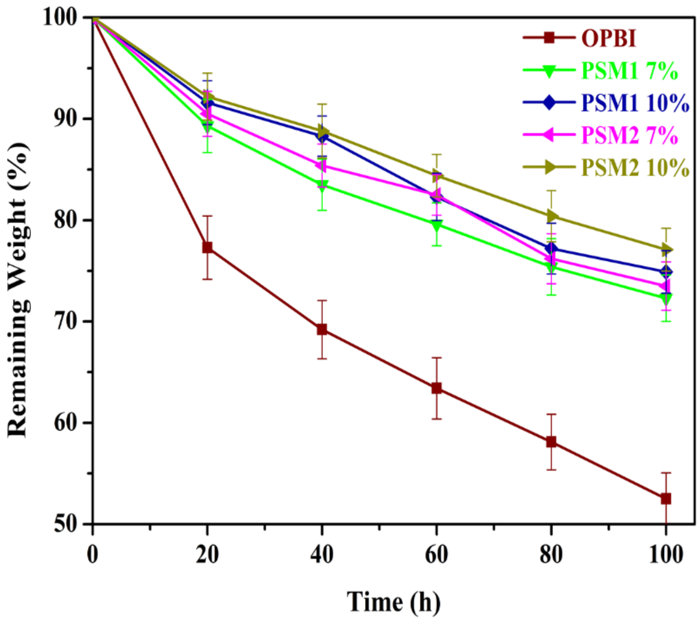

Figure 3.6. Oxidative stability of **OPBI** nanocomposite membranes with different percentage loading of **PSM 1** and **PSM 2**.

Water uptake, swelling ratio and phosphoric acid (PA) loading

The water uptake, swelling ratio and PA doping level of all the composite membranes along with pristine **OPBI** are tabulated in **Table 3.3.** PBI based polymers are hygroscopic in nature and can absorb moisture from the atmosphere due to the tendency of '−N=' atom moiety to form H-bonds with water molecules.[55,57] In our earlier work, **PSM 1** and **PSM 2** MOFs were observed to exhibit highly hydrophilicity.[29] Thus, it is obvious that water uptake capacity of the composite membranes will be more than pristine **OPBI** (water uptake 11.66 wt%). Table 3 denotes that water uptake gradually increases with increasing the loading of the **PSM 1** and **PSM 2** in the polymer network. Of note, water uptake of **PSM 2-7%** (18.97 wt%) and **10%** (20.88 wt%) membranes are slightly higher than **PSM 1-7%** (18.88 wt%) and **10%** (19.75 wt%) membranes. This can be directly correlated with the slightly higher water sorption capacity of **PSM 2** than **PSM 1**.[29]

OPBI undergoes dimensional changes due to absorption of moisture and acid, which cause excessive swelling of the membrane. This serious demerit lowers the potential of pristine **OPBI** to be used as proton conducting membrane.

Table 3.3 exhibits that, swelling ratio decreases with increasing wt% of **PSM 1** and **PSM 2** in the composite membranes. The swelling ratio of **PSM 1-10**% in water and PA are respectively 2.62 wt% and 4.81 wt%. For **PSM 2-10%** membrane, also it is in quite comparable range and exhibits 2.56 wt% and 4.57 wt% in water and PA, respectively. The swelling ratio of both **PSM 1-10%** and **PSM 2-10% OPBI** composite membranes are significantly lower than swelling ratio of pristine **OPBI** in water (4.34 wt%) and PA (6.25 wt%). With the help of PXRD analysis and FT-IR analysis, it is proven that MOFs are involved in strong H-bonding interactions with the **OPBI** matrix. In case of the PSM MOF modified composite membranes, water and PA molecules are unable to penetrate in between the polymer chains to cause excessive swelling due to the presence of interfacial interactions into the ionically crosslinked composite membrane matrix.

PA loading is a very important parameter that dictates the proton conductivity of a PA doped membrane. The observed proton conductivity of a composite membrane is directly proportional with the PA loading level. Higher is the PA loading inside a membrane, higher is the number of labile protons and higher is the expected proton conductivity of the membrane. PA doping levels of all the composite membranes along with pristine **OPBI** are mentioned in **Table 3.3.** The PA doping level of **OPBI** is 16.48 mol/repeat unit. Addition of MOFs into **OPBI** matrix gradually increase the capacity of PA loading in composite membranes, and PA doping level increases with increase in filler concentration in both the cases of **PSM 1** and **PSM 2** composites. For **PSM 1-10%** and **PSM 2-10**% composites, the highest PA loading level of 29.09 mol/repeat unit and 31.35 mol/repeat unit are obtained respectively. The reason behind the higher PA loading of the composite membranes than the pristine **OPBI** can be a cumulative effect of several factors. **Firstly**, both **PSM 1** and **PSM 2** consist of hydrophilic '$-SO_3H$' groups, and with the increase in the loading of **PSM 1** and **PSM 2** in the composites network, more '$-SO_3H$' groups are able to undergo H-bonding interactions with PA molecules as shown in Scheme 2. **Secondly**, the sulfonic acid groups interact with nitrogen in the imidazole ring of **OPBI** to produce a more regular structure (a certain order of crystallinity has been observed in the PXRD analysis) and a bigger space between the chains that can easily accommodate a larger amount of absorbed PA.[61] PA doping disturbs the original crystalline ordering[62] and decreases the peak intensities of * marked peaks between 2θ range 25°–30° for PA doped samples [see **Figure A1.1(a and b)** in Appendix 1]. This change in the crystallinity is accompanied with partial disruption of the pre-existing H-bonded structure and development of new H-bonds involving the newly absorbed PA molecules and the '$-SO_3H$' groups and 'N-H' groups already present in the membrane. This results in the formation of ion pairs or H-bonds of the type: NH^+-H_2PO_4 or $N^+\cdot\cdot H\cdot\cdot H_2PO_{4-}$. Similar interactions are also possible between MOFs primary and secondary amines and PA molecules which help in uptake more PA. And **thirdly**, with increase in filler concentration, the development of highly porous fibrillar morphology may also be helpful towards increased PA uptake. It is important to mention that all these phenomena are facilitated by the increase in loading of PSM-MOF nanofillers in the **OPBI** matrix. Thus, the PA loading of the composite membranes are found to be much higher than the pristine **OPBI** membrane.

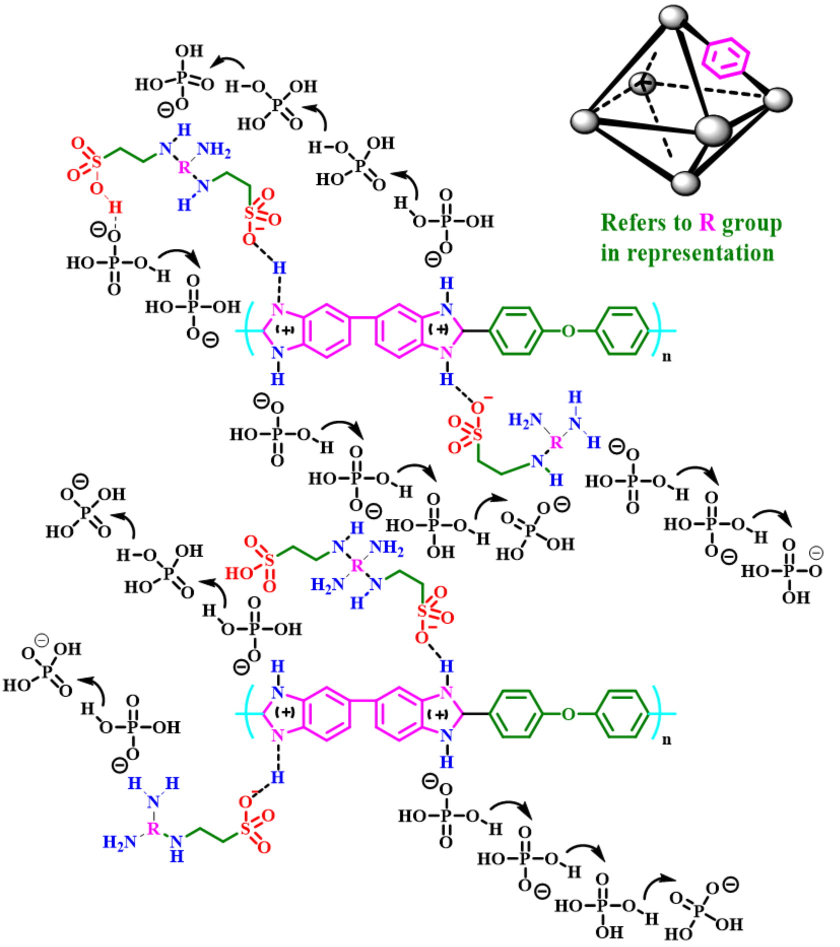

Scheme 3.2. Proposed interaction pattern of PA molecules with PSM composite membrane matrix.

The PA loading of **PSM 2-10%** is slightly more than **PSM 1-10%**, which can be attributed to the slightly higher amount of ‘$-SO_3H$’ groups presence in **PSM 2** over **PSM 1**.[29] Composite membrane containing pristine UiO-66-NH_2, in 10 wt% lacks the presence of ‘$-SO_3H$’ groups, which results in much lower PA loading compare to PSM composites. This explains the crucial role of the ‘$-SO_3H$’ group containing side arm of the **PSM 1** and **PSM 2** behind the high PA loading of the composite membranes.

Table 3.3. Water uptake, swelling ratio, PA loading level data of **OPBI** and PSM-OPBI composite membranes [a]

Sample name	*Water uptake (wt%)*	*Swelling ratio in water (%)*	*Swelling ratio in PA (%)*	*PA loading (no. of mol/OPBI r.u)*
OPBI	11.66 (1.52)	4.34 (1.1)	6.25 (1.21)	16.48 (1.72)
PSM 1-3%	13.28 (1.15)	4.27 (0.45)	5.80 (0.65)	22.31 (1.32)
PSM 1-5%	16.05 (2.12)	3.62 (0.56)	5.41 (0.51)	24.15 (2.04)
PSM 1-7%	18.88 (0.75)	2.91 (0.38)	5.05 (0.16)	26.30 (2.88)
PSM 1-10%	19.75 (0.67)	2.62 (0.23)	4.81 (0.32)	29.09 (1.78)
PSM 2-7%	18.97 (1.08)	2.67 (0.41)	5.06 (0.42)	28.85 (2.56)
PSM 2-10%	20.88 (0.59)	2.56 (0.27)	4.57 (0.85)	31.35 (1.56)
UiO-66-NH_2 10%	–	–	–	21.10 (1.44)

[a] *The number in the parentheses represents standard deviation value obtained from measurements.*

Proton conductivity

Proton conductivity analysis has been carried out for all the composite membranes, pristine **OPBI** membrane and also UiO-66-NH_2 (10 wt%) loaded **OPBI** membrane, by performing impedance spectroscopic analysis using a four-electrode set up. All the composite membranes were doped with PA for 5 days before the measurement. The membranes were placed between two Teflon plates of the conductivity cell. The proton conductivities of all the composite membranes were measured within the temperature range of 30 ºC to 160 ºC. The proton conductivities of the pristine **OPBI** membrane and that of the **OPBI** composite membranes were determined from the corresponding Nyquist plots [**Figure A1.8 (a and b)** in Appendix 1] by fitting with the most relevant equivalent circuit (for details, see Appendix 1). For both the **PSM 1** and **PSM 2** containing composites, proton conductivity increases with increase in the loading of the **PSM 1/ PSM 2 MOF** nanoparticles in the composites and are observed to be significantly higher than that of the pristine **OPBI** as shown in **Figure 3.7.** This result is in accordance with PA doping level (**Table 3.3**) of the composites. The composite membranes with high PA doping show better proton conductivity performance.

Unlike our previous work, where the **PSM 2** MOF was reported to perform proton conduction with almost 50 times lower efficiency than the **PSM 1**, the proton conductivities of **PSM 2-7%** and **PSM 2-10%** membranes are observed here to be slightly higher than those of **PSM 1-7%** and **PSM 1-10%** membranes (**Figure 3.7** and **Table A1.1-A1.3** in the Appendix 1). This reversal of trend of proton conduction between the only MOF particles, and the MOF containing polymer supported membranes, is a striking observation. The key factors behind this reversal of proton conductivity are two-folds: (a) participation of the dangling '−SO_3H' group in the interfacial H-bonding interactions with the **OPBI** matrix, which affects the internal H-bonding interactions, reported previously for the only MOF system and (b) PA acts as the main source of the labile protons in the PA doped composite membranes unlike the '−SO_3H' protons in the only MOFs.[29] Thus, it can be said that, the interfacial H-bond formation in the undoped composite membranes and also the H-bond formation involving absorbed PA molecule in case of the PA doped composite membranes have the capacity to completely change the H-bonding scheme, present in the MOF only system. This change in the H-bonding schemes from "the only **PSM 1** and **PSM 2** MOFs" to the "nanofillers doped composite polymer membranes" results in the reversal of the observed proton conductivity order in the present work.

The slightly higher PA loading of **PSM 2** containing composite membrane than **PSM 1** containing composite membrane may play a crucial role behind the enhanced proton conductivity of the former than the later. In addition, the presence of '−SO_3H' groups, primary amines and secondary amines in the composites facilitate the proton conduction by inducing additional H-bonding with PA and hence forming proton conduction path as described earlier. Hydrophilic '−SO_3H' groups help in the formation of proton conduction channel by H-bonding interaction with PA.[63,64] Thus more '−SO_3H' groups in the composite causes more hydrophilic ion channel formation and helps in higher amount of PA loading, which in turn facilitates the proton conduction. The slightly more grafting of '−SO_3H' in **PSM 2** over **PSM 1** helps in the increased PA loading, hence, more proton conduction.

The proton conductivity of pristine **OPBI** membrane is found to be 0.067 Scm^{-1} at 160 °C. Proton conductivity of **PSM 1-10%** is found to be the highest (0.290 Scm^{-1} at 160 °C) among **PSM 1** composites. On the other hand, the proton conductivity of 0.308 Scm^{-1} at 160 °C is obtained for **PSM 2-10%** membrane, which is the highest among all the **PSM 1** and **PSM 2** containing composites membranes. Proton conductivity of 0.138 Scm^{-1} has been obtained for UiO-66-NH_2 10%, membrane at 160 °C, which is even significantly lower than the proton conductivity of **PSM 1-3%** composite membrane (0.202 Scm^{-1}) at the same temperature. This tremendously low proton conduction can be directly correlated with the absence of '−SO_3H' groups in UiO-66-NH_2. Proton conductivity of **PSM 1-12.5%** and **PSM 2-12.5%** membranes are 0.261 Scm^{-1} and 0.283 Scm^{-1}, respectively at 160 °C which are lower than that of **PSM 1-10%** and **PSM 2-10%** (**Figure A1.8(c)** in Appendix 1). This observation can be explained by considering the probable agglomeration of PSM fillers in the membrane in case of higher filler loading (> 10%), which can obstruct the proton conduction pathway resulting in decreased proton conductivity.[50] Further, decrease in mechanical strength of the membranes is observed with increasing filler loading more than 10% as seen from the storage modulus *vs.* temperature plots of **PSM -10%** and **PSM-12.5%** [**Figure A1.6(c-d)** in Appendix 1].

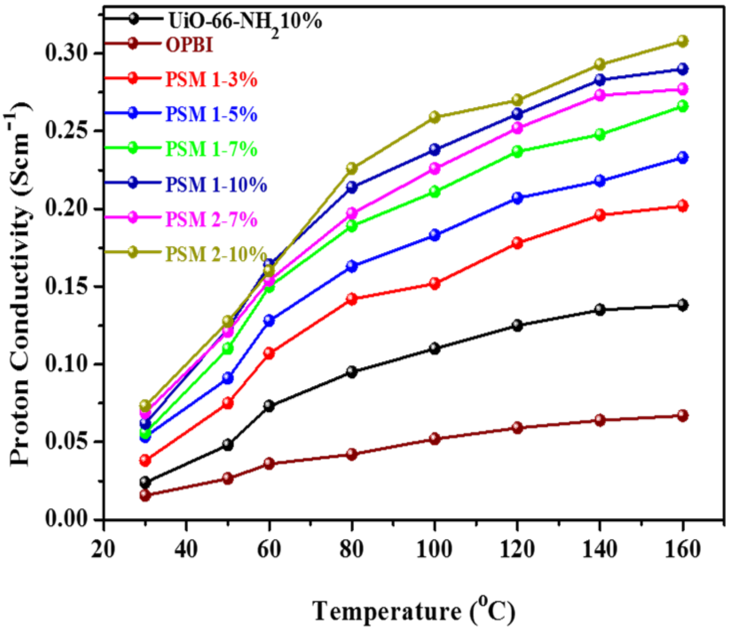

Figure 3.7. Proton conductivity values of **OPBI**, PSM composite membranes along with UiO-66-NH_2 10% membrane.

According to the work of Jana and co-worker, the presence of crystalline planes in the polymer matrix improves conductivity of PA acid doped PBI membranes.[55,56] Crystallinity induces more accessible proton conducting channels. Both undoped and PA doped composite membranes exhibit crystallinity unlike amorphous pristine **OPBI**. This helps in the increased proton conductivity of the composite membranes. In addition, the porous morphology obtained from FESEM [**Figure 3.3(a-c)** and **Figure A1.3(a-d)** in Appendix 1] is helpful towards more amount of PA molecules uptake into the pores, which further facilitates increased proton conductivity of composite membranes.

The **Figure A1.9** of Appendix 1 represents the isothermal proton conductivities of 7% and 10% PSM MOF composites and pristine **OPBI** plotted against time. The membranes were isothermally kept at 160 °C for 24 h. Under this condition, the conductivity of each composite membranes and pristine **OPBI** membrane were measured for every 2 h up to 24 h. From the **Figure A1.9** (Appendix 1), it can be observed that, within the first 2–4 h, there is an initial decrease in observed proton conductivity values for each material. After the initial period, the observed proton conductivities are stable up to 24 h. The PA doped **PSM 1** and **PSM 2** containing composite membranes exhibit much less decrease in conductivity compared to the PA doped pristine **OPBI**. This is due to the presence of the PSM MOF nanofillers in the composite membranes. The extensive interfacial H-bonding interactions between the **PSM 1 / PSM 2 MOF** and **OPBI** matrix provide the composite membranes with the enhanced stability that help them to retain their proton conductivity under long-term isothermal measurement at elevated temperature. This proves the enhancement of stability of the composite membranes due to the presence of the PSM MOF nanofillers.

For hopping-like temperature dependent proton conduction mechanism, conductivity follow Arrhenius equation,[65]

$$\ln(\sigma T) = \ln \sigma_o - \frac{E_a}{RT} \qquad \text{------} (1)$$

where σ is the proton conductivity of the membrane (Scm^{-1}), σ_o is the pre-exponential factor ($SK^{-1}\ cm^{-1}$), E_a is the proton conducting activation energy ($kJ\ mol^{-1}$), R is the ideal gas constant ($J\ mol^{-1}K^{-1}$) and T is the temperature (K). E_a, which is the minimum energy required for proton conduction, is obtained from the slope of linear fit of (eq.1).

The Arrhenius plots of acid doped pristine **OPBI** and all the nanocomposite membranes are illustrated in **Figure 3.8.** From the Arrhenius plot, activation energy (E_a) values have been calculated based on the proton conductivity values obtained within the temperature range of 30 ^oC- 160 ^oC. E_a values, obtained from **OPBI**, **PSM 1-10%** and **PSM 2-10**% membranes are 14.56 kJ/mol (0.15eV), 14.76 kJ/mol (0.152 eV) and 14.30 kJ/mol (0.148 eV) respectively, which implies that the proton conduction in all these materials follow Grotthuss proton transport mechanism. This occurs as a result of proton hopping between PA molecules, **OPBI** and uncoordinated functional groups of the PSM MOF nanofillers through continuous construction and destruction of H-bonding network. Under the application of bias, the pre-existing proton conduction channel possessing extensive H-bonding facilitates this proton hopping.[66,67] Also, in the case of composites membranes, some irregularities from linear shape of the plots are observed, and this might suggest that proton conduction is partly contributed by vehicular mechanism as well. Self-assembly of PSM fillers causes self-diffusion of protons through the proton conducting channels created by the former, or a vehicle mechanism could operate through transfer of the protons from the surface of the PSM nano-filler to the next PSM nano-filler via PA network as proton carriers. The E_a value to the composite membranes found to be slightly higher than that of pristine OPBI, because nanofillers act as carrier bridge for proton conduction, and this process requires more energy.[50,55,57,67]

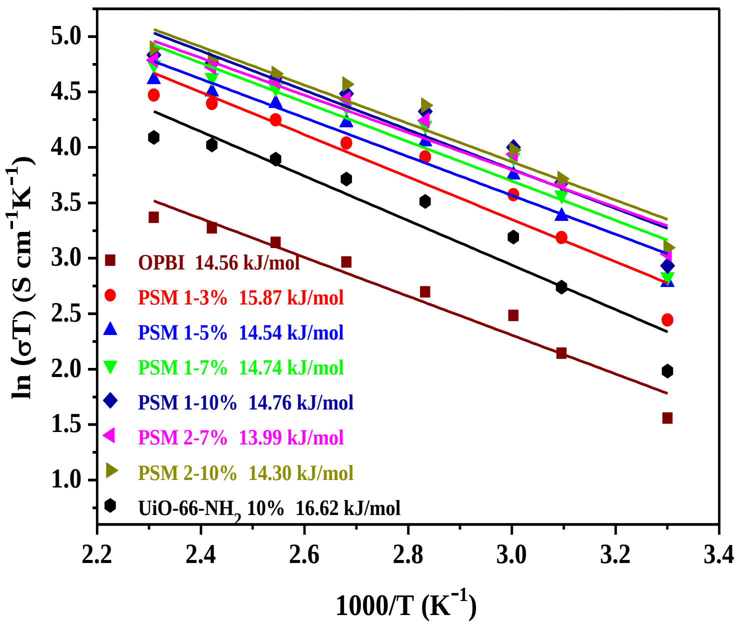

Figure 3.8. Arrhenius activation energy plot of **OPBI** and nanocomposite membranes at indicated loadings.

Stress-strain studies

In order to use any membrane in PEM fuel cell, dimensional stability of the PA doped membrane has always been a matter of discussion. The various mechanical properties, like, tensile strength, elongation at break values depend on the amount of the PSM MOF nanofillers loading as shown in **Table 3.4.** As shown in the **Figure 3.9(a and b),** huge increase in tensile strength observed in case of PA loaded nanocomposites as compared with PA loaded pristine **OPBI**. The presence of interfacial interactions between **OPBI** and MOFs, owing to the formation of fibrillar morphology and self-assembled structural anisotropy of the nanocomposites, causes mechanical and tensile reinforcement of the composites with respect to the pristine **OPBI**. As the loading level of the nanofillers increases *i.e.*, moving from **PSM 1-5%** to **PSM 1-10%**, and from **PSM 2-7%** to **PSM 2-10%** composite membrane, tensile strength value of the composites decreases with huge increase in elongation at break value. This is due to the fact that, the acid-base interactions between imidazole of **OPBI** and sulfonic acid groups of **PSM 1** and **PSM 2** are affected (observed from decreased peak intensity in PXRD) by the PA molecules after PA doping. This phenomenon was also reported in various

PA doped membranes[62,68,69] and can be explained by considering the fact that PA molecules exert plasticizing effect on polymer membranes and therefore loosen the compact packing of polymer backbones. This makes the chain movement much flexible.[69] Increase in filler loading causes more PA loading, which makes the membranes more flexible and that results into decrease in tensile stress and significantly improve in their elongation at break. Tensile strength values of **PSM 2-7%** and **PSM 2-10%** membranes are slightly lower than those of **PSM 1-7%** and **PSM 1-10%** membranes. This may be attributed to the lower storage modulus value, obtained from **PSM 2** composites over **PSM 1**. But, **PSM 2-7%** and **PSM 2-10%** composites elongation values at break are quite comparable with **PSM 1** higher loading composites.

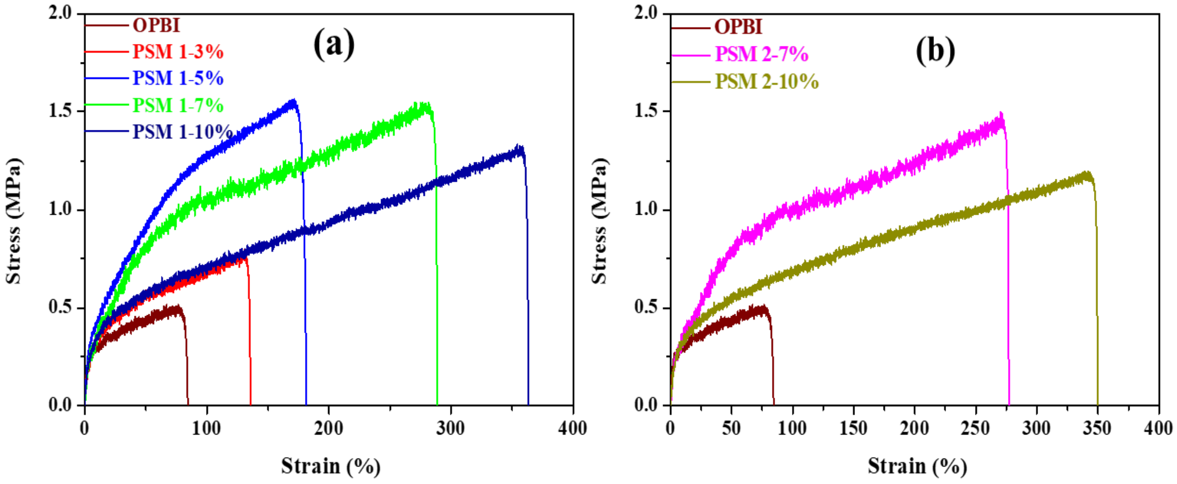

Figure 3.9. Stress-strain profile of phosphoric acid loaded **OPBI** nanocomposite **(a) PSM 1** and **(b) PSM 2** membranes.

Table 3.4. Tensile stress and elongation at break values of **OPBI** and **PSM-OPBI** composite membranes.

Sample	*Tensile stress (MPa)*	*Elongation at break (%)*	*Young Modulus*
OPBI	0.50	81.6	0.07
PSM 1-3%	0.76	134	0.087
PSM 1-5%	1.55	176.1	0.095
PSM 1-7%	1.51	285.2	0.080
PSM 1-10%	1.31	360.2	0.076
PSM 2-7%	1.45	274.3	0.078
PSM 2-10%	1.18	350	0.068

Acid leaching study

While performing proton conduction in the fuel cell, under actual operational condition (at elevated temperatures, under high humidity *etc.*), very often the PEM suffers from acid leaching from the PA doped membranes and lose its capacity to function as proton exchange membrane. Thus, acid leaching test has been performed with PA doped **OPBI** composite membranes as shown in **Figure 3.10(a)** (see also **Figure A1.10** in Appendix 1). The PA doped membranes were dried, weighed, and kept under saturated water vapour using a home-made set-up to check PA leaching via water condensation at 100 ºC for a period of 3 h. The protocol has adapted from previous studies of PA leaching.[49,70]

After every one hour, the weight of the acid leached membrane was measured carefully. The weight loss ratio of PA present in the membrane is calculated and the results are shown in **Figure 3.10(a).** In the case of **OPBI** itself, the weight loss occurs to 45% after first hour of leaching analysis, further decrease was observed in the 2nd and 3rd hour to 66% and 71%. Thus, **OPBI** is found to be unable to hold most of the doped acid molecules under operational condition within its matrix. On the other hand, the leaching experiment for the PSM MOF nanofiller containing composite membranes result in low acid leaching. Acid leaching decreases with increase in loading of the **PSM 1** and **PSM 2** nanofillers in the composites. **PSM 1-3%** exhibits weight loss of 31%, while **PSM 1-10%** losses 21.5 % of its initial weight after 3 hours of analysis. **PSM 2-10%** membrane leaches least amount of acid and the weight loss is only 18.8% after three hours of leaching study. Thus, **PSM 2** containing composite-membranes can be accounted as the most efficient one, in terms of acid retention capacity. The reason for this low acid leaching of the **PSM 1** and **PSM 2** containing composites are attributed to the presence of sulfonic acid groups in them, along with the presence of primary and secondary amines, causing all together strong H-bonding interactions with PA molecules. More loading of **PSM 1** and **PSM 2** nanofiller into the composite causes more uphold of PA through extensive H- bonding, which results in more PA loading and less leaching. Also, the porous morphology and a certain order of crystallinity help composites in retaining the PA inside the matrix. The slightly lower acid leaching by **PSM 2-10%** composite than **PSM 1-10%** composite can be explained by considering the slightly higher amount of sulfonic acid groups in **PSM 2** than in **PSM 1**. Acid uptake capacity of UiO-66-NH_2 modified **OPBI** membrane was similar to the pristine **OPBI** membrane, due to lack of hydrophilic sulfonic acid group in the UiO-66-NH$_2$ nanofiller containing composite leaches 44% of PA within three hours of analysis.

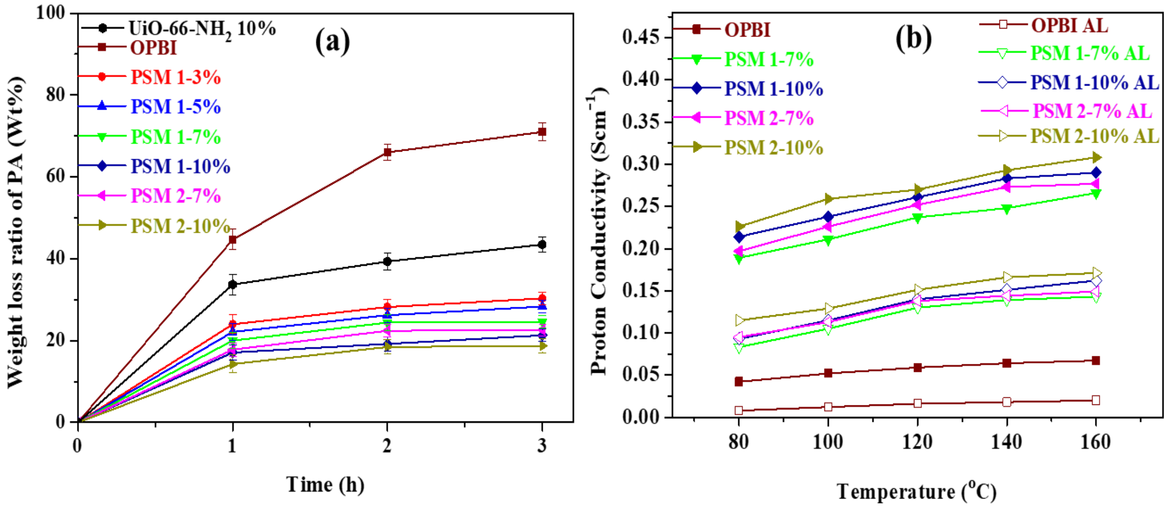

Figure 3.10. (a) Time dependent acid leaching study of **OPBI** and PSM composite membranes along with UiO-66-NH$_2$ 10%. **(b)** Proton conductivity of **OPBI** composite membranes before and after acid leaching study (* AL means after leaching).

The acid leaching ability has further been confirmed by measuring the proton conductivity of the composite membranes after acid leaching analysis for 3h. After the completion of acid leaching test, the moisture and acid were wiped from the membrane, and the conductivity was measured from 80 °C to 160 °C (fuel cell operating temperature). **Figure 3.10(b)** depicts the plots of proton conductivity of freshly acid doped membranes with acid leached pristine **OPBI** membrane, **PSM 1** and **PSM 2** composite membranes. The leached **PSM 1-7%**, **PSM 1-10%**, **PSM 2-7**%, and **PSM 2-10%**, composite membranes exhibit proton conductivity of 0.143, 0.162, 0.149 and 0.171 S/cm, respectively at 160 °C which is very high compared to the proton conductivity of 0.02 Scm^{-1} observed for acid leached **OPBI** at this temperature. It must be noted that the lowering of conductivity after leaching is more prominent in case of pristine **OPBI**, whereas it is relatively less in case of the PSM MOF nano-fillers containing composites. Thus, the role of porous UiO-66 type of MOF containing uncoordinated '−SO$_3$H' groups and '−NH$_2$' groups, in retaining acid and in elevating conductivity of the composite membranes are clearly understood.

Conclusion

Our current work ensembles preparation of **OPBI** nanocomposite membranes with different weight percent loadings of **PSM 1** and **PSM 2** MOFs by solution casting blending method and studied thoroughly with an objective to develop PEMs (proton exchange membranes) with enhanced or better properties for fuel cell application. We have demonstrated, in this work, a unique strategy to develop a superior PEM, by employing a super proton conductor MOF as nanofiller into a versatile polymer membrane PA doped **OPBI** via extensive interfacial H-bonding interactions**.** The highest proton conductivity of the fuel cell's PEM is not the only criterion for a superior PEM of an efficient fuel cell. Besides its super proton conductivity, the PEM should qualify many more crucial benchmarks, for example, high capacity of acid loading, high acid retention capacity, very good thermo-mechanical and tensile properties, excellent oxidative stability and high proton conductivity at the wide temperature range. **PSM 1-OPBI** and **PSM 2-OPBI** nano-composites not only exhibits super proton conduction but also new crystalline planes, self-assembled anisotropic net-like morphology, high capacity of PA loading, high acid retention capacity, excellent thermo-mechanical and tensile properties, excellent oxidative stability, and notably high proton conductivity. More specifically, the dangling uncoordinated '$-SO_3H$' groups along with primary and secondary '$-NH_2$' groups of the nanofiller (a super proton conductor MOF in the present case) are found to participate in interfacial H-bonding interactions during the formation of the membrane. It also helps in the high PA loading as well as retention of PA molecules. During the membrane formation and during the PA loading, these uncoordinated groups form extensive H-bonds with the (host) **OPBI** molecules and the PA molecules, respectively. In case of the PA loaded nano-composite membranes, the proton conductivity is dictated mainly by the amount of the PA loading and the number of '$-SO_3H$' groups present in the moiety. Thus, the proton conductivity of the **PSM 1** and **PSM 2** composite membranes (present work) are observed to be similar. Strictly speaking, the proton conductivity of **PSM 2** composite membrane is marginally higher than **PSM 1** composite membrane. This is a direct consequence of its slightly higher loading of '$-SO_3H$' functionality and thus higher loading of PA. The proton conductivity obtained by us for **PSM 1-10%** and **PSM 2-10%** composite membranes at 160 °C are among the highest proton conductivity reported in literature so far on MOF based proton conducting composite membranes. The parent UiO-66-NH_2 composite exhibits lower PA loading and lower proton conductivity than **PSM 1** and **PSM 2** modified composites due to absence of the dangling '$-SO_3H$' containing side arm. Thus, the PSM of the parent MOF plays a vital role in the **PSM-**

OPBI nanocomposites membranes and made them potential candidates for use in high temperature proton exchange fuel cells.

References

(1) Biyikoğlu, A. Review of Proton Exchange Membrane Fuel Cell Models. *Int. J. Hydrogen Energy* **2005**, *30*, 1181–1212.

(2) Peighambardoust, S. J.; Rowshanzamir, S.; Amjadi, M. *Int. J. Hydrogen Energy* **2010**, *35*, 9349–9384.

(3) Daud, W. R. W.; Rosli, R. E.; Majlan, E. H.; Hamid, S. A. A.; Mohamed, R.; Husaini, T. *Renew. Energy* **2017**, *113*, 620–638.

(4) Kraytsberg, A.; Ein-Eli, Y. *Energy and Fuels* **2014**, *28*, 7303–7330.

(5) Walkowiak-Kulikowska, J.; Wolska, J.; Koroniak, H. P*Phys. Sci. Rev.* **2017**, *2*, 1–36.

(6) Hickner, M. A.; Pivovar, B. S. *Fuel Cells* **2005**, *5*, 213-229.

(7) Kreuer, K. D. Proton Conductivity: Materials and Applications. *Chem. Mater.* **1996**, *8*, 610–641.

(8) Ramaswamy, P.; Wong, N. E.; Shimizu, G. K. H. *Chem. Soc. Rev.* **2014**, *43*, 5913–5932.

(9) Scofield, M. E.; Liu, H.; Wong, S. S. *Chem. Soc. Rev.* **2015**, *44*, 5836–5860.

(10) Laberty-Robert, C.; Vallé, K.; Pereira, F.; Sanchez, C. *Chem. Soc. Rev.* **2011**, *40*, 961–1005.

(11) Mauritz, K. A.; Moore, R. B. State of Understanding of Nafion. *Chem. Rev.* **2004**, *104*, 4535–4585.

(12) Sahu, A. K.; Pitchumani, S.; Sridhar, P.; Shukla, A. K. *Bull. Mater. Sci.* **2009**, *32,* 285-294.

(13) Nagarkar, S. S.; Unni, S. M.; Sharma, A.; Kurungot, S.; Ghosh, S. K. *Angew. Chemie. Int.. Ed.* **2014**, *53*, 2638-2642.

(14) Taylor, J. M.; Komatsu, T.; Dekura, S.; Otsubo, K.; Takata, M.; Kitagawa, H. *J. Am. Chem. Soc.* **2015**, *137*, 11498–11506.

(15) Dong, X.-Y.; Wang, R.; Wang, J.-Z.; Zang, S.-Q.; Mak, T. C. W. *J. Mater. Chem. A*, **2015**, *3*, 641-647.

(16) Liu, S.-S.; Han, Z.; Yang, J.-S.; Huang, S.-Z.; Dong, X.-Y.; Zang, S.-Q. *Inorg. Chem.* **2020**, *59*, 396-402.

(17) Phang, W. J.; Jo, H.; Lee, W. R.; Song, J. H.; Yoo, K.; Kim, B.; Hong, C. S. *Angew. Chemie. Int. Ed.* **2015**, *54*, 5142–5146.

(18) Dey, C.; Kundu, T.; Banerjee, R. *Chem. Commun,* **2012**, *48,* 266-268.

(19) Sasmal, H. S.; Aiyappa, H. B.; Bhange, S. N.; Karak, S.; Halder, A.; Kurungot, S.; Banerjee, R. *Angew. Chemie. Int.. Ed..* **2018**, 57, 10894–10898.

(20) Li, W. H.; Lv, J.; Li, Q.; Xie, J.; Ogiwara, N.; Huang, Y.; Jiang, H.; Kitagawa, H.; Xu, G.; Wang, Y. *J. Mater. Chem. A* **2019**, *7*, 10431–10438.

(21) Kim, S.; Joarder, B.; Hurd, J. A.; Zhang, J.; Dawson, K. W.; Gelfand, B. S.; Wong, N. E.; Shimizu, G. K. H. *J. Am. Chem. Soc.* **2018**, *140*, 1077–1082.

(22) Li, X. M.; Dong, L. Z.; Li, S. L.; Xu, G.; Liu, J.; Zhang, F. M.; Lu, L. S.; Lan, Y. Q. *ACS Energy Lett.* **2017**, *2*, 2313–2318.

(23) Elahi, S. M.; Chand, S.; Deng, W. H.; Pal, A.; Das, M. C. *Angew. Chemie. Int. Ed.* **2018**, *57*, 6662–6666.

(24) Yang, F.; Xu, G.; Dou, Y.; Wang, B.; Zhang, H.; Wu, H.; Zhou, W.; Li, J. R.; Chen, B. *Nat. Energy* **2017**, *2*, 877–883.

(25) Huang, S.-Z.; Liu, S.-S.; Zhang, H. J.; Han, Z.; Zhao, G.; Dong, X.-Y.; Zang, S.-Q. *ACS Appl. Mater. Interfaces* **2020,** *12*, 28720−28726.

(26) Yang, F.; Huang, H.; Wang, X.; Li, F.; Gong, Y.; Zhong, C.; Li, J. R. *Cryst. Growth Des.* **2015**, *15*, 5827–5833.

(27) Ragon, F.; Campo, B.; Yang, Q.; Martineau, C.; Wiersum, A. D.; Lago, A.; Guillerm, V.; Hemsley, C.; Eubank, J. F.; Vishnuvarthan, M.; Toulelle, F.; Horcajada, P.; Vimont, A.; Llewellyn, P. l.; Daturi, M.; Vinot, S. D.; Maurin, G.; Serre, C.; Devic, T.; Clet, G. *J. Mater. Chem. A* **2015**, *3*, 3294–3309.

(28) Dong, X.-Y.; Wang, J.-H.; Liu, S.-S.; Han, Z.; Tang, Q.-J.; li, F.-F.; zang, S.-Q. *ACS Appl. Mater. Interfaces* **2018**, *10*, 38209−38216.

(29) Mukhopadhyay, S.; Debgupta, J.; Singh, C.; Sarkar, R.; Basu, O.; Das, S. K. *ACS Appl. Mater. Interfaces* **2019**, *11*, 13423–13432.

(30) Smitha, B.; Sridhar, S.; Khan, A. A. *J. Membr. Sci.* **2005**, *259*, 10–26.

(31) Hickner, M. A.; Ghassemi, H.; Kim, Y. S.; Einsla, B. R.; McGrath, J. E. *Chem. Rev.* **2004**, *104*, 4587–4611.

(32) Li, Q.; Jensen, J. O.; Savinell, R. F.; Bjerrum, N. J. *Prog. Polym. Sci.* **2009**, *34*, 449–477.

(33) Li, Z.; He, G.; Zhang, B.; Cao, Y.; Wu, H.; Jiang, Z.; Tiantian, Z. *ACS Appl. Mater. Interfaces* **2014**, *6*, 9799–9807.

(34) Tsai, C. H.; Wang, C. C.; Chang, C. Y.; Lin, C. H.; Chen-Yang, Y. W. *Int. J. Hydrogen Energy* **2014**, *39*, 15696–15705.

(35) Kim, H. J.; Talukdar, K.; Choi, S. J. *J. Nanoparticle Res.* **2016**, *18*, 47.

(36) Rao, Z.; Tang, B.; Wu, P. *ACS Appl. Mater. Interfaces* **2017**, *9*, 22597–22603.

(37) Donnadio, A.; Narducci, R.; Casciola, M.; Marmottini, F.; D'Amato, R.; Jazestani, M.; Chiniforoshan, H.; Costantino, F. *ACS Appl. Mater. Interfaces* **2017**, *9*, 42239–42246.

(38) Li, Q.; He, R.; Jensen, J. O.; Bjerrum, N. J. *Chem. Mater.* **2003**, *15*, 4896–4915.

(39) Thompson, E. L.; Capehart, T. W.; Fuller, T. J.; Jorne, J. *J. Electrochem. Soc.* **2006**, *153*, 2351-2362.

(40) Wu, L.; Zhang, Z.; Ran, J.; Zhou, D.; Li, C.; Xu, T. *Phys. Chem. Chem. Phys.* **2013**, *15*, 4870–4887.

(41) Sun, H.; Tang, B.; Wu, P. *ACS Appl. Mater. Interfaces* **2017**, *9*, 26077–26087.

(42) Sun, H.; Tang, B.; Wu, P. *ACS Appl. Mater. Interfaces* **2017**, *9* , 35075–35085.

(43) Zhang, H.; Shen, P. K. *Chem. Rev.* **2012**, *112*, 2780–2832.

(44) Kim, S. K.; Choi, S. W.; Jeon, W. S.; Park, J. O.; Ko, T.; Chang, H.; Lee, J. C. *Macromolecules* **2012**, *45*, 1438–1446.

(45) Mader, J. A.; Benicewicz, B. C. *Macromolecules* **2010**, *43*, 6706–6715.

(46) Li, Q.; Hjuler, H. A.; Bjerrum, N. J. *Journal of Applied Electrochemistry* **2001,** *31*, 773-779.

(47) Tian, X.; Wang, S.; Li, J.; Liu, F.; Wang, X.; Chen, H.; Ni, H.; Wang, Z. *Int. J. Hydrogen Energy* **2017**, *42*, 21913–21921.

(48) Van De Ven, E.; Chairuna, A.; Merle, G.; Benito, S. P.; Borneman, Z.; Nijmeijer, K. *J. Power Sources* **2013**, *222*, 202–209.

(49) Kutcherlapati, S. R.; Koyilapu, R.; Jana, T. *J. Polym. Sci. Part A Polym. Chem.* **2018**, *56*, 365–375.

(50) Escorihuela, J.; Sahuquillo, Ó.; García-Bernabé, A.; Giménez, E.; Compañ, V. *Nanomaterials* **2018**, *8*, 775.

(51) Escorihuela, J.; Narducci, R.; Compañ, V.; Costantino, F. *Adv. Mater. Interfaces* **2019**, *6*, 1801146.

(52) Singha, S.; Koyilapu, R.; Dana, K.; Jana, T. *Polymer* . **2019**, *167*, 13–20.

(53) Singha, S.; Jana, T.; Modestra, J. A.; Naresh Kumar, A.; Mohan, S. V. *J. Power Sources* **2016**, *317*, 143–152.

(54) Sana, B.; Jana, T. *Eur. Polym. J.* **2016**, *84*, 421–434.

(55) Singha, S.; Jana, T. *ACS Appl. Mater. Interfaces* **2014**, *6*, 21286–21296.

(56) Singha, S.; Jana, T. *Polymer* **2014**, *55*, 594–601.

(57) Maity, S.; Singha, S.; Jana, T. *Polymer* **2015**, *66*, 76–85.

(58) Øien, S.; Wragg, D.; Reinsch, H.; Svelle, S.; Bordiga, S.; Lamberti, C.; Lillerud, P. K. *Cryst. Growth Des.* **2014,** *14,* 5370−5372.

(59) Maity, S.; Sannigrahi, A.; Ghosh, S.; Jana, T. *Eur. Polym. J.* **2013**, *49*, 2280–2292.

(60) Singha, S.; Jana, T. *Polymer* **2016**, *98*, 20–31.

(61) Lobato, J.; Cañizares, P.; Rodrigo, M. A.; Úbeda, D.; Pinar, F. J. *J. Memb. Sci.* **2011**, *369*, 105–111.

(62) Jiang, J.; Zhu, X.; Qian, H.; Xu, J.; Yue, Z.; Zou, Z.; Yang, H. *Sustain. Energy Fuels* **2019**, *3*, 2426–2434.

(63) Liu, Y. L. *Polym. Chem.* **2012**, *3*, 1373–1383.

(64) Kannan, R.; Parthasarathy, M.; Maraveedu, S. U.; Kurungot, S.; Pillai, V. K. *Langmuir* **2009**, *25*, 8299–8305.

(65) He, R.; Li, Q.; Xiao, G.; Bjerrum, N. J. *J. Membr. Sci.* **2003**, *226*, 169–184.

(66) Vilčiauskas, L.; Tuckerman, M. E.; Bester, G.; Paddison, S. J.; Kreuer, K. D. *Nat. Chem.* **2012**, *4*, 461–466.

(67) Singha, S.; Jana, T. *J. Indian Inst. Sci.* **2016**, *96*, 351–364.

(68) Yang, J.; Wang, J.; Liu, C.; Gao, L.; Xu, Y.; Che, Q.; He, R. *J. Membr. Sci.* **2015**, *493*, 80–87.

(69) Dang, J.; Zhao, L.; Zhang, J.; Liu, J.; Wang, J. *J. Membr. Sci.* **2018**, *545* , 88–98.

(70) Lee, K. S.; Spendelow, J. S.; Choe, Y. K.; Fujimoto, C.; Kim, Y. S. *Nat. Energy* **2016**, *1*, 16120.

Chapter 4

Covalent Organic Framework and Polybenzimidazole Composite Proton Exchange Membrane with superior Proton Conductivity

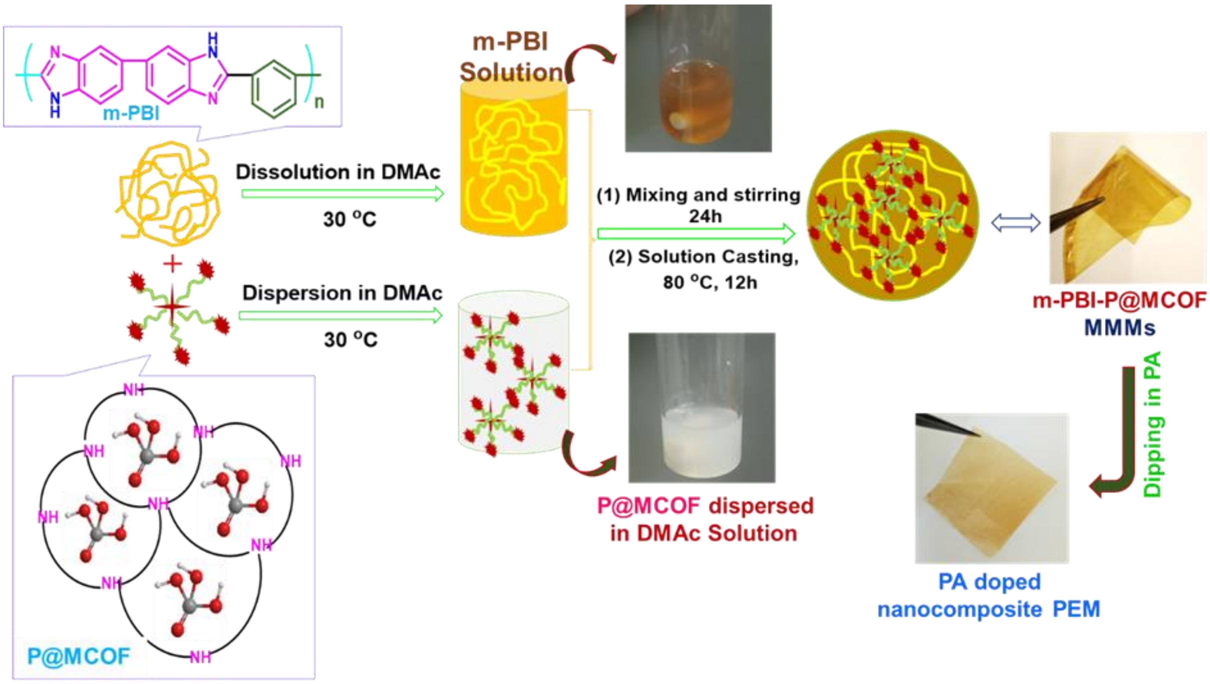

Anupam Das, Mousumi Hazarika, Balakondareddy Sana and Tushar Jana*. Covalent Organic Framework and Polybenzimidazole Composite Proton Exchange Membrane with superior Proton Conductivity. *Under revision: ACS Appl. Nano Mater.*

Abstract

Fabrication and design of efficient proton conduction nanochannels within the solid electrolyte materials is pivotal and challenging to develop energy-efficient devices like proton exchange membrane fuel cells (PEMFCs). In this work, we have synthesized melamine-based Schiff base network type porous covalent organic framework (MCOF) and impregnated phosphoric acid (H_3PO_4) as electrolyte into the pores of the MCOF via vacuum assisted method. Unfortunately, stable film/membrane did not form from H_3PO_4 loaded MCOF (P@MCOF) and hence in order to resolve this, mixed matrix membranes were fabricated for the first time with the P@MCOF and [2,2′-(m-phenylene)-5,5′-benzimidazole] or m-PBI. Formation of acid base pair occurred in m-PBI-P@MCOF composite membrane between the P@MCOF and m-PBI driven by H-bonding interfacial interaction. Also, the acidic−PO_3H_2 functionalities in the pores of P@MCOF provides abundant sites for labile proton transport, which enables uninterrupted proton conduction ion channels with low energy barrier in the composite membranes. Furthermore, all the composite membranes were immersed and loaded with phosphoric acid (PA) to obtain proton exchange membranes (PEMs). Use of H_3PO_4 impregnated P@MCOF framework structures as nanofillers into the m-PBI membrane matrix resulted into superior proton conductivity, excellent thermal, thermo-mechanical and tensile stress-strain profile, improved acid (PA) holding efficiency and improved chemical stability of the m-PBI-P@MCOF membranes in comparison with the pristine m-PBI. The resulted proton conductivity of m-PBI-P@MCOF-10% membrane at 180°C is **0.309 S cm^{-1}**, a five-fold increment with respect to pristine m-PBI proton conductivity (**0.061 S cm^{-1}**) under the identical experimental condition. This work clearly illustrates the nature of H-bonded interfacial interaction between the P@MCOF nanofillers with the m-PBI, which can efficiently execute proton conduction. This will be the first report of COF as nanofillers into the PBI matrix for generation of superior proton conducting membranes.

Introduction

In the modern world, consumption of fossils fuel has been increased significantly over the years due to extensive urbanization causing severe environmental pollution and resulted global warming. Also, the increased demand of limited source of fossil fuel is a warning to the society for its unavailability in near future. In the present scenario, fuel cell (FC) has considerable attraction to the entire scientific community as an alternative source of energy to mitigate the above shortcomings.[1-3] Technically, fuel cell is an efficient electrochemical device, which facilitates conversion of chemical energy into electrical energy with generation of heat and H_2O.[4–6] Proton exchange membrane fuel cell (PEMFCs) remains the most prominent energy conversion device among the fuel cells in which the efficiency of the FC is largely dependent upon ability of proton conduction of the PEM.[7–10] Nafion membrane as PEM has gained significant attention among the researchers for their promising proton conductivity along with chemical and mechanical stability, however Nafion membrane suffers from severe loss in proton conduction beyond 80 °C and relative humidity (RH) less than 50%.[11–13] A replacement to the conventional Nafion membranes, polybenzimidazole (PBI) based polymers evolve into literature as efficient PEM materials with reasonable proton conductivity when treated with phosphoric acid (PA), under anhydrous environment at elevated temperature (160°C-200°C) along with high thermal, thermomechanical stability, tensile properties, and promising oxidative stability in presence of harsh oxidative environment.[14–16] Though, PBI based PEMs also suffers from low PA doping level, severe PA leaching at elevated temperature, which causes loss in proton conductivity. Also under PA doped condition PBI membranes results excessive swelling followed by poor mechanical robustness which renders to achieve best fuel cell efficiency.[17–19]

Nanofillers can have a crucial contribution to resolve issues listed above and can improve PEM properties to make them superior materials for PEMFC application.[20] Nanofillers are basically inorganic, organic or hybrid nanoparticles/nanosheets, different from the polymer on basis of their structure and composition. Several research groups have utilized titania, silica, nanoclay, graphene oxide, carbon nanotubes (CNTs) etc. as nanofillers to prepare PBI based nanocomposite membranes with improved properties.[21–27]

In recent years, a new class of porous materials like metal-organic frameworks (MOFs), porous organic polymers (POPs) and covalent-organic frameworks (COFs) have developed as potential proton conductors.[28–35] The tailored mediated functional groups (carboxyl groups, sulfonate groups, phosphonate groups etc.) into the porous matrix contributes significantly in proton conduction due to their hydrophilic nature.[28,30] Furthermore, the porous network of MOFs and COFs allows them to impregnate guest molecules, which generates extensive proton conduction channel for proton transport into the porous network.[2,31,36] MOF materials have been utilized extensively in literature to fabricate hybrid proton exchange membranes.[37,38.] In our previous work, we have incorporated post synthetically modified UiO-66-NH_2 MOFs (PSM 1 & PSM 2) into OPBI matrix, which resulted superior proton conductivity of 0.308 S/cm at 160 °C.[29] Very recently we have reported mixed matrix OPBI supported membranes developed from utilization of synthetically modified MIL-53 and MIL-88B MOFs (53-S and 88B-S) as nanofillers, which exhibits proton conductivity 0.304 S/cm at 160°C under anhydrous environment.[38] Unlike MOFs, COFs are intrinsically constructed by strong covalent bonding interaction.[39] The covalently linked organic building blocks of moderate gravimetric weight ensure excellent thermal stability to the COF materials, and their exceptional compatibility with the polymer matrix.

Literature report reveals that, $–PO_3H_2$ groups conduct protons with superiority over $–SO_3H$ groups. Each amphoteric $–PO_3H_2$ group contains two proton-donor site and one proton-acceptor site, hence lower energy (37.2 kJ/mol) is required while conducting protons with respect to $–SO_3H$ groups (69.9 kJ/mol).[40] Banerjee et al. have developed phosphoric acid loaded azo (− N=N −) based (Tp-Azo) COFs which resulted proton conductivity of $6.7×10^{-5}$ S cm^{-1} at 340 K under anhydrous environment.[32] Mirica et al. developed 2D-Aza-Fused COFs acidified with H_3PO_4, with a resulted proton conductivity in 10^{-3} order at 323 K and 97% RH.[41] Zhang et al. reported (H_3PO_4@NKCOF-1) with an extraordinary proton conductivity of $1.13×10^{-1}$ at 353 K at 98 % RH.[42] Jiang et al. reported proton conductivity of 0.191 S cm^{-1} for H_3PO_4@TPB-DMeTP-COF at 160 °C in presence of anhydrous atmosphere.[2] In the recent years, great effort has been made by scientists all over the globe to fabricate PEMs based on $–PO_3H_2$ groups grafted filler materials as alternate proton conductors.[27,31,43] Development of proton transfer domains with amphoteric $-PO_3H_2$ groups enables continuous H-bonded network formation, hence predicted to be good choice to develop substantial proton conduction channels within the polymer supported PEM matrix. But so far all reported COF based proton conductors did not produce mechanically stable film and hence cannot be used as PEM in the PEMFC. In addition, there is no report of H_3PO_4 impregnated COF grafted PBI based PEMs in literature till date.

In this present work, we aim to synthesize melamine-based Schiff base network type microporous covalent organic framework (COF) following a modified synthetic procedure reported by Yin et al.,[31] followed by incorporation of phosphoric acid (H_3PO_4) molecules inside the porous region of COFs via vacuum assisted method (VAM). Then the COF based mixed matrix membranes (MMMs) were developed from the impregnated COFs (P@MCOF) in a [2,2′-(m-phenylene)-5,5′-benzimidazole] (m-PBI) polymer supported matrix for the first time. Acidic $−PO_3H_2$ groups incorporated in the pores of P@MCOF provide abundant sites for labile proton transfer into the composite matrix, causing efficient proton conduction. Also, acid-base pairs could generate between the P@MCOF frameworks and m-PBI polymer due to the presence of extensive H-bonding interfacial interaction between the polymer and the filler particles. We aim to give a keen and detailed observation to establish the interaction pattern in the composite matrix, leading to formation of MMMs with altered morphology responsible for mechanical and tensile reinforcement, high PA uptake followed by superior proton conduction.

Experimental Section

All the source of reagents and chemicals are given in **Chapter 2**. Synthesis of [2,2′-(m-phenylene)-5,5′-benzimidazole] (abbreviated as m-PBI) polymer was performed following a modified literature reported method.[44-46] (see **Chapter 2** for synthetic details).

Synthesis of MCOF

Melamine based Schiff base network type COF (MCOF) was synthesized by a literature reported procedure[31,47] A mixture of melamine (1.88 g, 14.92 mmol), terephthalaldeyde (3.00 g, 22.36 mmol) and DMSO (100 mL) were taken in a reflux condenser fitted with three-necked round bottomed flask. The mixture was kept for heating at 180 °C for 72 h in presence argon atmosphere. After reaction competition, the reaction mixture was subjected to cooling down to room temperature followed by separation of precipitated powder from the reaction mixture through filtration. The synthesized product was washed repeatedly with DMF and THF, followed by purification using Soxhlet extraction method with methanol, THF and methanol repeatedly. Finally, the MCOF powder was kept for drying inside vacuum oven at 120 °C overnight to get white fluffy powder [**Scheme 4.1(A)**].

Impregnation of H_3PO_4 into the MCOF structure to get P@MCOF

Following a literature reported procedure, H_3PO_4 was impregnated into the MCOF network through vacuum assisted method (VAM).[31] Firstly, MCOF powder was treated with CH_2Cl_2 for 24 h in refluxing condition for the replacement of high boiling point solvent by low boiling point solvent. After that, the MCOF was kept in a vacuum containing Schlenk flask at 120°C for 24 h to remove the residual CH_2Cl_2, absorbed moisture and trapped air present in the pores. In the next step, the Schlenk flask was cool down at 80 °C followed by addition of H_3PO_4 aqueous solution (25 wt%, 25 mL) into the Schlenk flask. Then the entire reaction mixture was kept under vacuum for 12 h, after that the vacuum was removed and the mixture was continued to stir for another 12 h. During this process, H_3PO_4 molecules were incorporated inside the cavities of MCOF due to the resulted pressure difference between the cavities and the outside atmosphere. Finally, the product was centrifuged, followed by washing with water until the supernatant liquid becomes pH neutral. Then the product was kept for drying at 60°C in a vacuum oven to obtain the H_3PO_4 impregnated MCOF (abbreviated as P@MCOF) [**Scheme 4.1(B)**].

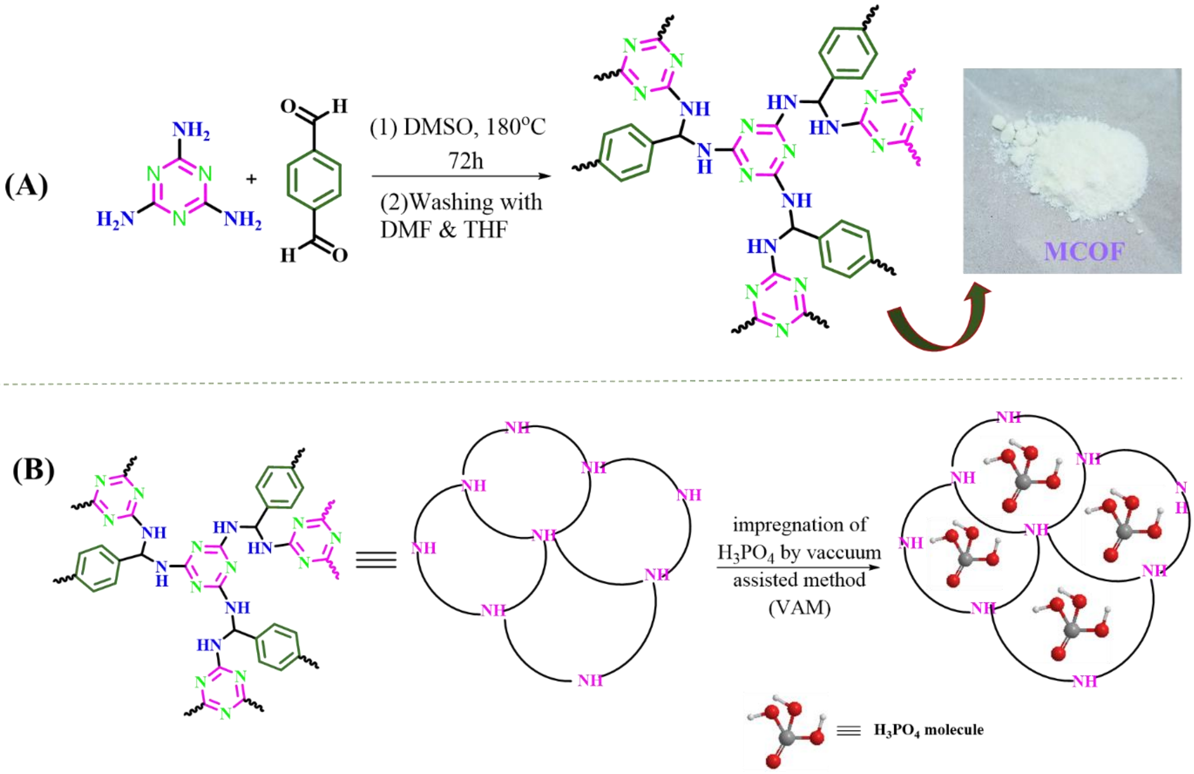

Scheme 4.1. (A) Reaction scheme for the synthesis of melamine-based Schiff base network type COF abbreviated as MCOF. **(B)** Incorporation of H_3PO_4 into the pores of MCOF, the H_3PO_4 impregnated MCOF is abbreviated as P@MCOF.

MCOF characterizations were performed using Solid state ^{13}C CP-MAS NMR spectra, FT-IR, FESEM, TEM & Brunauere-Emmete-Teller (BET) N_2 sorption profile analysis. P@MCOF materials were characterized through FT-IR, BET, FESEM and EDX with elemental mapping & TEM. ICP-OES were also performed for P@MCOF to get the total P content after H_3PO_4 incorporation and represented in the Appendix 2.

Preparation of m-PBI-P@MCOF composite MMMs

m-PBI-P@MCOF composite MMMs were obtained through a solution blending technique by addition of various loading wt% of P@MCOF powders (3, 5, 7, and 10 wt %) with respect to m-PBI as fillers dispersion in DMAc to a 2 wt % m-PBI solution in DMAc. The final m-PBI concentration in DMAC was maintained as 1 wt %. Then the mixture solution was kept under vigorous stirring at 30 °C for 24 h – 36 h, until formation of a homogeneous mixture, which was then poured on to a glass Petri dish followed by a gradual solvent evaporation in a heating oven at 80 °C for 12 h. The fabricated MMMs were then peeled out from the petri dish and kept for drying in a vacuum oven at 100 °C to remove the traces of absorbed solvent molecules and moisture. The synthesis protocols of m-PBI-P@MCOF MMMs are represented schematically in the **Figure 4.1.** m-PBI-MCOF-10% membrane also fabricated utilizing the same strategy for comparison purpose.

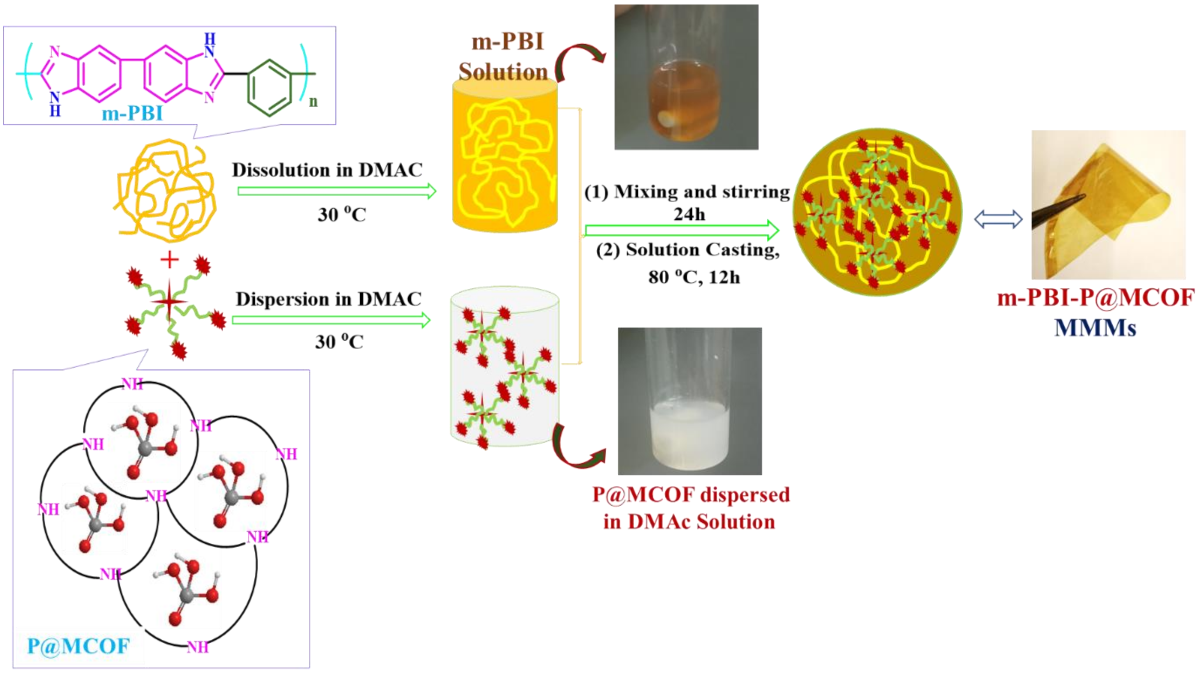

Figure 4.1. Schematic representation for the fabrication of m-PBI-P@MCOF nanocomposite MMMs by solution casting blend method.

PA doping of the m-PBI-P@MCOF MMMs

After keeping all the membranes at 100 °C under vacuum for 24 h, membranes were taken out from the oven and were treated with 85 wt% PA solution for prolong 5 days to obtain PA doped PEMs. After that, the PA doped MMMs were taken out from the PA container and the surface PA molecules were swabbed using tissue paper/filter paper. Finally, the membranes were stored in air tight zip-lock covers for further characterizations.

All the prepared m-PBI-P@MCOF nanocomposite membranes were characterized by Fourier-transform infrared spectroscopy (FT-IR), powder X-ray diffraction (PXRD), Field emission scanning electron microscopy (FESEM) and transmission electron microscopy (TEM), thermogravimetric analysis (TGA), thermomechanical studies by dynamic mechanical analyser (DMA) and tensile strength analysis by universal testing machine (UTM). The detailed experimental procedure for PA loading level, water uptake, swelling ratio studies, proton conductivity, isothermal proton conductivity, PA retention analysis was also performed and all these experimental details are given in the **Chapter 2.**

Results and discussion

Preparation of P@MCOF

The chemical structure of synthesized MCOF is verified by recording ^{13}C solid-state NMR spectra (**Figure A2.1** of Appendix 2). The NMR spectrum of MCOF exhibits three characteristics resonance signal at 167, 127 and 55 ppm. The resonance at 167 ppm is due to the carbon atoms in the triazine ring of melamine, the signal at 127 ppm corresponds to the aromatic carbons of benzene moiety, whereas the resonance at 55 ppm generates from the tertiary carbon atoms in aminal structures.[31] The generation of the Schiff base network type MCOF compound is also confirmed by FT-IR spectra (**Figure A2.2** of Appendix 2). The distinct bands at 3413-3415 cm^{-1} is attributed to the N-H stretching frequency and the band at 1545 and 1475 cm^{-1} are appeared due to the stretching of triazine in the MCOF framework.[31] The band at ~1192 cm^{-1} is generated due to the C-N bonds stretching frequency, which confirms the Schiff base network formation. The successful impregnation of H_3PO_4 into MCOF is confirmed by the FT-IR spectra of the P@MCOF (**Figure A2.2**). The new band emerged at 1145 cm^{-1} is ascribed to the P=O stretching vibration, which proves successful H_3PO_4 incorporation.[31] The FESEM morphology of MCOF remains unchanged after H_3PO_4 incorporation into the MCOF matrix by vacuum assisted method to obtain P@MCOF. Both MCOF & P@MCOF have shown identical morphology from FESEM though after H_3PO_4 impregnation MCOF particles displayed a bit more self-assembled morphology [**Figure A2.3(A, B**) of Appendix 2] and they are obtained as small particles with a diameter of 20-50 nm. **Figure A2.4** of Appendix 2 displays the FESEM EDX elemental mapping of P@MCOF where P molecules is uniformly dispersed all over the P@MCOF framework. In addition, ICP-OES analysis also have been performed to evaluate the P content present in the mesoporous P@MCOF framework (see **Table A2.1** of Appendix 2), and the P content is 3.97 % by mass. Identical morphology obtained from TEM study for both MCOF and P@MCOF [**Figure A2.5(A, B**) of Appendix 2], and each individual particles are of ~20-50 nm in size. In case of P@MCOF a bit of self-assembled particles with formation of patches are observed which could be due to the impregnation of H_3PO_4 molecules. The porous structure of MCOF and P@MCOF is analysed by N_2 sorption analysis. As shown in **Figure A2.6** of Appendix 2, the adsorption isotherms sorption profile of the samples displayed Type I isotherm, which is typical characteristics for microporous materials.[31] The Brunauere-Emmete-Teller (BET) surface area obtained from MCOF and P@MCOF is 490.05 m^2/g and 379.21 m^2/g and the total pore volumes of these materials are 2.32 cm^3/g 1.13 cm^3/g, respectively**.** Impregnation of H_3PO_4 molecules resulted slight decrement in the surface area and pore volume, which proves successful impregnation.

m-PBI-P@MCOF MMM as PEM:

Despite of having the presence of porous framework structure, melamine, amine functionalities and H_3PO_4 impregnation into the mesoporous region of the P@MCOF, this material cannot be directly utilise as PEM due to their non-processability of membrane. Hence, we have loaded P@MCOF into the m-PBI membrane in an aim to develop PEM with exceptional proton conductivity and improved mechanical robustness. The fabrication technique of the MMMs is described in the experimental section and represented in the **Figure 4.1.** After membrane preparation, we have performed several structural and physical characterizations to evaluate the MMMs quality and performances for their potential utilization as PEM in HT-PEMFC.

Structural characterization:

The powder X-ray diffraction pattern (PXRD) of m-PBI-P@MCOF composite MMMs along with pristine m-PBI are plotted in the **Figure 4.2A**. MCOF and P@MCOF materials are amorphous in nature as evident from the presence of a broad signal in the 2θ value between 15° - 30°. In case of P@MCOF, slight d value shift could be observed towards the higher 2θ region may be because of the H_3PO_4 impregnation into the MCOF network, owing to reduction of the framework inter planner spacing. PBI based polymer also exhibits a broad XRD signal in the 2θ value between 20° - 30°, associated with the amorphous nature of the PBI structure.[38,44,48] In the m-PBI-P@MCOF membranes, the presence of identical broad signal could be observed with slight shift in the 2θ value, and with the increase in the P@MCOF loading from 5-10 %, the shifting of broad halo could be observed towards the slight higher 2θ value. Also, the higher filler loaded m-PBI-P@MCOF-(5-10) % exhibits two less intense peak (marked with *) and a sharp crystalline peak in between 2θ range 14°- 15° (marked with #), which are not identical with PXRD pattern obtained from either MCOF materials or the polymer (**Figure 4.2A**). The intensity of the # marked sharp crystalline peak also increases in proportionality with the P@MCOF loading. Shifting of the broad signal in the composite MMMs along with formation of sharp crystalline peak indicates that the extensive H-bonding interfacial interaction operating between the P@MCOF and m-PBI resulting new crystalline plane.

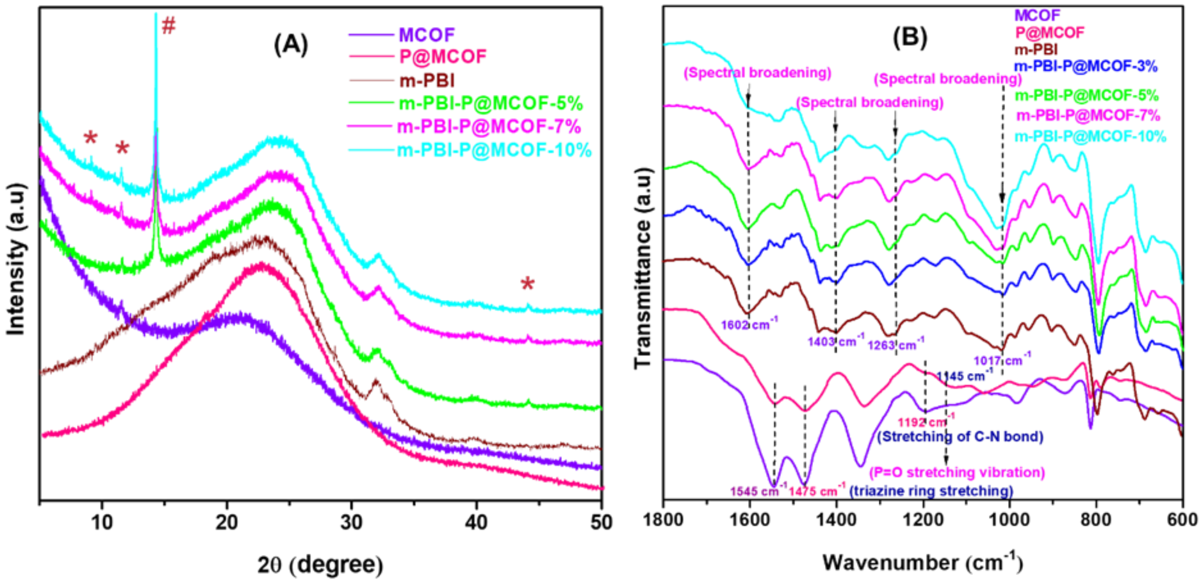

Figure 4.2. (A) PXRD patterns of m-PBI, MCOF, P@MCOF along with m-PBI-P@MCOF composite membranes of indicated loadings. **(B)** FT-IR plots of the m-PBI, MCOF, P@MCOF and m-PBI-P@MCOF MMMs at their indicated wt%.

The formation of extensive H-bonding interfacial interaction into the m-PBI-P@MCOF composite network was also further analysed by FT-IR. The FT-IR spectra of MMMs are given in the **Figure 4.2B** and **Figure A2.7** of Appendix 2. Three peaks present at 3415, 3143 and 3060 cm^{-1} in m-PBI are due to free ‘N-H’ groups, hydrogen bonded ‘N-H’ groups and aromatic C-H stretching, respectively.[48-50] A broad ‘N-H’ stretching frequency signal seen at 3415 cm^{-1} for MCOF and P@MCOF which overlaps with the 3415 cm^{-1} peak of m-PBI and appears as broad ‘N-H’ stretching in the case of m-PBI-P@MCOF composites. The ‘N-H’ stretching peak at 3143 cm^{-1} appears as a negligible broad peak in the composite membranes. Also, the peak corresponds to the aromatic C-H stretching at 3060 cm^{-1} and aliphatic C-H stretching at (2860-2920) cm^{-1} appeared in all the m-PBI-P@MCOF membranes. A broad band at 3625 cm^{-1}appears for m-PBI and its composites membranes due to ‘O-H’ of absorbed moisture.[51] The peak of m-PBI corresponds to the C=C/C=N stretching undergoes spectral broadening in the 7% and 10% P@MCOF loaded MMMs (**Figure 4.2B**). Also we have observed appearance of spectral broadening at 1403 cm^{-1}, 1263 cm^{-1}, and 1017 cm^{-1} for the higher filler loaded MMMs.

The characteristics picks of P@MCOF (**Figure A2.2** & **Figure A2.7** of Appendix 2) merges with the m-PBI peaks with some positional shifts. All these peak shifting and broadening are due to the presence of strong interfacial interaction between polymeric 'N-H' with the functional group of P@MCOF

Hence, the presence of crystallinity obtained from the PXRD analysis, and spectral shifts along with broadening obtained from the FT-IR analysis for the P@MCOF loaded MMMs clearly signify the interfacial interactions between the P@MCOF filler and polymer.

Morphology study

Figure 4.3(A, B) and **Figure A2.8(A-C)** of Appendix 2 represents the FESEM morphology of the composite membrane surface where nice homogeneous dispersion of P@MCOF fillers can be observed all over the surface. Cross-section FESEM morphology of the samples suggests interesting observation. Unlike bare m-PBI, fibrillar network type cross-sectional morphology with generation of triangular and rectangular porous cavity along with uniformly ordered dispersion of P@MCOF are seen in case of the composite MMMs [**Figure 4.3(C, D)** and **Figure A2.8(D-F)** of Appendix 2**]** This morphological features are expected outcome of extensive H-bonding between the organic functionalities ('-NH', '-PO_3H_2') of the P@MCOF fillers and the imidazole '–N=' and 'N-H' functionalities of the m-PBI polymers. Homogeneous dispersion pattern of fillers into the porous fibrillar network type cross-sectional interface become more distinguishable throughout the matrix in case of 7% and 10% of P@MCOF loaded MMMs than that of the lower (wt%) filler loaded samples.

P@MCOF nanofillers have formed structural self-assembly and framework type morphology into the composite matrix as seen from the TEM images shown in [**Figure 4.3 (E, F)**]. In higher filler loaded MMMs, P@MCOF materials are prone to form self-assembled framework structure among themselves as well as with the m-PBI matrix. The homogeneous dispersion pattern of P@MCOF material all over the polymer matrix generates self-assembled P@MCOF framework into dense the polymeric network which results network like self-assembled structure. Similar observation was reported by us earlier for post synthetically modified (PSM 1 and PSM 2) MOF grafted PEMs.[29] The dispersion pattern of the filler materials in 10% sample is more prominent followed by network like clusters formation over m-PBI-P@MCOF-7% membrane**.** At high filler loaded MMMs, two factors contribute significantly, these are: (a) presence of substantial H-bonding which contributes effectively towards the self-aggregation of fillers into the polymer network with uniformed dispersion and (b) Also, the acid-base type H-bonding between the donor and acceptor groups of m-PBI polymer and P@MCOF filler materials leads to formation of self-assembled network like morphology with structural anisotropy.[23,29] Self-assembly generates new crystalline planes as observed from the sharp PXRD peak intensity between 2θ range 14°−15° for the higher filler loaded MMMs which are absent in both parent m-PBI and P@MCOF XRD patterns also support this observation.

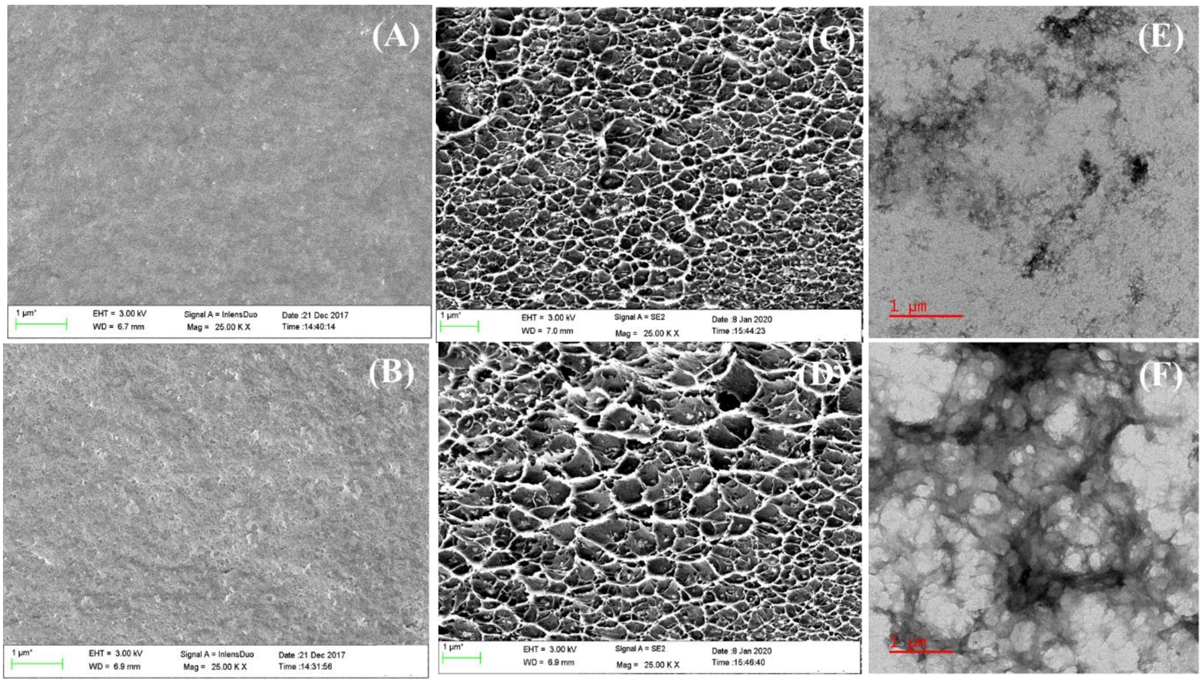

Figure 4.3. (A) FESEM surface morphology of pristine m-PBI-P@MCOF-7% and **(B)** m-PBI-P@MCOF-10% composite membranes. **(C)** FESEM cross-sectional morphology of m-PBI-P@MCOF-7% and **(D)** m-PBI-P@MCOF-10% composite membranes. **(E)** TEM morphology of m-PBI-P@MCOF-7% membrane. **(F)** TEM morphology of m-PBI-P@MCOF-10% membrane.

Thermal stability of the P@MCOF loaded MMMs

TGA thermogramms of the MCOF, P@MCOF and the composite membranes are plotted in **Figure 4.4(A)**. P@MCOF exhibits less thermal stability compared to MCOF and resulted thermal degradation in the temperature range of 300 – 400 °C due to the evaporation or condensation of impregnated H_3PO_4 molecules. Pristine m-PBI and composite MMMs show weight loss >200 °C and the weight loss % increases with the increase in P@MCOF loading in the MMMs due to polycondensation and evaporation of more H_3PO_4 functionality present in the pores of P@COF materials and also due to the degradation of more organic functionality from the P@MCOF. The degradation of polymeric backbone is observed after 550°C in all the samples.[44,46,52] All the membranes exhibit superior thermal stability compared to pure MCOF & P@MCOF owing to the much better thermal stability of the m-PBI.

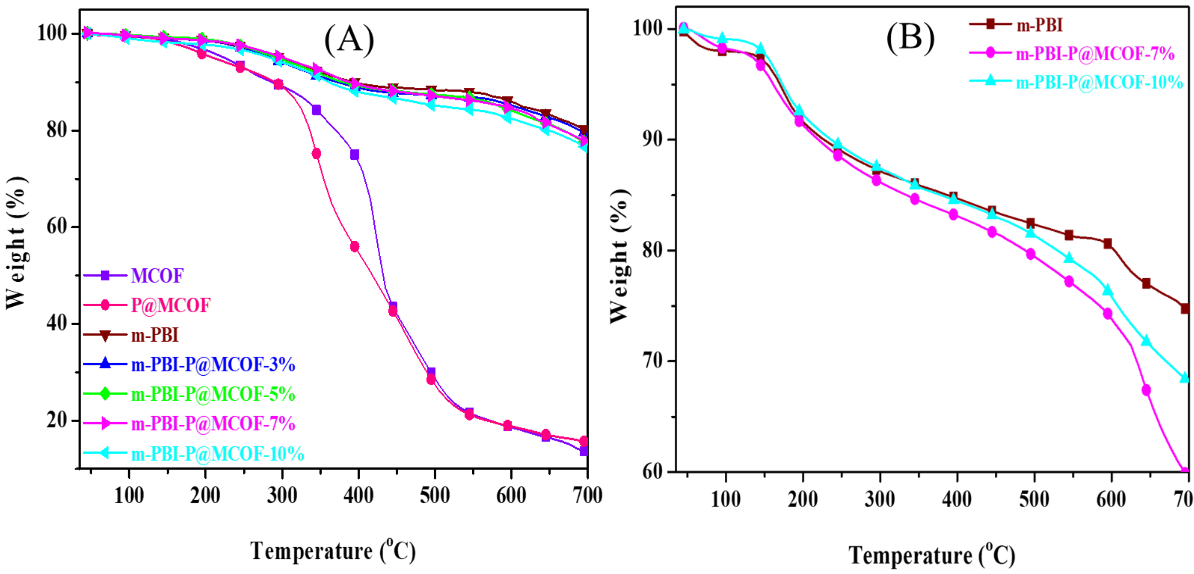

Figure 4.4. (A) TGA data of the composite MMMs along with pristine m-PBI, MCOF and P@MCOF (The zoomed TGA plot of the MMMs between 450 °C-700°C is given in the **Figure A2.9** of Appendix 2**. (B)** TGA of PA doped composite MMMs along with PA doped m-PBI.

The TGA diagram of PA loaded m-PBI along with 7% and 10% m-PBI-P@MCOF composite PEMs are plotted at **Figure 4.4(B).** The first weight loss is seen in between the temperature range of 100-200°C which corresponds to the evaporation of moisture and H-bonded H_2O molecules.[46,52,53] After that, gradual weight loss up to 550 °C is noticed either due to the degradation of polymer composite network or due to the polycondensation and evaporation of PA molecules.[38] Beyond 550 °C, a sharp degradation of the polymer backbone is observed.[54] A comparison between the TGA of undoped MMMs and PA doped MMMs indicates that the thermal stability of the PA doped m-PBI-P@MCOF-10% composite MMMs is better than that of the PA loaded pristine m-PBI, which is a reverse observation from the dry membranes TGA. This is due to the fact that the hydrophilic $–PO_3H_2$ groups of the P@COF filler materials present in the composite matrix can form intermolecular H-bonding with the PA molecules. Also, the imidazole ‘N-H’, ‘-N=’ group of the m-PBI and the heteroatom functionalities (‘N-H’, ‘$-PO_3H_2$’) present in the P@MCOF undergo formation of H-bonding interaction with PA molecules to uphold more PA followed by increase in the composite backbone thermal stability. Similar observation was reported earlier by us for post synthetically modified (53-S and 88B-S) MOF loaded MMMs.[38]

Mechanical properties of the MMMs

The dispersion of P@MCOF filler materials all over the m-PBI-P@MCOF membrane network plays a vital role for their mechanical reinforcement. The temperature responsive storage modulus (E′) plots [obtained from dynamic mechanical analysis (DMA)] of all the P@MCOF loaded MMMs along with the pristine m-PBI membrane are represented in **Figure 4.5** and the corresponding storage moduli values at 100 °C, 250 °C and 400 °C are tabulated in the **Table 4.1**. It can be inferred that the composite membranes introduce significant increment in storage modulus with respect to bare m-PBI, also the storage modulus found to be increasing with the increase in P@MCOF loading % in the composite membranes. For example, the storage modulus of m-PBI at 100 °C, 250 °C and 400 °C are 1844 MPa, 1594 MPa and 921 MPa, respectively, whereas, for m-PBI-P@MCOF-10% membrane storage moduli values are 3866 MPa, 3245 MPa and 1679 MPa at 100 °C, 250 °C and 400 °C, respectively. The widely different morphology associated with self-assembly of fillers into the polymeric network along with the homogeneous dispersion of P@COF particles into the surface and dense porous fibrillar network type cross-sectional region of the polymer composite are the driving forces behind this mechanical reinforcement. The presence of P@MCOF nanofillers network like dispersion and self-assembly generates a vast robust interfacial region into the composite matrix where the strong H-bonding interfacial interactions between the m-PBI functional groups with the P@MCOF functionalities make the MMM matrix rigid by decreasing the segmental mobility of the polymer chains and in turn responsible for significant mechanical reinforcement.

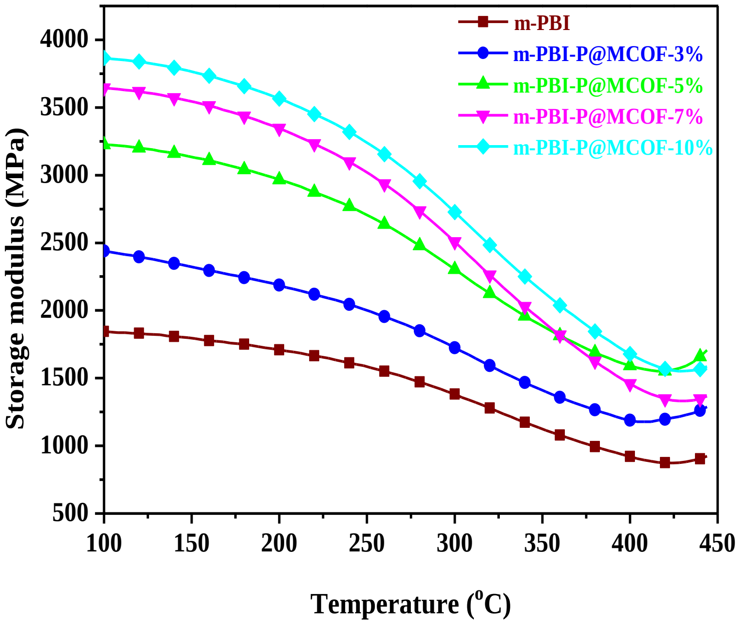

Figure 4.5. Storage modulus plots of m-PBI-P@MCOF nanocomposites obtained from DMA.

Table 4.1. Storage modulus values the m-PBI-P@MCOF nanocomposite MMMs at 100°C, 250°C, and 400°C obtained from DMA storage modulus plot.

Sample	*E' (MPa) at 100 °C*	*% of increase*	*E' (MPa) at 250 °C*	*% of increase*	*E' (MPa) at 400 °C*	*% of increase*
m-PBI	1844		1594		921	
m-PBI-P@MCOF-3%	2439	32.26	2017	26.53	1188	29.0
m-PBI-P@MCOF-5%	3226	74.94	2691	68.82	1592	72.85
m-PBI-P@MCOF-7%	3645	97.66	3043	90.90	1458	58.30
m-PBI-P@MCOF-10%	3866	109.65	3245	103.57	1679	82.30

The glass transition temperature (T_g) of the samples are obtained from the loss modulus (E″) and tan δ plots [**Figure A2.10 (A, B)** of Appendix 2] and the corresponding values are summarised in **Table 4.2.** Due to the formation of miscible blend membranes, loss modulus (E″) and tan δ plot exhibit only single relaxation peak for m-PBI-P@MCOF composite MMMs, and the temperature associated with that peak is considered as the glass transition temperature (T_g).[55-57] The T_g value of m-PBI is 320 °C (loss modulus plot) and 340 °C (tan δ plot), respectively. The incorporation of P@MCOF fillers results slight decrement in the T_g values, and with increase in the P@MCOF loading gradual decrement in T_g value is observed (**Table 4.2**), which might be due to the polymer-COF interaction present in the composite membrane matrix.

Table 4.2. Glass transition temperature (T_g) of the m-PBI-P@MCOF composite MMMs obtained from Loss modulus and tan δ plot.

Sample	*T_g (°C) obtained from E″*	*T_g (°C) obtained from Tan δ*
m-PBI	320	340
m-PBI-P@MCOF-3%	316	332
m-PBI-P@MCOF-5%	308	331
m-PBI-P@MCOF-7%	308	324
m-PBI-P@MCOF-10%	308	324

Oxidative stability of MMMs

Fuel cell operation generates hydrogen peroxide (H_2O_2) which can produce HO• and HOO• radicals in the electrodes sides and are responsible for chemical degradation of the PEMs.[48,58] Hence, determination of the chemical stability of MMMs are very crucial for the use as PEMs. Therefore, to analyse the effect of HO• and HOO• radical attack on P@MCOF loaded MMMs, membranes were immersed into Fenton's reagent (which is a 3% H_2O_2 containing solution in 2 ppm of $FeSO_4$) at 70°C for a certain time period (100 h) and the weights corresponds to the membranes before and after treatment with Fenton's reagent were noted to evaluate the degradation percentage of the MMMs. The chemical stability (in presence of oxidative environment) of the MMMs with respect to time (h) is plotted in the **Figure 4.6.** Composite MMMs are found to exhibit significantly improved chemical stability compared to m-PBI and the stability is boosted with increasing P@MCOF filler loading in the m-PBI. **Figure 4.6** shows that after 100 h of Fenton's reagent treatment m-PBI contains 54.5 % of its initial weight, while the remaining weight associated with m-PBI-P@MCOF membranes are 55.24%, 70.45%, 74.59% and 77.15%, for 3, 5, 7 and 10% membranes respectively, and hence indicating significant improvement in the composite membranes stability. The P@MCOF materials dispersed uniformly throughout the polymer matrix and generate a self-assembled network through involvement in H-bonding interfacial interaction with the m-PBI chains which protect the polar functional groups of the m-PBI from the HO• and HOO• radicals attack. With increasing P@MCOF loading, the presence of more donor-acceptor interfacial interaction provides better shielding of polymer chains, causes significant increment in the chemical stability of the MMMs under harsh oxidative environment.

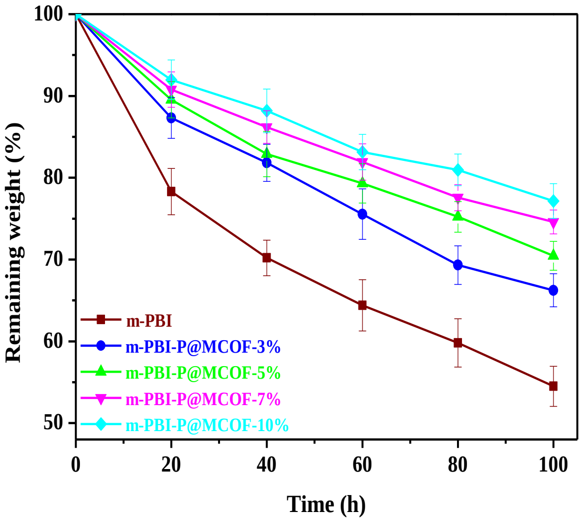

Figure 4.6. Oxidative durability study of m-PBI-P@MCOF composite membranes with different filler loading.

Water uptake (WU), Swelling ratio (SWR) and phosphoric acid (PA) loading of the MMMs

The water uptake (WU), swelling ratio (SWR) in (water and PA), and PA doping level of m-PBI and all the P@MCOF loaded membranes are given in **Table 4.3**. Due to the hygroscopic nature of the PBI based polymers, they prone to absorb atmospheric moisture through involvement of '−N=' of PBI to generate H-bonding with H_2O molecules.[54,59] Water uptake capacity of m-PBI-P@MCOF composites increases in comparison with pristine m-PBI and the increment is proportional with the P@MCOF loading percentage. The resulting water uptake of m-PBI is 10.32%, which is in well accordance with the literature reported value.[45] which increased to 13.10%, 15.62%, 16.66% and 18.34 % for 3, 5, 7 and 10 % respectively. As the P@MCOF filler materials contains hydrophilic $-PO_3H_2$ groups into the pores, those can form extensive H-bonding with water molecule, hence with the increase in the filler loading from 3-10%, tendency of filler materials to form H-bonding with water molecules also increase which results enhanced WU proportional with the P@MCOF loading. Due to absorption of excess moisture and PA, PBI based membranes display dimensional changes which is responsible for excessive swelling and is the reason for mechanical weakness of the membrane.

Swelling ratio both in water and PA tends to decrease quite significantly with increasing P@MCOF loading in the composite membranes (**Table 4.3**). These results clearly suggest that these PEMs obtained from composite MMMs will have better dimensional and mechanical stability than the PEM obtained from PA loaded bare m-PBI.

Table 4.3. Water uptake (WU), swelling ratio (SWR) in water and PA & PA doping level of m-PBI and m-PBI-P@MCOF composite MMMs along with m-PBI-MCOF-10% membrane [a]

Sample name	*Water uptake (wt%)*	*Swelling ratio in water (%)*	*Swelling ratio in PA (%)*	*PA loading (no.of mol/m-PBI r.u)*
m-PBI	10.32 (1.16)	9.73 (0.72)	25.40 (1.35)	10.39 (1.72)
m-PBI-P@MCOF-3%	13.10 (1.02)	6.69 (0.85)	23.54 (0.75)	16.20 (1.44)
m-PBI-P@MCOF-5%	15.62 (1.65)	6.25 (0.42)	21.86 (0.71)	18.36 (1.81)
m-PBI-P@MCOF-7%	16.66 (0.98)	5.88 (0.68)	18.35 (0.48)	19.30 (2.08)
m-PBI-P@MCOF-10%	18.34 (0.56)	5.40 (0.53)	17.95 (0.37)	22.15 (1.78)
m-PBI-MCOF-10%			16.55 (1.08)	15.41 (2.02)

[a] The number given in the brackets attributed to the standard deviations obtained from the analysis.

The proton conductivity of the PA doped PEMs is directly proportional with the PA doping level of the PBI based membrane. Hence, PA loading level determination is a vital parameter to be checked to see the stability of membrane as PEM. Higher PA doping level generates significant number of labile proton transfer sights inside the membrane matrix, which amplify the proton hopping efficiently resulting superior proton conduction.[60] PA doping levels of pristine m-PBI and composite membranes are summarized in **Table 4.3.** The PA doping level of m-PBI is 10.39 mol/repeat units, which is in accordance with the literature reported value.[44] A gradual increase in the PA loading of the composite membranes with increasing P@MCOF content in the membrane is observed. The PA doping levels of m-PBI-P@MCOF membranes are respectively 16.20, 18.36, 19.30 and 22.15 mol/repeat unit for 3, 5, 7 and 10 % loading, respectively. The remarkable PA loading enhancement in the MMMs is associated with several cumulative factors and these are: Firstly, P@MCOF filler material contains hydrophilic –PO_3H_2 groups into its porous region due to the impregnation of H_3PO_4 by VAM. Now, more the loading percentage in the composite membranes, formation of more intermolecular H-bonding results between the –PO_3H_2 groups with PA molecules, and hence increased PA doping level. Secondly, PA molecules penetrates into the interfacial region of the polymer composite backbone and exerts plasticizing effect to make the polymer rubbery in nature with partial disruption of the original crystalline packing.[38,61] Therefore, the H-bonding interfacial interaction between the m-PBI polymer and P@MCOF functional groups disrupts partially with generation of new H-bonding consisting the functional groups of polymer and P@MCOF materials with PA molecules. Hence, PA doping level increases proportionally with filler loading. Thirdly, composite MMMs exhibits formation of porous cavities in a fibrillar network type morphology with homogeneous dispersion of hydrophilic P@MCOF materials all over the matrix also responsible for generation of proton conducting nanochannels in the MMMs along with superior PA loading. In addition, the completely altered morphology of the composites allows incorporation of significant amount of PA inside composite matrix which can undergo intermolecular H-bonding interaction among themselves to uphold more PA (**Scheme 4.2**). All these factors are facilitated with increased hydrophilic P@MCOF materials loading into the polymer matrix. On the other hand, m-PBI-MCOF-10% membrane lacks the ability to reach high PA doping level due to the absence of hydrophilic –PO_3H_2 groups and results lower PA doping level (15.41 mol/repeat unit of m-PBI) with respect to P@MCOF grafted PEMs.

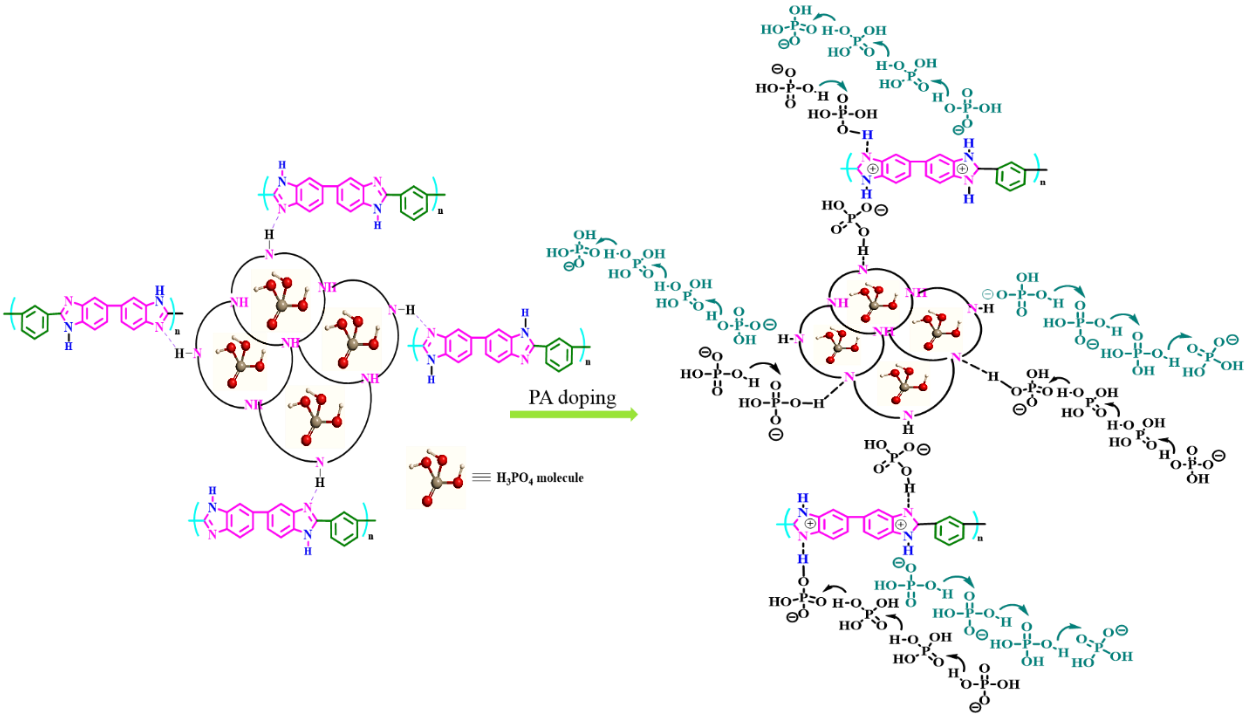

Scheme 4.2. Proposed mechanism of the interaction patterns between PA molecules with composite membrane.

Proton conductivity of the PA loaded MMMs.

Proton conductivity measurement was performed for PA loaded membranes between 30 °C - 180 °C and the proton conductivity values were calculated from the Nyquist plots [**Figure A2.11 (A** and **B)** of Appendix 2] using relevant equivalent circuit fitting (see Chapter 2 for circuit fitting details). Incorporation of P@MCOF filler into the composite matrix results significant improvement in proton conductivity with respect to pristine m-PBI under the same operational condition as shown in **Figure 4.7(A).** Also, the proton conductivity follows proportionality with the increasing P@MCOF loading. In addition, the trend of proton conduction values of all the MMMs maintains a good correlation with the PA doping level (**Table 4.3**) of the membrane.

The proton conductivity for pristine m-PBI membrane at 180 °C is 0.061 S cm^{-1}, whereas this increases to 0.14 S cm^{-1}, 0.186 S cm^{-1}, 0.233 S cm^{-1} and 0.309 S cm^{-1} at 180 ^{o}C, for 3, 5, 7 and 10% P@MCOF loading in m-PBI respectively (see **Table A2.2** of Appendix 2). This results can be attributed to the cumulative effect of several factors: which include, the H-bonding interfacial interaction between the donor and acceptor heteroatoms of P@MCOF and m-PBI generates more proton conducting channels for proton transport. Secondly, the hydrophilic –PO_3H_2 groups present in the porous filler materials can significantly contributes to uphold more PA by forming H-bonding interaction with PA molecules. Therefore, higher filler loaded membranes (7-10) % can cause more PA loading, and as PA loading is proportional to proton conduction, thus proton conductivity values increase with filler loading. Thirdly, for higher filler loaded membranes, the fibrillar porous cavity formation along with development of network type morphology with homogeneous dispersion of hydrophilic P@MCOFs all over the composite matrix and the nanofillers self-assembled framework into the dense polymeric network responsible for effective uphold of PA, hence efficient PA loading followed by superior proton conduction. On the other hand, m-PBI-MCOF-10% membrane dose not contains hydrophilic $–PO_3H_2$ functionalities which resulted significantly lower proton conductivity value of 0.115 S cm^{-1} at 180 °C, which is even inferior than the value obtained for m-PBI-P@MCOF-3% membrane. Hence, this describes the importance associated with the impregnation of H_3PO_4 by VAM to fabricate superior COF based fillers for PEMs.

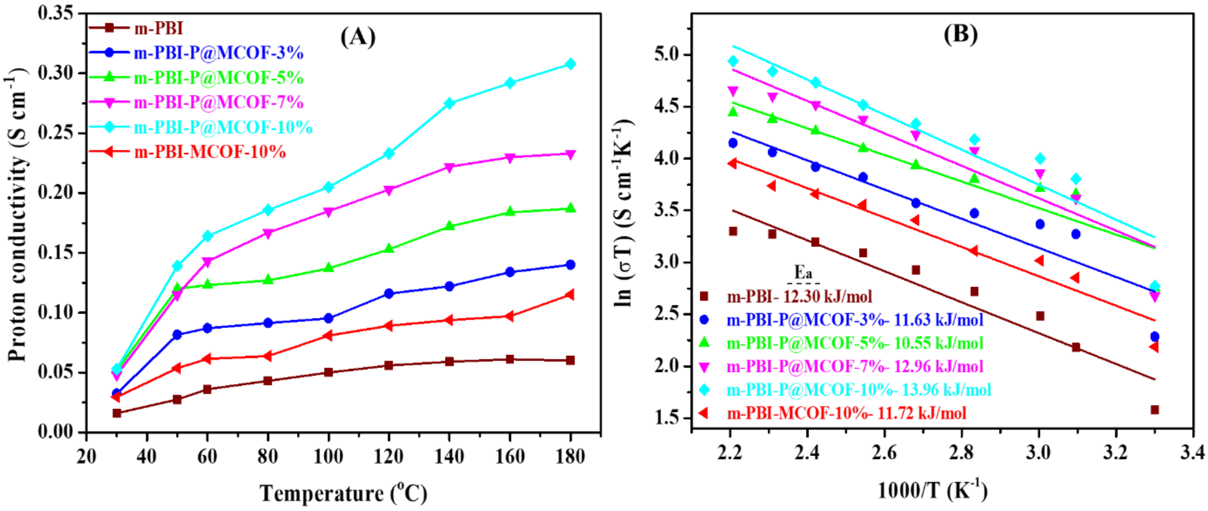

Figure 4.7. **(A)** Proton conductivity values of m-PBI and m-PBI-P@MCOF composite membranes of different filler loading percentage along with m-PBI-MCOF 10% membrane. **(B)** Arrhenius plot of conductivity vs temperature data to determine the activation energy for proton conduction.

Figure 4.7(B) shows the Arrhenius plot of m-PBI and composite MMMs. The calculation of activation energy (E_a) values from the Arrhenius plot was performed from the proton conductivity between 30 °C - 180 °C. E_a value for pristine m-PBI membrane is 12.30 KJ/mol (0.127 eV) and the E_a obtained from m-PBI-P@MCOF membranes are 11.63 kJ/mol (0.120 eV), 10.55 kJ/mol (0.109 eV), 12.96 kJ/mol (0.134 eV) and 13.96 kJ/mol (0.144 eV) for 3, 5, 7 and 10 wt%, respectively. For m-PBI-MCOF-10% membranes E_a appears to be 11.72 KJ/mol (0.121 eV). E_a obtained from the composite membranes implies that the proton conduction occurs through Grotthuss & vehicles mechanism, where the previous one predominates,[62] which is due to the proton hopping between the PA molecules with m-PBI and the functional groups of the fillers through continuous generation and destruction of H-bonding network (see **Scheme 4.2**).[38,60,63] In the case of P@MCOF loaded MMMs, some deviation of activation energy plot from linearity can be observed.[38,55] This is due to the involvement of partial vehicular mechanism, which can occur through proton hopping between one P@MCOF filler surface to another P@MCOF filler through PA network as proton carriers, or a vehicular mechanism could operate through self-assembly of fillers into the composite network which causes self-diffusion of protons.[64]

Isothermal proton conductivity analysis of the P@MCOF loaded membranes were also performed at 160 °C for 24 h to check the long term proton conductivity retention (**Figure A2.12** of Appendix 2**).** In the first 2–4 h of analysis, the membranes show slight decrease in proton conductivity value and that proton conductivity values remain unaltered for 24 h. The PA doped MMMs results much less decrease in proton conductivity in comparison to the PA doped pristine m-PBI due to the presence of hydrophilic P@MCOF framework into the composite. The presence of acidic $–PO_3H_2$ groups into the pores of P@MCOF filler materials can hold significant amount of PA through formation of H-bonding with PA molecules into the interfacial region of composites causing retention of proton conductivity under elevated temperature. Also, the presence of extensive H-bonding network, structural self-assembly, and generation of entirely altered porous morphology can enhance the stability of the MMMs under prolong treatment in elevated temperature.

Mechanical strength analysis of the PA doped MMMs.

Dimensional stability of the PA doped membranes is a key factor for their utilization in PEMFC. The dimensional stability of membranes (tensile strength, elongation at break, young modulus) values relies on the loading percentage of P@MCOF nanofillers as evidenced from the data shown in **Table 4.4.**

Stress strain profiles of PA doped m-PBI-P@MCOF composite MMMs display much improved mechanical reinforcement compared to PA doped m-PBI (**Figure 4.8** and **Table 4.4**). Presence of H-bonding interfacial interaction between the functional groups of P@MCOF particles and m-PBI polymer matrix is responsible for completely altered morphology which contributes effectively in the thermomechanical and tensile reinforcement of the MMMs. The tensile strength, elongation at break (%), and young modulus value increase significantly with the increase in the P@MCOF loading in the composite matrix due to the above-mentioned factors. But, m-PBI-P@MCOF-10% membrane shows increase in elongation at break value with respect to 7% filler loaded membrane but display decrease in tensile strength (**Figure 4.8** & **Table 4.4**). At higher filler loading, PA doping level increased significantly which causes partial disruption in the H-bonding interaction between the P@MCOF functional groups and m-PBI imidazole 'N-H' groups with the formation of new H-bonding of those functional groups with PA molecules and hence disrupts the organized closed packing. This phenomenon is reported in literature for various PA doped membranes [61,65] and can be explained by the plasticizing effect of PA resulting at higher filler loaded polymer composites.[65]

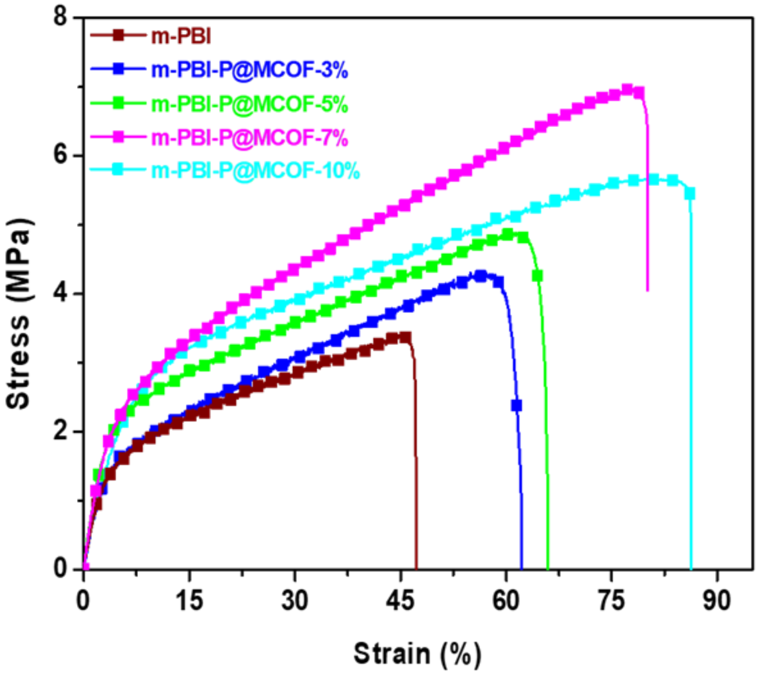

Figure 4.8. Stress-strain profile of PA loaded m-PBI and m-PBI-P@MCOF composite membranes of indicated P@MCOF loading.

Table 4.4. Tensile stress (MPa), elongation at break (%) & young modulus values of PA loaded m-PBI and m-PBI-P@MCOF-(3-10) % composite MMMs.

Sample	*Tensile strength (MPa)*	*Elongation at break (%)*	*Young Modulus (MPa)*
m-PBI	3.36	45.98	0.436
m-PBI-P@MCOF-3%	4.26	59.20	0.461
m-PBI-P@MCOF-5%	4.86	62.38	0.575
m-PBI-P@MCOF-7%	6.97	78.96	0.672
m-PBI-P@MCOF-10%	5.64	85.11	0.635

Acid retention studies of PA loaded MMMs.

During the fuel cell operation membrane suffers from the PA leaching out problem which in turn results deteriorating PEM performance. Thus, this problem has to be addressed via an effective way so that membranes can retain sufficient amount of PA.[66] To understand this, acid retention analysis has been performed with PA loaded composite MMMs **Figure 4.9(A)**. The PA doped MMMs were kept hanging over boiling water to check the PA leaching from the membranes in presence of saturated water vapour at 100 °C, over a certain time period of 3 h.[23,24] During every one-hour interval, weight loss at the PA leached membranes were analysed and from the weight loss difference the PA leaching from the MMMs was calculated and plotted in **Figure 4.9.** The resulting weight loss for m-PBI after 3rd hours is 66.32% which resembles that pristine m-PBI is no longer able to hold significant amount of PA molecules. But, on contrary m-PBI-P@MCOF composite membranes show much better acid retention capacity and PA leaching decreases with increasing filler loading. m-PBI-P@MCOF-3% membrane exhibits 39.46% weight loss of initial weight percentage after 3 h of leaching analysis. While, the weight loss in case of m-PBI-P@MCOF-5%, m-PBI-P@MCOF-7% and m-PBI-P@MCOF-10% membranes are 34.6%, 34.1% and 32.16%, respectively, after 3h of PA leaching analysis. The high PA retention ability of the composite MMMs is because of the several interactions which have been described in the previous sections.

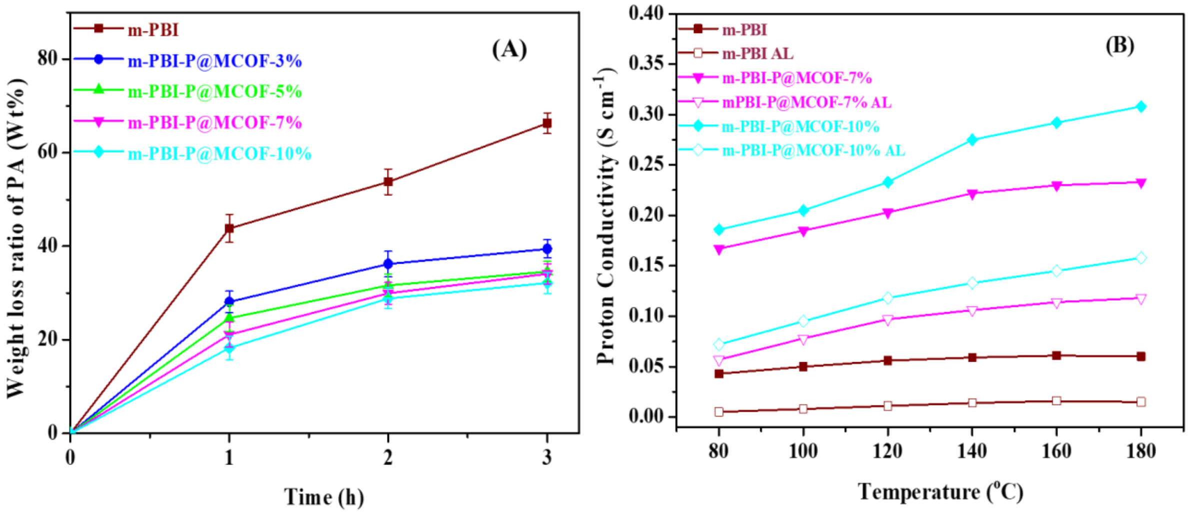

Figure 4.9. (A) Time dependent acid leaching study or PA retention test of PA loaded m-PBI and m-PBI-P@MCOF MMMs of indicated filler loadings. **(B)** Comparison of proton conductivity of the PA loaded m-PBI and m-PBI-P@MCOF-7% & 10% MMMs before and after the PA retention test (* AL indicate after leaching)

The excellent acid retention capacity of the composite membranes was further checked by proton conductivity measurement of post acid leached samples. Proton conductivity of freshly PA doped m-PBI along with m-PBI-P@MCOF (7% & 10%) composite membranes were compared with the post acid leached membranes of similar composition [**Figure 4.9(B)**]. PA leached m-PBI-P@MCOF-7% AL and m-PBI-P@MCOF-10% AL (AL mean after leaching) membranes proton conductivity values are 0.118 Scm^{-1} and 0.158 Scm^{-1}, respectively at 180 °C which is remarkably high in comparison with the PA leached m-PBI AL (0.015 S cm^{-1}) at 180 °C. A significant loss in proton conductivity can be observed for pristine m-PBI after post PA leached treatment whereas, P@MCOF composites still produce excellent proton conduction. This is due to the all possible interactions which have been discussed in earlier sections. The results clearly indicate the superiority of the composite MMMs in comparison to pristine m-PBI.

Conclusion

The current work demonstrates synthesis of melamine-based Schiff base network type covalent organic framework (MCOF) followed by impregnation of phosphoric acid (H_3PO_4) into the microporous region of MCOF via vacuum assisted method (VAM) to prepare P@MCOF. Then, a series of P@MCOF based hybrid mixed matrix composite (MMC) membranes with different filler loading have been developed for the very first time with [2,2′-(m-phenylene)-5,5′-benzimidazole] (m-PBI). Furthermore, the m-PBI-P@MCOF composites MMMs are characterized by FT-IR, PXRD, FESEM, TEM, TGA, DMA, UTM analysis. All these analyses confirmed the presence of H-bonding interfacial interaction between imidazole ‘N-H’ and ‘-N=’ groups of m-PBI with the functional groups of P@MCOF. The m-PBI-P@MCOF composite MMMs results formation of acid-base pairs between the filler (P@MCOF) and polymer (m-PBI) matrix which is governed by formation of H-bonding interfacial interaction. Proton conductivity analysis of all the PA loaded MMMs were performed, the acidic ‘$-PO_3H_2$’ functional groups into the pores of P@MCOF develops abundant proton carrier sights which generates proton transfer nanochannels with low energy barrier. The self-assembled network morphology of m-PBI-P@MCOF composite and the fibrillar porous cavity type morphology with dispersion of hydrophilic fillers all over the polymer also contributes significantly to uphold more PA followed by superior proton conduction. Proton conductivity of the m-PBI-P@MCOF MMMs found to be increasing in proportionality with the loading of P@MCOF in the m-PBI matrix. The incorporation of P@MCOF also protects the m-PBI polymeric interfacial region from harsh chemical environment and hence the m-PBI-P@MCOF nanocomposites exhibits high thermal and oxidative stability under oxidative environment with respect to pristine m-PBI. The self-assembled framework structure of the P@MCOF fillers in the polymeric interfacial region increased the rigidity of the polymer composite backbone which results significant increase in storage modulus values of the composite MMMs. The acid retention analysis demonstrates that due to the altered morphology and presence of hydrophilic functional groups m-PBI-P@MCOF membranes are very much effective in terms of PA retention, and exhibits efficient proton conduction even after PA leaching treatment. To the best of our knowledge, this work will be the first report on COF based proton conduction into the PBI network to develop highly efficient PEMs for PEMFC.

References

(1) Bakangura, E.; Wu, L.; Ge, L.; Yang, Z.; Xu, T. *Prog. Polym. Sci.* **2016**, *57*, 103–152.

(2) Tao, S.; Zhai, L.; Dinga Wonanke, A. D.; Addicoat, M. A.; Jiang, Q.; Jiang, D. *Nat. Commun.* **2020**, *11*, 8–15.

(3) Scofield, M. E.; Liu, H.; Wong, S. S. *Chem. Soc. Rev.* **2015**, *44*, 5836–5860.

(4) Li, Q.; Jensen, J. O.; Savinell, R. F.; Bjerrum, N. J. *Prog. Polym. Sci.* **2009**, *34*, 449–477.

(5) Jacobson, M. Z.; Colella, W. G.; Golden, D. M. *Science* **2005**, *308*, 1901–1905.

(6) Daud, W. R. W.; Rosli, R. E.; Majlan, E. H.; Hamid, S. A. A.; Mohamed, R.; Husaini, T. *Renew. Energy* **2017**, *113*, 620–638.

(7) Walkowiak-Kulikowska, J.; Wolska, J.; Koroniak, H. *Phys. Sci. Rev.* **2017**, *2*, 1–36.

(8) Peighambardoust, S. J.; Rowshanzamir, S.; Amjadi, M. *Int. J. Hydrogen Energy*, **2010**, *35*, 9349-9384.

(9) Kraytsberg, A.; Ein-Eli, Y. *Energy and Fuels* **2014**, *28*, 7303–7330.

(10) Hickner, M. A.; Pivovar, B. S. *Fuel cells* **2005**, 5, 213–229.

(11) Nasef, M. M. *Chem. Rev.* **2014**, *114*, 12278–12329.

(12) Mishra, A. K.; Bose, S.; Kuila, T.; Kim, N. H.; Lee, J. H. *Prog. Polym. Sci.* **2012**, *37*, 842–869.

(13) Zhang, L.; Chae, S. R.; Hendren, Z.; Park, J. S.; Wiesner, M. R. *Chem. Eng. J.* **2012**, *204–206*, 87–97.

(14) Kim, S. K.; Choi, S. W.; Jeon, W. S.; Park, J. O.; Ko, T.; Chang, H.; Lee, J. C. *Macromolecules* **2012**, *45*, 1438–1446.

(15) Mecerreyes, D.; Grande, H.; Miguel, O.; Ochoteco, E.; Marcilla, R.; Cantero, I. *Chem. Mater.* **2004**, *16*, 604–607.

(16) Mamlouk, M.; Scott, K. *Int. J. Hydrogen Energy* **2010**, *35*, 784–793.

(17) Zhang, H.; Shen, P. K. *Chem. Rev.* **2012**, *112*, 2780–2832.

(18) Quartarone, E.; Mustarelli, P.; Carollo, A.; Grandi, S.; Magistris, A.; Gerbaldi, C. *Fuel Cells* **2009**, *9*, 231–236.

(19) Mustarelli, P.; Quartarone, E.; Grandi, S.; Carollo, A.; Magistris, A. *Adv. Mater.* **2008**, *20*, 1339–1343.

(20) Tian, X.; Wang, S.; Li, J.; Liu, F.; Wang, X.; Chen, H.; Ni, H.; Wang, Z. *Int. J. Hydrogen Energy* **2017**, *42*, 21913–21921.

(21) Namazi, H.; Ahmadi, H. *J. Power Sources* **2011**, *196*, 2573–2583.

(22) Gorre, A.; Das, A.; Jana, T. *J. Macromol. Sci. Part A Pure Appl. Chem.* **2023,** *60*, 38-50.

(23) Mukherjee, N.; Das, A.; Dhara, M.; Jana, T. *Polymer*. **2021,** *236*, 124315.

(24) Mukherjee, N.; Das, A.; Jana, T. *ACS Appl. Nano Mater.* **2023,** *6*, 544-557.

(25) Chuang, S. W.; Hsu, S. L. C.; Hsu, C. L. *J. Power Sources* **2007**, *168*, 172–177.

(26) Wang, Y.; Shi, Z.; Fang, J.; Xu, H.; Ma, X.; Yin, J. *J. Mater. Chem.* **2011**, *21*, 505–512.

(27) Kannan, R.; Kagalwala, H. N.; Chaudhari, H. D.; Kharul, U. K.; Kurungot, S.; Pillai, V. K. *J. Mater. Chem.* **2011**, *21*, 7223–7231.

(28) Mukhopadhyay, S.; Debgupta, J.; Singh, C.; Sarkar, R.; Basu, O.; Das, S. K. *ACS Appl. Mater. Interfaces* **2019**, *11*, 13423–13432.

(29) Mukhopadhyay, S.; Das, A.; Jana, T.; Das, S. K. *ACS Appl. Energy Mater.* **2020**, *3*, 7964-7977.

(30) Ramaswamy, P.; Wong, N. E.; Gelfand, B. S.; Shimizu, G. K. H. *J. Am. Chem. Soc.* **2015**, *137*, 7640–7643.

(31) Yin, Y.; Li, Z.; Yang, X.; Cao, L.; Wang, C.; Zhang, B. Wu, H.; Jiang, Z. *J. Power Sources* **2016**, *332*, 265–273.

(32) Chandra, S.; Kundu, T.; Kandambeth, S.; BabaRao, R.; Marathe, Y.; Kunjir, S. M.; Banerjee, R. *J. Am. Chem. Soc.* **2014**, *136*, 6570–6573.

(33) Shinde, D. B.; Aiyappa, H. B.; Bhadra, M.; Biswal, B. P.; Wadge, P.; Kandambeth, S.; Garai, B.; Kundu, T.; Kurungot, S.; Banerjee, R. *J. Mater. Chem. A* **2016**, *4*, 2682–2690.

(34) Peng, Y.; Xu, G.; Hu, Z.; Cheng, Y.; Chi, C.; Yuan, D.; Cheng, H.; Zhao, D. *ACS Appl. Mater. Interfaces* **2016**, *8*, 18505–18512.

(35) Yuan, S.; Li, X.; Zhu, J.; Zhang, G.; Van Puyvelde, P.; Van Der Bruggen, B. *Chem. Soc. Rev.* **2019**, *48*, 2665–2681.

(36) Li, Z.; He, G.; Zhang, B.; Cao, Y.; Wu, H.; Jiang, Z.; Tiantian, Z. *ACS Appl. Mater. Interfaces* **2014**, *6*, 9799–9807.

(37) Escorihuela, J.; Narducci, R.; Compañ, V.; Costantino, F. *Adv. Mater. Interfaces* **2019**, *6*, 1801146.

(38) Basu, O.; Das, A.; Jana, T.; Das, S. K. *ACS Appl. Energy Mater.* **DOI**: 10.1021/acsaem.2c02972.

(39) Ding, S. Y.; Wang, W. *Chem. Soc. Rev.* **2013**, *42*, 548–568.

(40) Paddison, S. J.; Kreuer, K. D.; Maier, J. *Phys. Chem. Chem. Phys.* **2006**, *8*, 4530–4542.

(41) Meng, Z.; Aykanat, A.; Mirica, K. A. Proton Conduction in 2D Aza-Fused Covalent Organic Frameworks. *Chem. Mater.* **2019**, *31*, 819–825.

(42) Yang, Y.; He, X.; Zhang, P.; Andaloussi, Y. H.; Zhang, H.; Jiang, Z.; Chen, Y.; Ma, S.; Cheng, P.; Zhang, Z. *Angew. chem.* **2020**, *132*, 3707–3713.

(43) Wong, C. Y.; Wong, W. Y.; Ramya, K.; Khalid, M.; Loh, K. S.; Daud, W. R. W.; Lim, K. L.; Walvekar, R.; Kadhum, A. A. H. *Int. J. Hydrogen Energy* **2019**, *44*, 6116–6135.

(44) Hazarika, M.; Jana, T. *ACS Appl. Mater. Interfaces* **2012**, *4*, 5256–5265.

(45) Sannigrahi, A.; Arunbabu, D.; Murali Sankar, R.; Jana, T. *Macromolecules* **2007**, *40*, 2844–2851.

(46) Sannigrahi, A.; Arunbabu, D.; Sankar, R. M.; Jana, T. *J. Phys. Chem. B* **2007**, *111*, 12124–12132.

(47) Schwab, M. G.; Fassbender, B.; Spiess, H. W.; Thomas, A.; Feng, X.; Müllen, K. *J. Am. Chem. Soc.* **2009**, *131*, 7216–7217.

(48) Maity, S.; Singha, S.; Jana, T. *Polymer.* **2015**, *66*, 76–85.

(49) Singha, S.; Jana, T.; Modestra, J. A.; Naresh Kumar, A.; Mohan, S. V. *J. Power Sources* **2016**, *317*, 143–152.

(50) Hazarika, M.; Jana, T. *Eur. Polym. J.* **2013**, *49*, 1564–1576.

(51) Maity, S.; Jana, T. *Macromolecules* **2013**, *46*, 6814–6823.

(52) Lee, S.; Nam, K.-H.; Seo, K.; Kim, G.; Han, H. *Polymers.* **2020**, *12*, 1604.

(53) Jouanneau, J.; Mercier, R.; Gonon, L.; Gebel, G. *Macromolecules* **2007**, *40*, 983–990.

(54) Xiao, L.; Zhang, H.; Jana, T.; Scanlon, E.; Chen, R.; Choe, E. W.; Ramanathan, L. S.; Yu, S.; Benicewicz, B. C. *Fuel Cells* **2005**, *5*, 287–295.

(55) Singha, S.; Koyilapu, R.; Dana, K.; Jana, T. *Polymer.* **2019**, *167*, 13–20.

(56) Sana, B.; Koyilapu, R.; Dineshkumar, S.; Muthusamy, A.; Jana, T. *J. Polym. Res.* **2019**, *26*, 55.

(57) Ghosh, S.; Maity, S.; Jana, T. *J. Mater. Chem.* **2011**, *21*, 14897–14906.

(58) Chang, Z.; Pu, H.; Wan, D.; Liu, L.; Yuan, J.; Yang, Z. *Polym. Degrad. Stab.* **2009**, *94*, 1206–1212.

(59) Xiao, L.; Zhang, H.; Scanlon, E.; Ramanathan, L. S.; Choe, E. W.; Rogers, D.; Apple, T.; Benicewicz, B. C. *Chem. Mater.* **2005**, *17*, 5328–5333.

(60) Singha, S.; Jana, T. *ACS Appl. Mater. Interfaces* **2014**, *6*, 21286–21296.

(61) Jiang, J.; Zhu, X.; Qian, H.; Xu, J.; Yue, Z.; Zou, Z.; Yang, H. *Sustain. Energy Fuels* **2019**, *3*, 2426–2434.

(62) Yu, S.; Benicewicz, B. C. *Macromolecules* **2009**, *42*, 8640–8648.

(63) Vilčiauskas, L.; Tuckerman, M. E.; Bester, G.; Paddison, S. J.; Kreuer, K. D. *Nat. Chem.* **2012**, *4*, 461–466.

(64) Pu, H.; Meyer, W. H.; Wegner, G. *J. Polym. Sci. Part B Polym. Phys.* **2002**, *40*, 663–669.

(65) Dang, J.; Zhao, L.; Zhang, J.; Liu, J.; Wang, J. *J. Memb. Sci.* **2018**, *545*, 88–98.

(66) Quartarone, E.; Mustarelli, P. *Energy Environ. Sci.* **2012**, *5*, 6436–6444.

Chapter 5

Polymer Grafted Graphene Oxide/Polybenzimidazole Nanocomposites for Efficient Proton Conducting Membranes

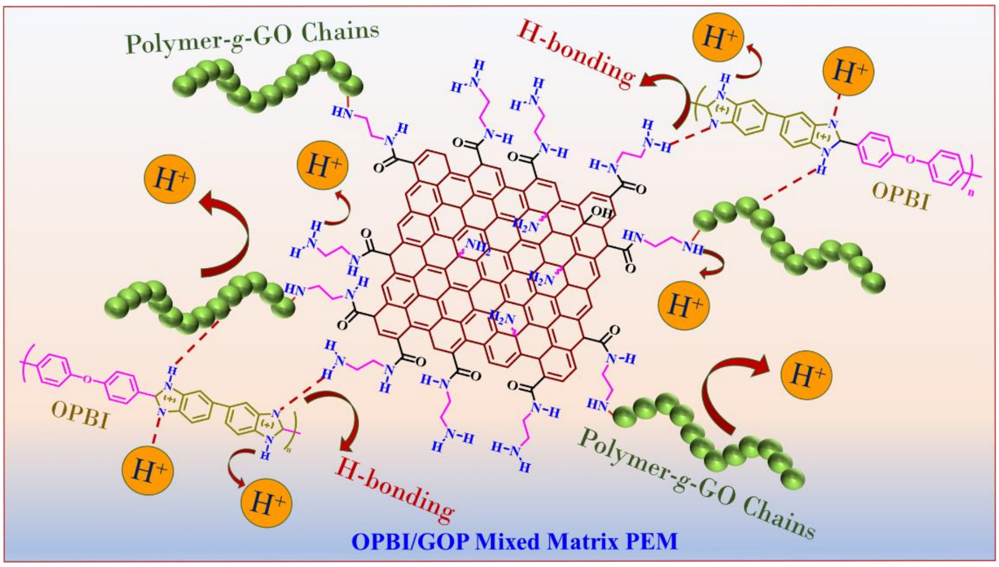

Anupam Das, Nilanjan Mukherjee and Tushar Jana*. Polymer Grafted Graphene Oxide/Polybenzimidazole Nanocomposites for Efficient Proton Conducting Membranes. *ACS Appl. Nano Mater.* **2023, [Article in Press].**

Abstract

In this study, we have functionalized graphene oxide (GO) by growing polymer chains on the and then utilized polymer-*g*-GO as nanofiller with oxypolybenzimidazole (OPBI) to make highly efficient nanocomposite-based proton exchange membrane (PEM). Three different monomers, namely acrylamide (AAM), 2-acrylamido-2-methyl-1-propanesulfonic acid (AMPS) and 3-sulfopropyl acrylate potassium salt (SPAK) were polymerized on the activated GO surface *via* surface initiated reversible addition fragmentation chain transfer (RAFT) polymerization to obtain three different types of polymer-*g*-GO namely pAAM-*g*-GO, pAMPS-*g*-GO and pSPAK-*g*-GO. Furthermore, chain length of grafted polymers in each case were altered in order to study the effects of grafted polymer structure and chain length on the properties of nanocomposite PEM. The exfoliation of GO nanosheets after polymer grafting was confirmed by studying the surface morphology using various microscopic techniques. GPC and TGA analysis helped in measuring the chain length of grafted polymers and grafting density on the GO surface. Further, we have impregnated polymer-*g*-GO as nanofillers by varying loading wt% into the OPBI to fabricate mixed matrix membrane (MMM) which upon doping with phosphoric acid (PA) converted into mixed matrix PEM. Prepared nanocomposite PEM displayed exceptionally good thermal stability, significantly improved tensile properties, improved PA loading followed by superior proton conductivity and remarkable PA retention when exposed to saturated water vapour. When the 2.5 wt% pSPAK-*g*-GO (where pSPAK chain length is 19.6 kDa) mixed with OPBI, the resulting PEM showed remarkably high proton conductivity value of 0.327 S cm^{-1} at 160 °C, a significant 5-fold increment compared to pristine OPBI membrane (0.067 S cm^{-1} at 160°C). To the best of our knowledge, this will be the first report on utilization of polymer-*g*-GO in a polybenzimidazole supported matrix for high temperature PEM application.

Introduction

In recent years, graphene oxide/polymer composite materials have been extensively utilized in the electrodes,[1] supercapacitors,[2,3] biosensors,[4] water desalination and waste water treatment,[5,6] and various other electrochemical devices owing to their superior physical properties. The large surface area, high aspect ratio and the presence of hydrophilic functionalities generate abundant proton transport sights in the graphene oxide (GO) and therefore, it has been considered and utilized as an effective organic filler in various types of composite based polymer electrolyte membranes (PEMs)[7,8] However, aggregation of GO in the membrane occurs owing to the poor dispersion of GO in organic solvents and hence significant property improvement of PEMs have often hampered.[9] In order to avoid this, researchers have *grafted* various active groups on the GO surface to increase the hydrophilicity so that the dispersion ability enhances. Lerf et. al. have functionalized the GO surface to prepare various modified GO derivatives and studied their properties.[10] Also, several research groups reported the incorporation of sulfonated GO (S-GO) into the polymer membrane which resulted various physical properties improvement in the PEMs.[11–13] Xu et al. have developed SGO-incorporated polybenzimidazole (S-GO/PBI) membranes and reported proton conductivity value of 0.052 S/cm at 175 °C under anhydrous environment, which is found to be 1.9 times higher than that of unmodified GO/PBI membranes (0.027 S/cm). Moreover, S-GO samples dispersion nature and compatibility with the PBI matrix found to be superior over unmodified GO.[14] Functionalized GOs possessing acidic and basic groups,[15–21] zwitterionic groups[22] and imidazole groups[23–25] have been prepared as nano-additives for PEMs with improved properties.

Furthermore, detailed literature findings suggest that suitable surface functionalization of the GO with polymer chains help in significant property improvement of the surface modified GO samples.[26–28] Surface modification of GO with strategically designed grafted polymer chains can be of great advantage as the molecular design and the attached functionalities of the grafted polymer structure can easily be tuned as desire to enhance the properties significantly. In order to grow polymer chains covalently on the surface of any nanomaterials, "*grafting to*" and "*grafting from*" are the two major approaches mostly utilized in literature. Researchers have utilized both of these strategies to graft polymer chains on the GO surface via atom transfer radical polymerization (ATRP) and reversible addition fragmentation chain-transfer (RAFT) polymerization techniques.[29–32] The *grafting from* method allows the effective *in situ* generation of nanomaterials surface modified with polymer chains,[33] and hence surface initiated RAFT (SI-RAFT) technique have been adapted by us in this work for the surface functionalization of GO, where we can control over the growth of the polymer chains and structure at the molecular level.

Therefore, in this work, first we have attached a RAFT agent on the GO surface in order to make a polymerizable surface. Then, three different types of monomers namely acrylamide (AAM), 2-acrylamido-2-methyl-1-propanesulfonic acid (AMPS) and 3-sulfopropyl acrylate potassium salt (SPAK) were polymerized via SI-RAFT technique to graft polymer chains on the GO surface using *grafting from* approach to obtain three different types of polymers *grafted*

GO namely pAAM-*g*-GO, pAMPS-*g*-GO and pSPAK-*g*-GO. These synthesized polymer-*g*-GO materials were thoroughly characterized by FT-IR analysis, thermogravimetric analysis (TGA), gel permeable chromatography (GPC), Brunauer-Emmett-Teller (BET) N_2 sorption analysis, Raman spectroscopy, field emission scanning electron microscopy with energy dispersive X-ray spectroscopy (FESEM-EDX), transmission electron microscopy (TEM), powder X-ray diffraction (PXRD), dynamic vapor sorption (DVS) and Zeta potential measurement. These monomers were chosen so that we can incorporate a large number of amine and hydrophilic sulfonic acid functionalities in the polymer-*g-GO* surface in order to improve the hydrophilicity and dispersion nature of the materials in polar solvents and also the grafting of amine (both primary and secondary) and $–SO_3H$ functionalities in the polymer modified GO can possibly contribute significantly towards the generation of hydrophilic ion channels for proton conduction into the PEMs interfacial region, which we have aimed to develop by blending these nanofillers with PBI.

We have impregnate these three sets of polymer-*g*-GO materials as a nanofiller into the aryl-ether type oxy-polybenzimidazole (OPBI) membrane to fabricate mixed matrix membrane (MMM) in order to evaluate the role of GO surface modification on the improved physical properties of the MMM. All these MMMs are converted to PEMs by doping with phosphoric acid. Utilization of surface polymer grafted GO samples as efficient nanofiller with any polymer membrane supported matrix have never been explored before in the literature. To the best of our knowledge this will be the first report on utilization of polymer-g-GO materials to develop mixed matrix super proton conducting PEMs.

Experimental Section

All the details about the source of reagents, preparation of graphene oxide (**Scheme A3.1** of Appendix 3) and synthesis of [3-benzylsulfanylthiocarbonylsufanyl-propionic acid] (BSPA) RAFT agents are included in the **Scheme A3.2** of Appendix 3. Structural characterization of BSPA through ^{1}H NMR, ^{13}C NMR and FT-IR spectra with assigned peak analysis are given in the **Figure A3.1, A3.2** of Appendix 3. The activation of RAFT agent (activated BSPA) is also described in details in the **Scheme A3.3** of Appendix 3**.** The synthesis of OPBI was adapted from literature following a modified procedure,[34,35] and descried in details in the Chapter 2.

Preparation of polymerizable graphene oxide surface.

In order to do the polymerization on the graphene oxide (GO) surface, at first surface was made polymerizable by multiple modification process as discussed below and shown in

Scheme A3.4 of Appendix 3**.** GO powder (1 g) was dispersed in approximately 50 mL of THF solution via ultrasonication process (10 min) and ethelenediamine (EDA) (2.5 mL, 37.4 mmol), 1,3-dicyclohexyl carbodiimide (DCC) (3 g, 15 mmol), and 4-dimethylamino pyridine (DMAP) (0.30 g, 2.46 mmol) were added into the reaction mixture and the reaction was continued for 72 h at 70°C under nitrogen atmosphere. Then the mixture was precipitated in *n*-hexane (~150 mL) followed by centrifugation at 10000 rpm. The obtained wet powder was further dispersed in THF solution and washed thrice with *n*-hexane to remove excess EDA and impurities. Finally, the obtained product which is EDA modified GO (GO-EDA) was dried in a vacuum oven at 50°C overnight. Attachment of [3-benzylsulfanylthiocarbonylsufanyl-propionic acid] (BSPA) RAFT agent on the GO-EDA was performed by dispersing 1 g of GO-EDA powder in 200 mL dry THF under N_2 atmosphere, followed by dropwise addition activated BSPA (60 mg, 0.16 mol) into the dispersion. Then the reaction mixture was allowed to stir under dark condition for 18 hours at room temperature. After 18 h reaction, GO-EDA with covalently attached activated BSPA (GO-BSPA) was separated from the reaction mixture using centrifuge at 14000 rpm for 10 minutes. The obtained black coloured GO-BSPA was further re-dispersed in THF for proper washing and removing the free RAFT agent followed by centrifugation to separate the pure product (**Scheme A3.4** of Appendix 3). This process was repeated thrice to separate the unbound RAFT agents. GO-BSPA was allowed to dry under vacuum at 50°C for 24 hours.

Polymerization of various monomers via SI-RAFT

In order to graft polymer chains on the functionalized GO surface through SI-RAFT polymerization, 150 mg (17.4 µmol) of GO-BSPA was dispersed in 4 mL of water: ethanol (3:1) mixture in a 25 mL Schlenk tube. 4.5 mg (17.4 µmol) of BSPA and 1.5 mg of AIBN (8.7 µmol) were also added in the reaction medium. Acrylamide (AAM) or 2-acrylamido-2-methyl-1-propanesulfonic acid (AMPS) or 3-sulfopropyl acrylate potassium salt (SPAK) (calculated amount to grow polymer of different chain lengths on the GO surface) were then added into the reaction mixture. We have varied three different monomers to grow three different types of polymers with different chain length on the GO surface. The Schlenk tube was sealed with a rubber septum and subjected to sonication for 5 minutes and stirred for 10 minutes for homogeneous dispersion of all the reactants present in the mixture. After that the Schlenk tube was subjected to undergo 3 freeze-thaw cycles to ensure complete removal of O_2, dissolved air and absorbed moisture from the reagent and solvent mixture. Furthermore, the tube was back filled with N_2 to maintain inert atmosphere and kept under stirring at 75 °C for 18 h. Upon the completion of 18 h, the reaction was quenched using liquid N_2 and was exposed to air for termination of the growing polymer chains. Liquid N_2 helps to freeze the propagating radicals present in the reaction mixture and exposure them to air, terminates the reactive radicals responsible for propagation of the polymer chain growth. Finally, the obtained polymers were precipitated in acetone and the precipitate was filtered and washed with ethanol-water mixture followed by re-precipitated in acetone. The polymers grafted GO were then kept at vacuum oven at 50 ºC overnight for drying. We have chosen three different sets of monomers namely AAM, AMPS and SPAK to grow three different types of polymers namely pAAM, pAMPS and pSPAK, respectively on the GO surface. Also, we have varied the amount of each monomer by keeping all other reagents same to graft different chain length of polymer chains of each monomer in the GO surface. All together six different polymer grafted GO samples were obtained. GO surface modified with polymers of low molecular weight are named as (abbreviated as) pAAM(L)-*g*-GO (GOP1), pAMPS(L)-*g*-GO (GOP3) and pSPAK(L)-*g*-GO (GOP5) and the polymers with high molecular weight are named as (abbreviated as) pAAM(H)-*g*-GO (GOP2), pAMPS(H)-*g*-GO (GOP4) and pSPAK(H)-*g*-GO (GOP6) (**Scheme 5.1**). The polymers grafted to the GO surface were detached from the GO by cleaving process as described and shown in the **Scheme A3.5** of Appendix 3**.** The cleaved polymer chains were subjected to molecular weight measurement via gel permeable chromatography (GPC).

Preparation of OPBI/GOP mixed matrix membrane (MMM)

To find the potential application of the polymer grafted GO materials (GOP), they were introduced as filler material into the oxy-polybenzimidazole (OPBI) to cast OPBI/GOP based MMM utilizing solution casting blending method (**Scheme 5.2**). We have varied the content of GOP materials loading from 1 wt% to 2.5 wt % with respect to the OPBI weight to prepare the MMMs. We have used three types of different polymers with high molecular weight polymers grafted on GO surface and these are GOP2, GOP4 and GOP6. In a culture tube GOP sample (1 mg and 2.5 mg, calculated with respect to OPBI) was allowed to mix in 5 mL of formic acid (FA). In a separate culture tube 100 mg of OPBI polymer are taken in 5 mL of FA (2 wt % solution) and kept under stirring for complete dissolution of the polymer in FA. After that the GOP dispersed FA solution was mixed with the 2 wt% OPBI solution, which resulted the final concentration of OPBI in FA solution as 1 wt%. Finally, the solution mixture was allowed to stir for 24 h -36 h at room temperature until formation of a homogeneous dispersion. The mixture was then poured on to a glass petri dish followed by gradual evaporation of FA at 60 °C for 12 h. The formed homogeneous composite MMMs were then peeled off and vacuum dried at 100 °C for 24 h to remove the traces of the solvent and absorbed moisture. The obtained mixed matrix membranes are named as GOP2-1% and GOP2-2.5%, GOP4-1% and GOP4-2.5%, GOP6-1% and GOP6-2.5%. GOP1-2.5%, GOP3-2.5% GOP5-2.5% and GO-EDA-2.5% nanocomposite MMMs were also prepared for the purpose of comparison.

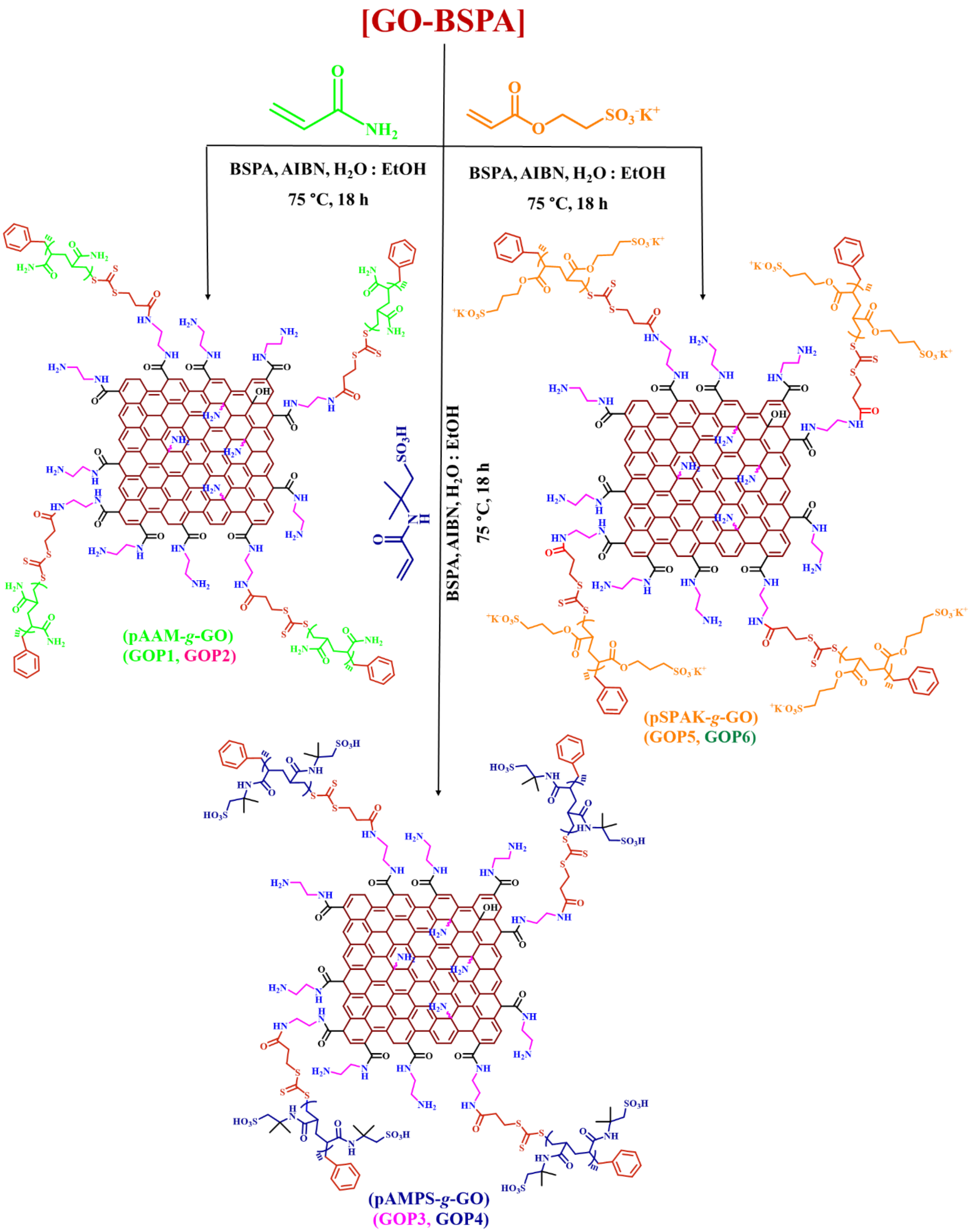

Scheme 5.1. Schematic representation of SI-RAFT polymerization to graft various polymer chains on the GO surface.

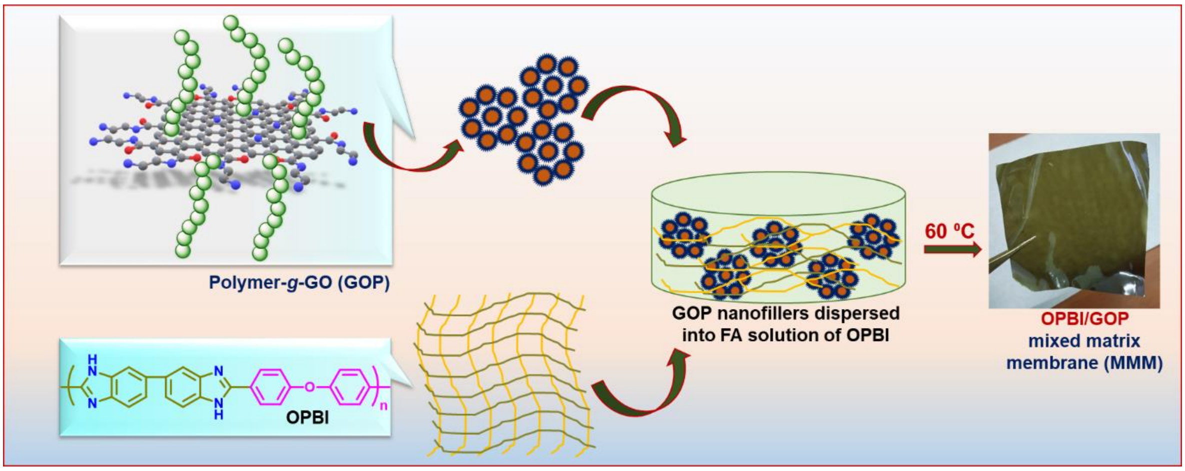

Scheme 5.2. Schematic representation for the preparation of **OPBI/GOP** MMM.

Phosphoric Acid (PA) doping of the obtained Mixed Matrix Membranes

PA doped polyelectrolyte PEMs were obtained by immersing fully vacuum dried OPBI and OPBI/GOP membranes into 85% PA solution for 5 days. After completion of the 5 days the PA doped MMMs were taken out of the PA container, quickly wiped the surface adsorbed PA and stored in zip-lock air tight covers for further analysis.

The instrumental details used for the physical characterizations of the GO and GOP loaded mixed matrix membranes are given in the **Chapter 2.**

Results and discussion

Grafting of polymer chains on GO surface

The FT-IR spectra of the synthesized GO, GO-EDA, GO-BSPA and the polymer-*g*-GO (GOP) are given in the Appendix 3, **Figure A3.3.** In case of GO, the peak at 1049 cm^{-1} appeared due to C-O-C stretching vibrations, 1223 cm^{-1} for C-OH stretching vibrations, 1406 cm^{-1} due to the O-H deformation of the C-OH groups and 1724 cm^{-1} peak generates due to the –C=O stretching vibrations of the –COOH groups.[36] The -OH vibrational frequency of GO appeared as a broad peak in the 3000-3600 cm^{-1} region. The C=C stretching vibration of GO is observed at 1640 cm^{-1} and 1575 cm^{-1}.[27] After reacting with EDA, several new peaks emerged in the GO-EDA structure. A new peak at 1072 cm^{-1} evolved due to the amine groups N-H stretching. Medium and low intensity peaks were observed between 1300-1460 cm^{-1} in the GO-EDA structure due to antisymmetric C-N stretching merged with the out-of-plane NH and NH_2 linkage. The intense peak at 2850-2930 cm^{-1} attributed to the aliphatic C-H stretching of the EDA, and the less intense broad peak at 3320 cm^{-1} appeared due to the N-H stretching vibrations.[27] All the characteristics peaks of GO-EDA are present in the GO-BSPA with the appearance of few new peaks due to the RAFT agent (BSPA) attachment.[37] After surface grafted polymerization in the GO-BSPA, all the characteristics peaks of surface functionalized GO found to be present in the polymer modified samples with the generation of new peaks due to the functional groups present in the grafted polymer chains. The peak at 1660 cm^{-1} appears in the GOP2 sample (pAAM-*g*-GO) is due to the –C=O stretching of $–CONH_2$ group, and the peak at 1442 cm^{-1} and 1551 cm^{-1} are due to the bending of acrylamide N-H bonds.[38] In the GOP4 (pAMPS-*g*-GO)**,** the peak at 1656 cm^{-1} attributed to the –C=O stretching of $–CONH_2$ group and the peak at 1535 cm^{-1} appeared due to the N-H bending. The peak at 1361 cm^{-1}, 1150 cm^{-1} and 1031 cm^{-1} are related to the asymmetric and symmetric stretching of the -S=O of $–SO_3H$.[38,39] In the GOP6 (pSPAK-*g*-GO), ester -C=O peak depicted at 1720 cm^{-1}, the band at 1446 cm^{-1} is attributed to saturated ester,[40,41] and the peaks at 1372 cm^{-1}, 1180 cm^{-1} and 1038 cm^{-1} are attributed to the asymmetric and symmetric stretching of SO_3.[42] In all the polymers aliphatic C-H stretching frequency are observed at 2860-2930 cm^{-1} due to the presence of the EDA structure in the surface modified GO.

The TGA data of graphite powder, GO, GO-EDA, GO-BSPA and the GOP samples are shown in the **Figure 5.1(A, B)** display a negligible degradation in thermal stability of the graphite powder in the entire temperature range of 35 -700 ºC. In the GO and GO-EDA sample, a minor mass loss is observed around 100 ºC, which is due to the evaporation of the absorbed moisture and water molecules from the GO surface.[43] The mass loss around 100 ºC for GO and GO-EDA is 3.03 wt% and 1.12 wt%, respectively. The decreased moisture absorption of GO-EDA resulted due to the reduction effect of EDA.[44] GO nanosheets displays one sharp degradation of ~25 wt% in the temperature range 110 ºC- 210 ºC due to the thermal degradation of CO, CO_2, H_2O molecules from the labile epoxide functionalities present in the GO surface,[45] followed by a gradual degradation of the thermal stability between 210 ºC- 700 due to the degradation of comparatively stable oxygen functionalities (**Figure 5.1A**).[46] After modification with EDA, the first stage thermal degradation shifted from 140 ºC- 195 ºC with an approximate mass loss of ~8 wt%. Also, a sharp degradation is observed after 225 ºC which continues with a gradual thermal degradation up to 400 ºC with a $T_{d,\,max}$ of 311.7 ºC [27] and can be attributed to the degradation of ethylene diamine functionalities covalently attached to the surface of GO nanosheets. The thermal stability of the RAFT agent BSPA is only up to 200 ºC after that it shows a sharp degradation (**Figure A3.4** of Appendix 3). Therefore, after BSPA attachment, the thermal stability of the GO-BSPA decreases. The wt% difference between GO-EDA and GO-BSPA materials at 700 ºC is used to calculate the grafting density of the covalently attached

RAFT on the GO-EDA surface and found to be 30.04 mg/g (see **Table 5.1).** In the polymer grafted samples (GOP1-GOP6), the thermal degradation increases with increasing the grafted polymer chains on the GO-BSPA surface or in other words the higher molecular weights polymers GOP2, GOP4 and GOP6 show higher degradation than GOP1, GOP3 and GOP5. But all the GOP materials are found to be stable up to 250-300 °C [**Figure 5.1(B)**], and the main degradation of the surface grafted polymer chains started after 225 °C followed by gradual thermal degradation up to 400 °C. There is also the relatively weak influence of polymer structure on the thermal stability [**Figure 5.1(B)** and **Table 5.1**]. The calculated grafting density of the polymer chains found to be increased with increasing polymer chain lengths. The maximum polymer grafting density of 220.42 mg/g of GO was achieved for pSPAK(H)-*g*-GO (GOP6) sample.

Gel permeation chromatography (GPC) of all the polymer-*g*-GO samples (GOP1-GOP6) were performed after chemical treatment of the polymer grafted GO samples with N-hexylamine in presence of sodium dithionite [see **Scheme A3.5** of Appendix 3]. The resulted chemical environment produced by these reagents causes breaking of the trithiocarbonate bond, linking between the grafted homopolymer chains with the GO surface, and liberates the free polymer chains in the solution mixture[35,47] The bare polymer chains were then purified and then run through a GPC using HPLC water as eluent solvent to measure the molecular weight. The GPC chromatograms are shown in **Figure 5.1(C)** and molecular weights and polydispersity index are tabulated in the **Table 5.1**. The molecular weights of the surface grafted polymers acquired from the GPC technique are in good agreement with the targeted molecular weight as planned before the reaction. Also, the samples resulted very narrow polydispersity index (Đ) which gives a direct proof that the surface polymer grafting resulted via RAFT polymerization technique. The degree of polymerization, the number of monomeric units in each grafted polymer chain, is calculated using GPC data and shown in **Table 5.1** (in sample type column) clearly shows that higher molecular weight polymer chain size is greater than double compared to its low molecular weight counterpart.

To further check the successful grafting of polymer chains on the GO surface, we have performed the Brunauer–Emmett–Teller (BET) N_2 sorption analysis which displayed a well-defined type-IV isotherm in all the cases (**Figure A3.5** of Appendix 3). The obtained surface area of the unmodified GO found to be 192.357 m^2/g whereas GOP samples show a huge decrement in surface area with respect to the unmodified GO. The obtained surface area of GOP2, GOP4 and GOP6 are 14.762 m^2/g, 16.530 m^2/g and 4.212 m^2/g, respectively. The huge decrease in the surface area is a direct consequence of the surface grafting of polymer chains on the GO surface which is entirely covered by the surface grafted polymers resulting low surface area.

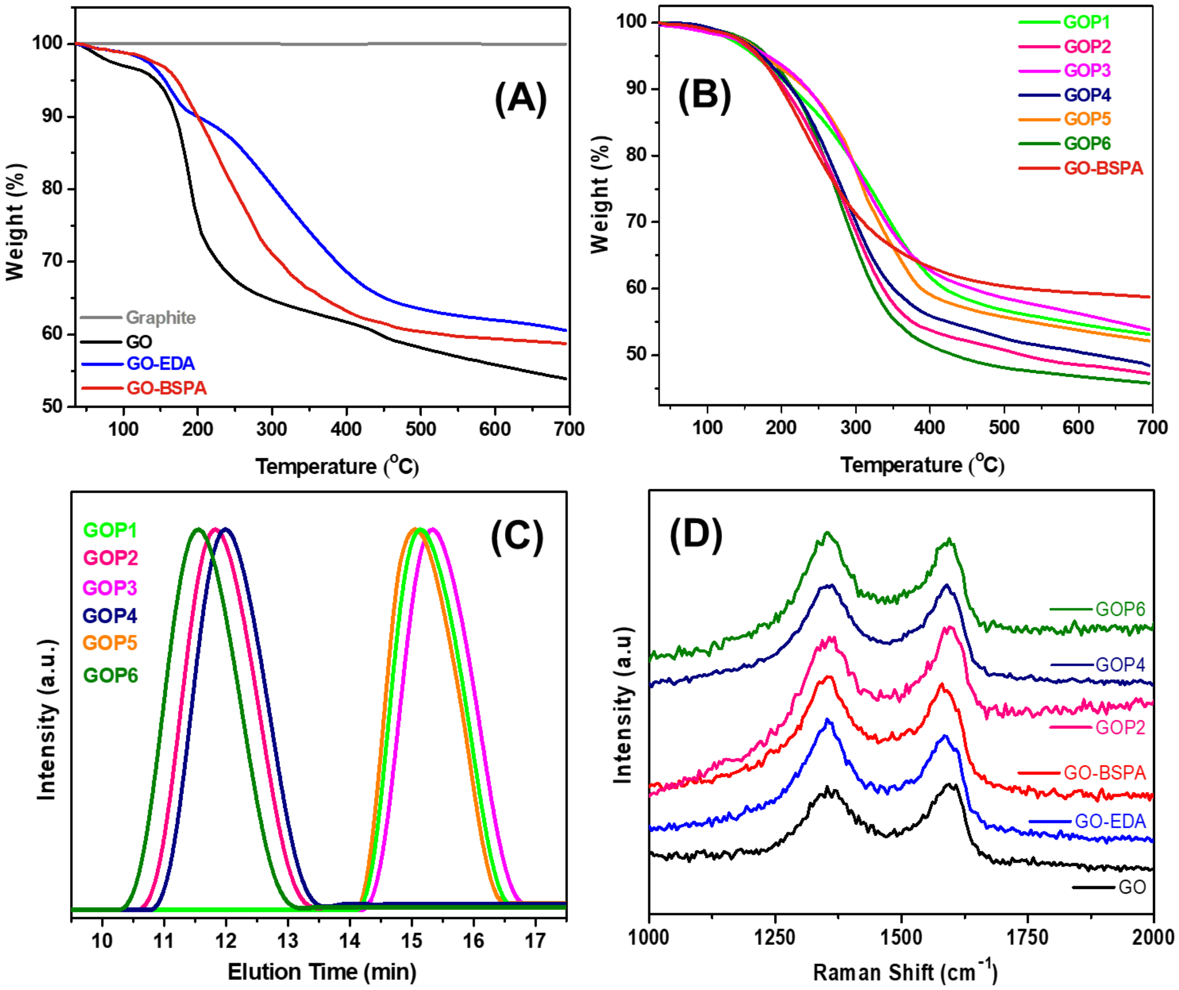

Figure 5.1. TGA of graphite powder, GO, GO-EDA and GO-BSPA **(A)**, polymer grafted GO (GOP) of altered chain length **(B)**. GPC plots of the polymer chains which are detached from the surface of GO after treating the GOP samples with cleaving agent **(C)**. Raman shifts of GO, surface functionalized GO and GOP samples **(D)**.

Raman spectrum of GO displays D band at 1352 cm^{-1} along with G band at 1590 cm^{-1} (**Figure 5.1D**) and I_D/I_G value is found to be 1.023 which indicates the decrement in the size of the in-plane SP^2 domain and formation of defects i.e. SP^3 carbon atoms due to the oxidation reaction performed in the graphite structure.[28] GO-EDA and GO-BSPA show further increment in the I_D/I_G values to 1.13-1.17 attributing the further decrement of in-plane SP^2 structure and formation of more defect structure due to the EDA reduction reaction performed on the GO surface. No notable increment in the I_D/I_G values are observed for the GOP samples, instead slight decrement in I_D/I_G values are observed (0.9-1.1), which suggests that the ordered structure of the reduced GO is preserved after surface grafting of polymer chain.

Table 5.1. Physical properties of the surface functionalized polymer-*g*-GO samples.

Sample name	Sample type[a]	Remaining weight % at 700 °C (wt%)[b]	Polymer content[c]	$\bar{M}_n$[d]	$\bar{M}_w$[e]	Đ[f]	Zeta potential (mV)[g]
GO	-	53.94	-	-	-	-	-11.2
GO-EDA	-	60.57	-	-	-	-	-11.9
GO-BSPA	-	58.75	30.04	-	-	-	-10.4
GOP1	pAAM(L)$_{128}$-*g*-GO	53.13	95.65	9081	9353	1.03	-10.4
GOP2	pAAM(H)$_{269}$-*g*-GO	47.21	196.42	19134	20090	1.05	-13.1
GOP3	pAMPS(L)$_{43}$-*g*-GO	53.86	83.23	8831	9272	1.05	-10.6
GOP4	pAMPS(H)$_{91}$-*g*-GO	48.40	176.17	18841	19594	1.04	-13.5
GOP5	pSPAK(L)$_{40}$-*g*-GO	52.14	112.51	9223	9407	1.02	-15.2
GOP6	pSPAK(H)$_{84}$-*g*-GO	45.80	220.42	19610	20786	1.06	-17

[a] sample type describes the polymer chain identity which is grafted on the GO surface and the degree of polymerization for each homopolymers are included in the suffix which have been calculated from the molecular weight measurements data obtained from the GPC analysis. [b] calculated from the data obtained from the TGA analysis (at 700 °C) and [c] Calculation of the GO surface grafted polymer content from TGA data analysis (at 700 °C) in **Figure 5.1(B)** which is expressed as amount (in mg) of polymer chains /g of GO-BSPA, in case of GO-BSPA polymer content represents the amount of covalently attached RAFT agent on GO surface. [d], [e] and [f] are determined by gel permeation chromatography of the detached polymer from the Polymer-*g*-GO, and [g] obtained from Zeta potential analysis**.**

The FESEM and TEM images of GO and the polymer-*g*-GO samples are represented in the **Figure 5.2(A-F)** and **Figure A3.6-A3.16** of Appendix 3. The FESEM morphology of GO, GO-EDA and GO-BSPA displays almost identical features consisting of layers with roughness and wrinkles on the surface which might be due to the presence of epoxide or carboxylic acid functionalities (**Figure A3.6-A3.8** of Appendix 3). After GO surface modification with EDA and BSPA, presence of small clusters could be observed in the layered surface which indirectly confirms the successful amine modification and RAFT attachment on the GO surface. EDX elemental mapping of GO-EDA shows that the nitrogen content increases significantly as compared to GO (**Figure A3.6-A3.7**) which again slightly decreases with presence of trace amount of sulfur content in the GO-BSPA sample due to the presence of RAFT agent, which gives an additional proof for the successful RAFT attachment (**Figure A3.8**). The polymer-*g*-GO samples exhibits entirely altered morphology with respect to GO and GO-BSPA wherein the grafted polymer chains covered the entire surface of the GO, and the sheets become thick and dense with increased surface roughness [**Figure 5.2(A-C)** and **Figure A3.9-A3.14]**, which is a direct proof for the GO surface modification with the grown polymer chains. Comparison of FESEM morphology and EDX elemental analysis of **GOP1** and **GOP2** clearly show that the GO surface becomes comparatively more thick, dense, rough and exfoliated in the higher chain length polymer **(GOP2).** Also, the nitrogen content of GOP2 (50.87 wt%) is higher than GOP1 (45.91%) due to the more grafting of polymer chains in the former. Similarly, comparison of **GOP3** and **GOP4** results **(Figure 5.2B, Figure A3.11** and **A3.12)** clearly show the increased S content with higher polymer chain length. Further, exactly similar conclusion can be drawn from the FESEM and EDX results of **GOP5** and **GOP6** **(Figure 5.2C, Figure A3.13** and **A3.14).**

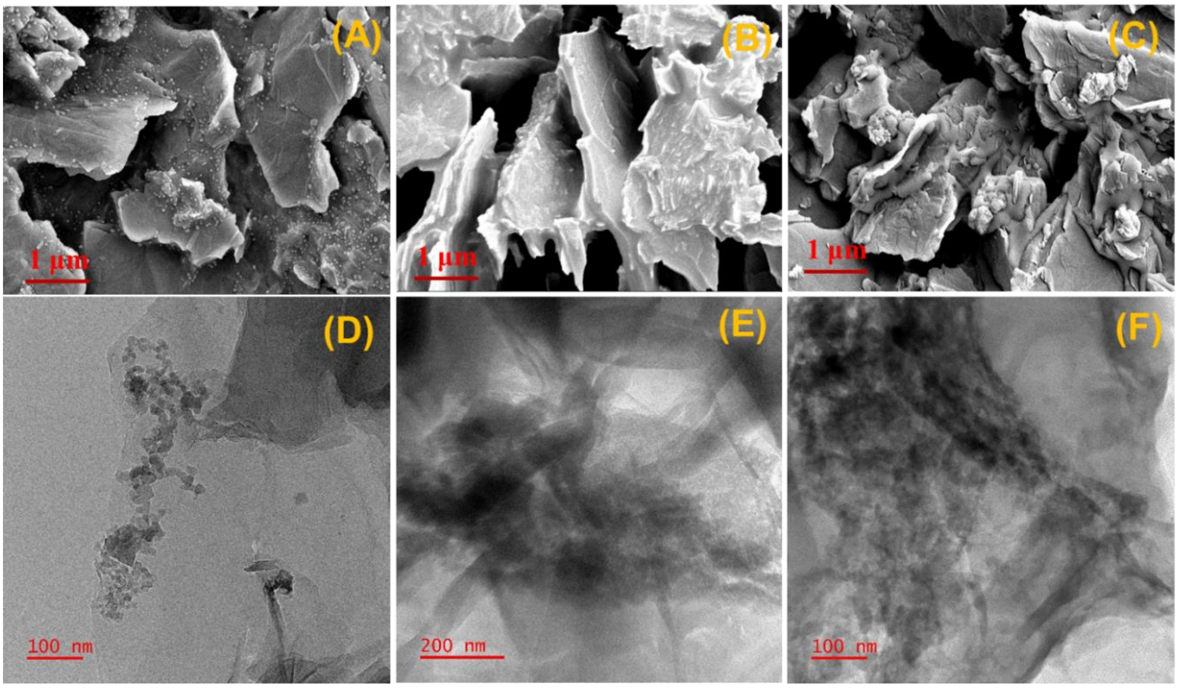

Figure 5.2. FESEM images of **(A)** pAAM-*g*-GO (GOP2) **(B)** pAMPS-*g*-GO (GOP4), **(C)** pSPAK-*g*-GO (GOP6). TEM images of GOP2 **(D)**, GOP4 **(E)** and GOP6 **(F)**.

TEM analysis of the GO and GOP samples were also performed and represented in the **Figure 5.2(D-F)** and **Figure A3.15-A3.16** of Appendix 3**.** GO exhibits few layered transparent planner sheets with wrinkles and folding in the surface, and the sheets are found to be overlapped with each other. The SAED pattern consists of hexagonal lattice with sixfold symmetry (**Figure A3.15**).[48] The TEM morphology of GO-BSPA is similar along with formation of black spots in the layered surface of the GO sheets due to the sulfur deposition after RAFT attachment (**Figure A3.16**). Grafting of the pAAM, pAMPS and pSPAK polymer chains on the GO surface resulted entirely altered morphology, all the polymer-*g*-GO samples exhibit less transparent thick plates with dark contrast due to the polymer grafting attributing that the surface of the RAFT modified GO sheets have been covered by the polymer chains [**Figure 5.2(D-F)**]. The polymer chains are not only grown on the surface of GO but also grown in between the surface of the interlayer sheets which makes the GO sheets thick and exfoliated with dark contrast. Also, the associated H-bonding between the intra and interlayered GOP nanosheets functional groups resulted partial intercalated structure in the GOP samples. Therefore, TEM images clearly demonstrates the formation of partially intercalated and exfoliated structure in the polymer attached GO.

Dynamic vapour sorption (DVS) studies were performed in order to verify the water sorption ability of GOP samples. Unmodified GO is found to be not much susceptible for water vapour sorption (only 0.04084g of water/g of GO) (see **Figure A3.17** of Appendix 3). Whereas, the GOP samples show much improved water sorption ability, the values of GOP2, GOP4 and GOP6 are 0.1154, 0.2616, 0.3203 g of water/g of samples, respectively. The remarkably higher water sorption ability is due to the presence of primary and secondary ammines, and hydrophilic sulfonic acid (-SO_3H) functionalities present in the polymer structures which can form extensive H-bonding interaction with the water molecules. Hence, through the extensive H-bonding network in the polymer-*g*-GO samples, the presence of hydrophilic ion channels formation or hydrophilic domains formation into the surface polymer grafted GO nanosheets make the materials highly efficient as nanofillers into the proton conducting MMMs as the hydrophilic ion channels can generate efficient proton conducing pathway into the MMMs interfaces. The Zeta potential values recorded from aqueous dispersion of samples are included in **Table 5.1,** suggests the good dispersion ability of GOP samples in polar solvents which is needed for making the composite with any polymer using solution blending process. In addition, it is clearly evident that higher chain length polymer modified samples have higher Zeta potential suggesting better dispersion ability.

Further we have tried to utilize these GO surface functionalized polymer materials as a nanofiller to prepare nanocomposite with OPBI to make proton conducting membrane and also to evaluate the role of the surface modification in improving polymer membrane properties. The fabrication technique of the MMMs is described in the experimental section (**Scheme 5.2**). After fabrication, we have characterized these membranes through various techniques to evaluate the utility of these MMMs as PEM which are discussed in the following section.

OPBI/GOP nanocomposites

GO exhibits a diffraction peak at $2\theta = 10.39^o$ corresponding to the interlayer spacing of 0.85 nm (**Figure 5.3A**) which is also analysed from the HRTEM SAED pattern of GO (**Figure A3.15** of Appendix 3). After BSPA attachment, the diffraction peak shifted to $2\theta = 7.59^o$ corresponding to the interlayer spacing of 1.16 nm which indicates that RAFT attachment have been successfully occurred in the GO surface resulting increment in the interlayer spacing.[32] In the case of GOP samples, the obtained 2θ values are in the range of (8.82-9.98) ^{o} with interlayer spacing between 0.89-1.00 nm (**Figure 5.3A**). The decrement in the interlayer spacing after polymer modification in the GO-BSPA surface is a direct consequence of H-bonding interaction between the primary amines, secondary amines and carboxylic acid moiety present in the GO surface with the $–CONH_2$ functionalities of the pAAM , -NH and $–SO_3H$ groups of the pAMPS, and $–SO_3H$ functionalities present in the grafted pSPAK polymers, respectively which has resulted crouched molecular chains of polymer-*g*-GO samples (GOP2, GOP4 and GOP6) and hence the interlayer spacing decreased. The PXRD data of OPBI membrane given in the **Figure 5.3(B)** exhibits a broad amorphous signal in the 2θ (degree) range between 20–35^o.[49,50] Incorporation of GOP2 or GOP4 or GOP6 polymers as fillers (1 wt% and 2.5 wt%) into the OPBI matrix resulted totally altered PXRD patterns with appearance of three unique semi-crystalline peaks in the 2θ value 10.30^o, 14.02^o and 18.70^o (marked with # in the **Figure 5.3B**) which are absent in both the GOP and pristine OPBI samples indicating the formation of an ordered structure into the MMM after incorporation of polymer modified GO nanosheets. Also, with increasing GOP loading from 1 wt% to 2.5 wt% in the OPBI, the intensity of the semi-crystalline planes increases. The $–CONH_2$ functionalities present in the GOP2, -NH and $–SO_3H$ groups present in the GOP4, and $–SO_3H$ functionalities present in the GOP6 polymer surface contributes remarkably towards the formation of acid-base and H-bonding interfacial interactions with the imidazole N-H functionalities of the OPBI which are responsible for such unique semi-crystallinity and structural ordering into the composite MMMs.

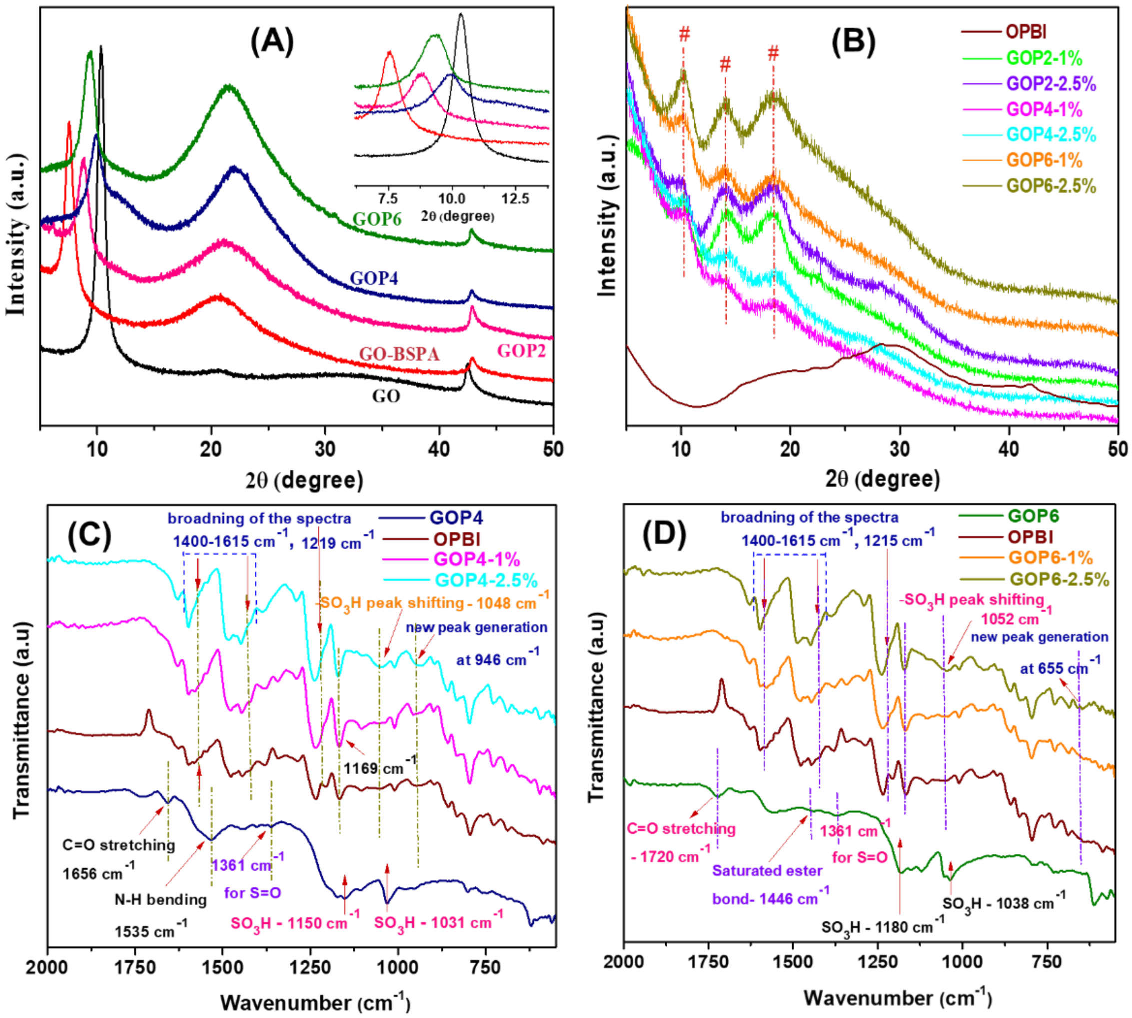

Figure 5.3. (A) PXRD plots of GO, GO-BSPA, GOP2, GOP4 and GOP6 (Inset: zoomed portion in the 2θ = 7-13°) **(B)** PXRD plots of OPBI and OPBI/GOP MMMs. **(C, D)** FT-IR spectra of OPBI, GOP and the OPBI/GOP MMMs.

FT-IR spectra of the GOP4 and GOP6 loaded MMMs were recorded and given in the **Figure 5.3(C, D)** and **Figure A3.18(A, B)** of Appendix 3. Appearance of new FT-IR signals, peak shifting, spectral broadening and disappearance of FT-IR signals are analysed to understand the various interactions between nanofillers (GOP) and the polymer (OPBI). The non-hydrogen bonded N-H vibration of OPBI at 3413 cm^{-1} shows less peak intensity in the composite samples (**Figure A3.18**) and disappearance in case of GOP4-2.5% and GOP6-2.5% membranes, which signifies the strong interaction between nanofillers and OPBI. The interactions in the composite samples lead to generate few positional shift, new peak appearances, and spectral broadening (**Figure 5.3C** and **D**). A new peak appears at 946 cm^{-1}

for GOP4-1% and GOP4-2.5% membranes and at 655 cm^{-1} for GOP6-1% and GOP6-2.5% membranes. –SO_3H peak shifts is observed for both the GOP4 and GOP6 samples at 1048-1052 cm^{-1}. Spectral broadening is observed around 1215- 1219 cm^{-1} and in the 1400-1615 cm^{-1} region for both GOP4-2.5% and GOP6-2.5% samples. Also, the OPBI peak at 1169-1173 cm^{-1} appeared with increased peak intensity in case of composite membranes. In addition, due to the incorporation of GOP nanofillers the OPBI/GOP composites shows increased aliphatic C-H stretching signals between 2851-2921 cm^{-1} (**Figure A3.18** of Appendix 3).

Morphological study of composite membranes

The FESEM cross-sectional morphology of the GOP2, GOP4 and GOP6 loaded MMMs displayed completely different morphology when compared with pristine OPBI (**Figure 5.4** and **Figure A3.19** of Appendix 3). Unlike OPBI, the MMMs show sponge like layered morphology with formation of thin fibrils along with homogeneous dispersion of GOP nanosheets throughout the membrane cross-section, and the dispersion pattern is more prominent in case of MMMs obtained from GOP6 (see the **Figure 5.4C** and **A3.19C**). It is to be noted that higher loading of GOP samples in the membranes display crater like cavity formation and thick dense fibrillar network generation with impregnation of GOP nanosheets into the porous fibrillar cross-section of the membranes [compare **Figure 5.4(A-C**) and **Figure A3.19 (A-C)**]. This kind of morphology develops due to the involvement of extensive H-bonding network between the OPBI imidazole N-H and –N= functionalities with the primary and secondary amines, -C=O, and the hydrophilic –SO_3H functionalities present in the polymer modified GOP surface. The thick fibrillar porous morphology can remarkably contributes towards improved electrolyte (phosphoric acid) uptake, proton conductivity, improved PA retention under saturated water vapour, and mechanical reinforcement in the mixed matrix PEMs.[50] TEM surface morphology of the MMMs displaying the homogeneous dispersion of GOP all over the membrane surface. However, a flower like self-aggregated network structure can be observed from the image in all the cases [**Figure 5.4(D-F)** and **Figure A3.19 (D-F)** of Appendix 3]. The formation of such structure with uniform dispersion of surface modified GO nanosheets all over the membrane matrix provides remarkable improvement in the various physical properties of the MMMs which are discussed in the following section. Increasing polymer-*g*-GO loading beyond >2.5 wt% may cause uncontrollable agglomeration of nanosheets in the polymer matrix which in-turn can destroy the proton conducting hydrophilic ion channel formation and also may cause mechanical damage in the membranes. Therefore, an optimization of nanofiller loading has to be maintained to retain better mechanical properties along with efficient proton conduction in the mixed matrix PEMs.

Furthermore, the 2D surface topology of the MMMs was analysed utilizing atomic force microscopy (AFM) technique to evaluate the dispersion nature of the polymer modified GO nanosheets into the membrane matrix. The 2D surface topology of OPBI found to be uniform, whereas in case of GOP2, GOP4 and GOP6 loaded MMMs, dispersion of polymer-*g*-GO nanosheets were observed at certain areas with formation of bright and dark domains into the membrane matrix which are may be associated with the hydrophilic and hydrophobic functionalities, respectively, [**Figure A3.20(A-G)** of Appendix 3**]**.[51,52] The appearance of brighter spots in the MMMs surface is attributed to the incorporation of hydrophilic GOP fillers. Due to the nanosheets incorporation and because of the proposed interaction pattern fibrillar layered morphology are also observed in the membrane matrix, hence the surface roughness also resulted remarkable increment after polymer modified GO nanosheets loading (see **Figure A3.21** and **Table A3.1** of Appendix 3 for surface roughness). The three-dimensional AFM morphology along with the surface height profiles for all the membranes are given in the **Figure A3.21(A-G)** of Appendix 3**,** which validities the data analysed from the surface topology. 3D surface morphology confirms the fibrillar structure, hydrophilic and hydrophobic domains formation and increased height profiles of the MMMs, which resulted remarkably high surface roughness with respect to OPBI.

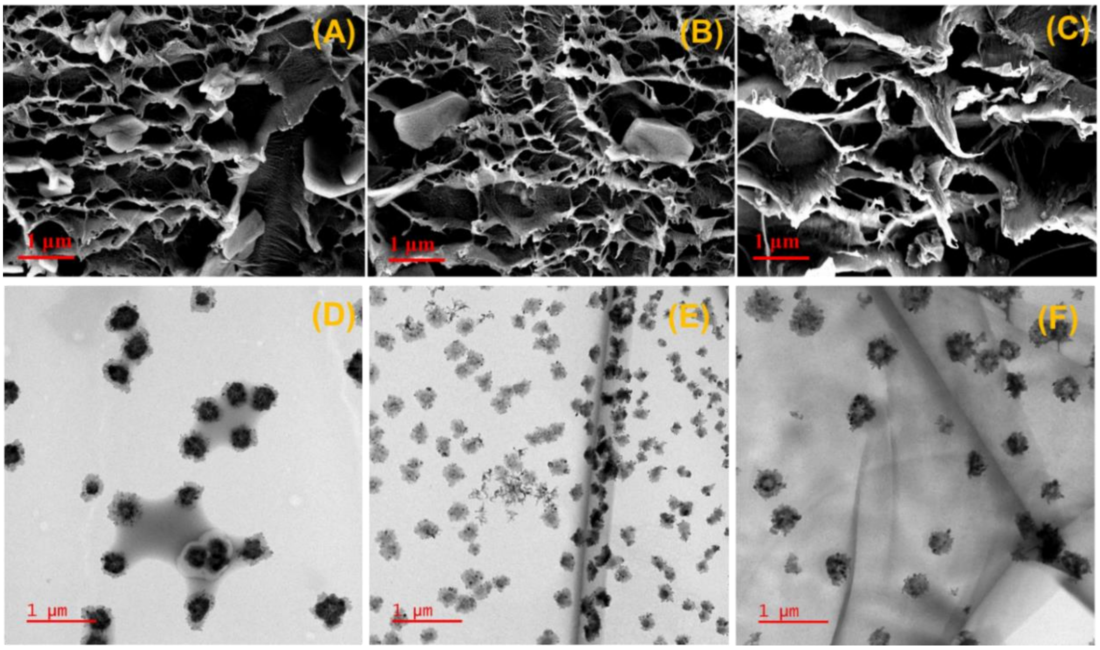

Figure 5.4. FESEM cross-sectional image of GOP2-2.5% **(A)**, GOP4-2.5% **(B)** and GOP6-2.5% **(C)** membranes. TEM images of GOP2-2.5% **(D)**, GOP4-2.5% **(E)** and GOP6-2.5% **(F)** membranes.

Thermal stability and thermomechanical study of MMMs.

TGA data of OPBI and GOP loaded MMMs **[Figure 5.5(A)]** show that the GOP loaded MMMs are quite stable without any weight loss up to 200 °C, a very minor weight loss is observed due to the evaporation of bound water molecules due to the presence of hydrophilic polymer grafted GO nanosheets in the membrane matrix. The thermal degradation initiates for OPBI and all the MMMs after 200 °C and with increasing GOP loading in the MMMs, the thermal degradation increases a bit due to the degradation of more hydrophilic functionalities (-C=O, $-SO_3H$), long alkyl chains, primary ammines and secondary ammines present in the GOP. The main polymeric backbone degradation is observed after 550 °C.[53] The loading percentage along with the dispersion pattern of the GOPs have impacted the storage modulus (E′) values of the MMMs significantly as seen from the temperature-dependent storage modulus (E′) plot in the **Figure 5.5 (B)** and the data are tabulated in the **Table A3.2** of Appendix 3. All the MMMs display remarkably high storage modulus (E′) when compared with OPBI, and the (E′) values are proportional with increasing GOP loading. **Table A3.2** data also suggests that the type of polymer grafted on the GO surface has impacted the values in the composite samples. The glass transition temperature (T_g) of the MMMs obtained from the loss modulus (E″) and tan δ plots are given in the **Figure A3.22** of Appendix 3**.** The T_g values obtained for OPBI and all the GOP loaded MMMs ranges between 265 – 295 °C which is in well accordance with the literature reported PBI based membranes.[34,49] The interfacial interaction between the GOP nanofillers and the OPBI responsible for slight T_g shifts in the composite MMMs with respect to OPBI (**Figure A3.22**).

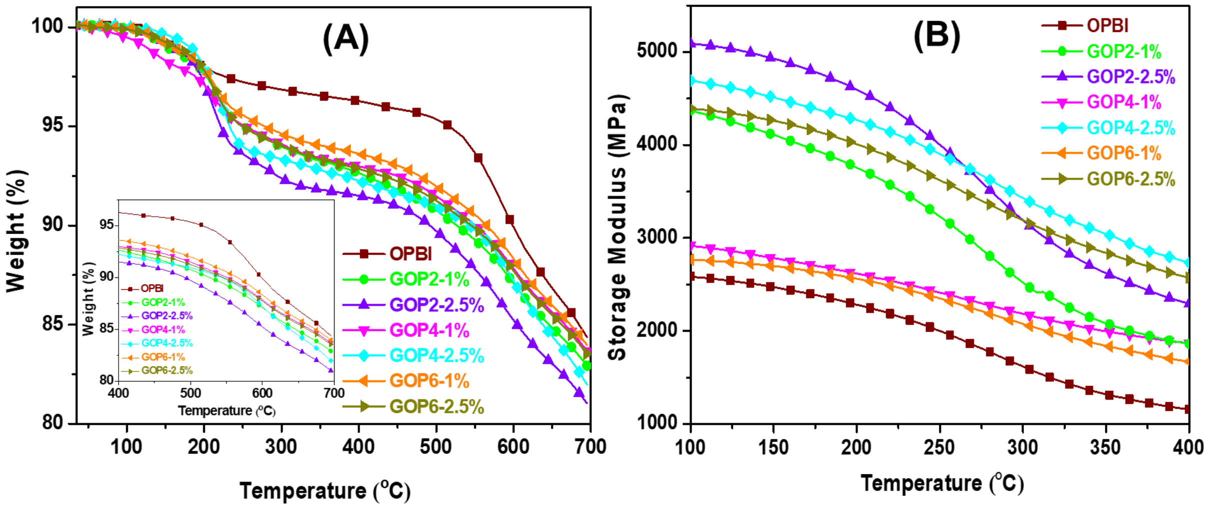

Figure 5.5. (A) TGA plot of the OPBI/GOP MMMs and OPBI membranes (Inset portrayed the zoomed TGA plot in the temperature range 400 ºC – 700 ºC). **(B)** Temperature dependent storage modulus plot of the OPBI/GOP MMMs of different filler loading.

Water uptake (WU), swelling ratio (SWR) and phosphoric acid (PA) loading of MMMs

The water uptake (WU) of OPBI is 10.57 wt% which decreases in case of GOP2 loaded MMMs **(Table 5.2)** as the –CONH$_2$ groups of the GO surface modified pAAM involves in substantial H-bonding with the OPBI 'N-H' and '-N=' groups, hence water molecules are unable to form H-bonding with the MMM network resulting lower WU. On the contrary, WU of the GOP4 and GOP6 loaded MMMs increases remarkably with increasing filler loading. This is attributed to the presence of hydrophilic –SO$_3$H functionalities present in the GO surface modified pAMPS and pSPAK polymer chains which involves in H-bonding with the water molecules. The swelling ratio (SWR) of the MMMs in water and PA decreases compared to OPBI and the decrement of SWR follows proportionality with the increasing GOP loading in the MMMs (**Table 5.2**). Only in case of GOP6 loaded membrane SWR both in water and PA shows an increment with increasing GOP loading, which might be due to the hydrophilic –SO$_3$H functionalities and flexible long chain present in the polymer chain (pSPAK) grafted on the GO surface.

Table 5.2. Water uptake, swelling ratio in water and PA, PA loading level of OPBI and MMMs**.** GO-EDA loaded membrane data also included for comparison purpose [a]

Sample name	*Water uptake (wt%)*	*Swelling ratio in water (%)*	*Swelling ratio in PA (%)*	*PA loading (no. of mol/PBI r.u)*
OPBI	10.57 (1.71)	4.31 (1.21)	5.87 (1.17)	15.21 (2.11)
GOP2-1%	10.31 (1.04)	1.89 (0.77)	3.76 (0.92)	20.52 (1.65)
GOP2-2.5%	9.77 (0.67)	0.96 (0.37)	2.72 (0.39)	22.51 (0.56)
GOP4-1%	14.47 (1.11)	2.41 (0.93)	2.68 (0.83)	24.41 (1.01)
GOP4-2.5%	17.71 (1.37)	1.77 (0.59)	2.33 (0.51)	27.14 (1.16)
GOP6-1%	16.28 (1.03)	2.67 (1.09)	1.85 (1.14)	24.88 (1.37)
GOP6-2.5%	20.04 (1.24)	2.93 (0.85)	3.31 (0.87)	29.94 (1.19)
GO-EDA-2.5%	10.79 (1.17)	1.19 (0.54)	4.18 (0.97)	19.97 (1.51)

[a] The number in the bracket represents the standard deviation value obtained from measurements.

PA doping level demonstrates the efficacy of proton conduction in a PA doped PEM as the proton conductivity of the membranes maintain proportionality with the PA doping level.

The PA doping level of OPBI is 15.21 mol/repeat unit, and displays an increasing trend with increasing loading of the GOP in the MMMs **(Table 5.2)**. The calculated PA doping level of GOP2-2.5%, GOP4-2.5% and GOP6-2.5% membranes are 22.51, 27.14 and 29.94 mol/repeat unit of PBI, respectively. The significantly improved PA doping level of the GOP4 and GOP6 loaded MMMs compared to GOP2 membranes are the combined effect of various factors. Firstly, GOP2 only consists of primary amines, secondary amines and $–CONH_2$ functionalities which can generate H-bonding with the PA molecules to improve the PA doping level when compared with OPBI. On the contrary, the exceptional PA doping level of the GOP4 and GOP6 loaded MMMs is due to the presence of hydrophilic $–SO_3H$ groups dangling with the flexible long alkyl chains, which can enhance the PA doping level of the MMMs due to the effective H-bonding associated between the $–SO_3H$ functionalities with PA molecules (**Scheme 5.3**). Secondly, the primary amines, secondary amines, $-CONH_2$, $-SO_3H$ functionalities available in the GOP interacts with the 'N-H' and '-N=' groups of OPBI to form donor-acceptor type acid base H-bonded structure which generates certain order of crystallinity in the composite matrix responsible for improved PA loading.[54] Thirdly, in higher filler loaded MMMs, PA molecules deploy plasticizing effect responsible for destroying the existing crystalline ordering in the membrane followed by formation of H-bonding of the PA molecules with the $–SO_3H$ and amine functionalities present in the MMMs.[55] In addition, the crater like cavity formation along with uniform dispersion pattern of the hydrophilic GOP nanosheets all over the membranes surface and interfacial region also effectively contributes towards higher PA uptake.

Proton conductivities of PEMs obtained from PA loaded MMMs

Proton conductivity of all the PEMs prepared by loading PA into the GOP loaded MMMs were measured and analysed in the temperature range 80-160 ºC. The obtained proton conductivity values of the MMMs are calculated from the Nyquist plot by relevant electrochemical circuit fitting (**Figure A3.23** of Appendix 3). GOP loaded MMMs show excellent proton conductivity compared to pristine OPBI [**Figure 5.6(A)**], while the observed proton conductivity value of OPBI is only 0.067 S cm^{-1} at 160 °C, the GOP2-1% and GOP2-2.5% MMMs are 0.188 Scm^{-1} and 0.224 Scm^{-1}, respectively at 160 ºC, which are ~ 3.5-fold high. The proton conductivity values of the GOP4-1% and GOP4-2.5% MMMs show further increase and the values are 0.251 S cm^{-1} and 0.276 S cm^{-1}, respectively at 160 ºC which are an enhancement of ~ 4.0- fold. Finally, the highest obtained proton conductivities are obtained in case of GOP6 loaded MMMs and the values are 0.260 S cm^{-1} and 0.327 S cm^{-1}, respectively at 160 °C for GOP6-1% and GOP6-2.5% membranes which are remarkably high (~5-fold) than pristine OPBI. Similar

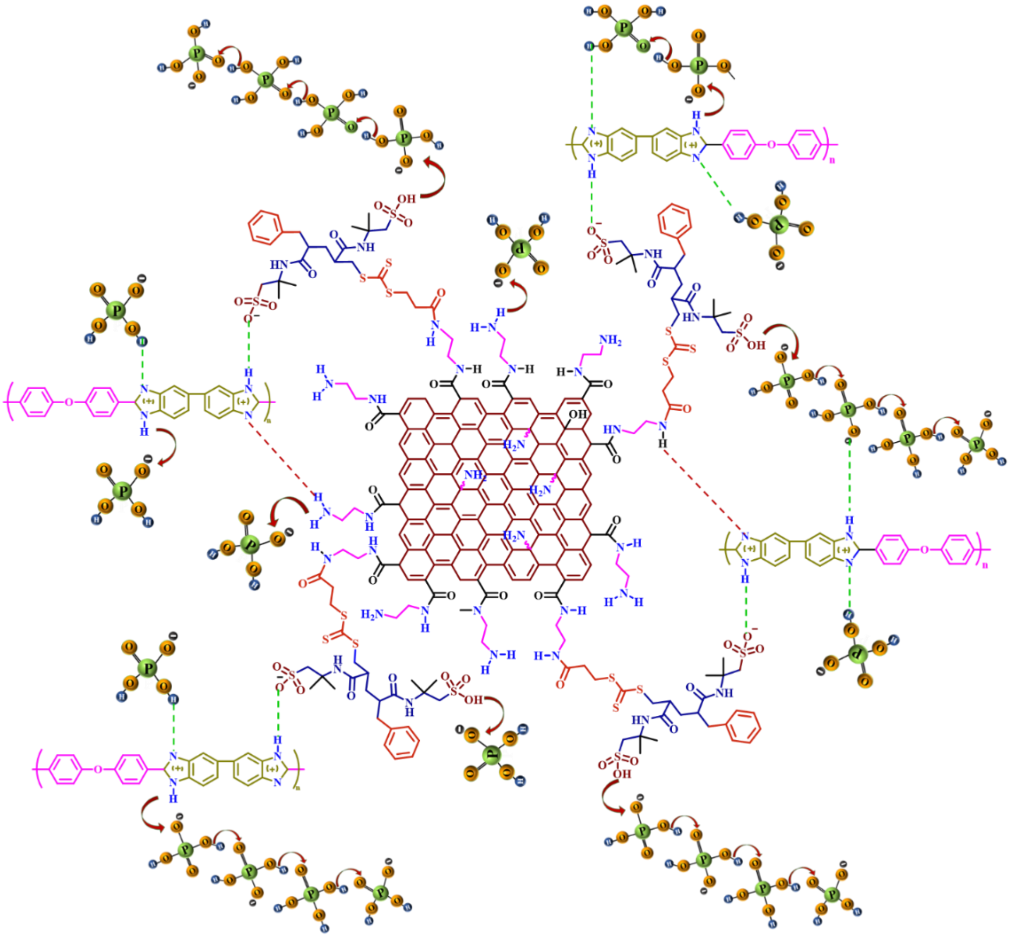

Scheme 5.3. Interaction pattern of PA with GOP loaded OPBI composite MMMs (a representative figure for OPBI/GOP6 composite membrane sample is given).

results and increment in proton conductivity are also observed for all other GOP loaded MMMs (**Figure A3.24** of Appendix 3). PA doping level of the membranes plays the important role in proton conductivity, it is clear from the data shown in **Figure 5.6A** and **Table 5.2** that higher PA loading results high proton conductivity. For example, the higher PA doping level of the GOP6 loaded MMMs over the GOP2 and GOP4 loaded MMMs provides higher proton conductivity of the MMMs in the former case. It is important to note that the proton conductivity of PEMs obtain from the PA doped GOP loaded MMMs are dependent on various features of GOP and these are: (1) type of polymer grafted on the surface of GO – this can be realized by simply comparing the data shown in **Figure 5.6A** and **Figure A3.24** which clearly show that as we change the GOP structure, the proton conductivity varies a lot, (2) the molecular weight of the grafted polymer chain – this can be understood by simply comparing GOP1-GOP2 data (or GOP3- GOP4 or GOP5-GOP6), for example GOP5-2.5% shows proton conductivity 0.246 S cm^{-1} whereas GOP6-2.5% results 0.327 S cm^{-1} at 160 °C, and (3) the loading also influences undoubtedly – higher the GOP loading higher is the conductivity. At higher temperature (>100 ºC), the segmental mobility of the polymer chains also contributes effectively towards efficient proton conductions,[56] hence, the coordinated motion of OPBI and the GO surface modified polymer chains contributed cumulatively at higher temperatures and resulted well-ordered proton transport channels in the nanocomposite membranes, especially for the GOP4-2.5% and GOP6-2.5% membranes. GO-EDA-2.5% membrane resulted very less proton conductivity (0.147 S cm^{-1}) with respect to all other MMMs due to the absence of hydrophilic –C=O, -SO_3H functionalities in the membrane. The Arrhenius activation energy values of proton conduction for the GOP loaded MMMs observed to be in between 7-11 kJ/mol (see **Figure A3.25** of Appendix 3) which suggests that the proton conduction in the membranes occurring through Grotthuss proton hopping mechanism[35,57] where the PA molecules acts as labile proton conductors.

The membranes were further treated for prolong isothermal proton conductivity analysis at 160 ºC for 36 h (see **Figure 5.6B**). Isothermal proton conductivities of the GOP2-2.5%, GOP4-2.5% and GOP6-2.5% membranes were measured and compared with the pristine OPBI. Initially, within the first 2-4 h of analysis a bit decrease of proton conductivity was observed for all the membranes. After the initial period, proton conductivities of the MMMs found to be stable up to the entire experimental time range. The MMMs found to be retained superior proton conductivity with respect to the bare OPBI polymer due to the presence of substantial H-bonding network inside the membrane's interfacial region, and due to the highly altered morphology and remarkably high PA doping level. Even after elevated temperature long term treatment (160 ºC for 36 h) membranes barely loses any conductivity and retained its superiority.

To check the suitability of the PEMs obtained from MMMs for HT-PEMFC application, PA retention efficacy of the membranes were measured and the results are summarized in the **Figure 5.6(C)**. The maximum PA leaching of all the membranes are observed within the first hour of analysis. OPBI loses 44.1 wt% PA while GOP2-2.5%, GOP4-2.5% and GOP6-2.5% membranes leach 23.47 wt%, 21.86 wt% and 18.22 wt% PA, respectively after 1 h of treatment. At the end of 3 h of analysis, the total PA leaching of these three membranes are 30.23 wt%, 28.74 wt% and 23.35 wt%, respectively, on the contrary, the pristine OPBI membrane leaching >70 wt% PA and the slope of the leaching curve continues to increase, whereas in case of MMMs the curve reaches saturation with further negligible PA loss (**Figure 5.6C**). The layered GOPs and the dispersion pattern of the GOPs played a crucial role in the PA retention capacity of the membranes owing to the presence of H-bonded partial intercalation of GOP present in the MMMs which enables the PA molecules retention within the membranes. In addition, GOP generates substantial H-bonding and ionic interactions of the PA molecules associated with the dangling surface grafted hydrophilic polymer functionalities (-CONH$_2$, -NH, -SO$_3$H) present in the GOP surface which prevents the PA molecules leaching away from the MMM interface.

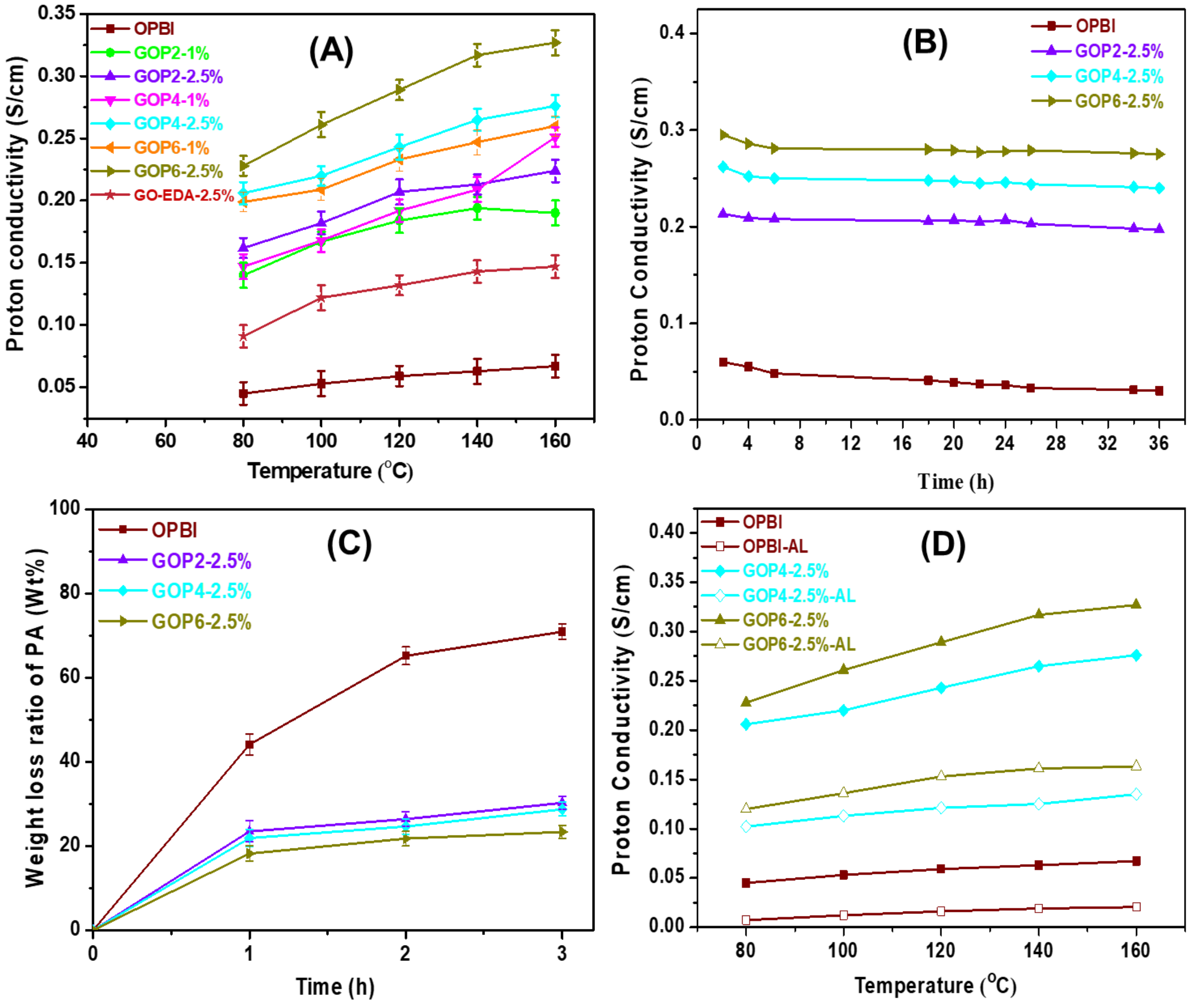

Figure 5.6. (A) proton conductivity of PA doped OPBI and GOP loaded MMMs. **(B)** Isothermal proton conductivity at 160°C for OPBI, GOP2-2.5%, GOP4-2.5% and GOP6-2.5% membranes. **(C)** Acid leaching analysis of the PA loaded MMMs. **(D)** Proton conductivity measurement of the PA loaded MMMs after PA leaching treatment (AL corresponds to the membranes after acid leaching test).

The post PA leaching proton conduction analysis of the GOP4-2.5% and GOP6-2.5% membranes were also performed in a comparison with OPBI to establish the PA retention superiority of the flexible hydrophilic polymeric chains modified GO nanosheets loaded MMMs (**Figure 5.6D**). The proton conductivity of OPBI-AL is resulted only 0.0204 S cm^{-1} at 160 ^{o}C, on the contrary PA leached GOP4-2.5%-AL and GOP6-2.5%-AL membranes exhibit proton conductivity values of 0.135 S cm^{-1} and 0.163 S cm^{-1} under identical experimental condition. The retention of proton conductivity values >0.1 S cm^{-1} even after acid leaching treatment makes our membrane highly robust in terms of utilization in prolong HT-PEMFC operation. The specific H-bonding interaction of the primary, secondary amines, and the hydrophilic flexible long chain –SO_3H groups present in the surface modified GOP nanostructure with the PA molecules, and the completely altered morphology contributes towards substantial PA retention followed by excellent proton conduction in the PA leached PEMs.

Mechanical and thermal stabilities of the PEMs obtained from PA loaded MMMs

The stress-strain profiles of the PA loaded MMMs were analysed in Universal Testing Machine (UTM) analysis and plotted in the **Figure 5.7(A, B, C).** The tensile strength and elongation at break values are tabulated in the **Table A3.3** of Appendix 3**.** All the PA loaded MMMs exhibit huge mechanical reinforcement in comparison to OPBI clearly suggesting that the GOP nanofiller has helped in improving the mechanical strength of the resulting membrane. It is to be noted that, with increasing GOP loading in the MMMs the little decrease in strength is observed but remarkable increase in elongation at break is noticed. Stress-strain profiles of the GOP2 loaded membranes are found to be better over the GOP4 and GOP6 loaded MMMs suggesting the influence of type of grafted polymer chains on the GO surface.

Furthermore, the thermal stability of the PA doped MMMs were performed to evaluate the PA retention capability of the MMMs and interestingly the observation obtained from the TGA plot validates the data analysed from the PA leaching analysis. In our earlier assessment PA undoped MMMs found to be less thermally stable with respect to bare OPBI polymer due to the degradation of the organic functionalities present in the GOP (**Figure 5.5A**), but the PA doped MMMs exhibit reverse order of thermal stability in between 100 °C - 400 °C, and the highest thermal stability is obtained in case of GOP6-2.5% membrane **(Figure 5.7D)**.

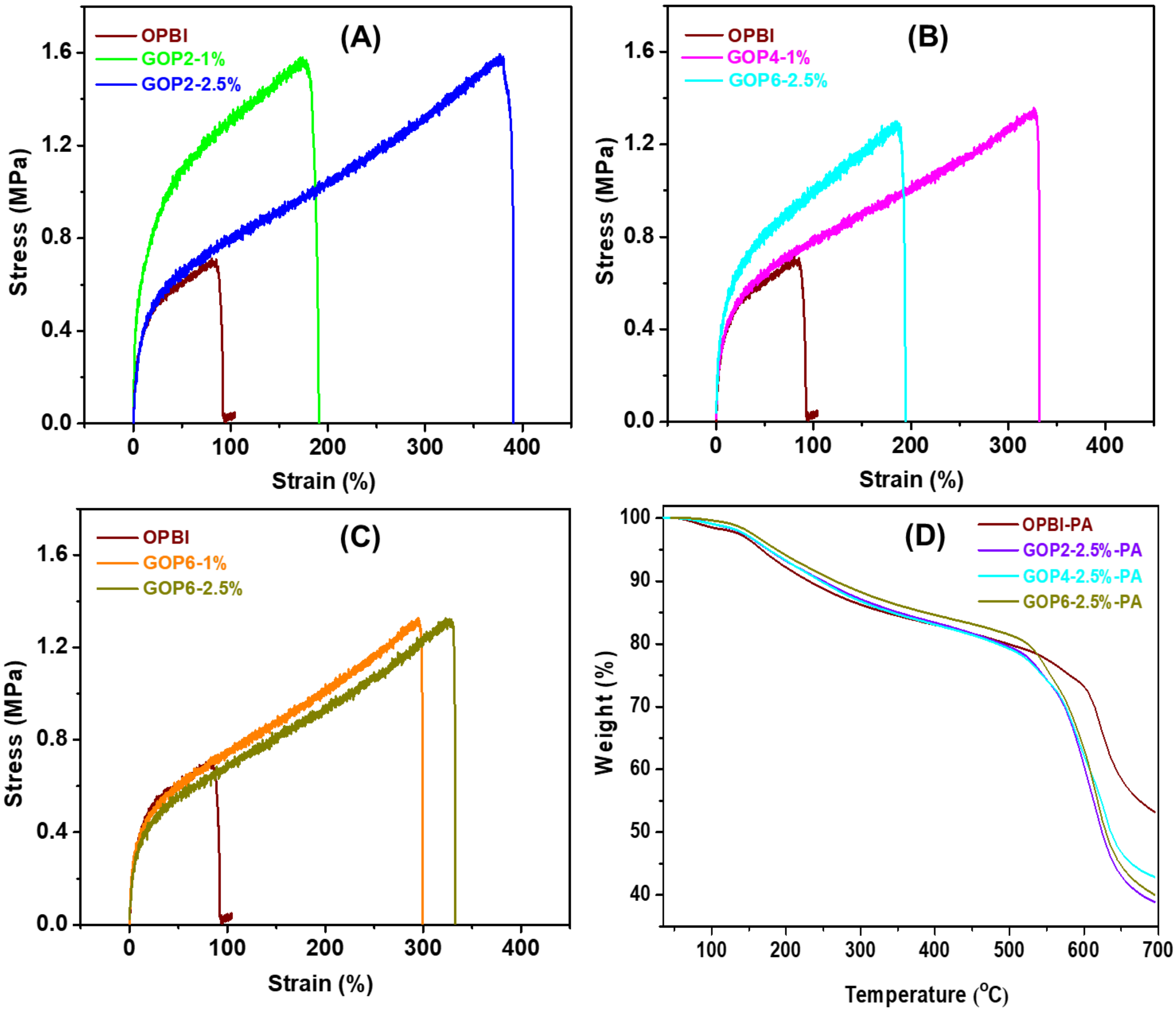

Figure 5.7. Stress-strain plots of PEMs obtained from (A) GOP2, (B) GOP4 and GOP6 (C) loaded MMMs. Plot for PEM obtained from pristine OPBI has been included in each case for comparison purpose. TGA plot of the PA doped OPBI and GOP loaded MMMs.

Conclusion

Our current work illustrates a highly effective strategy for the surface modification of GO with various kinds of polymer chains along with the precise control over the surface functionalization. A surface initiated reversible addition fragmentation "*grafting from*" polymerization approach has been used to covalently grow three different polymer chains namely pAAM-*g*-GO, pAMPS-*g*-GO and pSPAK-*g*-GO on the surface of the GO. We have carefully chosen heteroatoms (-NH and –SO_3H) containing monomers to grow the polymer chains in the GO surface which ensured formation of hydrophilic nanochannels throughout the GO surface and enabled the preparation of hydrophilic nanofiller in order to increase the dispersion nature of the nanomaterials in the polar solvents. The surface modified polymers have been further utilized as a nanofiller with oxypolybenzimidazole (OPBI) to make mixed matrix membranes (MMMs). The H-bonding interaction between the OPBI imidazole ‘N-H’ groups with the functional groups (-NH and –SO_3H) present in the grafted polymer chains on the GO surface resulted newly generated crystalline planes in the MMMs, and highly altered surface and cross-sectional morphology. All these factors contributed significantly towards the remarkably high PA doping level followed by superior proton conductivity improvement, outstanding PA retention capacity at elevated temperature, and noteworthy improvement of mechanical properties of the MMMs. Even, all the MMMs retained their proton conductivity under prolong treatment at elevated temperature (160 °C). After PA leaching analysis, membranes were able to possess proton conductivity >0.15 S cm^{-1} which demonstrates the stability and the robustness of the fabricated MMMs. So far, surface functionalized polymer-*g*-GO materials have never been explored in literature for their effective utilization in improving PEM properties. To the best of our knowledge this will be the first report on utilization of surface polymer modified GO nanosheets in PBI membrane supported matrix to evaluate the role of super proton conducting mixed matrix PEMs in HT-PEMFC application.

Reference

(1) Wu, S.; Yin, Z.; He, Q.; Huang, X.; Zhou, X.; Zhang, H. *J. Phys. Chem. C* **2010**, *114*, 11816–11821.

(2) Wang, H.; Hao, Q.; Yang, X.; Lu, L.; Wang, X. *ACS Appl. Mater. Interfaces* **2010**, *2*, 821–828.

(3) Hou, J.; Shao, Y.; Ellis, M. W.; Moore, R. B.; Yi, B. *Phys. Chem. Chem. Phys.* **2011**, *13*, 15384–15402.

(4) Zhang, J.; Zhang, J.; Zhang, F.; Yang, H.; Huang, X.; Liu, H.; Guo, S. *Langmuir* **2010**, *26*, 6083–6085.

(5) Padmavathy, N.; Behera, S. S.; Pathan, S.; Ghosh, L. D.; Bose, S. *ACS Appl. Mater. Interfaces* **2019,** *11*, 7566–7575.

(6) Maiti, S.; Islam, S. S.; Bose, S. *Environ. Sci.: Water Res. Technol.*, **2023,** *9*, 249-264.

(7) Tseng, C. Y.; Ye, Y. S.; Cheng, M. Y.; Kao, K. Y.; Shen, W. C.; Rick, J.; Chen, J. C.; Hwang, B. J. *Adv. Energy Mater.* **2011**, *1*, 1220–1224.

(8) Shukla, G.; Pandey, R. P.; Shahi, V. K. *J. Membr. Sci.* **2016,** *520,* 972-982.

(9) Luong, N. D.; Hippi, U.; Korhonen, J. T.; Soininen, A. J.; Ruokolainen, J.; Johansson, L. S.; Nam, J. Do; Sinh, L. H.; Seppälä, J. *Polymer* **2011**, *52*, 5237–5242.

(10) Lerf, A.; He, H.; Riedl, T.; Forster, M.; Klinowski, J. *Solid State Ionics* **1997**, *101–103*, 857–862.

(11) Vinothkannan, M.; Kim, A. R.; Gnana Kumar, G.; Yoo, D. J. *RSC Adv.* **2018**, *8*, 7494–7508.

(12) Beydaghi, H.; Javanbakht, M.; Kowsari, E. *Ind. Eng. Chem. Res.* **2014**, *53*, 16621–16632.

(13) Feng, K.; Tang, B.; Wu, P. *J. Mater. Chem. A* **2014**, *2*, 16083–16092.

(14) Xu, C.; Cao, Y.; Kumar, R.; Wu, X.; Wang, X.; Scott, K. A *J. Mater. Chem.* **2011**, *21*, 11359–11364.

(15) Zarrin, H.; Higgins, D.; Jun, Y.; Chen, Z.; Fowler, M. *J. Phys. Chem. C* **2011**, *115*, 20774–20781.

(16) Liang, M.; Luo, B.; Zhi, L. Application of Graphene and Graphene-Based Materials in Clean Energy-Related Devices. *Int. J. Energy Res.***2009,** *33*, 1161–1170.

(17) Kowsari, E.; Zare, A.; Ansari, V. *Int. J. Hydrogen Energy* **2015**, *40* , 13964–13978.

(18) Pandey, R. P.; Shukla, G.; Manohar, M.; Shahi, V. K. *Adv. Colloid Interface Sci.* **2017**, *240*, 15–30.

(19) Jiang, Z.; Zhao, X.; Fu, Y.; Manthiram, A. *J. Mater. Chem.* **2012**, *22* , 24862–24869.

(20) Wu, W.; Li, Y.; Chen, P.; Liu, J.; Wang, J.; Zhang, H. *ACS Appl. Mater. Interfaces* **2016**, *8*, 588–599.

(21) Cai, Y. Y.; Zhang, Q. G.; Zhu, A. M.; Liu, Q. L. *J. Colloid Interface Sci.* **2021**, *594*, 593–603.

(22) Chu, F.; Lin, B.; Feng, T.; Wang, C.; Zhang, S.; Yuan, N.; Liu, Z.; Ding, J. *J. Memb. Sci.* **2015**, *496*, 31–38.

(23) Yang, J.; Liu, C.; Gao, L.; Wang, J.; Xu, Y.; He, R. *RSC Adv.* **2015**, *5*, 101049–101054.

(24) Ko, T.; Kim, K.; Lim, M. Y.; Nam, S. Y.; Kim, T. H.; Kim, S. K.; Lee, J. C. *J. Mater. Chem. A* **2015**, *3*, 20595–20606.

(25) Kim, J.; Kim, K.; Ko, T.; Han, J.; Lee, J. C. *Int. J. Hydrogen Energy* **2021**, *46*, 12254–12262.

(26) Yang, Y.; Song, X.; Yuan, L.; Li, M.; Liu, J.; Ji, R.; Zhao, H. *J. Polym. Sci. Part A Polym. Chem.* **2012**, *50*, 329–337.

(27) Samadaei, F.; Salami-Kalajahi, M.; Roghani-Mamaqani, H. *Int. J. Polym. Mater. Polym. Biomater.* **2016**, *65* , 302–309.

(28) Namvari, M.; Biswas, C. S.; Wang, Q.; Liang, W.; Stadler, F. J. *J. Colloid Interface Sci.* **2017**, *504*, 731–740.

(29) Wang, S.; Meng, H.; Li, Y.; Sun, D.; Zhan, Y.; Ge, X.; Chen, L. *J. Polym. Sci. Part A Polym. Chem.* **2019**, *57*, 689–698.

(30) Badri, A.; Whittaker, M. R.; Zetterlund, P. B. *J. Polym. Sci. Part A Polym. Chem.* **2012**, *50* , 2981–2992.

(31) Deng, Y.; Li, Y.; Dai, J.; Lang, M.; Huang, X. *J. Polym. Sci. Part A Polym. Chem.* **2011**, *49*, 1582–1590.

(32) Zhang, X.; Su, Y.; Lei, L.; Wu, S.; Shen, J. *Colloids Surfaces A Physicochem. Eng. Asp.* **2021**, *610*, 125925.

(33) Dhara, M.; Rudra, S.; Mukherjee, N.; Jana, T. *Polym. Chem.* **2021**, *12*, 3976–3991.

(34) Basu, O.; Das, A.; Jana, T.; Das, S. K. *ACS Appl. Energy Mater.* **DOI:** 10.1021/acsaem.2c02972.

(35) Mukherjee, N.; Das, A.; Jana, T. *ACS Appl. Nano Mater.* **2023,** *6*, 544-557.

(36) Roghani-Mamaqani, H.; Haddadi-Asl, V.; Khezri, K.; Zeinali, E.; Salami-Kalajahi, M. *J. Polym. Res.* **2014**, 21, 333.

(37) Yeole, N.; Kutcherlapati, S. N. R.; Jana, T. *J. Colloid Interface Sci.* **2015**, *443*, 137–142.

(38) Pandey, R. P.; Das, A. K.; Shahi, V. K. *ACS Appl. Mater. Interfaces* **2015**, *7*, 28524–28533.

(39) Wang, J.; Yu, X.; Wang, C.; Xiang, K.; Deng, M.; Yin, H. *J. Alloys Compd.* **2017**, *709*, 596–601.

(40) Patel, R.; Chi, W. S.; Ahn, S. H.; Park, C. H.; Lee, H. K.; Kim, J. H. *Chem. Eng. J.* **2014**, *247*, 1–8.

(41) Degirmenci, M. *J. Macromol. Sci. - Pure Appl. Chem.* **2005**, *42*, 21–30.

(42) Sangthumchai, T.; Kamjornsupamitr, T.; Saengsaen, S.; Pumingdawn, N.; Panawong, C.; Sumranjit, J.; Budsombat, S. *Polymer.* **2020**, *207*, 122910.

(43) Rahimi-Razin, S.; Salami-Kalajahi, M.; Haddadi-Asl, V.; Roghani-Mamaqani, H. *J. Polym. Res.* **2012**, *19*. 9954.

(44) Kim, N. H.; Kuila, T.; Lee, J. H. *J. Mater. Chem. A* **2013**, *1*, 1349–1358.

(45) Stankovich, S.; Dikin, D. A.; Piner, R. D.; Kohlhaas, K. A.; Kleinhammes, A.; Jia, Y.; Wu, Y.; Nguyen, S. B. T.; Ruoff, R. S. *Carbon* **2007**, *45*, 1558–1565.

(46) Shen, J.; Hu, Y.; Shi, M.; Lu, X.; Qin, C.; Li, C.; Ye, M. *Chem. Mater.* **2009**, *21*, 3514–3520.

(47) Li, C.; Wang, C.; Ji, Z.; Jiang, N.; Lin, W.; Li, D. *Eur. Polym. J.* **2019**, *113*, 404–410.

(48) Roy, M.; Kusurkar, T. S.; Maurya, S. K.; Meena, S. K.; Singh, S. K.; Sethy, N.; Bhargava, K.; Sharma, R. K.; Goswami, D.; Sarkar, S.; Das, M. *3 Biotech* **2014**, *4*, 67–75.

(49) Gorre, A.; Das, A.; Jana, T. *J. Macromol. Sci. Part A Pure Appl. Chem.* **2023,** *60*, 38-50.

(50) Mukhopadhyay, S.; Das, A.; Jana, T.; Das, S. K. *ACS Appl. Energy Mater.* **2020**, *3*, 7964–7977.

(51) Priyangga, A.; Mumtazah, Z.; Junoh, H.; Jaafar, J.; Atmaja, L. *J. Membr. Sci. Res.* **2021**, *7*, 295–304.

(52) Muthumeenal, A.; Neelakandan, S.; Kanagaraj, P.; Nagendran, A. *Renew. Energy* **2016**, *86*, 922–929.

(53) Mukherjee, N.; Das, A.; Dhara, M.; Jana, T. *Polymer* **2021**, *236* , 124315.

(54) Lobato, J.; Cañizares, P.; Rodrigo, M. A.; Úbeda, D.; Pinar, F. J. *J. Memb. Sci.* **2011**, *369*, 105–111.

(55) Jiang, J.; Zhu, X.; Qian, H.; Xu, J.; Yue, Z.; Zou, Z.; Yang, H. *Sustain. Energy Fuels* **2019**, *3*, 2426–2434.

(56) Koyilapu, R.; Subhadarshini, S.; Singha, S.; Jana, T. *Polymer* **2021**, *212* , 123175.

(57) Escorihuela, J.; Mancilla, J. O.; Alexandrova, L.; Castillo, L. F. D.; Compañ, V. *Polymers* **2020**, *12*, 1861.

Chapter 6

Cross-Linked Alkaline Anion Exchange Membrane from N-Spirocyclic Quaternary Ammonium and Polybenzimidazole.

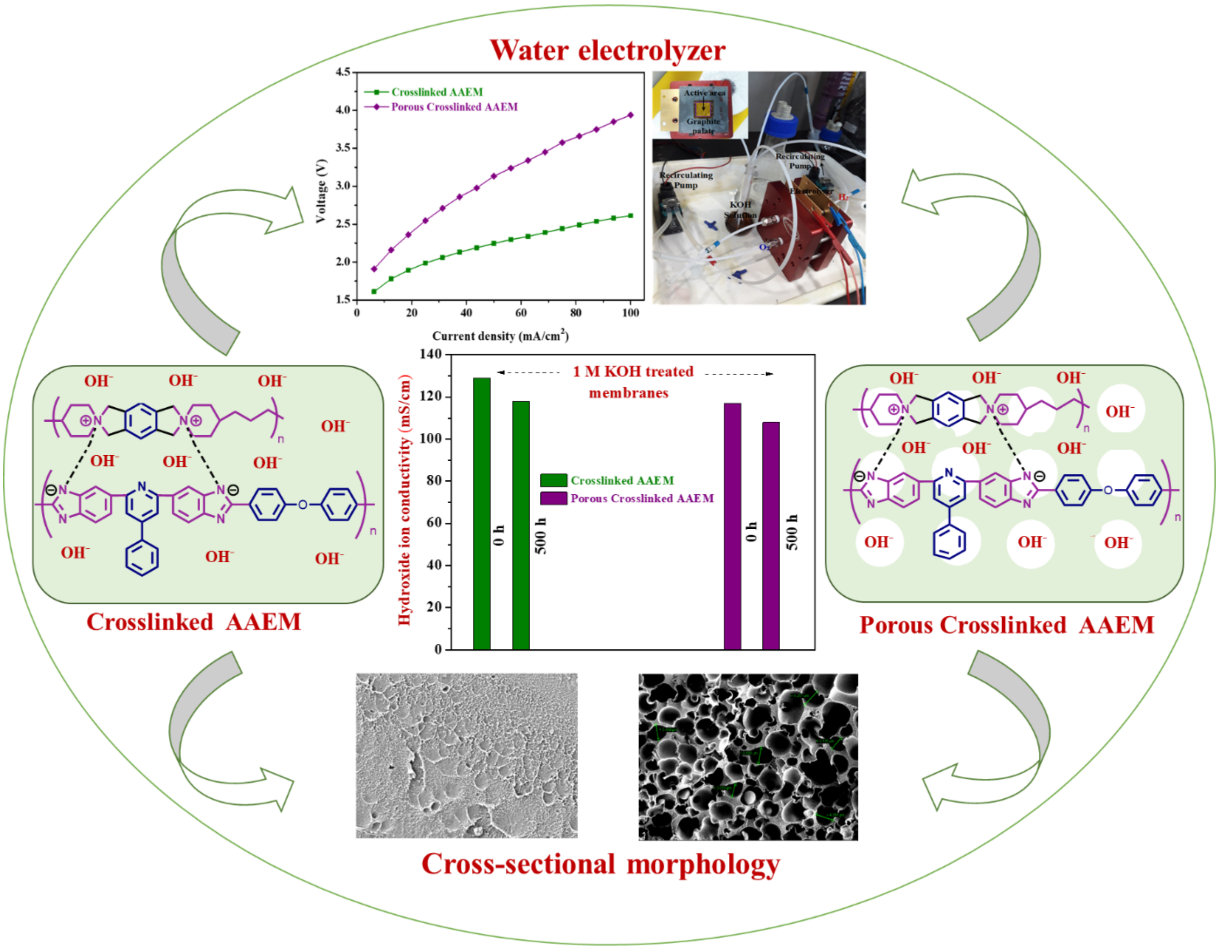

<u>Anupam Das</u>, Balakondareddy Sana, Rama Bhattacharyya, Prakash Chandra Ghosh and Tushar Jana* Cross-Linked Alkaline Anion Exchange Membrane from N-Spirocyclic Quaternary Ammonium and Polybenzimidazole. *ACS Appl. Polym. Mater.* **2022,** *4,* 1523−1534.

Abstract

In spite of significant research outcomes on alkaline anion exchange membrane (AAEM) in recent past, two major challenges namely hydroxide conductivity and alkaline stability of the polymer membrane yet to be resolved adequately. To address these challenges, in this work development of ionically crosslinked AAEMs has been achieved by blending pyridine bridged polybenzimidazole (PyPBI) and N-spirocyclic quaternary ammonium spiro ionene polymer (SP). Further, membranes were converted to porous membranes by adding different weight % of porogen in the membrane matrix and then leaching out the porogen followed by crosslinking. All the membranes (both non-porous and porous) were converted to hydroxide conducting AAEM by dipping into 1 M KOH solution and under this condition, a part of the -NH- groups of PyPBI was deprotonated to form ammonium-imidazolate complexes with SP which resulted ionic crosslinking in the AAEM. Hydroxide ion conductivity, one of the highest among the reported so far, of 129 mS/cm at 90 °C was obtained in case of S70P30-OH membrane which was a hydroxide form membrane obtained from the blend of 70 wt% SP and 30 wt% PyPBI and this membrane showed the highest KOH uptake among all other AAEMs prepared in this study. On the other hand, among the porous ionically crosslinked membranes S50P50-P25-OH (blends of 50 wt% SP and 50 wt% PyPBI with 25% porogen) membrane showed the highest hydroxide ion conductivity (117 mS/cm at 90 °C) among all the porous membrane studied here. All the ionically crosslinked AAEMs (both non porous and porous) displayed excellent alkaline stability and remains unaffected during alkaline stability test in 1M KOH at 80 °C as long as testing was carried out (960 h). Observing the exceptional stability in 1 M KOH of S50P50-OH and S50P50-P25-OH membranes, OH^- conductivity analysis and alkaline stability tests of these samples have been carried out even in 2 M KOH, and we found that these membranes retained ~80% of their OH^- conductivity value even after 500 h of alkaline treatment in 2 M KOH at 60 °C. Furthermore, membranes were found to be useful in alkaline water electrolysis and the best performance is shown by S70P30-OH membrane which displayed a current density of 100 mA cm^{-2} at 2.6 V. Overall as these recently developed membranes retained hydroxide conductivity, structural, thermal stability even after harsh alkaline treatment for longer period of time.

Introduction

With the development of fossils free renewable energy resources, electrochemical energy conversion devices such as fuel cells,[1–4] electrodialysis,[5] redox flow batteries,[6,7] and alkaline water electrolysis[8,9] have gained a lot of focus in current times. The ion exchange membrane, an important component of the electrochemical devices, plays a vital role in the ion conduction and electrode separation.[5] Huge benefits, particularly use of non-precious metal catalyst like Co and Ni and faster electrode kinetics of alkaline anion exchange membrane fuel cell (AAEMFC) over proton exchange membrane fuel cell (PEMFC) have generated great deal of attention in developing various kinds of alkaline anion exchange membrane (AAEM) in recent years.[1-5,7] Generally, cationic functional moieties such as pyridinium,[10,11] quaternary ammonium (QA),[12-16] imidazolium,[17-19] benzimidazolium,[10,19] phosphonium,[20] tertiary sulphonium,[21] guanidinium,[22] piperidinium,[23,24] pyrrolidinium,[25] azepanium,[26] morpholinium,[26] quinuclidium[26] have been often introduced into the polymer chain to create anion exchange sites. A promising anion exchange membrane must possess high hydroxide ion conductivity, excellent alkaline stability, good thermal stability, moderate to high mechanical robustness and sufficiently long-term durability at elevated temperature in presence of harsh alkaline condition.[17,27,28] Development of such kind of AAEM with all above mentioned features is a major challenge. Because of its highly basic and nucleophilic nature, the hydroxide ion is prone to attack and degrade the conventional QA[29] and other cationic groups via, e.g., Hofmann eliminations and nucleophilic substitutions.[30] In addition, polymer backbones may degrade via such as cleavage of activated ether bridges.[31] Also, the hydroxide ion conductivity and mechanical properties of AAEMs normally deteriorate over time[32] and therefore severely limits their applicability especially at temperatures beyond 60 °C.

Several successful strategies have been utilized to improve the alkaline stability of cationic groups including the utilization of steric protection,[33] conformational restrictions,[34] inductive effects[35] and metal complexes.[36] In recent years, N-spirocyclic QA moiety has been evolved as an area of keen interest among the researchers due to its superior alkaline stability.[16,34,37-44] Marino and Kreuer reported on the exceptional alkaline stability of certain N-spirocyclic QA salts, especially 6-azonia spiro[5.5]undecane.[45] Jannasch et al. has developed a new class of AAEM functionalized with N-spirocyclic QA cations formed via cycloquaternization reactions involving pyrrolidine, piperidine, and azepane, respectively. After that these cations were introduced in poly(arylene ether sulfone) backbones resulting OH^- conductivity of 110 mS/cm at 80 °C.[34] In another report, the same group has developed cross-linked AAEMs by copolymerizing N, N-diallylpiperidinium Chloride (DAPipCl) and diallylmethyl QA tethered to poly(phenylene oxide) and reported OH^- conductivity above 0.1 S cm^{-1} at 80 °C.[46] Sung, Kim, Henkensmeier and co-workers have introduced spirobiindane group to poly(arylene ether sulfone) to synthesize anion conducting membrane where they have achieved ion exchange capacity (IEC) value 1.18 meq/g and OH^- conductivity 27 ms/cm at 80 °C.[42] Zhang et al. reported an AAEM which showed OH^- ion conductivity of 63.1 mS cm^{-1} at 80 °C despite of its relatively low IEC (0.93 meq/g), and the constrained ring conformation of N-spirocyclic QA results in improved stability of the membrane.[44] Recently, Zhu and co-workers have tethered single N-spirocyclic cation to the PPO backbone via long side chains.[47] After alkaline treatment (1 M NaOH/H_2O, 80 °C, 1500 h), the sample showed satisfactory stability, but the fragility of membrane is of a profound disadvantage to their practical application. Guiver and co-workers reported PPO incorporating spirocyclic 3,6-diazaspiro[5.5]undecane membrane with IEC of 1.91 meq/g and OH^- conductivity (31.9 mS/cm) with 76% water uptake and 9.6% linear dimensional swelling at 20 °C, and observed 72-77% retention of OH^- conductivity after 360 h of alkaline stability test at 1 M NaOH 80 °C.[38]

Inspired by the profound stability of spirocyclic structure as seen in several reports in the above discussion, in our current work, we have synthesized N-spirocyclic quaternary ammonium ionene (abbreviated as SP) following a modified literature reported procedure[37] and observed that SP is highly water soluble due to the presence of long alkyl chains, and hence cannot be utilized as AAEMs directly for AAEMFC and alkaline water electrolysis. Therefore, we aimed to fabricate water insoluble ionically crosslinked AAEM by blending spiro ionene polymer (SP) with pyridine bridge polybenzimidazole (PyPBI)[48] polymer in different weight ratios. We can expect promising ion conductivity, excellent mechanical and tensile properties with improved alkaline durability at elevated temperature for a longer period of time due to the induced crosslinking.

Further we noted that several literatures demonstrated that the introduction of porosity into the pristine polymer membrane in a controlled manner increases ionic conductivity, IEC value etc. Induced pores brings porous morphology leading to attract more water and electrolyte molecules to enter into the membrane and therefore improves properties.[49-52] Literature also supports the existence of porous crosslinked membranes with excellent mechanical and tensile properties along with promising ion conductivity.[53] Therefore, we also introduced porosity in a controlled manner by varying the porogen ratio into the blend membrane of SP/PyPBI, then porogen were leached out by solvent treatment,[49] followed by ionic crosslinking to develop ionically crosslinked porous blend AAEM. Therefore, we expect to achieve more improved properties like ionic conductivity, IEC, water and KOH uptake into this porous AAEM. Thus, both the non-porous and porous ionically crosslinked (ICL) membranes have been developed and studied in this work with the objective to improve the properties of AAEM.

Experimental Section

All the source of materials, synthesis and characterization of PyPBI and spiro ionene polymer (SP), all the membranes characterization methods and instrumentation techniques utilized in this work are discussed in details in the **Chapter 2** and **Appendix 4.**

Preparation of ionically crosslinked (ICL) alkaline anion exchange membranes

SP and PyPBI polymers were dissolved in 10 mL of DMSO by keeping total polymer concentration 4 wt%. The solution of these mixture was stirred for 48 h at 30 °C. Then the solution was transferred to a Petri dish and the solvent was evaporated slowly to cast membrane in a ventilated oven at 80 °C for 48 h. The resulting membrane was easily detached from the Petri dish and subsequently immersed in a 1 M aqueous KBr solution for 24 h to make Br^- form membrane. After that, membrane in the Br^- form was converted to the OH^- form by immersing in a 1 M aqueous KOH solution under nitrogen atmosphere for 24 h. Upon KOH loading, the -NH- groups of PyPBI were deprotonated to form ammonium-imidazolate complex with SP **(Scheme 6.1)** resulting ionically crosslinked (ICL) AAEM. Finally, the membranes were thoroughly washed with degassed deionized water and stored in degassed deionized water under N_2 atmosphere for further measurements.

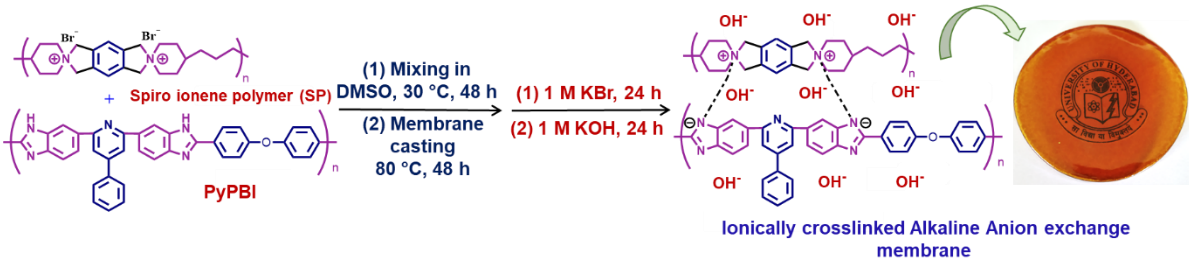

Scheme 6.1. Ionically crosslinked (ICL) AAEM formation by ammonium-imidazolate complexation (shown using dotted line). Transparent membrane was obtained as clearly seen from the picture where the emblem seen through the membrane is sourced from the webpage of the University of Hyderabad and used after approval from the appropriate authority.

The blend composition was varied by altering the relative weight ratios of SP and PyPBI in the mixture. Three blends were prepared where weight ratios of SP: PyPBI were 70:30, 50:50 and 30:70, and these are identified as S70P30, S50P50 and S30P70, respectively where S and

P represents SP and PyPBI polymers, respectively. The AEM in the Br^- and OH^- form are named as S70P30-Br and S70P30-OH, respectively and similar notations are used for other two samples as well.

Preparation of porous ionically crosslinked AAEM

Porous ionically crosslinked AAEM **(Scheme 6.2)** also prepared by the similar solution blending procedure as applied for the preparation of pristine ionically crosslinked membranes **(Scheme 6.1)** but in addition to polymers, dibutyl-phthalate (DBP) was added as porogen into the polymer mixture solution. After formation of the membrane by solvent casting and evaporation method, membrane was dipped into methanol for one hour to leach out the porogen completely.[49] Then, the membranes were taken out from methanol and dried. After that, porous membranes were ionically crosslinked by treating with 1 M KBr for 24 h and followed by 1 M KOH for 24 h. The porosity was introduced with one representative blend membrane namely S50P50 sample. However, the amount of porogen (DBP) in the membrane was altered with respect to total polymers weight %. Three different porous ionically crosslinked membranes were prepared by following the procedure as given in **Scheme 6.2** and these samples are named as S50P50-P10, S50P50-P25 and S50P50-P40 where P10, P25 and P40 indicates the 10, 25 and 40 wt% of porogen, respectively with respect to the total polymer weight.

Induced expected experimental porosity (P) was calculated for porous membranes by following literature reported procedure[49] by subtracting the membrane weight obtained after porogen removal from the initial weight before porogen removal by following eq. 1 and represented in **Table A4.1**. in Appendix 4.

$$P = \frac{W_{\text{polymer+DBP}} - W_{\text{polymer}}}{W_{\text{polymer+DBP}}} \qquad (1)$$

Where, $W_{\text{Polymer+DBP}}$ is the weight of dried membrane before DBP removal and W_{Polymer} is the weight of dried membrane after DBP removal.

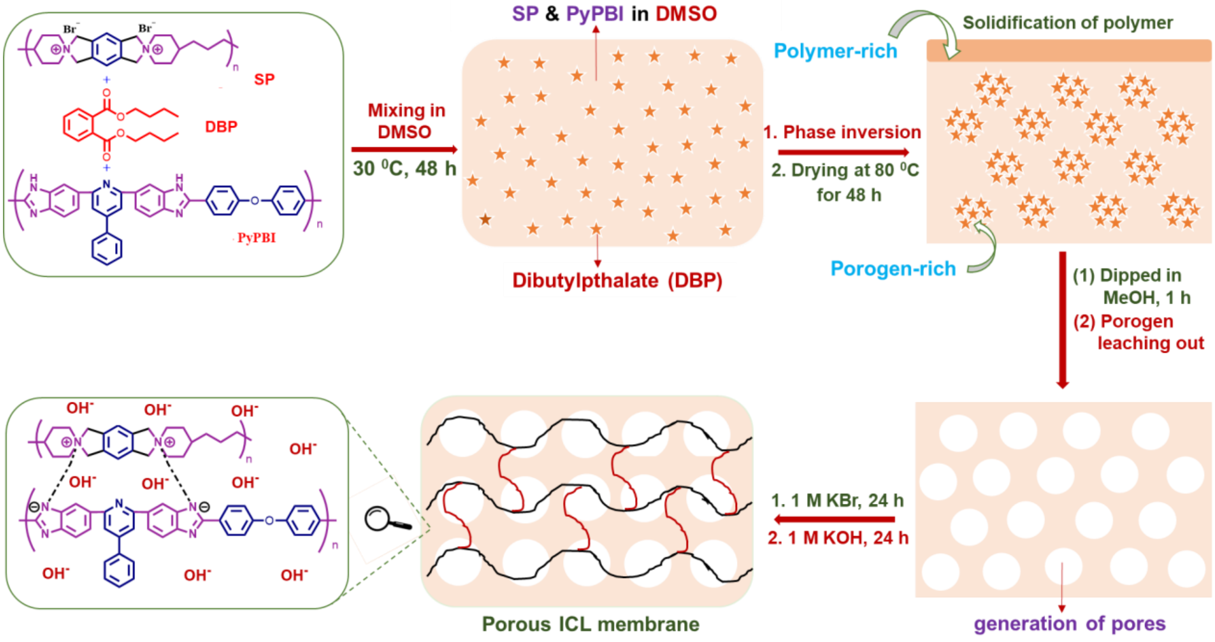

Scheme 6.2. Fabrication of ionically crosslinked (ICL) porous AAEM by the formation of ammonium-imidazolate complex (shown using dotted line) after leaching out the porogen through MeOH treatment.

Results and discussion

Spectral evidences for various interactions

Infrared spectra of all the Br^- form and ionically crosslinked (ICL) OH^- form membranes along with their parent polymers (PyPBI & SP) are shown in **Figure A4.4,** Appendix 4. PyPBI spectra shows three characteristic broad peaks at 3413, 3175, and 3063 cm^{-1} attributed to non-hydrogen bonded free N−H groups, self-associated hydrogen-bonded N−H groups and stretching modes of aromatic C−H groups, respectively.[48,54] In case of SP, a sharp and intense band at 2840-2950 cm^{-1} is ascribed to the vibrational frequency of aliphatic C-H stretching,[31,54,55] and also a peak at 3393 cm^{-1} is due to absorbed moisture.[56] The stretching intensity of C-H bond of SP increases with increasing SP content in the samples as can be seen in both Br^- and OH^- form samples (see the highlighted portions). The two important peaks at 1592 cm^{-1} and 1440-1470 cm^{-1} which are ascribed to the C=C/C=N in plane benzimidazole ring deformation[48,57,58] of PyPBI are present in all the samples proving the presence of PyPBI. In all the Br^- form membranes a broad band around 3400 cm^{-1} observed due to non-hydrogen bonded free N-H stretching frequency, however, intensity of this band becomes weak and almost negligible in OH^- form membranes indicating the formation of the ionically crosslinked ammonium-imidazolate complex where significant amount of –NH- vanishes after crosslinking. A closer look of this peak (see the highlighted portion in **Figure A4.4,** Appendix

4) shows that the –NH- peak intensity of S70P30-OH is weaker than S50P50-OH and this peak appears with increased intensity in case of S30P70-OH which is may be due to unreacted –NH- owing to the unavailability of sufficient SP content in the sample.

Similarly, the FT-IR spectra of all the ICL porous membranes are also analyzed. S50P50-P25 and S50P50-P40 membranes are given as representative samples in the Appendix 4, **Figure A4.4** and **A4.5.** The peaks at around 1125 cm^{-1} and 1716 cm^{-1} owing to the stretching vibration of O-C-O and C=O bonds,[49] respectively of DBP are visible before porogen (DBP) removal both in case of S50P50-P25-Br and S50P50-P40-Br samples. The two peaks around 2958 cm^{-1} and 2871 cm^{-1} are attributed to the stretching vibrations of CH_3, CH_2, and CH groups in the dibutyl chains of DBP.[49] After DBP removal by methanol treatment, all those peaks corresponds to DBP completely disappears and the porous Br^- form and ICL (OH^- form) membranes spectra look identical with the non-porous Br^- form and ICL membranes (compare with **Figure A4.3** spectra where no porogen was added). Hence, ionic crosslinking results in the porous network in the membrane as well as structural integrity of the membrane does not affect due to porogen treatment. In addition, disappearance of peak intensity at 3396 cm^{-1} (as indicated in **Figure A4.3–A4.5,** Appendix 4) clearly indicates that ammonium-imidazolate complex (as shown in **Scheme 6.1 and 6.2** using dotted line) is formed both in ICL and porous ICL AAEMs when treated with 1 M KOH which also make the membranes insoluble in DMSO further suggesting crosslinking.

Thermogravimetric analysis

TGA plots of S70P30, S50P50 and S30P70 membranes (both in Br^- and OH^- form) along with their parent polymers (PyPBI & SP) are shown in **Figure 6.1.** PyPBI polymer backbone is highly stable and main polymer backbone degradation observed only above 550 °C.[54] SP shows 5% degradation ($T_{d,\,95}$) at 336 °C[37] and then stiff decrease in the thermal stability is observed due to quaternary ammonium substituent degradation along with degradation of alkyl chains in the spirocyclic polymer backbone. All the membrane show stability in between PyPBI and SP, and found to be largely dependent on the composition of the sample. All the OH^- form membranes are displaying higher stability than that of Br^- membranes. This may be due to: (1) thermal stability depends on the counter ion nucleophilic strength and due to the lower nucleophilic strength, membranes with hydroxide counter ion shows higher thermal stability[59], (2) thermal stability also depends on polymer backbone structure and composition. As after OH^- loading, membranes are forming ionically crosslinked network structure, thus imposing of this crosslinking also helping to improve the thermal stability than that of un-crosslinked Br$^-$ form membranes. The thermal stability trend of OH$^-$ form membrane follows S30P70-OH > S50P50-OH> S70P30-OH order. As PyPBI content predominates over SP in S30P70-OH membrane, thus it is the most stable membrane where ionically crosslinked network started degradation only after 400 °C which is close to PyPBI main chain degradation temperature. S50P50 OH membrane shows moderate thermal stability due to increase in SP content into the membrane matrix, and the ionically crosslinked network started degradation at around 380 °C, which decreases further following the same trend for S70P30-OH at around 360 °C, which is close to the initial degradation temperature of spirocyclic polymer backbone.

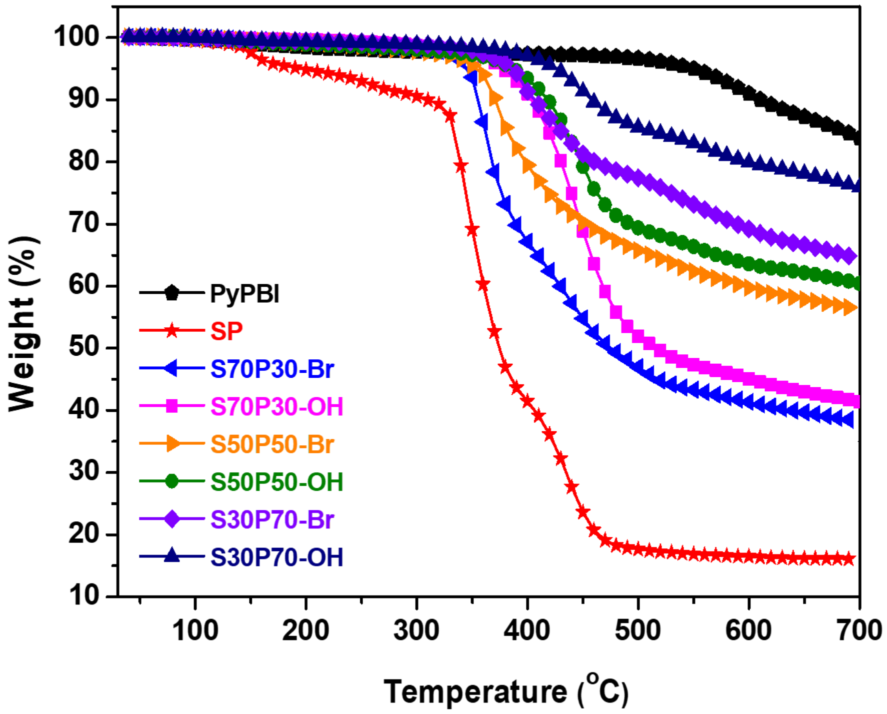

Figure 6.1. Thermogravimetric analysis plots of all the non-porous Br$^-$ form membranes and ICL OH$^-$ form membranes along with their parent polymers (PyPBI and SP).

Similarly, in the Appendix 4**, Figure A4.6,** TGA data of S50P50-P25 and S50P50-P40 membranes (both in Br$^-$ and OH$^-$ form) are presented. It is noticed that, before leaching out the porogen from the porous membranes, the initial weight loss observed is in between 250 °C - 330 °C which can be attributed to weight loss obtained due to presence of DBP. After leaching out the DBP by methanol treatment, again TGA analysis of the porous Br$^-$ and OH$^-$ form membranes were performed and represented along with pristine (S50P50- Br and OH) membranes. Both S50P50-P25-Br and S50P50-P40-Br membranes have less thermal stability with respect to S50P50-Br, but as expected the thermal stability of S50P50-P25-OH and

S50P50-P40-OH membranes have increased significantly with respect to their Br^- form membranes, and S50P50-P40-OH exhibits the highest thermal decomposition temperature. The reason may be attributed to the induced crosslinking into the porous network generates structural ordering into the polymer matrix which decreases the free volume fraction of the polymer and hence responsible for the significantly increased thermal stability. Thus, the higher thermal stability of ICL & porous ICL membranes provides evidence for their suitability as AAEMs.

Morphology and porosity of the porous membrane

It is important to note that the boiling point of the porogen DBP is 340 °C which is far higher than that of DMAc (166 °C). As a result, when the solvent evaporates from the solution at 80 °C during casting of the membrane then the porogen remains in the solution and its concentration increases, thus inducing phase inversion of the polymer solution into a polymer-rich (porogen-poor) and a porogen-rich (polymer-poor) phase (see **Scheme 6.2**). Further evaporation of the solvent lead to solidification of the polymer membranes.[50] FESEM cross-sectional morphology of the porous membranes of different compositions (compositions are given in **Table A4.1,** Appendix 4) are represented in **Figure 6.2.** In a comparison with pristine S50P50-Br membrane, pores are clearly seen into the membrane matrix after DBP removal with MeOH treatment.

FE-SEM image (**Figure 6.2**) of S50P50-Br clearly shows no pores into the cross-sectional region but pore size is in the range of 1.3-1.8, 3.0-4.3 and 5.0-6.5 µm in case of S50P50-P10-Br, S50P50-P25-Br and S50P50-P40-Br membranes, respectively. Therefore, it is clear that increasing the DBP concentration increases pore size significantly. In addition, BET results supports the formation of pores in the membrane after porogen removal. **Figure 6.2(E)** compares the BET isotherms of the porous membranes. The average pore size obtained from the BET isotherm for these membranes are $2.34 \times 10^{+3}$, $4.12 \times 10^{+3}$ and $5.58 \times 10^{+3}$ Å for S50P50-P10-Br, S50P50-P25-Br and S50P50-P40-Br membranes, respectively. Similarly, the surface area of these membrane increases with increasing porogen content as 8.993, 25.574 and 35.112 m^2/g. Therefore, results obtained from BET analysis conclude that with increasing porogen (DBP) content in the membrane matrix both the surface area and average pore size are increasing and hence porosity increasing. Also, it is to be noted that the data obtained from BET analysis followed the similar trend with the data obtained from FESEM cross-sectional analysis.

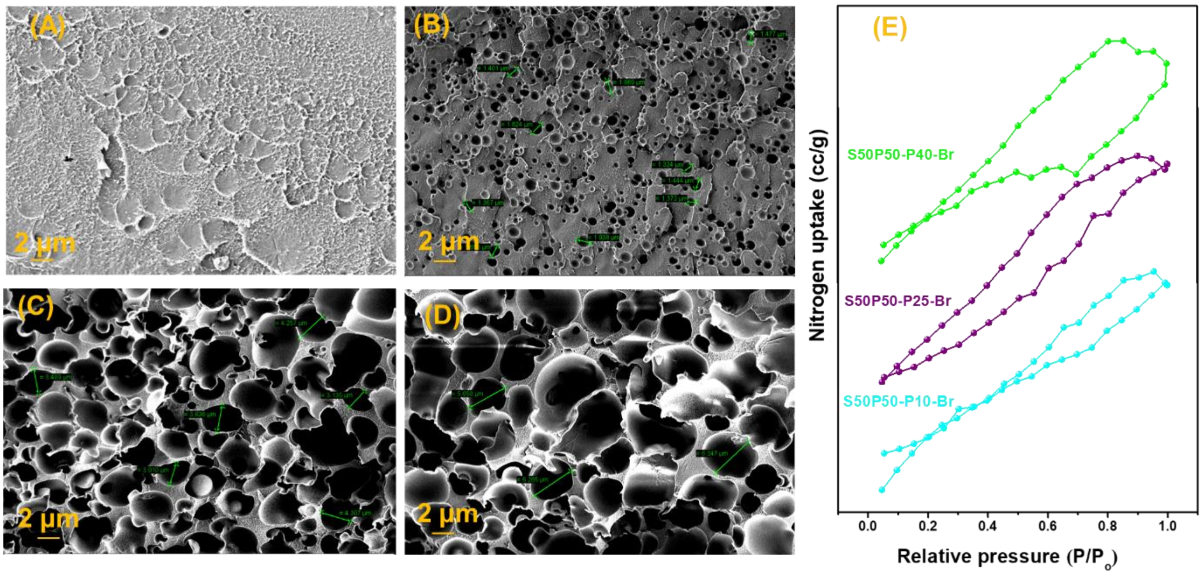

Figure 6.2. Cross-sectional morphology of S50P50-Br (A) and the porous samples S50P50-P10-Br (B), S50P50-P25-Br (C), S50P50-P40-Br (D). BET isotherms of porous membranes (E).

Water uptake, KOH uptake and Ion exchange capacity (IEC)

Water uptake, KOH uptake and IEC values of all the ICL and porous ICL hydroxide form membranes are measured and shown in **Table 6.1**. Highest values of water uptake, KOH uptake & IEC are observed in case of S70P30-OH sample as this membrane consists 70 wt% ratio of hydrophilic spiro ionene polymer (SP) which is responsible for increasing all these properties in the ICL membrane. As expected, lowest values of water uptake, KOH uptake and IEC are obtained for S30P70-OH membrane due to more hydrophobicity produced by 70 wt% of PyPBI polymer in the membrane. In a similar trend, moderate values of water uptake, KOH uptake and IEC are achieved for S50P50-OH membrane as the wt% ratio of SP and PyPBI polymer in this case is equal. However, introduction of porosity in the S50P50 membrane increases water uptake, KOH uptake and IEC values significantly[49] as the pores present in the crosslinked AAEMs are able to accommodate more water and electrolytes (KOH) inside their pores. Also, these values increase with increasing porogen content owing to the increased porosity. A significant amount of swelling both in length-wise (L_{SWR}) and cross-section-wise (C_{SWR}) are also observed in S70P30-OH and S50P50-P40-OH membranes under hydrated condition. Similarly, both L_{SWR} and C_{SWR} are showing increasing trend with increasing porogen content in the membranes. For all the membranes water uptake increases with increase in temperature, which is in agreement with the literature reports.[44]

Table 6.1. Water uptake, KOH uptake, IEC, swelling ratio of all the hydroxide form membranes.

Sample Identity	Lengthwise swelling ratio L_{SWR} (%)	Crosswise swelling ratio C_{SWR} (%)	KOH uptake (wt %)	Titrated IEC [a] (meq/g)	Water uptake [b] (wt %) at 35°C	Water uptake [b] (wt %) at 80°C
S70P30-OH	10.59	12.5 (±1.4)	37.49 (±2.72)	2.39	43.06 (±3.04)	70.08 (±4.16)
S50P50-OH	5.64	12.5 (±1.4)	22.22 (±1.47)	1.82	21.20 (±2.72)	51.12 (±3.23)
S30P70-OH	3.04	11.1 (±1.4)	15.92 (±2.03)	1.48	13.26 (±1.36)	31.19 (±2.44)
S50P50-P10-OH	6.02	12.5 (±1.4)	28.32 (±1.78)	2.16	27.85 (±2.54)	58.54 (±2.49)
S50P50-P25-OH	7.79	18.18 (±1.81)	36.66 (±3.37)	2.37	41.40 (±2.90)	75.57 (±3.21)
S50P50-P40-OH	12.83	22.22 (±2.22)	51.50 (±1.61)	2.65	49.33 (±3.14)	88.54 (±2.95)

[a] measured using titration method, [b] standard deviation of various data are given in the parenthesis after the data.

Hydroxide ion conductivity of the membranes

IEC, water uptake and KOH uptake values can significantly influence the hydroxide ion conductivity (σ_{OH^-}) which plays crucial role in the development of AAEM.[10,60] Infact more the water uptake, KOH uptake and IEC of the membrane, more will be the ionic conductivity. The σ_{OH^-} of all the ionically crosslinked AAEMs were measured after dipping the membranes in 1 M KOH alkaline solutions for 24 hours followed by keeping the membranes under fully hydrated condition in deionized water for 24h at ambient temperature before measurement. The ionic conductivity of all the ionically crosslinked hydroxide form membranes is studied as a function of temperature and plotted in **Figure 6.3(A).** The σ_{OH^-} of the membranes are increasing with the temperature as expected due to the increasing free volume for ion transport and the enhancement of the mobility of anions.[10] All the membranes show excellent of ionic conductivity and S70P30-OH membrane is the best among all, which is following a similar trend observed for water uptake, KOH uptake and IEC values for the membranes. Among the three ICL membranes, the σ_{OH^-} of S70P30-OH at 25 °C is 50.7 mS/cm which is more than two-fold increase than that of S30P70-OH (22 mS/cm). This increase in σ_{OH^-} is a direct consequence of KOH and IEC values of these two membranes which are 37.49% and 2.39 meq/g for S70P30-OH and 15.92% and 1.48 meq/g for S30P70-OH (**Table 6.1**). Highest ionic conductivity of 129 mS/cm is obtained in case of S70P30-OH at 90 °C, which is again almost two-fold increase than that of S30P70 OH membrane's σ_{OH^-} (70 mS/cm) at 90 °C. To the best of our knowledge, this value of σ_{OH^-} (129 mS/cm) at 90 °C is one of the highest value reported so far in the literature. S50P50-OH (KOH uptake 22.22% and IEC 1.82 meq/g) membrane also exhibits very good σ_{OH^-} of 39 mS/cm and 108 mS/cm at 25 °C and 90 °C, respectively, little bit less but very much close with the value of S70P30-OH membrane.

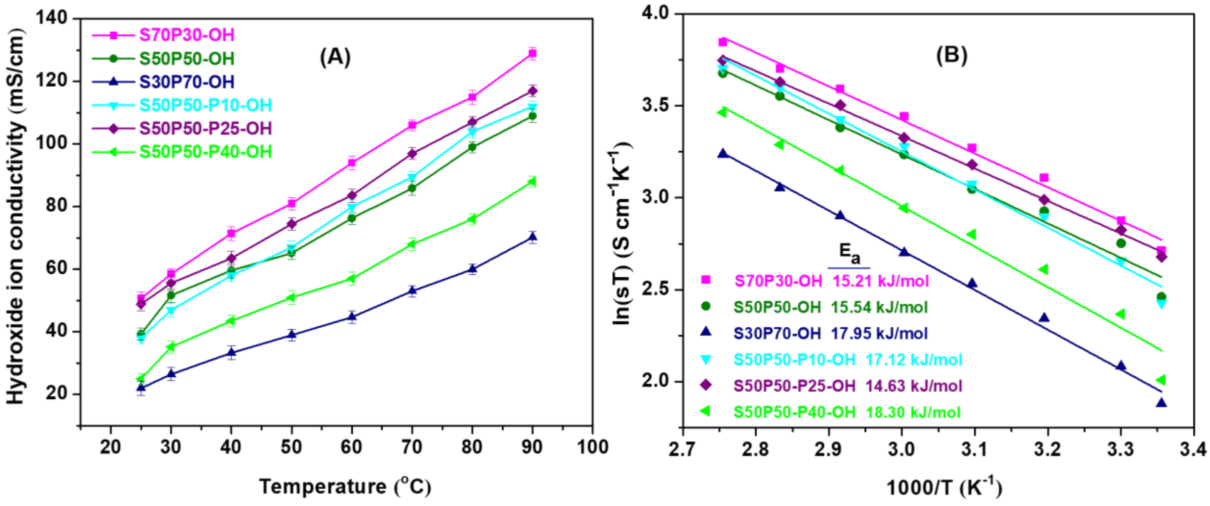

Figure 6.3. Hydroxide ionic conductivity (σ_{OH^-}) of ICL and membranes along with ICL porous membranes. **(A)** σ_{OH^-} vs temperature plot and **(B)** temperature dependent Arrhenius plot of σ_{OH^-}

Addition of porogen into the membrane followed by leaching out of the porogen generates voids (see **Figure 6.2**) in the crosslinked membrane matrix, which is able to uphold more water and more KOH resulting more IEC[49] (see **Table 6.1**). The σ_{OH^-} of S50P50-P10-OH is found to be 38 mS/cm at 25 °C & 112 mS/cm at 90 °C which is more than the σ_{OH^-} value obtained from pristine S50P50-OH membrane. S50P50-P25-OH membrane shows further increase in ionic conductivity 48 mS/cm at 25 °C & 117 mS/cm at 90 °C. However, further increase in porogen content in S50P50-P40-OH membrane surprisingly shows decrease in hydroxide ionic conductivity (25 mS/cm at 25 °C & 88 mS/cm at 90 °C). Two reasons can be attributed for this observation: First, due to introduction of high degree of porosity (40 wt%), membrane swells excessively under hydrated condition (**Table 6.1**) and results in decrement of ionic conductivity and secondly, when the membrane is highly water swollen condition, the dilution of charge carries leads to decrease of the ion conductivity.[37,61] Overall, all the membranes are yielding excellent hydroxide ionic conductivities even at 90 °C indicates highly conducting ionically crosslinked AAEMs are also thermally very much stable and thus, these robust membranes found to be highly promising as AAEMs.

The conductivities of ionically crosslinked hydroxide (OH^-) form membranes exhibit an Arrhenius type temperature dependence as evident from the linear fit of Arrhenius plot shown in **Figure 6.3(B).** The activation energy obtained from the slope of the linear fit also listed in the **Figure 6.3(B).** The activation energy of all the AAEMs are obtained in the range of 14.63-18.30 kJ/mol (0.151 - 0.189 eV/atom) which is in well accordance with the already literature reported data.[10,62,63] Therefore, we can conclude that the hydroxide ion conduction throughout the AAEMs are carried out by the Grotthuss mechanism.

σ_{OH^-} of S50P50-OH & S50P50-P25-OH membranes were also measured after dipping them in 2 M KOH solution for 24 h, which resulted σ_{OH^-} values of 113 mS/cm and 124 mS/cm at 90 °C for S50P50-OH and S50P50-P25-OH membranes, respectively. These values are slightly higher than the values obtained in 1 M KOH treated samples (**Figure 6.3A**) and this phenomenon of rising OH^- conductivity with increasing electrolyte (KOH) concentration is well reported in literature.[10,64-66] The σ_{OH^-} vs temperature plot for these two samples are shown in Appendix 4, **Figure A4.8.**

Chemical Stability

Chemical stability of AAEMs in the alkaline condition is an important parameter to be examined as the working fuel cell operates in the basic environment.[67] The chemical stability of ionically crosslinked AAEMs was studied by soaking them into 1 M aqueous KOH solutions at 30 °C and at 80 °C and the stability was monitored as a function of time for ~960 hours (which is ~ 40 days). We did not perform alkaline stability test beyond 960 hours as the membranes were profoundly stable. It is to be noted that the chemical stability was monitored as function of time by checking the membrane flexibility, brittleness and by observing the colour change of the alkaline solution. Ionically crosslinked membranes are completely insoluble in any solvent because of the formation of ammonium-imidazolate complex as proved earlier. In a similar way, the porous membranes after leaching out the porogen by methanol treatment followed by the crosslinking also results similar insolubility observation. Thus, NMR analysis of these crosslinked membranes could not be performed as it was done in earlier reports.[10] Therefore, we confirmed the membranes chemical stability by analysing FT-IR spectra. All the AAEMs did not show any visible change after treating with 1 M KOH for 960h at 80 °C with regard to the colour change, flexibility etc. as can be seen very clearly from the image of the membrane (**Figure A4.9,** Appendix 4). FT-IR spectra of all the AAEMs were recorded during the alkali stability study at various time interval [**Figure A4.10 (A-F**), Appendix 4]. All the spectra are identical indicating that there is no change in the structure which means no degradation happened during the 1 M KOH treatment for 960h at 80 °C. Neither any peaks obtained in IR spectra, nor the colour of the membrane affected during alkaline treatment. Membranes are flexible enough to handle with tweezers even after long term stability test. Again, we measured σ_{OH^-} after 500h treatment with 1 M KOH at 80 °C and represented in **Figure 6.4(A)**. A comparison of σ_{OH^-} value at 90 °C of all the AAEMs before and after alkaline stability test (1 M KOH, 500h at 80 °C) are also shown in **Table 6.2** and **Figure A4.11,** Appendix 4. These data clearly show that a negligible decrease (~ 10%, see **Table 6.2**) in conductivity and also negligible decrease (~ 7-8 %, see **Table 6.2**) in IEC after 500h alkaline treatment at 80 °C of the AAEMs are observed, indicating very high stability of the membranes in KOH for longer duration. We also carried out TGA analysis of the 500h alkali treated membranes and compared with the freshly alkali treated samples **[Figure 6.4(B)]**. Interestingly, both sets of membranes are showing identical thermal stability proving the zero degradation of the membrane. This remarkably high alkaline stability of the crosslinked AAEMs is very significant considering the fact that both PBI and PyPBI samples known to degrade quickly in 1 M KOH solution as mentioned in earlier literature by several research groups.[10,68] Additionally, S50P50-OH and S50P50-P25-OH membranes were also treated with 2 M KOH for 500h at 60 °C, and they show exceptional alkaline stability even at 2 M KOH (no detectable change in the colour of membranes). Therefore, hydroxide ionic conductivity measurement was performed for these two membranes after treating with 2 M KOH for 500h at 60 °C, and compared with the freshly alkali treated membranes conductivity at 2 M KOH **(**see **Figure A4.12** and **Table A4.2,** Appendix 4**).** Once again, a very small loss in σ_{OH^-} values are observed after long hour of treatment in 2 M KOH at 60 °C attributing superior stability of our membrane. Gravimetric analysis was also performed before and after alkaline stability test for S50P50-OH and S50P50-P25-OH membranes at both 1 M and 2 M aqueous KOH solution **[Figure A4.13(A) & (B),** Appendix 4**].** Very minor (less than 5%) weight changes of the two above mentioned AAEMs are noted after alkaline stability test for 500h both in 1 M KOH and 2 M KOH reinforces our all-other data with regards to excellent alkaline durability of the membranes.

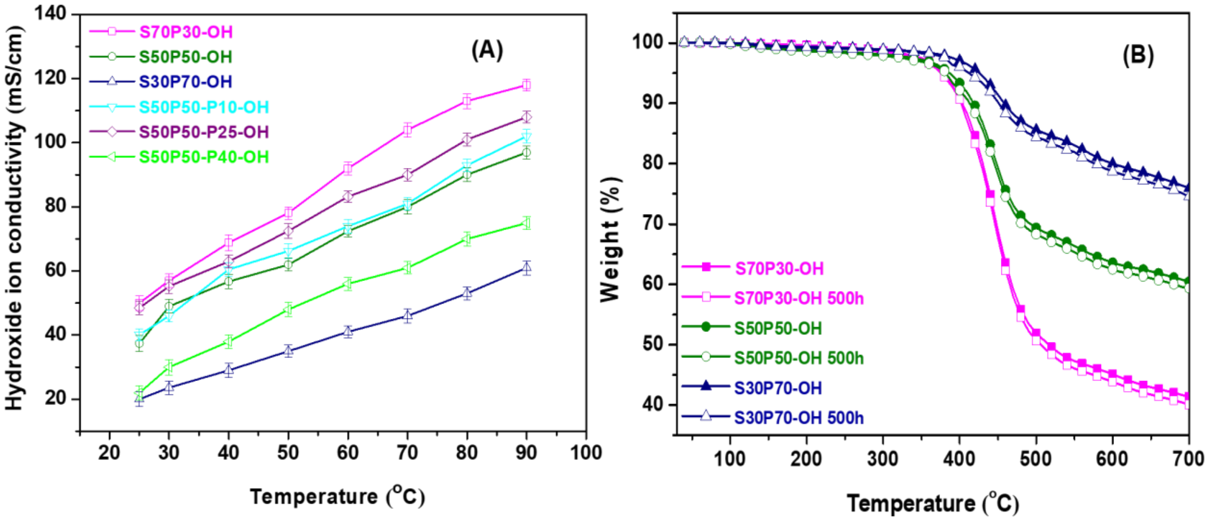

Figure 6.4. (A) Hydroxide ionic conductivity and **(B)** thermal stability of the ionically crosslinked AEMs after 500 h alkaline treatment with 1 M KOH at 80 °C. TGA data are compared with freshly alkali treated membranes. The comparison of σ_{OH^-} at 90 °C between freshly prepared sample and samples after 1 M KOH treatment for 500 h at 80 °C is shown in **Figure A4.12.**

Table 6.2. Comparison of σ_{OH^-} and IEC values of membranes before and after 1 M KOH treatment for 500 h at 80 °C.

Sample identity	OH$^-$ conductivity (mS/cm) at 90 °C [a]	OH$^-$ conductivity (mS/cm) at 90 °C after 500h treatment in 1 M KOH	Decrease in σ_{OH^-} after 500 h (%)	Titrated IEC (meq/g)	Titrated IEC (meq/g) after 500h treatment in 1 M KOH	Decrease in IEC after 500 h (%)
S70P30-OH	129	118	8.52	2.39	2.25	5.85
S50P50-OH	108	97	10.18	1.82	1.69	7.15
S30P70-OH	70	61	12.85	1.48	1.37	7.43
S50P50-P10-OH	112	102	8.92	2.16	2.01	6.94
S50P50-P25-OH	117	108	7.70	2.37	2.21	6.75
S50P50-P40-OH	88	75	14.77	2.65	2.43	8.30

[a] Values obtain from Figure 3(A).

Thermal transition and mechanical properties of the membranes

Temperature dependent dynamic mechanical analysis of all the ICL membranes were measured using the dynamic mechanical analyser (DMA) and the various parameter [storage modulus (E'), loss modulus (E'') and Tan δ] against temperature plots are shown in **Figure 6.5(A)** and **Figure A4.14,** Appendix 4. Among the three ICL AAEMs, S50P50-OH exhibits highest storage modulus and S30P70-OH exhibits lowest storage modulus. The reason might be that some portion of the non-hydrogen bonded 'N-H' of PyPBI polymer backbone still remains unreacted due to the lack of spiro-ionene quaternary ammonium functionality in the blend composition in case of S30P70-OH membrane, resulting less storage modulus owing to the less cross-linking. S70P30-OH exhibits moderate storage modulus and S50P50 OH showing the highest due to the formation maximum crosslinking of 1:1 blend composition. Storage modulus data (**Table A4.3**) clearly suggests that mechanical strength of the membranes becomes poorer at higher temperatures for example, E' of all the samples decrease drastically beyond 400 °C (see **Table A4.3**). This is due to the degradation of spiro ionene polymer (SP) present in the membrane. Interestingly, S30P70-OH membrane E' at 400 °C is more than other two samples as it contains 70 wt % of PyPBI in the composition which is quite stable up to 550 °C. However porous ICL membranes DMA data shows the decrement in E' values with respect to pristine S50P50-OH and the decrement increases with increasing porogen content from 10 wt% to 40 wt%. This may be due to the increased porosity causing more swelling in water and KOH of these membranes (see **Table 6.1**) and therefore increases membranes flexibility but decreases the storage modulus.

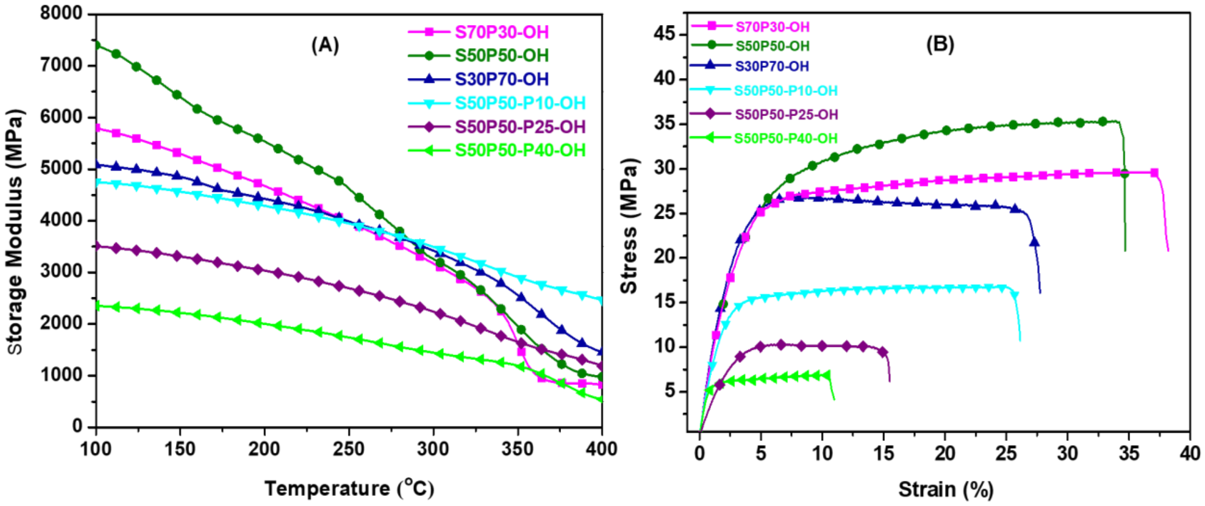

Figure 6.5. Storage modulus (E') vs temperature plot **(A)** and stress-strain plot **(B)** of ionically crosslinked hydroxide form membranes.

Loss modulus (E'') and tan δ plots of all the above AEMs are shown in **Figure A4.14** and the T_g values obtained from these are tabulated in **Table A4.3** of Appendix 4. The glass transition temperatures (T_g) values of the pyridine-bridged polybenzimidazoles are reported to be in between 350 °C to 450 °C depending on the polymer structure and molecular weight.[48] For the ICL AAEMs, both porous and non-porous samples the T_g varies between 340 °C to 385 °C (see **Table A4.3,** Appendix 4). T_g increases a bit with increase in PyPBI polymer content in the membrane sample and it increases further by introducing porosity into the membrane with respect to samples of the alike composition (compare with S50P50-OH sample). Introducing crosslinking into the porous membrane ensembles structural ordering into the porous network, and this kind of porous morphology of the membranes decreases the free volume fraction of the polymer and hence requirement of a higher temperature to cause the free volume segmental mobility of the polymer chains,[69] resulting higher (T_g) value with increasing porosity.

Figure 6.5(B) shows the stress-strain profiles of all the water doped ICL membranes and various data like tensile strength and elongation at break (%) obtained from these plots are listed in **Table 6.3**. Among the three non-porous AAEMs, S50P50-OH yields much higher tensile stress which is in the agreement with higher storage modulus from DMA as compared to other membranes. This is due to the maximum crosslinking because of 1:1 composition of SP and PyPBI which enables maximum formation of ammonium-imidazolate complex. Tensile stress is less for S30P70-OH alike with the trend obtained from DMA storage modulus value (at 100 °C) as some of the N-H groups of PyPBI remain free and cannot take part in crosslinking. Elongation at break value is higher for S70P30-OH membrane due to its higher water uptake and KOH uptake among the three AAEMs because more hydrophilicity introduced in the membrane which makes the membrane flexible with respect to other membranes. As water and KOH uptake of S30P70-OH is less among the three membranes thus it exhibits less elongation at break value.

Stress-strain profiles of the porous ICL membranes are also quite promising [**Figure 6.5(B)**] though the tensile properties (**Table 6.3**) show a bit decrease compared to non-porous composition samples because water uptake and KOH uptake increases significantly after porosity formation (see **Table 6.1**) which is responsible for decrement in tensile stress of the porous AAEMs. Due to the increased porosity S50P50-P40-OH membrane swells excessively in presence of aqueous KOH and water which results decrement in membranes mechanical properties significantly, also resulted lower storage modulus value as obtained from DMA analysis **(Figure 6.5A)** and **Table A4.3,** Appendix 4. Overall, the mechanical study data (both DMA and stress-strain) clearly suggest that these membranes are suitable to be used as promising materials for AAEM.

Table 6.3. Tensile strength & Elongation at break data of all the AEMs obtained from stress-strain profiles.

Sample identity	Tensile Strength (MPa)	Elongation at break (%)
S70P30-OH	29.70 (±0.5)	37.14 (±3)
S50P50-OH	35.23 (±0.5)	34.06 (±2)
S30P70-OH	25 (±0.5)	26.6 (±2)
S50P50-P10-OH	16.77 (±0.5)	25.5 (±1.5)
S50P50-P25-OH	9.5 (±0.5)	14.96 (±1.5)
S50P50-P40-OH	6.90 (±0.5)	10.35 (±2)

Membranes performance on alkaline water electrolysis

A membrane electrode assembly (MEA) was fabricated (pictorially shown in **Figure 6.6B**) using the few representative membranes, which are developed in this work, to demonstrate the suitability of electrolyzer applications. The MEAs were obtained by sandwiching the membrane between the anode and cathode electrodes. On both the electrodes, platinised carbon was used as the catalyst and Nafion solution as a binder. The catalyst ink was prepared by mixing 40 wt % of platinised and 7 wt % Nafion solution suspended in isopropyl alcohol. An equal amount of membrane ionomer solution was added for improving the binding between the electrodes and the membrane and sonicated for 30 minutes. The slurry was brush-coated manually on the microporous layer of a gas diffusion layer (GDL) of thickness 0.37 µm and area 4 cm^2. Finally, it was dried at 60 ºC for 30 minutes to achieve a catalyst loading of 0.5 mg cm^{-2} on the electrodes. MEAs were evaluated with parallel serpentine flow field machined on graphite plates in electrolyzer mode at 60 ºC. 1 M KOH electrolyte solution was circulated at a flow rate of 24 mL/min on both the electrodes. The polarisation behaviour of the electrolyzer was obtained using Biologic VMP 300 as shown in **Figure 6.6(A & B).** It is clear from **Figure 6.6(A)**, the best performance is shown by S70P30-OH membrane and achieve a current density of 100 mA cm^{-2} at 2.6 V, which is in well accordance with the trend obtained from the OH$^-$ conductivity of the membranes. Also, significant improvement in electrolysis performance could be observed from S50P50-OH membrane to S50P50-P25-OH membrane which is again in agreement with their trends of OH$^-$ conductivity values. The porous membrane (S50P50-P25-OH) exhibits a current density of 100 mA cm^{-2} at 3.9 V whereas the non-porous (S50P50-OH) shows only ~ current density 50 mA cm^{-2} at 7 V. Similarly, the other porous membrane S50P50-P10-OH shows better performance than S50P50-OH but lower than S50P50-P25-OH. These results clearly attribute the effect of membrane structure and hydroxide conductivity on the performance of membrane as AAEM in water electrolyzer.

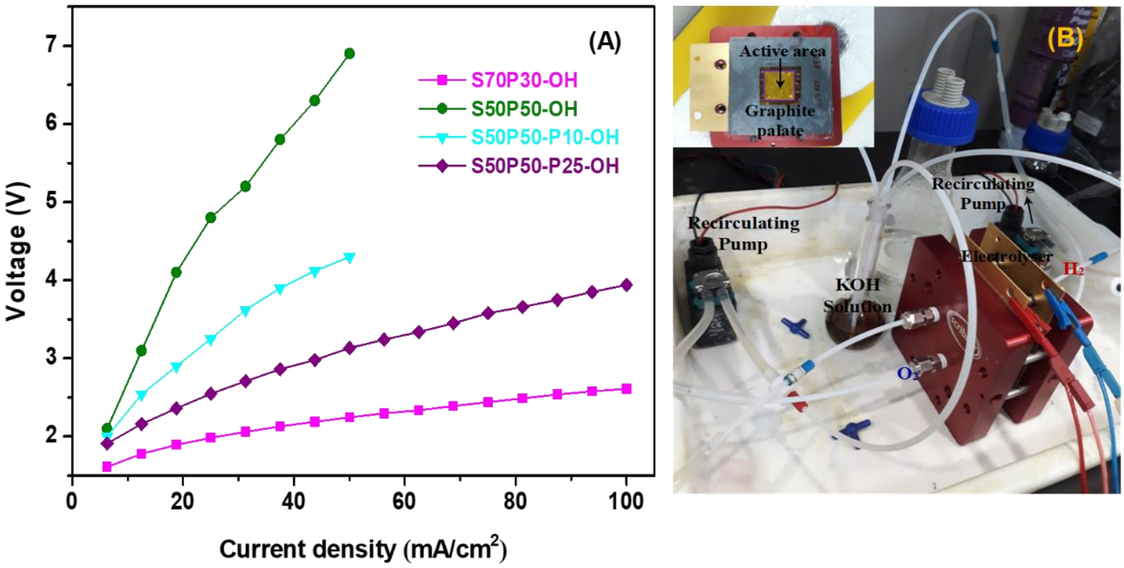

Figure 6.6. (A) The current-voltage characteristic behaviour of MEA, made from different AAEM, in alkaline water electrolyzer. **(B)** Experimental setup for membrane testing in electrolyzer mode.

A comparison of the current results with literature report

We have made an effort to put up a comparative perspective of the current work with the already reported data (see **Figure 6.7** and supporting information **Table A4.4,** Appendix 4). The comparison results clearly indicate that our membrane has promising IEC and hydroxide conductivity at room temperature and 80 °C. Our hydroxide conductivity values are one of the best among the reported data. There are only few reports in which >100 mS/cm hydroxide conductivity have been reported so far. The present work membranes come under this category with very high IEC values and alkaline stability along with good dimensional stability as discussed throughout the manuscript. It is to be also noted that, our current membranes have displayed very high alkaline stability in 1 M KOH at 80 °C for prolong treatment period (960 h), and even in 2 M KOH for 500 h, and show significantly high thermal, mechanical/tensile stability.

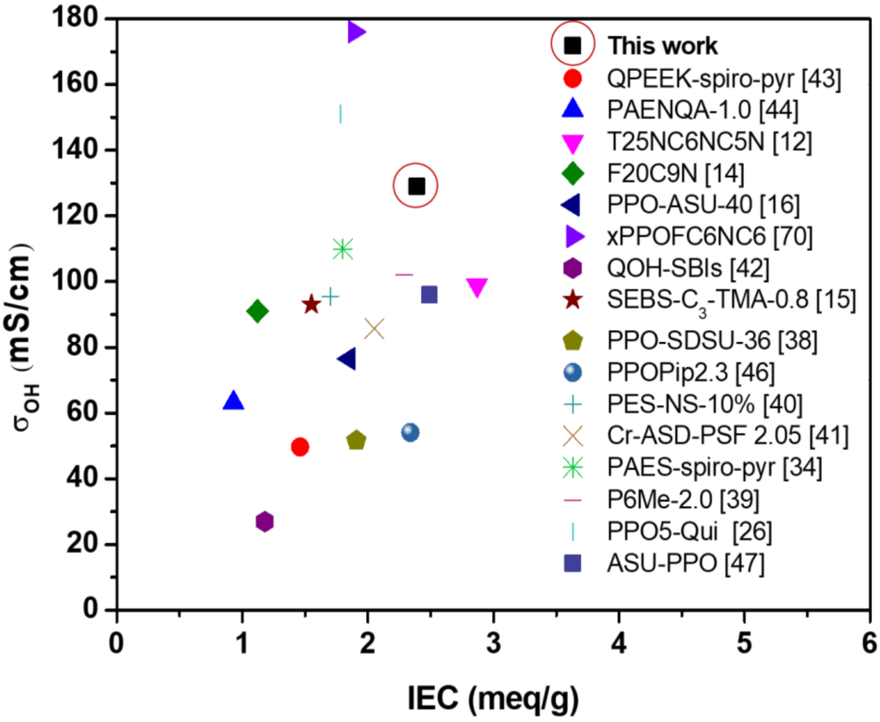

Figure 6.7. Currently obtained OH$^-$ conductivity and IEC value of S70P30-OH membrane in a comparison with literature reported quaternary ammonium (QA) and N-Spirocyclic quaternary ammonium (NSQA) based membranes.

Conclusion

Ionically crosslinked alkaline anion exchange membranes (AAEMs) with improved properties have been developed from the blends of different wt% of PyPBI and spirocyclic polymer (SP), and further porosity has been introduced in the membrane to enhance the properties of AAEM. The formation of ammonium-imidazolate complex among the constituent polymers as confirmed by the FT-IR analysis is found to be the driving force of the ionic crosslinking in the membrane. The current results also confirmed that the introduction of porosity did not affect the structural integrity of the ionically crosslinked membrane. The highest hydroxide ionic conductivity of 129 mS/cm at 90 °C and highest IEC (2.39 meq/g) have been achieved for the membrane with 70% SP and 30% PyPBI as this membrane has highest KOH uptake among all the other membranes composition. Introduction of porosity in the crosslinked membrane is found to improve the hydroxide conductivity along with IEC value. All the membranes showed very good thermal stability though the degradation temperature displays the dependence on the blend composition and porogen content of the membrane. The alkaline stability test at harsh alkaline condition proved the long-term chemical stability of the membranes. Even after 960 h of alkaline treatment in 1 M KOH at 80 °C, all the membrane maintained their structural integrity and showed negligible (less than 10%) decrease in hydroxide conductivity. Further, alkaline stability test in 2 M KOH solution at 60 °C for few representative samples showed the retention of ~80% of their OH^- conductivity value after 500 h of alkaline treatment. Thermo-mechanical analysis and stress-strain studies confirmed very high mechanical stability of all the membranes, though among the membrane when composition is 1:1, the stability found to be the best because of the highest degree of crosslinking. Also, our membranes found to be suitable for alkaline water electrolysis, the best performance is obtained from S70P30-OH membrane which showed a current density of 100 mA cm^{-2} at 2.6 V. Overall, the current work clearly showed that the membranes developed in this work have very high hydroxide conductivity, excellent alkaline stability even at harsh condition and higher temperature, and finally very robust mechanical stability. Therefore, we believe this new strategy of membrane development would be useful in the production of AAEMs for alkaline electrochemical applications.

References

(1) Gottesfeld, S.; Dekel, D. R.; Page, M.; Bae, C.; Yan, Y.; Zelenay, P.; Kim, Y. S. *J. Power Sources* **2018**, *375*, 170–184.

(2) Dekel, D. R. *J. Power Sources* **2018**, *375*, 158–169.

(3) You, W.; Noonan, K. J. T.; Coates, G. W. *Prog. Polym. Sci.* **2020**, *100*, 101177.

(4) He, G.; Li, Z.; Zhao, J.; Wang, S.; Wu, H.; Guiver, M. D.; Jiang, Z. *Adv. Mater.* **2015**, *27*, 5280–5295.

(5) Varcoe, J. R.; Atanassov, P.; Dekel, D. R.; Herring, A. M.; Hickner, M. A.; Kohl, P. A.; Kucernak, A. R.; Mustain, W. E.; Nijmeijer, K.; Scott, K.; Xu, T.; Zhuang, L. *Energy Environ. Sci.* **2014**, *7*, 3135–3191.

(6) Lee, Y.; Kim, S.; Maljusch, A.; Conradi, O.; Kim, H. J.; Jang, J. H.; Han, J.; Kim, J.; Henkensmeier, D. *Polymer* **2019**, *174*, 210-217.

(7) Maurya, S.; Shin, S. H.; Kim, Y.; Moon, S. H. *RSC Adv.* **2015**, *5*, 37206–37230.

(8) Park, H. J.; Lee, S. Y.; Lee, T. K.; Kim, H. J.; Lee, Y. M. *J. Membr. Sci.* **2020**, *611*, 118355.

(9) Cho, M. K.; Park, H.Y.; Lee, H. J.; Kim, H. J.; Lim, A.; Henkensmeier, D.; Yoo, S. J.; Kim, J. Y.; Lee, S. Y.; Park, H. S.; Jang, J. H. *J. Power Sources* **2018**, *382*, 22-29.

(10) Sana, B.; Das, A.; Jana, T. *Polymer.* **2019**, *172*, 213–220.

(11) Li, X.; Yu, Y.; Liu, Q.; Meng, Y. *Int. J. Hydrogen Energy* **2013**, *38*, 11067–11073.

(12) Zhu, L.; Pan, J.; Wang, Y.; Han, J.; Zhuang, L.; Hickner, M. A. *Macromolecules* **2016**, *49*, 815–824.

(13) Choi, J.; Byun, Y. J.; Lee, S. Y.; Jang, J. H.; Henkensmeier, D.; Yoo, S. J.; Hong, S. A.; Kim, H. J.; Sung, Y. E.; Park, J. S. *Int. J. Hydrogen Energy* **2014**, *39*, 21223–21230.

(14) Zhu, L.; Peng, X.; Shang, S. L.; Kwasny, M. T.; Zimudzi, T. J.; Yu, X.; Saikia, N.; Pan, J.; Liu, Z. K.; Tew, G. N.; Mustain, W. E.; Yandrasits, M.; Hickner, M. A. *Adv. Funct. Mater.* **2019**, *29*, 1902059.

(15) Jeon, J. Y.; Park, S.; Han, J.; Maurya, S.; Mohanty, A. D.; Tian, D.; Saikia, N.; Hickner, M. A.; Ryu, C. Y.; Tuckerman, M. E.; Paddison, S. J.; Kim, Y. S.; Bae, C. *Macromolecules* **2019**, *52*, 2139–2147.

(16) Chu, X.; Liu, L.; Huang, Y.; Guiver, M. D.; Li, N. *J. Membr. Sci.* **2019**, *578*, 239–250.

(17) Hugar, K. M.; Kostalik, H. A.; Coates, G. W. *J. Am. Chem. Soc.* **2015**, *137*, 8730–8737.

(18) You, W.; Hugar, K. M.; Coates, G. W. *Macromolecules* **2018**, *51*, 3212-3218.

(19) Aili, D.; Yang, J.; Jankova, K.; Henkensmeier, D.; Li, Q. *J. Mater. Chem. A* **2020**, *8*, 12854–12886.

(20) Noonan, K. J. T.; Hugar, K. M.; Kostalik, H. A.; Lobkovsky, E. B.; Abruña, H. D.; Coates, G. W. *J. Am. Chem. Soc.* **2012**, *134*, 18161–18164.

(21) Jang, H.; Hossain, M. A.; Sutradhar, S. C.; Ahmed, F.; Choi, K.; Ryu, T.; Kim, K.; Kim, W. *Int. J. Hydrogen Energy* **2017**, *42*, 12759–12767.

(22) Xue, B.; Wang, Q.; Zheng, J.; Li, S.; Zhang, S. *J. Membr. Sci.* **2020**, *601*, 117923.

(23) Chu, X.; Shi, Y.; Liu, L.; Huang, Y.; Li, N. *J. Mater. Chem. A* **2019**, *7*, 7717–7727.

(24) Olsson, J. S.; Pham, T. H.; Jannasch, P. *Adv. Funct. Mater.* **2018**, *28*, 1702758.

(25) Dong, X.; Lv, D.; Zheng, J.; Xue, B.; Bi, W.; Li, S.; Zhang, S. *J. Membr. Sci.* **2017**, *535*, 301–311.

(26) Dang, H. S.; Jannasch, P. A. *J. Mater. Chem. A* **2017**, *5*, 21965–21978.

(27) Sana, B.; Das, A.; Sharma, M.; Jana T. *ACS Appl. Energy Mater.* **2021**, *4*, 9792-9805.

(28) Zhu, Y.; He, Y.; Ge, X.; Liang, X.; Shehzad, M. A.; Hu, M.; Liu, Y.; Wu, L.; Xu, T. A *J. Mater. Chem. A* **2018**, *6*, 527–534.

(29) Vega, J. A.; Chartier, C.; Mustain, W. E. *J. Power Sources* **2010**, *195*, 7176–7180.

(30) Chempath, S.; Einsla, B. R.; Pratt, L. R.; Macomber, C. S.; Boncella, J. M.; Rau, J. A.; Pivovar, B. S. *J. Phys. Chem. C* **2008**, *112*, 3179–3182.

(31) Chen, D.; Hickner, M. A. *ACS Appl. Mater. Interfaces* **2012**, *4*, 5775–5781.

(32) Kreuer, K. D.; Jannasch, P. A *J. Power Sources* **2018**, *375*, 361–366.

(33) Thomas, O. D.; Soo, K. J. W. Y.; Peckham, T. J.; Kulkarni, M. P.; Holdcroft, S. *J. Am. Chem. Soc.* **2012**, *134*, 10753–10756.

(34) Pham, T. H.; Jannasch, P. *ACS Macro Lett.* **2015,** *4*, 1370–1375.

(35) Lee, W. H.; Kim, Y. S.; Bae, C. *ACS Macro Lett.* **2015**, *4*, 814–818.

(36) Mao, C.; Kudla, R. A.; Zuo, F.; Zhao, X.; Mueller, L. J.; Bu, X.; Feng, P. *J. Am. Chem. Soc.* **2014**, *136*, 7579–7582.

(37) Pham, T. H.; Olsson, J. S.; Jannasch, P. *J. Am. Chem. Soc.* **2017,** *139*, 2888–2891.

(38) Xue, J.; Liu, X.; Zhang, J.; Yin, Y.; Guiver, M. D. *J. Membr. Sci.* **2020**, *595*, 117507.

(39) Pham, T. H.; Olsson, J. S.; Jannasch, P. *J. Mater. Chem. A* **2018**, *6*, 16537–16547.

(40) Liu, F. H.; Yang, Q.; Gao, X. L.; Wu, H. Y.; Zhang, Q. G.; Zhu, A. M.; Liu, Q. L. *J. Membr. Sci*. **2020**, *595*, 117560.

(41) Zhang, Y.; Chen, W.; Yan, X.; Zhang, F.; Wang, X.; Wu, X.; Pang, B.; Wang, J.; He, G. *J. Membr. Sci.* **2020**, *598*, 117650.

(42) Choi, J.; Kim, M. H.; Han, J. Y.; Chae, J. E.; Lee, W. H.; Lee, Y. M.; Lee, S. Y.; Jang, J. H.; Kim, J. Y.; Henkensmeier, D.; Yoo, S. J.; Sung, Y. E.; Kim, H. J. *J. Membr. Sci.* **2018**, *568*, 67–75.

(43) Shang, L.; Yao, D.; Pang, B.; Zhao, C. *Int. J. Hydrogen Energy* **2021**, *46*, 19116–19128.

(44) Lin, C.; Yu, D.; Wang, J.; Zhang, Y.; Xie, D.; Cheng, F.; Zhang, S. *Int. J. Hydrogen Energy* **2019**, *44*, 26565–26576.

(45) Marino, M. G.; Kreuer, K. D. *ChemSusChem* **2015**, *8*, 513–523.

(46) Olsson, J. S.; Pham, T. H.; Jannasch, P. *Macromolecules* **2017**, *50*, 2784–2793.

(47) Chen, N.; Long, C.; Li, Y.; Lu, C.; Zhu, H. *ACS Appl. Mater. Interfaces* **2018**, *10*, 15720–15732.

(48) Maity, S.; Jana, T. *Macromolecules* **2013**, *46*, 6814–6823.

(49) Zarrin, H.; Jiang, G.; Lam, G. Y. Y.; Fowler, M.; Chen, Z. *Int. J. Hydrogen Energy* **2014**, *39*, 18405–18415.

(50) Peng, S.; Yan, X.; Wu, X.; Zhang, D.; Luo, Y.; Su, L.; He, G. *RSC Adv.* **2017**, *7*, 1852–1862.

(51) Mecerreyes, D.; Grande, H.; Miguel, O.; Ochoteco, E.; Marcilla, R.; Cantero, I. *Chem. Mater.* **2004**, *16*, 604–607.

(52) Liang, N.; Fang, J.; Guo, X. A *J. Mater. Chem. A* **2017**, *5*, 15087–15095.

(53) Shen, C. H.; Jheng, L. C.; Hsu, S. L. C.; Tse-Wei Wang, J. *J. Mater. Chem.* **2011**, *21*, 15660–15665.

(54) Mukhopadhyay, S.; Das, A.; Jana, T.; Das, S. K. *ACS Appl. Energy Mater.* **2020**, *3*, 7964–7977.

(55) Ghosh, S.; Sannigrahi, A.; Maity, S.; Jana, T. *J. Phys. Chem. C* **2011**, *115*, 11474–11483.

(56) Rewar, A. S.; Bhavsar, R. S.; Sreekumar, K.; Kharul, U. K. *J. Membr. Sci.* **2015**, *481*, 19–27.

(57) Rewar, A. S.; Shaligram, S. V.; Kharul, U. K. *J. Membr. Sci.* **2016**, *497*, 282–288.

(58) Sannigrahi, A.; Ghosh, S.; Lalnuntluanga, J.; Jana. T. *J. Appl. Polym. Sci.* **2009**, *111*, 2194–2203.

(59) Lee, H. J.; Choi, J.; Han, J. Y.; Kim, H. J.; Sung, Y. E.; Kim, H.; Henkensmeier, D.; Ae Cho, E.; Jang, J. H.; Yoo, S. J. *Polym. Bull.* **2013**, *70*, 2619–2631.

(60) Zhegur-Khais, A.; Kubannek, F.; Krewer, U.; Dekel, D. R. *J. Membr. Sci.* **2020**, *612*, 118461.

(61) Marino, M. G.; Melchior, J. P.; Wohlfarth, A.; Kreuer, K. D. *J. Membr. Sci.* **2014**, *464*, 61–71.

(62) Tanaka, M.; Fukasawa, K.; Nishino, E.; Yamaguchi, S.; Yamada, K.; Tanaka, H.; Bae, B.; Miyatake, K.; Watanabe, M. *J. Am. Chem. Soc.* **2011**, *133*, 10646–10654.

(63) Yan, J.; Hickner, M. A. *Macromolecules* **2010**, *43*, 2349–2356.

(64) Zeng, L.; Zhao, T. S.; An, L.; Zhao, G.; Yan, X. H. *J. Membr. Sci.* **2015**, *493*, 340-348.

(65) Lue, S. J.; Wang, W. T.; Mahesh, K. P. O, Yang, C. C. *J. Power Sources*, **2010,** *195*, 7991-7999.

(66) Cai, X.; Zhang, Y.; Li, C.; Zhang, G.; Wang, X.; Zhang, X.; Wang, Q.; Wang, F. *Membranes* **2021**, *11*, 224.

(67) Chen, Y.; Tao, Y.; Wang, J.; Yang, S.; Cheng, S.; Wei, H.; Ding, Y. *J. Polym. Sci. Part A Polym. Chem.* **2017**, *55*, 1313–1321.

(68) Henkensmeier, D.; Cho, H. R.; Kim, H. J.; Nunes Kirchner, C.; Leppin, J.; Dyck, A.; Jang, J. H.; Cho, E.; Nam, S. W.; Lim, T. H. *Polym. Degrad. Stab.* **2012**, *97*, 264–272.

(69) Maity, S.; Singha, S.; Jana, T. *Polymer.* **2015**, *66*, 76–85.

(70) Zhu, L.; Pan, J.; Christensen, C. M.; Lin, B.; Hickner, M. A. *Macromolecules* **2016**, *49*, 3300–3309.

Multicationic Anion Exchange Membranes from Pyridine-bridged Polybenzimidazole and Polymer Ionic Liquid Grafted Graphene Oxide

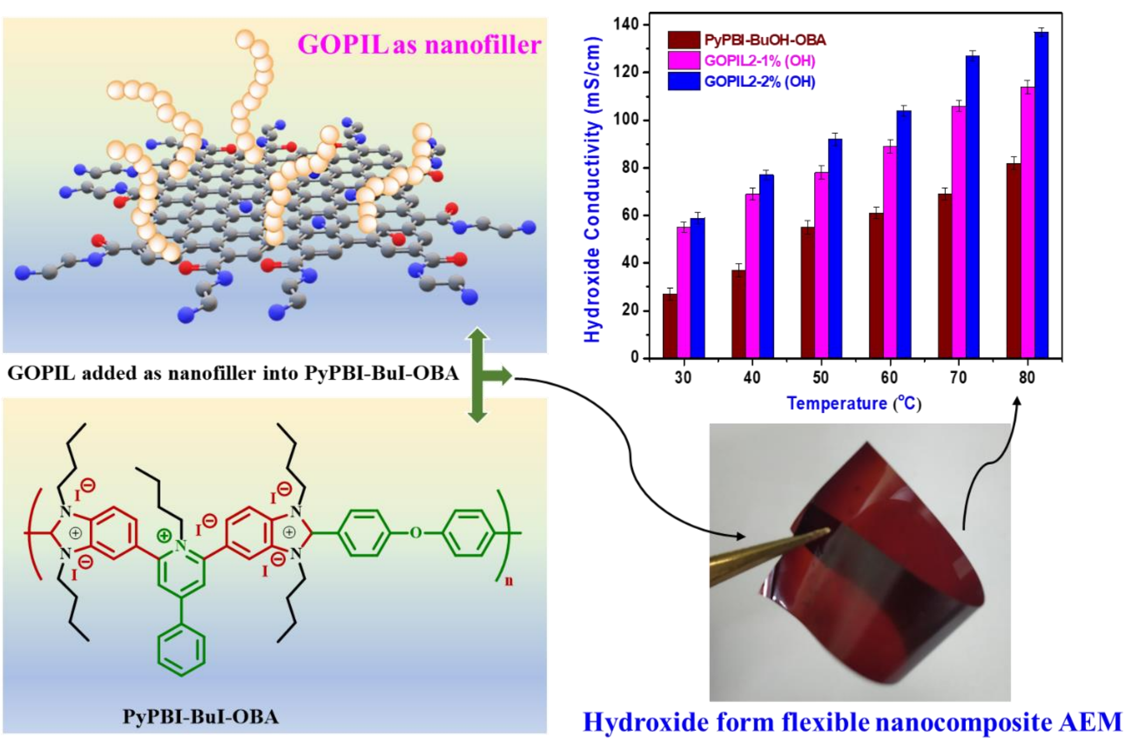

Anupam Das, Nilanjan Mukherjee, Ritu Saraswat and Tushar Jana*. Multicationic Anion Exchange Membranes from Pyridine-bridged Polybenzimidazole and Polymer Ionic Liquid Grafted Graphene Oxide *(To be Communicated). (Chapter 7)*

Abstract

In this study, we have functionalized the surface of graphene oxide (GO) nanosheets by grafting polymeric ionic liquid (PIL) chains of verities of structures and then utilized PIL-g-GO materials as nanofiller with poly(butylated pyridinium benzimidazolium)iodide (PyPBI-BuI-OBA) in order to prepare hydroxide ion conducting mixed matrix alkaline anion exchange membranes with multiple ion exchange sites. Three different ionic liquid based monomers namely [2-(methacryloyloxy)ethyl]trimethylammonium chloride (MATMA), 3-butyl-1-vinylimidazolium iodide [VImBu][I] and 1-butyl-2-methyl-1-(4-vinylbenzyl)imidazolium iodide [VBImBu][I] were polymerized on the activated GO surface via surface initiated reversible addition fragmentation chain transfer process to obtain three different types of PIL grafted GO namely pMATMA-*g*-GO (GOPIL1), pVImBu-*g*-GO (GOPIL2) and PVBImBu-g-GO (GOPIL3). Exfoliation of GO sheets upon grafting of PIL was observed and were verified from the electron microscopic studies. The grafted PIL chains found to have narrow polydispersity (Đ) and precise control over the molecular weight confirming the grafting through SI-RAFT polymerization. Amount of polymer grafted on the GO surface were obtained from TGA analysis and strong dependence on polymer structure were found. The mixed matrix membranes (MMMs) were prepared by solution blending of PyPBI-BuI-OBA with varying loading of GOPIL materials and then MMMs were immersed in KOH in order to develop alkaline anion exchange membranes (AAEMs) containing of imidazolium, pyridinium quaternary ammonium ion exchange sites. Among all AAEMs with 2 wt% GOPIL2 and GPIL3 exhibited superior hydroxide ion conductivity of 137 mS/cm and 127 mS/cm, respectively at 80 °C. These mixed matrix AAEMs displayed no noticeable change under alkaline stability treatment for prolong time at elevated temperature in 1 M and 5 M KOH. The structural, chemical, thermal, mechanical and conducing properties of the membranes remained unaltered after alkaline treatment at elevated temperature. These AAEMs exhibited ~90% and ~80% retention of IEC and ~90% and ~70% retention in OH^- conductivity after alkaline treatment in 1 M KOH, at 60 °C for 500 h and in 5 M KOH, at 60°C for 375 h, respectively. To the best of our knowledge, this will be the first report on utilization of surface PIL grafted GO nanosheets in a AAEM.

Introduction

Electrochemical devices consist of alkaline anion exchange membrane (AAEM) as electrolyte separates electrodes is considered as the most promising device for the use as fuel cell and electrolyzer in order to generate clean electricity from H_2 and produce green H_2, respectively and has drawn significant popularity among the scientists in the past two decades.[1,2] In comparison to conventional proton exchange membranes based electrochemical devices, AAEM based devices has many advantages including enhanced oxygen reduction kinetics, utilization of non-noble metal like Co, Ni catalysts which helps in cost reduction along with better cell performance.[3,4] Several research groups have focused on the development of large variety of AAEM in past couple of years. The main challenge associated with the development of AAEM is to prepare AAEM with high hydroxide conductivity and long term durability under strong alkaline environment.[5] In addition to these, an efficient AAEM must possess good thermal stability, high mechanical robustness, chemical stability and high ion exchange capacity (IEC).[6] The alkaline stability of the AAEM is primarily influenced by the types of cationic groups which are tethered into the polymer for the reaction of anion exchange sites along the polymer backbone structure, and hence development of AAEM with a delicate balance of cationic group and polymer structure remains a major challenge.

Polymer backbone structures such as poly(aryl ether),[7] poly(arylene ether sulfone),[8] polysulfone,[9] poly(ether ether ketone),[10] polyethylene,[11] poly(phenylene oxide),[12] poly(styrene-co-vinylbenzyl chloride),[13] poly(vinylbenzyl chloride),[14] polybenzimidazole,[15,16] fluorinated polymers[17] are utilized so far in literature for the development of AAEM. These polymeric structures can be easily tethered with various types of cationic functionalities such as pyridinum,[18] piperidinium,[19] pyrrolidinium,[20] azepanium,[21] morpholinium,[21] quinuclidinium[21] quaternary ammonium (QA),[22–24] phosphonium,[25] tertiary sulfonium,[26] imidazolium,[27-30] guanidinium,[31] in their backbone to develop AAEM. In order to increase the hydroxide conductivity of the AAEM, the ion exchange capacity (IEC) of the membranes can be improved through multiple structural modifications by the introduction of more labile ion conducting groups into the polymer backbones. However, such processes can lead to the excessive swelling of the membrane resulting poor dimensional stability and hence deteriorates the overall durability of the membranes despite of increment in OH^- conduction.[32] To mitigate these problems researches have come up with various pathways over the years such as: cross-linking of polymer chains to develop robust AAEM,[33] steric protection in the polymeric backbone to restrict attack by alkali, various structural modifications of the polymer structures via grafting different types chains,[34] and development of inorganic-organic composite membranes.[5,35]

The addition of inorganic nano materials into the polymer membrane has significant advantages in terms of enhancement of ionic conductivity and chemical stability of the ion exchange membranes. Over the past decades, we have demonstrated that the use of verities of inorganic fillers with polybenzimidazole (PBI) can significantly improve the PBI based PEM properties.[36-38] In our previous work we found the polymer-grafted-graphene oxide (polymer-g-GO) is very effective nanofiller in improving the PBI based PEM properties significantly (see Chapter 5). We noticed that grafting of polymer chain on the GO surface significantly enhances the dispersibility of the GO in the common organic solvent and also facilities the formation of composite with PBI provided the grafted polymer chain has strong interaction with PBI (see details in Chapter 5). Therefore, in order to grow polymer chains on the GO surface *grafting from* reversible addition fragmentation chain-transfer (RAFT) polymerization technique has been found to be the most effective in our previous work.

As mentioned earlier in the discussion, the increase of number of ion exchange sites by tethering multiple cationic site in the polymer backbone can significantly improve the AAEM efficiency but it is also a fact that tethering many ion exchange site can also enhance the possibility of membrane degradation. Therefore, if one can bring the ion exchange site via making composites where nanofiller contributes to enhancing the ion exchange site both stability and IEC can increase without any compromise. Considering this fact, we plan to polymerize three different sets of ionic liquid monomers namely [2-(methacryloyloxy)ethyl]trimethylammonium chloride (MATMA), 3-butyl-1-vinylimidazolium iodide [VImBu][I] and 1-butyl-2-methyl-1-(4-vinylbenzyl)imidazolium iodide [VBImBu][I] via SI-RAFT polymerization on GO using *"grafting from"* approach to obtain three different types of PIL *grafted* GO namely pMATMA-*g*-GO, pVImBu-*g*-GO and pVBImBu-*g*-GO and characterized through various techniques. We have chosen the monomers in such a way through which we can incorporate hydrophilic quaternary ammonium (QA) and imidazolium (Im) cationic functionalities tethered with the surface functionalized PIL-*g-GO* nanosheets in order to improve the hydrophilicity and dispersion nature of the materials in various polar solvents, also the *grafting* of cationic sights comprised of PIL chains in the PIL-*g-GO* surface can contribute significantly towards the generation of more ion exchange sites for OH^- conduction into the mixed matrix AAEMs.

Further, we impregnate these three sets of PIL-*g*-GO materials as nanofillers into the poly(alkylated pyridinium benzimidazolium) iodide [PyPBI-BuI-OBA] membrane matrix then multicationic mixed matrix alkaline anion exchange membrane (MMAAEM) have formed with improved ionic conductivities. Utilization of surface PIL *grafted* GO nanosheets as efficient nanofiller with any polymer membrane supported matrix have never been explored before in literature. To the best of our knowledge this will be the first report on utilization of PIL-*g*-GO materials to develop efficient mixed matrix hydroxide conducting AAEMs for potential applications in multiple electrochemical devices.

Experimental Section

Synthesis of graphene oxide (GO), amine modified GO (GO-EDA), [3-benzylsulfanylthiocarbonylsufanyl-propionic acid] or BSPA RAFT agent, activation of BSPA RAFT agent and its covalent attachment to GO surface in order to synthesize GO-BSPA were performed and are discussed in details in the Chapter 5**.** Synthesis of 3-butyl-1-vinylimidazolium iodide [VImBu][I] and 1-butyl-2-methyl-1-(4-vinylbenzyl)imidazolium iodide [VBImBu][I] was performed following literature reported procedure and characterization data are given in the Appendix 5 **(Figure A5.1, A5.2).** Synthesis of PyPBI polymer was adapted from literature and given in the Chapter 2**.**

Synthesis of pMATMA-*g*-GO, pVImBu-*g*-GO and pVBImBu-*g*-GO via RAFT polymerization

In a typical SI-RAFT polymerization of GO in order to graft polymer chains on the functionalized GO surface, 150 mg (17.4 µmol) of GO-BSPA was dispersed in 4 mL of water: ethanol (3:1 w/v) mixture in a 25 mL Schlenk tube. 4.5 mg (17.4 µmol, 1eq) of BSPA and 1.5 mg of AIBN (8.7 µmol, 0.5eq) were also added in the reaction medium. After that, calculated amount of [2-(methacryloyloxy)ethyl]trimethylammonium chloride (MATMA) or 3-butyl-1-vinylimidazolium iodide [VImBu][I] or 1-butyl-2-methyl-1-(4-vinylbenzyl)imidazolium iodide [VBImBu][I] monomer (calculated amount to grow polymer of targeted chain lengths on the GO surface) were then added into the reaction mixture to grow three different polymers of targeted chain length on the GO surface. The Schlenk tube was then sealed with a rubber septum and subjected to sonication for 5 minutes, and stirred for 10 min for homogeneous dispersion of all the reactants present in the mixture. After that the Schlenk tube was subjected to undergo 3 freeze-thaw cycles to ensure complete removal of O_2, dissolved air and absorbed moisture from the reagent and solvent mixture. Furthermore, the tube was back filled with N_2 to maintain inert atmosphere and kept under stirring at 75 °C for 18 h. Upon the completion of 18 h, the reaction was quenched using liquid N_2 and was exposed to air for termination of the growing polymer chains. Liquid N_2 helps to freeze the propagating radicals present in the

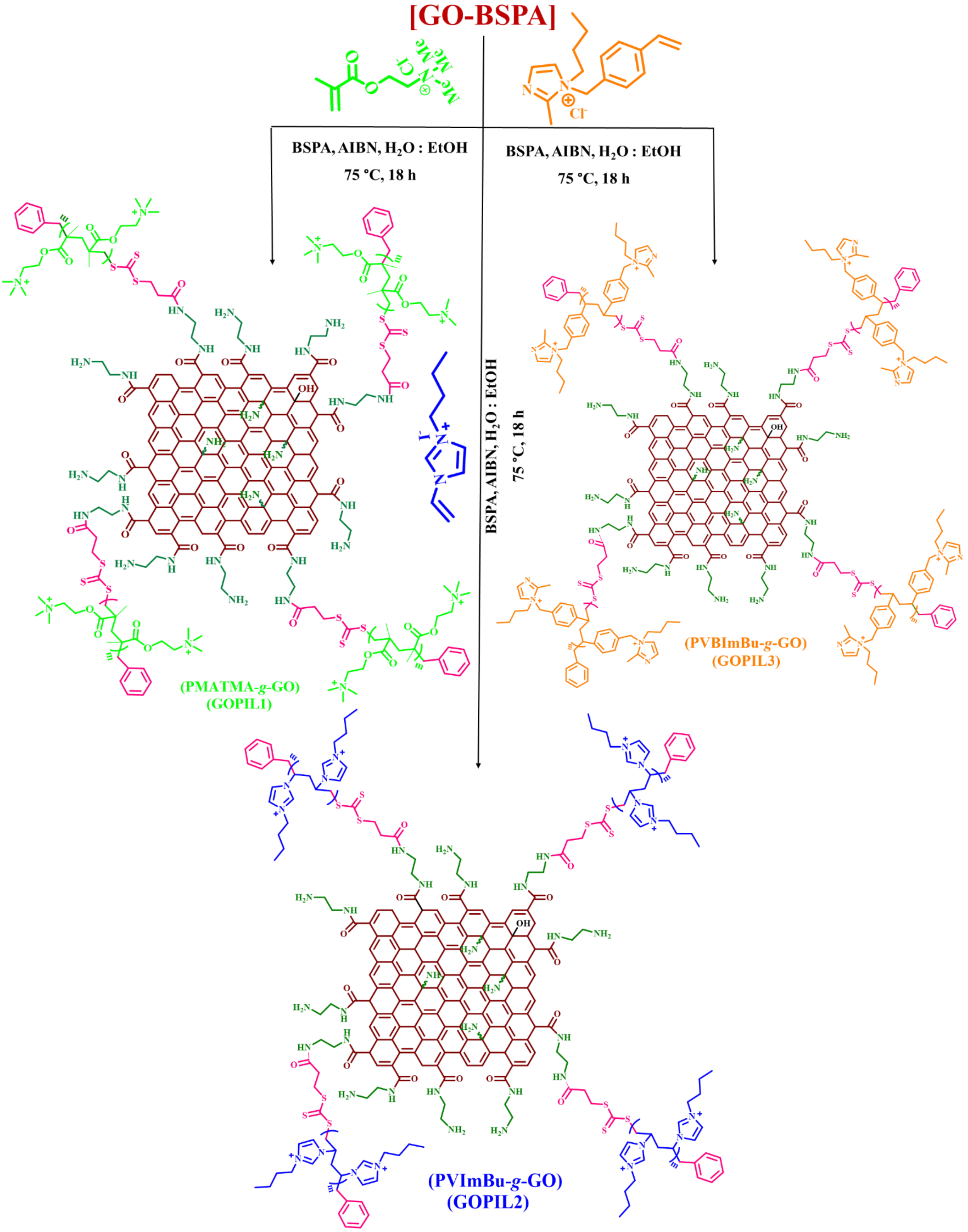

Scheme 7.1. Schematic representation for the polymerization of various monomers on the GO surface using grafting from approach of SI-RAFT polymerization process.

reaction mixture and exposure them to air which terminates the reactive radicals responsible for propagation of the polymer chain growth. Finally, the obtained polymers were precipitated in acetone and the precipitate was filtered and washed with ethanol-water mixture followed by re-precipitated in acetone. The surface grafted polymers were then kept at vacuum oven at 50 ⁰C overnight for drying. The GO surface modified polymers are abbreviated as pMATMA-*g*-GO (GOPIL1), pVImBu-*g*-GO (GOPIL2) and pVBImBu-*g*-GO (GOPIL3) and schematically represented in the **Scheme 7.1**. The obtained molecular weights and polydispersity index of the GO surface modified polymer chains are given in the **Table 7.1.**

Synthesis of poly(butylated pyridinium benzimidazolium) iodide [PyPBI-BuI-OBA]

Following a procedure reported in our previous work,[15] 1.0 g (1.80 mmol) of PyPBI-OBA polymer we have dissolved into 60 mL of dry DMSO at 80 °C temperature and the dissolved solution was then transferred in a 100 mL round bottom flask fitted with a reflux condenser. Inert atmosphere was maintained throughout the reaction process under N_2 purging. After dissolving, the polymer solution was kept for cooling until it comes to ambient temperature. After that, a required amount of sodium hydride (0.0867 g, 3.61 mmol) was added into the solvent reaction mixture, and temperature was raised to 80 °C. Under such condition, we kept the reaction mixture under stirring for 12 h, followed by cooling into the room temperature. Into this solution mixture, a required amount of butyl iodide (BuI=1.663 g, 9.05 mmol) was then added and the stirring was further continued for 4 h at 80 °C. The molar ratio of the polymer, alkyl iodide and sodium hydride was maintained as 1:5:2. After 4h we again added same amount of butyl iodide, and the reaction mixture was kept under stirring at 80°C for prolong 16 h. After completion of the reaction, the entire reaction mixture was dropwise poured into the water which generated a reddish brown coloured precipitation. The precipitate was then filtered off and repeatedly washed Millipore water several times for total removal of excess NaH or butyl iodide present in the precipitated product. Finally, the PyPBI-BuI-OBA polymer (**Scheme 7.2**) was kept for drying under vacuum oven at 60 °C for overnight, and the dried alkylated polymer was kept in vacuum desiccator for future use. The ^{1}H-NMR spectra with individual peak assignments is given in the **Figure A5.3.**

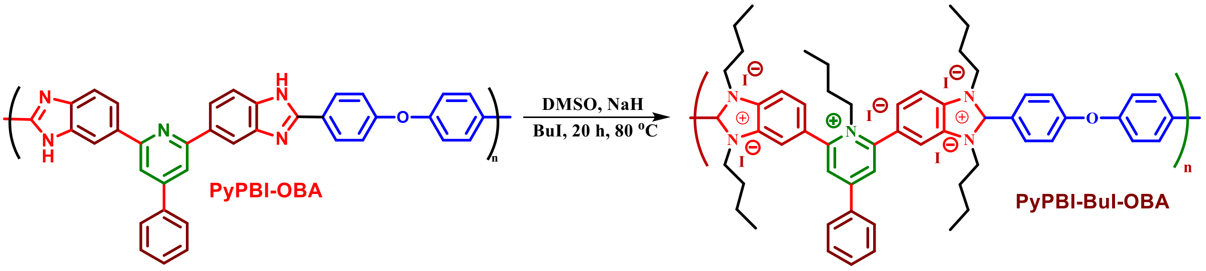

Scheme 7.2. Synthesis of poly(alkylated pyridinium benzimidazolium) iodide (PyPBI-BuI-OBA).

Preparation of [GOPIL@PyPBI-BuI] multicationic mixed matrix membranes

polymeric ionic liquid (PIL) grafted GO materials, pMATMA-*g*-GO (GOPIL1), pVImBu-*g*-GO (GOPIL2) and pVBImBu-*g*-GO (GOPIL3) were introduced as nanofiller materials into poly(alkylated pyridinium benzimidazolium) iodide (PyPBI-BuI-OBA) in order to prepare GOPIL loaded mixed matrix composite anion exchange membranes utilizing solution casting blending method. We have varied the content of GOPIL materials (GOPIL1, GOPIL2 and GOPIL3) loading from 1 wt% to 2 wt % with respect to the PyPBI-BuI-OBA weight to fabricate the MMAAEMs. All the GOPIL samples and calculated amount of PyPBI-BuI-OBA were mixed together in presence of dimethyl sulfoxide. Finally, the solution mixture was stirred for 24 h -36 h at room temperature to form a homogeneous dispersion of GOPILs in the alkylated PyPBI matrix which was then poured on to a glass petri dish followed by gradual evaporation of DMSO at 80 °C for 24 h. The formed homogeneous composite MMAAEMs were then peeled off and vacuum dried at 100 °C for 24 h to remove the traces of the solvent and absorbed moisture. The obtained mixed matrix anion exchange membranes (MMAAEMs) in their iodide form GOPILX-Y%(I), where X indicates the type of grafted polymer chains (for example 1 means pMATMA chains grafted on GO), Y indicates the % of loading and (I) means the membrane in iodide form. Six membranes were prepared and named as **GOPIL1-1%(I)** and **GOPIL1-2%(I), GOPPIL2-1%(I)** and **GOPIL2-2%(I), GOPIL3-1%(I)** and **GOPIL3-2%(I),** respectively.

Exchange of iodide (I^-) with (OH^-) ion to prepare hydroxide doped membranes

The obtained GOPILs loaded multicationic mixed matrix composite AAEMs were kept immersed into 1 M KOH aqueous solutions at 30°C for 24 h to convert the membranes from iodide (I^-) form to hydroxide (OH^-) form. Then, the OH^- form membranes were thoroughly washed with DI water repeated times to remove excess KOH present on the surface of the membranes. These membranes were soaked in DI water for 24 h prior to conductivity measurement and other experimental analysis. All the six iodide form membranes were converted to OH^- doped membranes and they are symbolised as **GOPIL1-1%(OH)** and **GOPIL1-2%(OH), GOPPIL2-1%(OH)** and **GOPIL2-2%(OH), GOPIL3-1%(OH)** and **GOPIL3-2%(OH)**.

Result and discussion

Grafting of Polymeric ionic liquid on the GO surface:

The grafting of polymer on the GO surface has been carried out in a multiple steps: first the GO surface is activated with the RAFT agent to make the surface polymerizable (see details in Chapter 5) and then the polymerization is carried out. The grafting process is schematically shown in the Appendix 3 and **Scheme 7.1.** The obtained products are thoroughly characterized as described below.

The FT-IR spectra of the synthesized GO, GO-EDA and GO-BSPA samples are already discussed in details in the Chapter 5, and the FT-IR of PIL-*g*-GO samples (GOPIL1, GOPIL2 and GOPIL3) are given in the Appendix 5, **Figure A5.4.** After surface grafted polymerization in the GO-BSPA all the characteristics peaks of surface functionalized GO is found to be present in the polymer modified samples with generation of few new peaks due to the functional groups presence in the *grafted* polymer chains. The peak at 1726 cm^{-1} appears in the pMATMA-*g*-GO (GOPIL1) sample due to the –C=O stretching of -COO functional group present in the polymer structure,[39,40] and we also observed spectral broadening in the FI-IR signal due to the polymer grafting in the GO-BSPA surface. In case of pVImBu-*g*-GO (GOPIL2) sample, the imidazole ring vibrations at 1500 cm^{-1} and 1450 cm^{-1} [41] merges with the RAFT modified GO signals and appears as broad signals. In the pVBImBu-*g*-GO (GOPIL3) the appearance of relatively more signals are occurred due to the presence of C-C and C-H stretching vibration of aromatic benzylic moiety.[42,43] In case of all the PIL-*g*-GO samples, the aliphatic C-H stretching frequency is observed at 2860-2930 cm^{-1} due to the presence of the EDA structure in the surface modified GO. Also, the amide –C=O stretching of GO-EDA at 1660 cm^{-1} is present in all the three GOPIL samples which indicates that the amine modified GO nanosheets backbone structural identity remains even after polymer grafting.

The TGA plots of GO-BSPA and the surface polymeric ionic liquid modified GO samples (GOPIL1-GOPIL3) are represented in the **Figure 7.1(A)**. The TGA data of the GO, GO-EDA and GO-BSPA samples are discussed in details in the Chapter 5. The calculated grafting density of the attached RAFT on the GO surface is given in **Table 7.1.** The calculation is carried out from the wt% difference obtained from TGA. In the PIL-*g*-GO samples the thermal degradation is increased compared to GO-BSPA after grafting of PIL chains on the GO-BSPA surface, but all the GOPIL materials are stable up to 250-300 °C [**Figure 7.1(A)**] and the main degradation of the surface grafted PILs is started after 220 °C followed by gradual thermal degradation up to 400 °C. We have calculated the grafting density of the PIL chains on the GO surface by from TGA analysis. The maximum polymer grafting density of 260.08 mg/g (**Table 7.1**) of GO was observed for GOPIL3 polymer. Therefore, it is clear from the **Table 7.1** data that the type of polymer chain grafted on the surface has a strong influence on the amount of polymer which can be attached to the surface.

Gel permeation chromatography (GPC) of GOPIL1-GOPIL3 were performed after chemical treatment of the PIL grafted GO samples with N-hexylamine (5-fold excess) in presence of sodium dithionite ($Na_2S_2O_4$) in HPLC water medium. The resulted chemical environment causes breaking of the trithiocarbonate bond linking between the grafted polymer chains with the GO surface and liberates the free polymer chains in the solution mixture[44] (see Chapter 5). The bare polymer chains were then purified and the molecular weight of each bare polymer chain was measured by GPC analysis using HPLC water as eluent solvent [**Figure 7.1(B)**] and the molecular weights are tabulated in the **Table 7.1**. The molecular weights of the GO surface grafted polymers are in agreement with the targeted molecular weight of each of the individual polymers. We have targeted ~20000 KDa molecular weight for all the three GOPILs and **Table 7.1** data show that almost similar molecular weight obtained with all GOPILs. Also, the samples display very narrow polydispersity index (Đ) which is a direct proof that the surface polymer *grafting* taken place via RAFT polymerization. To further check the successful grafting of three different type of polymer chains on the GO surface we have performed the Brunauer–Emmett–Teller (BET) N_2 sorption analysis at the GOPIL samples [**Figure A5.5**]. The PIL-*g*-GO samples show a well-defined type-IV isotherm and the obtained surface area of GOPIL1, GOPIL2 and GOPIL3 are 30.351, 29.938 and 28.717 m^2/g, respectively, which are much less than the GO surface area 192.357 m^2/g (Chapter 5). The remarkable decrement in the surface area is a direct consequence of the PIL modified exfoliated GO nanosheets where after the surface polymer modification the interlayer spacing between the GO nanosheets are entirely covered by the surface *grafted* polymeric ionic liquids resulting significant exfoliation in the GO nanosheets.

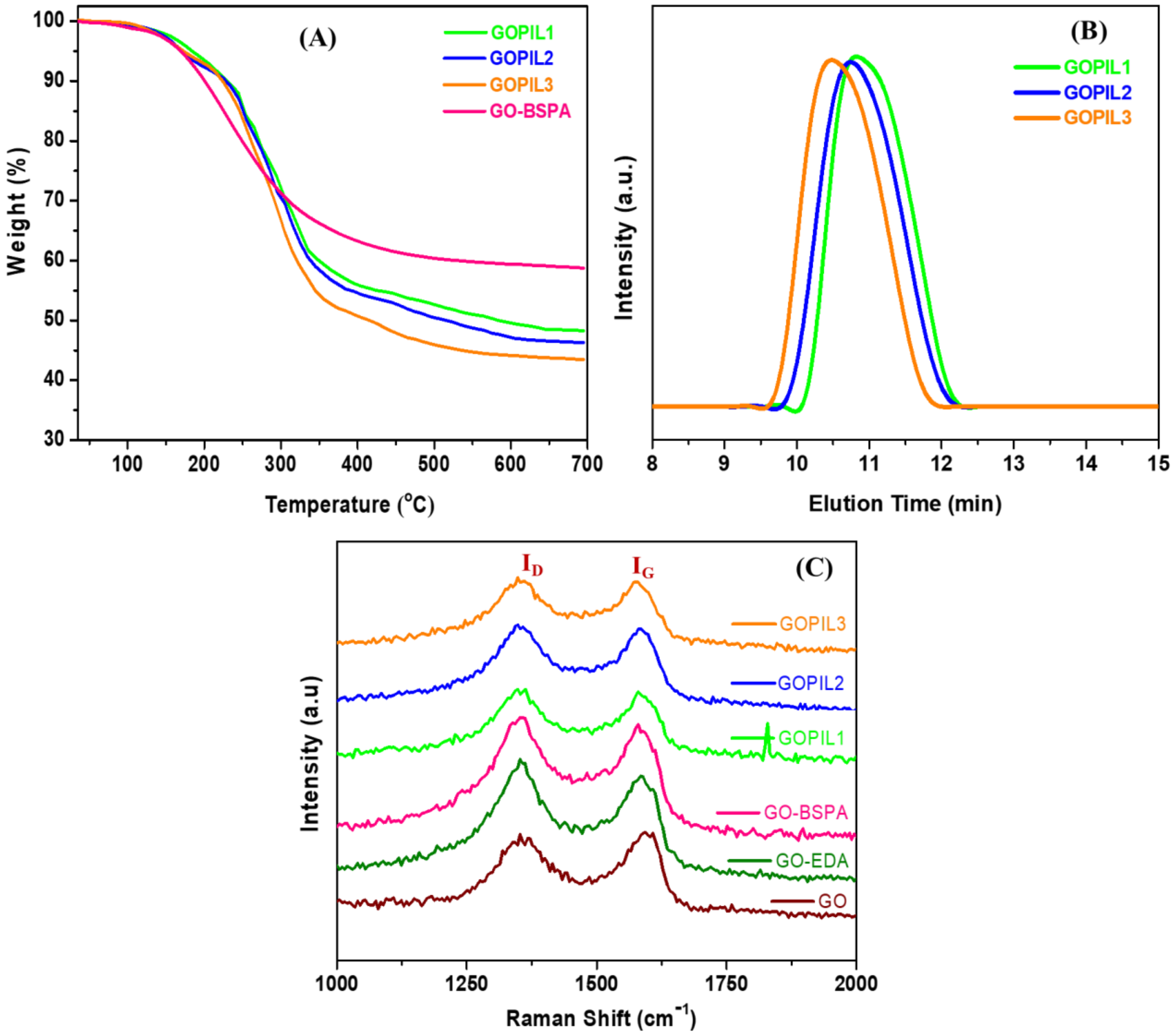

Figure 7.1. (A) TGA of polymeric ionic liquid modified GO (GOPIL1, GOPIL2, GOPIL3) along with GO-BSPA for comparison. **(B)** GPC plots of the PIL chains which are detached from the surface of GO after treating the GOPIL samples with cleaving agent. **(C)** Raman shifts of GO, surface functionalized GO and GOPIL samples.

The Raman spectra of GO and GO-EDA is already discussed in the Chapter 5. Raman spectra of GO-BSPA shows that I_D/I_G value is 1.18, which indicates the decrease of in-plane sp^2 structure and formation of more ordered structure compare to bare GO which has I_D/I_G value 1.025. No notable change in the I_D/I_G values is observed for the PIL-*g*-GO samples instead slight decrease in I_D/I_G is noticed in GOPIL samples (0.9-1.1) which attributes that the ordered structure of the reduced GO is preserved after surface grafting of polymer[45] [**Figure 7.1(C)**].

Table 7.1. Physical properties of the surface functionalized PIL *grafted* GO samples.

Sample name	Sample type[a]	Remaining weight % at 700 °C (wt%)[b]	Grafting density[c] (mg/g)	$\bar{M}_n$[d]	$\bar{M}_w$[e]	Đ[f]	Zeta potential (mV)[g]
GO-BSPA	-	58.71	30.06	-	-	-	-10.4
GOPIL1	pMATMA$_{115}$-*g*-GO	48.27	178.38	19876	20472	1.03	45.4
GOPIL2	pVImBu$_{132}$-*g*-GO	46.28	212.25	19996	21196	1.06	-52.5
GOPIL3	pVBClmBu$_{80}$-*g*-GO	43.47	260.08	20420	21236	1.04	67.5

[a] sample type describes the chain sequence and the degree of polymerization for each random polymer included in the suffix which are obtained from the molecular weight measurements using gel permeation chromatography.
[b] estimated from the TGA analysis (at 700 °C) and [c] Polymer content was obtained from the analysis of the TGA curves and expressed as amount (in mg) of polymer chains /g of GO-BSPA, in case of GO-BSPA polymer content represents the amount of RAFT agent on GO surface. [d], [e] and [f] are determined by gel permeation chromatography of the GOPILs, and [g] obtained from Zeta potential analysis.

The FESEM and TEM data of GO and the GO-BSPA samples are given in the Chapter 5 along with related discussion. FESEM of the GOPIL samples are represented in the **Figure 7.2(A-C)** and **Figure A5.6-A5.8** of Appendix 5. The PIL-*g*-GO samples exhibits entirely different morphology compared to GO and GO-BSPA (compare with Chapter 5), where the grafted polymeric IL chains covered the entire surface of the GO and hence the sheets become thick and dense with increased surface roughness, which is a direct proof for the GO surface modification with the PIL chains (**Figure 7.2A-C**). Morphology along with EDX elemental analysis of GOPIL1 clearly demonstrates that the GO surface becomes comparatively more thick, dense, rough and exfoliated after PIL grafting. Similarly, in case of GOPIL2 the grafting of dense pVImBu polymer layers has covered the entire GO surface which causes the increment in the nitrogen (N) content to 37.16 wt% obtained from the EDX analysis, due to the introduction of imidazolium functionalities through PIL grafting on GO surface. Similarly, GO surface exfoliation with thick polymer agglomeration is also observed in case of GOPIL3 sample (**Figure 7.2C** and **Figure A5.8**). The overall nitrogen content slightly decreases in case of GOPIL1 and GOPIL3 compared to GO-BSPA because after polymer grafting the aromatic functionalities present in the GOPIL1 and GOPIL3 polymers also contributes towards increase in the overall carbon contents of the polymers.

TEM analysis of the **PIL-*g*-GO** (**Figure 7.2D-F**) display entirely altered morphology, all the GOPIL samples exhibit less transparent thick plates with dark contrast due to the polymer grafting. This demonstrates that the surface of the GO nanosheets sheets have been covered by pMATMA, pVImBu and pVBImBu polymers (**Figure 7.2D-F**). The PIL chains are not only grown on the surface of GO but also grown in between the surface of the interlayer sheets, which makes the GOPIL sheets thick and exfoliated with dark contrast. Also, the associated H-bonding between the intra and interlayered GOPIL nanosheets functional groups results partial intercalated structure in the PIL-g-GO samples.

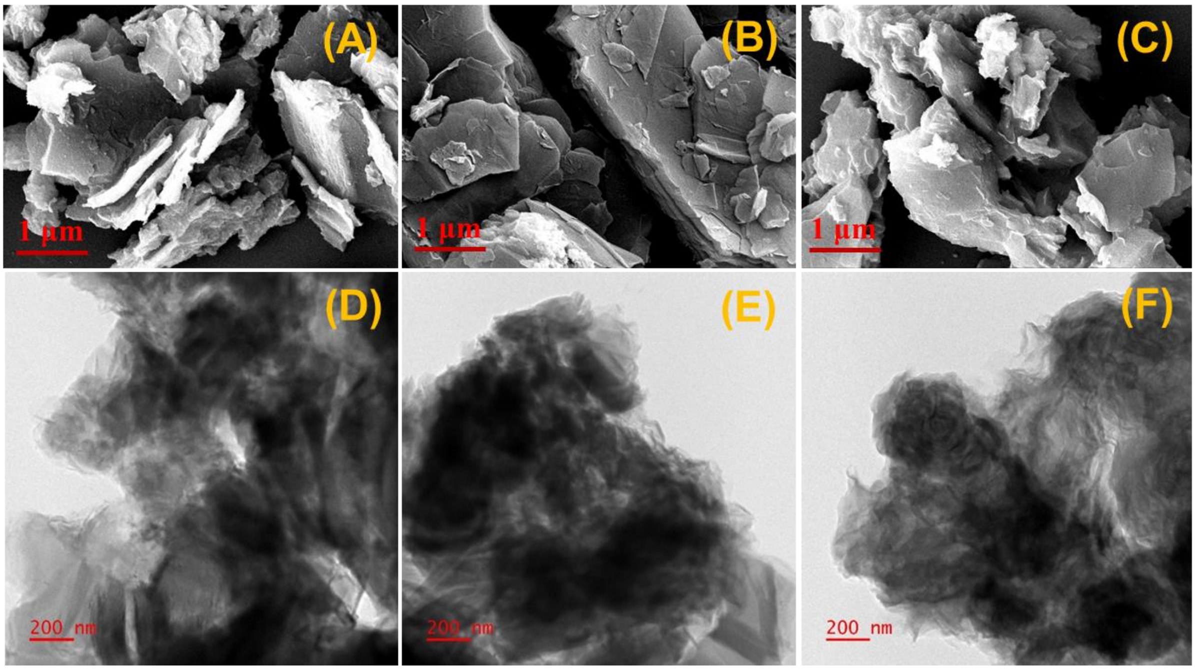

Figure 7.2. FESEM images of GOPIL1 **(A),** GOPIL2 **(B),** GOPIL3 **(C).** TEM images of GOPIL1 **(D),** GOPIL2 **(E)** and GOPIL3 **(F).**

Dynamic vapour sorption (DVS) studies of the PIL-*g*-GO samples were performed and which shows that GOPILs samples has improved water sorption compared to GO due to the grafting of hydrophilic PILs on the surface **Figure A5.9**, Appendix 5. The water vapour sorption values of GOPIL1 is 0.0491 g of water/g of GOPIL1 which is due to the presence of primary and secondary ammines and quaternary ammonium functionalities in the GOPIL1. Similarly, for GOPIL2 and GOPIL3, the water sorption values are 0.0867 and 0.0731 g of water/g, respectively. The remarkably higher water sorption is due to the presence of primary and secondary ammines, and hydrophilic imidazolium ionic functionalities present in grafted polymer chains which can form H-bonding interaction with the water molecules and can improve water sorption. Thus these results indicate the absorption of large quantity of water which might help in taking up more KOH and hence may results super hydroxide conducting AAEMs.

We have also measured the Zeta potential of the PIL-*g*-GO samples in aqueous dispersion and presented in **Table 7.1**. The Zeta potential data implies that due to the strong H-bonding interaction between the functional groups present in the GOPILs with the water molecules the dispersive nature of the polymer modified GO samples has improved much compared to bare GO (compare with Chapter 5). This in turn suggests a better stability of the PIL modified GO samples in aqueous dispersion. Hence, the hydrophilicity and the stability in the aqueous dispersion of the GOPIL materials makes them suitable choice for their utilization as nanofillers for developing AAEMs with high processability.

GOPIL as nanofiller to make PyPBI/GOPIL nanocomposite based AAEM.

We have extended our work in an aim to utilize these GO surface functionalized GOPIL materials as a nanofiller material for the preparation of hydroxide conducting mixed matrix AAEM (MMAAEM) with high mechanical durability, improved alkaline stability, very high hydroxide conductivity and to evaluate the role of the nanomaterials surface modification in improving overall polymeric membrane properties, more specifically their OH^- conduction, chemical & mechanical stability. The solution casting blending preparation of the MMAAEM is described in the experimental section. All these different types of GOPIL namely GOPIL1, GOPIL2 and GOPIL3 were mixed with PyPBI-BuI-OBA in various wt% of loading in DMSO for 24 h followed by casting and evaporation of the solution to produce nanocomposite based AAEM and then these membranes were dipped into 1 M KOH convert into KOH doped AAEMs. The whole process is described in the experimental section. We have also characterized these membranes through various techniques to evaluate their performance as potential membrane material for the use as AAEM in fuel cell or water electrolysis.

PXRD and thermal study

The PXRD patterns of GO, GO-BSPA, GOPIL samples and the composites are given in the **Figure 7.3A & B.** The PXRD data of GO, GO-EDA and GO-BSPA samples are already discussed in details in the Chapter 5. GOPIL samples show diffraction pattern at 2θ = 8.8-10.0 °, corresponding to d value between 0.9-1.0 nm (**Figure 7.3A**). The decrease in the interlayer spacing in the GOPIL samples compared to GO-BSPA (d = 1.17 nm) surface is a direct consequence of polymer grafting on the surface. This happens as grafted polymer chain helps in collapsing the spacing because of interaction. The PXRD pattern of PyPBI-BuOH-OBA exhibits a broad amorphous halo in the 2θ region between (15–35)º.[16] However, incorporation of GOPILs as fillers into the PyPBI-BuOH-OBA results significantly crystalline PXRD patterns with appearance of several new sharp crystalline signals particularly peaks in the 2θ 9.56º, 20° - 35º and 42.80º (marked with # in the **Figure 7.3B**). The peak at 2θ = 9.56º is due to the presence of GOPIL in the composite. both GOPIL and PyPBI-BuOH-OBA samples do not show any crystalline peaks but the presence of large number of sharp crystalline peaks in composite samples attributed generation of a certain structural ordering in the composite samples may be due to the generation of interfacial interaction between the GOPIL and the PyPBI-BuOH-OBA structural functionalities. This kind of crystallinity with ordered structure can assists the nanocomposite to accommodate more electrolyte into their interfacial region which helps in improvement of physical properties including ion conducting properties.

The thermal stability of the alkylated PyPBI membranes and the GOPIL nanofiller loaded mixed matrix AAEMs (both I^- and OH^- form membranes) are given in the **Figure 7.3 (C, D)** and Appendix 5, **Figure A5.10.** The alkylated PyPBI-OBA and the nanocomposite AAEMs exhibit exhibit similar type of thermal degradation. All the samples show two major degradation: the first major step is observed between 200 °C -300 °C which is due to the cleavage of the imidazolium rings and QA moieties present in the PyPBI backbone structure and in the GOPIL nanosheets, respectively,[46,47] then the final degradation step is found above 400 °C temperature which is the main chain decomposition of the polymer membrane.[16,33] The **GOPIL** loaded (1 wt% and 2 wt%) membranes display slightly lower thermal stability with respect to alkylated PyPBI due to the degradation of the organic functionalities present in the PIL modified GO nanosheets. The hydroxide form membranes exhibit higher thermal stability than that of corresponding iodide from membranes which are clearly observed from the TGA plots represented in the **Figure 7.3(C, D)** and Appendix 5, **Figure A5.10** because of OH^- counter ions which displays higher thermal stability owing to the lower nucleophilic strength of the hydroxide ions.[48]

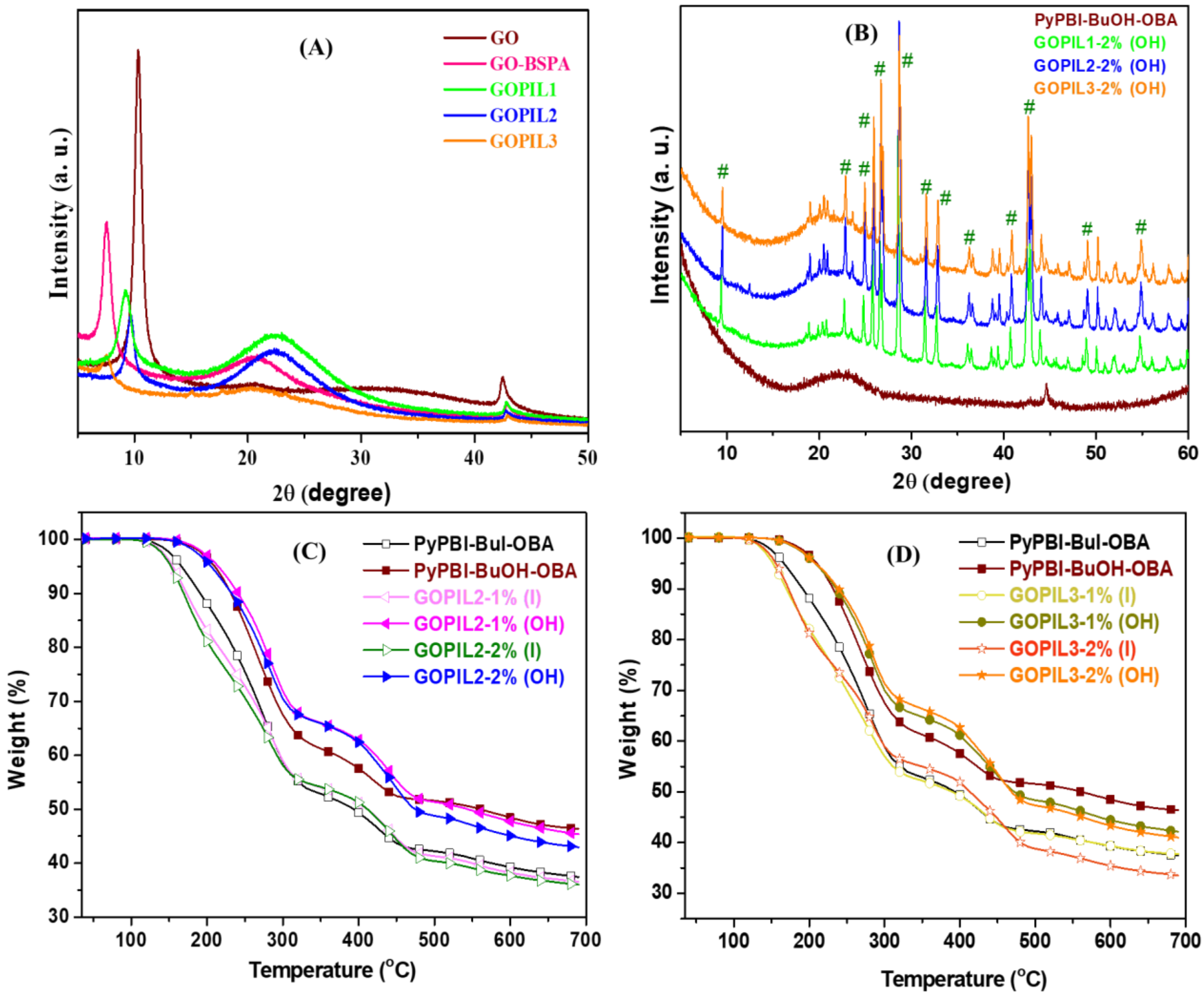

Figure 7.3. (A) PXRD plots of GO, GO-BSPA, GOPIL1, GOPIL2 and GOPIL3. **(B)** PXRD plots of PyPBI-BuI-OBA and GOPIL loaded mixed matrix membranes. **(C, D)** TGA plot of alkylated PyPBI and GOPIL2 and GOPIL3 loaded nanocomposite AAEMs of different loading wt% (both iodide and hydroxide form membranes).

Morphological study

The 2D surface morphologies of the GOPIL loaded MMAAEMs (iodide form membranes) have been analysed through atomic force microscopy (AFM) technique in order to evaluate the dispersion nature of the GOPIL nanofillers into the PyPBI-BuI matrix. Though PyPBI-BuI-OBA shows a uniform featureless morphology (**Figure A5.11A**) whereas, GOPIL loaded membranes display dispersion of PIL-*g*-GO nanosheets in the samples with bright domains [**Figure 7.4(A-C), Figure A5.11(B-D)**].[49,50] The appearance of brighter spots in the GOPIL loaded membrane surface is attributed to the incorporation of hydrophilic GOPIL nanosheets. It is to be noted that the size and intensity of the brighter spots in the AFM images increases with the increasing GOPIL loading and also depends on the nature of grafted polymer chain on the GOPIL. Due to the nanofillers incorporation, the membrane surface roughness also displays remarkable enhancement after GOPIL loading (see **Table A5.1**, Appendix 5). The three dimensional (3D) AFM morphology along with the surface height profiles for all the GOPIL loaded membranes along with pristine PyPBI-BuI-OBA are given in the **Figure A5.12** and **A5.13.** The surface roughness also greatly influenced by the GOPIL type and % of loading.

The FESEM morphology of the **GOPIL** loaded composite AAEMs (iodide form membranes) are given in the **Figure A5.14 – A5.16.** which display formation of sponge like porous granular type rough membrane surface with dispersion of GOPIL nanofillers all over the surface. This kind of sponge like porous granular morphology development observed after performing butylation on the PyPBI-OBA matrix due to the formation of polymeric salt structure. After GOPILs loading into the PyPBI-BuI-OBA, the hydrophilic nanofillers becomes compatible with the PyPBI-BuI-OBA polymeric salt structure and a miscible blend surface morphology with sponge like porous granules formation is observed all over the matrix due to the compatibility between the polymeric matrix and the added nanofillers. Also, this feature increases with increasing GOPILs loading from 1 wt% to 2 wt% in the composite. Cross-sectional FESEM analysis of the hydroxide form membranes also have been performed, which exhibit sponge like fibrillar morphology with generation of similar type of granular surface with presence of hydrophilic GOPILs in the membranes cross-section **[Figure 7.4(D-F)].** This kind of porous sponge like nano granular generation with hydrophilic GOPIL incorporation in the surface and interfacial region can accelerate accommodation of significant amount of KOH molecules into the membrane matrix which can enhance the hydroxide ion conduction of the composite AAEMs significantly. In addition, the sponge like fibrillar morphology and the surface modified GOPILs incorporation in the membrane can result significant improvement in mechanical strength of the nanocomposite AAEMs.

TEM analysis also has been performed for the hydroxide form membranes [**Figure 7.4(G-I)**] and it display a highly dense polymeric network with dispersion of GOPILs all over the composite. Also, the hydroxide form composite AAEMs show generation of ionic clusters all over the sample after incorporation of KOH electrolyte which can effectively contribute towards high IEC (>2.0 meq/g) and eventually superior OH^- conduction of the membranes.

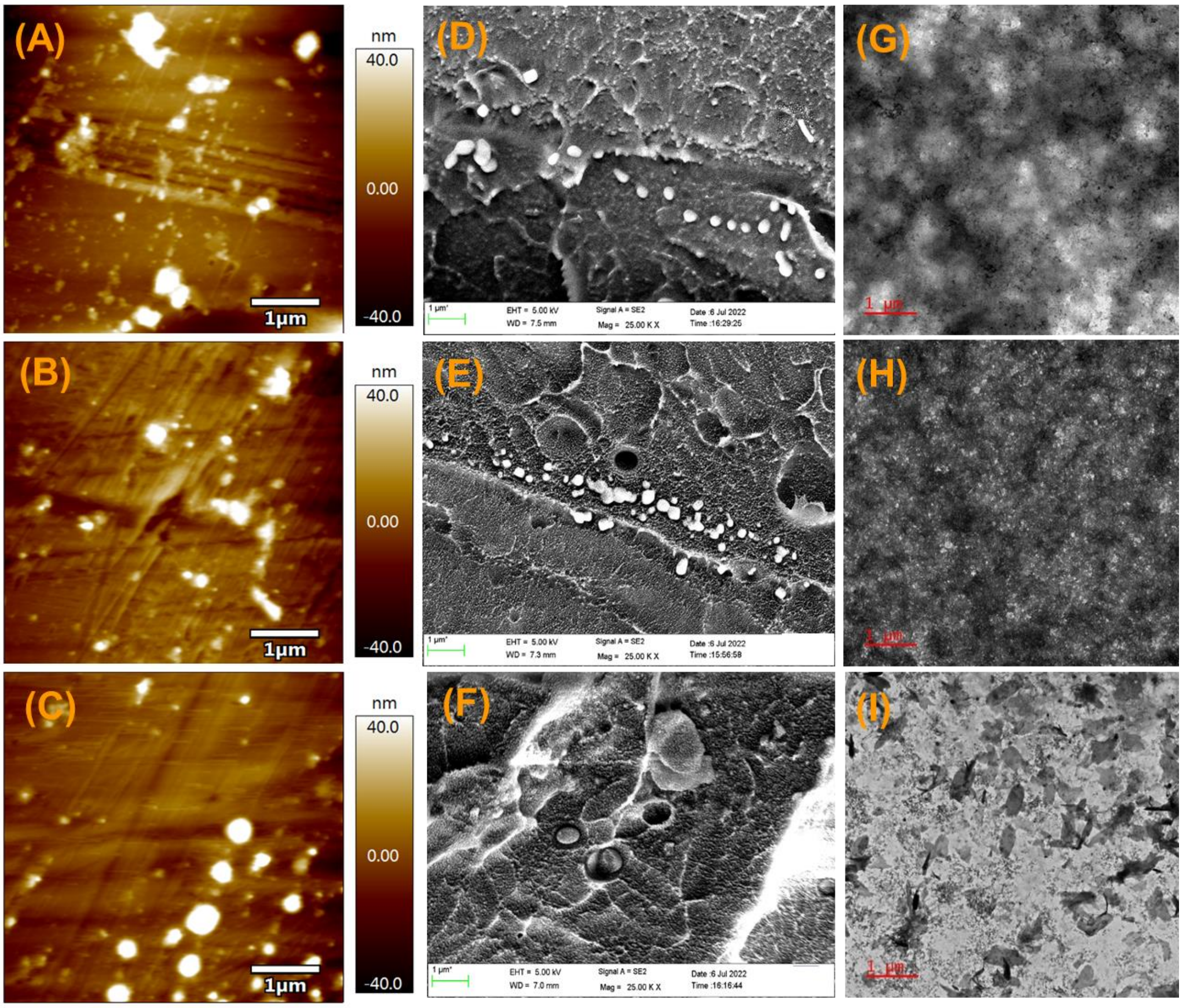

Figure 7.4. Surface AFM images of GOPIL2-2%(I), GOPIL2-2%(I), and GOPIL3-2%(I) **(A, B, C).** FESEM cross-sectional image of GOPIL2-2%(OH), GOPIL2-2%(OH) and GOPIL3-2%(OH) **(D, E, F).** TEM images of GOPIL2-2%(OH), GOPIL2-2%(OH) and GOPIL3-2%(OH) **(G, H, I).**

Water uptake (WU), swelling ratio and ion exchange capacity (IEC):

Water uptake (%), dimensional stability (measured in the form of swelling ratio) and IEC of the membranes are three important parameters need to be evaluated for their potential as AAEMs. The water uptake of the hydroxide treated dry composite membranes have been evaluated at 30 °C, 60 °C and 80 °C (**Table 7.2).** It is observed that, the water uptake increases with increasing temperature and also dependent upon both % of GOPIL loading and type of GOPIL. In all the cases composite membranes shows higher water uptake than the pristine polymer membrane because of hydrophilic nature of GOPIL. The swelling ratio (SWR) of the mixed matrix AAEMs also have been evaluated at 30 °C, 60 °C and 80 °C (**Table A5.2,** Appendix 5). All the GOPIL loaded AAEMs display much less swelling with respect to PyPBI-

BuOH-OBA membrane despite of having high WU values due to the loading of GOPIL nanofiller, which helps in reducing the swelling of the AAEMs. Also, the SWR of the membranes decreases with increasing GOPIL filler loading and found to be not much dependent on the type of GOPIL. The results of ion exchange capacity (IEC) in milliequiv.g^{-1} of 1 M KOH treated composite membranes are listed in **Table 7.2.** The results clearly indicate that both IEC of the membranes follows proportionality with the WU (%) values. Also, the IEC of all the composite AAEMs display much improved values with respect to the PyPBI-BuOH-OBA due to the more electrolyte uptake into the membranes provided by GOPILs loading. The highest IEC value of 3.39 meq/g was observed for the GOPIL2-2%(OH) membrane. We have also estimated the IEC of the 1 M KOH treated samples after keeping them at 60 °C for 500 h. Interestingly, we did not find any notable change in the IEC values even after such a prolong alkaline stability test indicating superior stability of these GOPIL loaded membranes in harsh alkaline environment.

Table 7.2. The IEC and water uptake of the PyPBI-BuI-OBA and GOPIL loaded anion exchange membranes.

Sample identity	***Water uptake at 30 °C (%)***	***Water uptake at 60 °C (%)***	***Water uptake at 80 °C (%)***	***IEC (meq/g) at 1 M KOH*** [a]	***IEC (meq/g) after alkaline stability treatment*** [b]
PyPBI-BuOH-OBA	3.52	5.58	7.33	2.68	2.39
GOPIL1-1%(OH)	3.97	6.01	8.17	2.87	2.60
GOPIL1-2%(OH)	4.04	8.55	10.16	3.03	2.78
GOPIL2-1%(OH)	4.75	6.51	10.0	3.07	2.71
GOPIL2-2%(OH)	7.00	11.0	30.0	3.39	3.11
GOPIL3-1%(OH)	3.44	6.32	8.67	2.96	2.65
GOPIL3-2%(OH)	8.00	8.66	10.66	3.25	2.91

[a] IEC of freshly 1 M KOH treated membranes measured using titration method; [b] IEC measurement was carried out using titration method after membranes were treated with 1 M KOH at 60 °C for 21 days (500 h).

Hydroxide conductivity of the AAEMs.

The hydroxide ionic conductivity of the membranes is the key parameter which is significantly influenced by the water uptake and IEC values of the AAEMs and generally follows proportionality relationship with them. The hydroxide conductivity of the PyPBI-BuOH-OBA and the GOPILs loaded composite AAEMs have been measured after doping them in 1 M KOH solutions for 24 hours. Membranes were kept in water bath for 24 h at room temperature before measurement in order to remove the surface KOH of the membranes prior to analysis. The hydroxide conductivity of the AAEMs as a function of temperature is represented in **Figure 7.5 (A-C).** The OH^- conductivity of all the composite AAEMs and the PyPBI-BuOH-OBA increases with the increasing temperature as with increasing temperature as expected from the increasing hydroxide ions mobility. Also OH^- conductivity follows proportionality relationship with increasing IEC due to the enhancement of water uptake which contributes towards the enhanced local mobility of water and induced long-range ionic domain percolation.[51] The OH^- conductivity of PyPBI-BuOH-OBA is 82 mS/cm at 80 °C. All the composite AAEMs display improved OH^- ion conduction over pristine PyPBI-BuOH-OBA membrane due to their improved IEC. Also with increasing GOPIL nanosheets loading from 1 wt% to 2 wt% in the AAEMs, the OH^- conductivity show significant enhancement. The GOPIL1-2%(OH), GOPIL2-2%(OH) and GOPIL3-2%(OH**)** membranes OH^- conductivities are 113 mS/cm, 137 mS/cm and 127 mS/cm at 80 °C, respectively [**Figure 7.5 (A-C)],** which is in well accordance with their excellent IEC values. The ionic conductivities of the GOPIL loaded composite AAEMs have been considerably improved in contrast to the imidazolium and other types of cationic sites based polymeric membranes reported so far in literature.[15,33,52] The presence of multicationic functionalities (imidazolium, pyridinium of the PyPBI-BuI-OBA polymer and the quaternary ammonium or imidazolium functionalities grafted in the GOPILs) in the composite AAEMs accounts for superior hydroxide (OH^-) ions transport through the AAEMs which contributes remarkably towards significantly improved OH^- conduction. The reason for highest OH^- conductivity in case of GOPIL2 loaded membrane is because of more water uptake and more IEC of the membrane. The hydroxide conductivity of the nanocomposite AAEMs displays an Arrhenius type temperature dependence **[Figure 7.5(D)].** The activation energy (E_a) was calculated from the slopes of the Arrhenius plot which ranges from 15-22 kJ/mol or ~0.15-0.22 eV. These values are comparable with the reported literature data,[16] suggests that OH^- conduction happens through Grotthuss hopping mechanism.

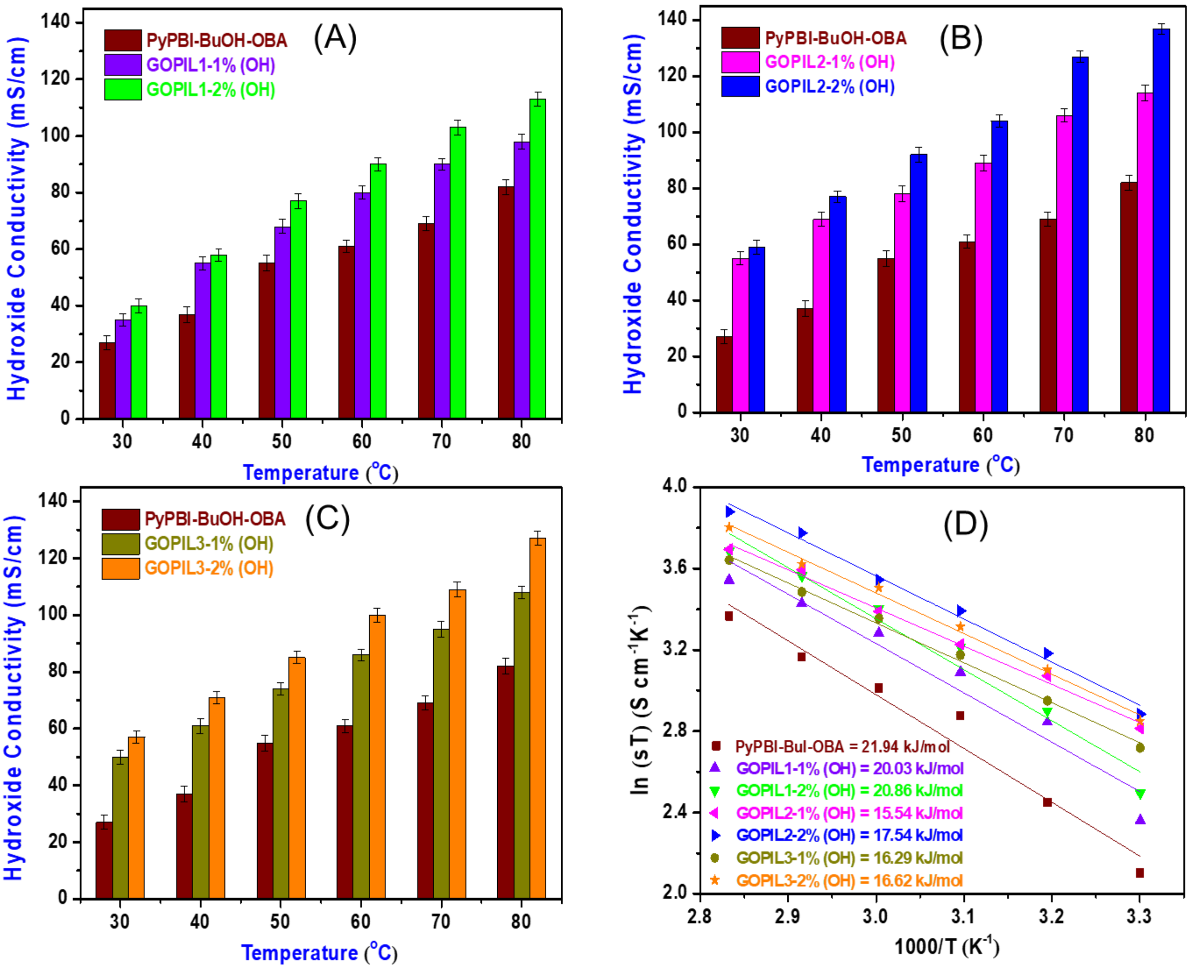

Figure 7.5. Hydroxide ionic conductivity of GOPIL1 loaded AAEMs of different wt% **(A),** GOPIL2 loaded AAEMs of different wt% **(B),** GOPIL3 loaded AAEMs of different wt% **(C),** Arrhenius plots of the mixed matrix AAEMs **(D).** These membranes were doped by dipping in 1 M KOH alkaline solution for 24 h before measurements.

Tensile properties of the mixed matrix AAEMs

The stress-strain profiles of the hydroxide form AAEMs were checked using Universal Testing Machine (UTM) and the data are plotted in the **Figure 7.6.** The obtained tensile stress and elongation at break values of all the membranes are also tabulated in the **Table A5.3.** All the composite AAEMs exhibit very high mechanical reinforcement after GOPIL loaded into PyPBI-BuOH-OBA membrane, while with increasing GOPIL loading in the membrane shows significant improvement in the tensile strength along with little variation in elongation at break (%). Particularly GOPIL1-2%(OH) and GOPIL3-2%(OH) membranes exhibit ~2-3 fold increased tensile strength and ~1.5 – 2% improved elongation at break with respect to the pristine PyPBI-BuOH-OBA. The enhanced mechanical strength of the composite AAEM is clearly due to the presence of GOPIL nanofiller. It is to be noted that the stress-strain properties of the current composite AAEMs are much superior compare to other imidazolium and QA based AAEMs reported in literature.[15,16,53]

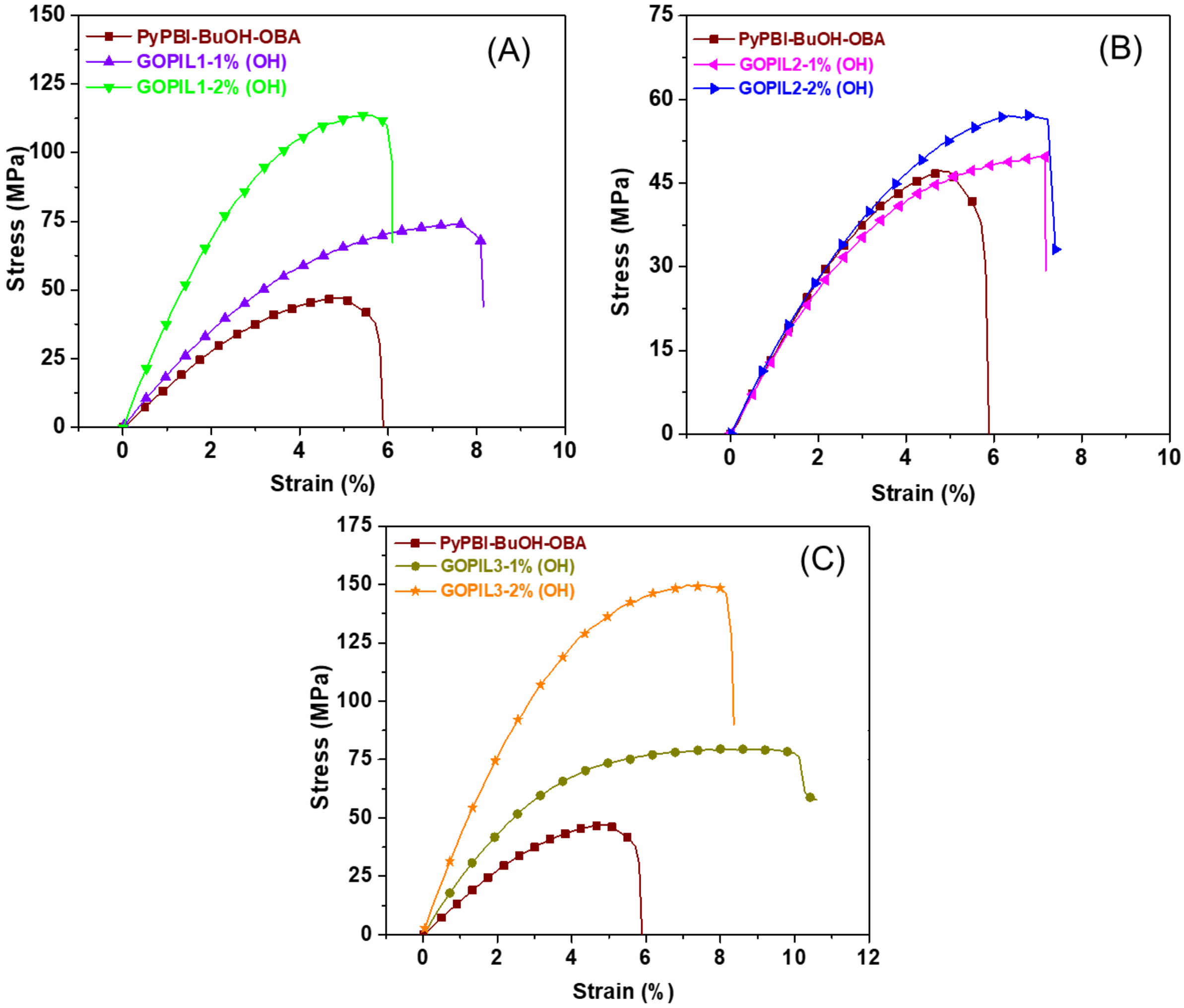

Figure 7.6. Stress strain profile of the GOPIL loaded hydroxide form AAEMs: **(A)** GOPIL1 loaded AAEMs **(B)** GOPIL2 loaded AAEMs and **(C)** GOPIL3 loaded AAEMs.

Alkaline stability of the composite AAEMs

In order to predict the potential of any membrane to be used as AAEM the alkaline stability of the membrane needs to be evaluated in presence of harsh alkaline environment. The chemical stability of an AAEM in presence high pH alkaline environment is a major challenging issue as harsh alkaline environment causes degradation of the AAEMs and reduces their dimensional and chemical stability under prolong alkaline treatment.[54] Therefore, in our work we have treated the PyPBI-BuI-OBA and all the GOPIL loaded MMAAEMs with 1 M KOH at 60 °C for 500 h, and after that we have repeated all the characterizations (structural and physical characterizations) in order to evaluate the stability and performance of the membranes under harsh alkaline condition for such a prolong treatment. The PXRD signals of the membranes (represented by putting AT which meant after alkali treatment) remains intact even after harsh alkaline treatment (compare **Figure 7.7A** with **Figure 7.3B**), except that intensity of few peaks decreases a little bit. The FT-IR signals of the composite AAEMs after treatment with alkali also remain unaltered as can be seen from **Figure 7.7B** and **Figure A5.17,** Appendix 5. The peak at 3060 cm^{-1} for aromatic C-H stretching vibration, the aliphatic C-H bond vibrational stretching signal at 2982-2880 cm^{-1} due to the aliphatic alkyl chains present in all the samples,[33,53] the pyridine ring C-H stretching frequency at 830 cm^{-1}, the peaks at 1600 cm^{-1} and 1477 cm^{-1} due to the stretching vibration of C=C/C=N and in plane benzimidazole ring deformation,[33,55] are present in all the GOPIL loaded AAEMs. However, we have observed spectral broadening in the 900 – 1480 cm^{-1} region due to the GOPIL loading and existing interfacial interaction between the nanofillers and the alkylated PyPBI functionalities present in the composite AEM matrix. We did not find any notable change for any of the composite membranes FT-IR signals even after 500 h treatment in 1 M KOH solution at elevated temperature. In addition, the cross-sectional FESEM and TEM morphology of the composite AAEMs remains unchanged (alike the fresh OH$^-$ form AAEMs shown in the **Figure 7.4**) even after alkaline treatment at elevated temperature for 500 h in 1 M KOH (**Figure 7.7 C & D**) and **Figure A5.18A-D**, appendix 5. Visually we have observed no degradation in the membranes after treatment (**Table A5.4,** Appendix 5) and all the AAEMs remains flexible and can be nicely handled with tweezers after stability treatment (**Figure 7.7E-G**). The steric factors and the electronic factors induced by the bulky butyl chains in the PyPBI backbone and GOPIL loading in the PyPBI-BuI-OBA matrix makes the composite AEMs highly durable towards the attack of alkali under such harsh environment. The bulky nature of the butyl groups present in the polymer backbone and in the GOPIL is very much helpful for prevention of attack by the hydroxide ion nucleophile to C2 position of the imidazolium moiety, pyridinium and QA functionalities present in the composite membrane matrix.

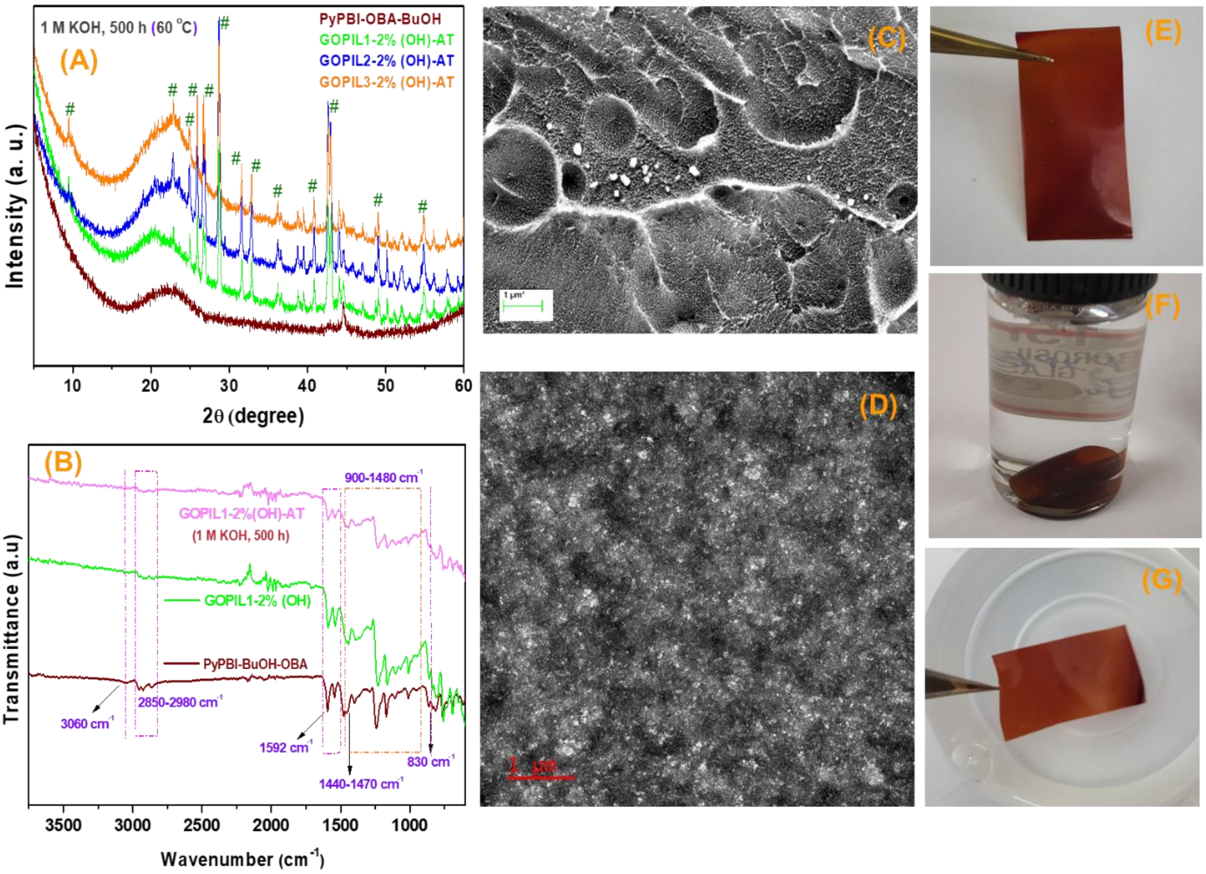

Figure 7.7. PXRD plot of mixed matrix AAEMs after alkaline stability treatment in 1 M KOH at 60 °C, 500 h **(A).** FT-IR spectra of GOPIL1-2%(OH) membrane (before and after alkaline stability treatment in 1 M KOH at 60 °C for 500 h) along with pristine PyPBI-BuOH-OBA membrane **(B).** An image of GOPIL loaded composite membrane in (I^-) form before doping into KOH **(C),** image of composite membrane under 1 M KOH treated condition at 60 °C **(D),** image of composite membrane after completion of alkaline stability treatment in 1 M KOH at 60 °C for 500 h (the membrane is nicely flexible and can be handled with tweezer nicely) **(E).**

It is very important to evaluate the thermal and mechanical durability of the membranes after performing alkaline stability treatment as membranes often loses their mechanical durability and become brittle in nature in presence of alkaline degradation. The weight loss pattern analysed from the TGA after alkaline stability test remains identical with the OH^- form fresh membranes (**Figure A5.19,** Appendix 5). The weight retention of the membranes was measured also gravimetrically, where the 2 wt% GOPIL loaded MMAEMs able to retain >98% of their initial weight after alkaline stability treatment at 1 M KOH for 500 h at 60 °C (see **Figure 7.8A**). Even the tensile stress-strain studies of the composites also have been performed after alkaline stability test under identical experimental condition and compared with the freshly prepared hydroxide form membranes (**Figure 7.8B**), which shows that membranes retain almost similar mechanical behaviour even after prolong alkaline treatment, and all the composite AAEMs still exhibit ~1.5 – 2.0 fold higher tensile strength (MPa) compared to the freshly alkali treated PyPBI-BuOH-OBA membrane sample.

Finally, the superiority of any AAEM depends upon the retention of IEC and hydroxide ion conductivity after alkaline stability test as many AAEMs tend to loose these properties over time in alkali treated condition. Therefore, IEC values of all the GOPILs loaded MMAAEMs after alkaline stability test was measured and the results are reported in the **Table 7.2.** The composite AAEMs exhibit almost identical IEC values with ~90% of their initial IEC even after keeping under long term harsh alkaline atmosphere. Furthermore, the alkali treated membranes hydroxide conductivity was again evaluated at 80 °C and compared with the fresh OH^- form membranes (**Figure 7.8C**). Here also composite membranes exhibit ~87 – 90% retention of their OH^- conductivity, and their conductivity still remains more than 100 mS/cm.

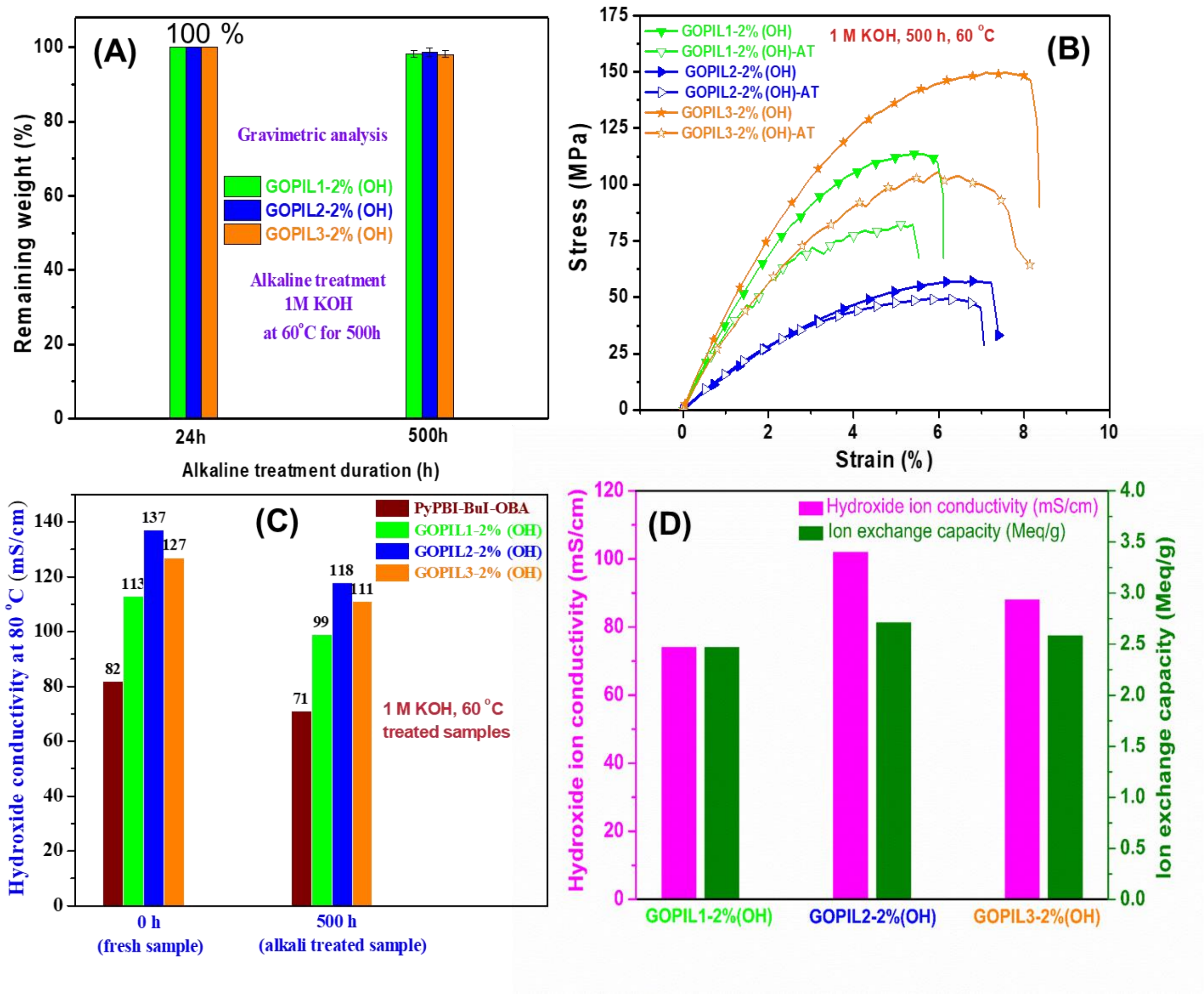

Figure 7.8. (A) Gravimetric analysis of membranes remaining weight after alkaline stability treatment in 1 M KOH, 60 °C, 500 h. **(B)** Stress-strain plot of the membranes before and after

alkaline stability treatment at 1 M KOH, 60 °C, 500 h. **(C)** Hydroxide ion conductivity of the membranes before and after alkaline stability treatment at 1 M KOH, 60°C, 500 h. **(D)** Hydroxide conductivity at 80 °C and IEC of the indicated composite membranes after alkaline stability treatment at 5 M KOH, 60°C for 375 h (15 d).

Due to the exceptional alkaline stability in 1 M KOH the membranes were further treated with 5 M KOH, at 60°C for 375 h (15 d). We observed that the membranes remain flexible and nicely handled with tweezers (**Table A5.5,** Appendix 5), only the colour of the membranes change a bit to light yellow from brown colour. To evaluate whether the 5 M KOH treatment for 375 h (15 d) affects the hydroxide conductivity or not, we have also measured the IEC and the OH^- conductivity of the composite membranes and data are shown in the **Figure 7.8D.** Here also we have observed not much change in the IEC of the membranes with respect to the fresh samples IEC (compare **Table 7.2** and **Figure 7.8D**) and the membranes retained ~80% of their initial IEC values after stability treatment in 5 M KOH. Also, the 80°C hydroxide ionic conductivity data of these alkali treated samples shows ~70% retention of their ionic conductivity (**Figure 7.8D**).

Conclusion

This work has demonstrated a SI-RAFT "*grafting from*" approach to covalently graft three different types of ionic liquid (PIL) on the surface of the GO with accurate control over the molecular weight and with narrow Đ. The formation of polymer chains has been confirmed by measuring the molecular weight of the covalently attached PIL chains upon detachment from the GO surface. The grafting density of the synthesized GOPILs (PIL-g-GO) has been analysed by TGA and the totally exfoliated polymer modified GO nano sheets has been confirmed by FESEM and TEM analysis. The GO surface functionalized nanosheets have been further introduced into PyPBI-BuI-OBA membrane matrix as potential nanofiller by varying wt% loading in order to fabricate multicationic mixed matrix AAEMs with improved thermal, chemical, mechanical and ion conducting properties. These membranes then loaded with KOH to develop AAEM with PIL-g-GO loaded membrane. Superior hydroxide ion conductivity of in the range of >100 mS/cm are obtained at 80 °C. Our mixed matrix AAEMs has not shown any notable change under alkaline stability treatment for prolong duration at elevated temperature (60 °C) in 1 M and 5 M KOH. The structural, chemical, thermal, mechanical and conducing properties of the membranes remained well maintained even after long term alkaline stability treatment at elevated temperature. The mixed matrix AAEM exhibited ~90% retention of IEC and > 85 % retention in their OH^- conductivity after alkaline stability test. All these observations and findings of PIL-g-GO loaded mixed matrix AAEM indicated their potential use in for their potential application in several electrochemical devices. So far, surface functionalized PIL-*g*-GO materials have never been explored in literature for their effective utilization in improving AAEM properties. To the best of our knowledge this will be the first report on utilization of surface polymer modified GO nanosheets in a membrane supported matrix to evaluate the role of anion conducting mixed matrix AAEMs.

Reference

(1) Dekel, D. R. *J. Power Sources* **2018**, *375*, 158–169.

(2) You, W.; Noonan, K. J. T.; Coates, G. W. *Prog. Polym. Sci.* **2020**, *100*, 101177.

(3) Xie, L.; Kirk, D. W. *Electrochim. Acta* **2020**, *364*, 137091.

(4) Gottesfeld, S.; Dekel, D. R.; Page, M.; Bae, C.; Yan, Y.; Zelenay, P.; Kim, Y. S. *J. Power Sources* **2018**, *375*, 170–184.

(5) Long, C.; Lu, C.; Li, Y.; Wang, Z.; Zhu, H. *Int. J. Hydrogen Energy* **2020**, *45*, 19778–19790.

(6) Hugar, K. M.; Kostalik, H. A.; Coates, G. W. *J. Am. Chem. Soc.* **2015**, *137* (27), 8730–8737.

(7) Du, X.; Wang, Z.; Liu, W.; Xu, J.; Chen, Z.; Wang, C. *J. Membr. Sci.* **2018**, *566*, 205–212.

(8) Guo, D.; Lai, A. N.; Lin, C. X.; Zhang, Q. G.; Zhu, A. M.; Liu, Q. L. *ACS Appl. Mater. Interfaces* **2016**, *8*, 25279–25288.

(9) Zhang, Y.; Chen, W.; Yan, X.; Zhang, F.; Wang, X.; Wu, X.; Pang, B.; Wang, J.; He, G. *J. Membr. Sci.* **2020**, *598*, 117650.

(10) Son, T. Y.; Kim, D. J.; Vijayakumar, V.; Kim, K.; Kim, D. S.; Nam, S. Y. *J. Ind. Eng. Chem.* **2020**, *89*, 175–182.

(11) You, W.; Ganley, J. M.; Ernst, B. G.; Peltier, C. R.; Ko, H. Y.; DiStasio, R. A.; Knowles, R. R.; Coates, G. W. *Chem. Sci.* **2021**, *12*, 3898–3910.

(12) Zhu, L.; Pan, J.; Christensen, C. M.; Lin, B.; Hickner, M. A. *Macromolecules* **2016**, *49*, 3300–3309.

(13) Jeevanantham, S.; Hosimin, S.; Vengatesan, S.; Sozhan, G. *New J. Chem.* **2018**, *42*, 380–387.

(14) Hu, E. N.; Lin, C. X.; Liu, F. H.; Yang, Q.; Li, L.; Zhang, Q. G.; Zhu, A. M.; Liu, Q. L. *ACS Appl. Energy Mater.* **2018**, *1*, 3479–3487.

(15) Sana, B.; Das, A.; Jana, T. *Polymer* **2019**, *172*, 213–220.

(16) Sana, B.; Das, A.; Sharma, M.; Jana, T. *ACS Appl. Energy Mater.* **2021**, *4*, 9792–9805.

(17) Mahmoud, A. M. A.; Elsaghier, A. M. M.; Otsuji, K.; Miyatake, K. *Macromolecules* **2017**, *50*, 4256–4266.

(18) Choi, Y. J.; Park, J. M.; Yeon, K. H.; Moon, S. H. *J. Memb. Sci.* **2005**, *250*, 295–304.

(19) Chu, X.; Shi, Y.; Liu, L.; Huang, Y.; Li, N. *J. Mater. Chem. A* **2019**, *7*, 7717–7727.

(20) Dong, X.; Lv, D.; Zheng, J.; Xue, B.; Bi, W.; Li, S.; Zhang, S. *J. Membr. Sci.* **2017**, *535*, 301–311.

(21) Dang, H. S.; Jannasch, P. *J. Mater. Chem. A* **2017**, *5*, 21965–21978.

(22) Zhu, L.; Peng, X.; Shang, S. L.; Kwasny, M. T.; Zimudzi, T. J.; Yu, X.; Saikia, N.; Pan, J.; Liu, Z. K.; Tew, G. N.; Mustain, W. E.; Yandrasits, M.; Hickner, M. A. *Adv. Funct. Mater.* **2019**, *29*, 1902059

(23) Jeon, J. Y.; Park, S.; Han, J.; Maurya, S.; Mohanty, A. D.; Tian, D.; Saikia, N.; Hickner, M. A.; Ryu, C. Y.; Tuckerman, M. E.; Paddison, S. J.; Kim, Y. S.; Bae, C. *Macromolecules* **2019**, *52*, 2139–2147.

(24) Pham, T. H.; Olsson, J. S.; Jannasch, P. *J. Mater. Chem. A* **2018**, *6*, 16537–16547.

(25) Papakonstantinou, P.; Deimede, V. *RSC Adv.* **2016**, *6*, 114329–114343.

(26) Jang, H.; Hossain, M. A.; Sutradhar, S. C.; Ahmed, F.; Choi, K.; Ryu, T.; Kim, K.; Kim, W. *Int. J. Hydrogen Energy* **2017**, *42*, 12759–12767.

(27) Park, H. J.; Lee, S. Y.; Lee, T. K.; Kim, H. J.; Lee, Y. M. *J. Membr. Sci.* **2020**, *611*, 118355.

(28) Zhao, Y.; Yoshimura, K.; Mahmoud, A. M. A.; Yu, H. C.; Okushima, S.; Hiroki, A.; Kishiyama, Y.; Shishitani, H.; Yamaguchi, S.; Tanaka, H.; Noda, Y.; Koizumi, S.; Radulescu, A.; Maekawa, Y. *Soft Matter* **2020**, *16*, 8128–8143.

(29) He, X.; Cheng, C.; Huang, S.; Zhang, F.; Duan, Y.; Zhu, C.; Guo, Y.; Wang, K.; Chen, D. *Polymer.* **2020**, *195*, 122412.

(30) Aili, D.; Yang, J.; Jankova, K.; Henkensmeier, D.; Li, Q. *J. Mater. Chem. A* **2020**, *8*, 12854–12886.

(31) Xue, B.; Wang, Q.; Zheng, J.; Li, S.; Zhang, S. *J. Memb. Sci.* **2020**, *601*, 117923.

(32) Zhang, D.; Xu, S.; Wan, R.; Yang, Y.; He, R. *J. Power Sources* **2022**, *517*, 230720.

(33) Sana, B.; Das, A.; Jana, T. *ACS Appl. Energy Mater.* **2022**, *5*, 3626–3637.

(34) Lin, C. X.; Huang, X. L.; Guo, D.; Zhang, Q. G.; Zhu, A. M.; Ye, M. L.; Liu, Q. L. *J. Mater. Chem. A* **2016**, *4*, 13938–13948.

(35) Arunkumar, I.; Kim, A. R.; Lee, S. H.; Yoo, D. J. *Int. J. Hydrogen Energy* **DOI:** 10.1016/j.ijhydene.2022.10.184.

(36) Basu, O.; Das, A.; Jana, T.; Das, S. K. *ACS Appl. Energy mater.* **DOI:** 10.1021/acsaem.2c02972.

(37) Mukherjee, N.; Das, A.; Jana, T. *ACS Appl. Nano Mater.* **2023,** *6*, 544-557.

(38) Mukhopadhyay, S.; Das, A.; Jana, T.; Das, S. K. *ACS Appl. Energy Mater.* **2020**, *3*, 7964–7977.

(39) Patel, R.; Chi, W. S.; Ahn, S. H.; Park, C. H.; Lee, H. K.; Kim, J. H. *Chem. Eng. J.* **2014**, *247*, 1–8.

(40) Degirmenci, M. *J. Macromol. Sci. - Pure Appl. Chem.* **2005**, *42*, 21–30.

(41) Yassin, F. A.; El Kady, F. Y.; Ahmed, H. S.; Mohamed, L. K.; Shaban, S. A.; Elfadaly, A. K. *Egypt. J. Pet.* **2015**, *24*, 103–111.

(42) Hermán, V.; Takacs, H.; Duclairoir, F.; Renault, O.; Tortai, J. H.; Viala, B. *RSC Adv.* **2015**, *5*,

51371–51381.

(43) Subramani, M.; Sepperumal, U. *Sch. Res. Libr. Ann. Biol. Res.* **2016**, *7*, 55–61.

(44) Li, C.; Wang, C.; Ji, Z.; Jiang, N.; Lin, W.; Li, D. *Eur. Polym. J.* **2019**, *113*, 404–410.

(45) Namvari, M.; Biswas, C. S.; Wang, Q.; Liang, W.; Stadler, F. J. *J. Colloid Interface Sci.* **2017**, *504*, 731–740.

(46) Jheng, L. C.; Tai, C. K.; Hsu, S. L. C.; Lin, B. Y.; Chen, L.; Wang, B. C.; Chiang, L. K.; Ko, W. C. *Int. J. Hydrogen Energy* **2017**, *42*, 5315–5326.

(47) Liu, M.; Wang, Z.; Mei, J.; Xu, J.; Xu, L.; Han, H.; Ni, H.; Wang, S. *J. Membr. Sci.* **2016,** *505*, 138-147.

(48) Henkensmeier, D.; Kim, H. J.; Lee, H. J.; Lee, D. H.; Oh, I. H.; Hong, S. A.; Nam, S. W.; Lim, T. H. *Macromol. Mater. Eng.* **2011**, *296*, 899–908.

(49) Priyangga, A.; Mumtazah, Z.; Junoh, H.; Jaafar, J.; Atmaja, L. *J. Membr. Sci. Res.* **2021**, *7*, 295–304.

(50) Muthumeenal, A.; Neelakandan, S.; Kanagaraj, P.; Nagendran, A. *Renew. Energy* **2016**, *86*, 922–929.

(51) Lin, B.; Dong, H.; Li, Y.; Si, Z.; Gu, F.; Yan, F. *Chem. Mater.* **2013**, *25*, 1858–1867.

(52) Abdi, Z. G.; Chiu, T. H.; Pan, Y. Z.; Chen, J. C. *React. Funct. Polym.* **2020**, *156*, 104719.

(53) Das, A.; Sana, B.; Bhattacharyya, R.; Chandra Ghosh, P.; Jana, T. *ACS Appl. Polym. Mater.* **2022**, *4*, 1523–1534.

(54) Wang, Y. J.; Qiao, J.; Baker, R.; Zhang, J. *Chem. Soc. Rev.* **2013**, *42*, 5768–5787.

(55) Maity, S.; Jana, T. *Macromolecules* **2013**, *46*, 6814–6823.

Summary & Conclusion

SUMMARY

This thesis entitled ***"Mixed Matrix Membranes of Polybenzimidazoles as Proton and Anion Exchange Membranes"*** describes the development of mixed matrix nanocomposite proton exchange membranes by incorporating MOFs, COFs, Polymer-*g*-GO in different loading wt% into the polybenzimidazole membrane supported matrix in order to develop superior quality hybrid mixed matrix membranes (MMMs) with super proton conductivity and mechanical durability. Under phosphoric acid doped conditions these MMMs acts as proton exchange membranes and exhibits superior proton conductivity, chemical and mechanical robustness. In another part of the thesis development of pyridine bridged polybenzimidazoles (PyPBIs) based ionically crosslinked anion exchange membranes (AAEMs) and polymer ionic liquid grafted graphene oxide (GOPIL) loaded PyPBI matrix supported robust hybrid AAEMs were prepared, where the main challenge is to make the AAEMs structurally and chemically stable in presence of harsh alkaline treatment (1 M – 5 M KOH, 80ºC, 500 h) for their superior application in alkaline fuel cell (AEMFC), alkaline water electrolysis and various other membrane based electrochemical applications. The thesis contains eight chapters, an introductory chapter, then materials & methods followed by five working chapters with corresponding appendix. The summary of the contents of each chapter is as follows.

CHAPTER 1

In this chapter a brief introduction of fuel cells (FC) is discussed along with various types of fuel cells, PEMFC working principle, PA doped PBI membranes proton conduction solution blending techniques for fabrication of mixed matrix PEMs have been discussed. In addition, in this chapter the AEMFC working principle have been discussed, properties of AEMs, different cationic sights and the associated degradation mechanisms of AAEMs have been discussed. Also, how to restrict degradation to improve the alkaline durability also have been discussed in details. Finally, this chapter describes the scope of the thesis work.

CHAPTER 2

The detailed experimental methods and characterization techniques of the MOFs, POPs, COFs, polymer-g-GO samples, Spiro-ionene polymers, and the fabricated nanocomposite proton exchange membranes (PEMs) and anion exchange membranes (AEMs) are discussed in the Chapter 2.

CHAPTER 3. *Fabricating a MOF Material with Polybenzimidazole into an Efficient Proton Exchange Membrane.*

Metal organic frameworks (MOFs) have received considerable importance as proton conducting materials in recent times. However, most of the MOFs lack the ability to form film, which limits their application. In the present work, polybenzimidazole (PBI) composite membranes have been prepared by loading post synthetically modified (PSM) UiO-66-NH_2 MOFs, denoted as **PSM 1** and **PSM 2** into the arylether-type polybenzimidazole (**OPBI**) polymer. The pristine **OPBI**, and MOF nanofiller loaded membranes were doped with phosphoric acid (PA) to prepare proton exchange membranes (PEMs). Use of thermally stable, hydrophilic MOFs resulted into enhanced proton conductivity, higher PA retention capacity and increased stability against oxidative degradation for the composite membrane than the pristine OPBI polymer. Interestingly, the order of proton conductivity of the PA doped MOF containing polymer membranes were exactly opposite to that of the used MOFs as such. The proton conductivities of the composite membranes (0.29 Scm^{-1} for **PSM 1**-10% and 0.308 Scm^{-1} for **PSM 2**-10% membranes at 160˚C, anhydrous environment) were notably higher than the conductivities of the constituents and also higher than most of the MOF based polymer supported membranes. Extensive interfacial H-bonding plays the most crucial role behind the enhanced proton conductivities of the PA doped MOF containing polymer membranes reported here. This work clearly demonstrates the benefits of using rationally designed **PSM 1** and **PSM 2** MOFs as nanofiller to prepare OPBI supported membranes that perform excellent proton conduction in a wide temperature range spanning up to 160 °C. This provides a generalized approach towards achieving an efficient proton conducting membrane for the fuel cell.

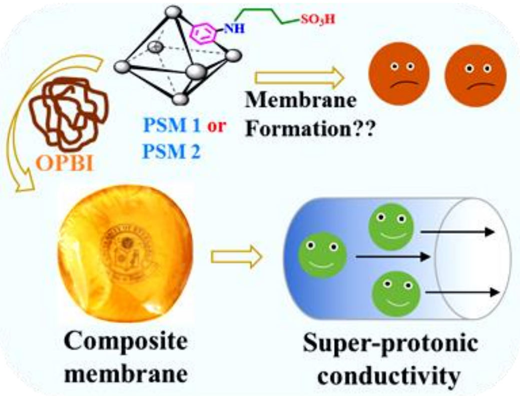

CHAPTER 4. *Covalent Organic Framework and Polybenzimidazole Composite Proton Exchange Membrane with superior Proton Conductivity.*

Fabrication and design of efficient proton conduction nanochannels within the solid electrolyte materials is pivotal and challenging to develop energy-efficient devices like proton exchange membrane fuel cells (PEMFCs). In this work, we have synthesized melamine-based Schiff base network type porous covalent organic framework (MCOF) and impregnated phosphoric acid (H_3PO_4) as electrolyte into the pores of the MCOF via vacuum assisted method. Unfortunately, stable film/membrane did not form from H_3PO_4 loaded MCOF (P@MCOF) and hence in order to resolve this, mixed matrix membranes were fabricated for the first time with the P@MCOF and [2,2′-(m-phenylene)-5,5′-benzimidazole] or m-PBI. Formation of acid base pair occurred in m-PBI-P@MCOF composite membrane between the P@MCOF and m-PBI driven by H-bonding interfacial interaction. Also, the acidic$-PO_3H_2$ functionalities in the pores of P@MCOF provides abundant sites for labile proton transport, which enables uninterrupted proton conduction ion channels with low energy barrier in the composite membranes. Furthermore, all the composite membranes were immersed and loaded with phosphoric acid (PA) to obtain proton exchange membranes (PEMs). Use of H_3PO_4 impregnated P@MCOF framework structures as nanofillers into the m-PBI membrane matrix resulted into superior proton conductivity, excellent thermal, thermo-mechanical and tensile stress-strain profile, improved acid (PA) holding efficiency and improved chemical stability of the m-PBI-P@MCOF membranes in comparison with the pristine m-PBI. The resulted proton conductivity of m-PBI-P@MCOF-10% membrane at 180°C is **0.309 S cm^{-1}**, a five-fold increment with respect to pristine m-PBI proton conductivity (**0.061 S cm^{-1}**) under the identical experimental condition. This work clearly illustrates the nature of H-bonded interfacial interaction between the P@MCOF nanofillers with the m-PBI, which can efficiently execute proton conduction. This will be the first report of COF as nanofillers into the PBI matrix for generation of superior proton conducting membranes.

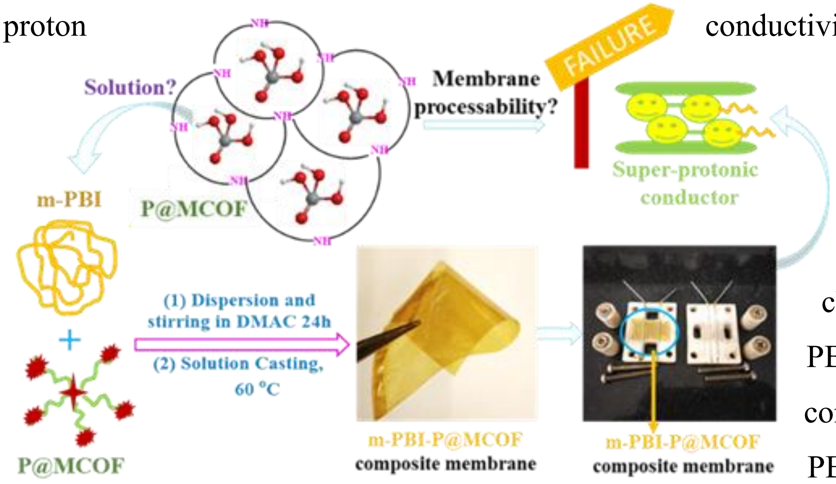

CHAPTER 5. *Polymer grafted Graphene Oxide/Polybenzimidazole Nanocomposites: Highly Efficient Proton Conducting Membranes.*

In this study, we have functionalized graphene oxide (GO) by growing polymer chains and then utilized polymer-*g*-GO as nanofiller with oxypolybenzimidazole (OPBI) to make highly efficient nanocomposite-based proton exchange membrane (PEM). Three different monomers, namely acrylamide (AAM), 2-acrylamido-2-methyl-1-propanesulfonic acid (AMPS) and 3-sulfopropyl acrylate potassium salt (SPAK) were polymerized on the activated GO surface *via* surface initiated reversible addition fragmentation chain transfer (RAFT) polymerization to obtain three different types of polymer-*g*-GO namely pAAM-*g*-GO, pAMPS-*g*-GO and pSPAK-*g*-GO. Furthermore, chain length of grafted polymers in each case were altered in order to study the effects of grafted polymer structure and chain length on the properties of nanocomposite PEM. The exfoliation of GO nanosheets after polymer grafting was confirmed by studying the surface morphology using various microscopic techniques. GPC and TGA analysis helped in measuring the chain length of grafted polymers and grafting density on the GO surface. Further, we have impregnated polymer-*g*-GO as nanofillers by varying loading wt% into the OPBI to fabricate mixed matrix membrane (MMM) which upon doping with phosphoric acid (PA) converted into mixed matrix PEM. The prepared nanocomposite PEM displayed exceptionally good thermal stability, significantly improved tensile properties, improved PA loading followed by superior proton conductivity and remarkable PA retention when exposed to saturated water vapour. When the 2.5 wt% pSPAK-*g*-GO (where pSPAK chain length is 19.6 kDa) mixed with OPBI, the resulting PEM showed remarkably high proton conductivity value of 0.327 S cm^{-1} at 160 °C, a significant 5-fold increment compared to pristine OPBI membrane (0.067 S cm^{-1} at 160°C). To the best of our knowledge, this will be the first report on utilization of polymer-*g*-GO in a polybenzimidazole supported matrix for high temperature PEM application.

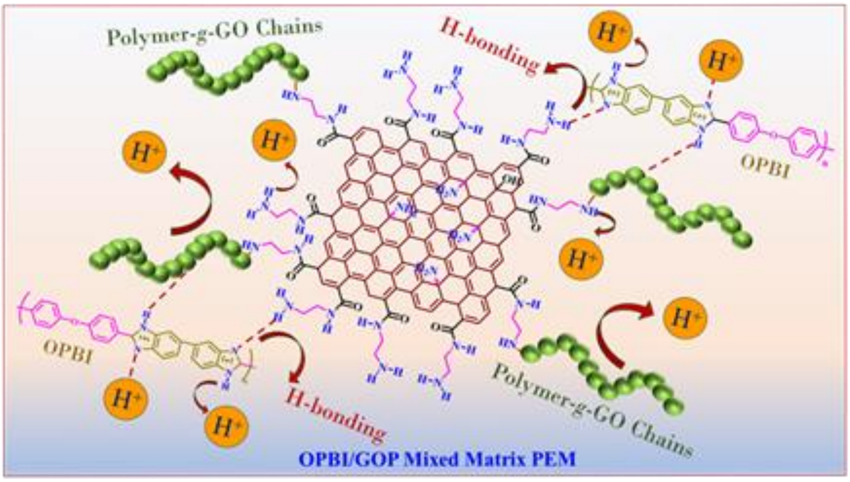

CHAPTER 6. *Crosslinked Alkaline Anion Exchange Membrane from N-Spirocyclic Quaternary Ammonium and Polybenzimidazole.*

In spite of significant research outcomes on alkaline anion exchange membrane (AAEM) in recent past, two major challenges namely hydroxide conductivity and alkaline stability of the polymer membrane yet to be resolved adequately. To address these challenges, in this work development of ionically crosslinked AAEMs has been achieved by blending pyridine bridged polybenzimidazole (PyPBI) and N-spirocyclic quaternary ammonium spiro ionene polymer (SP). Further, membranes were converted to porous membranes by adding different weight % of porogen in the membrane matrix and then leaching out the porogen followed by crosslinking. All the membranes (both non-porous and porous) were converted to hydroxide conducting AAEM by dipping into 1 M KOH solution and under this condition, a part of the -NH- groups of PyPBI was deprotonated to form ammonium-imidazolate complexes with SP which resulted ionic crosslinking in the AAEM. Hydroxide ion conductivity, one of the highest among the reported so far, of 129 mS/cm at 90 °C was obtained in case of S70P30-OH membrane which was a hydroxide form membrane obtained from the blend of 70 wt% SP and 30 wt% PyPBI and this membrane showed the highest KOH uptake among all other AAEMs prepared in this study. On the other hand, among the porous ionically crosslinked membranes S50P50-P25-OH (blends of 50 wt% SP and 50 wt% PyPBI with 25% porogen) membrane showed the highest hydroxide ion conductivity (117 mS/cm at 90 °C) among all the porous membrane studied here. All the ionically crosslinked AAEMs (both non porous and porous) displayed excellent alkaline stability and remains unaffected during alkaline stability test in 1M KOH at 80 °C as long as testing was carried out (960 h). Observing the exceptional stability in 1 M KOH of S50P50-OH and S50P50-P25-OH membranes, OH^- conductivity analysis and alkaline stability tests of these samples have been carried out even in 2 M KOH, and we found that these membranes retained ~80% of their OH^- conductivity value even after 500 h of alkaline treatment in 2 M KOH at 60 °C. Furthermore, membranes were found to be useful in alkaline water electrolysis and the best performance is shown by S70P30-OH membrane which displayed a current density of 100 mA cm^{-2} at 2.6 V. Overall as these recently developed membranes retained hydroxide conductivity, structural, thermal stability even after harsh alkaline treatment for longer period of time.

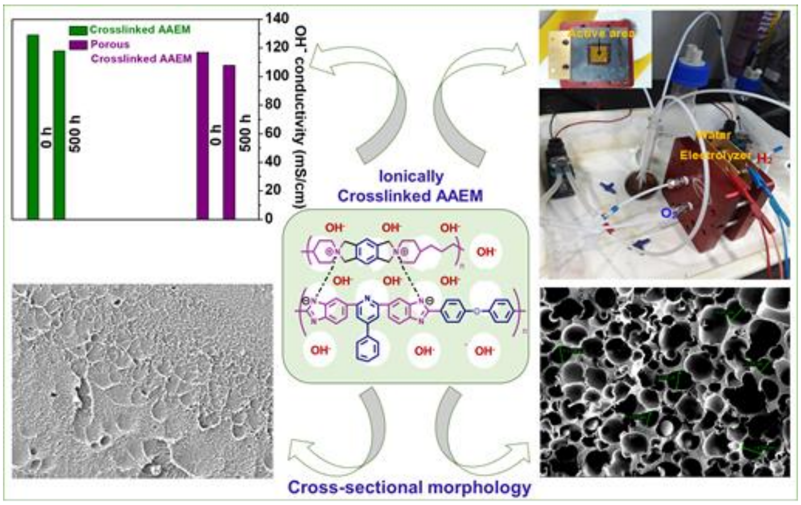

CHAPTER 7. *Multicationic Anion Exchange Membranes from Pyridine-bridged Polybenzimidazole and Polymer Ionic Liquid Grafted Graphene Oxide*

In this study, we have functionalized the surface of graphene oxide (GO) nanosheets by grafting polymeric ionic liquid (PIL) chains of verities of structures and then utilized PIL-g-GO materials as nanofiller with poly(butylated pyridinium benzimidazolium)iodide (PyPBI-BuI-OBA) in order to prepare hydroxide ion conducting mixed matrix alkaline anion exchange membranes with multiple ion exchange sites. Three different ionic liquid based monomers namely [2-(methacryloyloxy)ethyl]trimethylammonium chloride (MATMA), 1-vinylbutylimidazolium iodide [VImBu][I] and 1-(4-vinylbenzyl)-2-methyl-3-butylimidazolium iodide [VBImBu][I] were polymerized on the activated GO surface via surface initiated reversible addition fragmentation chain transfer process to obtain three different types of PIL grafted GO namely pMATMA-*g*-GO (GOPIL1), pVImBu-*g*-GO (GOPIL2) and PVBImBu-g-GO (GOPIL3). Exfoliation of GO sheets upon grafting of PIL was observed and were verified from the electron microscopic studies. The grafted PIL chains found to have narrow polydispersity (Đ) and precise control over the molecular weight confirming the grafting through SI-RAFT polymerization. Amount of polymer grafted on the GO surface were obtained from TGA analysis and strong dependence on polymer structure were found. The mixed matrix membranes (MMMs) were prepared by solution blending of PyPBI-BuI-OBA with varying loading of GOPIL materials and then MMMs were immersed in KOH in order to develop alkaline anion exchange membranes (AAEMs) containing of imidazolium, pyridinium quaternary ammonium ion exchange sites. Among all AAEMs with 2 wt% GOPIL2 and GPIL3 exhibited superior hydroxide ion conductivity of 137 mS/cm and 127 mS/cm, respectively at 80 °C. These mixed matrix AAEMs displayed no noticeable change under alkaline stability treatment for prolong time at elevated temperature in 1 M and 5 M KOH. The structural, chemical, thermal, mechanical and conducing properties of the membranes remained unaltered after alkaline treatment at elevated

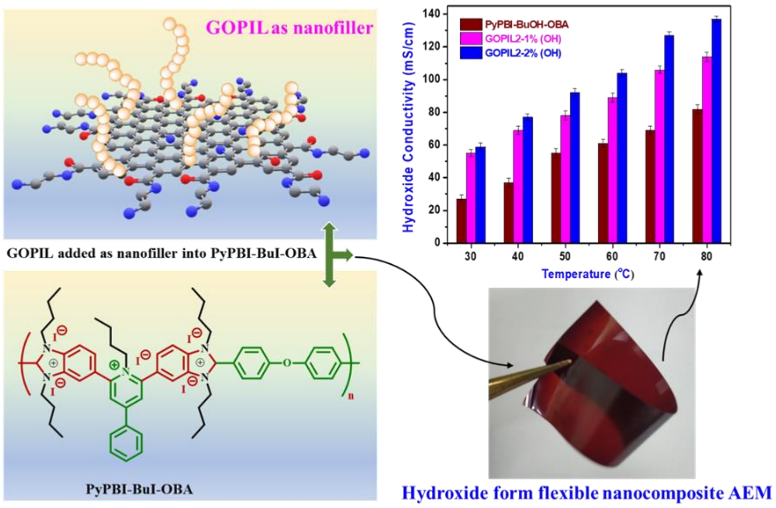

temperature. These AAEMs exhibited ~90% and ~80% retention of IEC and ~90% and ~70% retention in OH^- conductivity after alkaline treatment in 1 M KOH, at 60 °C for 500 h and in 5 M KOH, at 60°C for 375 h, respectively. To the best of our knowledge, this will be the first report on utilization of surface PIL grafted GO nanosheets in a AAEM.

Conclusion

- *Post synthetically modified UiO-66-NH_2 MOFs abbreviated as PSM 1 and PSM 2 has been incorporated into the aryl ether-type polybenzimidazole (**OPBI**) matrix via solution blending method in order to fabricate **OPBI@PSM1 or OPBI@PSM2** nanocomposite membranes with exceptional mechanical robustness, significantly increased PA doping level (PDL) followed by ultrahigh proton conductivity. Of note, the **PSM1-10%** membrane exhibits proton conductivity of **0.29 Scm^{-1}** and the **PSM2-10%** membrane resulted **0.308 Scm^{-1}**, at 160 °C under anhydrous condition.*

- *Melamine-based Schiff base network type porous covalent organic framework (COF), abbreviated as **MCOF** was prepared. After that impregnation of phosphoric acid (H_3PO_4) molecules into the microporous domains of the COFs structure were performed via vacuum assisted method (VAM) and abbreviated as **P@MCOF**. Then the COF based mixed matrix membranes (MMMs) were fabricated for the first time with the H_3PO_4 impregnated COFs **(P@MCOF)** and **[2,2'-(m-phenylene)-5,5'-benzimidazole]** abbreviated as (meta-PBI) or **m-PBI**. Impregnation of hydrophilic COF resulted huge improvement in the PDL of the membranes. As a result, proton conductivity of **m-PBI-P@MCOF-10%** membrane at 180°C was observed to be **0.309 S cm^{-1}**, a five-fold increment with respect to pristine **m-PBI** proton conductivity **(0.061 S cm^{-1})** under the identical experimental condition.*

- *Surface functionalization of the graphene oxide (GO) nanosheets via SI-RAFT technique was performed. Three different sets of monomers [acrylamide (AAM), 2-Acrylamido-2-methyl-1-propanesulfonic acid (AMPS) and 3-Sulfopropyl acrylate potassium salt (SPAK)] were utilized via SI-RAFT technique to grow covalently grafted polymer chains on the RAFT attached GO-BSPA surface to obtain three different types of polymers grafted GO **(PAAM-g-GO, PAMPS-g-GO** and **PSPAK-g-GO).** Also, the amount of each monomer was varied to graft two different chain length of each polymer in the GO surface. All together six different SI-RAFT modified polymers have been synthesized in the GO surface. Furthermore, impregnation of these three sets of **polymer-g-GO** materials as potential nanofillers (by varying wt% loading) into the poly(4,4' - diphenylether-5,5' - bibenzimidazole) (OPBI) membrane matrix to fabricate six different MMMs was performed. The **PSPAK-g-GO** loaded **GOP6-2.5%** membrane resulted remarkably high proton conductivity value of **0.327 S cm^{-1}** at 160 °C under PA doped condition.*

- *Development of ionically crosslinked **(ICL)** AAEMs has been performed by blending different wt% of pyridine bridged polybenzimidazole **(PyPBI)** and N-spirocyclic quaternary ammonium spiro ionene polymer **(SP).** Furthermore, membranes were converted to porous membranes by adding different weight % of porogen (DBP) into the membrane matrix and then leaching out the porogen followed by crosslinking. All together six different **ICL and porous ICL** membranes were fabricated. The **S70P30-OH** membrane displayed hydroxide conductivity of **129 mS/cm** at 90 °C (100 % RH),* *with a current density of 100 mA cm^{-2} at 2.6 V, when applied for the alkaline water electrolysis treatment.*

- ***Polymer-g-GOPILs** have been utilized as potential nanofiller (by varying wt% loading) into the **poly(alkylated pyridinium benzimidazolium) iodides [PyPBI-BuI-OBA]** membrane matrix in order to fabricate mixed matrix hybrid multicationic alkaline anion exchange membranes (AAEMs). Introduction of multicationic [pyridinium (Pyr), quaternary ammonium (QA), Imidazolium (Im)] functionalities together into the mixed matrix AAEMs resulted significantly high OH^- conductivity of the fabricated AAEMs. The **GOPIL2-2%(OH)** membrane exhibits OH^- conductivity of **137 mS/cm at 80 °C** (100% RH). Furthermore, AAEMs were found to be stable in presence of 1 M KOH at 60 °C for prolong 21 days (500 h), and at 5 M KOH, 60 °C for prolong 15 days (375 h) without notable changes.*

Future Scope

- *Several new mixed matrix PEM materials can be fabricated utilizing different types of MOFs, POPs, COFs, or Polymer-g-GO loaded into the different types of PBI matrix in order to develop superior proton conducting PEMs with much improved thermal and mechanical durability.*

- *All the PBI based mixed matrix nanocomposite PEMs developed in the current thesis should be tested for their fuel cell efficiency.*

- *Not only PBI but different types of other polymers (SPEEK, SPPO) can also be utilized as matrix supported PEMs for incorporating several nanofillers in order to develop various kinds of novel MMMs.*

- *In order to develop durable alkaline anion exchange membranes cross-linked AAEMs can be fabricated utilizing different structural variations of PyPBIs and alkylated PyPBIs.*

- *Several other mixed matrix AAEMs can also be developed utilizing various hydrophilic inorganic fillers in order to enhance the OH^- conduction into the AAEM network.*

- *All the synthesized blend and nanocomposite AAEMs in the current work and in the future work can be utilized in Alkaline anion exchange membrane fuel cells (AEMFC), alkaline water electrolysis treatment, Zn-Air batteries and various other electrochemical devices.*

APPENDIX 1 (for Chapter 3)

Fabricating a MOF Material with Polybenzimidazole into an Efficient Proton Exchange Membrane

Synthesis of UiO-66-NH_2

Synthesis of UiO-66-NH_2 was adapted from the works of Farha and coworkers.[1] UiO-66-NH_2 MOF was prepared using 5.4 mmol of $ZrCl_4$, which was dissolved in 50 mL DMF in presence of 10 ml conc. HCl by sonication. Then 6.75 mmol. BDC-NH_2 was added along with 100 mL of DMF. The reaction mixture was kept at 80 °C temperature for 24 hours in a sealed Teflon capped container. After slow cooling over a period of 6 hours the reaction mixture was filtered and washed. Next, the crude UiO-66-NH_2 was stirred in dry ethanol for 72 hours to remove absorbed DMF molecules prior to further characterizations.

Synthesis of PSM 1 and PSM 2 MOFs

According to our earlier literature reported procedure,[2] freshly prepared and purified UiO-66-NH_2 was treated with 1,3-Propane Sultone and 1,4-Butane Sultone separately in presence of DCM as solvent at room temperature for a period of 24 hours. UiO-66-NH_2 and sultone were taken in such a manner that the reaction mixture had sultone in equivalent amount to that of NH_2 groups of UiO-66-NH_2 framework. After 24 hours the post synthetically modified compounds **PSM 1** and **PSM 2** were filtered and repeatedly washed with DCM, water and ethanol to get rid of any unreacted and trapped sultone/ hydrolyzed sulfonic acid from the pores. Finally, the post synthetically modified compounds were subjected to further studies.

X-ray study (PXRD)

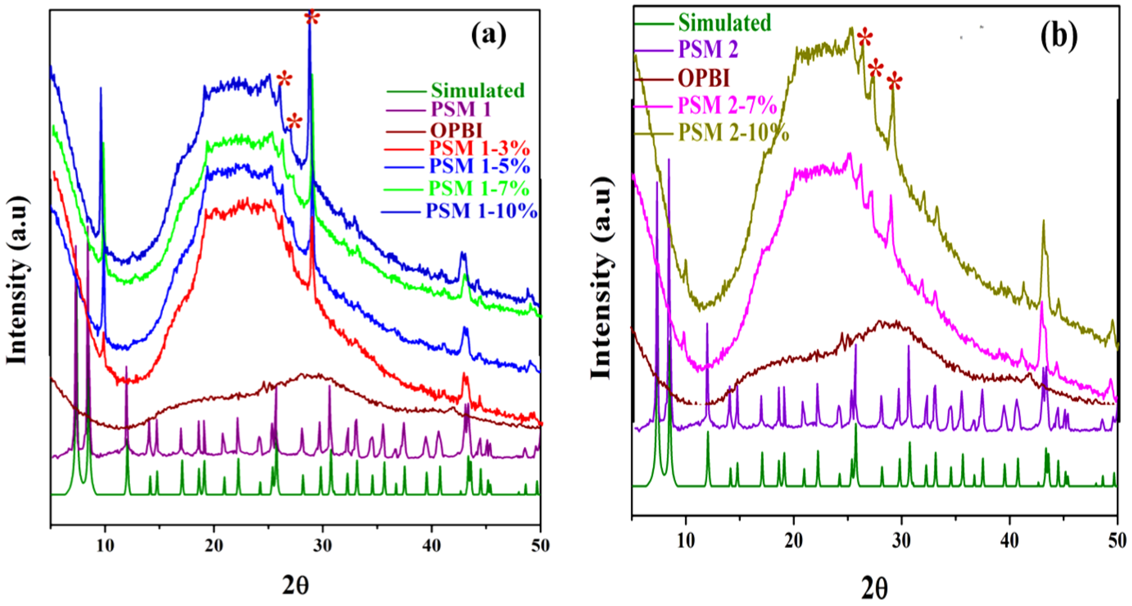

Figure A1.1. (a) PXRD pattern of PA doped **PSM 1** composite membranes with different filler loading. **(b)** PXRD pattern of PA doped **PSM 2** composite membranes with different filler loading.

FT-IR characterization

IR spectra of **PSM 1** and **PSM 2** have notable similarities.[2] The peak at 1565 cm^{-1} attributed to C=O bond of the carboxylate linkage is present in both **PSM 1** and **PSM 2**. Also, due to the presence of $-SO_3H$ group, two peaks near 1037 and 1143-1150 cm^{-1} obtained in both PSM 1 and **PSM 2**.[2] **OPBI** also exhibits three characterises picks at 3413, 3145 and 3060 cm^{-1} due to presence of non-hydrogen bonded free N-H, self- associated hydrogen bonded N-H groups and aromatic C-H stretching, respectively.[3]

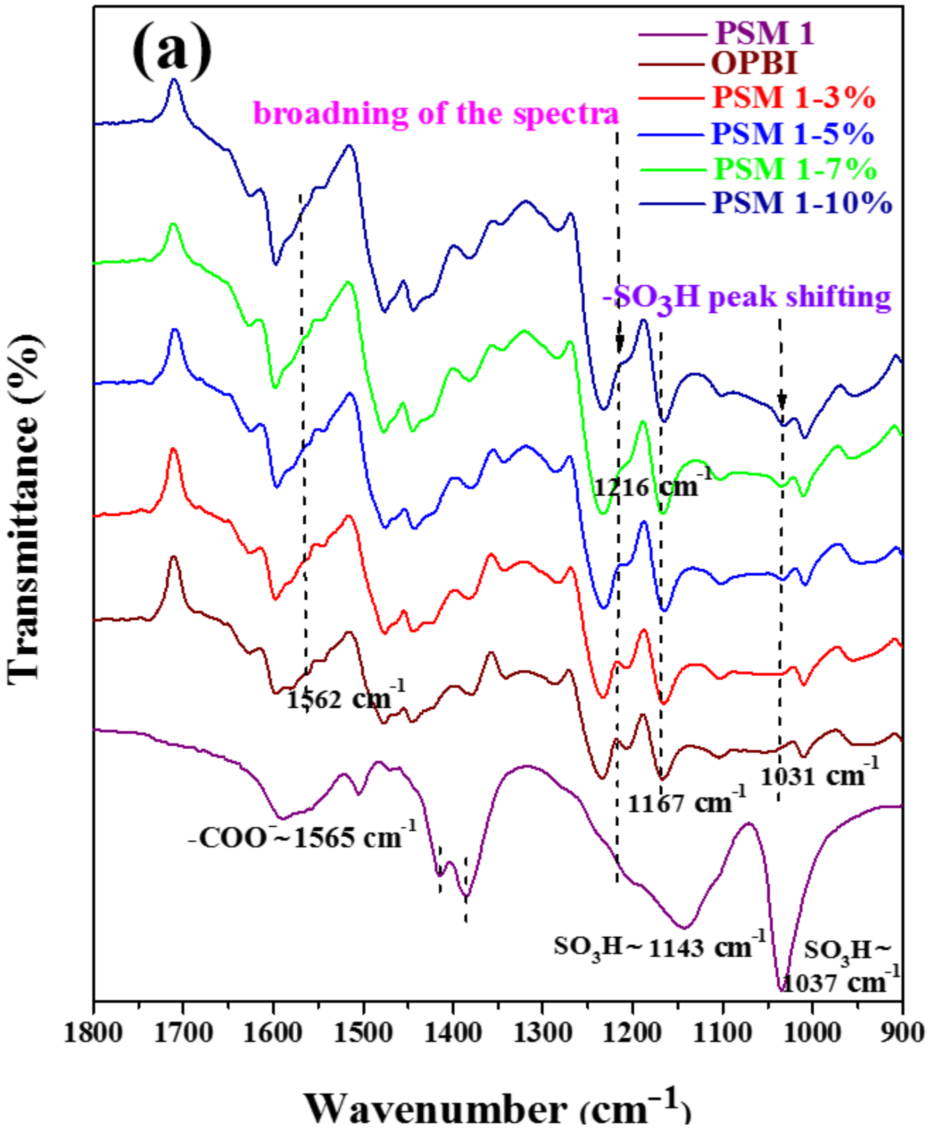

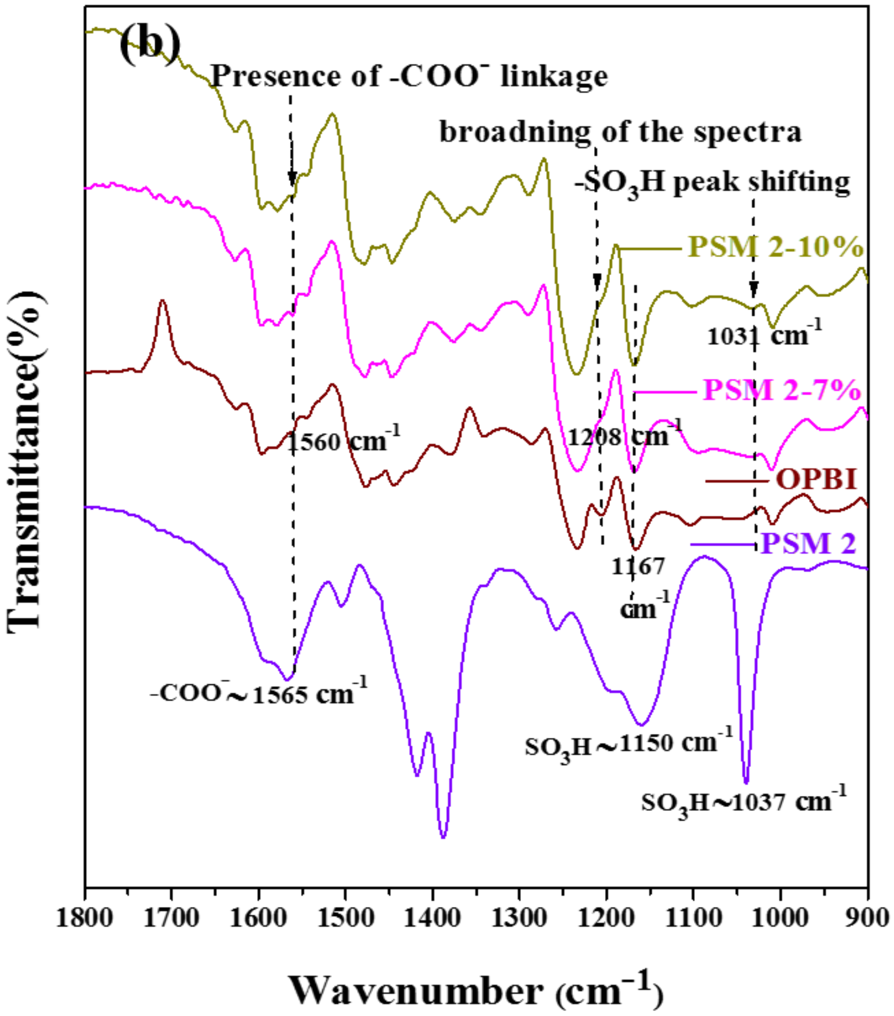

Figure A1.2. (a) FT-IR spectra of **PSM 1** composite membranes along with **OPBI** and **PSM 1**. **(b)** FT-IR spectra of **PSM 2** composite membranes along with **OPBI** and **PSM 2**.

Morphology study

Field Emission Scanning Electron Microscopy (FESEM)

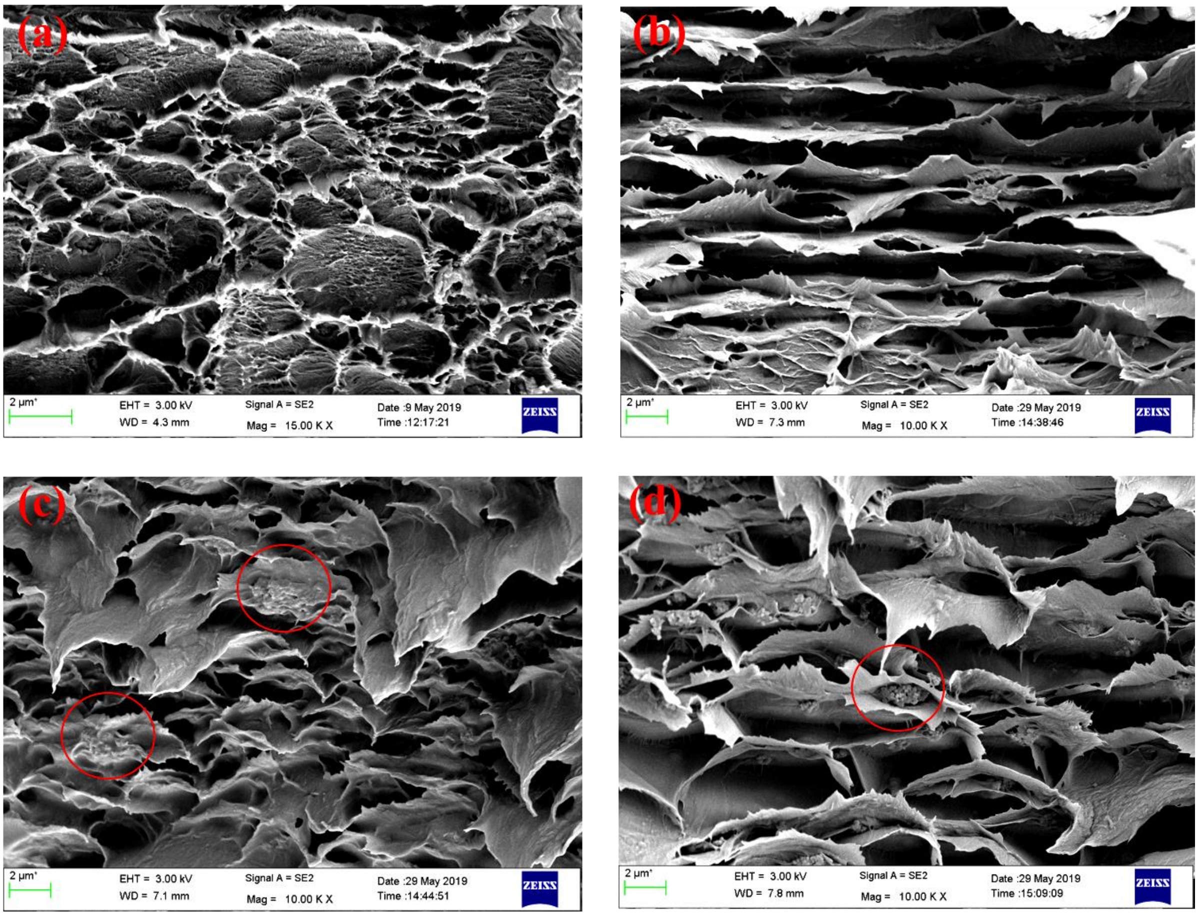

Figure A1.3. (a) FESEM cross-sectional image of **PSM 1**-3%, **(b) PSM 1**-5%, **(c) PSM 1**-7%, **(d) PSM 2**-7% (Nanofillers are scattered into the cross-section of composite membranes marked with red circle).

TEM analysis of composite membranes

The samples were prepared by placing a drop of formic acid dispersed **PSM 1**-10% and **PSM 2**-10% solution on carbon coated copper (200 mesh) grids. d values are obtained by analysis of different portion of the high resolution TEM images by generating Reduced FFT through Digital Micrograph software. Inverse FFT images were generated from Reduced FFT through Digital Micrograph software.

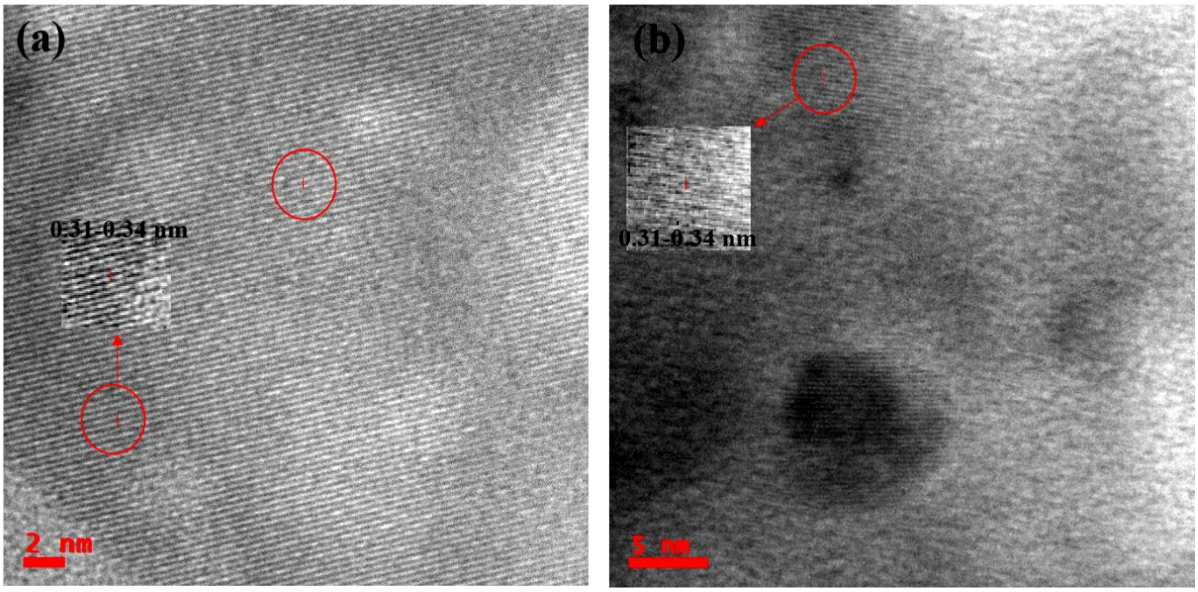

Figure A1.4. (a) High resolution TEM image of **PSM 1**-10% composite. (Inset: Inverse FFT image of **PSM 1**-10% composite obtained from Digital Micrograph software) **(b)** High resolution TEM image of **PSM 2**-10% composite. (Inset: Inverse FFT image of **PSM 2**-10% composite obtained from Digital Micrograph software).

Thermal study

We have kept all the samples at 100 °C isothermally for 30 minutes before measurement to evaporate excess water from the composite membranes and PSM MOFs. After that we have cooled the samples, allow them to achieve RT and start our measurement.

From TGA analysis of both **PSM 1** and **PSM 2** a steeper slope from 200 °C can be observed. This might be due to oxidation of the pendant alkyl chain and $-SO_3H$ group of these two compounds. In this region weight loss obtained for **PSM 2** is more than **PSM 1** due to presence of more '$-SO_3H$' group. Around 400°C significant weight loss was observed for both the MOFs due to structural changes in the framework structure as 'Zr-OH' functionalization of the metal node gets converted to 'Zr=O' while losing water. Complete disintegration of PSM framework takes place around 550°C. In higher temperature the residual compound completely converts into oxides as obtained from literature.[2]

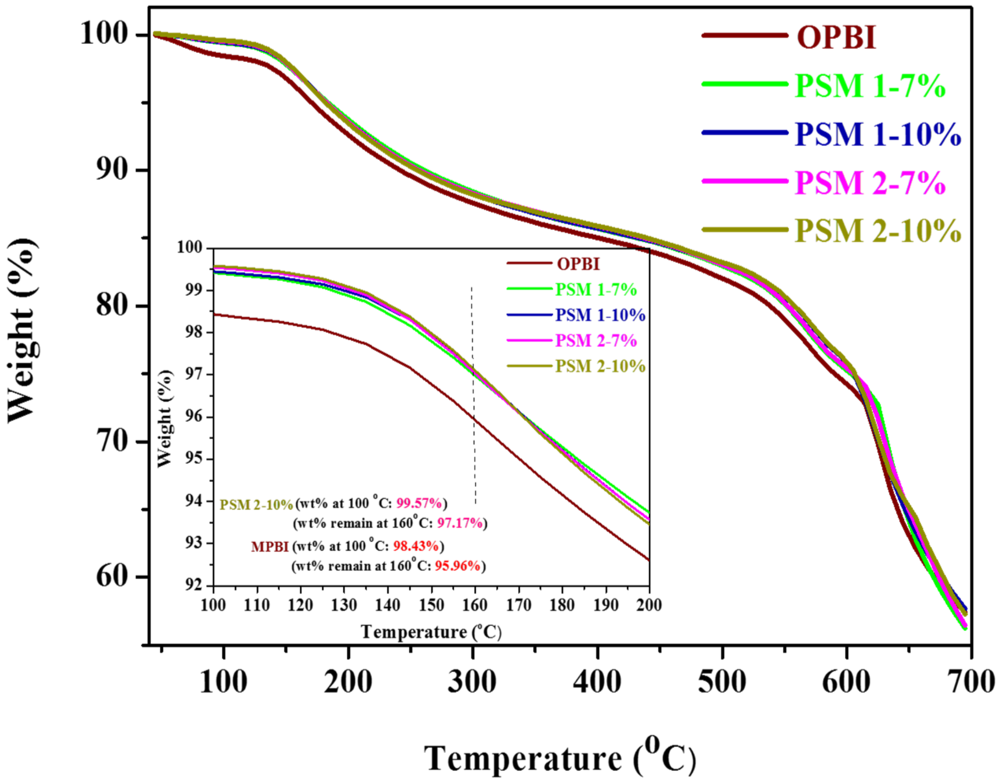

Figure A1.5. TGA of PA doped **PSM 1** and **PSM 2** composite membranes of above-mentioned loading (%) along with PA doped **OPBI**. (Inset- Zoomed TGA plot given in temperature range 100 °C- 200 °C)

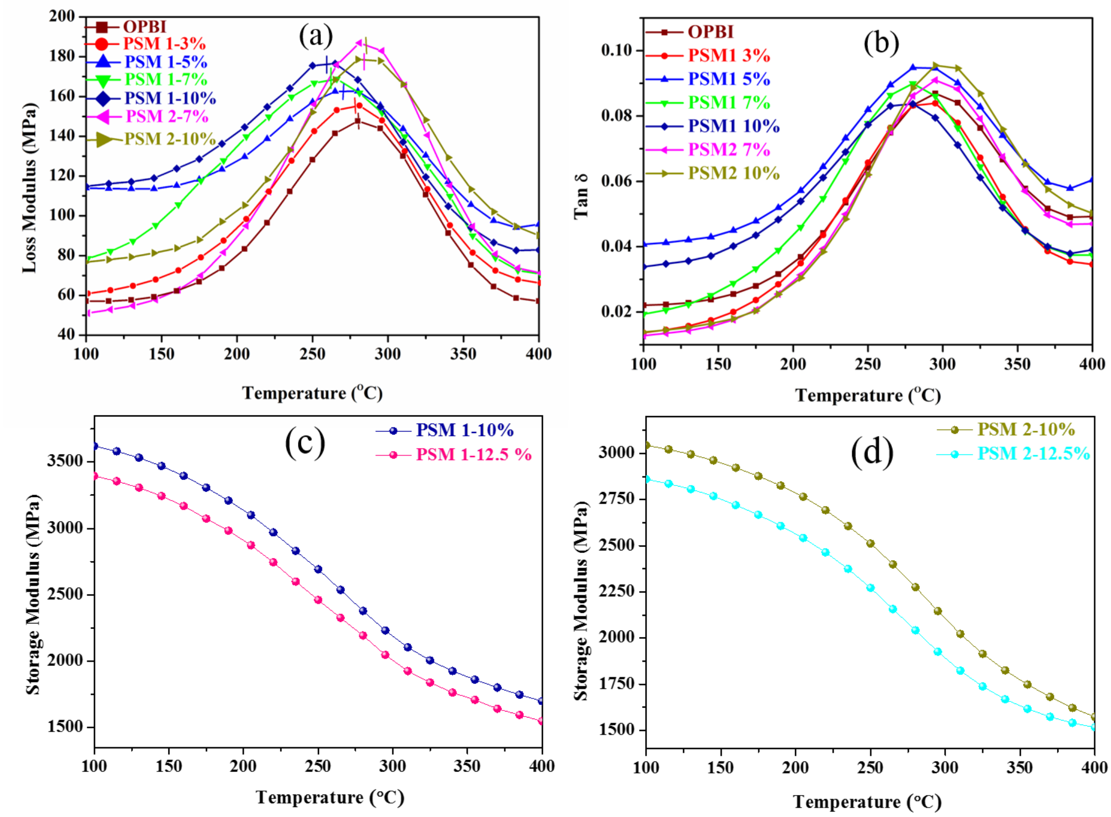

Figure A1.6. (a) Loss modulus and **(b)** tan δ plots of all the nanocomposite membranes of different filler loading along with pristine **OPBI**. (The T_g values are mentioned in **Table 2** of the main manuscript). **(c)** Storage modulus comparison of **PSM 1-**10% and **PSM 1-**12.5% membrane. **(d)** Storage modulus comparison of **PSM 2-**10% and **PSM 2-**12.5% membrane.

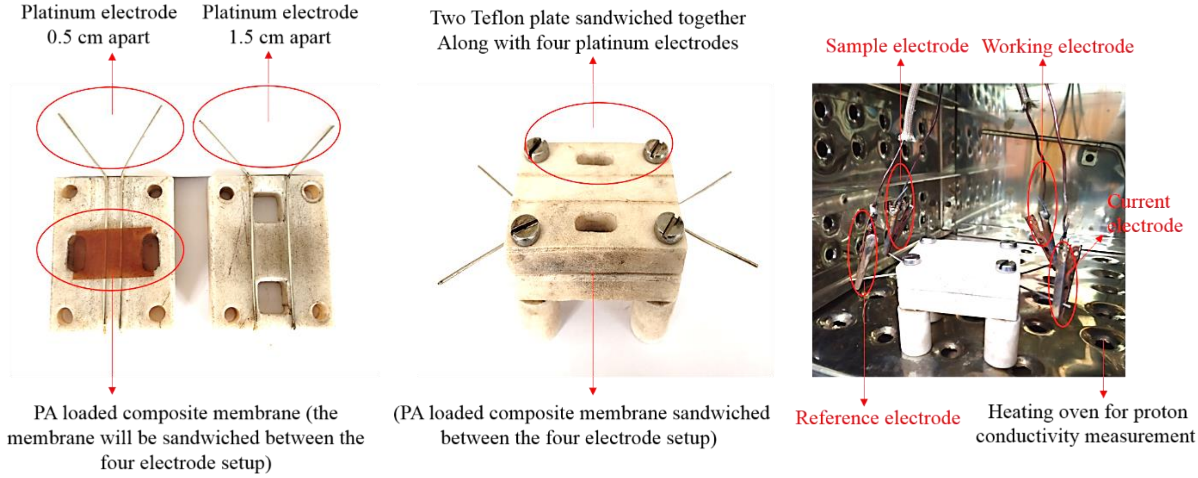

Figure A1.7. Pictorial representation of two Teflon plate with four platinum electrodes utilized in proton conductivity measurement.

Calculation of proton conductivity from Impedance spectra by fitting with equivalent circuit:

Equivalent circuit

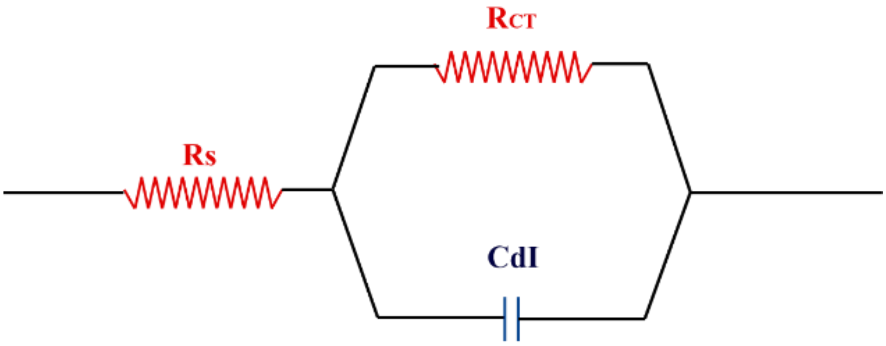

Impedance data were fitted to the most suitable equivalent circuit mentioned above with the help of EC-Lab software. The equivalent circuit is composed of three major components connected to each other in series. The bulk resistance (R_S) connected in series with a parallel combination of charge transfer resistance (R_{CT}) and a capacitor (CdI). Here R_S accounts for the bulk resistance of the membrane while R_{CT} represents the charge transfer resistance existing between the electrodes and the membrane electrolyte. Here, it should be noted that, charge transfer resistance R_{CT} is not associated with the conductivity of the electrolyte. Instead R_S is the crucial factor which quantifies the resistance of the bulk electrolyte. The bulk resistance of electrolyte i.e., R_S is of our primary interest as it represents conductivity of the membrane. R_S depends on (a) intrinsic conductivity of the PA loaded membrane sample (b) thickness of the membrane and (c) area of cross section of the membrane. Thus, to determine the proton conductivity of the membrane sample from the R_S value both of the other two factors (*i.e.*, area of cross section and thickness of membrane) should be taken into consideration.

Here we provide the values of R_S, and R_{CT} by fitting the experimentally obtained data points along the curve generated by the equivalent circuit mentioned above. The accuracy of the fitting was measured by the factor χ^2.

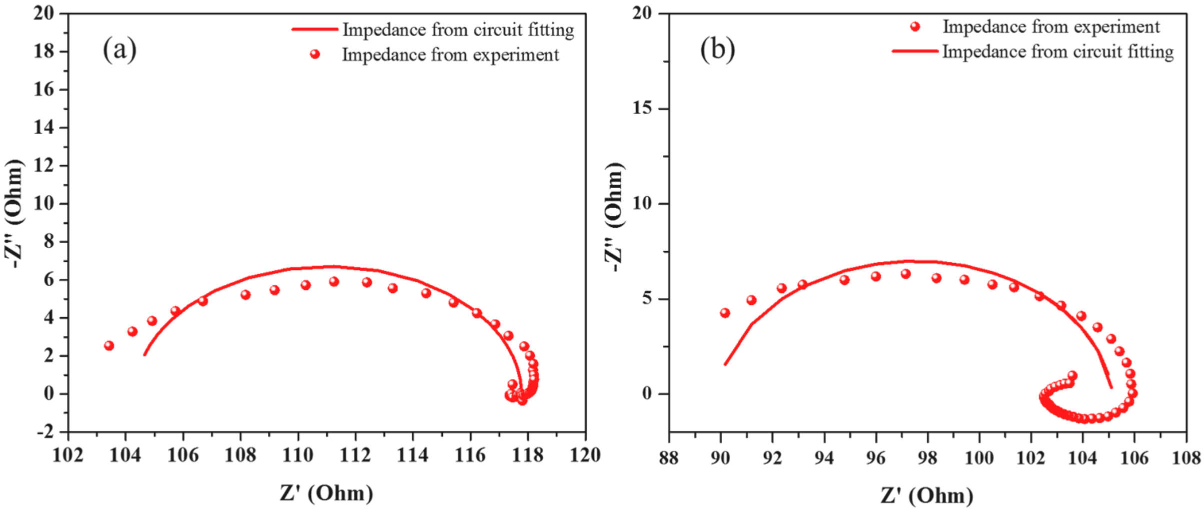

Figure A1.8. (a) Nyquist plot of **PSM 1-10%** and **(b) PSM 2-10%** composite membrane after equivalent circuit fitting at 160 °C.

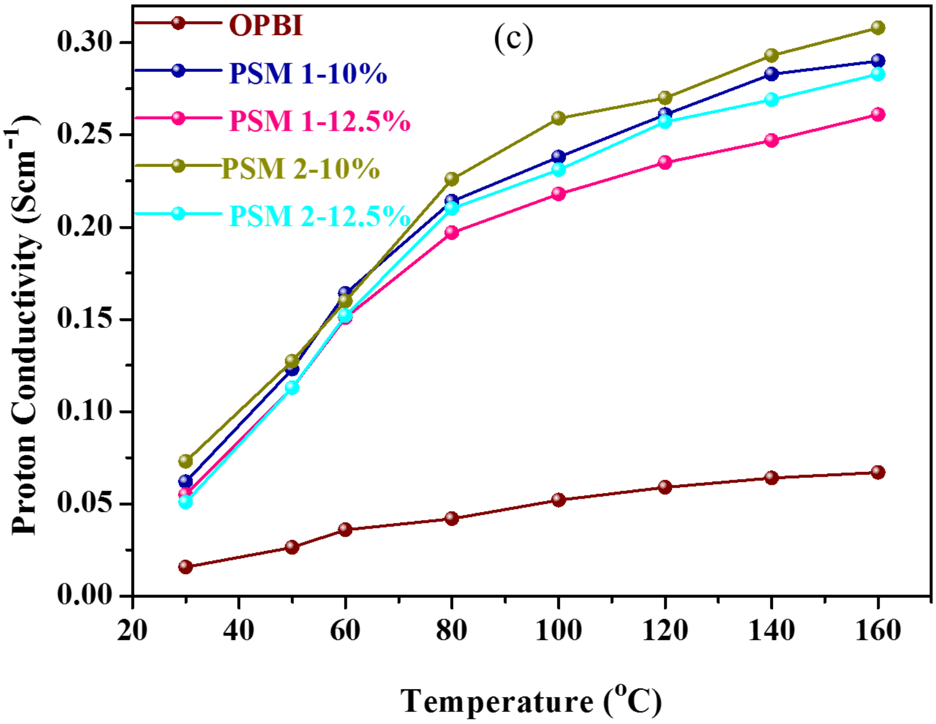

Figure A1.8. (c) Proton conductivity comparison of **PSM 1**-10% and **PSM 2**-10% membranes with **PSM 1-12.5%** and **PSM 2-12.5%** membranes under identical experimental condition.

Table A1.1. Fitting parameters to determine proton conductivity of **PSM 1-10%** composite membrane in various temperatures**: Membrane thickness = 0.011 cm** or **0.11 mm.**

Temperature (° C)	**Value of Rs (Ohm)**	**Conductivity (Scm^{-1})**	**χ^2 value**
30 °C	493.85	0.061	0.1996
50 °C	245.5	0.123	0.003737
60 °C	184.54	0.164	0.0011313
80 °C	141.54	0.214	0.00090132
100 °C	127.26	0.238	0.0015824
120 °C	116.08	0.261	0.00087793
140 °C	106.71	0.284	0.001123
160 °C	104.33	0.290	0.0013447

Table A1.2. Fitting parameters to determine proton conductivity of **PSM 2-10%** composite membrane in various temperatures**: Membrane thickness =0.012 cm** or **0.12 mm.**

Temperature (° C)	**Value of Rs (Ohm)**	**Conductivity (Scm^{-1})**	**χ^2 value**
30 °C	379.92	0.0731	0.00752
50 °C	218.12	0.127	0.34196
60 °C	174.32	0.160	0.18017
80 °C	122.38	0.226	0.055859
100 °C	107.1	0.259	0.032464
120 °C	102.68	0.270	0.0049207
140 °C	94.64	0.293	0.00251
160 °C	90.16	0.308	0.0090341

Table A1.3. Fitting parameters to determine proton conductivity of **PSM 1** and **PSM 2** composite membranes along with **OPBI** and **UiO-66-NH$_2$ 10%** membrane at **160 °C**.

Sample	Value of Rs (Ohm) at 160 °C	Thickness (cm)	Conductivity (Scm^{-1}) at 160 °C	χ^2 value
OPBI	411.19	0.012	0.067	0.0080366
UiO-66-NH$_2$ 10%	218.19	0.011	0.138	0.0051513
PSM 1-3%	137.53	0.012	0.202	0.0062789
PSM 1-5%	119.18	0.012	0.233	0.0023559
PSM 1-7%	104.5	0.012	0.266	0.006487
PSM 2-7%	100.3	0.012	0.277	0.0063149

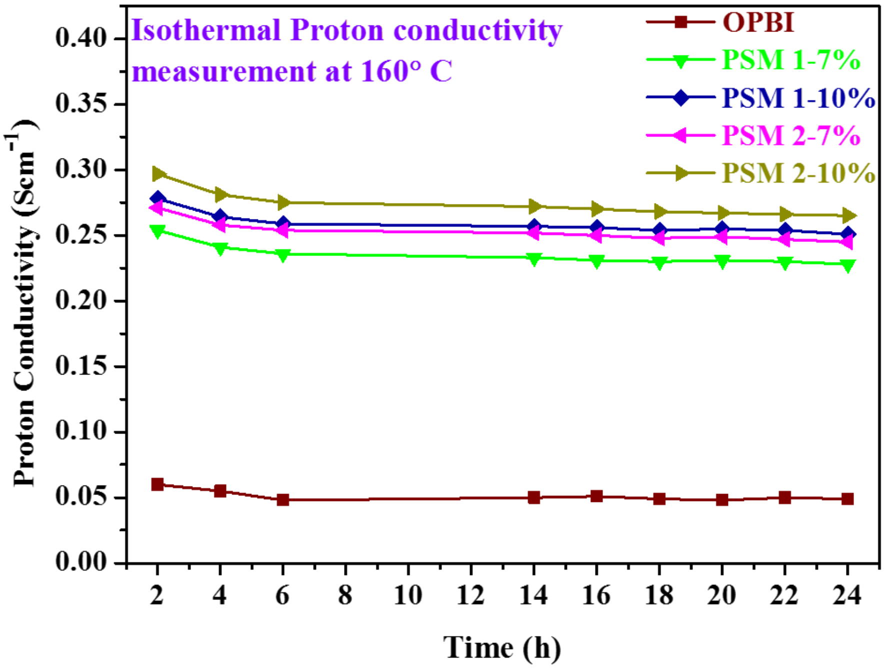

Figure A1.9. Isothermal proton conductivity of **OPBI** nanocomposite membranes at 160 °C for 24 h.

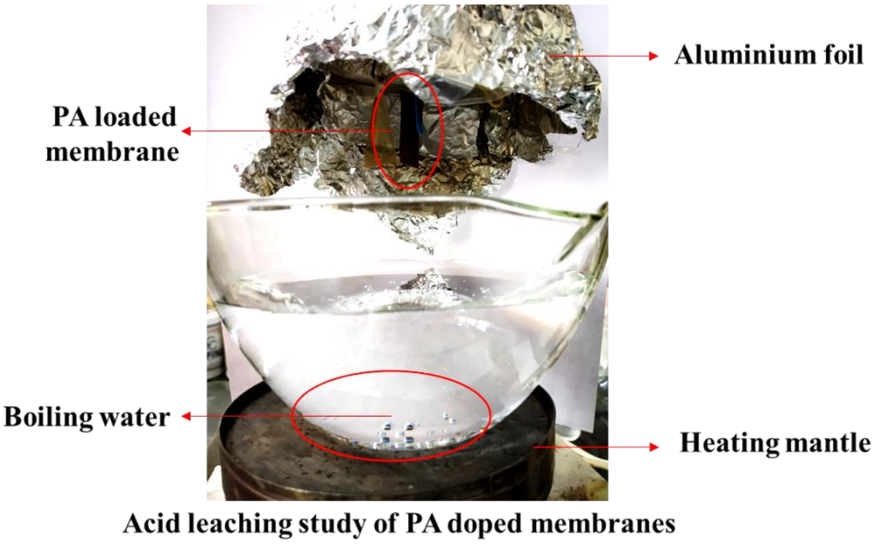

Figure A1.10. Acid leaching study of PA loaded **OPBI** composite membranes.

Table A1.4. Recent reports of MOF based polymer composite membranes

Polymer	**MOF (loading) (%)**	**Additive**	**Proton conductivity value (Scm^{-1})**	**Temperature (°C) and Relative Humidity (%)**	**Ref.**
Nafion	MIL-101 (12 wt%)	Phytic acid	0.228	100 °C and 100% RH	4
Nafion	ZIF-8 (1 wt%)	GO	0.28	120 °C and 40% RH	5
Nafion	HKUST-1 (2.5 wt%)	Phosphoric acid	0.018	25 °C and 100% RH	6
Nafion	UiO-66-NH$_2$ (1 wt%)	GO	3.4×10^{-3}	120 °C and Anhydrous	7
Nafion	2:1 UiO-66-NH$_2$: UiO-66- SO$_3$H (0.6 wt%)		0.256	90 °C and 95% RH	8
Nafion	UiO-66-SO$_3$H (2 wt%)		0.17	80 °C and 95% RH	9
SPEEK	ZIF-8 (2.5 wt%)		0.025	120 °C and 30% RH	10

SPEEK	MIL-101-SO$_3$H (7.5 wt%)		0.306	79 °C and 100% RH	11
SPEEK	NH$_2$-MIL-53 (5 wt%)		0.017	80 °C and 100% RH	12
PVP	chiral MOF (50 wt%)		3.2×10^{-4}	25 °C and 97% RH	13
PVA	ZIF-8 (5 wt%)	PAMS	0.134	80 °C and 100% RH	14
PVPA	ZIF-8 (25 wt%)		3.2×10^{-3}	140 °C and anhydrous	15
PVDF	MOF-808		7.3×10^{-3}	42 °C and 99% RH	16
PVDF	MOF-801 (60 wt%)		1.84×10^{-3}	52 °C and 95% RH	17
PBI	ZIF-8 (5 wt%)	Phosphoric acid	3.1×10^{-3}	120 °C and anhydrous	18
PBI	ZIF-67 (5 wt%)	Phosphoric acid	0.042	120 °C and anhydrous	18
PBI	1:1 ZIF-8: ZIF-67 (5 wt%)	Phosphoric acid	0.092	120 °C and anhydrous	18
SPPO	Fe-MIL-101-NH$_2$ (6%)		0.25	90 °C	19
Chitosan	MIL-101-SO$_3$H (7.5 wt%)		0.095	100 °C and 100% RH	20
PEI	ZIF-8 (20 wt%)	TBA	1.2×10^{-4}	anhydrous	21
PEI	ZIF-67 (20 wt%)	TBA	0.8×10^{-4}	anhydrous	21
PEI	1:1 ZIF-8: ZIF-67 (20 wt%)	TBA	0.8×10^{-5}	anhydrous	21
DNA	ZIF-8 (20 wt%)		3.4×10^{-4}	25 °C and 100% RH	22
OPBI	**PSM 1-10%**	**Phosphoric acid**	**0.290**	**160 °C and anhydrous**	**This work**
OPBI	**PSM 2-10%**	**Phosphoric acid**	**0.308**	**160 °C and anhydrous**	**This work**

References

(1) Katz, M. J.; Brown, Z. J.; Colón, Y. J.; Siu, P. W.; Scheidt, K. A.; Snurr, R. Q.; Hupp, J. T.; Farha, O. K. *Chem. Commun.* **2013**, *49*, 9449–9451.

(2) Mukhopadhyay, S.; Debgupta, J.; Singh, C.; Sarkar, R.; Basu, O.; Das, S. K. *ACS Appl. Mater. Interfaces* **2019**, *11*, 13423–13432.

(3) Singha, S.; Jana, T. *ACS Appl. Mater. Interfaces* **2014**, *6*, 21286–21296.

(4) Li, Z.; He, G.; Zhang, B.; Cao, Y.; Wu, H.; Jiang, Z.; Tiantian, Z. *ACS Appl. Mater. Interfaces* **2014**, *6*, 9799–9807.

(5) Yang, L.; Tang, B.; Wu, P. *J. Mater. Chem. A* **2015**, *3*, 15838–15842.

(6) Kim, H. J.; Talukdar, K.; Choi, S. J. *J. Nanoparticle Res.* **2016**, *18*, 47.

(7) Sun, H.; Tang, B.; Wu, P. *ACS Appl. Mater. Interfaces* **2017**, *9*, 26077–26087.

(8) Rao, Z.; Tang, B.; Wu, P. *ACS Appl. Mater. Interfaces* **2017**, *9*, 22597–22603.

(9) Donnadio, A.; Narducci, R.; Casciola, M.; Marmottini, F.; D'Amato, R.; Jazestani, M.; Chiniforoshan, H.; Costantino, F. *ACS Appl. Mater. Interfaces* **2017**, *9*, 42239–42246.

(10) Sun, H.; Tang, B.; Wu, P. *ACS Appl. Mater. Interfaces* **2017**, *9*, 35075–35085.

(11) Li, Z.; He, G.; Zhao, Y.; Cao, Y.; Wu, H.; Li, Y.; Jiang, Z. *J. Power Sources* **2014**, *262*, 372–379.

(12) Ahmadian-Alam, L.; Mahdavi, H. *Renew. Energy* **2018**, *126*, 630–639.

(13) Liang, X.; Zhang, F.; Feng, W.; Zou, X.; Zhao, C.; Na, H.; Liu, C.; Sun, F.; Zhu, G. *Chem. Sci.* **2013**, *4*, 983–992.

(14) Erkartal, M.; Usta, H.; Citir, M.; Sen, U. *J. Membr. Sci.* **2016**, *499*, 156–163.

(15) Sen, U.; Erkartal, M.; Kung, C. W.; Ramani, V.; Hupp, J. T.; Farha, O. K. *ACS Appl. Mater. Interfaces* **2016**, *8*, 23015–23021.

(16) Luo, H. Bin; Wang, M.; Liu, S. X.; Xue, C.; Tian, Z. F.; Zou, Y.; Ren, X. M. *Inorg. Chem.* **2017**, *56*, 4169–4175.

(17) Zhang, J.; Bai, H. J.; Ren, Q.; Luo, H. Bin; Ren, X. M.; Tian, Z. F.; Lu, S. *ACS Appl. Mater. Interfaces* **2018**, *10*, 28656–28663.

(18) Escorihuela, J.; Sahuquillo, Ó.; García-Bernabé, A.; Giménez, E.; Compañ, V. *Nanomaterials* **2018**, *8*, 775.

(19) Wu, B.; Lin, X.; Ge. L.; Wu, L.; Xu, T. *Chem. Commun.* **2013**, *49*, 143-145.

(20) Fadzallah, I. A.; Majid, S. R.; Careem, M. A.; Arof, A. K. *J. Membr. Sci.* **2014**, *463*, 65–72.

(21) Vega, J.; Andrio, A.; Lemus, A. A.; del Castillo, L. F.; Compañ, V. *Electrochim. Acta* **2017**, *258*, 153–166.

(22) Guo, Y.; Jiang, Z.; Ying, W.; Chen, L.; Liu, Y.; Wang, X.; Jiang, Z. J.; Chen, B.; Peng, X. *Adv. Mater.* **2018**, *30*, 1705155.

APPENDIX 2 (for Chapter 4)

Covalent Organic Framework and Polybenzimidazole Composite Proton Exchange Membrane with superior Proton Conductivity

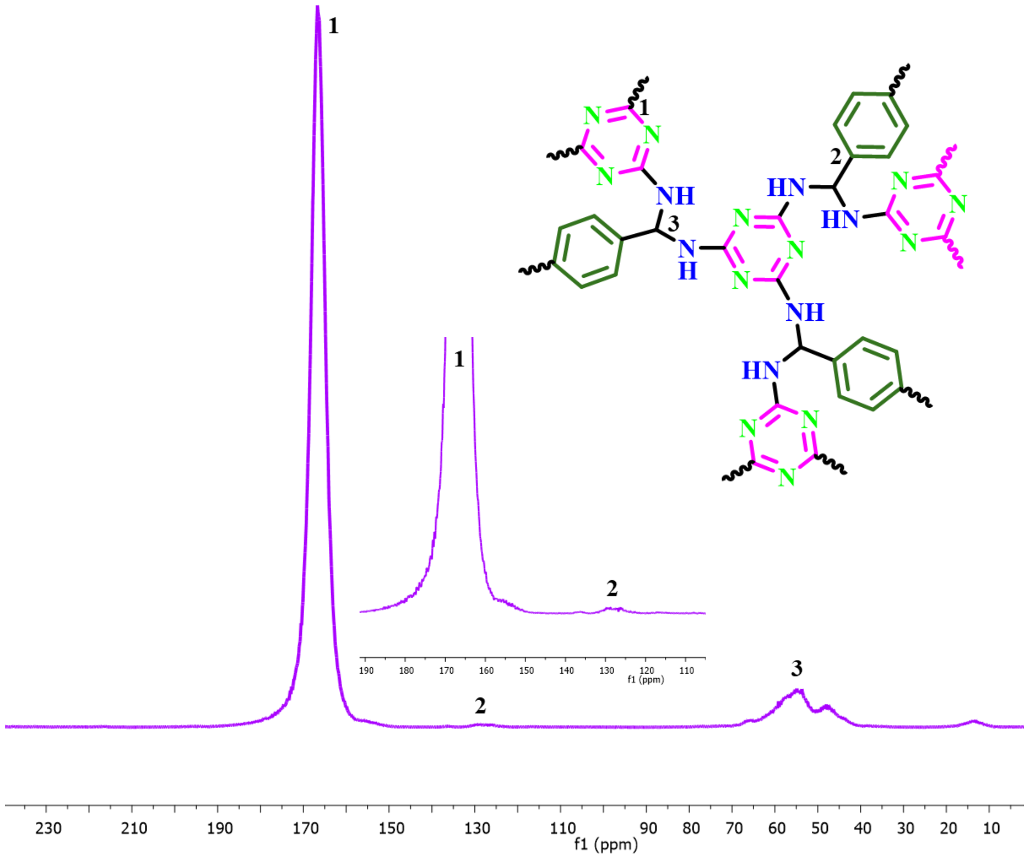

Figure A2.1. Solid state ^{13}C CP-MAS NMR spectra of MCOF.

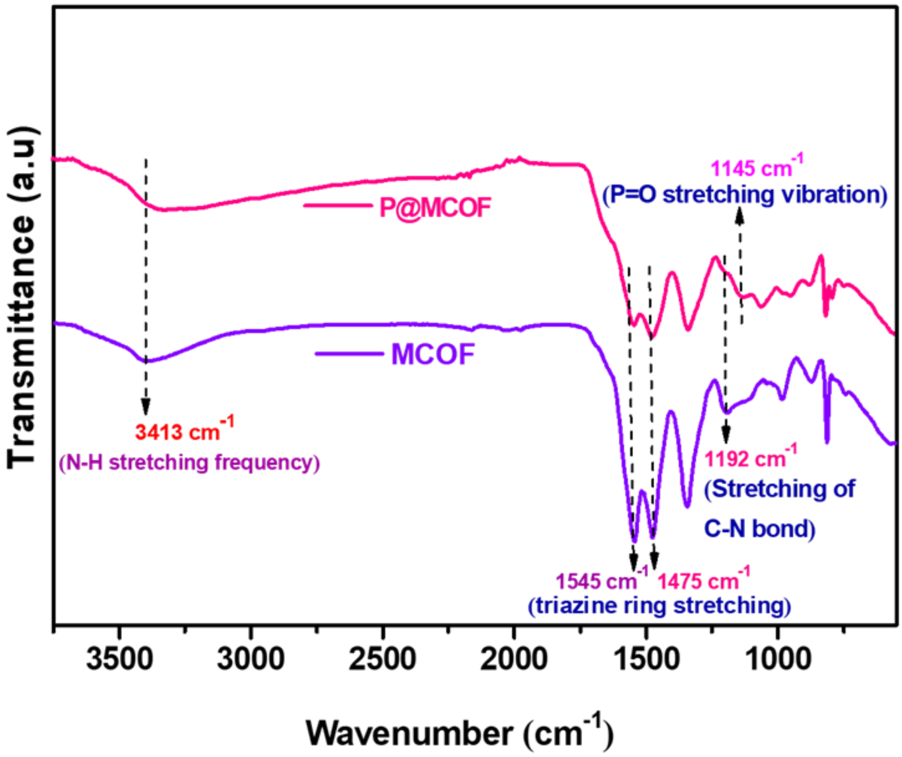

Figure A2.2. FT-IR spectra of MCOF & P@MCOF.

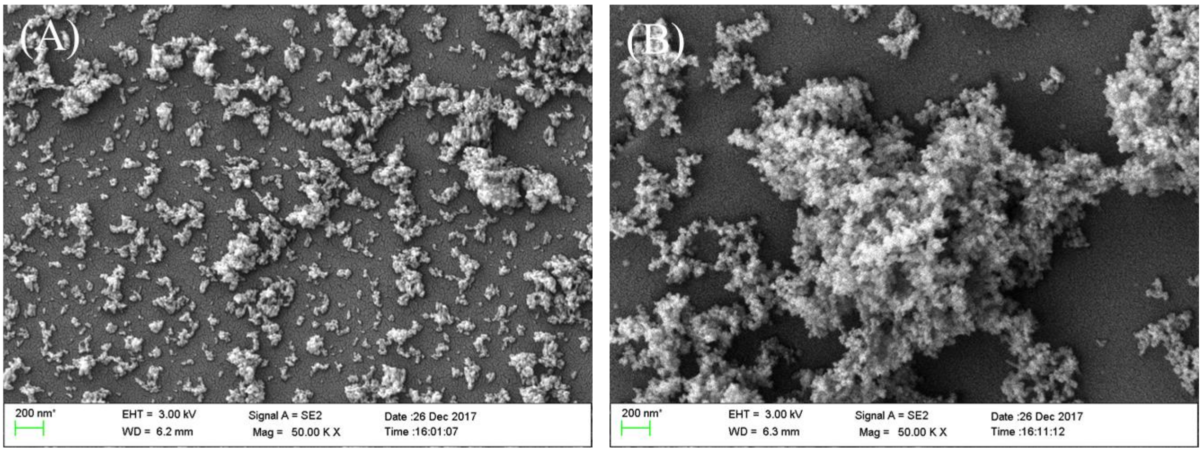

Figure A2.3. (A) FESEM image of MCOF, **(B)** FESEM images of P@MCOF.

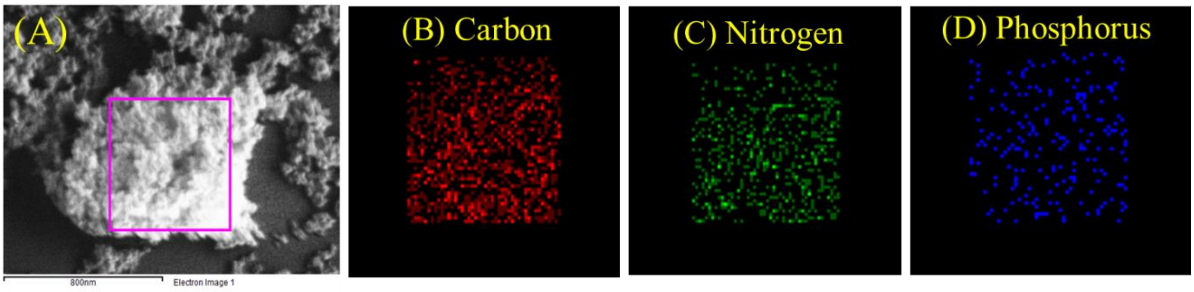

Figure A2.4 (A-D). EDX analysis and elemental mapping of P@MCOF obtained from FESEM. [EDX elemental mapping shows that, Carbon (C), Nitrogen (N) and Phosphorus (P) is scattered all over the matrix, presence of (P) detected in elemental mapping].

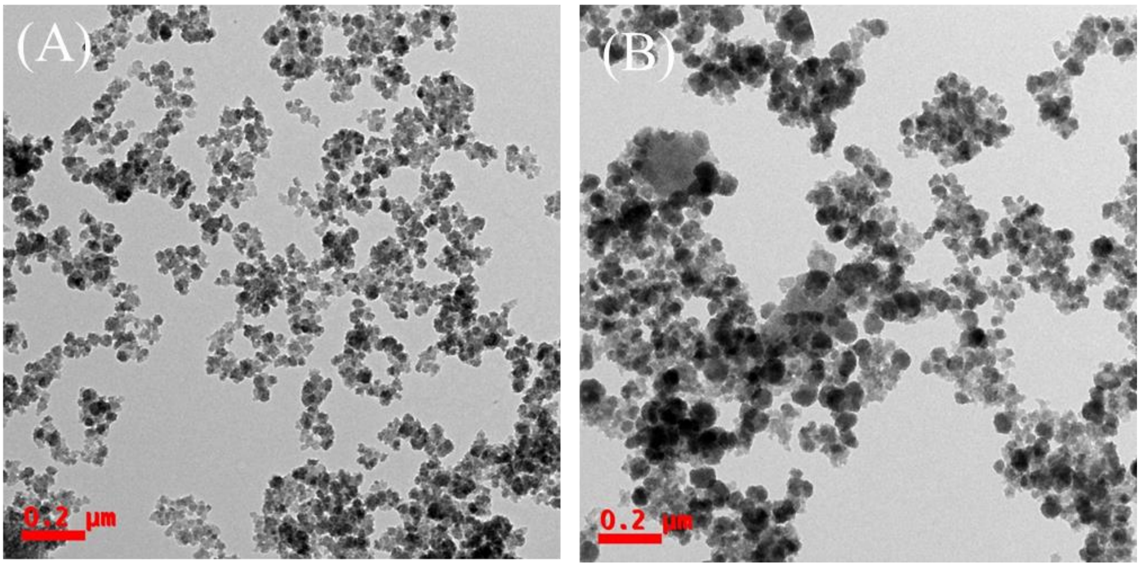

Figure A2.5. TEM images of MCOF **(A)** and P@MCOF **(B)**.

Table A2.1. ICP-OES analysis of P@MCOF

Sample Particulars : **P@MCOF**

Qty. Received : 10 mg X 1 No Vial

Test Parameters : Phosphrous as P

Date of Receipt of Sample : 30/10/2020
Date of completion of analysis : 03/11/2020

Date of Starting of Analysis : 02/11/2020

SAMPLE TESTED AS RECEIVED

TEST RESULTS

S.No.	**Parameters**	**Units**	**Results**
1	Phosphrous as P	% by mass	3.97

Instrument Used: ICP-OES, Varian 720-ES

NOTE : This report and results relate only to the sample / items tested.

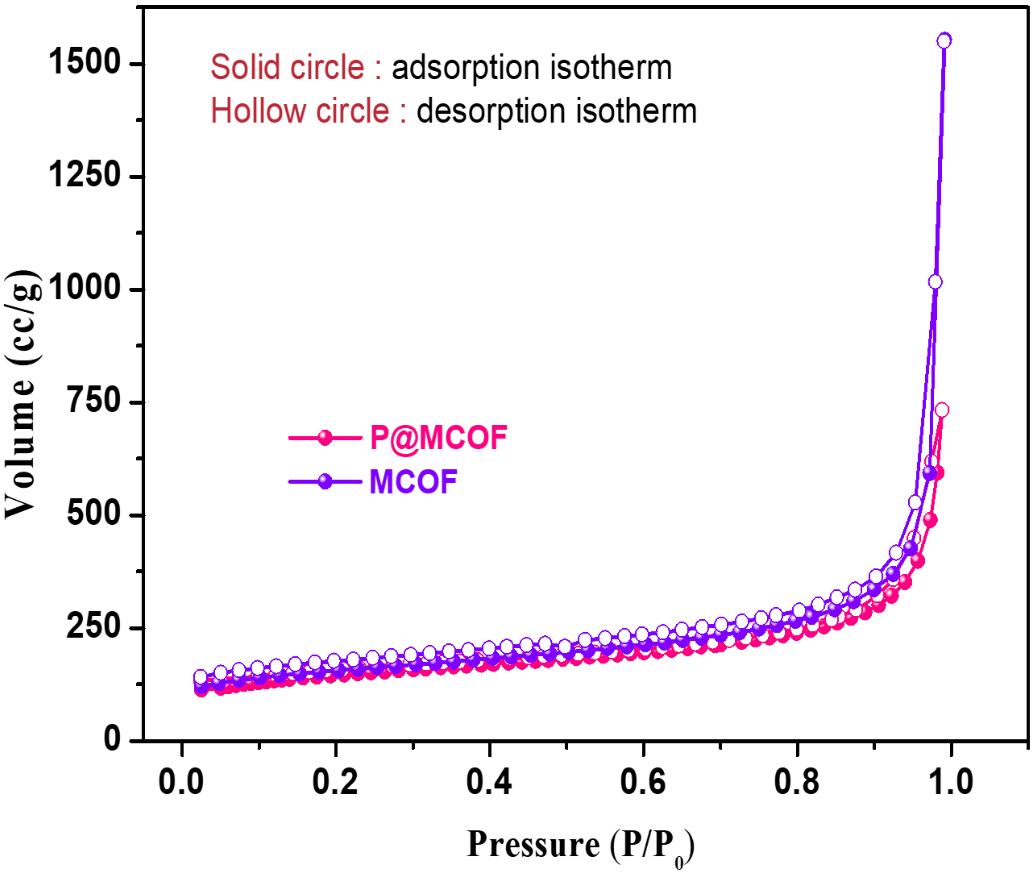

Figure A2.6. N_2 adsorption and desorption isotherm of MCOF and P@MCOF obtained from BET.

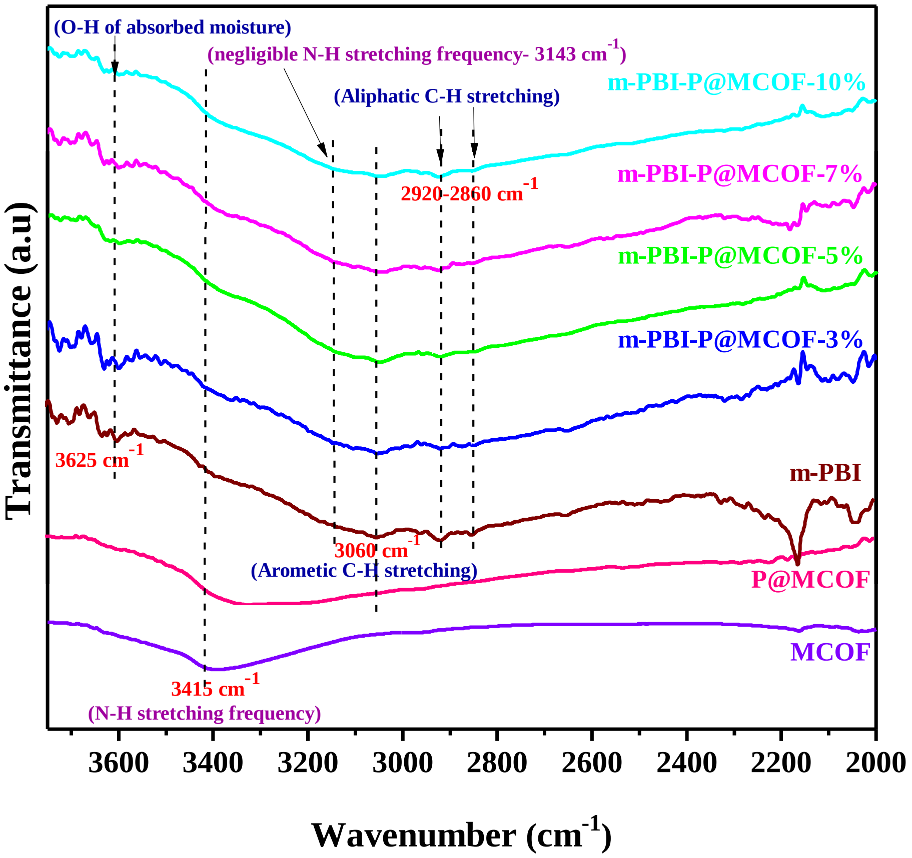

Figure A2.7. FT-IR spectral analysis of m-PBI-P@MCOF composite membranes along with m-PBI.

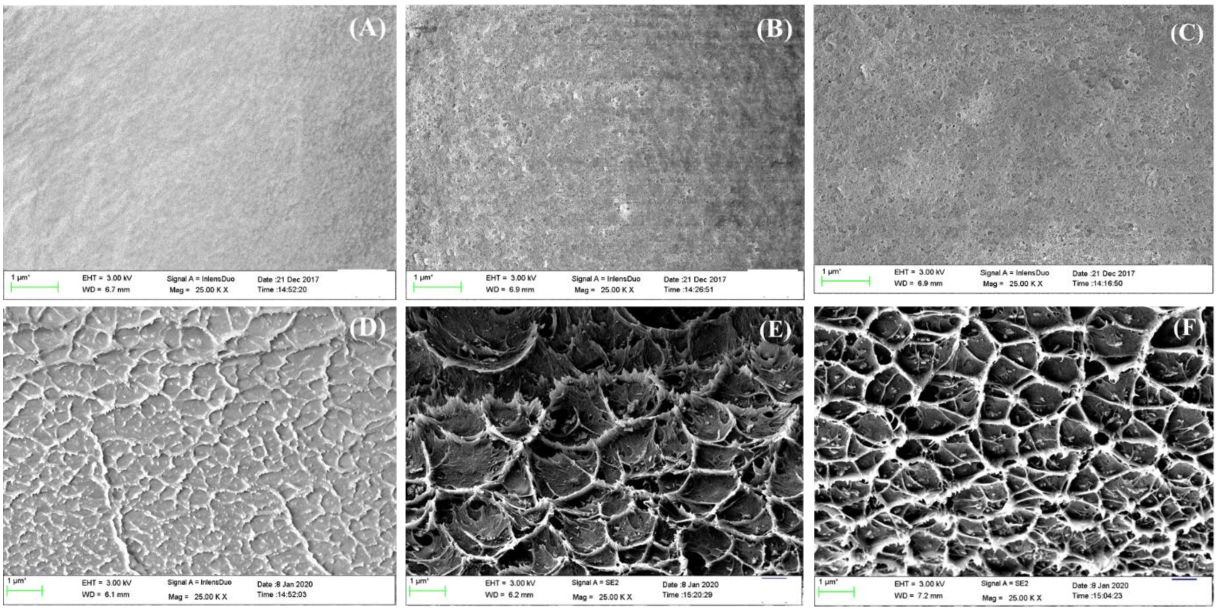

Figure A2.8. (A) FESEM surface morphology of m-PBI, **(B)** m-PBI-P@MCOF-3%, **(C)** m-PBI-P@MCOF-5%, **(D)** FESEM cross-sectional morphology of m-PBI, **(E)** m-PBI-P@MCOF-3%, **(F)** m-PBI-P@MCOF-5%.

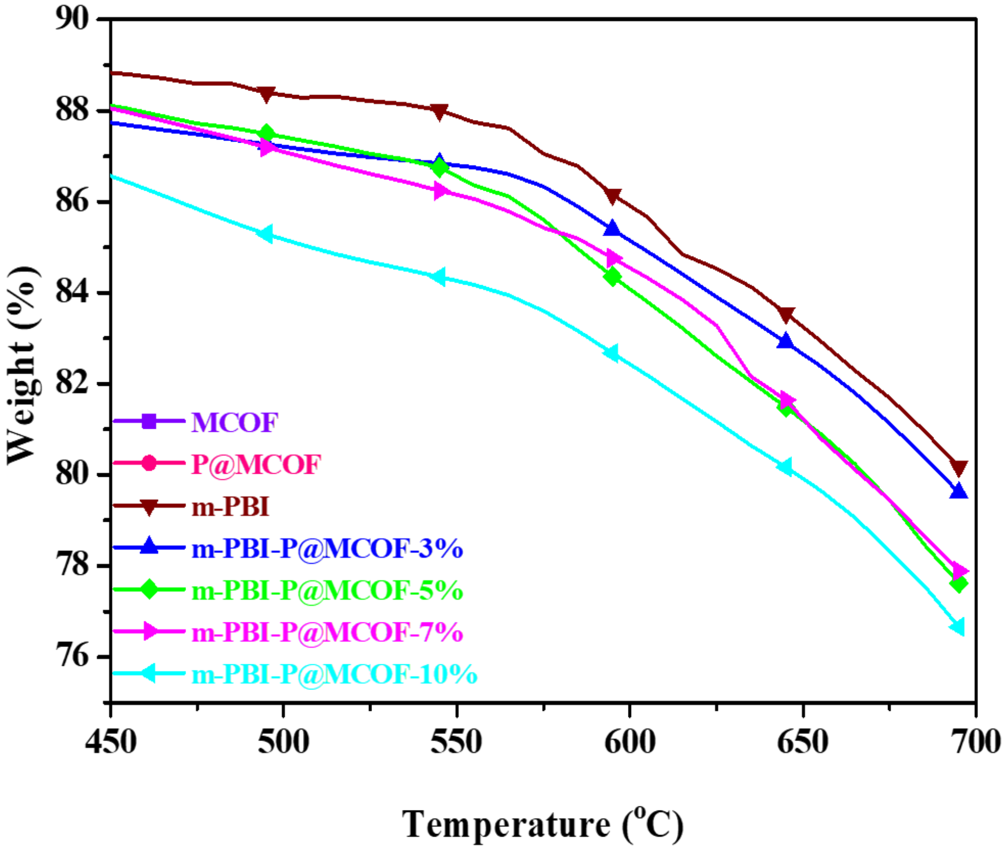

Figure A2.9. Zoomed TGA plot of m-PBI, MCOF, P@MCOF and nanocomposite membranes (450 °C -700°C) range.

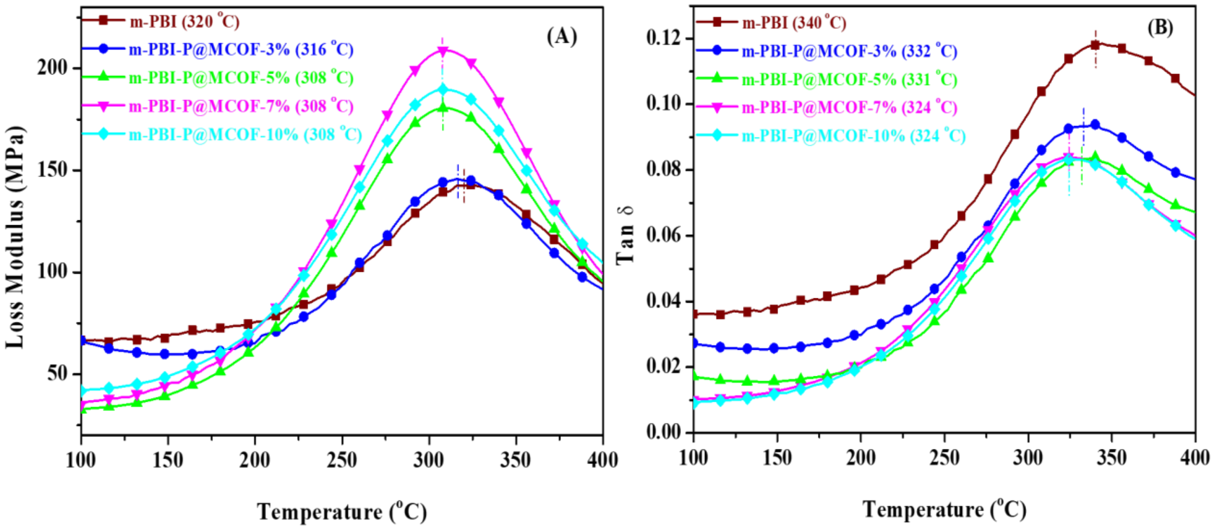

Figure A2.10. (A) Loss modulus and **(B)** tan δ plots of all the m-PBI-P@MCOF nanocomposite membranes of different filler loading along with pristine m-PBI. The T_g values are mentioned in **Table 2** of the main manuscript.

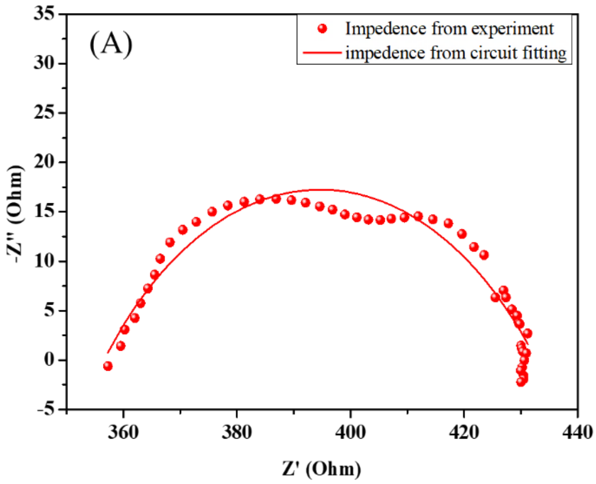

Figure A2.11. (A) Nyquist plot of m-PBI-P@MCOF-7% and **(B)** m-PBI-P@MCOF- 10% composite membranes after equivalent circuit fitting at 180 °C.

Table A2.2. Fitting parameters to determine proton conductivity of m-PBI-P@MCOF composite membranes of different loading along with m-PBI and m-PBI-MCOF-10% membranes at 180°C.

Sample	Value of Rs (Ohm) at 180 °C	Thickness (cm)	Conductivity (Scm^{-1}) at 180 °C	χ^2 value
m-PBI	1353.17	0.004	0.061	0.01509
m-PBI-P@MCOF-3%	594.522	0.004	0.140	0.0059931
m-PBI-P@MCOF-5%	446.623	0.004	0.186	0.0035392
m-PBI-P@MCOF-7%	357.259	0.004	0.233	0.024906
m-PBI-P@MCOF-10%	269.236	0.004	0.309	0.0035979
m-PBI-MCOF-10%	722.258	0.004	0.115	0.010653

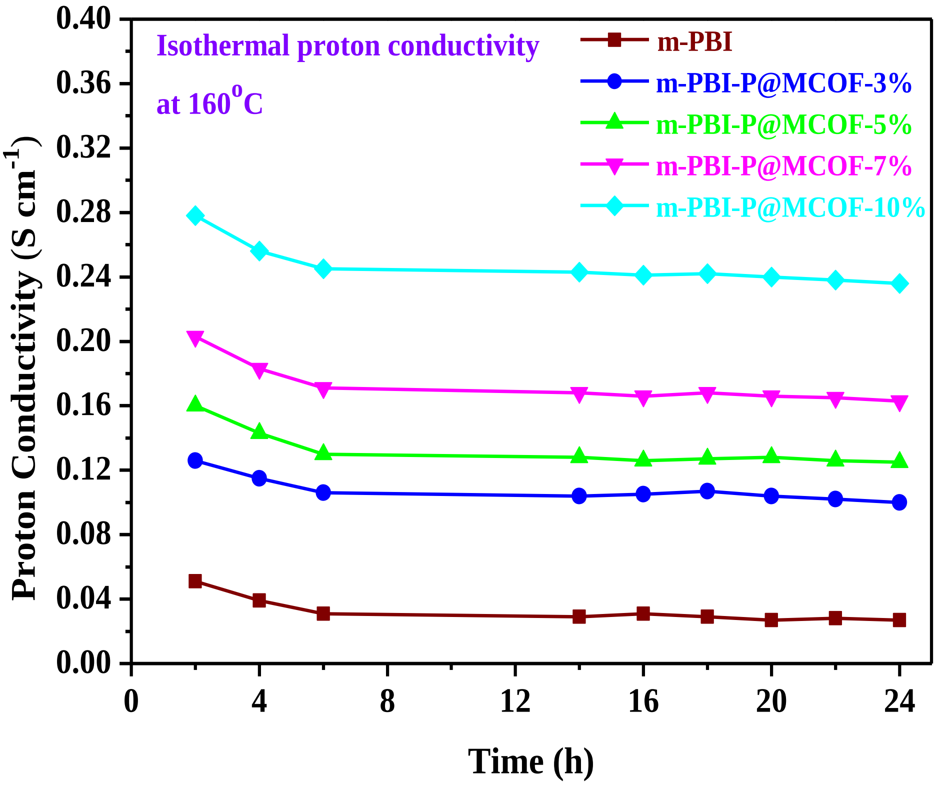

Figure A2.12. Isothermal proton conductivity of m-PBI-P@MCOF nanocomposite membranes along with pristine m-PBI at 160 °C for 24 h.

APPENDIX 3 (for Chapter 5)

Polymer Grafted Graphene Oxide/Polybenzimidazole Nanocomposites for Efficient Proton Conducting Membranes

Synthesis of graphene oxide (GO)

Graphene oxide (GO) was synthesized utilizing modified Hummers method from pure the graphite powder (**Scheme A3.1**).[1] In this method, approximately 120 mL of sulfuric acid (H_2SO_4) and 14 mL of 85% ortho-phosphoric acid (H_3PO_4) (volume ratio 9:1) were mixed and stirred until it becomes a homogeneous mixture. Then 1 g of graphite powder was added into the solution under stirring condition. Then 5.86 g of potassium permanganate ($KMnO_4$) was added slowly into the solution as an oxidising agent. This mixture was allowed to stir for 6 hours until the solution turns dark green colour. To eliminate excess amount of $KMnO_4$, ~3 mL of hydrogen peroxide (H_2O_2) was added dropwise and stirred for 30 minutes, in this process vigorous exothermic reaction was occurred. After that the reaction mixture was allowed to cool at room temperature. Then, 45-50 mL of hydrochloric acid (HCl) and 100 mL of deionized water was added and centrifuged using REMI 430S centrifuge machine at 14000 rpm for 25 minutes. Then, the supernatant liquid was decanted away with repeated washing using HCl and DI water, and finally repeated washing with water. The washed GO solution was then dried in a heating oven at 80 °C for 24 hours to obtain pure GO powders.

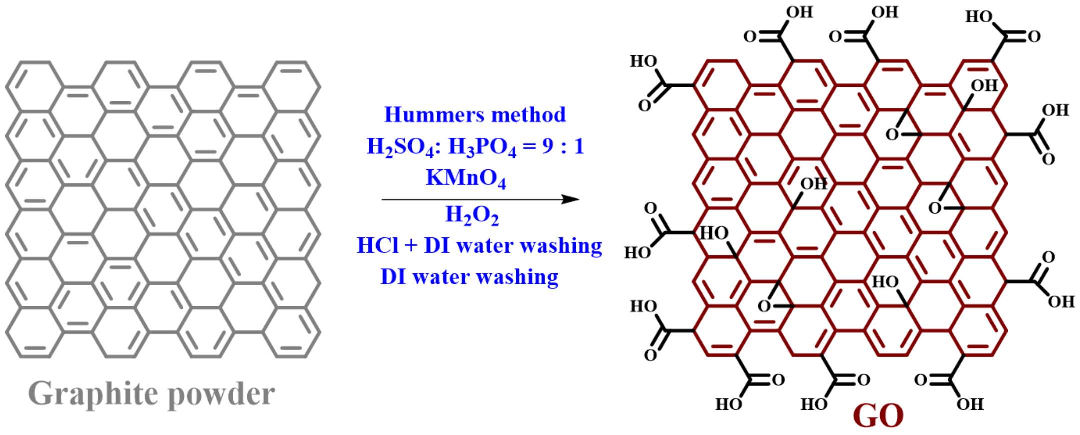

Scheme A3.1. Schematic representation for the synthesis of graphene oxide (GO).

Synthesis of BSPA RAFT agent

BSPA [3-benzylsulfanylthiocarbonylsufanyl-propionic acid] RAFT agent was synthesized using the modified literature reported synthetic procedure.[2,3] 9.42 mmol of 3-MPA, 9.42 mmol of K_3PO_4 and 10.4 mmol of CS_2 were taken in a round bottom flask consists of 15-20 mL of dry acetone under nitrogen atmosphere. The reaction mixture was then allowed to stir under ice bath condition for 30 min followed by addition of 9.42 mmol of benzyl bromide slowly into the solution with the help of a syringe. The reaction was further stirred for an hour and quenched with water. The compound was extracted with ethyl acetate and the yellow liquid was dried under reduced pressure. The compound was further purified using column chromatography and yellow crystalline compound was obtained. The synthesized compound was characterized by FT-IR, ^{1}H-NMR and ^{13}C-NMR studies for structural conformation (**Figure A3.1** and **Figure A3.2**).

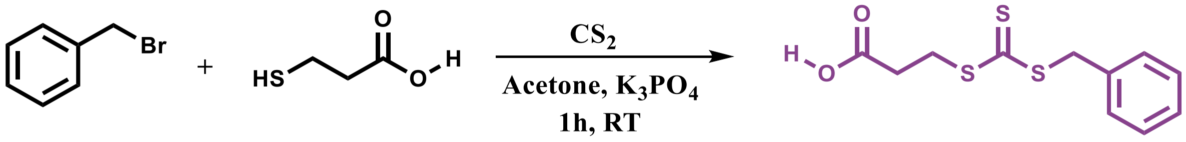

Scheme A3.2. The synthetic scheme for the preparation of 3-benzylsulfanylthiocarbonylsufanyl-propionic acid [BSPA] RAFT agent.

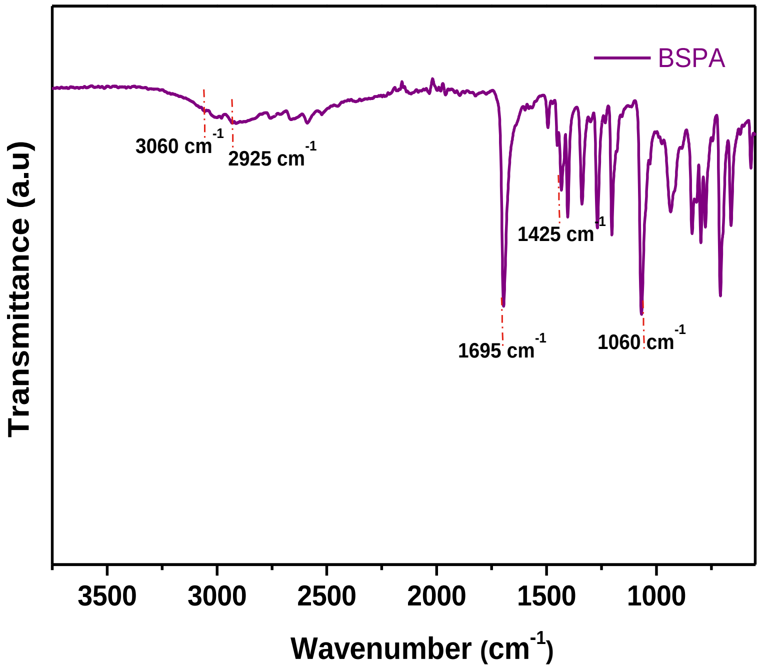

Figure A3.1. FT-IR spectra of BSPA.

BSPA RAFT agent shows the FT-IR signals at 3060 cm^{-1}, 2925 cm^{-1}, 1695 cm^{-1}, 1425 cm^{-1} and 1060 cm^{-1} which are attributed to the vibration of aromatic hydrogen, aliphatic C-H stretching, carbonyl –C=O, saturated C-H bending and presence of C=S bonds, respectively.[4]

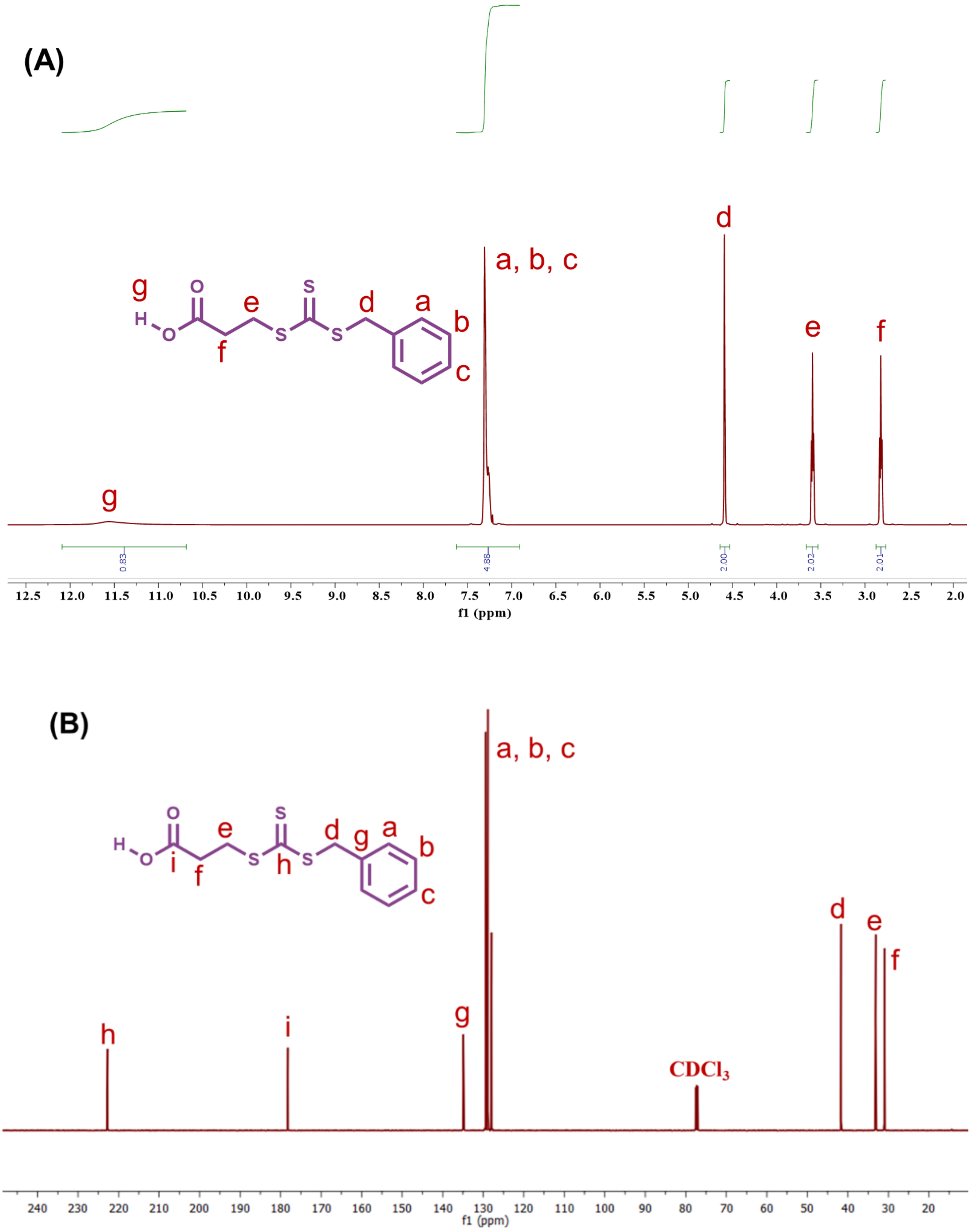

Figure A3.2. ^{1}H NMR **(A),** ^{13}C NMR **(B)** spectra of BSPA.

Synthesis of activated RAFT agent (activated BSPA)

Following a literature reported procedure[5] to activate the carboxylic acid group of BSPA RAFT agent, 0.122 mmol of BSPA, 0.183 mmol of DCC along with 0.012 mmol of DMAP was taken in a round bottom flask filled with 20 mL dry DCC under N_2 atmosphere. The reaction was kept at 0 °C for 15 minutes and then slowly added 0.159 mmol NHS dissolved in 5 mL dry THF. The reaction was continued at 0 °C for 18 h and then the reaction mixture was kept in refrigerator for overnight which helps to precipitate out excess DCC from the solution. The reaction mixture was filtered out in cold condition to remove solids from the reaction mixture and purified. The purified activated BEPA was then used for further reaction.

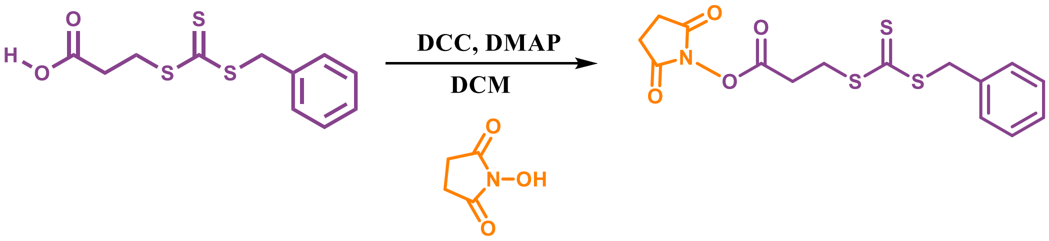

Scheme A3.3. The synthetic pathway to prepare activated BSPA RAFT agent.

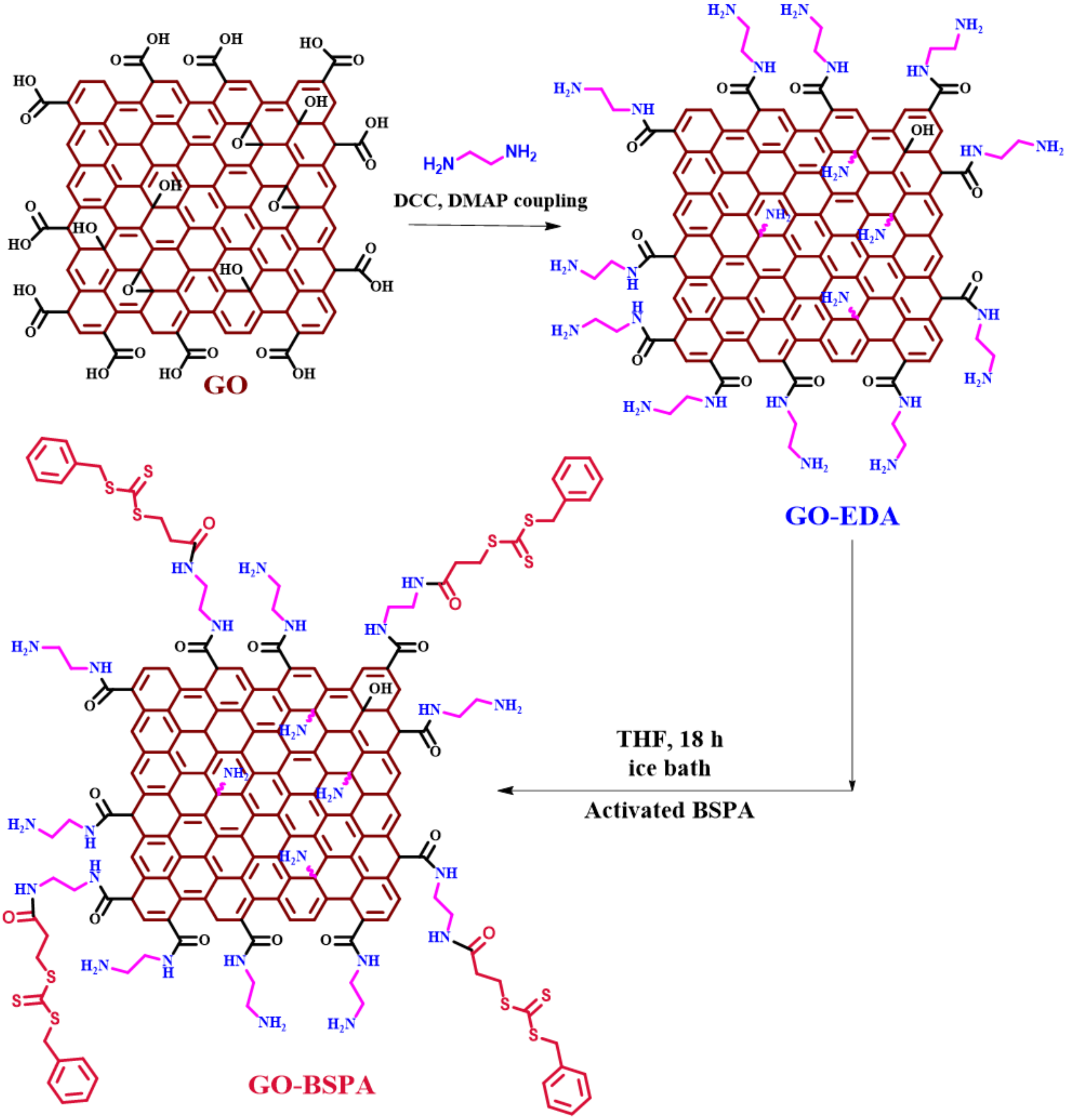

Scheme A3.4. Schematic representation of GO-EDA and GO-BSPA synthesis.

Detachment of polymer chains from the GO surface and molecular weight measurement

The molecular weights analysis and polydispersity index (Đ) of the grafted polymers were obtained after detaching the grafted polymer chains from the GO surface by breaking the trithiocarbonate moiety linked between the polymer chains and the amine modified GO surface. The grafted polymer chains of all the six polymer grafted GO (GOP1-GOP6) described in the article were subjected to polymer detachment using excess N-hexylamine in presence of sodium dithionite and purified in order to isolate the bare polymer chains.[6] The detached bare polymer chains were dissolved in HPLC water and the molecular weight of the detached polymers were determined by gel permeation chromatography (GPC) using polystyrene standards and eluted in HPLC water at flow rate of 0.5 mL/min at 30 °C on a GPC (Waters 515 HPLC) fitted with Waters 2414 refractive index detector and using Waters Ultra hydrogel 250 column.

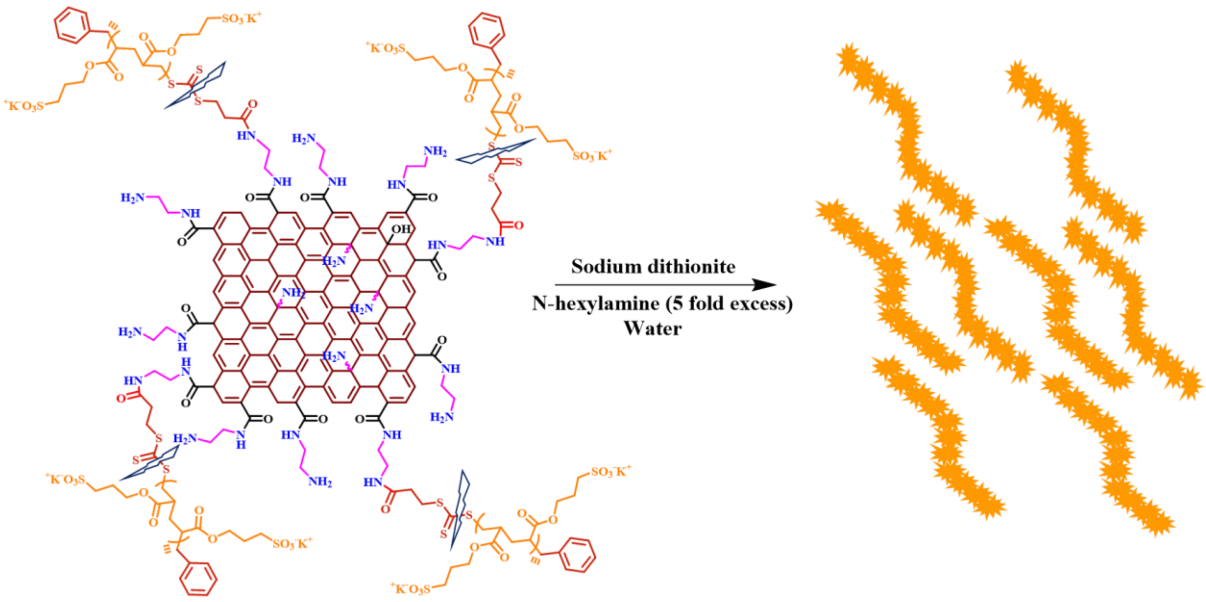

Scheme A3.5. Representative scheme to show the detachment of polymer chain from the GO surface for the measurement of molecular weight of the polymer using GPC analysis.

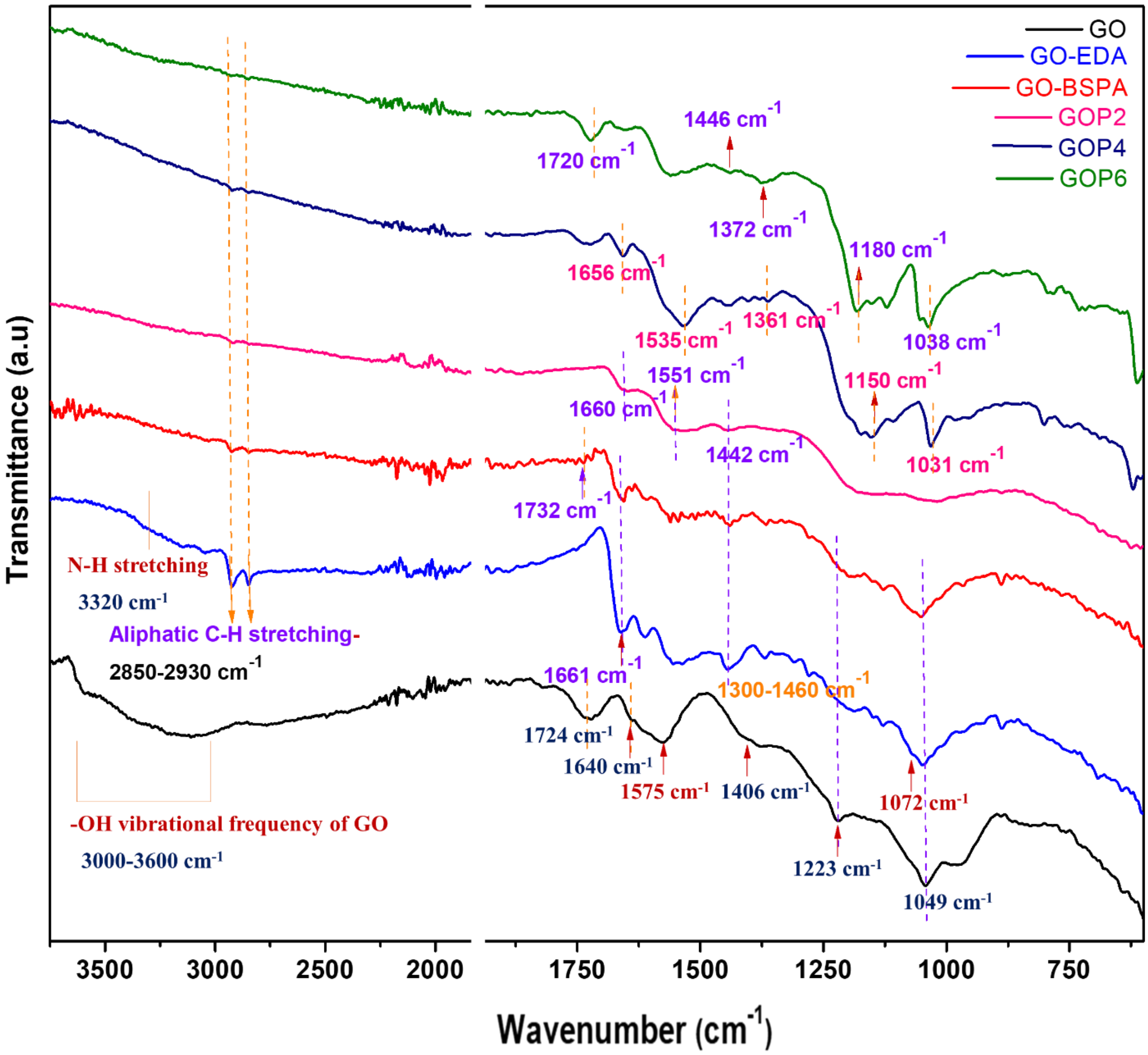

Figure A3.3. FT-IR spectra of GO, GO-EDA, GO-BSPA, GOP2, GOP4 and GOP6.

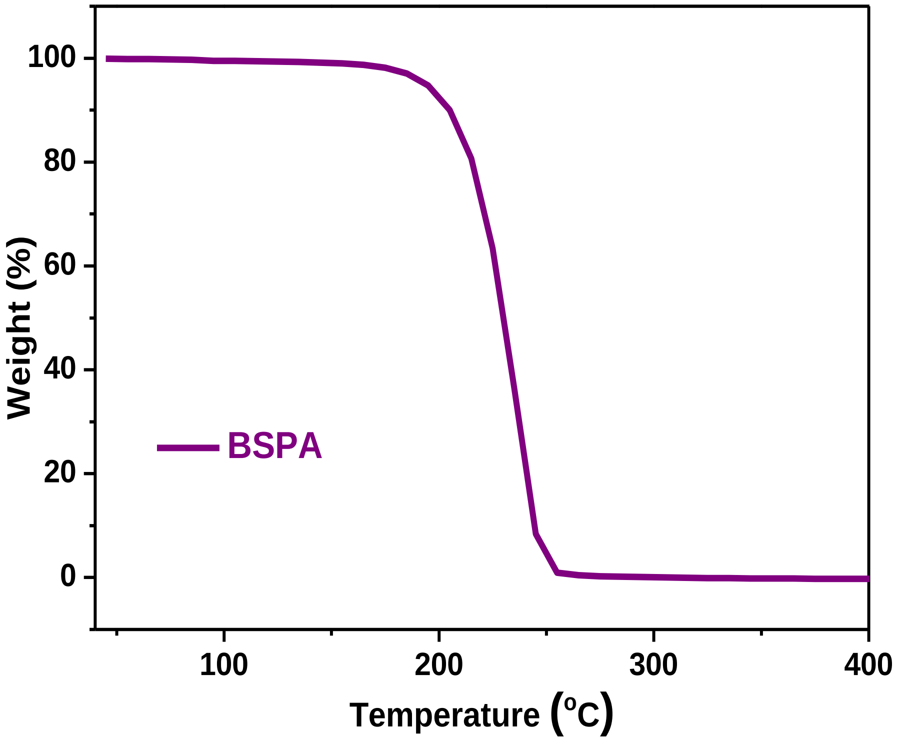

Figure A3.4. TGA plot of RAFT agent BSPA.

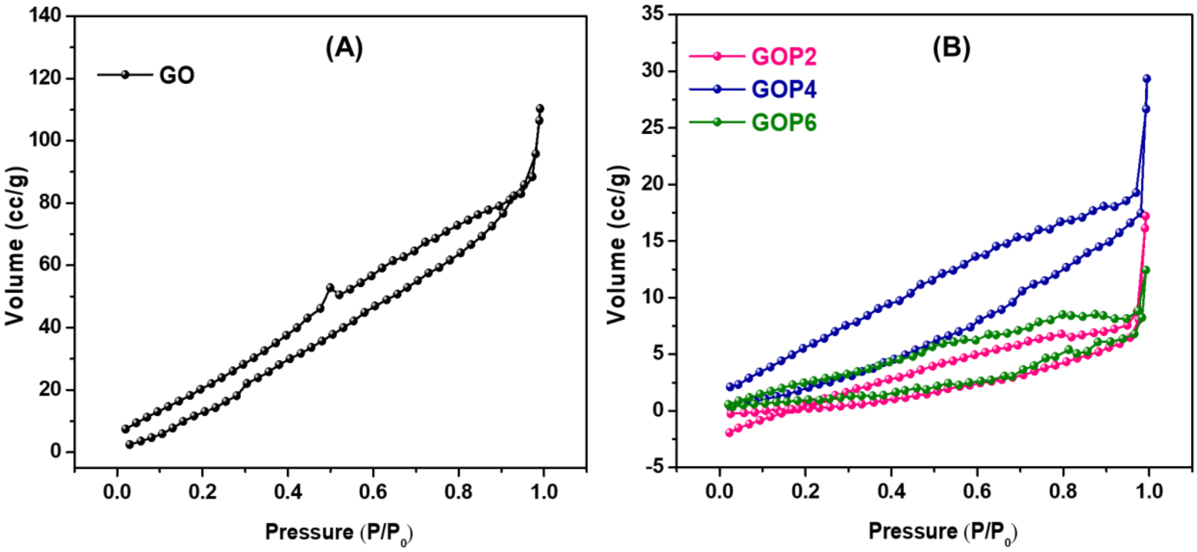

Figure A3.5. BET N_2 sorption isotherms of (A) GO and (B) GOP2, GOP4, GOP6 samples.

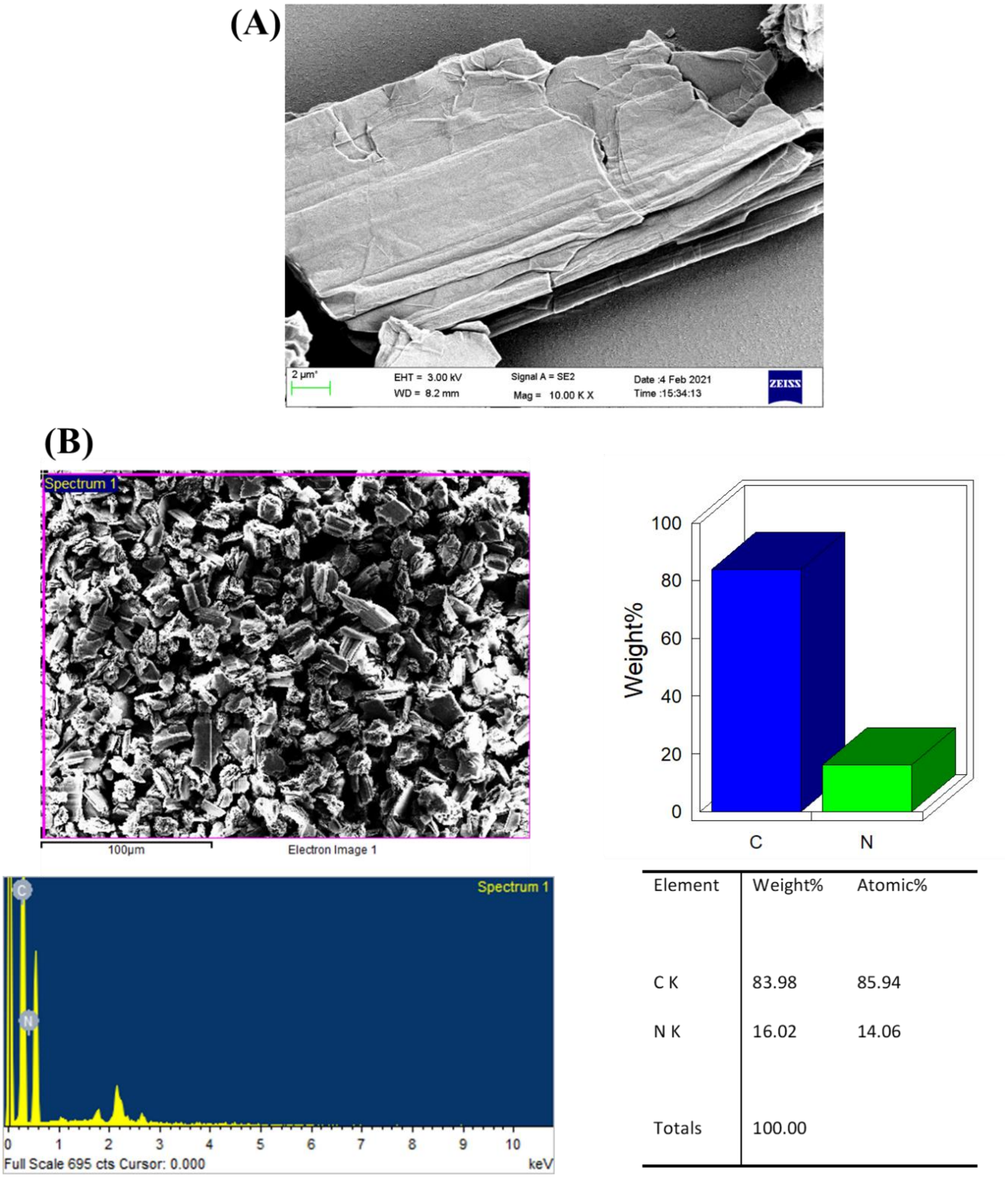

Element	Weight%	Atomic%
C K	83.98	85.94
N K	16.02	14.06
Totals	100.00	

Figure A3.6. (A) FESEM image (B) EDX elemental analysis of GO**.**

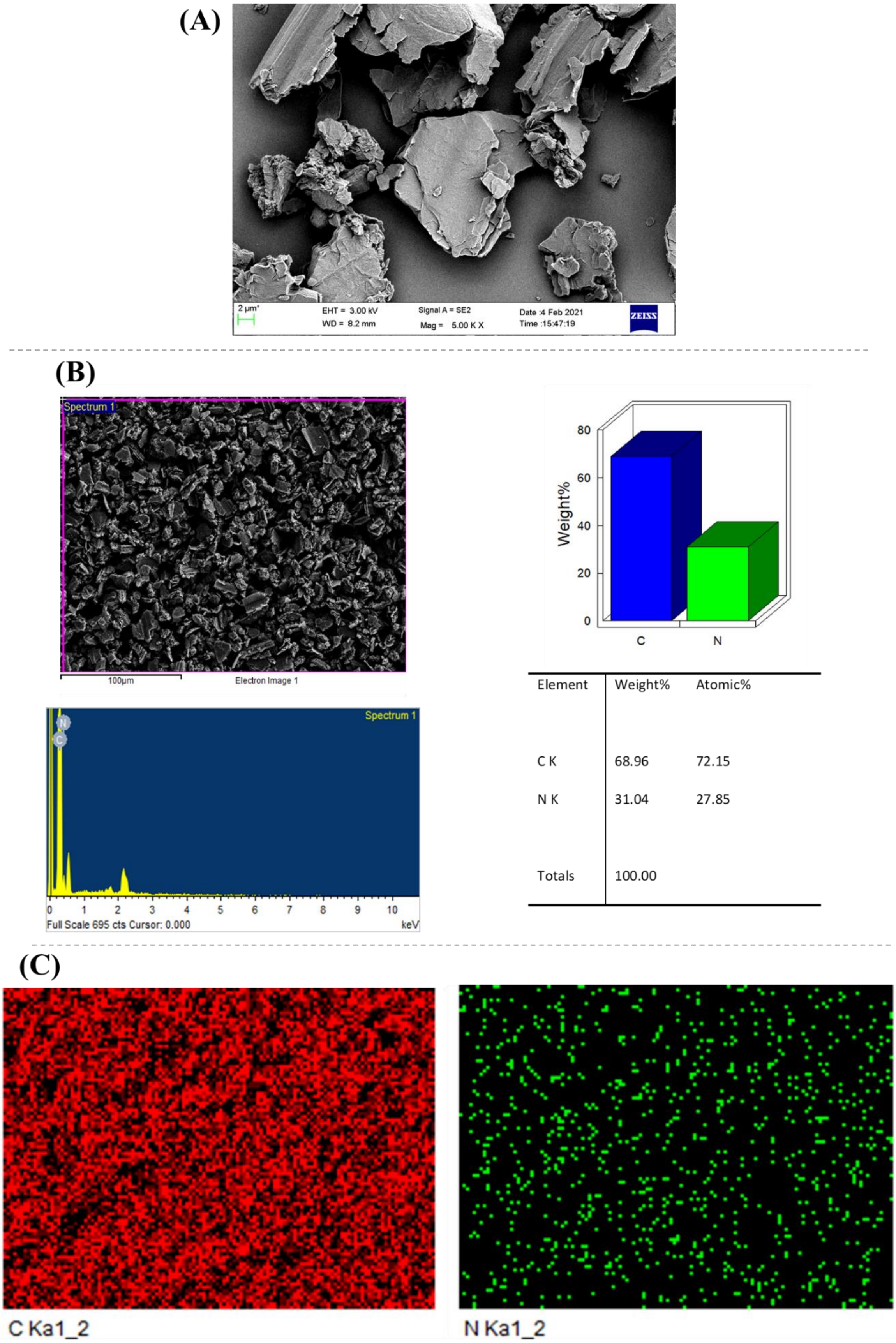

Element	Weight%	Atomic%
C K	68.96	72.15
N K	31.04	27.85
Totals	100.00	

Figure A3.7. (A) FESEM image, (B) EDX elemental analysis and (C) elemental mapping (for C and N) of GO-EDA.

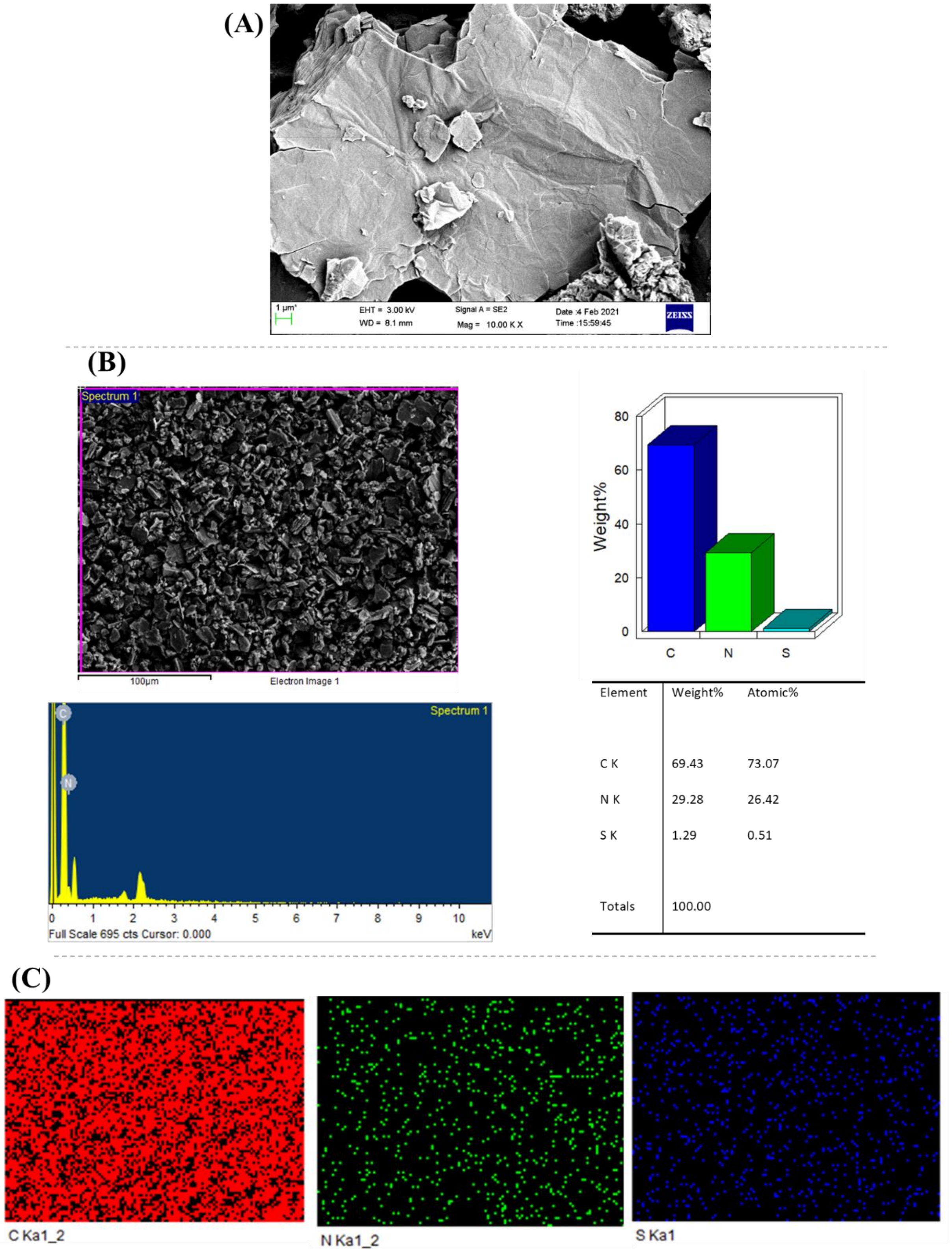

Element	Weight%	Atomic%
C K	69.43	73.07
N K	29.28	26.42
S K	1.29	0.51
Totals	100.00	

Figure A3.8. (A) FESEM image (B) EDX elemental analysis and (C) elemental mapping of GO-BSPA. The distribution of N and S throughout the image prove the successful BSPA grafting on GO.

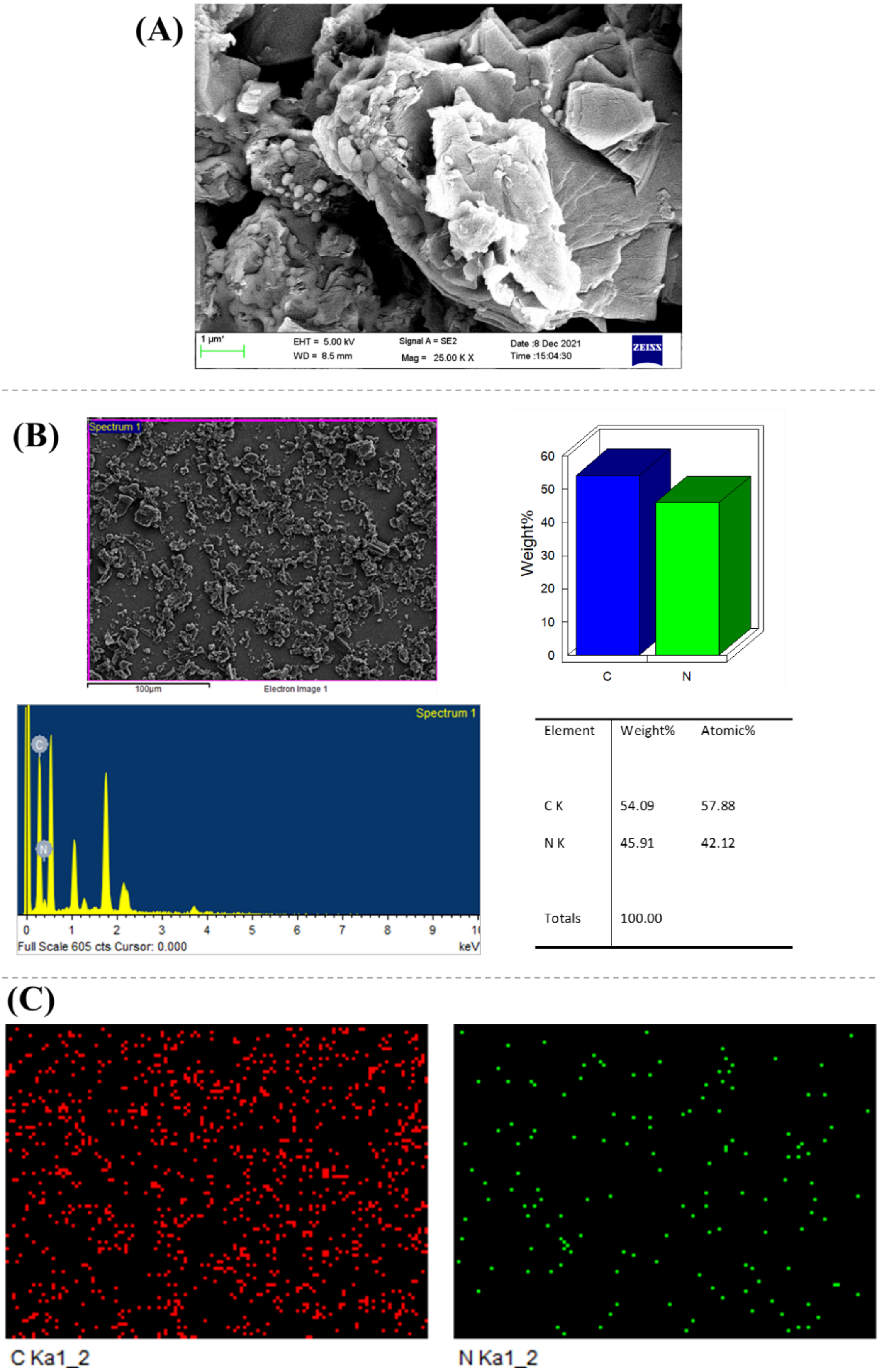

Element	Weight%	Atomic%
C K	54.09	57.88
N K	45.91	42.12
Totals	100.00	

Figure A3.9. (A) FESEM image, (B) EDX elemental analysis and (C) elemental mapping (for C and N) of pAAM(L)-*g*-GO (GOP1).

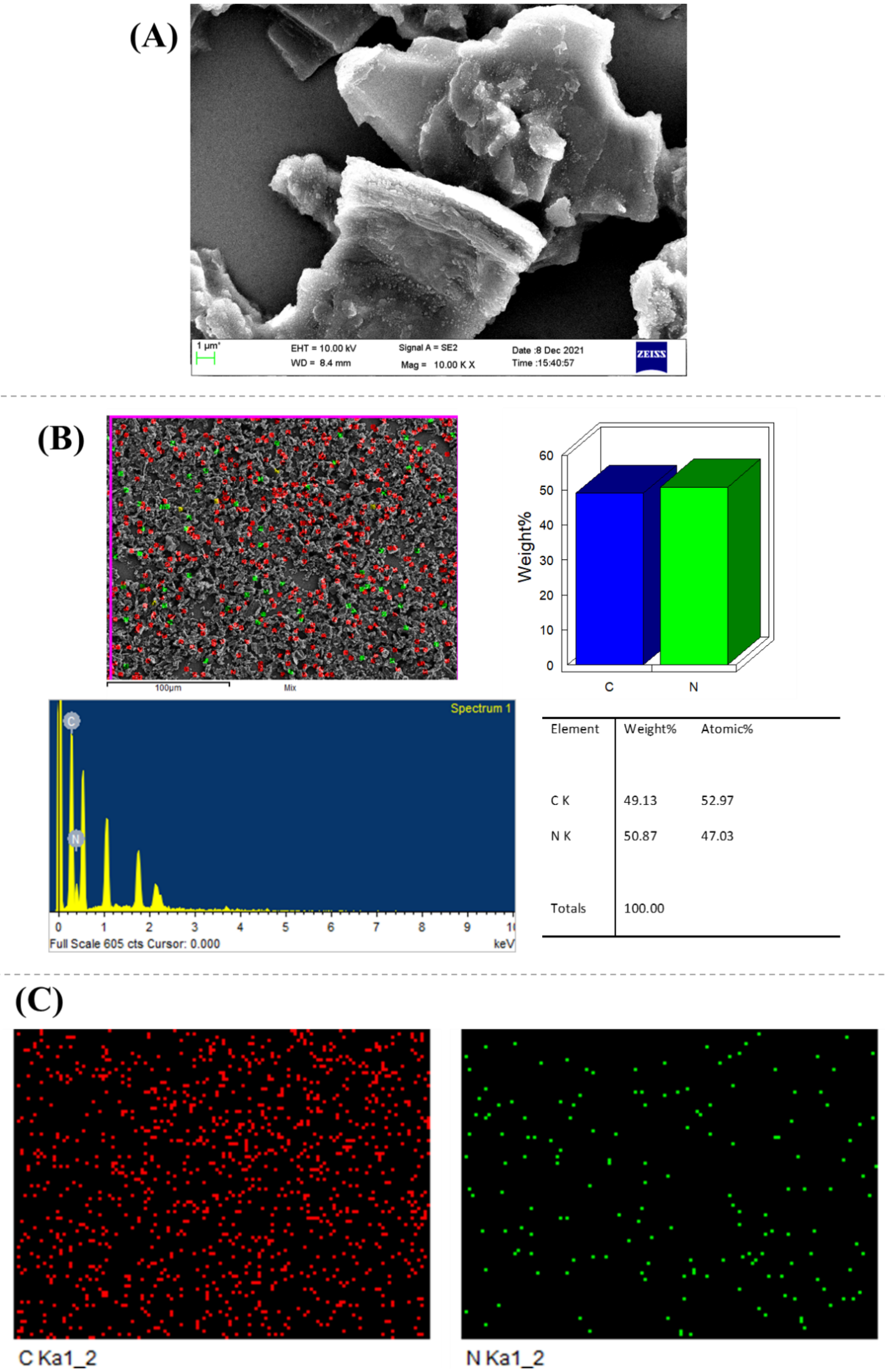

Element	Weight%	Atomic%
C K	49.13	52.97
N K	50.87	47.03
Totals	100.00	

Figure A3.10. (A) FESEM image, (B) EDX elemental analysis and (C) elemental mapping (for C and N) of pAAM(H)-*g*-GO (GOP2).

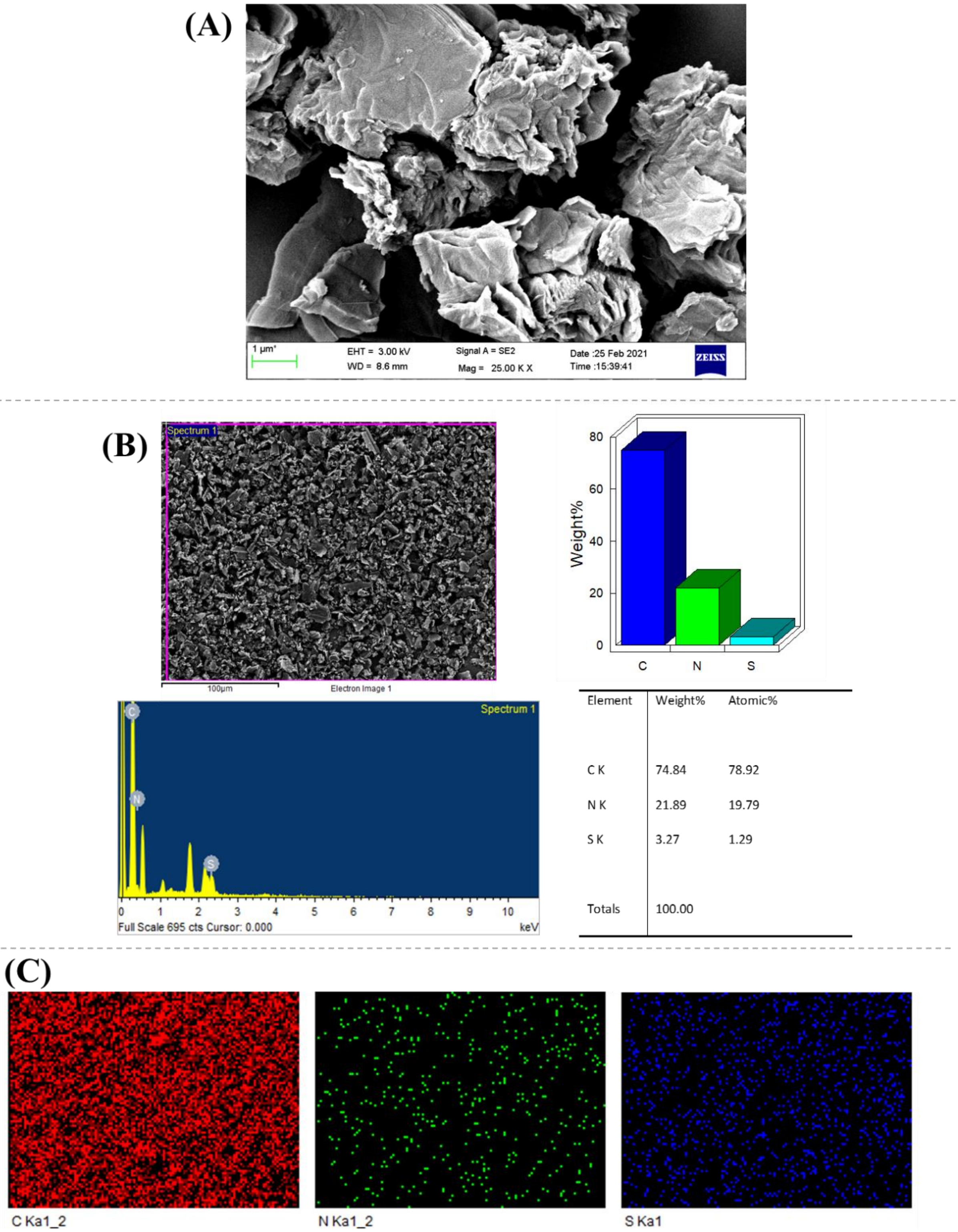

Element	Weight%	Atomic%
C K	74.84	78.92
N K	21.89	19.79
S K	3.27	1.29
Totals	100.00	

Figure A3.11. (A) FESEM image, (B) EDX elemental analysis and (C) elemental mapping (for C, N and S) of pAMPS(L)-*g*-GO (GOP3).

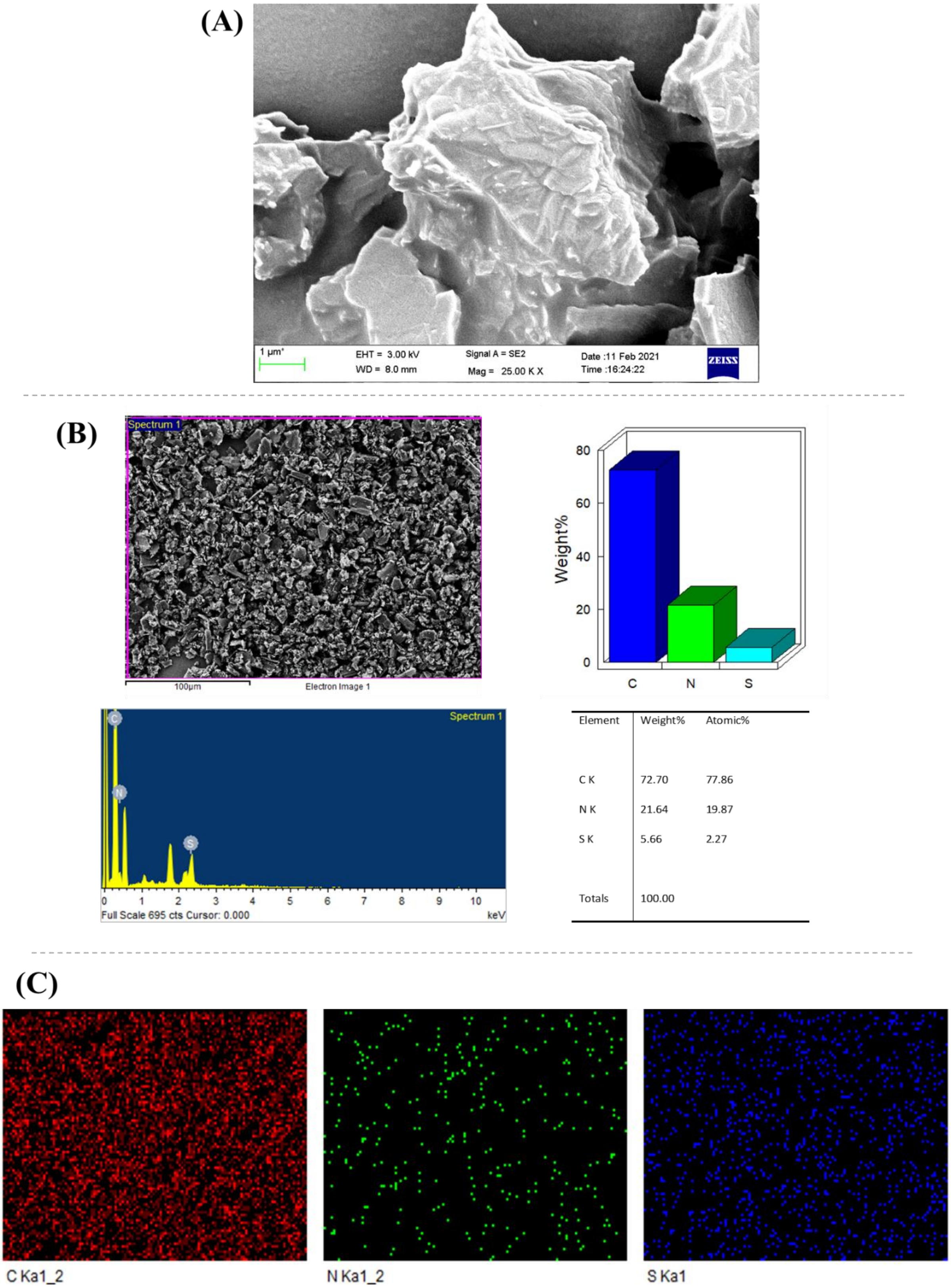

Element	Weight%	Atomic%
C K	72.70	77.86
N K	21.64	19.87
S K	5.66	2.27
Totals	100.00	

Figure A3.12. (A) FESEM image, (B) EDX elemental analysis and (C) elemental mapping (for C, N and S) of pAMPS(H)-*g*-GO (GOP4).

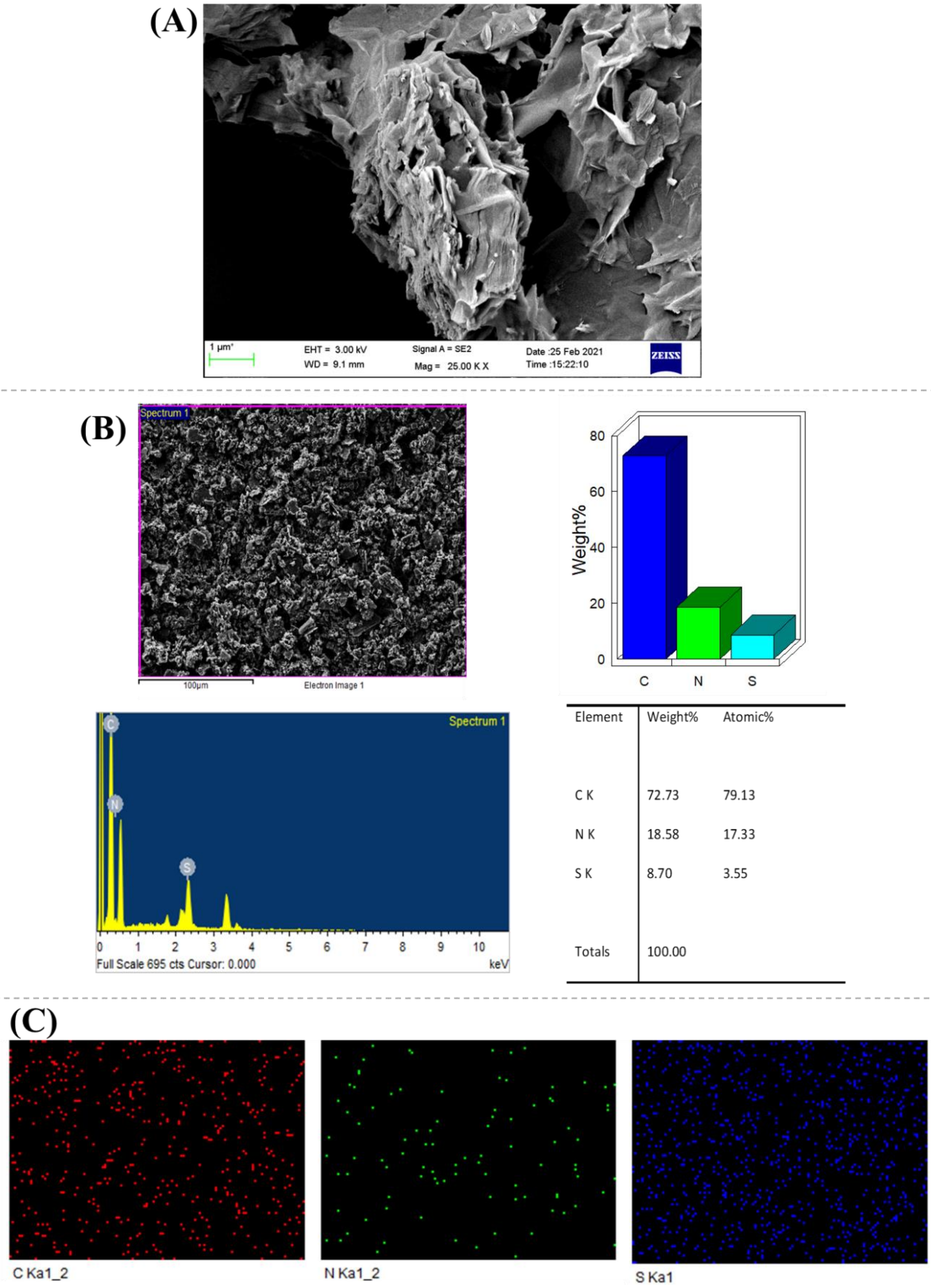

Element	Weight%	Atomic%
C K	72.73	79.13
N K	18.58	17.33
S K	8.70	3.55
Totals	100.00	

Figure A3.13. (A) FESEM images, (B) EDX elemental analysis and (C) elemental mapping (for C, N and S) of pSPAK(L)-*g*-GO (GOP5).

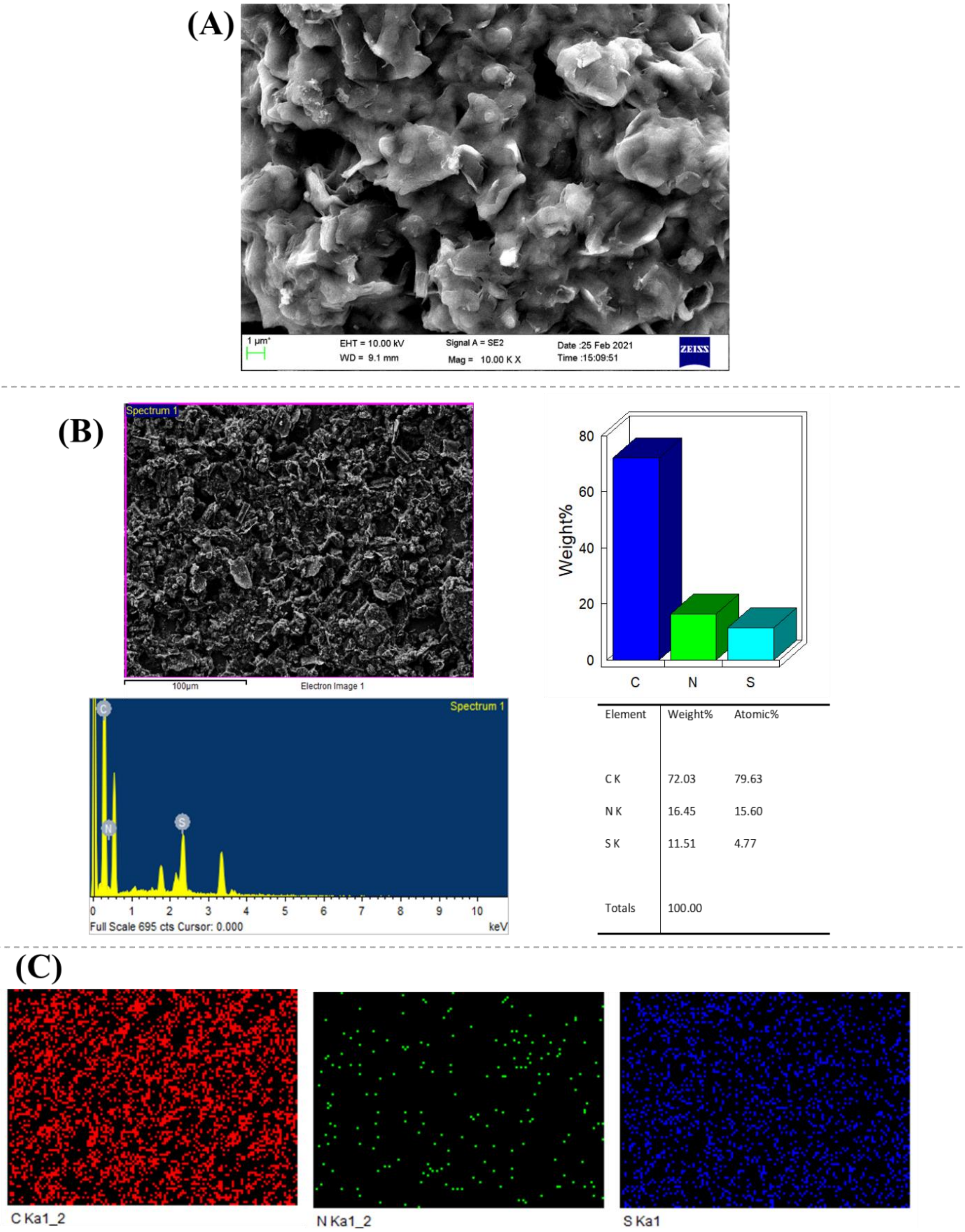

Element	Weight%	Atomic%
C K	72.03	79.63
N K	16.45	15.60
S K	11.51	4.77
Totals	100.00	

Figure A3.14. (A) FESEM images, (B) EDX analysis and (C) elemental mapping (for C, N and S) of pSPAK(H)-*g*-GO (GOP6).

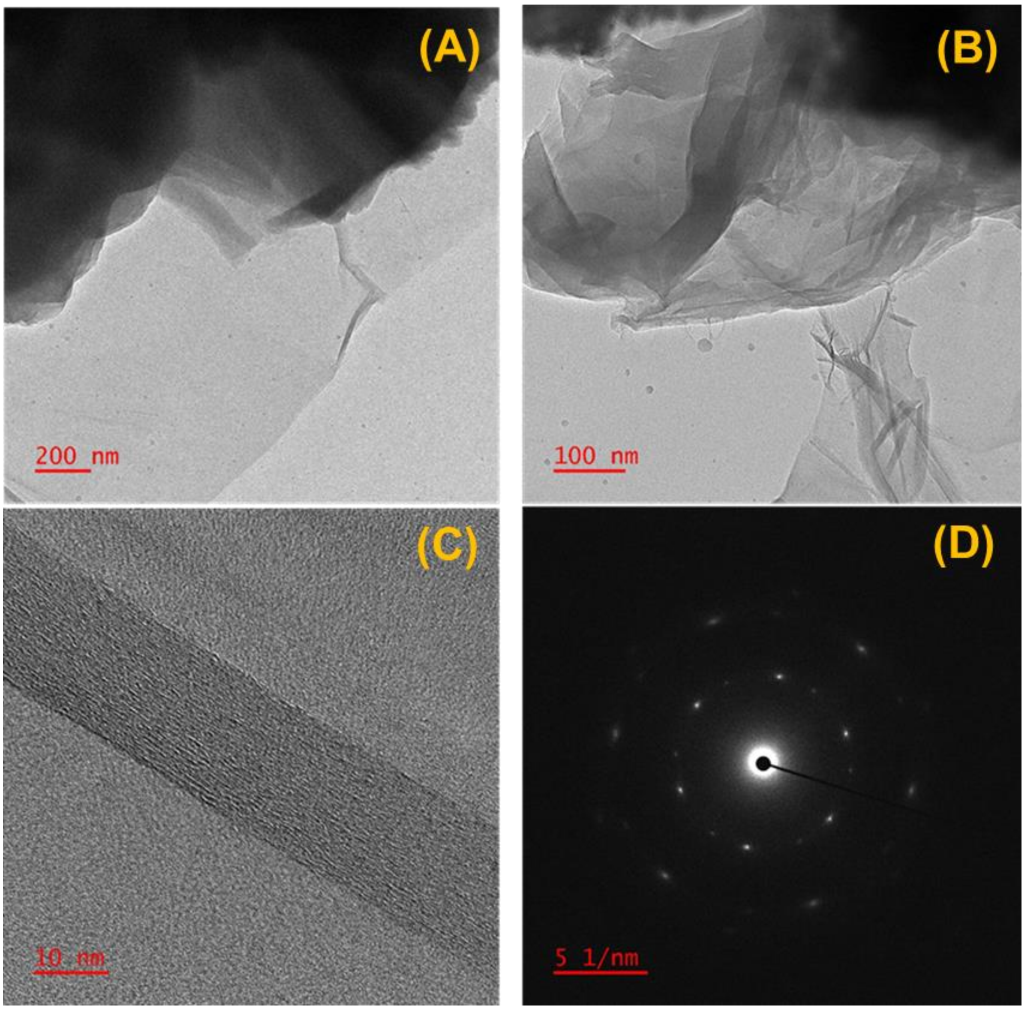

Figure A3.15. TEM images of GO in different magnification **(A, B),** HR-TEM image and SAED pattern of **GO** hexagonal lattice **(C, D).**

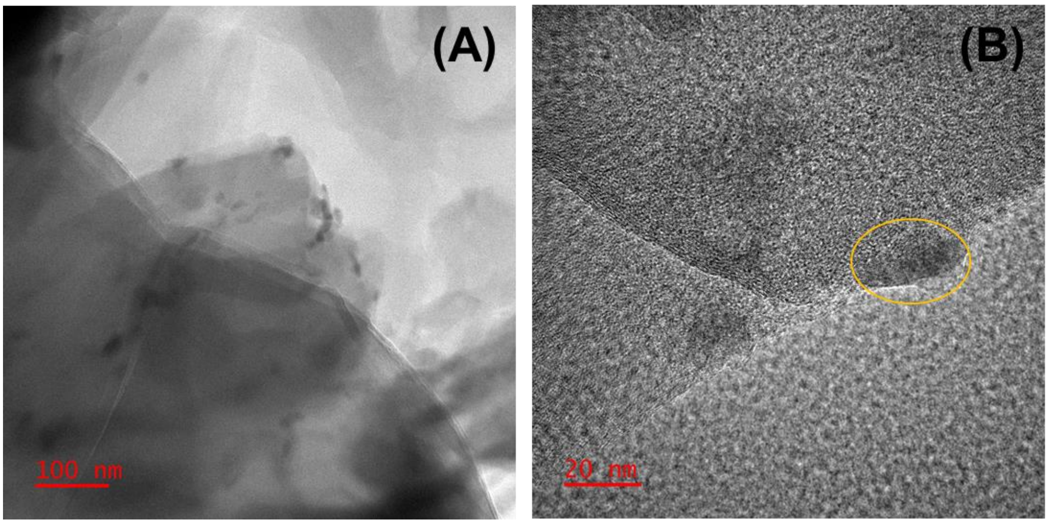

Figure A3.16. Surface TEM morphology of GO-BSPA in different magnification (A, B). Yellow circle represents sulfur deposition due to RAFT attachment.

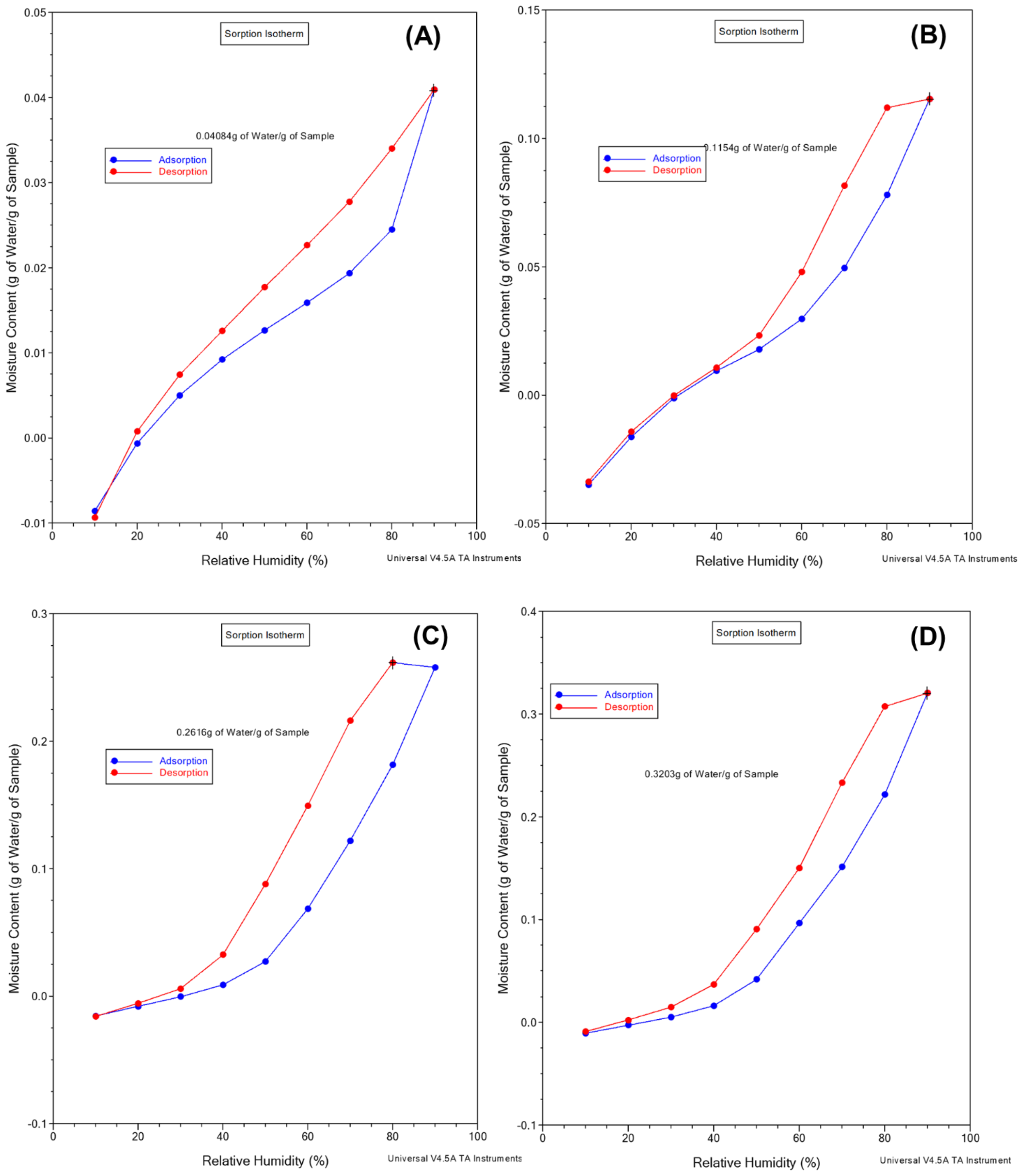

Figure A3.17. Dynamic vapour sorption analysis plot of GO (A), GOP2 (B), GOP4 (C) and GOP6 (D) polymers.

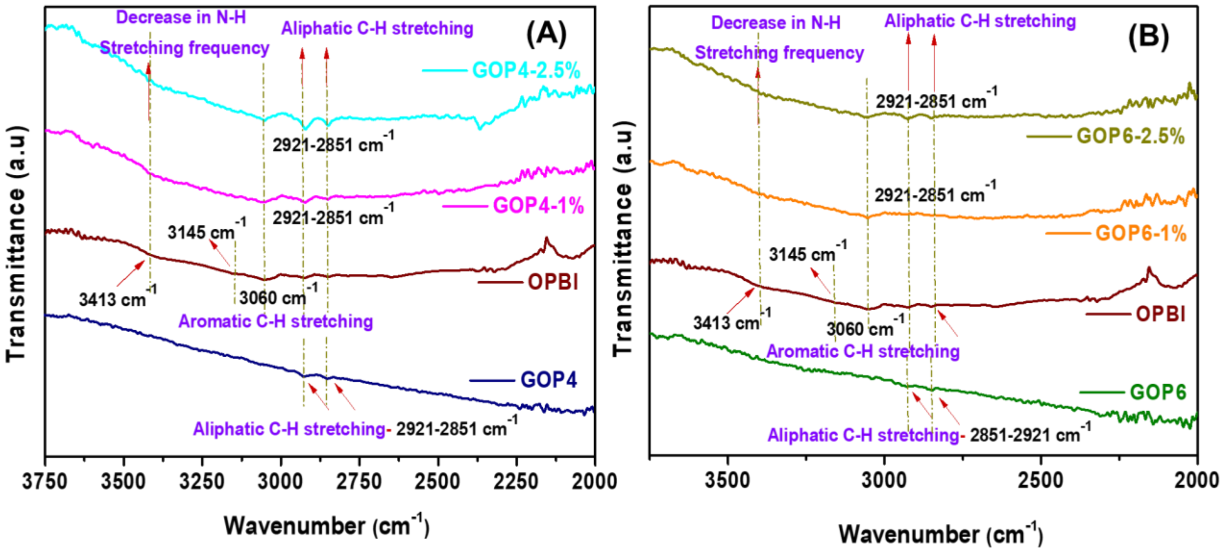

Figure A3.18. FT-IR spectra (3750 – 2000 cm^{-1}) of OPBI/GOP membranes along with OPBI and GOP4 **(A)**. FT-IR spectra (3750 – 2000 cm^{-1}) of OPBI/GOP membranes along with OPBI and GOP6 **(B)**.

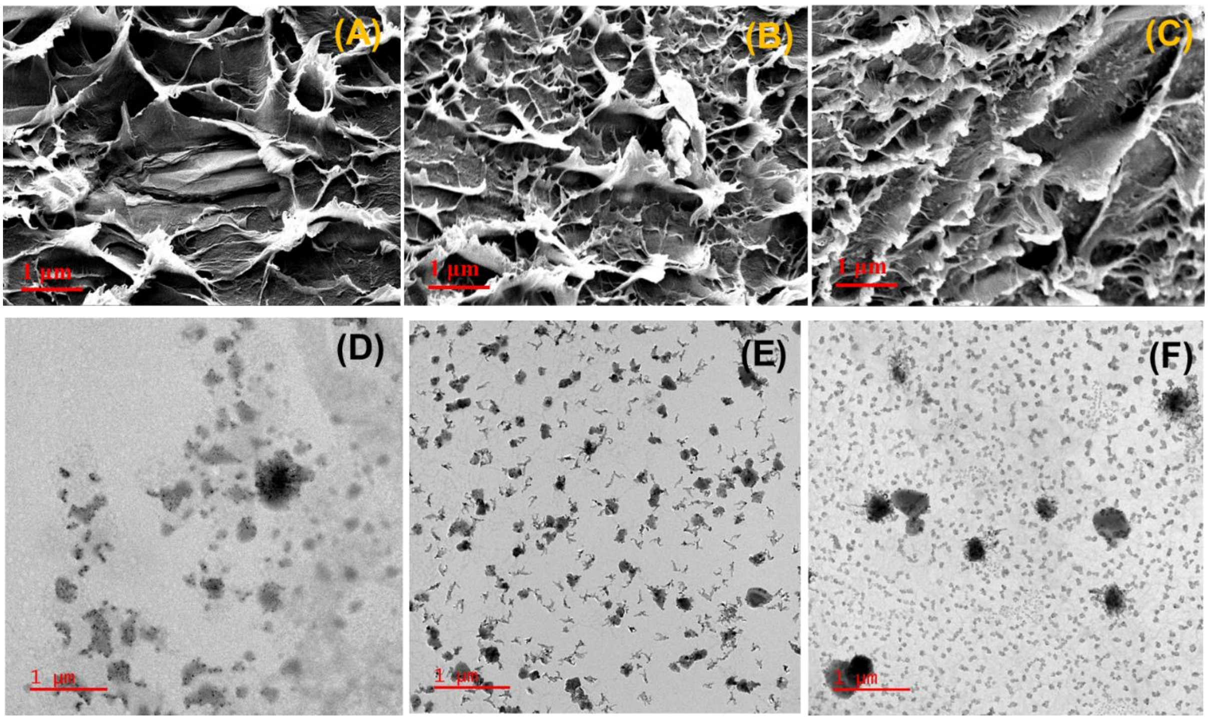

Figure A3.19. FESEM cross-sectional image of GOP2-1% **(A)**, GOP4-1% **(B)** and GOP6-1% **(C)** membranes. TEM images of GOP2-1% **(D)**, GOP4-1% **(E)** and GOP6-1% **(F)** membranes.

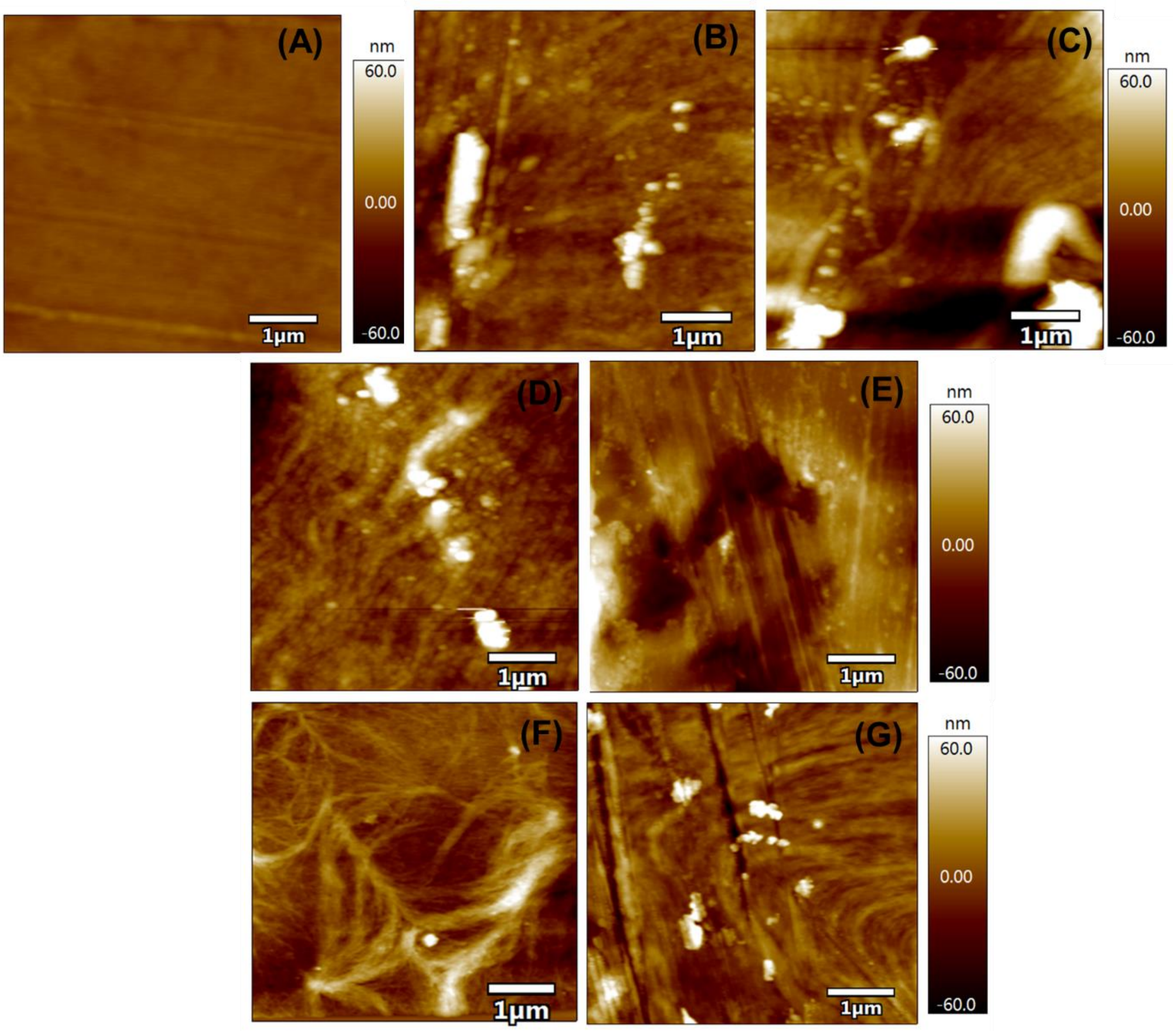

Figure A3.20. AFM surface images of OPBI **(A)**, GOP2-1% and GOP2-2.5% **(B, C)**, GOP4-1% and GOP4-2.5% **(D, E)** and GOP6-1% and GOP6-2.5% membranes **(F, G)**.

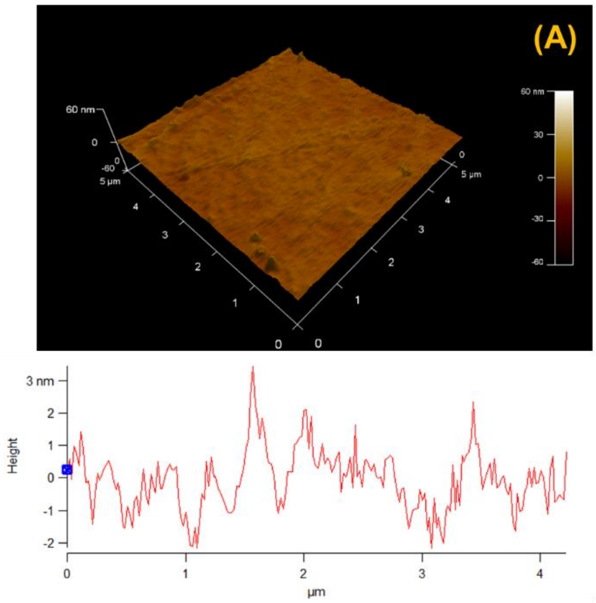
(A)
60 nm
0
-60
5 µm
4
3
2
1
0
0
1
2
3
4
5 µm
60 nm
30
0
-30
-60
3 nm
2
1
0
-1
-2
Height
0
1
2
3
4
µm

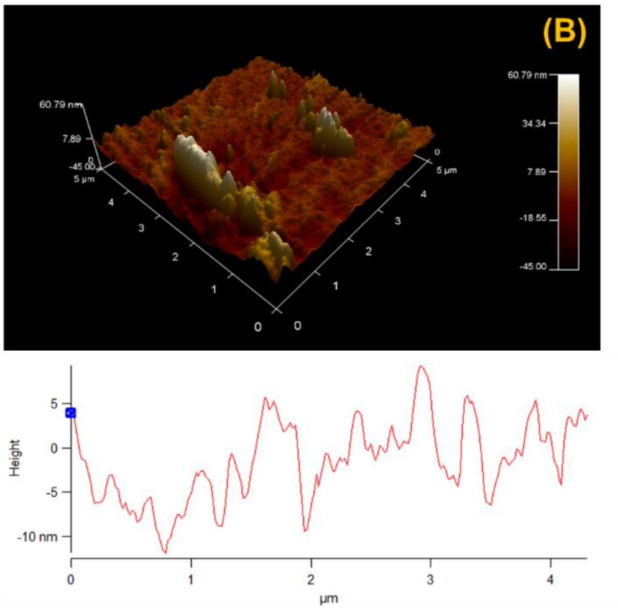
(B)
60.79 nm
7.89
-45.00
5 µm
4
3
2
1
0
0
1
2
3
4
5 µm
60.79 nm
34.34
7.89
-18.55
-45.00
5
0
-5
-10 nm
Height
0
1
2
3
4
µm

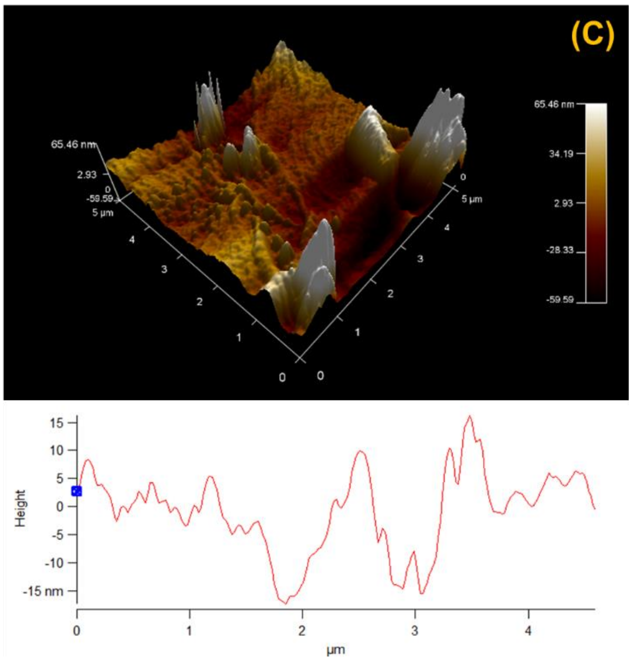
(C)
65.46 nm
2.93
-59.59
5 µm
4
3
2
1
0
0
1
2
3
4
5 µm
65.46 nm
34.19
2.93
-28.33
-59.59
15
10
5
0
-5
-10
-15 nm
Height
0
1
2
3
4
µm

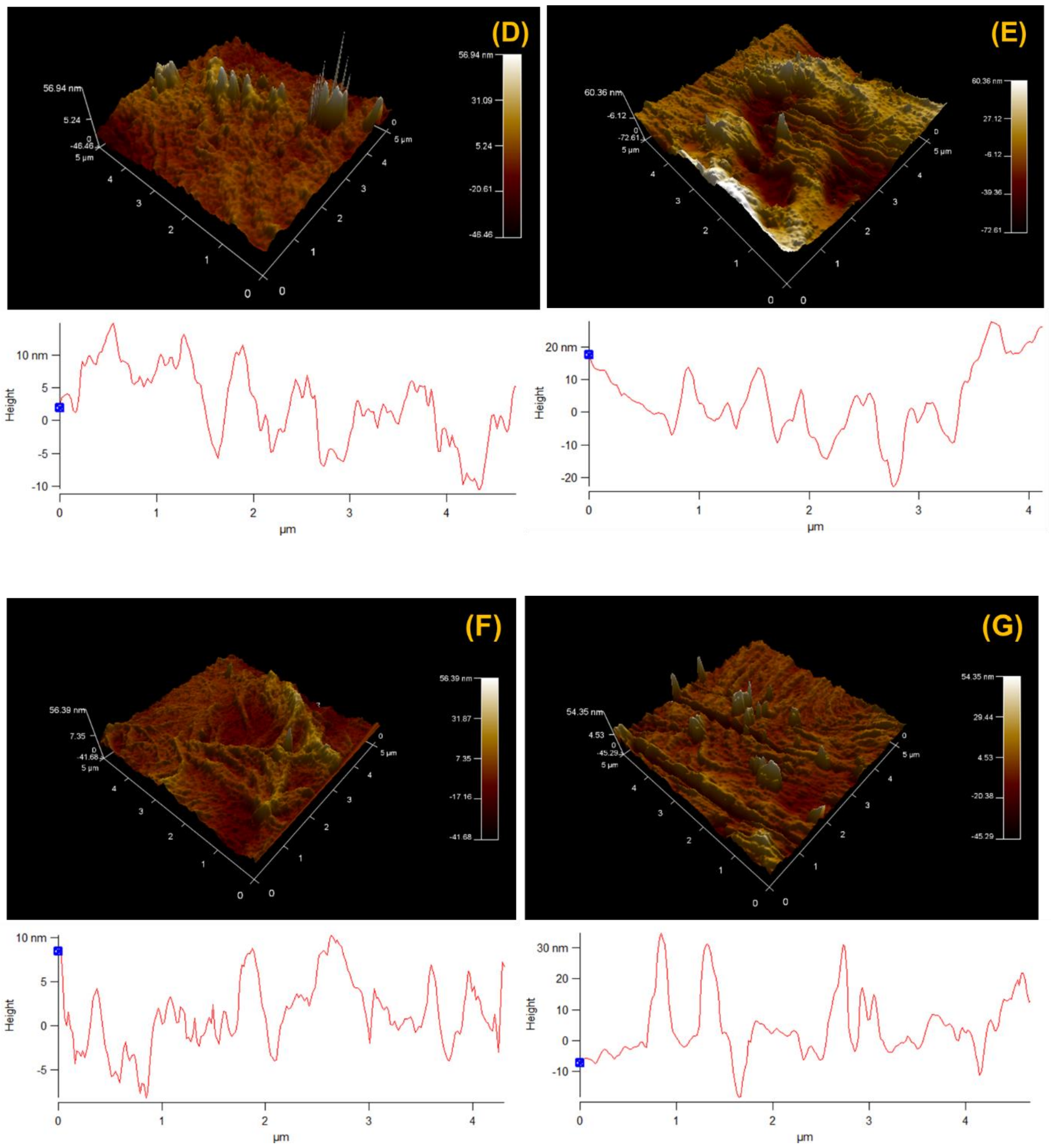

Figure A3.21. AFM 3D images of the surface morphology of **(A)** OPBI, **(B)** GOP2-1% and **(C)** GOP2-2.5%, **(D)** GOP4-1%, **(E)** GOP4-2.5%, **(F)** GOP6-1% and GOP6-2.5% **(G)** membranes along with the height profiles.

Table A3.1. Surface roughness of OPBI/GOP composite MMMs in a comparison with OPBI.

Sample	Root mean square roughness (S_q) (nm)
OPBI	2.273
GOP2-1%	9.740
GOP2-2.5%	26.082
GOP4-1%	9.310
GOP4-2.5%	18.539
GOP6-1%	7.116
GOP6-2.5%	7.381

Table A3.2. Storage modulus values (at 100 °C, 250 °C and 400 °C) of OPBI/GOP mixed matrix membranes obtained from DMA storage modulus plot.

Sample	*E' (MPa) at 100 ℃*	*% of increase*	*E' (MPa) at 250 °C*	*% of increase*	*E' (MPa) at 400 ℃*	*% of increase*
OPBI	2587		1986		1158	
GOP2-1%	4374	69.07	3204	61.32	1863	60.88
GOP2-2.5%	5092	96.83	3971	99.94	2296	98.27
GOP4-1%	2925	13.06	2404	21.04	1869	61.39
GOP4-2.5%	4694	81.44	3884	95.56	2735	136.18
GOP6-1%	2768	6.99	2339	17.76	1670	44.21
GOP6-2.5%	4397	69.96	3604	81.47	2573	122.19

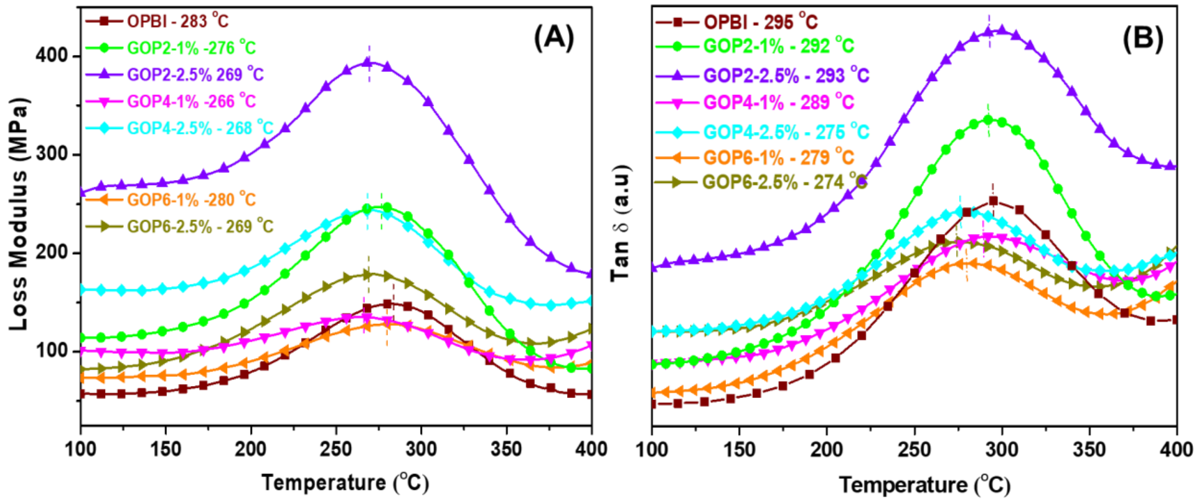

Figure A3.22. Loss Modulus **(A)** and tanδ plots **(B)** of all the GOP loaded MMMs of different filler loading along with pristine OPBI.

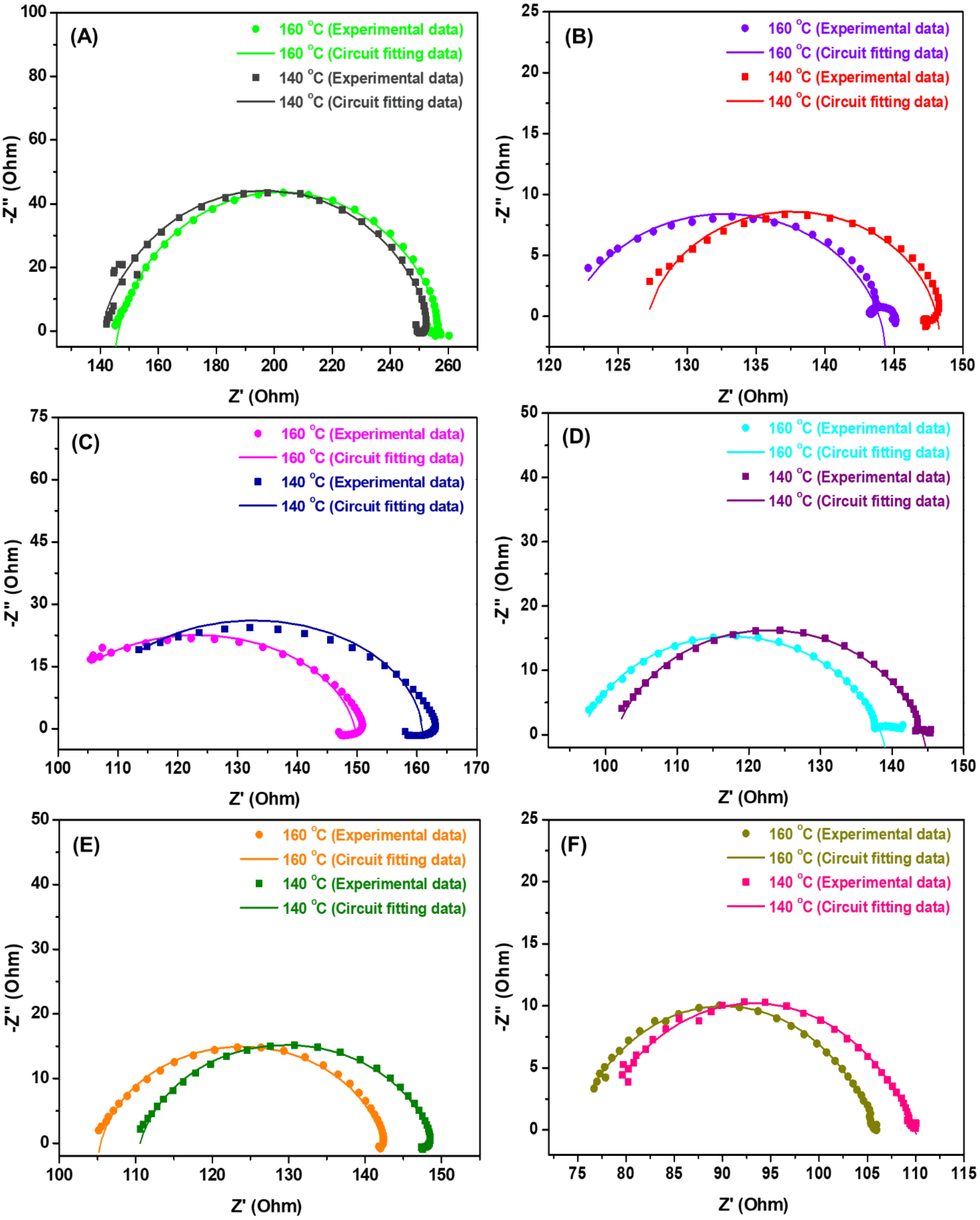

Figure A3.23. Nyquist plots of **(A)** GOP2-1%, **(B)** GOP2-2.5%, **(C)** GOP4-1%, **(D)** GOP4-2.5%, **(E)** GOP6-1% and **(F)** GOP6-2.5% membranes after equivalent circuit fitting at 140 °C and 160 ºC**.**

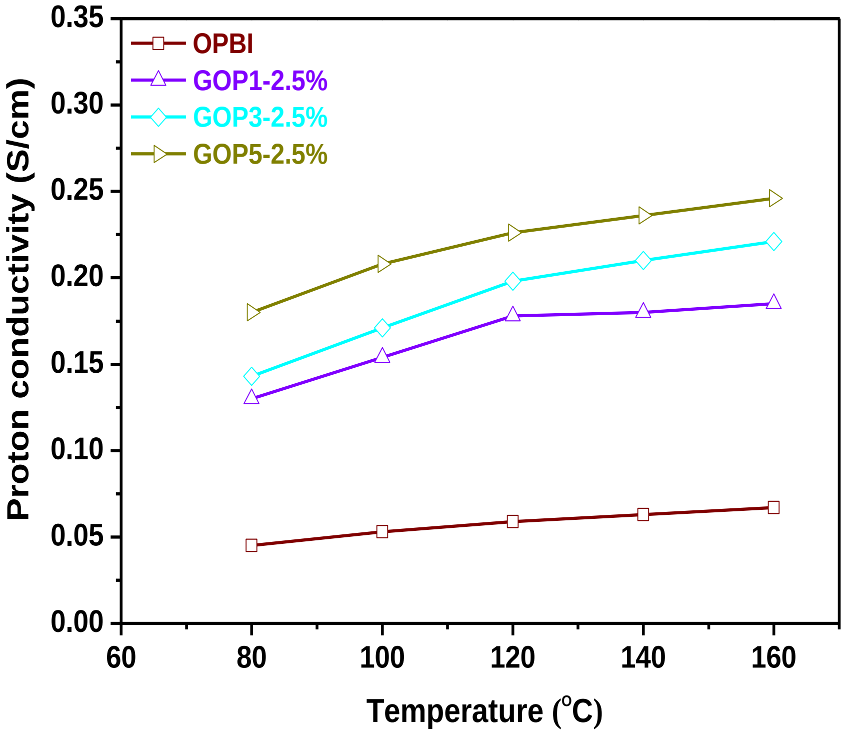

Figure A3.24. Proton conductivity vs temperature plot of GOP1-2.5%, GOP3-2.5% and GOP5-2.5% membranes.

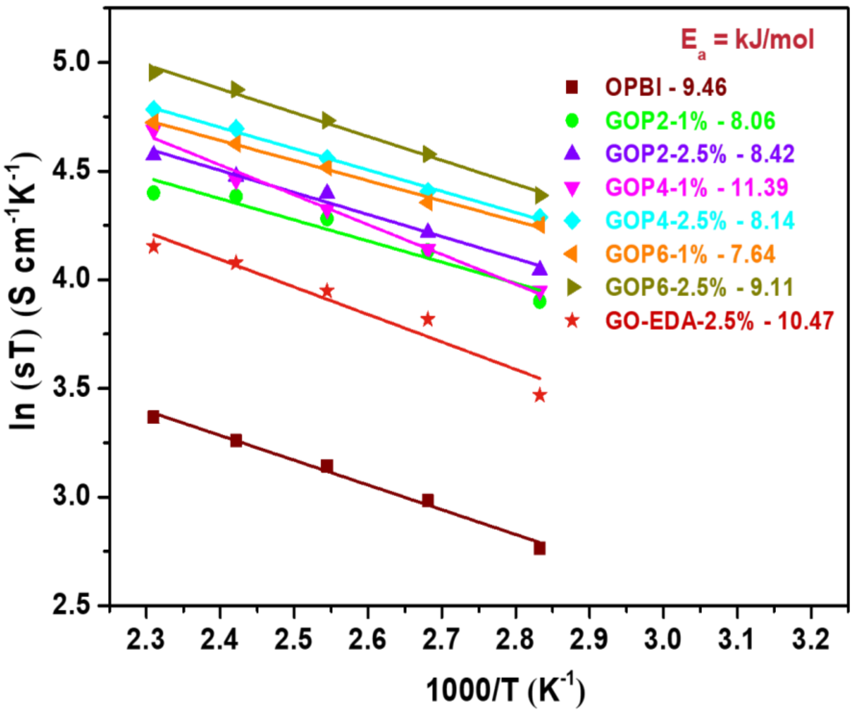

Figure A3.25. Activation energy of proton conduction for the OPBI and GOP loaded MMMs.

Table A3.3. Tensile strength and elongation at break values of PA loaded OPBI, and OPBI/GOP Composite Membranes.

Sample	**Tensile stress at break (MPa)**	**Elongation at break (%)**
OPBI	0.71	81
GOP2-1%	1.58	175
GOP2-2.5%	1.60	376
GOP4-1%	1.30	186
GOP4-2.5%	1.33	323
GOP6-1%	1.33	295
GOP6-2.5%	1.32	326

References

(1) Zaaba, N. I.; Foo, K. L.; Hashim, U.; Tan, S. J.; Liu, W. W.; Voon, C. H. *Procedia Eng.* **2017**, *184*, 469–477.

(2) Stenzel, M. H.; Davis, T. P. *J. Polym. Sci. Part A Polym. Chem.* **2002**, *40*, 4498–4512.

(3) Jesberger, M.; Barner, L.; Stenzel, M. H.; Malmström, E.; Davis, T. P.; Barner-Kowollik, C. *J. Polym. Sci. Part A Polym. Chem.* **2003**, *41*, 3847–3861.

(4) Yeole, N.; Kutcherlapati, S. N. R.; Jana, T. *J. Colloid Interface Sci.* **2015**, *443*, 137–142.

(5) Dhara, M.; Rudra, S.; Mukherjee, N.; Jana, T. *Polym. Chem.* **2021**, *12*, 3976–3991.

(6) Li, C.; Wang, C.; Ji, Z.; Jiang, N.; Lin, W.; Li, D. *European Polymer Journal* **2019**, *113* 404–410.

APPENDIX 4 (for Chapter 6)

Crosslinked Alkaline Anion Exchange Membrane from N-Spirocyclic Quaternary Ammonium and Polybenzimidazole

Synthesis of 1,2,4,5-tetrakis(bromomethyl)benzene

A literature reported procedure was followed,[1] Chloroform (80 mL) was added to a mixture of durene (5.16 g, 38.45 mmol), NBS (27.25 g, 153.1 mmol) and AIBN (0.642 g, 3.90 mmol). The mixture was kept under reflux for 2 h during which the reaction mixture turned orange. When the boiling became too vigorous because of the exothermic reaction, the heating was temporarily stopped. More NBS (6.75 g, 37.92 mmol) and AIBN (0.17 g, 1.03 mmol) were added and the reaction mixture was refluxed overnight. The hot mixture was then filtered to remove insoluble NBS. Chloroform was evaporated under reduced pressure until a dry residue was obtained. The residue was washed with cold methanol (3×50 mL) to give an off-white powder. The product was purified by two-fold recrystallization in chloroform, yielding colourless crystals (3.00 g, ≈17% isolated yield).

^{1}H NMR (500 MHz, $CDCl_3$) δ (ppm): 7.37 (s, 2H, Ar-*H*), 4.60 (s, 8H, Ar-CH_2-Br). Both ^{1}H and ^{13}C NMR spectra along with peak assignments are shown in **Figure A4.1.**

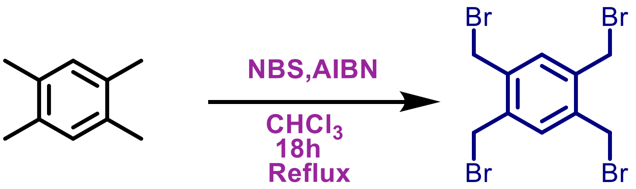

Scheme A4.1. Synthesis of 1,2,4,5-tetrakis(bromomethyl)benzene.

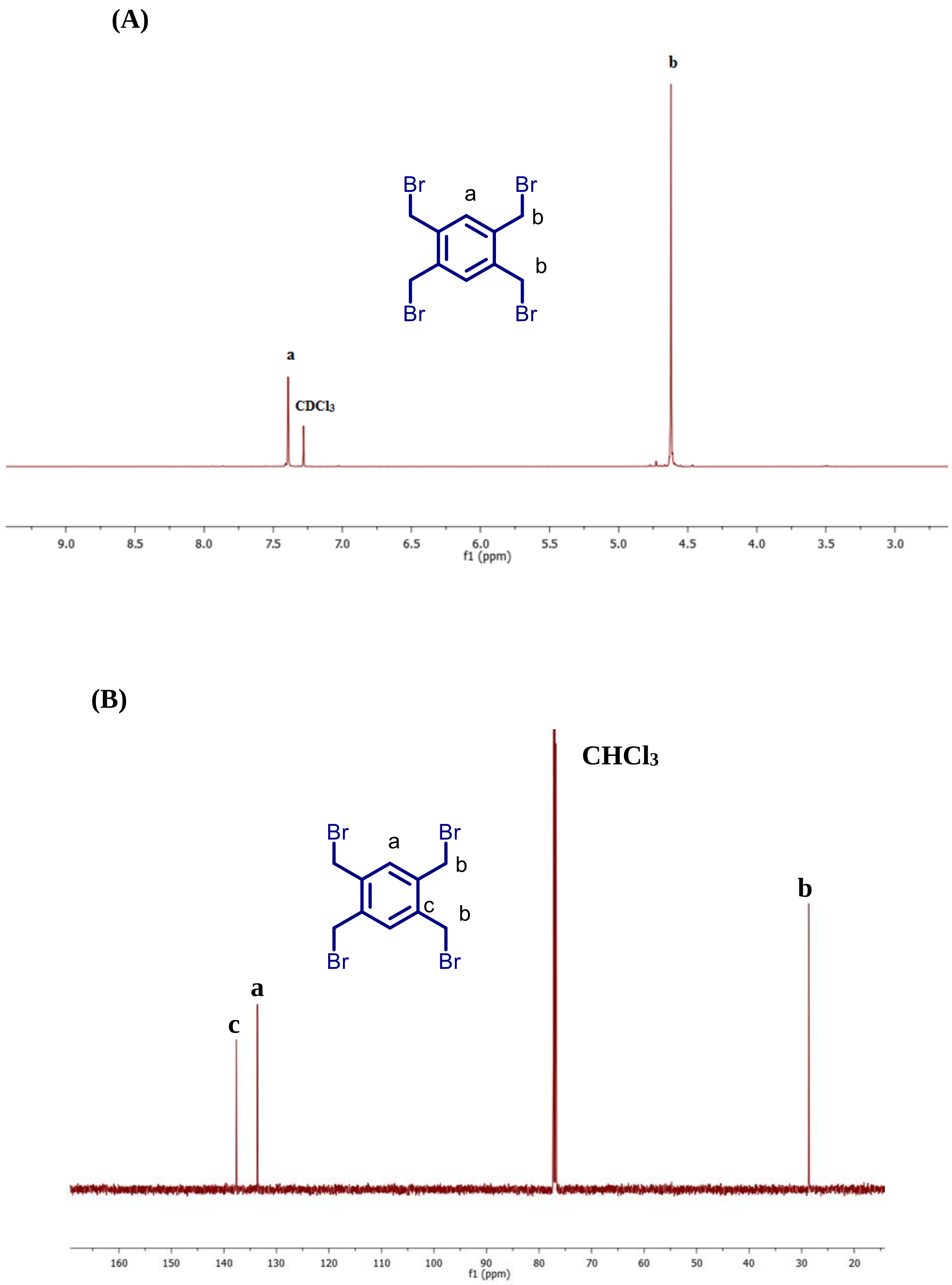

Figure A4.1. ^{1}H NMR (A) and ^{13}C NMR (B) spectra of 1,2,4,5-tetrakis(bromomethyl)benzene. $CDCl_3$ was used as NMR solvent.

Synthesis of Spiro ionene polymer (SP)

A reported procedure was modified for this synthesis[1] 1,2,4,5-Tetrakis(bromomethyl) benzene (1.17 g, 2.60 mmol) was dissolved in DMF (35 mL) in a 250 mL round flask. Next, DIPEA (2 mL, 12 mmol) and solution of 4,4′- trimethylenedipiperidine (0.554 g, 2.64 mmol) in a mixture of DMF (15 mL) and deionized water (8 mL) was added. The reaction mixture remained optically clear during 1 h stirring at 60 °C. The product was then precipitated in acetone (150-200 mL). Next, the white precipitate was washed with fresh acetone (2×150 mL), followed by drying under vacuum at 50 °C to yield an off-white powder (1.33 g, ≈100% isolated yield).

^{1}H NMR (500 MHz, D_2O) δ (ppm): 7.32 (s, 2H, Ar-*H*), 4.82 (d, 8H, J = 6.7 Hz, Ar-CH_2-N), 3.63 (d, 4H, J = 11.6 Hz, N-CH_2), 3.42 (t, 4H, J = 11.0 Hz, N-CH_2), 1.91 (d, 4H, J = 11.5 Hz, N-CH_2-CH_2), 1.63-1.55 (m, 6H, N-CH_2-CH_2 and C*H*), 1.30 (s, 6H, CH-CH_2 and CH-CH_2-CH_2).

^{13}C NMR (100 MHz, D2O) δ (ppm): 133.8, 118.9,70.8, 62.6, 61.0, 34.3, 32.1, 27.1, 22.6. Both ^{1}H and ^{13}C NMR spectra along with peak assignments are shown in **Figure A4.2.**

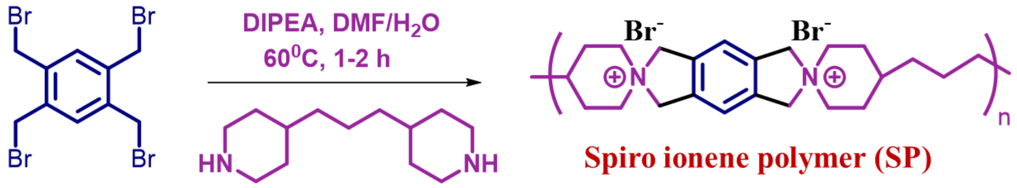

Scheme A4.2. Synthesis of spiro ionene polymer (SP)**.**

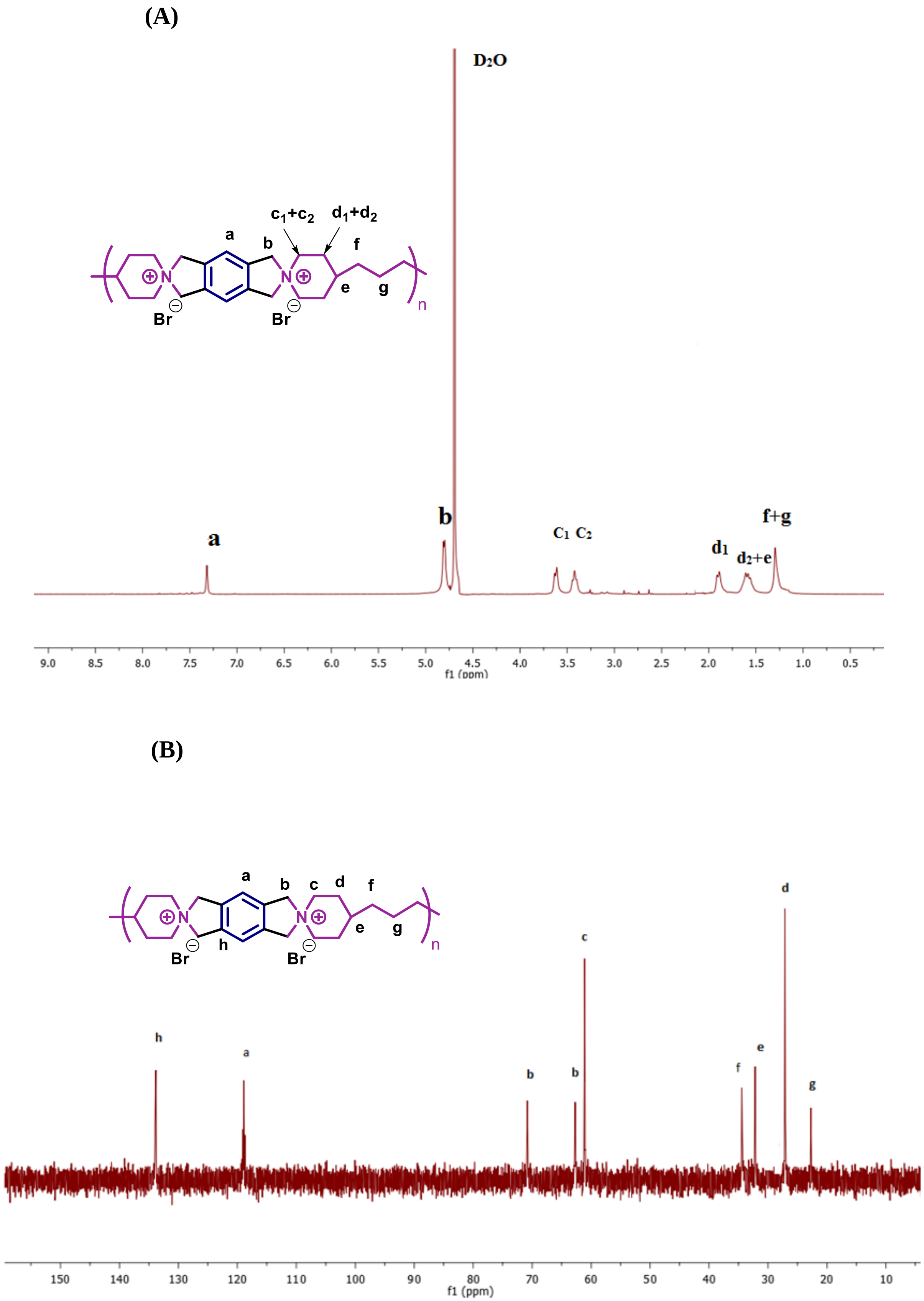

Figure A4.2. ^{1}H (A) and ^{13}C (B) NMR spectra of SP.

Table A4.1. Composition of porous blend membranes containing different porogen content in wt %.

Sample identity[#]	SP (wt %)	PyPBI (wt %)	DBP (wt %)	Induced expected experimentally porosity (P) (wt %)
S50P50-P10	50	50	10	9.49
S50P50-P25	50	50	25	26.13
S50P50-P40	50	50	40	39.31

[#] Porous AEMs in the Br^- and OH^- form are named as S50P50-P10-Br and S50P50-P10-OH, respectively and so on.

Membrane characterizations

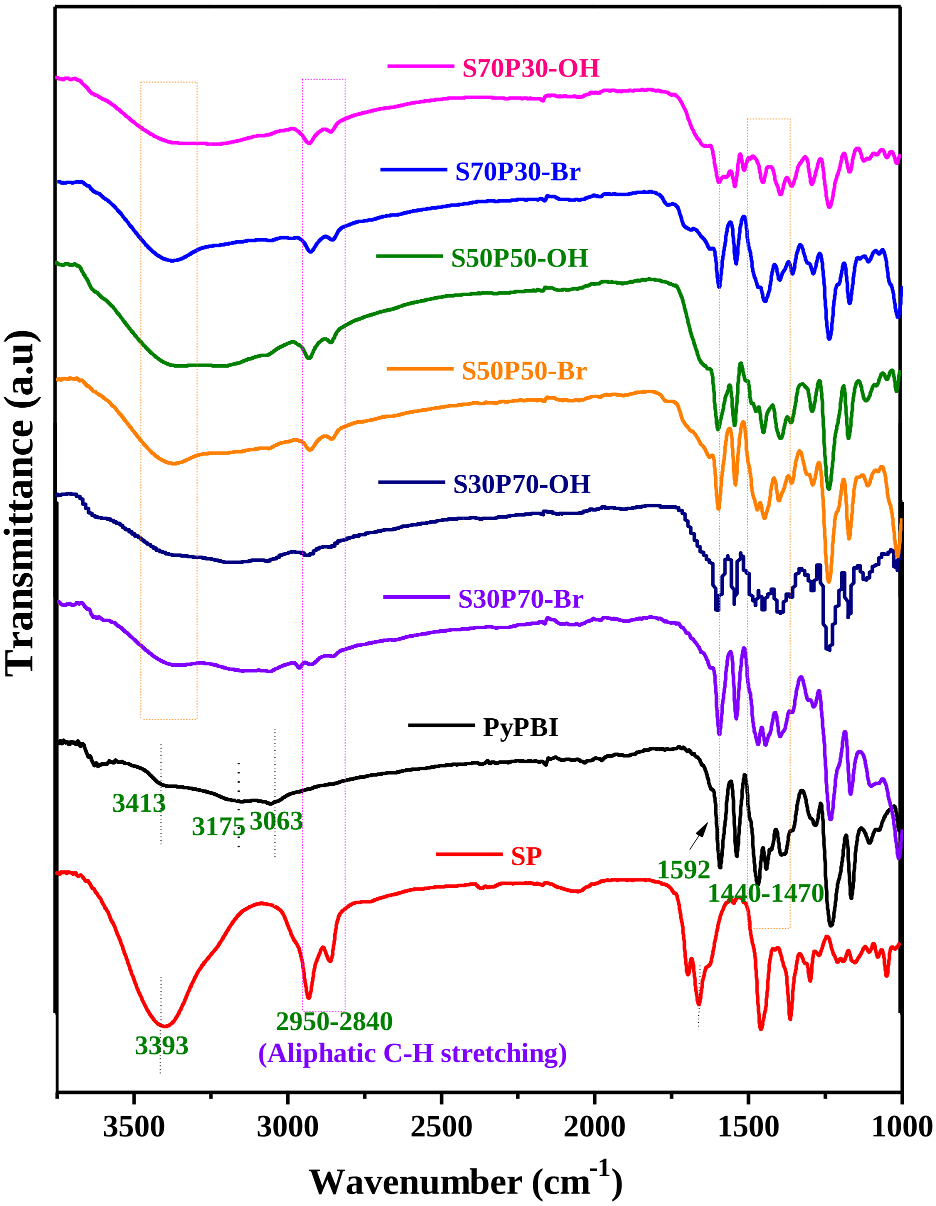

Figure A4.3. Infrared spectra (FT-IR) of all the Br$^-$ form membranes and ionically crosslinked OH$^-$ form membranes along with their parent polymers (PyPBI and SP).

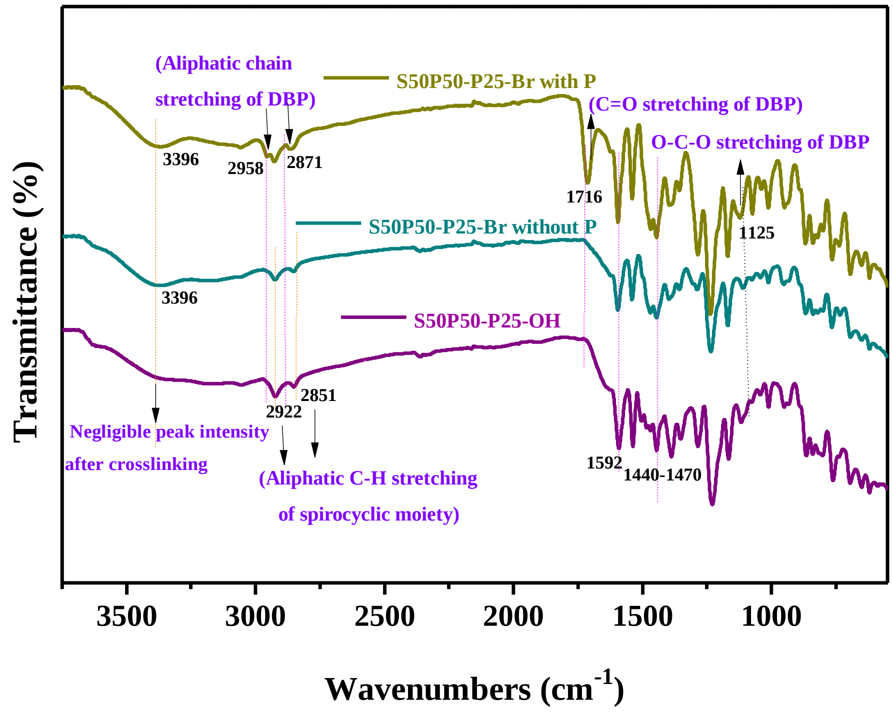

Figure A4.4. FT-IR spectra of S50P50-P25-Br with P (before porogen removal), without P (after porogen removal) and ionically crosslinked S50P50-P25-OH.

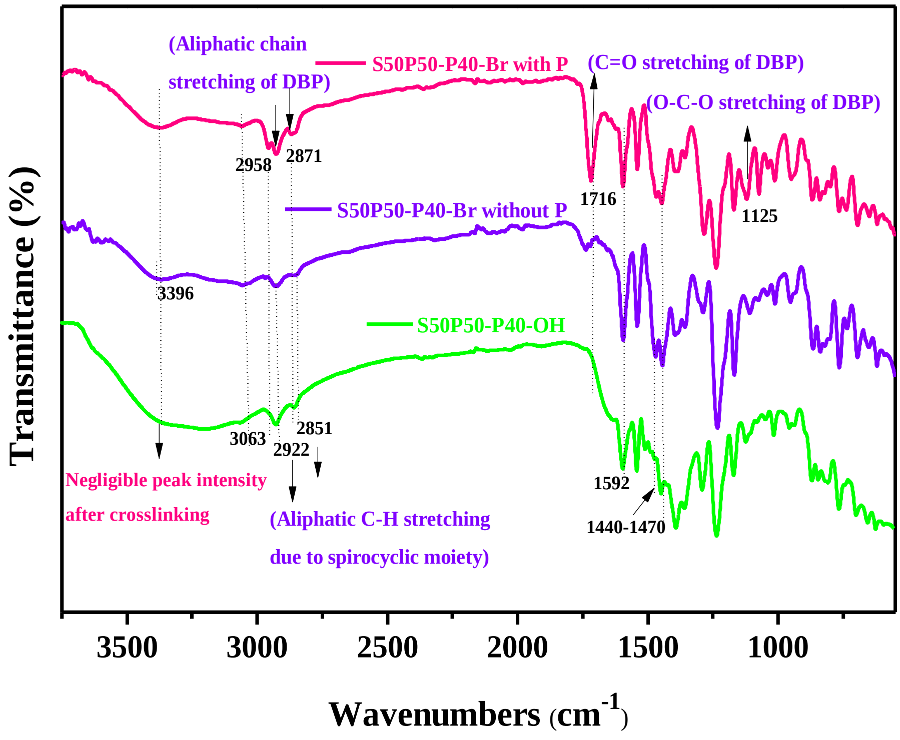

Figure A4.5. FT-IR spectra of S50P50-P40-Br with P (before porogen removal), without P (after porogen removal) and ionically crosslinked S50P50-P40-OH.

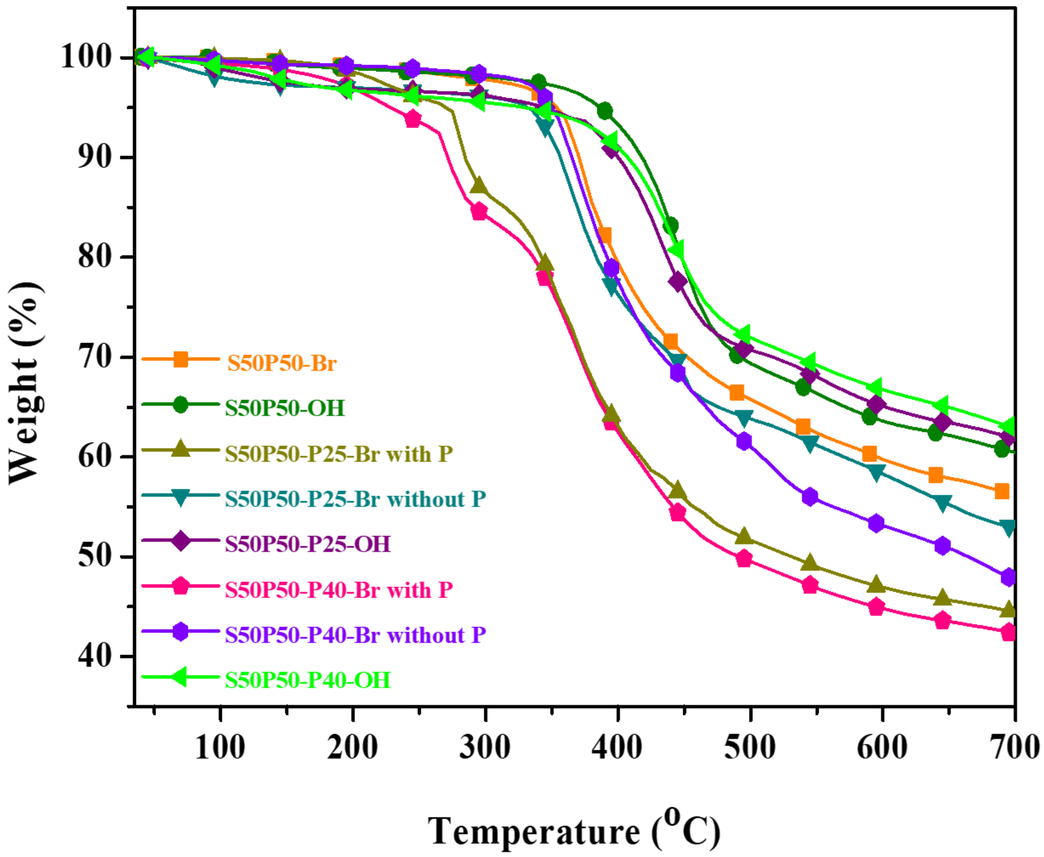

Figure A4.6. TGA analysis of S50P50-P25 & S50P50-P40 with P (before porogen removal), without P (after porogen removal) Br^- form membranes, and ionically crosslinked S50P50-P25-OH & S50P50-P40-OH membranes in a comparison with S50P50-Br and S50P50-OH membranes.

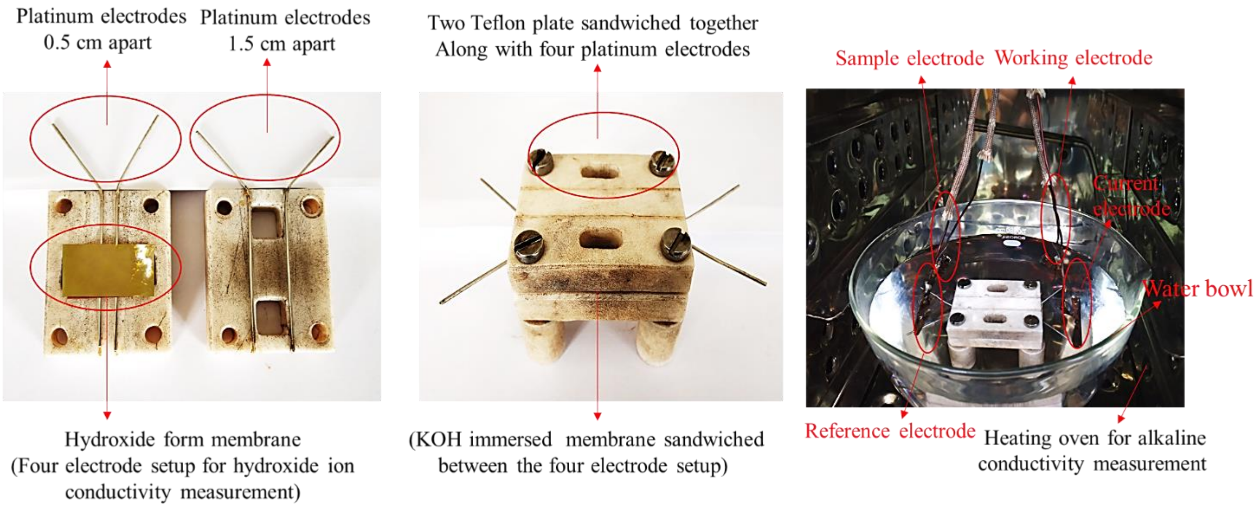

Figure A4.7. Pictorial representation of two Teflon plates with four platinum electrode set-up utilized in hydroxide (OH^-) ion conductivity measurement under hydrated condition.

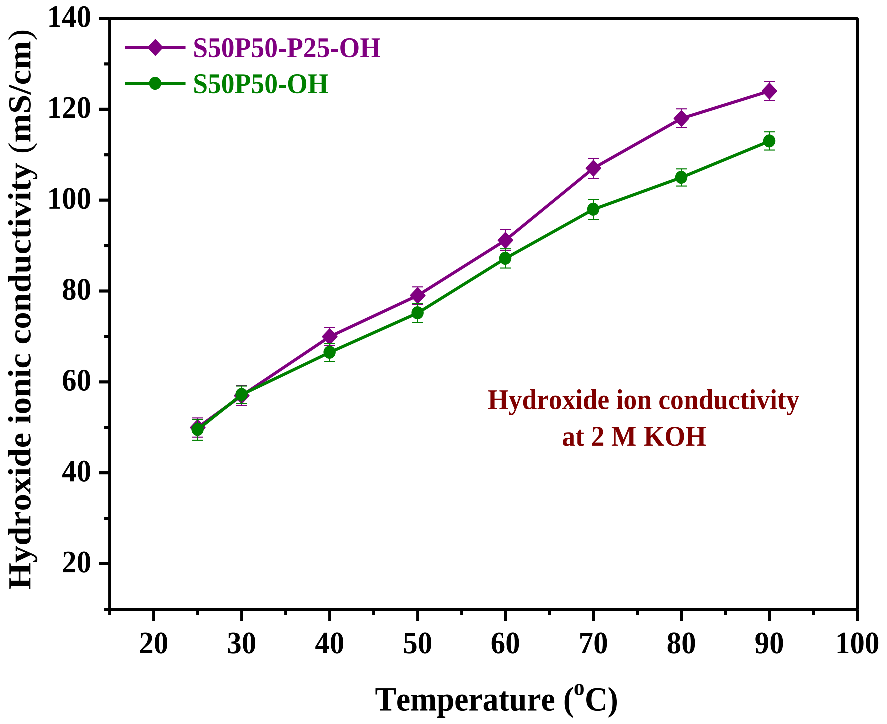

Figure A4.8. Hydroxide ion conductivity of S50P50-OH and S50P50-P25-OH membranes at 2 M KOH.

Alkaline stability

All the ICL and porous ICL membranes were immersed in 1 M aqueous KOH solution at room temperature and at 80 °C for a longer period of time (960h). Also, S50P50-OH and S50P50-P25-OH membranes were treated with 2 M KOH solution for 500 h at 60 °C to check their alkaline stability. The alkaline stability of all the anion exchange membranes in basic condition was studied with the time by measuring the weight loss (%) through thermogravimetric analysis (TGA) before and after alkaline stability test and gravimetric analysis by taking the membrane weight before and after alkaline treatment, IEC & hydroxide ion conductivity measurement after 500 h alkaline treatment and comparing with the freshly alkali treated samples, and also from FT-IR spectroscopy analysis before and after alkaline stability test.

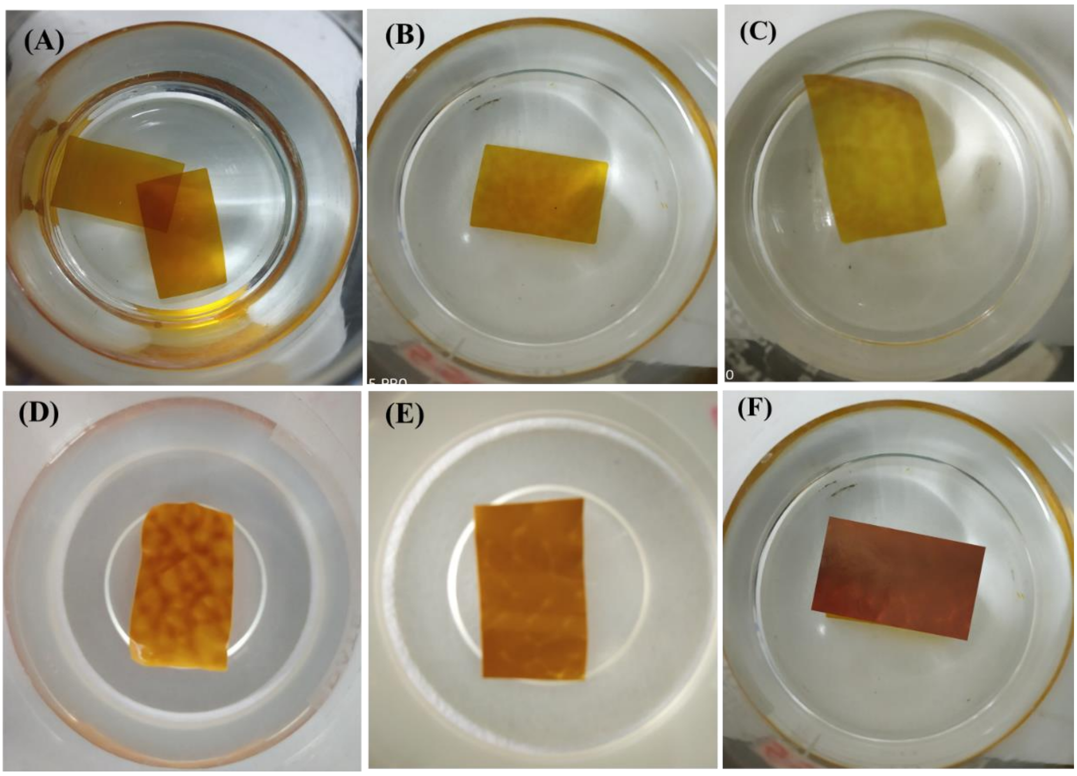

Figure A4.9. Images of ionically crosslinked AAEMs after 960 h of alkaline treatment at 80 °C in 1 M KOH. **(A)** S30P70-OH, **(B)** S50P50-OH, **(C)** S70P30-OH, **(D)** S50P50-P10-OH, **(E)** S50P50-P25-OH and **(F)** S50P50-P40-OH.

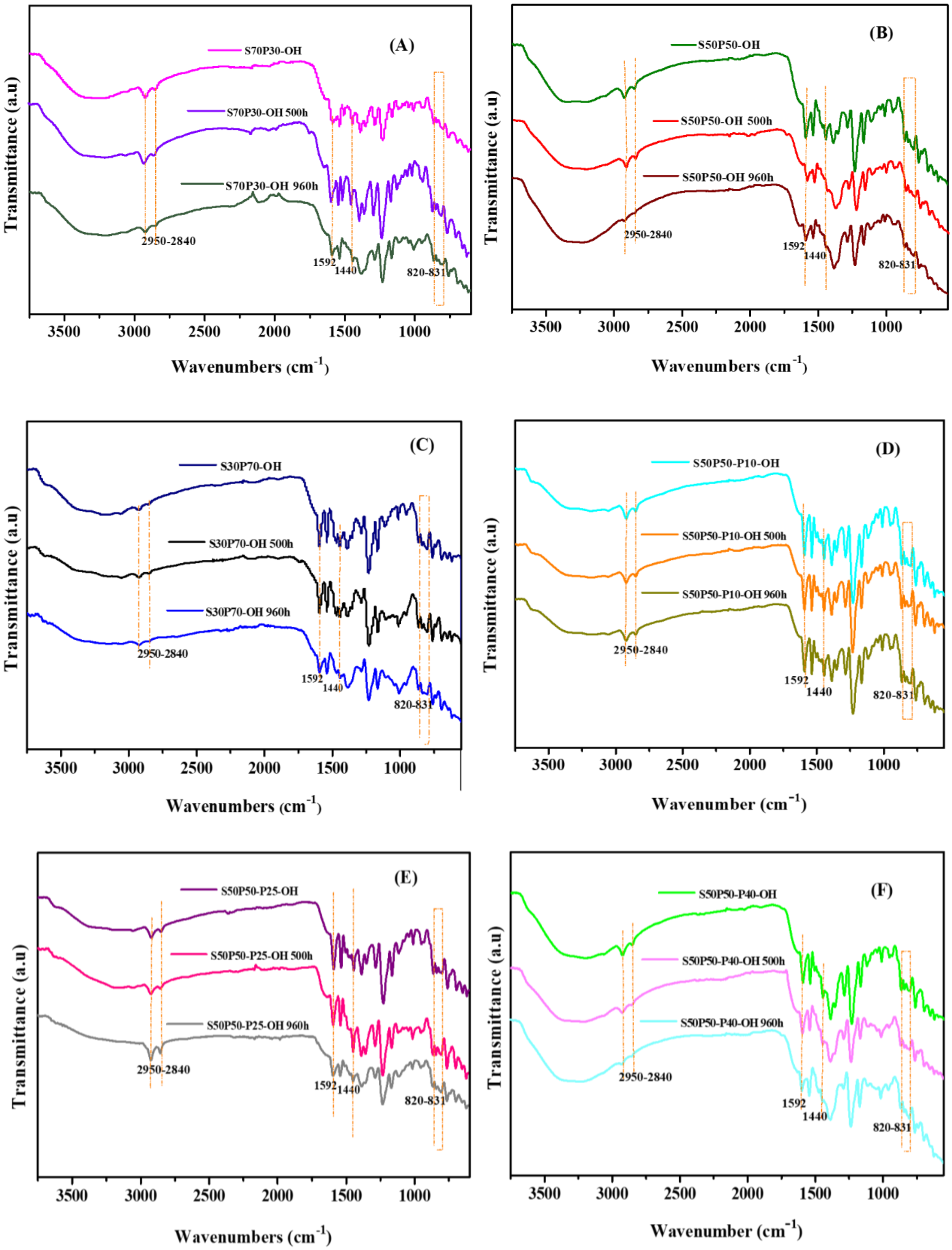

Figure A4.10 (A-F). The membranes at various time interval during the 1 M KOH treatment at 80 °C. For all the samples spectra were recorded after 500 h and 960 h, and compared with the spectra before the stability test.

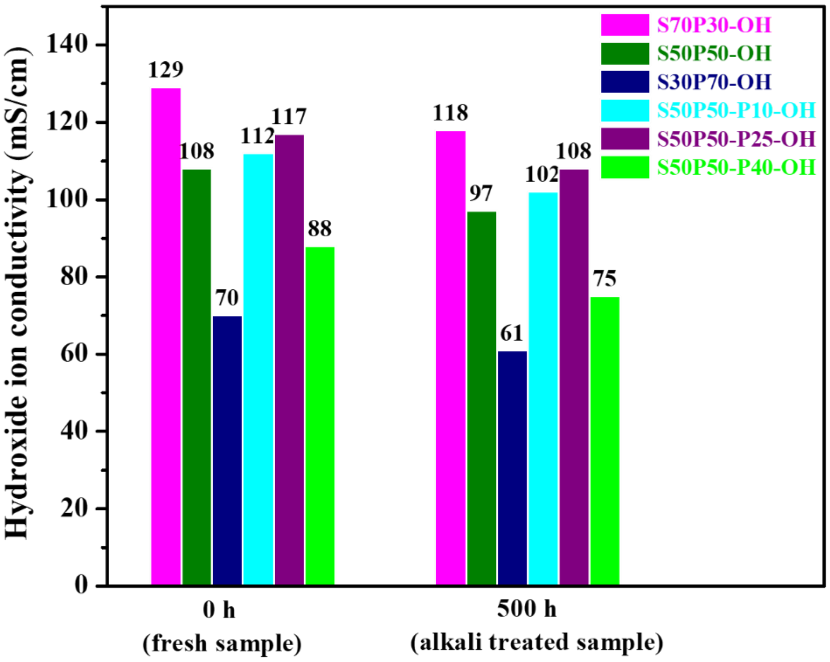

Figure A4.11. Comparison of hydroxide (OH$^-$) ion conductivity at 90 °C of all the ICL and porous ICL AAEMs before alkaline treatment and after 500 h alkaline (1 M KOH at 80 °C) treatment.

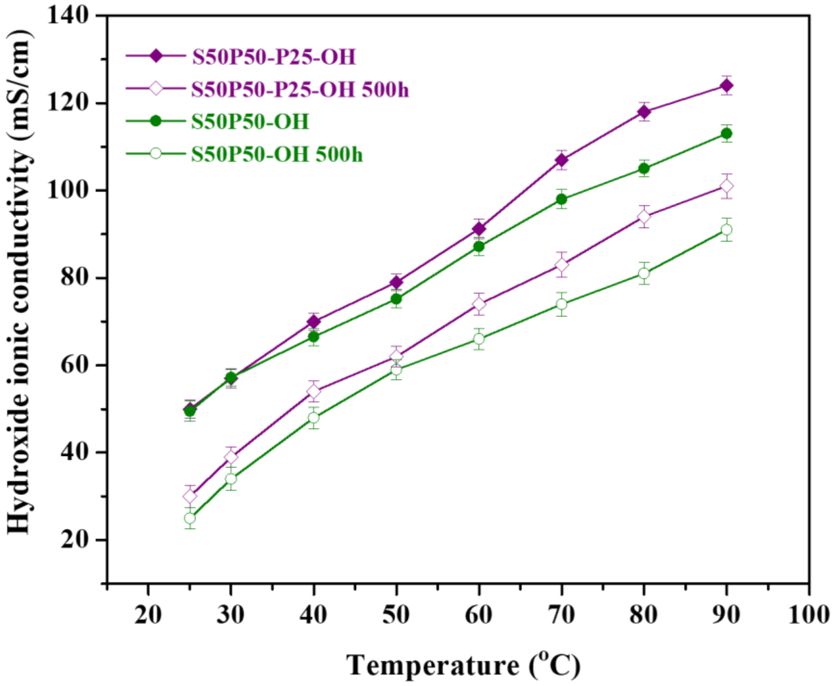

Figure A4.12. Comparison of hydroxide (OH$^-$) ion conductivity of S50P50-OH & S50P50-P25- OH AAEMs after treatment with 2 M KOH for 500 h alkaline treatment at 60 °C.

Table A4.2. OH^- conductivity comparison of ionically crosslinked AEMs after 500h alkaline treatment in 2 M KOH at 60 °C in a comparison with freshly alkali treated AEMs in 2 M KOH.

Sample identity	OH^- ion conductivity (mS/cm) at 90 °C	OH^- conductivity at 90 °C after 500h of treatment in 2 M KOH	Decrease in σ_{OH^-} (%)
S50P50-OH	113	91	19.47
S50P50-P25-OH	124	101	18.54

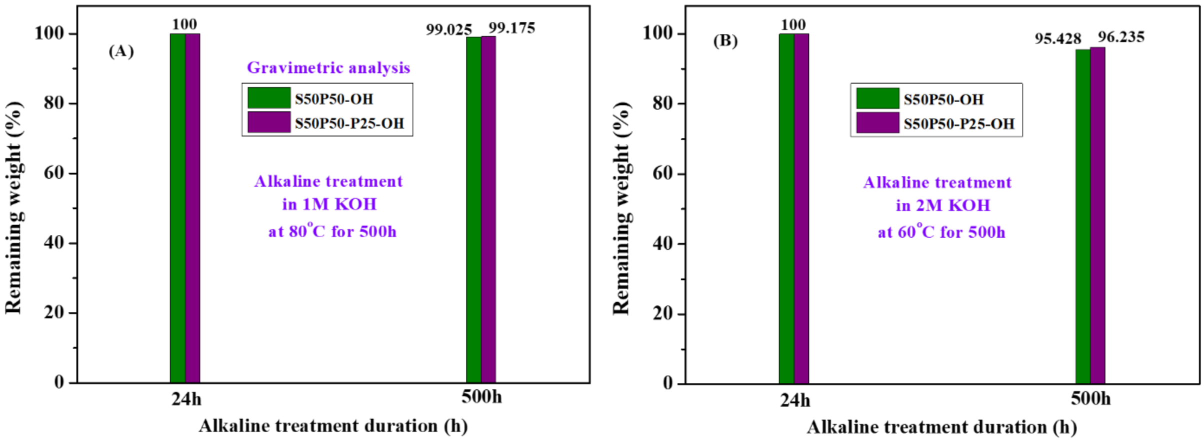

Figure A4.13. Gravimetric analysis of S50P50-OH and S50P50-P25- OH membranes before and after alkaline stability test (A) 1 M KOH at 80 °C, 500 h. (B) 2 M KOH at 60 °C, 500 h.

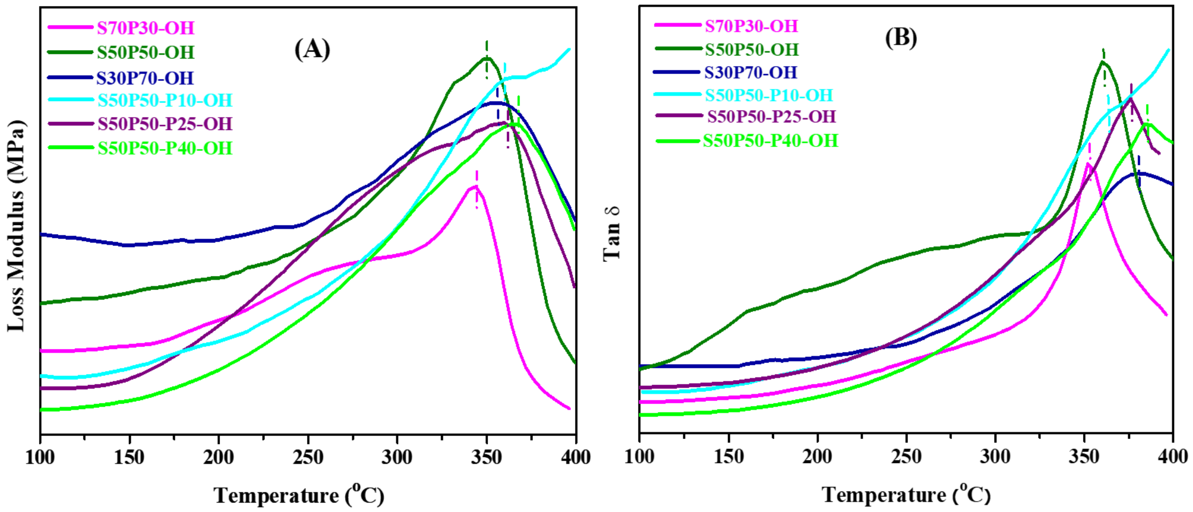

Figure A4.14. Glass transition temperature (T_g) obtained from **(A)** temperature dependent Loss Modulus plot and **(B)** Tan δ of ionically crosslinked AEMs. The peak indicated with dotted vertical line is the T_g.

Table A4.3. Thermo-mechanical and glass transition temperature data of ionically crosslinked hydroxide (OH^-) form membranes obtained from DMA analysis.

Sample	E′(MPa) at 100 °C	E′(MPa) at 400 °C	T_g °C from E″	T_g °C from Tan δ
S70P30-OH	5801	821	343	352
S50P50-OH	7397	977	350	360
S30P70-OH	5087′	1456	356	377
S50P50-P10-OH	4751	2466	359	363
S50P50-P25-OH	3512	1188	361	376
S50P50-P40-OH	2354	542	367	385

Table A4.4. The IEC and hydroxide ionic conductivity data of the present work compared with literature data.

Polymer backbones and references	Cationic site	IEC (meq/g)	Hydroxide conductivity (mS/cm)
Present work (Ionically crosslinked AEM) (S70P30 OH)	***NSQA***	***2.39***	***50.7 (25 °C) & 129 (90 °C)***
poly(2,6-dimethyl-1,4-phenylene oxide)-based AEMs[2]	QA	2.87	99 (RT)
Fluorinated poly(olefin)-based AEMs[3]	QA	1.12	91 (80 °C)
Poly(p-phenylene-co-aryl ether ketone)s[4]	QA	1.58	37.6 (80 °C)
Polyphenylene oxide with long alkyl side chains[5]	QA	2.75	43 (RT)
Poly phenylene oxide with fluorine side chains[6]	QA	1.89	176 (80 °C)
spirobiindane-based microporous poly(ether sulfone)s[7]	NSQA	1.18	27 (80 °C)
polystyrene-b-poly(ethylene-co-butylene)-b-polystyrene (SEBS)[8]	QA	1.55	93 (80 °C)
Olefinic-type copolymer based AEMs[9]	QA, Pyr & Im	1.24, 1.26 & 1.24	60 (80 °C), 50 (80 °C) & 40 (80 °C)
Poly(phenylene oxide)s incorporating *N*-spirocyclic quaternary ammonium based AEMs[10]	NSQA (Qpip)	1.91	51.6 (60 °C)
bis-six-membered N-cyclic quaternary ammonium cations in advanced anion exchange membranes[11]	QA	1.85	76.5 (80 °C)
Quaternized aromatic/perfluoroalkyl copolymer (QPAF) based AEMs[12]	QA	1.33	152 (80 °C)
Hexyl bis(quaternary ammonium)-mediated partially crosslinked SEBSs as AEMs[13]	QA	2.13	174.8 (80 °C)
Anion exchange membranes with dense N-spirocyclic cations as side-chain[14]	NSQA	1.70	95.5 (80 °C)

Polymer backbones and references	Cationic site	IEC (meq/g)	Hydroxide conductivity (mS/cm)
grafted quaternized side chains as AEMs[15]	QA	1.84	82.4 (80 °C)
cross-linked (AEM) based on poly(2,6-dimethylphenylene oxide) (PPO)[16]	QA	3.21	31 (RT)
tethered poly(phenylene oxide) (PPO) different hetero-cycloaliphatic QA cations via pentyl spacer chains[17]	QA, Pip, Qui Aze Mor	1.90 1.78 1.78 1.72 1.78	139 (80 °C) 117 (80 °C) 151 (80 °C) 78 (80 °C) 101 (80 °C)
Ether spaced N-spirocyclic quaternary ammonium functionalized crosslinked polysulfone based AEM[18]	NSQA	2.05	85.7 (80 °C)
Bis-N-spirocyclic Quaternary Ammonium Moieties as AEMs[19]	NSQA (Spiro-Pyr)	1.80	110 (80 °C)
Poly(arylene alkylene)s with pendant N-spirocyclic quaternary ammonium cation as AEMs[20]	NSQA	2.29	102 (80 °C)
PPO tethered with Six- Membered N-Spirocyclic Ammonium cation as AEMs[21]	NSQA	2.49	96 (80 °C)
poly (ether ether ketone) containing N-spirocyclic quaternary ammonium based AEM[22]	NSQA (Spiro-Pyr)	1.46	49.6 (80 °C)
poly(arylene ether)s-based anion exchange membranes bearing pendent N-spirocyclic quaternary ammonium[23]	NSQA	0.93	63.1 (80 °C)

QA= Quaternary ammonium, NSQA= N-Spirocyclic Quaternary ammonium, Im=Imidazolium, Pip= Piperidinium, Qpip= Quaternary piperidinium, Pyr=Pyrrolidinium, Qui= Quinuclidinium, Aze= Azepanium, Mor= Morpholinium.

References

(1) Pham, T. H.; Olsson, J. S.; Jannasch, P. *J. Am. Chem. Soc.* **2017,** *139*, 2888–2891.

(2) Zhu, L.; Pan, J.; Wang, Y.; Han, J.; Zhuang, L.; Hickner, M. A. *Macromolecules* **2016**, *49*, 815–824.

(3) Zhu, L.; Peng, X.; Shang, S. L.; Kwasny, M. T.; Zimudzi, T. J.; Yu, X.; Saikia, N.; Pan, J.; Liu, Z. K.; Tew, G. N.; Mustain, W. E.; Yandrasits, M.; Hickner, M. A. *Adv. Funct. Mater.* **2019**, *29*, 1902059.

(4) Dong, X.; Xue, B.; Qian, H.; Zheng, J.; Li, S.; Zhang, S. *J. Power Sources* **2017**, *342*, 605–615.

(5) Li, N.; Leng, Y.; Hickner, M. A.; Wang, C. Y. *J. Am. Chem. Soc.* **2013**, *135*, 10124–10133.

(6) Zhu, L.; Pan, J.; Christensen, C. M.; Lin, B.; Hickner, M. A. *Macromolecules* **2016**, *49*, 3300–3309.

(7) Choi, J.; Kim, M. H.; Han, J. Y.; Chae, J. E.; Lee, W. H.; Lee, Y. M.; Lee, S. Y.; Jang, J. H.; Kim, J. Y.; Henkensmeier, D.; Yoo, S. J.; Sung, Y. E.; Kim, H. J. *J. Memb. Sci.* **2018**, *568*, 67–75.

(8) Jeon, J. Y.; Park, S.; Han, J.; Maurya, S.; Mohanty, A. D.; Tian, D.; Saikia, N.; Hickner, M. A.; Ryu, C. Y.; Tuckerman, M. E.; Paddison, S. J.; Kim, Y. S.; Bae, C. *Macromolecules* **2019**, *52*, 2139–2147.

(9) Pan, J.; Zhu, H.; Cao, H.; Wang, B.; Zhao, J.; Sun, Z.; Yan, F. *J. Membr. Sci.* **2021**, *620*, 118794.

(10) Xue, J.; Liu, X.; Zhang, J.; Yin, Y.; Guiver, M. D. *J. Membr. Sci.* **2020**, *595*, 117507.

(11) Chu, X.; Liu, L.; Huang, Y.; Guiver, M. D.; Li, N. *J. Membr. Sci.* **2019**, *578*, 239–250.

(12) Mahmoud, A. M. A.; Elsaghier, A. M. M.; Otsuji, K.; Miyatake, K. *Macromolecules* **2017**, *50*, 4256–4266.

(13) Al Munsur, A. Z.; Hossain, I.; Nam, S. Y.; Chae, J. E.; Kim, T. H. *Int. J. Hydrogen Energy* **2020**, *45*, 15658–15671.

(14) Liu, F. H.; Yang, Q.; Gao, X. L.; Wu, H. Y.; Zhang, Q. G.; Zhu, A. M.; Liu, Q. L. *J. Membr. Sci.* **2020**, *595*, 117560.

(15) Wang, X.; Chen, W.; Yan, X.; Li, T.; Wu, X.; Zhang, Y.; Zhang, F.; Pang, B.; He, G. *J. Power Sources* **2020**, *451*, 227813.

(16) Zhu, L.; Zimudzi, T. J.; Wang, Y.; Yu, X.; Pan, J.; Han, J.; Kushner, D. I.; Zhuang, L.; Hickner, M. A. *Macromolecules* **2017**, *50*, 2329–2337.

(17) Dang, H. S.; Jannasch, P. *J. Mater. Chem. A* **2017**, *5*, 21965–21978.

(18) Zhang, Y.; Chen, W.; Yan, X.; Zhang, F.; Wang, X.; Wu, X.; Pang, B.; Wang, J.; He, G. *J. Membr. Sci.* **2020**, *598*, 117650.

(19) Pham, T. H.; Jannasch, P. *ACS Macro Lett.* **2015,** *4*, 1370–1375.

(20) Pham, T. H.; Olsson, J. S.; Jannasch, P. *J. Mater. Chem. A* **2018**, *6*, 16537–16547.

(21) Chen, N.; Long, C.; Li, Y.; Lu, C.; Zhu, H. *ACS Appl. Mater. Interfaces* **2018**, *10*, 15720–15732.

(22) Shang, L.; Yao, D.; Pang, B.; Zhao, C. *Int. J. Hydrogen Energy* **2021**, *46*, 19116–19128.

(23) Lin, C.; Yu, D.; Wang, J.; Zhang, Y.; Xie, D.; Cheng, F.; Zhang, S. *Int. J. Hydrogen Energy* **2019**, *44*, 26565–26576.

APPENDIX 5 (for Chapter 7)

Multicationic Anion Exchange Membranes from Pyridine-bridged Polybenzimidazole and Polymer Ionic Liquid Grafted Graphene Oxide

Synthesis of 3-butyl-1-vinylimidazolium iodide [VImBu][I]: Following a literature reported methodology,[1] [VImBu][I] was synthesized by stirring a mixture containing 1-vinylimidazole (2.0 g, 0.021 mol), butyl iodide (4.0 g, 0.021 mol), and KOH (1.22 g, 0.021 mol) in acetonitrile (30 mL) at room temperature under a nitrogen atmosphere for 48 h. The KBr precipitate was removed by filtration. After the evaporation of solvent, the mixture was washed three times with diethyl ether to obtain [VImBu][I]. The synthesized product was thoroughly characterized by ^{1}H and ^{13}C NMR spectroscopy for structure confirmation (**Figure A5.1A, B**), with detailed ^{1}H-NMR integration.

Synthesis of 1-(4-vinylbenzyl)-2-methylimidazole.

Following a literature reported procedure,[2] 1-(4-vinyl benzyl)-2-methylimidazole was synthesized by stirring a mixture containing 4.10 g (0.05 mol) of 2-methylimidazole, 7.65 g (0.05 mol) of 4-vinylbenzyl chloride, and 5.60 g (0.14 mol) NaOH in acetonitrile (40 mL) was stirred at room temperature for 36 h under an argon atmosphere. The solvent was removed under dynamic vacuum, and the crude product was extracted with CH_2Cl_2 three times. The combined organic phase was washed with distilled water and dried over anhydrous $MgSO_4$ and the solvent was removed under vacuum. The resultant yellow oil was dried in dynamic vacuum at room temperature.

Synthesis of 1-butyl-2-methyl-1-(4-vinylbenzyl)imidazolium iodide [VBImBu][I]: [VBImBu][I] was synthesized by stirring a mixture containing 1-(4-vinylbenzyl)-2-methylimidazole and an equivalent molar amount of 1-iodobutane for 24 h at 0 °C. The resultant viscous oil was washed with ethyl ether four times and then dried in vacuum at room temperature. The synthesized product was thoroughly characterized by ^{1}H and ^{13}C NMR spectroscopy for structure confirmation (**Figure A5.2A, B**).

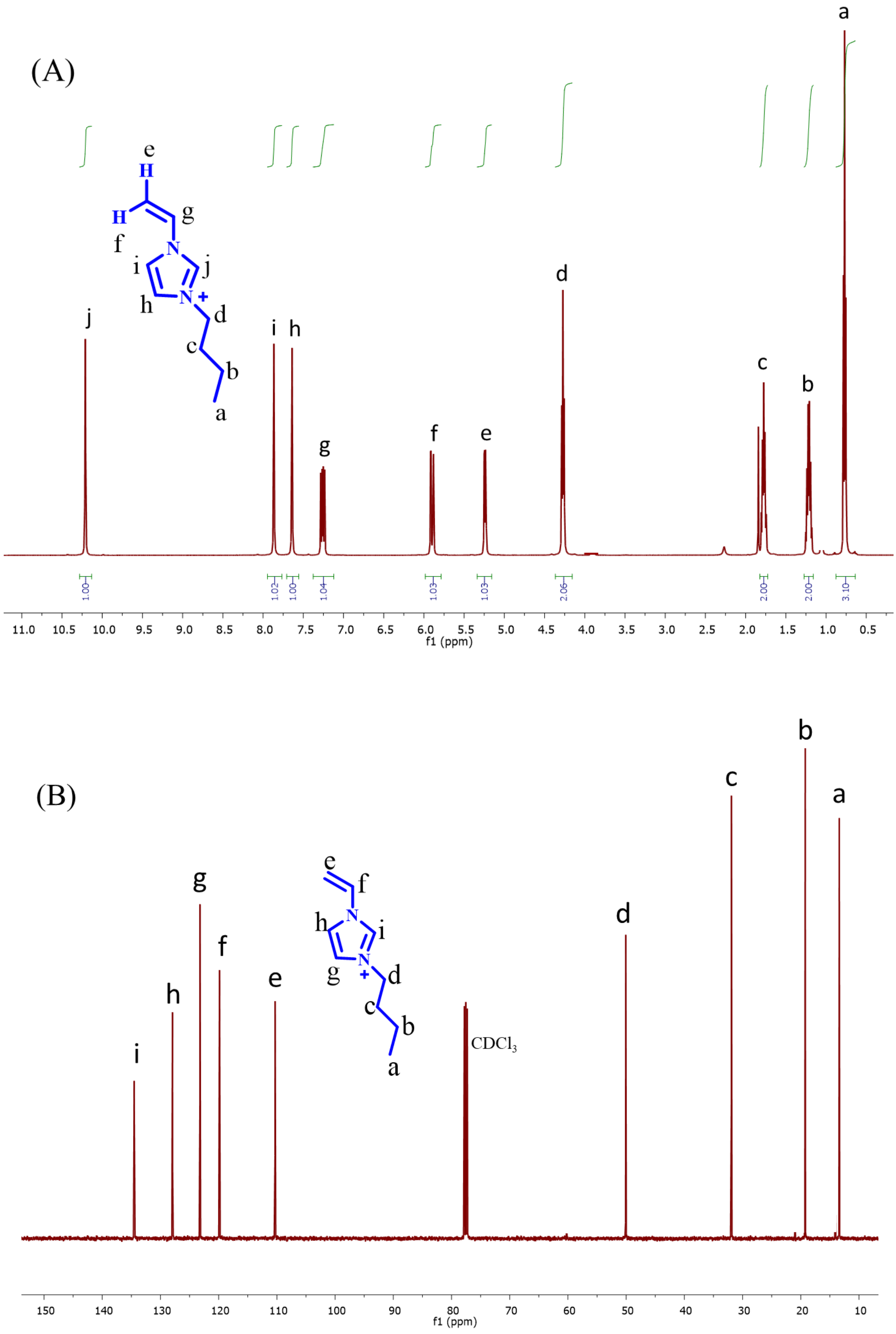

Figure A5.1. ^{1}H NMR data **(A),** ^{13}C NMR data **(B)** of 1-vinylimidazolium Iodide ([VImBu][I]).

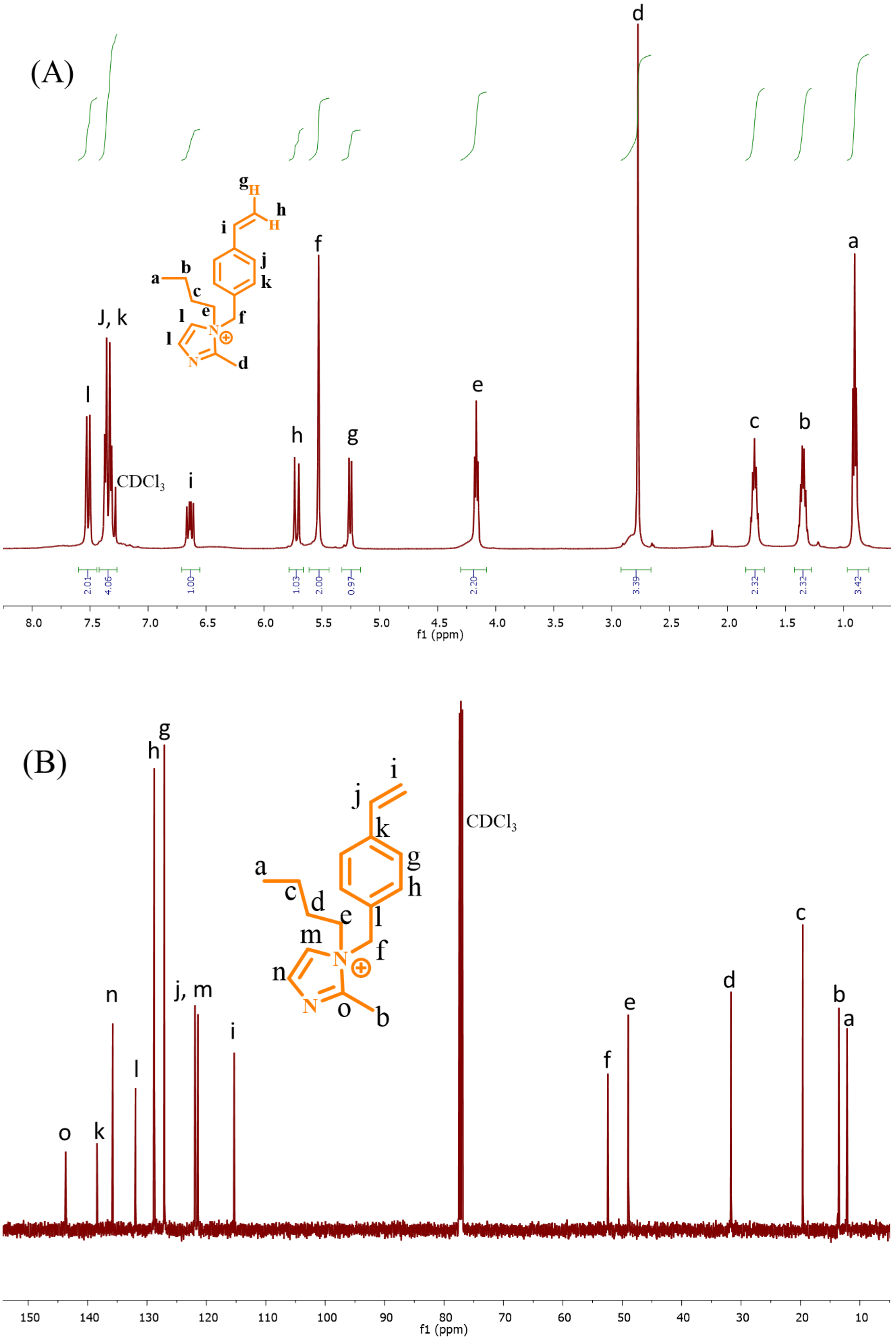

Figure A5.2. ^{1}H NMR data **(A),** ^{13}C NMR data **(B)** of [VBImBu][I].

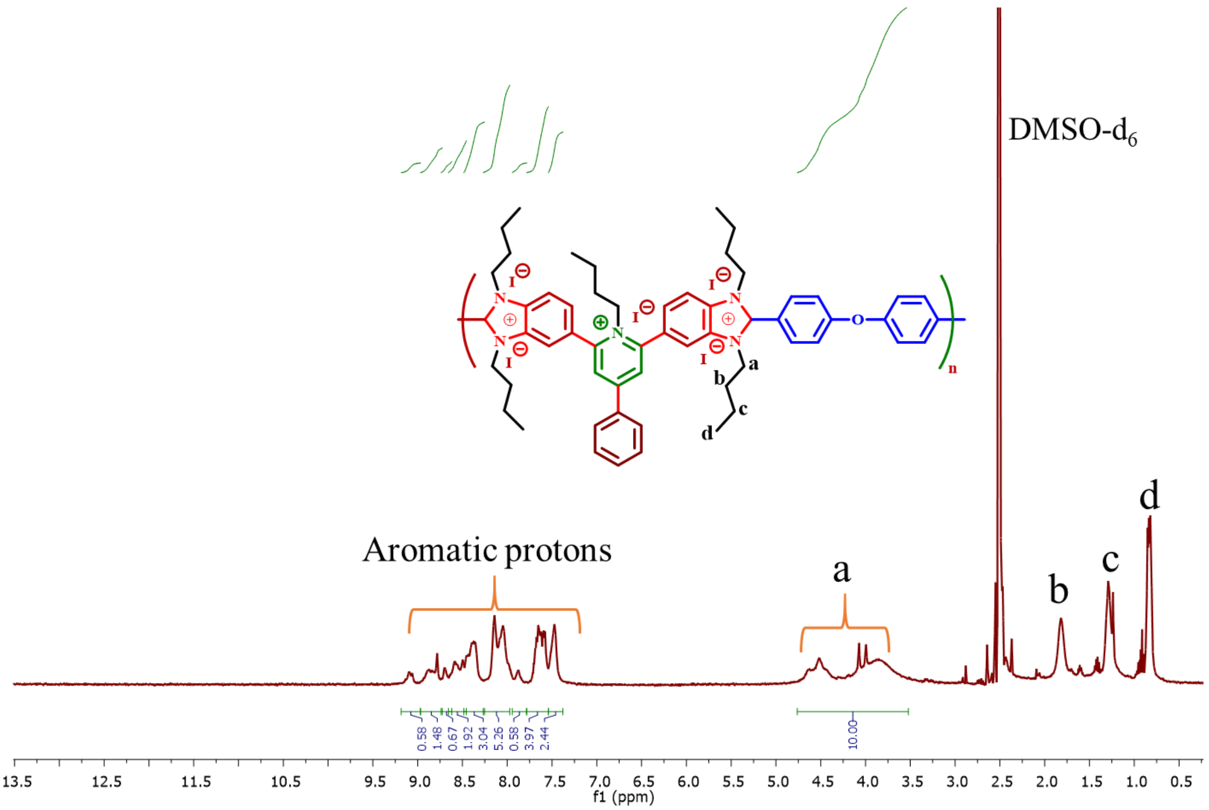

Figure A5.3. ^{1}H NMR data **of** PyPBI-BuI-OBA.

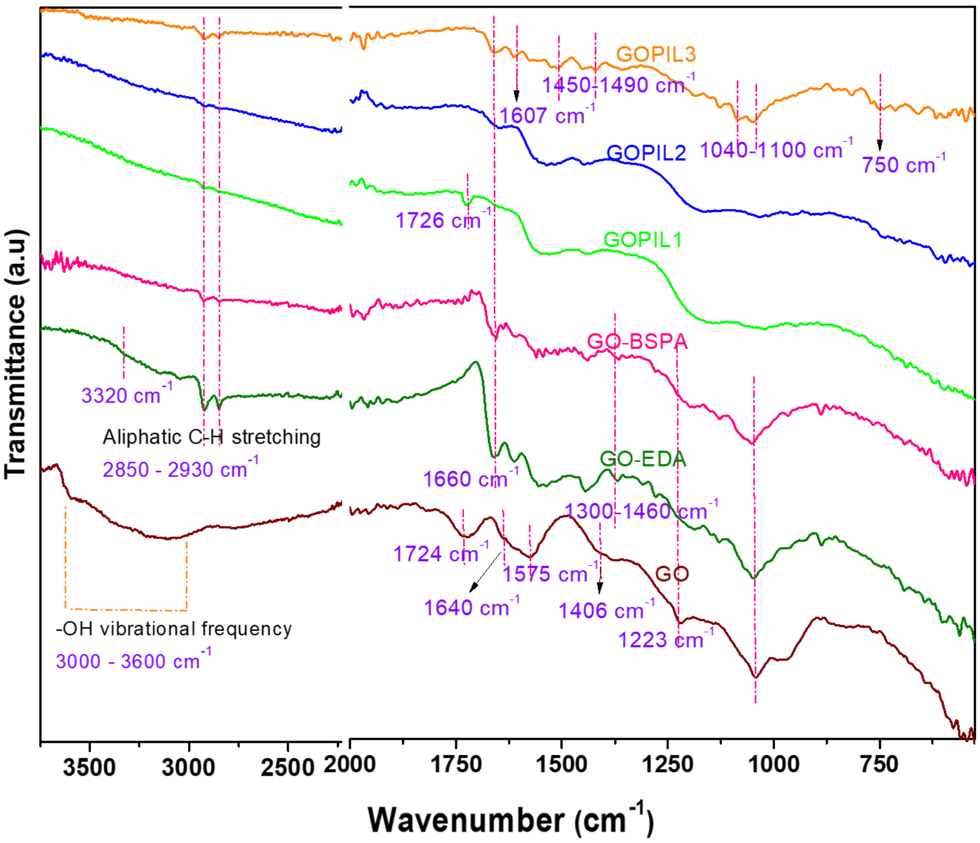

Figure A5.4. FT-IR analysis data of GO, GO-EDA, GO-BSPA, GOPIL1, GOPIL2 and GOPIL3 samples.

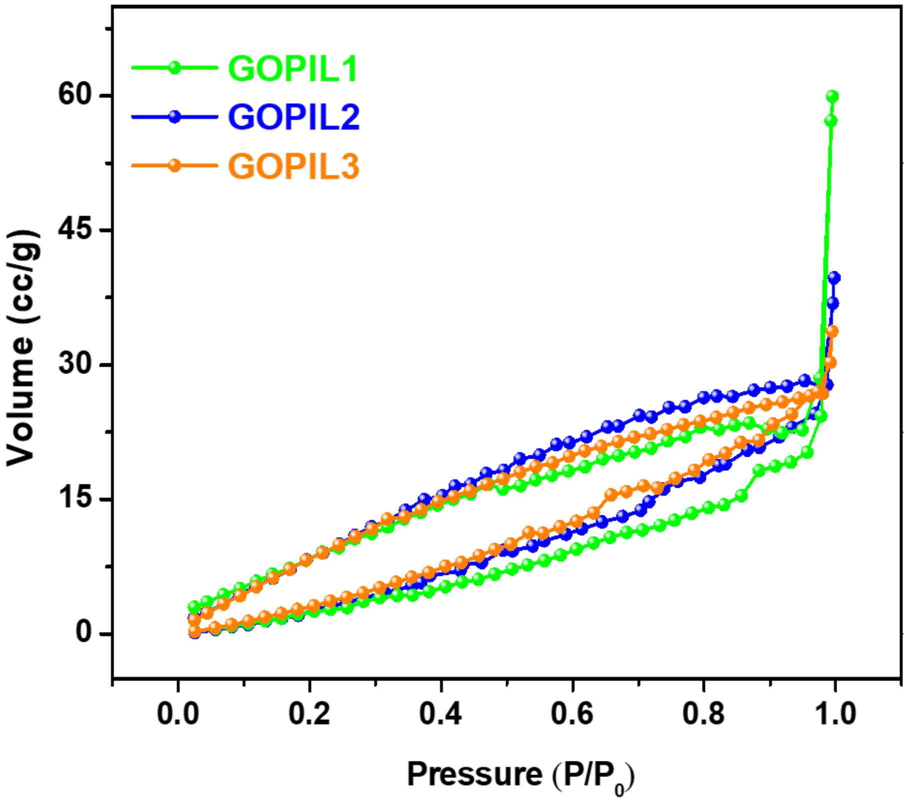

Figure A5.5. BET N_2 sorption isotherms of GOPIL1, GOPIL2 and GOPIL3 samples.

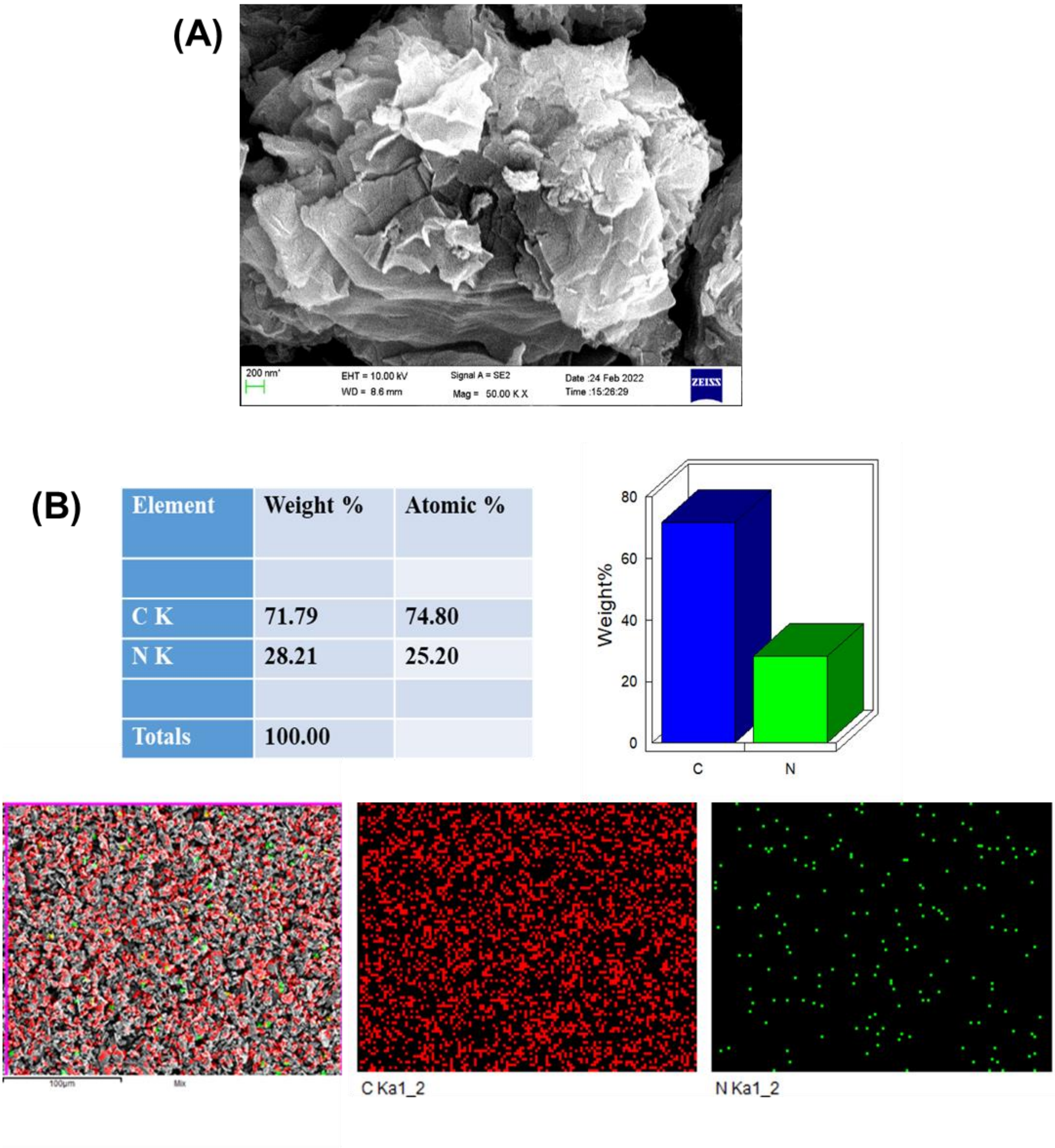

Element	Weight %	Atomic %
C K	71.79	74.80
N K	28.21	25.20
Totals	100.00	

Figure A5.6. (A) FESEM image and (B) EDX analysis data with elemental mapping (C and N) of pMATMA$_{115}$-*g*-GO (GOPIL1).

(A)

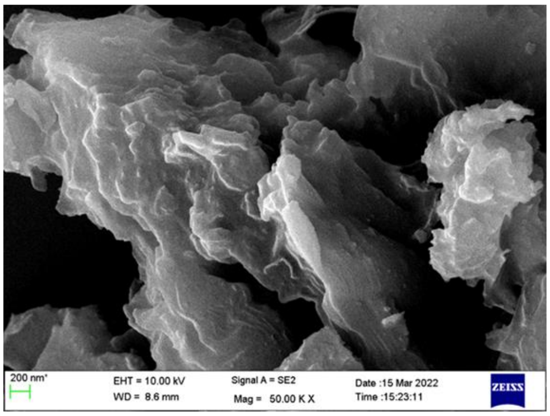

(B)

Element	Weight%	Atomic%
C K	59.18	62.84
N K	40.82	37.16
Totals	100.00	

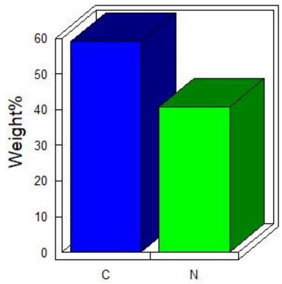

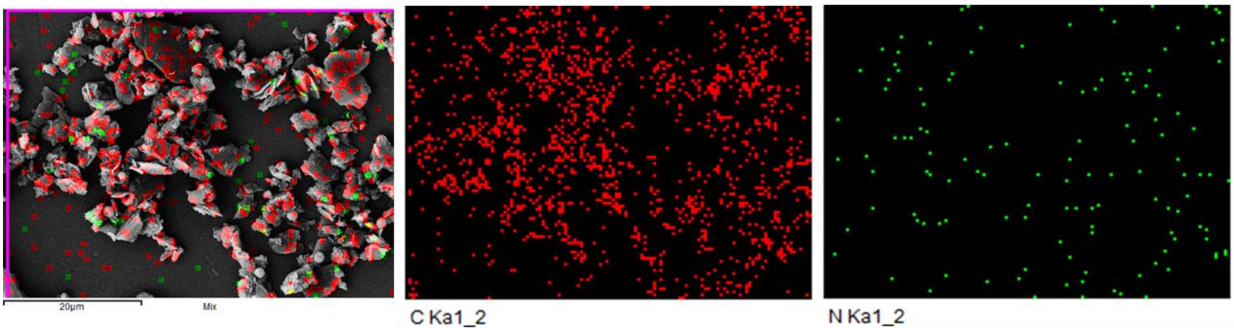

Figure A5.7. (A) FESEM image and (B) EDX analysis data with elemental mapping (C and N) of pVimBu$_{132}$-*g*-GO (GOPIL2).

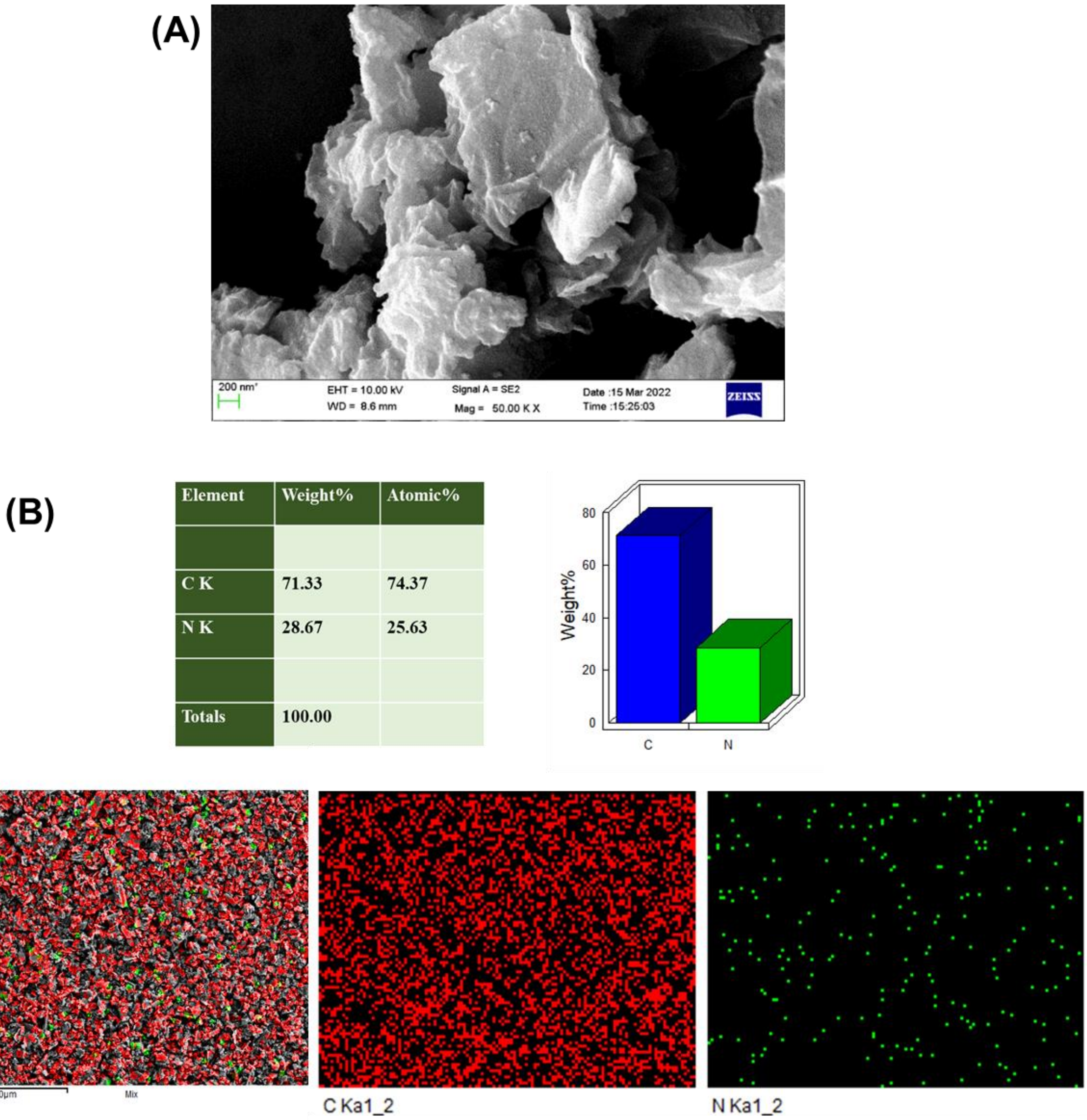

Element	Weight%	Atomic%
C K	71.33	74.37
N K	28.67	25.63
Totals	100.00	

Figure A5.8. (A) FESEM image and (B) EDX analysis data with elemental mapping (C and N) of pVBImBu$_{80}$-*g*-GO (GOPIL3).

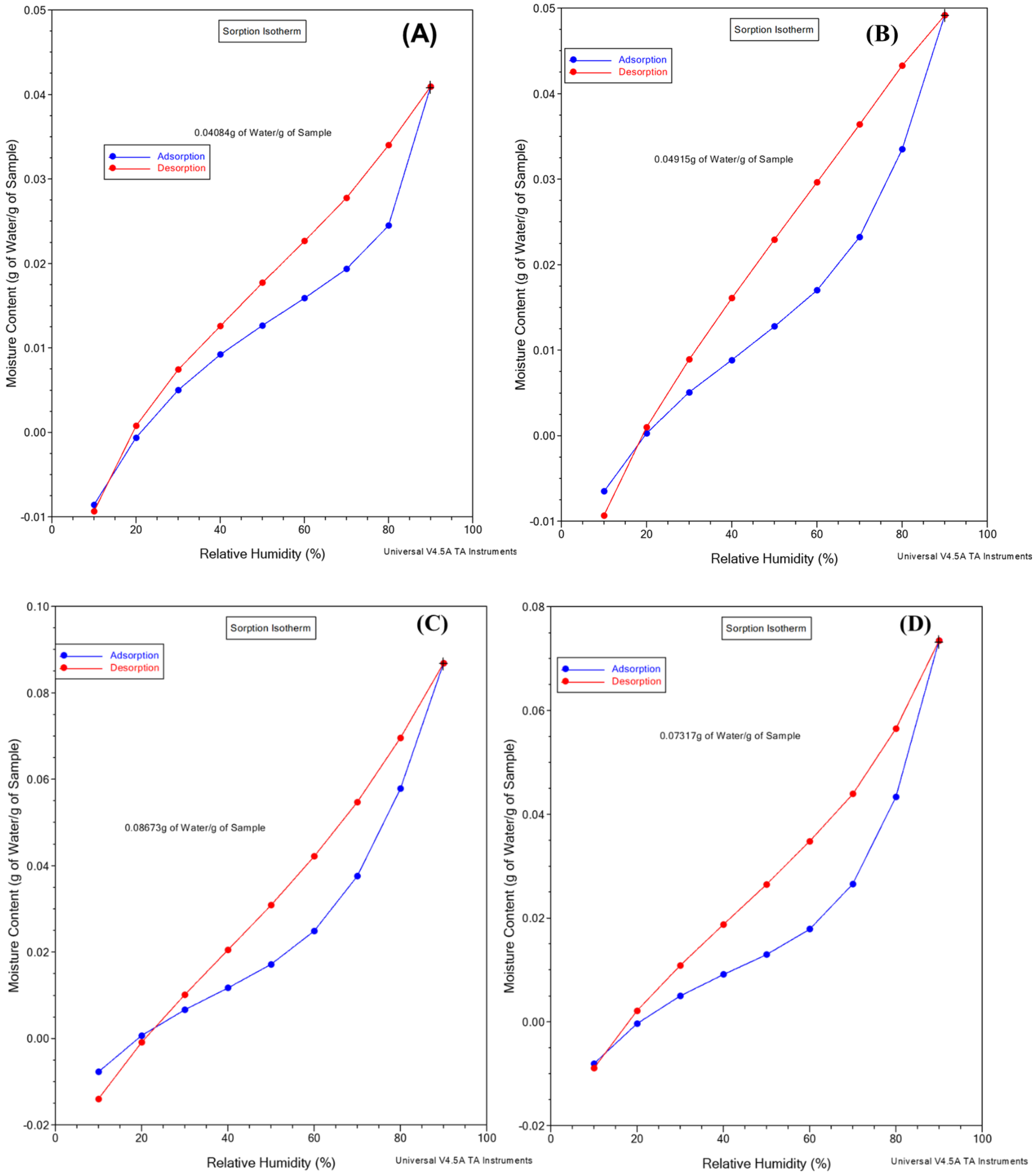

Figure A5.9. Dynamic vapour sorption analysis plot of GO (A), GOPIL1 (B), GOPIL2 (C) and GOPIL3 (D).

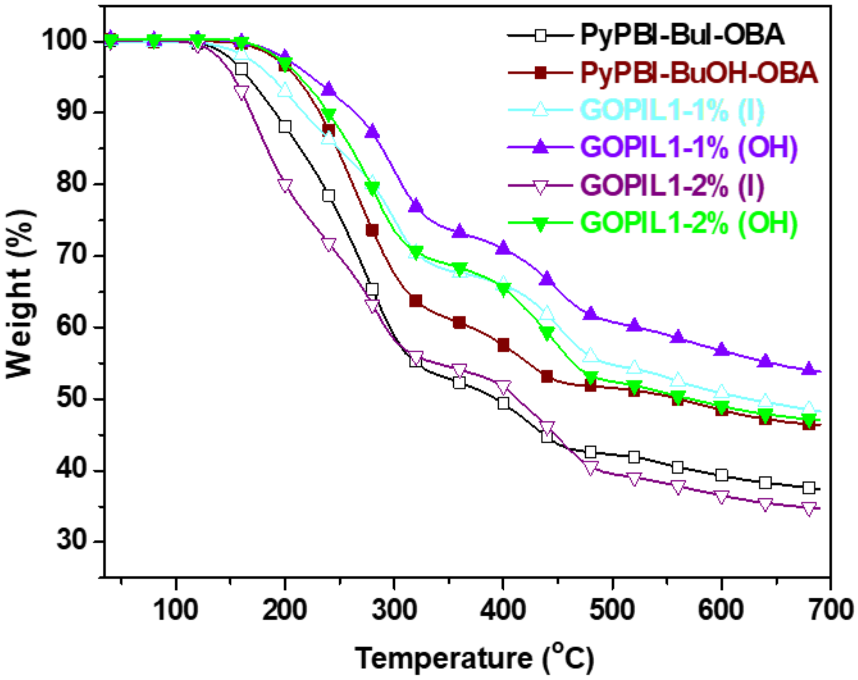

Figure A5.10. TGA plot of GOPIL1-1% and GOPIL1-2% (both iodide and hydroxide form) membranes.

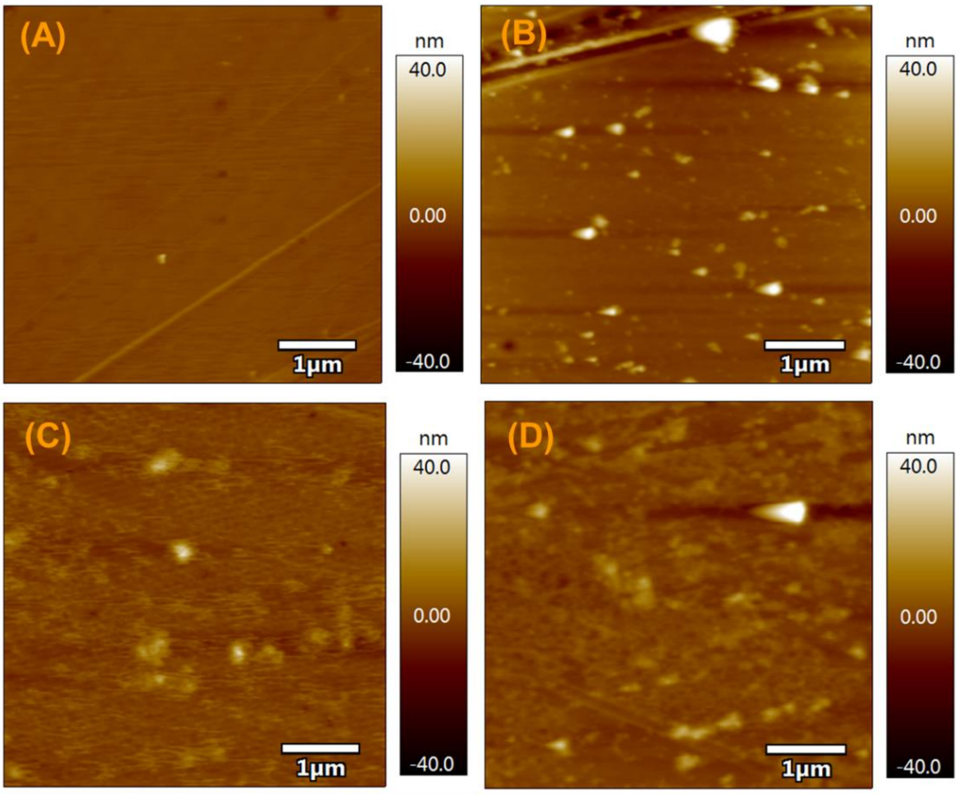

Figure A5.11. (A) AFM surface images of PyPBI-BuI-OBA (A), GOPIL1-1%(I) (B), GOPIL2-1%(I) (C), GOPIL3-1%(I) (D).

Table A5.1. Surface roughness of composite anion exchange MMMs in a comparison with PyPBI-BuI-OBA

Sample	Root mean square roughness (S_q) (nm)
PyPBI-BuI-OBA	1.056
GOPIL1-1%(I)	5.830
GOPIL1-2%(I)	16.215
GOPIL2-1%(I)	2.997
GOPIL2-2%(I)	11.537
GOPIL3-1%(I)	4.194
GOPIL3-2%(I)	13.006

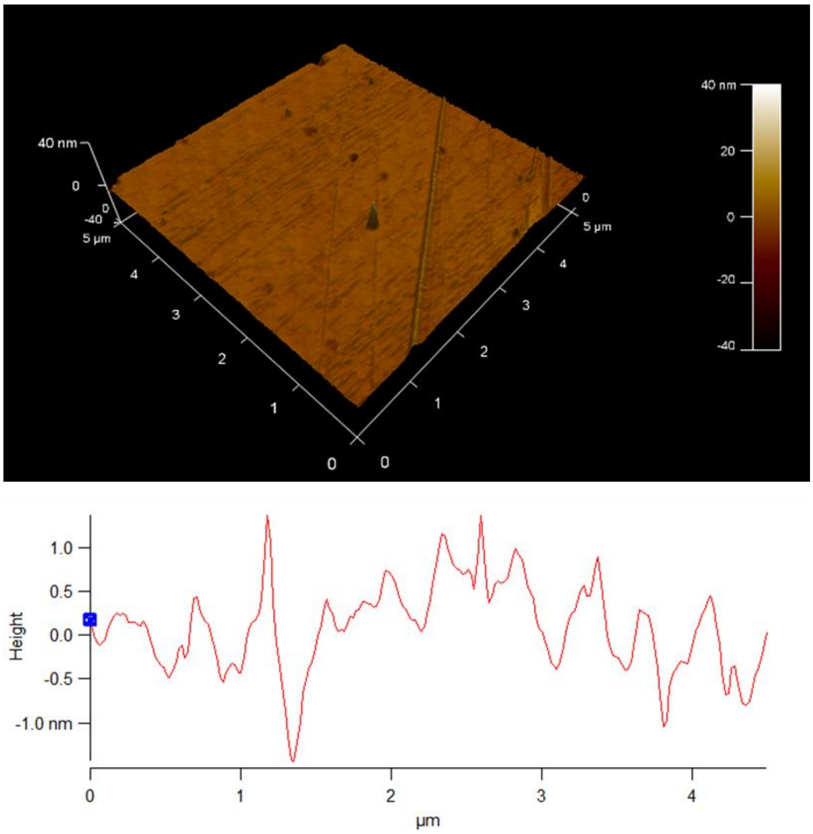

Figure A5.12. AFM 3D image of the surface morphology of PyPBI-BuI-OBA. Height profile is also measured (shown below the image) in order to estimate the surface roughness of the membranes.

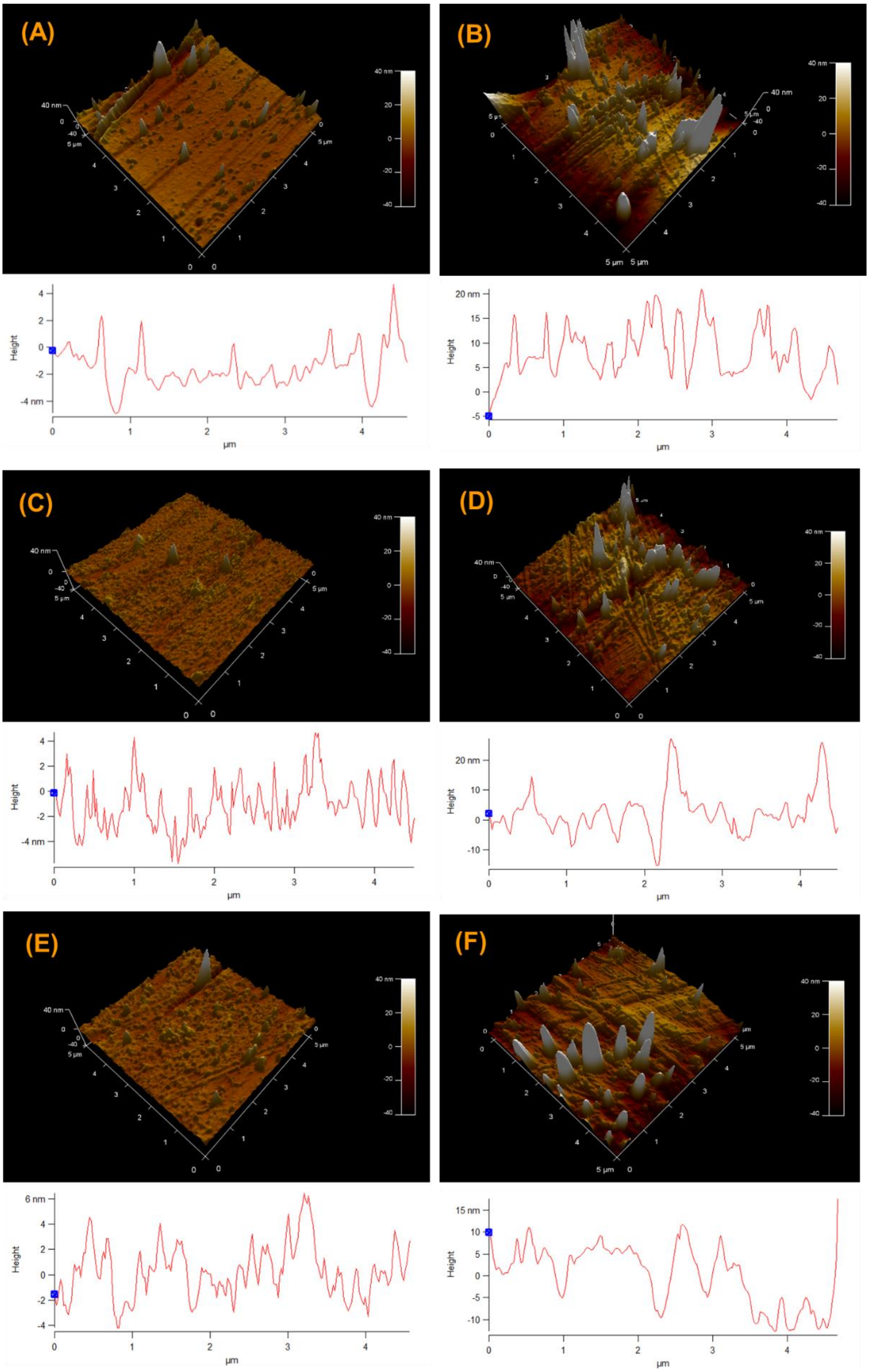

Figure A5.13. AFM 3D images of the surface morphology of **(A)** GOPIL1-1%(I), **(B)** GOPIL1-2%(I), and **(C)** GOPIL2-1%(I), **(D)** GOPIL2-2%(I), **(E)** GOPIL3-1%(I), and **(F)** GOPIL3-2%(I). Height profile is also measured (shown below the images) in order to estimate the surface roughness of the membranes.

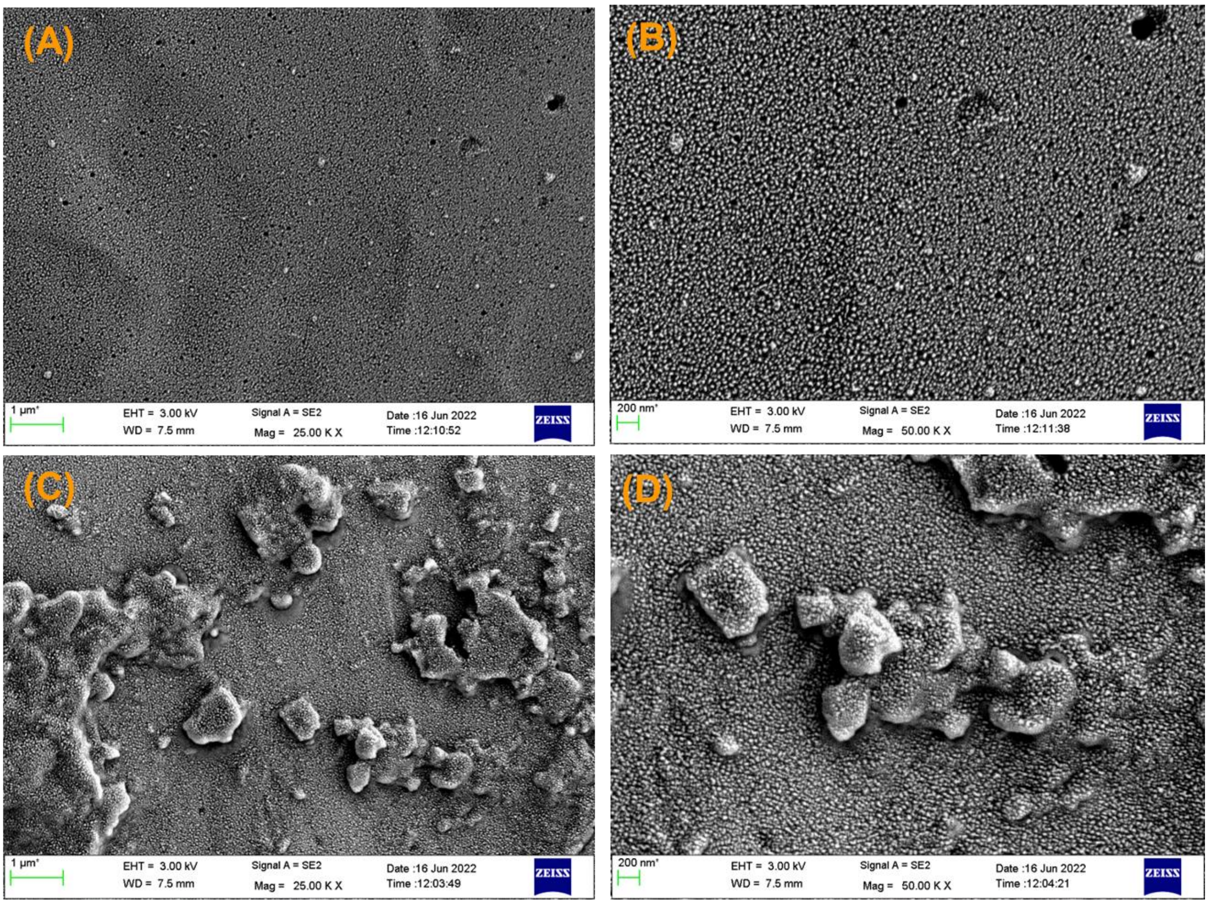

Figure A5.14. Surface FESEM images of GOPIL1-1%(I) in different magnification (A, B), GOPIL1-2%(I) in different magnification (C, D).

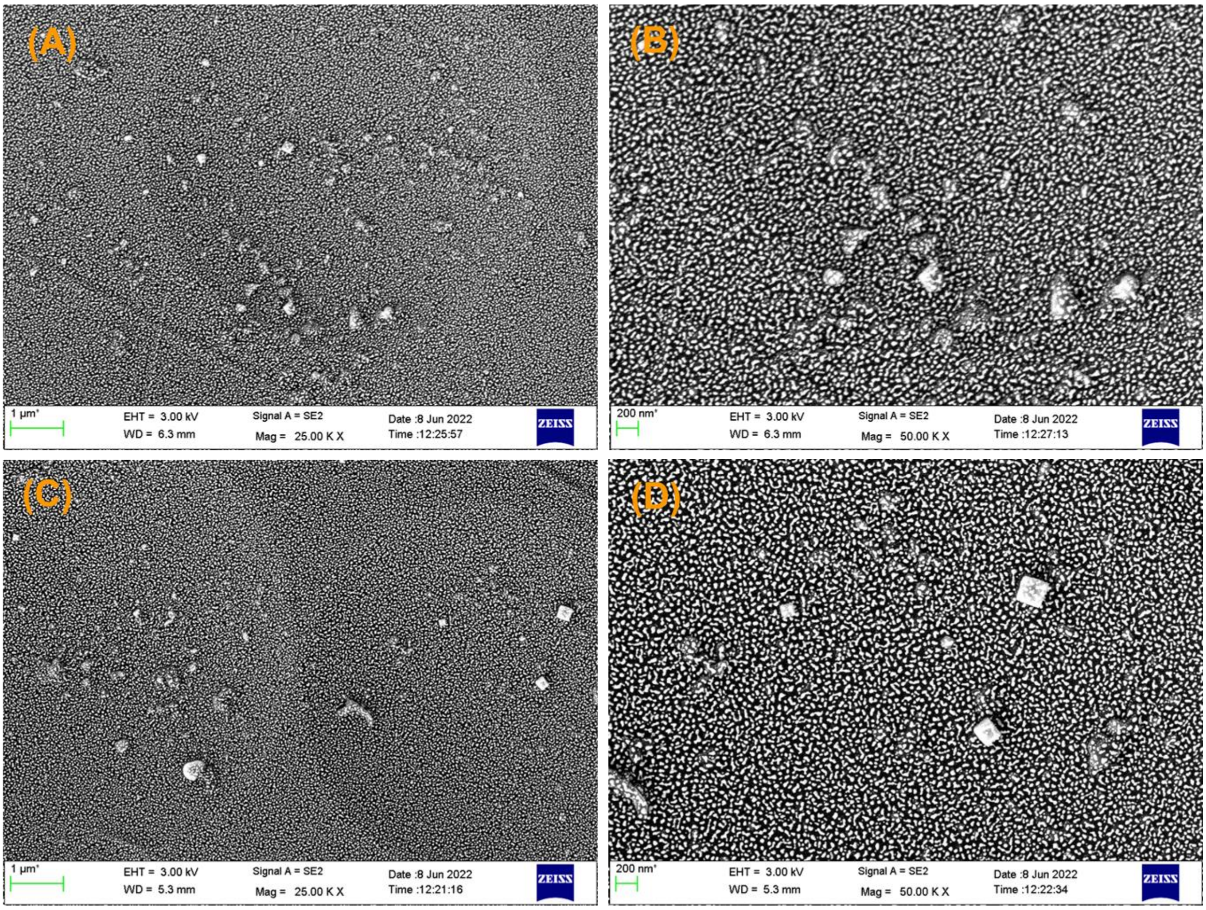

Figure A5.15. Surface FESEM images of GOPIL2-1%(I) in different magnification (A, B), GOPIL2-2%(I) in different magnification (C, D).

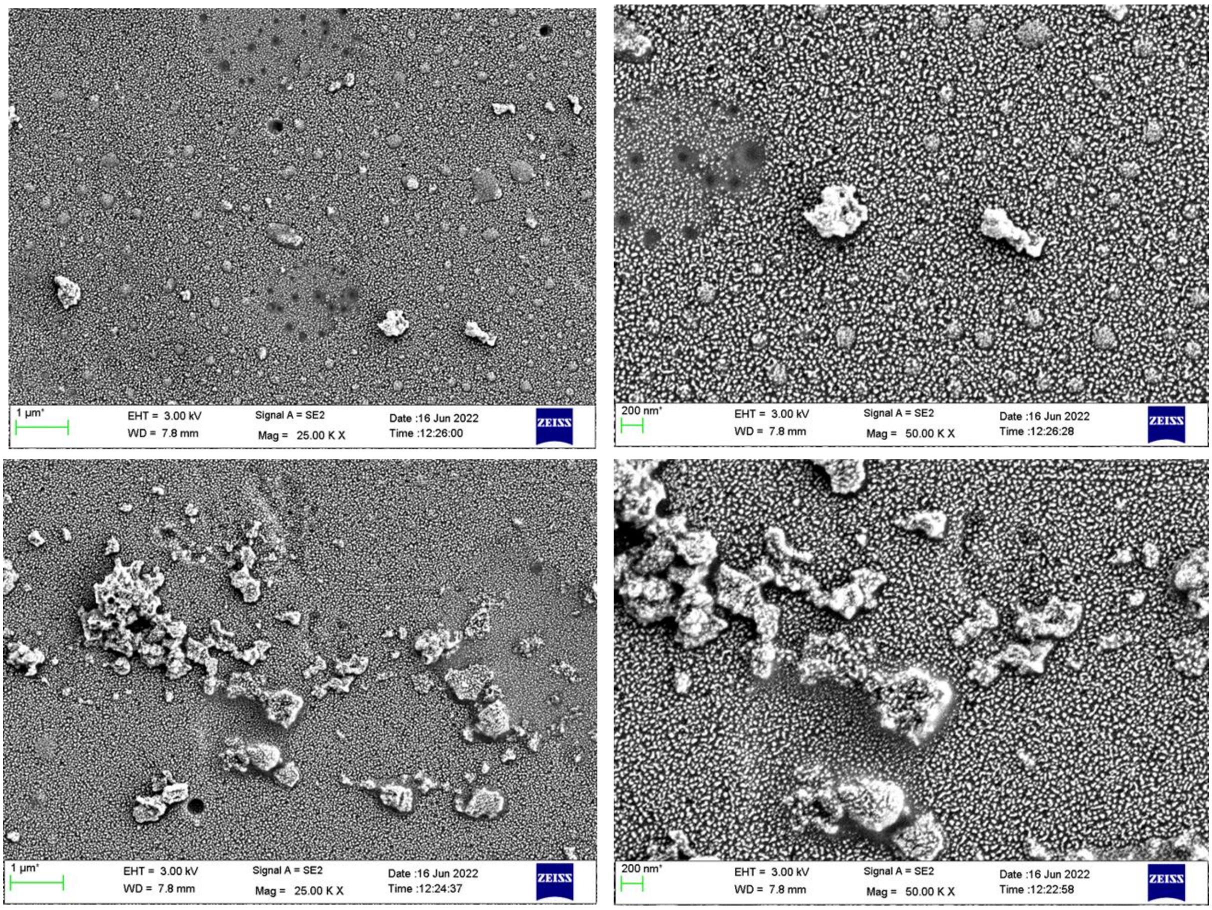

Figure A5.16. Surface FESEM images of GOPIL3-1%(I) in different magnification (A, B), GOPIL3-2%(I) in different magnification (C, D).

Table A5.2. Swelling ratio (%) of PyPBI-BuI-OBA composite AAEMs at various temperatures.

Sample identity	*Swelling ratio at 30 °C (%)*	*Swelling ratio at 60 °C (%)*	*Swelling ratio at 80 °C (%)*
PyPBI-BuOH-OBA	**2.76**	**3.35**	**3.98**
GOPIL1-1%(OH)	**2.03**	**2.45**	**3.52**
GOPIL1-2%(OH)	**1.39**	**1.87**	**2.33**
GOPIL2-1%(OH)	**1.04**	**1.89**	**2.30**
GOPIL2-2%(OH)	**7.60**	**8.42**	**8.83**
GOPIL3-1%(OH)	**1.25**	**2.13**	**2.54**
GOPIL3-2%(OH)	**1.77**	**1.92**	**2.26**

Table A5.3. Tensile Stress and Elongation at Break Values of the hydroxide form membranes.

Sample	**Tensile strength (MPa)**	**Elongation at break (%)**
PyPBI-BuOH-OBA	47.13	5.8
GOPIL1-1%(OH)	73.97	8.1
GOPIL1-2%(OH)	113.73	6.1
GOPIL2-1%(OH)	49.79	7.0
GOPIL2-2%(OH)	57.14	7.1
GOPIL3-1%(OH)	76.8	10.0
GOPIL3-2%(OH)	149.8	8.0

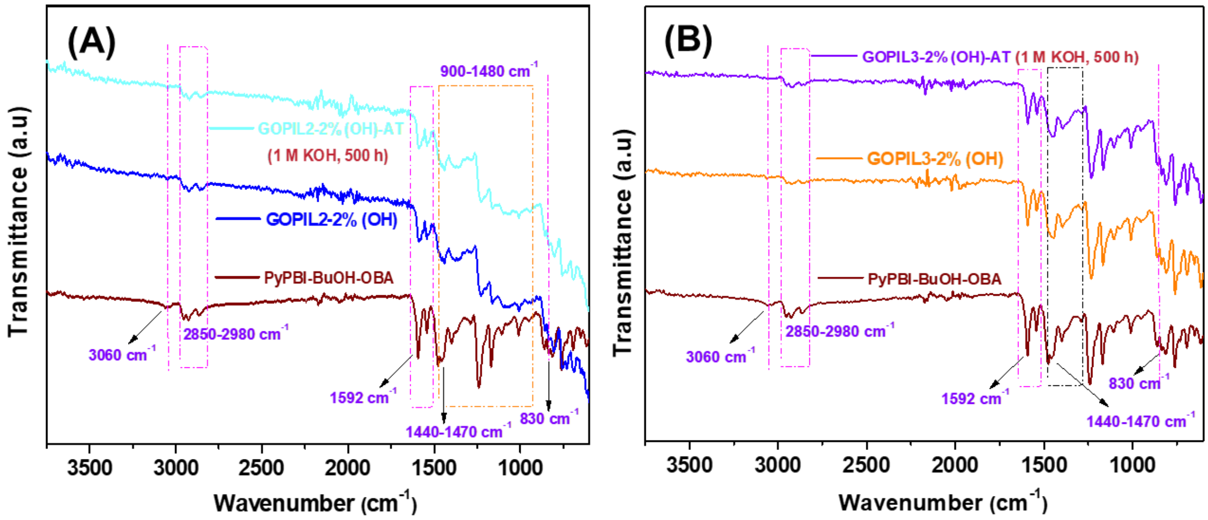

Figure A5.17. FT-IR spectra of GOPIL2-2%(OH) (A) GOPIL3-2%(OH) membrane (B) (before and after alkaline stability treatment in 1 M KOH at 60 °C for 500 h) along with pristine PyPBI-BuOH-OBA membrane.

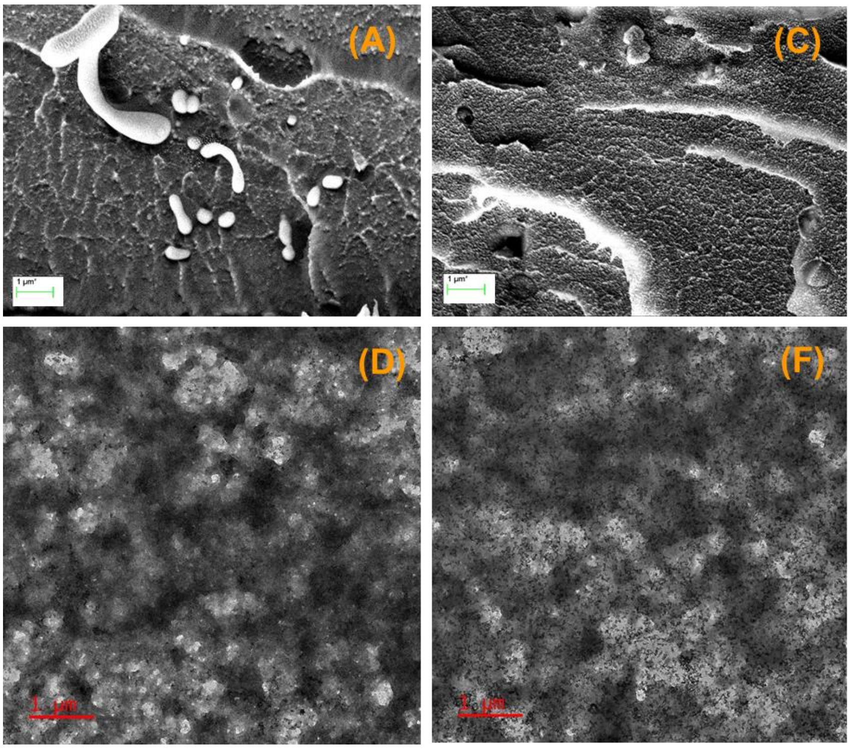

Figure A5.18. FESEM and TEM of GOPIL1-2%(OH) membrane after alkaline stability treatment in 1 M KOH at 60 °C for 500 h (A), FESEM and TEM of GOPIL3-2%(OH) membrane after alkaline stability treatment in 1 M KOH at 60 °C for 500 h

Table A5.4. Alkaline stability of the composite AAEMs in 1 M KOH at 60 °C for 21 days (500 h) [the images of the composite membranes are 1 M KOH treated membrane after alkaline stability treatment].

Sample	Time	Temperature (°C)	Observation
PyPBI-BuOH-OBA	500 h	60	No degradation observed
GOPIL1-1%(OH)	500 h	60	No degradation observed
GOPIL1-2%(OH)	500 h	60	No degradation observed
GOPIL2-1%(OH)	500 h	60	No degradation observed
GOPIL2-2%(OH)	500 h	60	No degradation observed
GOPIL3-1%(OH)	500 h	60	No degradation observed
GOPIL3-2%(OH)	500 h	60	No degradation observed

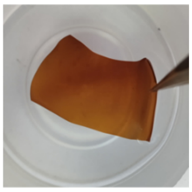

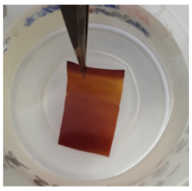

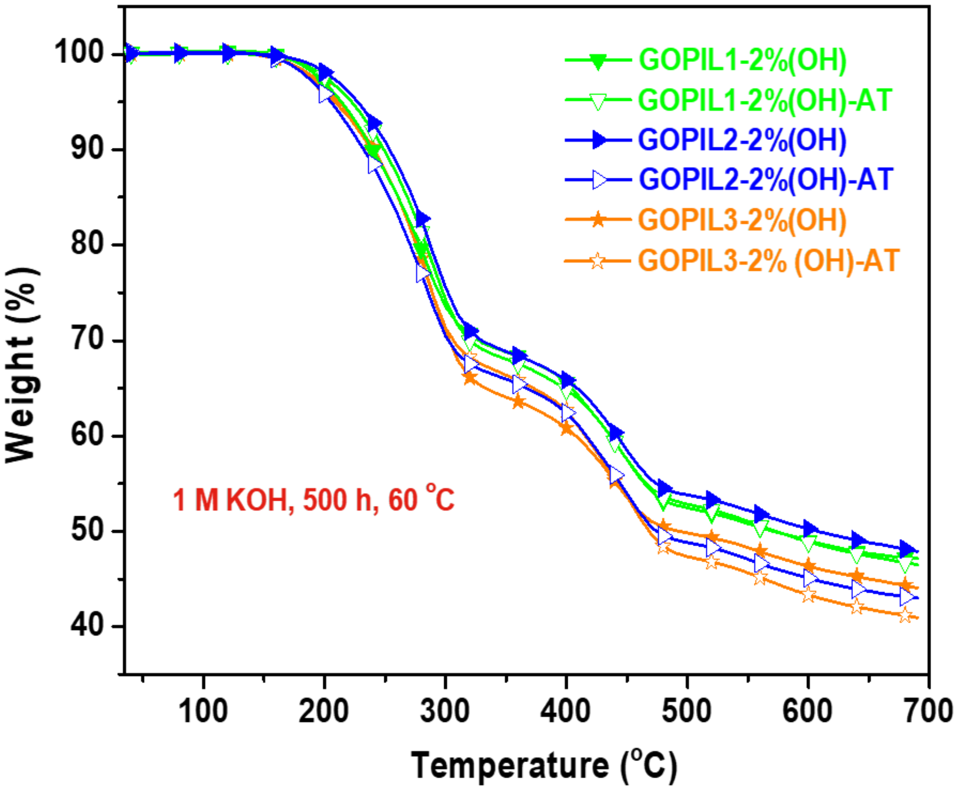

Figure A5.19. TGA plot of composite AAEMs before and after alkaline stability treatment in 1 M KOH at 60 °C for 500 h.

Table A5.5. Alkaline stability of the composite AAEMs in 5 M KOH, 60 °C for 15 d (375 h) [the images of the composite membranes are 5 M KOH treated membrane after alkaline stability treatment]

Sample	Time	Temperature$^{\#}$ (°C)	Observation
PyPBI-BuOH-OBA	15 d	60	Membranes remains flexible with slight color changes (brown to yellow)
GOPIL1-1%(I)	15 d	60	Membranes remains flexible with slight color changes (brown to yellow)
GOPIL1-2%(I)	15 d	60	Membranes remains flexible with slight color changes (brown to yellow)
GOPIL2-1%(I)	15 d	60	Membranes remains flexible with slight color changes (brown to yellow)
GOPIL2-2%(I)	15 d	60	Membranes remains flexible with slight color changes (brown to yellow)
GOPIL3-1%(I)	15 d	60	Membranes remains flexible with slight color changes (brown to yellow)
GOPIL3-2%(I)	15 d	60	Membranes remains flexible with slight color changes (brown to yellow)

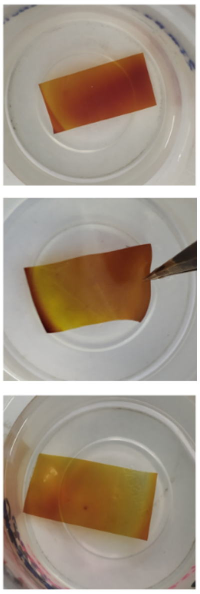

References

(1) Sun, Z.; Pan, J.; Guo, J.; Yan, F. *Adv. Sci.* **2018**, *5*, 1800065.

(2) Gu, F.; Dong, H.; Li, Y.; Si, Z.; Yan, F.; *Macromolecules* **2014,** *47*, 208−216.

Publications
&
Presentations

List of Publications & Presentations

Thesis Chapter Publications:

1. Subhabrata Mukhopadhyay†, **Anupam Das**†**,** Tushar Jana* and Samar K. Das*. Fabricating a MOF Material with Polybenzimidazole into an Efficient Proton Exchange Membrane. *ACS Appl. Energy Mater.* **2020**, *3*, 7964–7977. **[†] Co-First Authors.** ***(Chapter 3)***

2. **Anupam Das,** Mousumi Hazarika, Balakondareddy Sana and Tushar Jana*. Covalent Organic Framework and Polybenzimidazole Composite Proton Exchange Membrane with superior Proton Conductivity**.** Under Revision: *ACS Appl. Nano Mater.* ***(Chapter 4)***

3. **Anupam Das,** Nilanjan Mukherjee and Tushar Jana*. Polymer Grafted Graphene Oxide/Polybenzimidazole Nanocomposites for Efficient Proton Conducting Membranes**.** *ACS Appl. Nano Mater.* **2023** **[Article in Press].** ***(Chapter 5)***

4. **Anupam Das,** Balakondareddy Sana, Rama Bhattacharyya, Prakash Chandra Ghosh and Tushar Jana* Cross-Linked Alkaline Anion Exchange Membrane from N-Spirocyclic Quaternary Ammonium and Polybenzimidazole. *ACS Appl. Polym. Mater.* **2022,** *4,* 1523−1534. ***(Chapter 6)***

5. **Anupam Das,** Nilanjan Mukherjee, Ritu Saraswat and Tushar Jana*. Multicationic Anion Exchange Membranes from Pyridine-bridged Polybenzimidazole and Polymer Ionic Liquid Grafted Graphene Oxide *(To be Communicated).* ***(Chapter 7)***

Other Publications:

6. Akhil Gorre, **Anupam Das*** and Tushar Jana***.** Mixed matrix composite PEM with super proton conductivity developed from ionic liquid modified silica nanoparticle and polybenzimidazole. *J. Macromol. Sci. A, Pure Appl. Chem.* **2023,** *60,* 38-50. **[*] Co- Corresponding Authors.**

7. Nilanjan Mukherjee, **Anupam Das,** and Tushar Jana*. Poly(N-vinyl triazole-b-N-vinyl imidazole) Grafted on MWCNTs as Nanofillers to Improve Proton Conducting Membranes. *ACS Appl. Nano Mater.* **2023,** *6,* 544-557.

8. Shailja Rai, Poorm Prakash Pande, Krishna Kumar*, Rudramani Tiwari, S. Krihnamoorthy, **Anupam Das** and Tushar Jana. Enhancement of Urease Properties by Introducing New Interface based on pH responsive Polymer-Enzyme Bioconjugates via Grafting Through-RAFT Polymerization Technique. *Mater. Chem. Phys.* **2023,** *305,* 128009.

9. Olivia Basu†**, Anupam Das**†**,** Tushar Jana* and Samar K. Das*. Designing of Flexible MOF based Super Protonic Conductors: Potential Nanofiller for Mixed Matrix PEMs. *ACS Appl. Energy Mater.* **2022**, ***DOI :*** 10.1021/acsaem.2c02972 **[†] Co-First Authors.**

10. Balakondareddy Sana, **Anupam Das** and Tushar Jana*. Cross-Linked Polybenzimidazole as Alkaline Stable Anion Exchange Membrane. *ACS Appl. Energy Mater.* **2022,** *5,* 3626-3637.

11. Anuradha, **Anupam Das**, Sandip Pal and Suresh K. Jewrajka*. Physical, Electrochemical, and Solvent Permeation Properties of Amphiphilic Conetwork Membranes Formed through Interlinking of Poly(vinylidene fluoride)-*Graft*-Poly[(2-dimethylamino)ethyl Methacrylate] with Telechelic Poly(ethylene glycol) and Small Molecular Weight Cross-Linkers. *Langmuir* **2022,** *38,* 15340–15352.

12. Nisha Yadav, Krishna Kumar*, V.K. Singh, Shailja Rai, Kunal Blahatia, **Anupam Das** and Tushar Jana. Newly Designed Acrylamide Derivative-based pH-responsive Hydrogel-Urease Bioconjugates: Synthesis and Catalytic Urea Hydrolysis. *Soft Matter,* **2022,** *18,* 8647-8655.

13. Balakondareddy Sana, **Anupam Das,** Manju Sharma* and Tushar Jana*. Alkaline Anion Exchange Membrane from Alkylated Polybenzimidazole**.** *ACS Appl. Energy Mater.* **2021**, *4,* 9792-9805.

14. Nilanjan Mukherjee, **Anupam Das,** Moumita Dhara and Tushar Jana*. Surface initiated RAFT polymerization to synthesize N-heterocyclic block copolymer grafted silica nanofillers for improving PEM properties. *Polymer* **2021,** *236,* 124315.

15. Olivia Basu, Subhabrata Mukhopadhyay, Avik De, **Anupam Das** and Samar K. Das*. Tuning the electrochemical and catalytic ORR performance of C_{60} by its encapsulation in ZIF-8: a solid state analogue of dilute fullerene solution. *Mater. Chem. Front.* **2021,** *5,* 7654.

16. Balakondareddy Sana, **Anupam Das** and Tushar Jana*. Polybenzimidazole as alkaline anion exchange membrane with twin hydroxide ion conducting sites. *Polymer* **2019,** *172,* 213-220.

17. Vinay K. Singh, Krishna Kumar*, **Anupam Das,** Rudramani Tiwari, S. Krishnamoorthy. Fabrication of Microgel-GO@Ag/CuO Nanocatalyst and Explore their Ultrafast Catalytic Applications on Environmental Remediation. *Iranian Polymer Journal,* **2023,** *32,* 687-701.

18. Aradhana Chaudhuri, Krishna Kumar*, Vinay K. singh, Shailja Rai, Vinod Kumar, **Anupam Das,** and Tushar Jana. Hybrid Crosslinked Hydrogel Platform for Urease: Improved Stability, Storage and biocatalytic Activity. Under Review: *Polymer Engineering & Science*

19. Pinky Saha†, Hema Kumari Kolli†**,** **Anupam Das†,** Tushar Jana* and Samar K. Das*. Solid Nanoblackberries of $\{W_{72}Fe_{30}\}$ with the Highest Polyoxometalates based Proton Conductivity and Their Fabrication into Proton Transport Membranes. *(To be Communicated)* **[†] Co-First Authors.**

20. **Anupam Das,** Mousumi Hazarika, Namrata Deka and Tushar Jana*. Mixed Matrix PEM of Functionalized Porous Organic Polymer (POP) loaded Polybenzimidazole**.** *(To be Communicated).*

21. Nilanjan Mukherjee, **Anupam Das,** Subhabrata Mukhopadhyay and Tushar Jana*. Polybenzimidazole based Mixed Matrix Membranes Utilizing SI-RAFT initiated Polymer-*g*-UiO-66-NH_2 as Nanofillers to Fabricate Super Proton Conducting PEMs. *(To be Communicated).*

22. Sandip Ghosh, **Anupam Das** and Tushar Jana*. A New Strategy to Develop Acid Doped OPBI Gel Membranes for PEM Fuel Cell. *(Patent ready for filing).*

CONFERENCES ATTENDED:

- **Received the BEST ORAL presentation award** for the ORAL presentation entitled *"Proton Exchange Membrane of Polybenzimidazole Loaded with Porous MOF & POP"* in the ChemFest-2021, organized by School of Chemistry (University of Hyderabad), March 2021.

- **Presented ORAL** in the topic entitled *"Development of superior proton conducting PBI composite membranes by incorporating Phosphoric acid-loaded Covalent Organic Framework"* in the 13th International Conference on Advance Polymeric Materials (APM-2022), Organized by CIPET-Chennai.

- **Presented ORAL** in the topic entitled *"Cross-Linked Alkaline Anion Exchange Membrane from N-Spirocyclic Quaternary Ammonium and Polybenzimidazole"* in the KV Rao Scientific Society (KVRSS) Research Awards, 2022.

- **Presented POSTER** in the topic entitled *"Mixed Matrix PEM of Functionalized Porous Organic Polymer (POP) loaded Polybenzimidazole"* in 16th International conference on Polymer Science & Technology (SPSI-MACRO-November 2022) organized by IISER Pune & CSIR-NCL Pune.

- **Presented POSTER** in the topic entitled *"N-Spirocyclic Quaternary ammonium ionene based ionically crosslinked pristine and porous alkaline exchange membranes"* in the In-House Symposium ChemFest-2020, organized by School of Chemistry (University of Hyderabad), February 2020.

- Participated in 15th International conference on Polymer Science and Technology (SPSI-MACRO-December 2018) organized by IISER Pune & CSIR-NCL Pune.

Mixed Matrix Membranes of Polybenzimidazoles as Proton and Anion Exchange Membranes

by Anupam Das

Submission date: 24-Mar-2023 05:12PM (UTC+0530)
Submission ID: 2045338541
File name: Anupam_Das.pdf (7.19M)
Word count: 50678
Character count: 270172

Jana
27/03/2023

Prof. TUSHAR JANA
School of Chemistry
University of Hyderabad
HYDERABAD-500 046. INDIA.

Mixed Matrix Membranes of Polybenzimidazoles as Proton and Anion Exchange Membranes

ORIGINALITY REPORT

33%	7%	32%	2%
SIMILARITY INDEX	INTERNET SOURCES	PUBLICATIONS	STUDENT PAPERS

PRIMARY SOURCES

1	Anupam Das, Balakondareddy Sana, Rama Bhattacharyya, Prakash Chandra Ghosh, Tushar Jana. "Cross-Linked Alkaline Anion Exchange Membrane from N-Spirocyclic Quaternary Ammonium and Polybenzimidazole", ACS Applied Polymer Materials, 2022 Publication	12%
2	Subhabrata Mukhopadhyay, Anupam Das, Tushar Jana, Samar K. Das. "Fabricating a MOF Material with Polybenzimidazole into an Efficient Proton Exchange Membrane", ACS Applied Energy Materials, 2020 Publication	8%
3	Subhabrata Mukhopadhyay, Anupam Das, Tushar Jana, Samar Kumar Das. "Fabricating a MOF Material with Polybenzimidazole into an Efficient Proton Exchange Membrane", ACS Applied Energy Materials, 2020 Publication	7%

Jana

Prof. TUSHAR JANA
School of Chemistry
University of Hyderabad
HYDERABAD-500 046. INDIA.

Jana

Prof. TUSHAR JANA
School of Chemistry
University of Hyderabad
HYDERABAD-500 046. INDIA.

Jana

Prof. TUSHAR JANA
School of Chemistry
University of Hyderabad
HYDERABAD-500 046. INDIA.

4	www.researchgate.net Internet Source	1 %
5	Submitted to University of Hyderabad, Hyderabad Student Paper	1 %
6	Yongheng Yin, Zhen Li, Xin Yang, Li Cao, Chongbin Wang, Bei Zhang, Hong Wu, Zhongyi Jiang. "Enhanced proton conductivity of Nafion composite membrane by incorporating phosphoric acid-loaded covalent organic framework", Journal of Power Sources, 2016 Publication	<1 %
7	Olivia Basu, Anupam Das, Tushar Jana, Samar K. Das. "Design of Flexible Metal–Organic Framework-Based Superprotonic Conductors and Their Fabrication with a Polymer into Proton Exchange Membranes", ACS Applied Energy Materials, 2022 Publication	<1 %
8	Nilanjan Mukherjee, Anupam Das, Tushar Jana. " Poly(-vinyl triazole- - -vinyl imidazole) on MWCNTs as Nanofillers to Improve Proton Conducting Membranes ", ACS Applied Nano Materials, 2022 Publication	<1 %
9	docs9.chomikuj.pl Internet Source	

		<1%
10	Akhil Gorre, Anupam Das, Tushar Jana. "Mixed matrix composite PEM with super proton conductivity developed from ionic liquid modified silica nanoparticle and polybenzimidazole", Journal of Macromolecular Science, Part A, 2022 Publication	<1%
11	Balakondareddy Sana, Tushar Jana. "Polybenzimidazole composite with acidic surfactant like molecules: A unique approach to develop PEM for fuel cell", European Polymer Journal, 2016 Publication	<1%
12	Balakondareddy Sana, Anupam Das, Tushar Jana. "Cross-Linked Polybenzimidazoles as Alkaline Stable Anion Exchange Membranes", ACS Applied Energy Materials, 2022 Publication	<1%
13	Balakondareddy Sana, Anupam Das, Manju Sharma, Tushar Jana. "Alkaline Anion Exchange Membrane from Alkylated Polybenzimidazole", ACS Applied Energy Materials, 2021 Publication	<1%
14	baadalsg.inflibnet.ac.in Internet Source	<1%

15	link.springer.com Internet Source	<1 %
16	Satyanarayana Raju Kutcherlapati, Rambabu Koyilapu, Tushar Jana. " Poly(-vinyl imidazole) grafted silica nanofillers: Synthesis by RAFT polymerization and nanocomposites with polybenzimidazole ", Journal of Polymer Science Part A: Polymer Chemistry, 2018 Publication	<1 %
17	Justin O. Zoppe, Nariye Cavusoglu Ataman, Piotr Mocny, Jian Wang, John Moraes, Harm-Anton Klok. "Surface-Initiated Controlled Radical Polymerization: State-of-the-Art, Opportunities, and Challenges in Surface and Interface Engineering with Polymer Brushes", Chemical Reviews, 2017 Publication	<1 %
18	hdl.handle.net Internet Source	<1 %
19	worldwidescience.org Internet Source	<1 %
20	www.mdpi.com Internet Source	<1 %
21	Sudhangshu Maity, Shuvra Singha, Tushar Jana. "Low acid leaching PEM for fuel cell based on polybenzimidazole nanocomposites	<1 %

	with protic ionic liquid modified silica", Polymer, 2015 Publication	
22	mafiadoc.com Internet Source	<1 %
23	pubs.rsc.org Internet Source	<1 %
24	cris.bgu.ac.il Internet Source	<1 %
25	Hoang Vinh-Thang, Serge Kaliaguine. "Predictive Models for Mixed-Matrix Membrane Performance: A Review", Chemical Reviews, 2013 Publication	<1 %
26	"Proton Exchange Membrane Fuel Cells", Wiley, 2023 Publication	<1 %
27	storage.googleapis.com Internet Source	<1 %
28	Dhamodaran Arunbabu, Arindam Sannigrahi, Tushar Jana. "Blends of Polybenzimidazole and Poly(vinylidene fluoride) for Use in a Fuel Cell", The Journal of Physical Chemistry B, 2008 Publication	<1 %

29	Hongwei Zhang, Pei Kang Shen. "Recent Development of Polymer Electrolyte Membranes for Fuel Cells", Chemical Reviews, 2012 Publication	<1 %
30	Liliang Tian, Weiqi Zhang, Zheng Xie, Kai Peng, Qiang Ma, Qian Xu, Sivakumar Pasupathi, Huaneng Su. "Enhanced Performance and Durability of High-temperature Polymer Electrolyte Membrane Fuel Cell by Incorporating Covalent Organic Framework into Catalyst Layer", Acta Physico Chimica Sinica, 2020 Publication	<1 %
31	Submitted to nith Student Paper	<1 %
32	uir.unisa.ac.za Internet Source	<1 %
33	www.freepatentsonline.com Internet Source	<1 %
34	Shuvra Singha, Tushar Jana. "Structure and Properties of Polybenzimidazole/Silica Nanocomposite Electrolyte Membrane: Influence of Organic/Inorganic Interface", ACS Applied Materials & Interfaces, 2014 Publication	<1 %
	pure.tue.nl	

35	Internet Source	<1 %
36	Kai Yu Wang, Martin Weber, Neal Tai-Shung Chung. "Polybenzimidazoles (PBIs) and state-of-the-art PBI hollow fiber membranes for water, organic solvent and gas separations: a Review", Journal of Materials Chemistry A, 2022 Publication	<1 %
37	upcommons.upc.edu Internet Source	<1 %
38	www.science.gov Internet Source	<1 %
39	"Organic-Inorganic Composite Polymer Electrolyte Membranes", Springer Science and Business Media LLC, 2017 Publication	<1 %
40	Cheng-Hsun Shen, Li-cheng Jheng, Steve Lien-chung Hsu, Jacob Tse-Wei Wang. "Phosphoric acid-doped cross-linked porous polybenzimidazole membranes for proton exchange membrane fuel cells", Journal of Materials Chemistry, 2011 Publication	<1 %
41	Fuel Cells, 2013. Publication	<1 %

42	Mousumi Hazarika, Tushar Jana. "Proton Exchange Membrane Developed from Novel Blends of Polybenzimidazole and Poly(vinyl-1,2,4-triazole)", ACS Applied Materials & Interfaces, 2012 Publication	<1%
43	Nilanjan Mukherjee, Anupam Das, Moumita Dhara, Tushar Jana. "Surface initiated RAFT polymerization to synthesize N-Heterocyclic block copolymer grafted silica nanofillers for improving PEM properties", Polymer, 2021 Publication	<1%
44	Qingting Liu, Xiaohe Wang, Xiaoxiao Zhang, Zhiwei Ling et al. "Polyethyleneimine-filled sepiolite nanorods-embedded poly(2,5-benzimidazole) composite membranes for wide-temperature PEMFCs", Journal of Cleaner Production, 2022 Publication	<1%
45	Rambabu Koyilapu, Shuvra Singha, Balakondareddy Sana, Tushar Jana. "Proton exchange membrane prepared by blending polybenzimidazole with poly (aminophosphonate ester)", Polymer Testing, 2020 Publication	<1%
46	pure.rug.nl Internet Source	<1%

47	"Polymer-Engineered Nanostructures for Advanced Energy Applications", Springer Science and Business Media LLC, 2017 Publication	<1%
48	Rambabu Koyilapu, Suchismita Subhadarshini, Shuvra Singha, Tushar Jana. "An in-situ RAFT polymerization technique for the preparation of poly(N-vinyl imidazole) modified Cloisite nanoclay to develop nanocomposite PEM", Polymer, 2020 Publication	<1%
49	Singha, Shuvra, and Tushar Jana. "Influence of interfacial interactions on the properties of polybenzimidazole/clay nanocomposite electrolyte membrane", Polymer, 2016. Publication	<1%
50	Wei You, Kristina M. Hugar, Ryan C. Selhorst, Megan Treichel, Cheyenne R. Peltier, Kevin J. T. Noonan, Geoffrey W. Coates. "Degradation of Organic Cations under Alkaline Conditions", The Journal of Organic Chemistry, 2020 Publication	<1%
51	www.research-collection.ethz.ch Internet Source	<1%
52	Xiuyu Zhao, Yao Chen, Zhifang Wang, Zhenjie Zhang. "Design and application of covalent	<1%

	organic frameworks for ionic conduction", Polymer Chemistry, 2021 Publication	
53	www.dovepress.com Internet Source	<1 %
54	Alexander Kraytsberg, Yair Ein-Eli. "Review of Advanced Materials for Proton Exchange Membrane Fuel Cells", Energy & Fuels, 2014 Publication	<1 %
55	Ji Young Chu, Kyu Ha Lee, Ae Rhan Kim, Dong Jin Yoo. "Study on the Chemical Stabilities of Poly(arylene ether) Random Copolymers for Alkaline Fuel Cells: Effect of Main Chain Structures with Different Monomer Units", ACS Sustainable Chemistry & Engineering, 2019 Publication	<1 %
56	Jin Zhang, Hui-Juan Bai, Qiu Ren, Hong-Bin Luo, Xiao-Ming Ren, Zheng-Fang Tian, Shanfu Lu. " Extra Water- and Acid-Stable with High Proton Conductivity and Its Composite Membrane for Proton-Exchange Membrane ", ACS Applied Materials & Interfaces, 2018 Publication	<1 %
57	Submitted to Morningside College Student Paper	<1 %

58	Qing Ju, Hongying Tang, Ge Chao, Tiegen Guo, Kang Geng, Nanwen Li. "Performance and stability of ether-free high temperature proton exchange membranes with tunable pendent imidazolium groups", Journal of Materials Chemistry A, 2022 Publication	<1 %
59	pubs.acs.org Internet Source	<1 %
60	scholarbank.nus.edu.sg Internet Source	<1 %
61	www.rsc.org Internet Source	<1 %

Exclude quotes	On	Exclude matches	< 14 words
Exclude bibliography	On		

ACS APPLIED ENERGY MATERIALS

Fabricating a MOF Material with Polybenzimidazole into an Efficient Proton Exchange Membrane

Subhabrata Mukhopadhyay,[†] Anupam Das,[†] Tushar Jana,* and Samar K. Das*

Cite This: ACS Appl. Energy Mater. 2020, 3, 7964−7977

Read Online

ACCESS | Metrics & More | Article Recommendations | SI Supporting Information

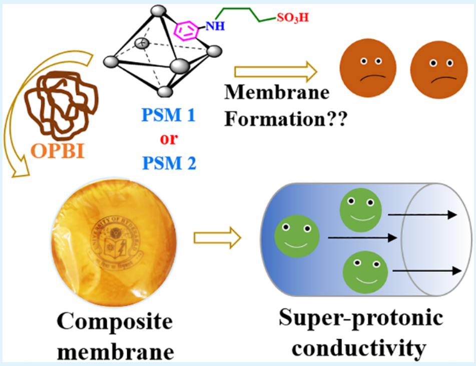

ABSTRACT: Metal organic frameworks (MOFs) have received considerable importance as proton conducting materials in recent times. However, most of the MOFs lack the ability to form film, which limits their application. In the present work, polybenzimidazole (PBI) composite membranes have been prepared by loading post synthetically modified (**PSM**) UiO-66-NH_2 MOFs, denoted as **PSM 1** and **PSM 2** into an aryl ether-type polybenzimidazole (**OPBI**) polymer. The pristine **OPBI**, and MOF nanofiller loaded membranes were doped with phosphoric acid (PA) to prepare proton exchange membranes (PEMs). Use of thermally stable, hydrophilic MOFs resulted in enhanced proton conductivity, higher PA retention capacity, and increased stability against oxidative degradation for the composite membrane than the pristine OPBI polymer. The proton conductivities of the composite membranes (0.29 S cm^{-1} for **PSM 1**-10% and 0.308 S cm^{-1} for **PSM 2**-10% membranes at 160 °C, under anhydrous environment) were notably higher than the conductivities of the constituents and also higher than most of the MOF based polymer supported membranes. To the best of our knowledge, the PA doped **PSM 2** loaded composite membrane shows the highest proton conductivity at 160 °C among all MOF based composite membranes. Extensive interfacial H-bonding plays the most crucial role behind the enhanced proton conductivities of the PA doped MOF containing polymer membranes reported here. This work clearly demonstrates the benefits of using rationally designed **PSM 1** and **PSM 2** MOFs as nanofiller to prepare **OPBI** supported membranes that can perform excellent proton conduction in a wide temperature range spanning up to 160 °C. This provides a generalized approach toward achieving an efficient proton conducting membrane for use in fuel cells.

KEYWORDS: *polymer-MOF, polybenzimidazole, proton exchange membrane, fuel cell, proton conduction, post-synthetic modification, UiO-66*

■ INTRODUCTION

Heavy vehicles or automobiles are one of the major reasons behind high consumption of fossil fuels and environmental pollution. Replacement of such conventional engines by fuel cells can produce the best environmentally friendly solution to this existing problem. A fuel cell is an electrochemical energy conversion device which can convert chemical energy directly into electrical energy.[1−3] In a fuel cell, hydrogen/fuel gets oxidized in the anode while oxygen gets reduced in the cathode. Protons travel through the proton exchange membrane (PEM) from cathode to anode while electrical energy is obtained in the outer circuit. The efficiency of a fuel cell largely depends on the efficiency of proton conduction through the PEM.[2,4−6] Therefore, proton conducting materials and proton transport phenomenon are very important for applied research in modern era.[7−10] In this context, polymers have been extensively studied in literature for PEMFC (proton exchange membrane fuel cell).[5] Perfluorosulfonated (Nafion) membranes have been evolved extensively as PEMs due to their promising conductivity, chemical and mechanical strengths, and long-term durability.[11,12] Recently, metal−organic framework (MOF) and other frameworks containing conducting compounds have emerged as potential materials for scientific research which generates bridges between inorganic cluster containing compounds and organic polymers in terms of availability of detailed crystal structure and their efficiency of proton conduction.[13−21] These MOFs are the coordination analogues of the conventional polymers and consist of organic molecules and metal ions.

Shimizu and co-workers developed two MOFs, namely, PCMOF2$^{1/2}$ (Pz) and PCMOF2$^{1/2}$ (Tz) (Pz = 1*H*-pyrazole and Tz = 1*H*-1,2,4-triazole) with promising proton conductivity under high relative humidity.[22] Lan and co-workers reported the synthesis of a sulfonic acid doped MIL-101 MOF (MIL-101-SO_3H) which displayed excellent proton conduc-

Received: June 7, 2020
Accepted: July 10, 2020
Published: July 10, 2020

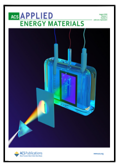

ACS APPLIED POLYMER MATERIALS

pubs.acs.org/acsapm Article

Cross-Linked Alkaline Anion Exchange Membrane from N-Spirocyclic Quaternary Ammonium and Polybenzimidazole

Anupam Das, Balakondareddy Sana, Rama Bhattacharyya, Prakash Chandra Ghosh, and Tushar Jana*

Cite This: *ACS Appl. Polym. Mater.* 2022, 4, 1523−1534 Read Online

ACCESS | Metrics & More | Article Recommendations | Supporting Information

ABSTRACT: Two major challenges, namely, hydroxide conductivity and alkaline stability of the polymer membrane, are yet to be resolved adequately in spite of significant research outcomes on alkaline anion exchange membrane (AAEM) in the recent past. To address these challenges, in this work, the development of ionically cross-linked AAEMs has been achieved by blending pyridine-bridged polybenzimidazole (PyPBI) and N-spirocyclic quaternary ammonium spiro ionene polymer (SP). Further, membranes were converted to porous membranes by adding different weight percentages of porogen in the membrane matrix. Membranes were converted to hydroxide-conducting AAEMs by dipping into 1 M KOH solution, and under this condition, a part of the −NH− groups of PyPBI was deprotonated to form ammonium−imidazolate complexes with SP, which resulted in ionic cross-linking in the AAEM. Hydroxide ion conductivity of 129 mS/cm at 90 °C was obtained in the case of the S70P30-OH membrane, which was a hydroxide-form membrane obtained from the blend of 70 wt % SP and 30 wt % PyPBI, and this membrane showed the highest KOH uptake among all other AAEMs prepared in this study. On the other hand, among the porous ionically cross-linked membranes studied here, the S50P50-P25-OH (blends of 50 wt % SP and 50 wt % PyPBI with 25% porogen) membrane showed the highest hydroxide ion conductivity (117 mS/cm at 90 °C). All the ionically cross-linked AAEMs displayed excellent alkaline stability and remained unaffected during alkaline stability test in 1 M KOH at 80 °C for as long as the test was carried out (960 h). Observing the exceptional stability in 1 M KOH of S50P50-OH and S50P50-P25-OH membranes, OH^- conductivity analysis and alkaline stability tests of these samples were carried out even in 2 M KOH, and we found that these membranes retained ∼80% of their OH^- conductivity value even after 500 h of alkaline treatment in 2 M KOH at 60 °C. Furthermore, membranes were found to be useful in alkaline water electrolysis, and the best performance was shown by the S70P30-OH membrane, which displayed a current density of 100 mA cm^{-2} at 2.6 V. Overall, these recently developed membranes retained hydroxide conductivity, structural and thermal stability even after harsh alkaline treatment for a longer period of time.

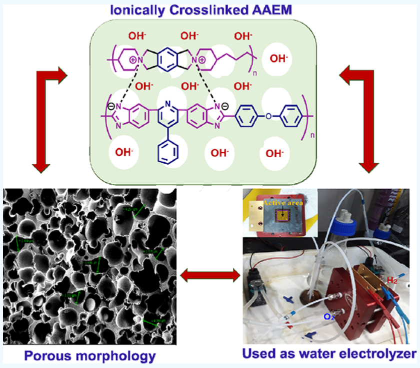

KEYWORDS: *alkaline anion exchange membrane, N-spirocyclic, polybenzimidazole, cross-linking, water electrolyzer*

INTRODUCTION

With the development of fossils free renewable energy resources, electrochemical energy conversion devices such as fuel cells,[1−4] electrodialysis,[5] redox flow batteries,[6,7] and alkaline water electrolysis[8,9] have gained a lot of focus in current times. The ion exchange membrane, an important component of the electrochemical devices, plays a vital role in ion conduction and electrode separation.[5] Huge benefits, particularly the use of non-precious metal catalysts like Co and Ni and faster electrode kinetics of the alkaline anion exchange membrane fuel cell (AAEMFC) over proton exchange membrane fuel cell, have generated great deal of attention in developing various kinds of AAEM in recent years.[1−5,7] Generally, cationic functional moieties such as pyridinium,[10,11] quaternary ammonium (QA),[12−16] imidazolium,[17−19] benzimidazolium,[10,19] phosphonium,[20] tertiary sulfonium,[21] guanidinium,[22] piperidinium,[23,24] pyrrolidinium,[25] azepanium,[26] morpholinium,[26] and quinuclidinium[26] have been often introduced into the polymer chain to create anion exchange sites. A promising anion exchange membrane must possess high hydroxide ion conductivity, excellent alkaline stability, good thermal stability, moderate to high mechanical robustness, and sufficiently long-term durability at an elevated temperature under harsh alkaline conditions.[17,27,28] The development of such kinds of AAEM with all the above-mentioned features is a major challenge. Because of its highly basic and nucleophilic nature, the hydroxide ion is prone to attack and degrade the conventional QA[29] and other cationic groups via, for example, Hofmann eliminations and nucleophilic substitutions.[30] In addition, polymer backbones may degrade via cleavage of activated ether bridges.[31] Also, the

Received: December 29, 2021
Accepted: January 4, 2022
Published: January 14, 2022

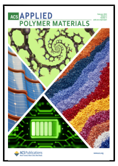

https://doi.org/10.1021/acsapm.1c01926

ACS APPLIED NANO MATERIALS

www.acsanm.org Article

Polymer-Grafted Graphene Oxide/Polybenzimidazole Nanocomposites for Efficient Proton-Conducting Membranes

Anupam Das, Nilanjan Mukherjee, and Tushar Jana*

Cite This: *ACS Appl. Nano Mater.* 2023, 6, 6365−6379

Read Online

ACCESS | Metrics & More | Article Recommendations | Supporting Information

ABSTRACT: In this study, we have functionalized graphene oxide (GO) by growing polymer chains on its surface and then utilized the polymer-*g*-GO as a nanofiller with oxypolybenzimidazole (OPBI) to make a highly efficient nanocomposite-based proton exchange membrane (PEM). Three different monomers, namely, acrylamide (AAM), 2-acrylamido-2-methyl-1-propanesulfonic acid (AMPS), and 3-sulfopropyl acrylate potassium salt (SPAK), were polymerized on the activated GO surface via surface-initiated reversible addition fragmentation chain-transfer polymerization to obtain three different types of polymer-*g*-GO, namely, pAAM-*g*-GO, pAMPS-*g*-GO, and pSPAK-*g*-GO. Furthermore, the chain length of grafted polymers in each case was altered in order to study the effects of the grafted polymer structure and chain length on the properties of nanocomposite PEMs. The exfoliation of GO nanosheets after polymer grafting was confirmed by studying the surface morphology using various microscopic techniques. Gel permeation chromatography and thermogravimetric analysis helped in measuring the chain length of grafted polymers and grafting density on the GO surface. Furthermore, we have impregnated polymer-*g*-GO as nanofillers by varying loading wt % into the OPBI to fabricate a mixed matrix membrane which upon doping with phosphoric acid (PA) converted into a mixed matrix PEM. The prepared nanocomposite PEM displayed exceptionally good thermal stability, significantly improved tensile properties, improved PA loading followed by superior proton conductivity, and remarkable PA retention when exposed to saturated water vapor. When the 2.5 wt % pSPAK-*g*-GO (where the pSPAK chain length is 19.6 kDa) mixed with OPBI, the resulting PEM showed a remarkably high proton conductivity value of 0.327 S cm^{-1} at 160 °C, a significant 5-fold increment compared to the pristine OPBI membrane (0.067 S cm^{-1} at 160 °C). To the best of our knowledge, this will be the first report on utilization of polymer-*g*-GO in polybenzimidazole membranes for high-temperature PEM application.

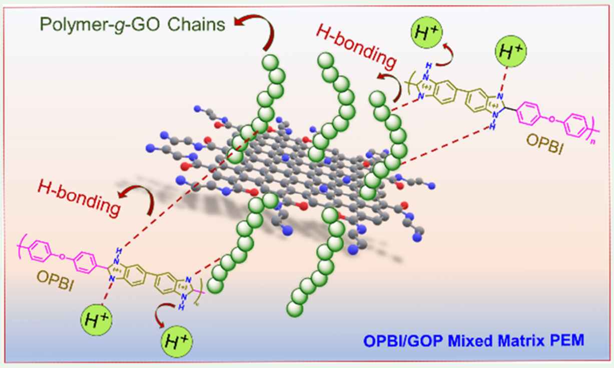

KEYWORDS: *graphene oxide (GO), polybenzimidazole, RAFT polymerization, proton exchange membrane, nanocomposites*

■ INTRODUCTION

In recent years, graphene oxide/polymer composite materials have been extensively utilized in electrodes,[1] supercapacitors,[2,3] biosensors,[4] water desalination and waste water treatment,[5,6] and various other electrochemical devices owing to their superior physical properties. The large surface area, high aspect ratio, and the presence of hydrophilic functionalities generate abundant proton transport sights in graphene oxide (GO), and therefore, it has been considered and utilized as an effective organic filler in various types of composite-based polymer electrolyte membranes (PEMs).[7−10] However, aggregation of GO in the membrane occurs owing to the poor dispersion of GO in organic solvents, and hence significant property improvement of PEMs has often been hampered.[11] In order to avoid this, researchers have *grafted* various active groups on the GO surface to increase the hydrophilicity so that the dispersion ability enhances. Lerf et al. have functionalized the GO surface to prepare various modified GO derivatives and studied their properties.[12] Also, several research groups reported the incorporation of sulfonated GO (SGO) into the polymer membrane which resulted in improvement of various physical properties in the PEMs.[13−15] Xu et al. have developed SGO-incorporated polybenzimidazole (SGO/PBI) membranes and reported a proton conductivity value of 0.052 S/cm at 175 °C under an anhydrous environment, which is found to be 1.9 times higher than that of unmodified GO/PBI membranes (0.027 S/cm). Moreover, SGO sample dispersion nature and compatibility with the PBI matrix were found to be superior over unmodified GO.[16] Functionalized GOs (FGOs) possess-

Received: February 23, 2023
Accepted: March 23, 2023
Published: April 3, 2023

https://doi.org/10.1021/acsanm.3c00834